*N82-16513*

50272-101

| REPORT DOCUMENTATION PAGE | 1. REPORT NO. | | 2. | 3. Recipient's Accession No. |
|---|---|---|---|---|
| **4. Title and Subtitle** UTD ANALYSIS OF ELECTROMAGNETIC SCATTERING BY FLAT PLATE STRUCTURES | | | | **5. Report Date** December, 1981 |
| | | | | **6.** |
| **7. Author(s)** F.A. Sikta and Leon Peters, Jr. | | | | **8. Performing Organization Rept. No.** 711930-2 |
| **9. Performing Organization Name and Address** The Ohio State University ElectroScience Laboratory Department of Electrical ENgineering Columbus, Ohio 43212 | | | | **10. Project/Task/Work Unit No.** |
| | | | | **11. Contract(C) or Grant(G) No.** (C) (G) NSG 1613 |
| **12. Sponsoring Organization Name and Address** National Aeronautics and Space Administration Langley Research Center Hampton, Virginia 23665 | | | | **13. Type of Report & Period Covered** Technical Report |
| | | | | **14.** |

**15. Supplementary Notes**

**16. Abstract (Limit: 200 words)**

The object of this research is to determine and analyze the different scattering mechanisms that contribute to the radar cross section of finite flat plates. The Geometrical Theory of diffraction, the Equivalent current and the newly developed corner diffraction, are used for this study. In addition, a study of the cross-polarized field for a monopole mounted on a plate is presented using novel edge wave mechanism in the analysis. The results are compared with Moment Method solutions as well as measured data when available.

**17. Document Analysis   a. Descriptors**

**b. Identifiers/Open-Ended Terms**

**c. COSATI Field/Group**

| 18. Availability Statement | 19. Security Class (This Report) Unclassified | 21. No. of Pages 366 |
|---|---|---|
| | 20. Security Class (This Page) Unclassified | 22. Price |

(See ANSI–Z39.18)                    *See Instructions on Reverse*                    OPTIONAL FORM 272 (4–77)
(Formerly NTIS–35)
Department of Commerce

## ACKNOWLEDGMENTS

I would like to express my sincere appreciation to both my graduate advisor, Professor Leon Peters, Jr. and Professor W.D. Burnside for their guidance and constant encouragement. A special thanks to Professor Peters for his patience with me during the course of this work, and a debt of gratitude is also owed to Professor Burnside for all his help and above all for his friendship.

THESIS / DISSERTATION
Typing Guide Paper

I thank Professor R.C. Rudduck for his helpful suggestions, and, both Dr. N. Wang and E. Newman for providing the moment method solutions used in our work. I would like, also to acknowledge the typist, the draftsmen, and photographer for an excellent job.

The material in this report has been used in partial fulfillment of the degree Doctor of Philosophy in Electrical Engineering at The Ohio State University.

1st page Chapter end line
— — — — — — — 1st page Chapter end line

LAST TEXT LINE

iii

PAGE LINE

1 inch

JAB/80

# TABLE OF CONTENTS

Chapter Line

THESIS/ DISSERTATION
Typing Guide Paper

1st page Chapter end line
1st page Chapter end line

LAST TEXT LINE

v iii

1 inch

JAB/80

2 inch Chapter Line

THESIS / DISSERTATION
Typing Guide Paper

1st page Chapter end line
— — — — — — — 1st page Chapter end line

Last Text Line

JAB/80

# LIST OF TABLES

## 2 iLIST OF FIGURES ne

THESIS / DISSERTATION
Typing Guide Paper

1st page Chapter end line

1st page Chapter end line

LAST TEXT LINE

PAGE NO. LINE    viii

1 inch

JAB/80

1½ inch

2 inch Chapter Line

THESIS / DISSERTATION
Typing Guide Paper

1 inch

1st page Chapter end line
1st page Chapter end line

LAST TEXT LINE

ix

PAGE NO. LINE

1 inch

JAB/80

1 inch

1½ inch

Page #

Figure

1 inch

Page

Type in Guide Paper

1st page Chapter end line

1st page Chapter end

1st page Chapter end line

LAST TEXT LINE

X

1 inch

JAB/80

1½ inch

1 inch

THESIS / DISSERTATION
Typing Guide Paper

First page chapter (end title)

LAST TEXT LINE

PAGE xi LINE

1 inch

JAB/80

1 inch

2 inch Chapter Line

THESIS / DISSERTATION
Typing Guide Paper

1st page Chapter end line
1st page Chapter end line

LAST TEXT LINE

JAB/80

JAB/80

2 inch, Chapter Line

THESIS / DISSERTATION
Typing Guide Paper

1 inch

1st page Chapter end line
1st page Chapter end line

PAGE NO. LINE

1 inch

JAB/80

xvi

JAB/80

1½ inch

1 inch

1st page Chapter end li

LAST TEXT LINE

xvii

JAB/80

1½ inch

1 inch

2 inch Chapter Line

THESIS / DISSERTATION
Typing Guide Paper

1st page Chapter end 1

LAST TEXT LINE

1 inch

JAB/80

1½ inch

1st page Chapter end line

─ ─ ─ ─ ─ ─ 1st page Chapter end

LAST TEXT LINE

xix

1 inch

JAB/80

Figure            Page

JAB/80

Figure | | Page

THESIS / DISSERTATION
Typing Guide Paper

1st page Chapter end line

LAST TEXT LINE

xxii

1 inch

JAB/80

1½ inch

1 inch

JAB/80

THESIS / DISSERTATION
Typing Guide Paper

1st page Chapter end line

— — — — — — — 1st page Chapter end line

LAST TEXT LINE

1 inch

JAB/80

# CHAPTER I
2 inch Chapter Line

## INTRODUCTION

The object of this research is to analyze the Radar Cross Section (RCS) of finite flat plates at high frequencies. The different physical mechanisms which contribute to the RCS are carefully studied and their important characteristics are explained.

Prior studies have suffered in several respects. First and foremost significant mechanisms have been neglected, particularly for rectangular, non-rectangular and non-circular plates both for angles of incidence in the principal and outside the principal planes. Second, the cost may be prohibitive for such computations even for large modern day computers for physical optics solutions for very large plates (in terms of wavelength) particularly when multiple interactions are significant and for Moment Method solutions where the size is increasing to the upper limit that may be so treated. Third, and perhaps least significant, fitting the shape of some non-rectangular plates with rectangular patches in the Moment Method solution can lead to significant errors.

Several authors have analyzed the RCS from finite plates using GTD techniques. One of the difficulties that they encountered is the calculation of RCS at and near broadside. The Physical Optics Theory (PO) was one of the first techniques used in estimating the RCS values at or near broadside, but it fails to account for polarization dependence for pattern regions beyond the main lobe, particularly for non principle planes. The Physical Optics solution also becomes quite expensive to run on modern computers for general shaped fins at higher frequencies where the fin is large in terms of wavelength. The Geometrical Theory

THESIS / DISSERTATION
Typing Guide Paper

1st page Chapter end line

LAST TEXT LINE

1

1 inch

JAB/80

of Diffraction (GTD) has also been used in conjunction with the forward scattering theorm to compute the fields in the direction of the shadow boundary for circular and square plates as did Keller [20], Ryan [21] and Millar [9-11] . Ross [28] modified the Geometrical Theory of Diffraction solution for the echo width of a perfectly conducting strip to compute the RCS for rectangular plates using a particular normalization procedure.  In all of the previous GTD solutions, the RCS is only computed in the principal plane.

The estimation of RCS at grazing incidence has also been discussed in the literature.  Ross [28] provided measured data of RCS as a function of the length of a rectangular plate.  Hey, et. al [31] , also presented measured data for rectangular and triangular plates but did not present an analytical model and did not describe the physical phenomena that led to the unexpectedly high RCS.

In this dissertation, we will attempt to present techniques that will enable one to compute the RCS at broadside and throughout the pattern in any pattern plane.  We will also present an analytical model that will describe the physical phenomena contributing to the RCS at grazing incidence.  These new techniques will be used to analyze the RCS of different plate geometries of different shapes.

Two basic methods are to be used to compute the RCS for plates. The first method for analysis of scattering from plates is a well known low frequency technique commonly referred to as the Moment Method (MM). The surface currents and the resulting scattered field can be found by enforcing the boundary conditions on the plate surface.  One of the first MM solutions applied to plates problems was the wire grid technique, developed by Richmond [1], which employed a point matching technique.  This solution required the determination of approximately 100 unknown currents per square wavelength in order that the wire grid adequately model the perfectly conducting surface.  Richmond [2] has developed a more sophisticated approach in which the reaction technique is

1½ inch

used to solve for the unknown currents. This solution still requires
approximately 100 unknown currents per square wavelength. Another ap-
proach is to divide the surface of the conducting plate into rectangular
patches each having two orthogonal unknown complex currents [3]. This
surface current patch approach reduces the unknown currents to about
20 per square wavelength. This allows a larger plate to be considered.
However, this approach is restricted to shapes that can be fit by an
array of square patches. All these techniques are restricted to low
frequencies due to the limitations imposed by the vast storage and com-
puter time required for such computations, which result in a high cost
per data point. The Geometrical Theory of Diffraction (GTD) and Equiva-
lent line source concepts are basically high frequency methods which
are based on two canonical problems, i.e., wedge diffraction and infin-
ite line source radiation. Some examples where this method has been
used include determining the diffracted fields by a body made up of
finite axially symmetric cone frustums [4], the radiation patterns of
rectangular wave guides [5], and horn antennas [6]. The MM solution
will be used in this dissertation primarily to provide data to be used
as a check on the GTD solutions developed herein. The author is in-
debted to Dr. Newman whose computer programs have been used to obtain
all of the Moment Method data presented here.

The basic approach used herein for the analysis of RCS of plates
is centered on using the Equivalent current technique in computing the
patterns including the main lobe region.

In Chapter III, the scattering from a perfectly conducting strip
is discussed in detail. The understanding of this problem is essential
in the analysis of RCS from plates.

Chapter IV discusses in detail the RCS pattern effects of the first
order interaction terms. In addition, the Equivalent current method
is compared to corner diffraction method. Note that the plate can have
an arbitrary orientation in space.

1 inch

THESIS / DISSERTATION
Typing Guide Paper

1st page Chapter end line
1st page Chapter end line

LAST LINE

3

JAB/80
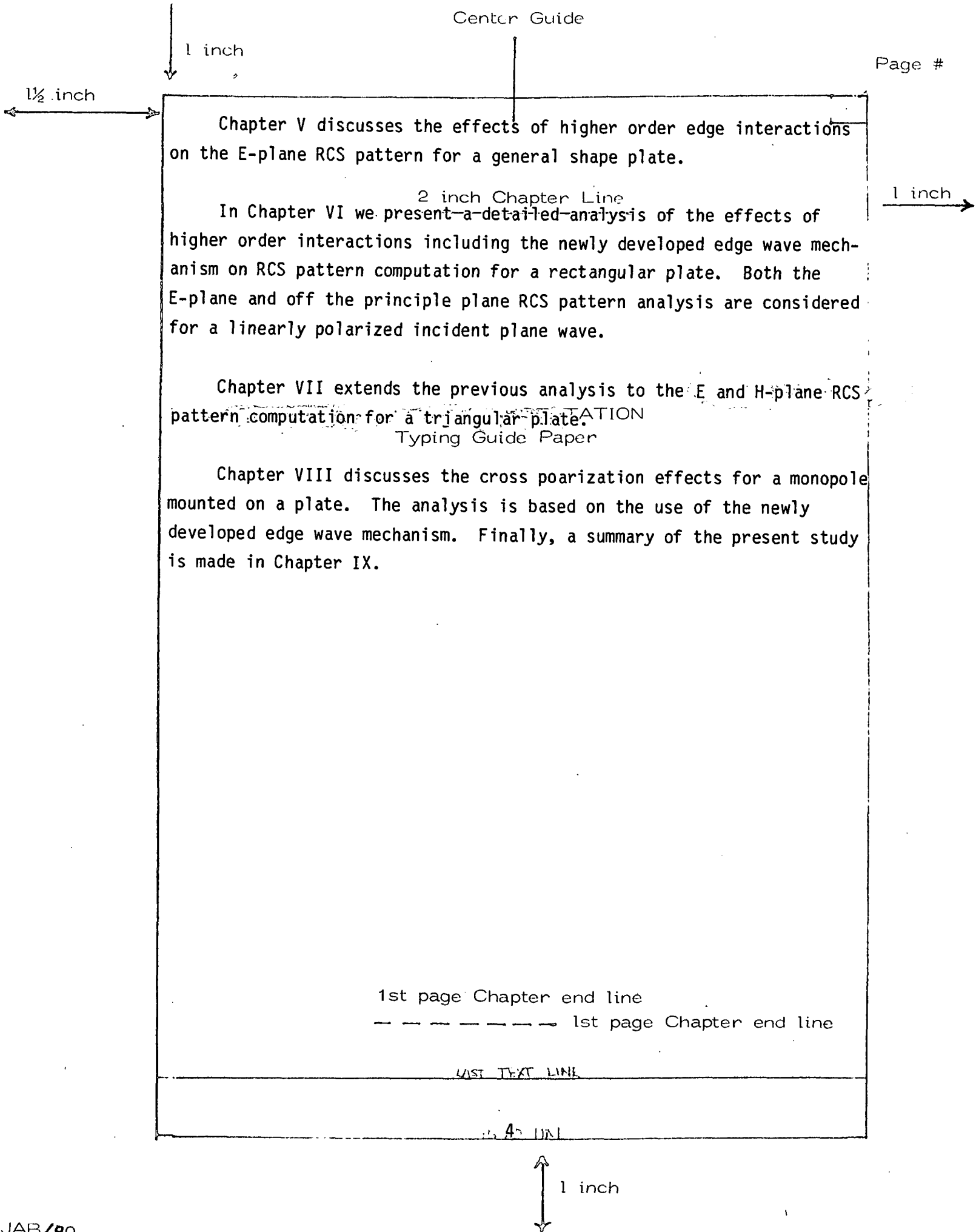
1½ inch

1 inch

Chapter V discusses the effects of higher order edge interactions on the E-plane RCS pattern for a general shape plate.

2 inch Chapter Line

In Chapter VI we present a detailed analysis of the effects of higher order interactions including the newly developed edge wave mechanism on RCS pattern computation for a rectangular plate. Both the E-plane and off the principle plane RCS pattern analysis are considered for a linearly polarized incident plane wave.

Chapter VII extends the previous analysis to the E and H-plane RCS pattern computation for a triangular plate.

Typing Guide Paper

Chapter VIII discusses the cross poarization effects for a monopole mounted on a plate. The analysis is based on the use of the newly developed edge wave mechanism. Finally, a summary of the present study is made in Chapter IX.

1st page Chapter end line

— — — — — — — 1st page Chapter end line

LAST TEXT LINE

1 inch

JAB/80

2 inch Chapter Line

CHAPTER II

THEORETICAL BACKGROUND

A.  INTRODUCTION

An analytic method for computing the radar cross section (RCS)of a general flat plate for all incident angles, has been developed using the Geometrical Theory of Diffraction (GTD) and the Equivalent Current (EC) concept.  The GTD is a ray optical technique and it, therefore, allows one to gain substantial physical insight into the significant physical mechanisms involved in the RCS.  Accordingly, one is able to determine the dominant diffraction mechansims for a given geometry. The basic GTD and the EC concepts needed in order to achieve this goal are discussed in this chapter.  In this dissertation, the far zone scattered fields are treated, the plates used are flat and perfectly conducting and the surrounding medium is free space.  An $e^{j\omega t}$ time dependence is assumed throughout and suppressed.

THESIS / DISSERTATION
Typing Guide Paper

B.  DIFFRACTION BY A WEDGE

The Uniform Theory of Diffraction (UTD) developed by Kouyomjian and Pathak [7] is sufficiently general to handle the three dimensional effects of the flat plate with straight edges.  Figure 1 shows the geometry used to evaluate the fields diffracted by a wedge.  A source whose radiated electric field is given by $E^i(s)$ at the edge, is located at

1st page Chapter end line

1st page Chapter end line

JAB/80

1 inch

1½ inch

1 inch

OBSERVATION
POINT
● P

z

$\hat{D}$

$\beta_0$

$(2-n)\pi$

$\hat{\beta}_0$

S

CONE OF
DIFFRACTED RAYS

$Q_E$

$\hat{\beta}_0'$

$\beta_0'$

y

x

S'

$\hat{I}$

● O

SOURCE POINT

y

$\hat{\phi}'$

S'

$\hat{\phi}$

$\phi'$

$\phi$

S

x

$(2-n)\pi$

SIDE VIEW
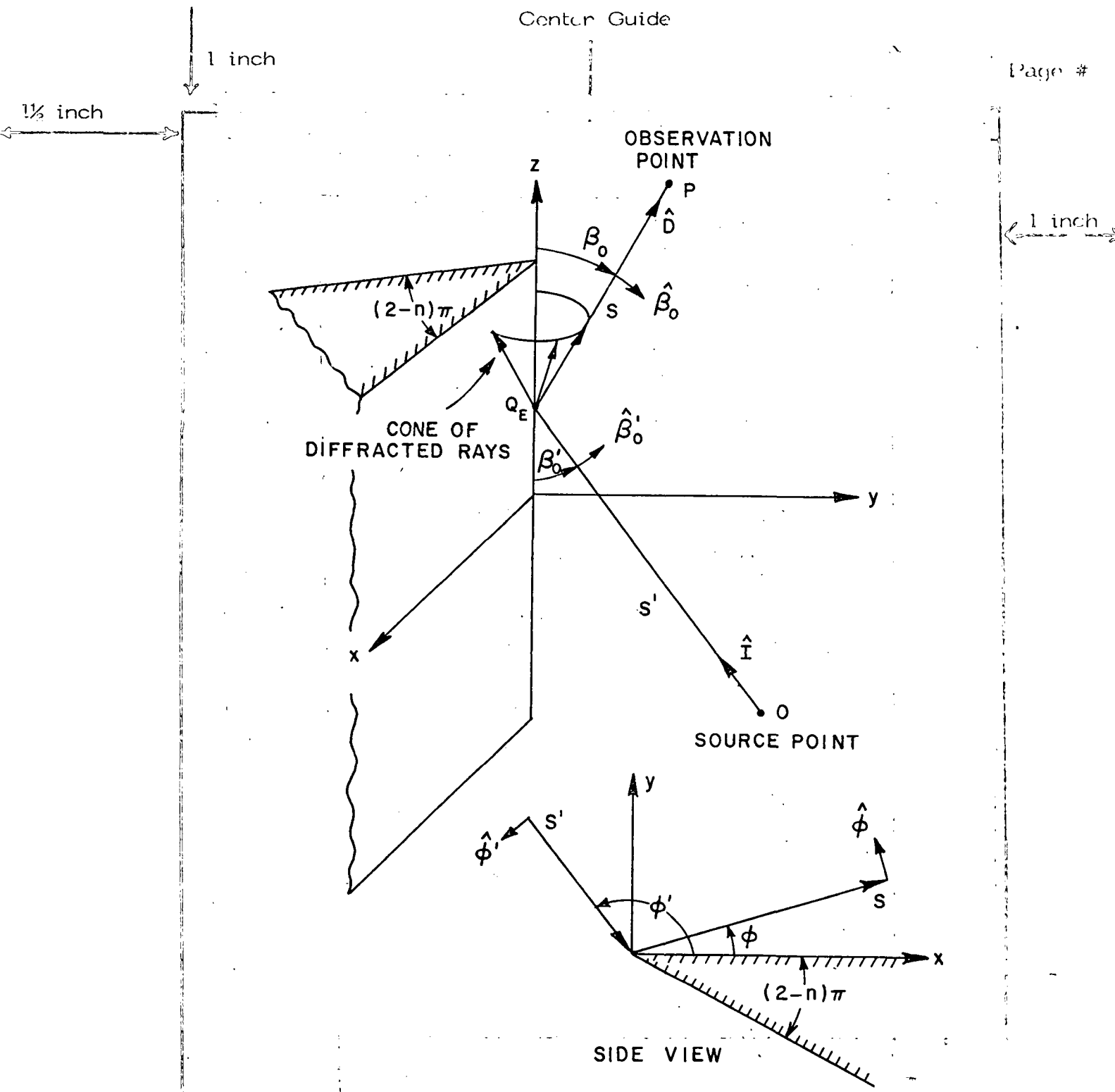
1st page Chapter end line

Figure 1.   Geometry for three-dimensional wedge diffraction problem.

1 inch

JAB/80
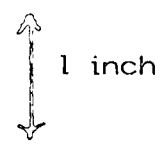
Point O $(\rho', \phi', z')$. This source can radiate a plane, cylindrical, conical or spherical wave incident on the wedge. Kouyoumjian and Pathak [7, 8], have shown that the diffracted fields at P $(\rho, \phi, z)$ can be written in a compact way if these fields are written in terms of a ray fixed coordinate system. This coordinate system is centered at the diffraction point $Q_E$, (or points of diffraction in case of plane wave), this point is unique for a given source and observation points. The incident ray diffracts as a cone of rays whose axis is the edge, such that $\beta_0 = \beta'_0$.

The orthogonal unit vectors associated with the ray fixed coordinate system are defined as

$$\hat{I} = -\hat{s}$$
$$\hat{I} = \hat{\beta}'_0 \times \hat{\phi}'$$
$$\hat{s} = \hat{\beta}_0 \times \hat{\phi}$$

where $\hat{I}$ is the incident direction unit vector, and $\hat{s}$ is the diffraction direction unit vector. The diffracted field is given by [7, 8]

$$\bar{E}^d(s) \sim \bar{E}^i(Q_E) \cdot \bar{\bar{D}}_E(\hat{s}, \hat{I}) \; A(s) \; e^{-jks} \tag{1}$$

where

$$\bar{\bar{D}}_E = -\hat{\beta}'_0 \hat{\beta}_0 D_s - \hat{\phi}' \hat{\phi} D_h \tag{2a}$$

and

$$
\begin{aligned}
D_{s,h}(L, \phi, \phi', \beta_0) = {} & \frac{-e^{-j\pi/4}}{2n\sqrt{2\pi k}\,\sin\beta_0} \Bigg[ \cot\left(\frac{\pi+\beta^-}{2n}\right) F\left(kL\, a^+(\beta^-)\right) \\
& + \cot\left(\frac{\pi-\beta^-}{2n}\right) F\left(kL\, a^-(\beta^-)\right) \mp \Bigg\{ \cot\left(\frac{\pi+\beta^+}{2n}\right) F\left(kL\, a^+(\beta^+)\right) \\
& + \cot\left(\frac{\pi-\beta^+}{2n}\right) F\left(kL\, a^-(\beta^+)\right) \Bigg\} \Bigg]
\end{aligned}
\tag{2b}
$$

with

$$F(x) = 2j \left| \sqrt{x} \right| e^{jx} \int_{\left| \sqrt{x} \right|}^{\infty} e^{-j\tau^2} \, d\tau \qquad (2c)$$

$$a^{\pm}(\beta) = 2 \cos^2\left(\frac{2n\pi N^{\pm} - (\beta)}{2}\right) \qquad (2d)$$

where $N^{\pm}$ are the integers which most nearly satisfy the equations:

$$2\pi n N^+ - (\beta) = \pi$$

and

$$2\pi n N^- - (\beta) = -\pi$$

with $\beta = \beta^{\pm} = \phi \pm \phi'$.

The magnitude and phase of the transition function $F(x)$ are shown in Figure 2. When x is small, $F(x)$ is given by:

$$F(x) \sim \left[ \pi x - 2x e^{j\pi/4} - \frac{2}{3} x^2 e^{-j\pi/4} \right] e^{j\left(\frac{\pi}{4} + x\right)} , \qquad (3a)$$

and when x is large

$$F(x) \sim 1 + \frac{j}{2x} - \frac{3}{4} \frac{1}{x^2} - j \frac{15}{8} \frac{1}{x^3} + \frac{75}{16} \frac{1}{x^4} . \qquad (3b)$$

If n=2, the wedge becomes a half plane and the form for $D_{s,h}$ reduces to:

$$D_{s,h}(L,\phi,\phi',\beta_0) = \frac{-e^{-j\pi/4}}{2 \sqrt{2\pi k} \sin \beta_0} \left[ \frac{F(kLa(\beta^-))}{\cos \beta^-/2} \mp \frac{F(kLa(\beta^+))}{\cos \beta^+/2} \right] . \qquad (4)$$

The diffracted fields can also be written in a matrix form as:

$$\begin{bmatrix} E_{\beta_0}^d(s) \\ E_{\phi}^d(s) \end{bmatrix} \sim \begin{bmatrix} -D_s & 0 \\ 0 & -D_h \end{bmatrix} \begin{bmatrix} E_{\beta_0}^i(Q_E) \\ E_{\phi'}^i(Q_E) \end{bmatrix} A(s) e^{-jks} \qquad (5)$$

1 inch

1½ inch

2 inch Chapter Line

1 inch



$$F(kLa) = 2j\sqrt{kLa}\ e^{jkLa}\int_{\sqrt{kLa}}^{\infty} e^{-j\tau^2}d\tau$$

MAGNITUDE OF F

PHASE OF F

MAGNITUDE

kLa
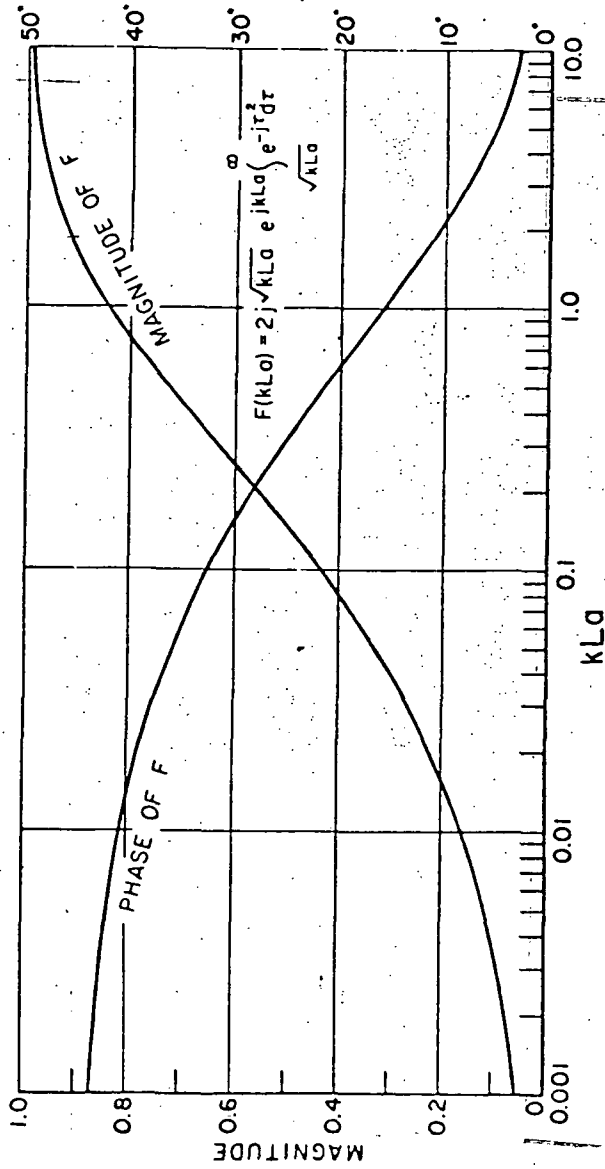
Figure 2.   Transition region correction factor F(kLa). (The positive branch of $\sqrt{kLa}$ is taken).

Chapter end line

1ST TEXT LINE

Chapter end line

LAST TEXT LINE

1 inch

JAB/80

1 inch

1½ inch

1 inch

The $D_s$ coefficient is referred to as the soft scalar diffraction coefficient when the soft boundary condition is used, i.e.,

$$\left(\overline{E}\ \Big|_{wedge}\right) = 0 \qquad \text{,} \underline{\text{2 inch Chapter Line}} \qquad (6a)$$

and the $D_h$ coefficient is referred to as the hard scalar diffraction coefficient obtained when the hard boundary condition is used, i.e.,

$$\left(\frac{\partial E}{\partial n}\ \Big|_{wedge}\right) = 0 \quad . \qquad (6b)$$

THESIS / DISSERTATION

Note that the $\beta^-$ terms are associated with the incident field and the $\beta^+$ terms are associated with the reflected field.

The spread factor is given by

$$A(s) = \begin{cases} \dfrac{1}{\sqrt{s}} & \text{plane, cylindrical, and conical wave incidence.} \\[2em] \sqrt{\dfrac{s'}{s(s+s')}} & \text{spherical wave incidence} \end{cases} \qquad (7a)$$

The L is a distance parameter, which is dependent on the type of illumination and is given by

$$L = \begin{cases} s\ \sin^2 \beta_0 & \text{for plane wave incidence,} \\[1em] \dfrac{ss'}{s+s'} & \text{for cylindrical wave incidence, and} \\[1em] \dfrac{ss'\ \sin^2\beta_0}{s+s'} & \text{for conical and spherical wave incidence.} \end{cases} \qquad (7b)$$

— — — — — — — 1st page Chapter end line

1 inch

JAB/80

## C. EQUIVALENT CURRENT CONCEPT

### 1. Introduction

The Equivalent Current (EC) concept has been used by many authors. Millar [9-11], developed the basic idea as early as 1955, he used it to solve different problems such as diffraction from apertures, fields along the caustic line, coupling through elliptical apertures. In 1968, Ryan and Rudduck [12] introduced the concept implicitly in a GTD solution. In 1969, the concept was formalized by Ryan and Peters [13-14] to obtain the same basic result as Millar. Burnside and Peters [15] used the concept to evaluate the axial RCS from a finite cone. They also corrected the misleading impressions generated in [16].

### 2. Equivalent Current Formulation

The UTD edge diffraction concept is suitable for the analysis of geometries where diffraction appears to come from a single or group of single isolated points along an edge. However, one must introduce an integral approach when the diffracted field at some observation point is the confluence of diffraction points on the edge. This point represents a caustic, in this case, the equivalent currents are used in conjunction with a free space Green's function to obtain the radiated fields. In the analysis to follow, no interactions such as higher order diffraction will be considered, although the method of equivalent currents allows these interactions to be included, as will be seen. The only limitation on the usage of this concept is that the edge diffracted fields must have the same spatial behavior as do the fields of the infinite line source, i.e., $\frac{1}{\sqrt{s}}$ . To compute the continuous diffracted fields in the vicinity of such a caustic, an equivalent current is set up on this edge and treated as a finite line source placed at the position of the finite edge. Figure 3 illustrates the geometry of a finite wedge illuminated by a plane wave, where the caustic lies in the far field of the finite edge. This wedge of length $\ell$ will be considered
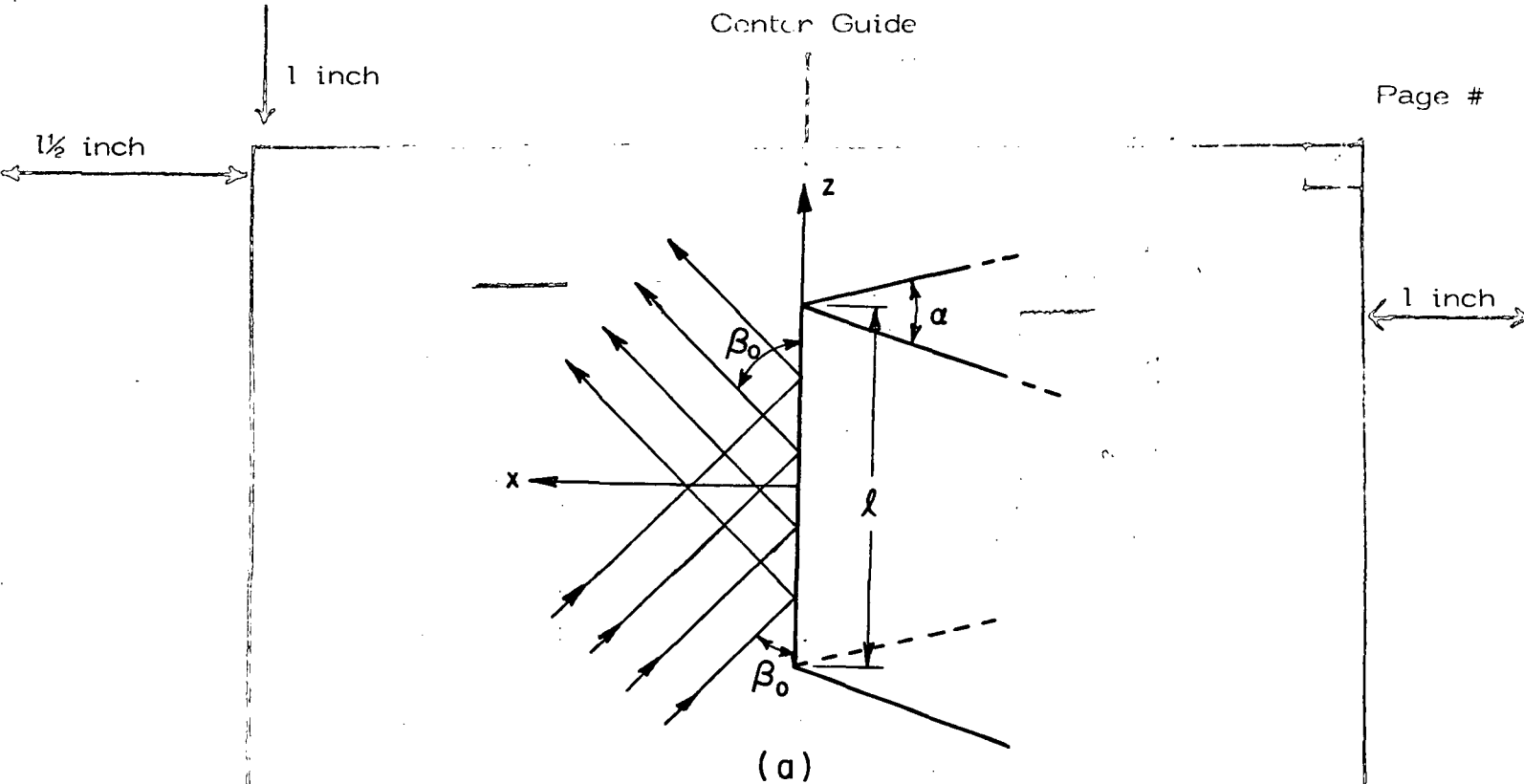
(a)
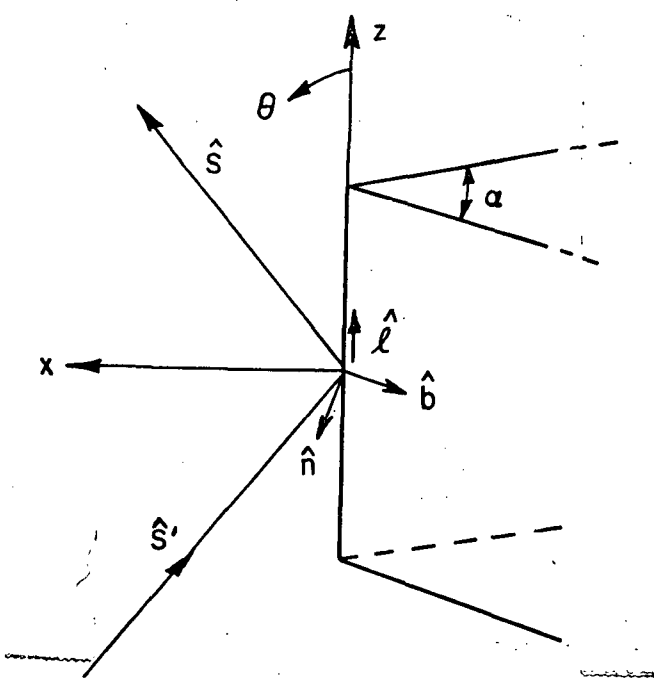
(b)

Figure 3.   Finite wedge geometry.

JAB/80
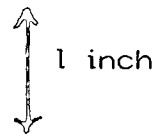
to be a segment of a wedge of infinite length (i.e., a two dimensional wedge). The equivalent current concept consists simply of determining the current flowing at the position of the edge of the infinite wedge (in the absence of the wedge) which would produce the same diffracted field as the edge of the wedge. The   component of the far electric field of a Z-directed infinite electric line source [17] is given by

$$E_\theta^S = Z_0 k_t I^e \frac{e^{j\pi/4}}{2\sqrt{2\pi k_t}} \frac{e^{-jk_t\rho}}{\sqrt{\rho}} e^{-jkz \cos \beta_0} \tag{8}$$

similarly for an infinite magnetic line source, one has

$$H_\theta^S = Y_0 k_t I^m \frac{e^{j\pi/4}}{2\sqrt{2\pi k_t}} \frac{e^{-jk_t\rho}}{\sqrt{\rho}} e^{-jkz \cos \beta_0} \tag{9}$$

where:  $Z_0$ is the impedance of free space

   $Y_0$ is the admittance of free space

   $k = \frac{2\pi}{\lambda}$ ,  $\lambda$ is the wave length

and

   $k_t = k \sin \beta_0$ ,  $\rho = s \sin \beta_0$ ,  $z = s \cos \beta_0$. $\tag{10}$

Figure 4 shows the infinite line source geometry, the Z component (i.e., parallel to the line source) of the far fields is given by:

$$E_Z^S = -E_\theta^S \sin \beta_0 \quad , \quad H_Z^S = -H_\theta^S \sin \beta_0$$

$$E_Z^S = -Z_0 k_t I^e \frac{e^{j\pi/4}}{2\sqrt{2\pi k_t}} \sin \beta_0 \frac{e^{-jk_t\rho}}{\sqrt{\rho}} e^{-jkz \cos \beta_0} \tag{11}$$

13
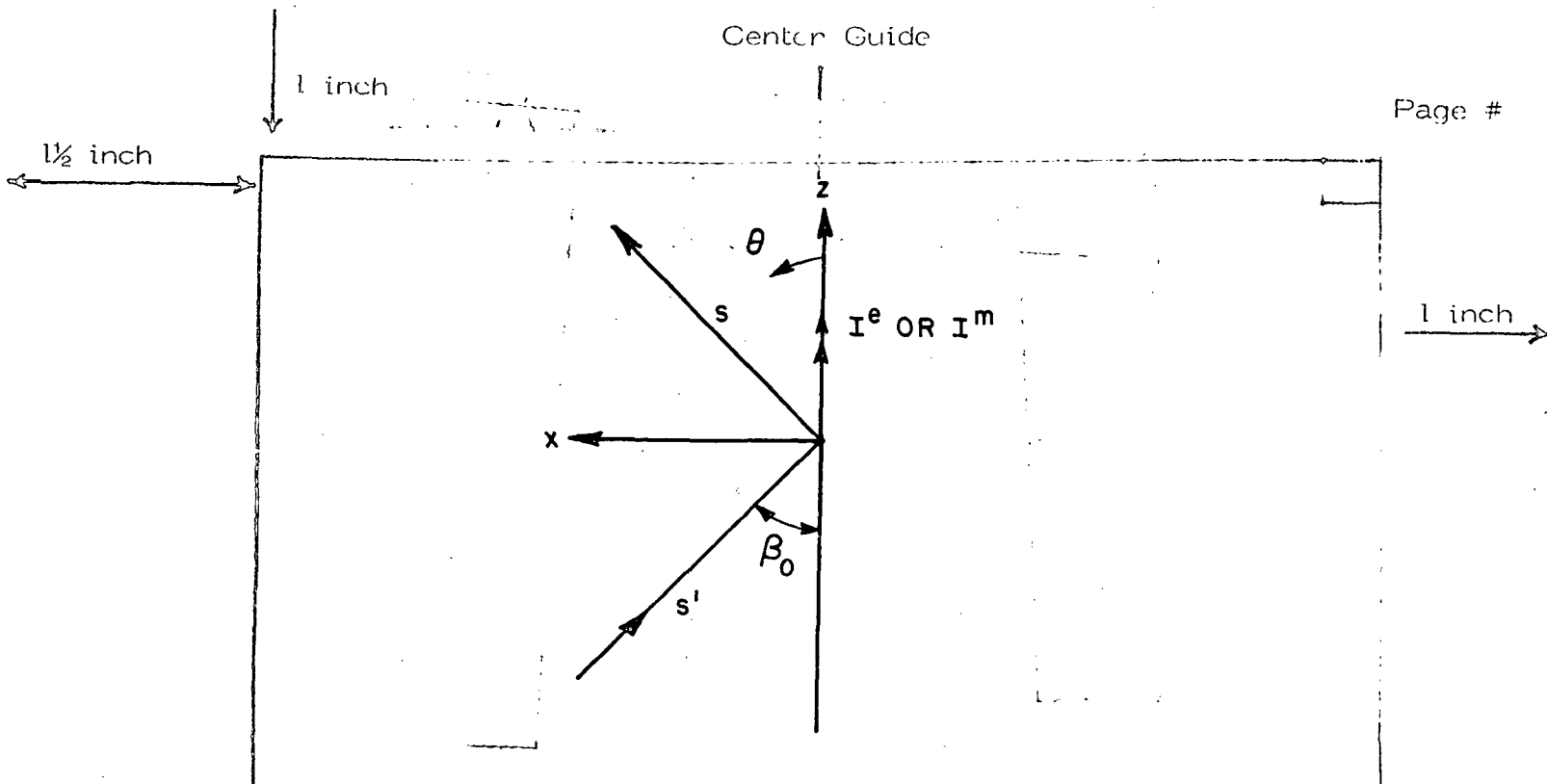
Figure 4. Infinite line source geometry.

$$H_Z^S = - Y_o \, k_t \, I^m \, \frac{e^{j\pi/4}}{2 \sqrt{2\pi k_t}} \, \sin \beta_o \, \frac{e^{-jk_t\rho}}{\sqrt{\rho}} \, e^{-jkz \cos \beta_o} \qquad (12)$$

The diffracted fields from an infinite wedge [7] are

$$E_Z^S = G^e(n,\phi,\phi') \, \frac{e^{-j\pi/4}}{\sqrt{2\pi k} \, \sin \beta_o} \, E_Z^i \, \frac{e^{-jks}}{\sqrt{s}} \, , \text{ and} \qquad (13)$$

$$H_Z^S = G^m(n,\phi,\phi') \, \frac{e^{-j\pi/4}}{\sqrt{2\pi k} \, \sin \beta_o} \, H_Z^i \, \frac{e^{-jks}}{\sqrt{s}} \, , \qquad (14)$$

where

$$G^e_m = R(n,\phi-\phi') \, \mp \, R(n,\phi+\phi')$$
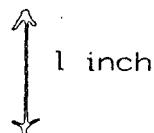
with $R(n,\psi) = \dfrac{1}{n} \sin \dfrac{\pi}{n} \left( \dfrac{1}{\cos \frac{\pi}{n} - \cos \frac{\psi}{n}} \right)$ .

One can rewrite equations (13) and (14) such that

$$E_Z^s = G^e(n,\phi,\phi') \frac{e^{-j\pi/4}}{\sqrt{2\pi k_t}} \; E_Z^i \; \frac{e^{-jk_t\rho}}{\sqrt{\rho}} \; e^{-jkz \cos \beta_0} \tag{15}$$

$$H_Z^s = G^m(n,\phi,\phi') \frac{e^{-j\pi/4}}{\sqrt{2\pi k_t}} \; H_Z^i \; \frac{e^{-jk_t\rho}}{\sqrt{\rho}} \; e^{-jkz \cos \beta_0} \tag{16}$$

where $k_t$, $\rho$ are defined in Equation (10)

Equating Equations (11) and (15) and also Equations (12) and (16) one obtains

$$I^e = \frac{2j}{Z_0 k} \; \frac{G^e(n,\phi,\phi')}{\sin^2 \beta_0} \; E_Z^i \qquad \text{and} \tag{17}$$

$$I^m = \frac{2j}{Y_0 k} \; \frac{G^m(n,\phi,\phi')}{\sin^2 \beta_0} \; H_Z^i \tag{18}$$

where the incident fields in Equation (17) and (18) represent the components of the incident field tangential to the edge. So Equations (17) and (18) are;

$$I^e = \frac{2j}{Z_0 k} \; \frac{G^e(n,\phi,\phi')}{\sin^2 \beta_0} \; E_{tan}^i \qquad \text{and} \tag{19}$$

$$I^m = \frac{2j}{Y_0 k} \; \frac{G^m(n,\phi,\phi')}{\sin^2 \beta_0} \; H_{tan}^i \quad , \tag{20}$$

15

JAB/80

1½ inch

where $E^i_{tan}$ and $H^i_{tan}$ are the tangential components to the edge of the incident electric and magnetic fields. One can now apply the vector potential functions given by

1 inch

$$\bar{A} = \frac{1}{4\pi} \int_L \bar{I}^e \; \frac{e^{-jk|\bar{r}-\bar{r}'|}}{|\bar{r}-\bar{r}'|} \; d\ell' \tag{21}$$

and

$$\bar{F} = \frac{1}{4\pi} \int_L \bar{I}^m \; \frac{e^{-jk|\bar{r}-\bar{r}'|}}{|\bar{r}-\bar{r}'|} \; d\ell' \; , \tag{22}$$

where L is the contour of the edge and $\bar{r}, \bar{r}'$ are defined as in Figure 5.

The equation for the far zone scattered field is

$$\bar{E}^e = -j\omega\mu \; \bar{A}_{trans} \tag{23}$$

and

$$\bar{H}^m = -j\omega\epsilon \; \bar{F}_{trans} \tag{24}$$

where $\bar{E}^e$ is the electric field due to $\bar{I}^e$ and $\bar{H}^m$ is the magnetic field due to $\bar{I}^m$ with

$$\bar{H}^e = \frac{\bar{E}^e}{Z_0} \quad \text{and} \quad \bar{E}^m = \frac{1}{Y_0}\bar{H}^m \tag{25}$$

page Chapter end line

1st page Chapter end line

1st page Chapter end line

LAST TEXT LINE

16

1 inch

JAB/80
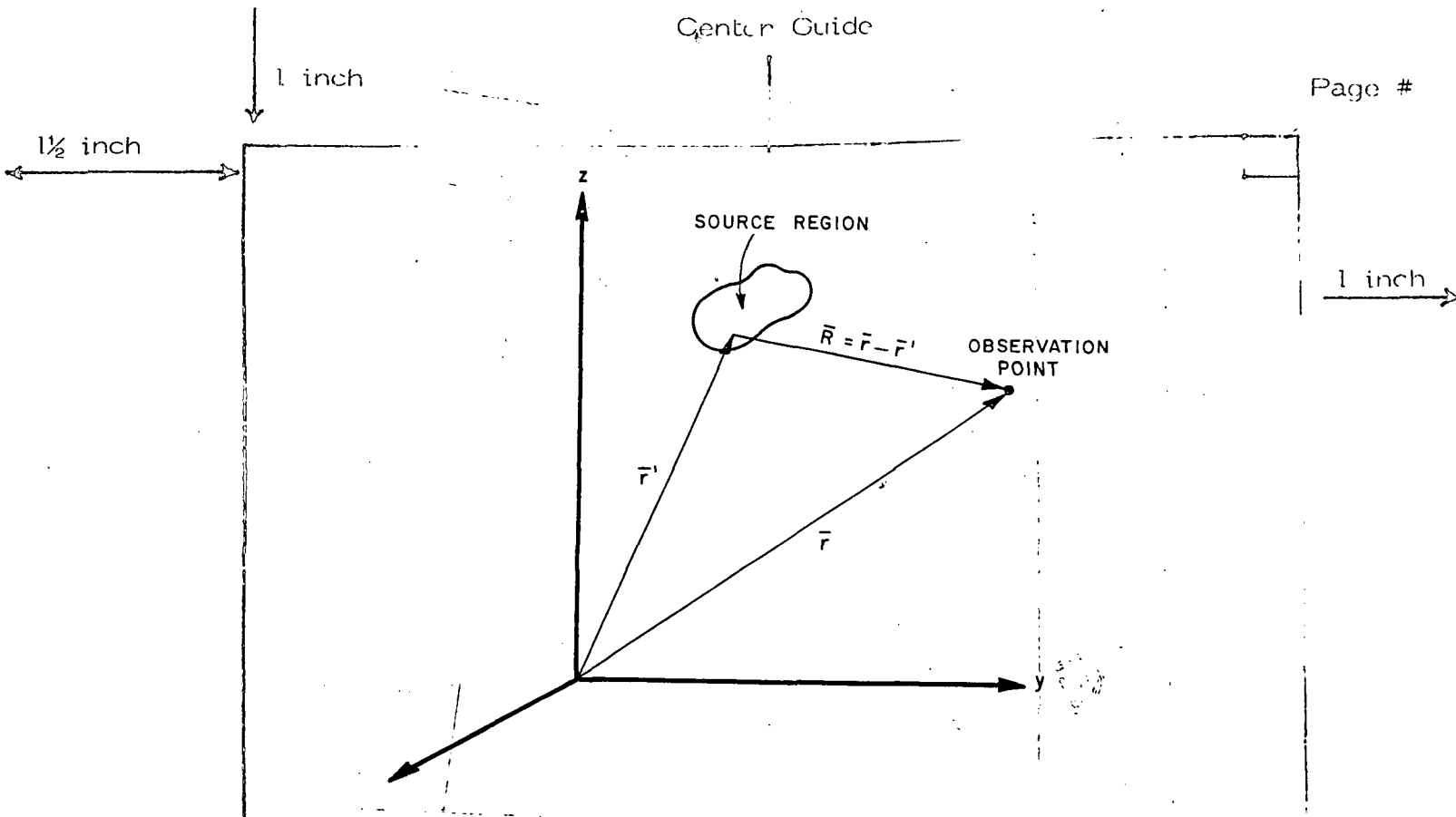
Figure 5.  Definition of the radiation integral parameters.

There has been some discussion about the use of the $\sin^2 \beta_0$ term in Equations (19) and (20), particularly for the case of a straight finite edge, where the observation point does not lie on the diffraction cone.  In this case, the solution fails to satisfy reciprocity.  Senior 18 has suggested that $\sin^2 \beta_0$ should be in the form $\sin \beta_0^i \sin \beta_0^d$ where the superscripts i and d refer to the incident and diffracted rays. This seems to be a "best fit" but, since the configuration of rays deviates sufficiently from the canonical solution, it can only be considered as approximate.  In reality, this difficulty occurs in that one is now trying to represent a corner diffraction for the finite edge, i.e., those observation points not lying in the usually conical bundle of rays can be reached only by rays diffracted by the corner.  This is not unlike the physical optics solution for a flat plate which also fails to satisfy reciprocity since it is forcing the physical optics currents to represent the edge diffraction.

1 inch

JAB/80

1 inch

1½ inch

## D. DIFFRACTION BY A CORNER

A corner is formed by the intersection of a pair of finite straight edges. Figure 6 shows the corner diffraction geometry. A new diffraction coefficient that handles diffraction from corners is needed. An empirical solution is proposed by Burnside and Pathak [19] and is based on the asymptotic evaluation of the radiation integral which employs the equivalent edge currents that would exist in the absence of the corner. The corner diffraction is then found by appropriately (but at present empirically) modifying the asymptotic result for the radiation integral which is characterized by a saddle point near an end point. The diffraction coefficient is still in its development stages. However, it has been shown to be very successful in predicting the fields diffracted by a corner for a number of plate structures. Accordingly, it is discussed here in this section and has been used to obtain some interesting results. The corner diffracted field associated with one corner and one edge in the near field with spherical wave incidence is given by

$$
\begin{bmatrix} E_{\beta_0}^C \\ E_\phi^C \end{bmatrix} = - \begin{bmatrix} E_{\beta_0}^i (Q_c) \, D_s^C(L,L_c,\phi,\phi',\beta_0,\beta_c,\beta_{oc}) \\ E_\phi^i (Q_c) \, D_h^C(L,L_c,\phi,\phi',\beta_0,\beta_c,\beta_{oc}) \end{bmatrix}
$$
$$
\sqrt{\frac{s'}{s''(s'+s'')}} \sqrt{\frac{s(s+s_c)}{s_c}} \; \frac{e^{-jks}}{s} \tag{26a}
$$

1st page Chapter end line

— — — — — — — 1st page Chapter end line

18

1 inch

1 inch

1½ inch

1 inch

2 inch Chapter Line
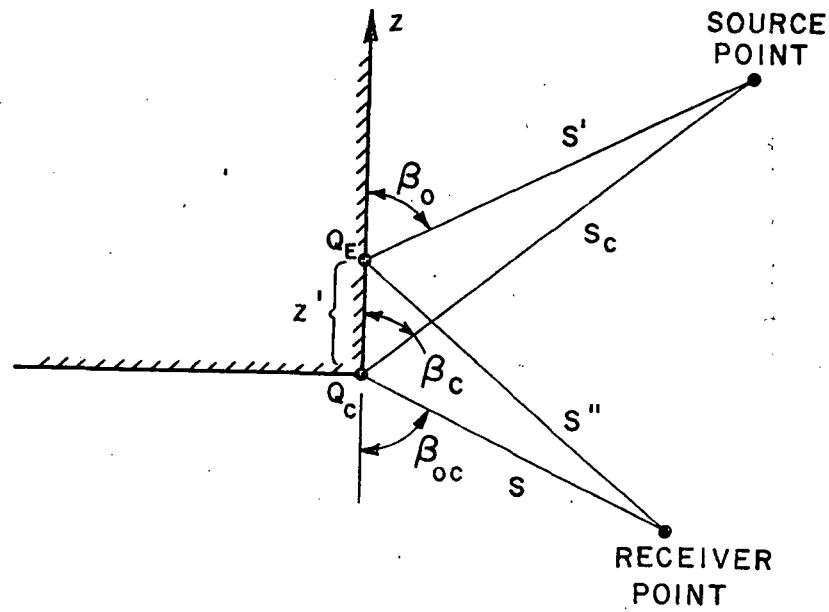


1st page Chapter end line

1st page Chapter end line

Figure 6.   Geometry for corner diffraction problem.

LAST TEXT LINE

1 inch

JAB/80

where

$$\begin{Bmatrix} D_s^c \\ \\ D_h^c \end{Bmatrix} = \begin{Bmatrix} C_s(Q_E) \\ \\ C_h(Q_E) \end{Bmatrix} \frac{\sqrt{\sin \beta_c \sin \beta_{oc}}}{(\cos \beta_{oc} - \cos \beta_c)}$$

$$F\left[kL_c \; a(\pi + \beta_{oc} - \beta_c)\right] \sqrt{\frac{8\pi}{k}} \; \frac{e^{-j\pi/4}}{4\pi} \qquad (26b)$$

and

$$C_{s,h}(Q_E) = \frac{-e^{-j\frac{\pi}{4}}}{2\sqrt{2\pi k} \; \sin \beta_0} \left[ \frac{F\left(kL\;a(\beta^-)\right)}{\cos \beta^-/2} \middle| F\left\{ \frac{L\;a(\beta^-)/\lambda}{kL_c a(\pi + \beta_{oc} - \beta_c)} \right\} \middle| \right. $$

$$\left. \pm \; \frac{F\left(kLa(\beta^+)\right)}{\cos \beta^+/2} \middle| F\left\{ \frac{L\;a(\beta^+)/\lambda}{kL_c a(\pi + \beta_{oc} - \beta_c)} \right\} \middle| \right] \qquad (26c)$$

The function F(x) was defined in Equation (2c), and
$$a(\beta) = 2 \cos^2 (\beta/2) \text{ where}$$

$$\beta^{\pm} = \phi \pm \phi'$$

$$L = \frac{s's''}{(s'+s'')} \sin^2 \beta_0 \quad \text{and} \quad L_c = \frac{s_c s}{s_c + s}$$

for spherical wave incidence.

2 inch Chapter Line

The function $D_{s,h}(Q_E)$ is a modified version of the diffraction coef-
ficient for the half plane case (n=2). The modification factor

$$\left| F\left[ \frac{L\;a(\beta)/\lambda}{kL_c a(\pi + \beta_{oc} - \beta_c)} \right] \right|$$

20

is a heuristic function that insures that the diffraction coefficient will not change sign abruptly when it passes through the shadow boundaries of the edge, i.e., the corner diffracted field will ensure the continuity of the fields as the edge diffracted field shadow boundary is crossed. In Figure 7, we show a corner formed by the intersection of two edges (a) and (b). With each edge there is a corner field component associated with it. While there is only one edge diffracted field component due to diffraction from edge (b), diffraction from edge (a) does not contribute since $Q_E^{(a)}$ lies on the edge extension. Another situation is shown in Figure 8, where both $Q_E^{(a)}$ and $Q_E^{(b)}$ lies on their edge extension. Therefore, no edge diffraction field component is present. Only corner fields will be present at the receiver. Observe that there are two components of the corner diffracted fields present, one for each of the coordinate systems shown. Figure 9 shows the case where edge and corner diffracted fields from both edges are incident upon the receiver.

## E. BROADSIDE ECHO AREA PATTERNS OF FLATE PLATES

The broadside echo area of flat plate structures can also be computed by use of Equivalent Current (EC) concepts provided this is done quite carefully. It is apparent that the EC cannot be used when a caustic and a shadow or reflection boundary coincide. This is because the EC is obtained from the far field diffraction coefficient (see Equations (19) and (20)), which becomes singular in the direction of the reflection or shadow boundary. Keller [20] showed that this singularity could be eliminated by considering the diffraction from points on the opposite sides of the plate (or aperture). He invoked the Forward scattering theorm and used only the imaginary component of the diffraction coefficient. Ryan [21] used essentially this approach as did Millar [9-11] to find the scattered field in the direction of the shadow boundary for square and circular plates. However, there is an error of a factor of two in Ryan's solution for the circular plate. Ryan also used both a set of electric and magnetic Equivalent Currents which corrected the error and lead to the correct result.

1 inch

1½ inch

inch

EDGE (a)

SOURCE

$S_c$

$\beta_c^{(a)}$

$S'(b)$

$\beta_o^{(b)}$

$Q_E^{(b)}$ $\beta_c^{(b)}$

EDGE (b)

$S'(a)$

$\beta_o^{(a)}$

$\beta_{o_c}^{(a)}$

$\beta_{o_c}^{(b)}$

$S''(b)$

$Q_E^{(a)}$

$S$

EDGE
DIFFRACTION
SHADOW BOUNDARY

$S''(a)$
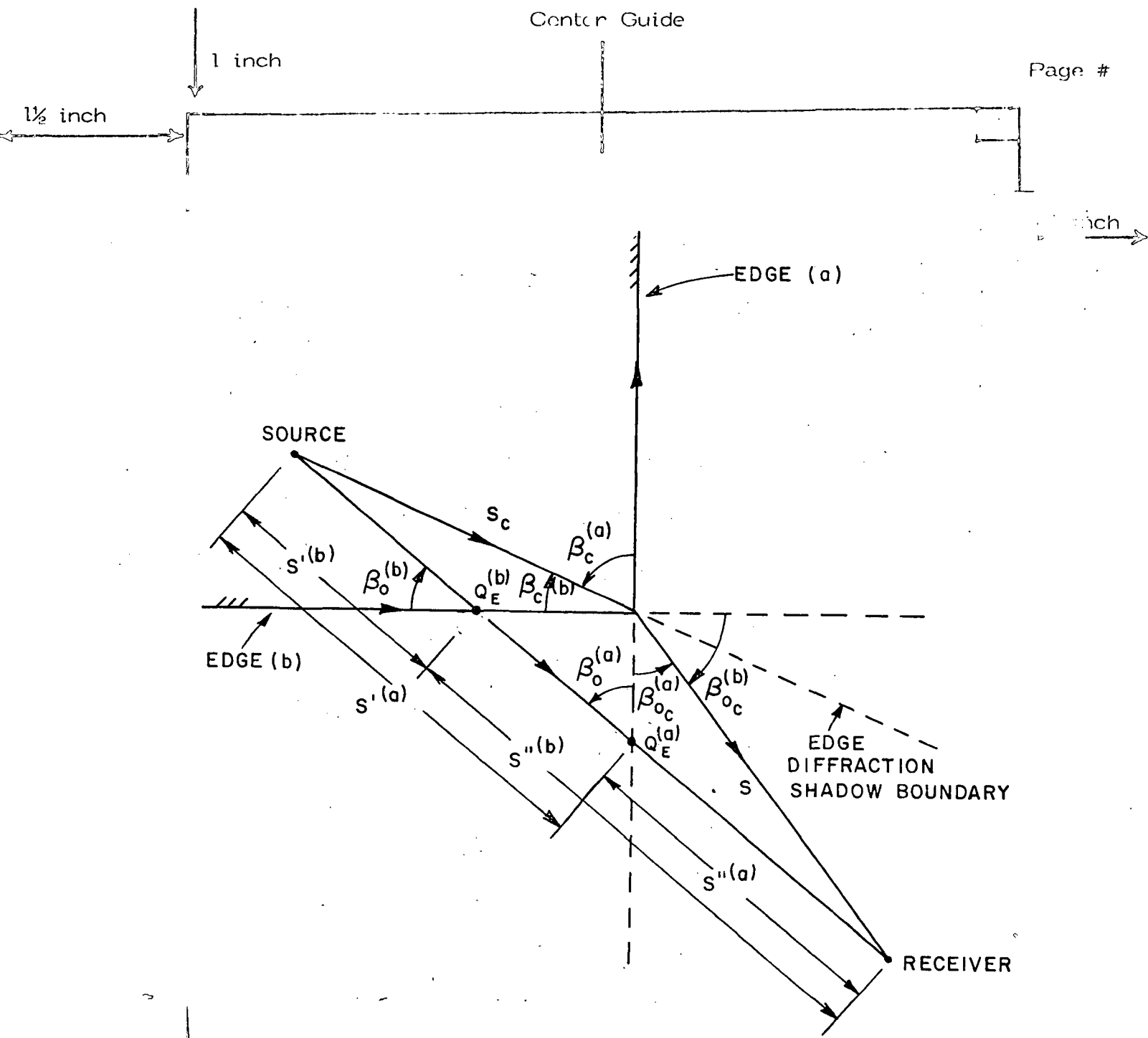
RECEIVER

1st page Chapter end line

Figure 7.  Case of only-one-edge-diffracted field and both corner
fields are received by the receiver.

22

1 inch

JAB/80

1 inch

1½ inch

1 inch

EDGE (a)

$\beta_c^{(a)}$

$Q_E^{(b)}$

$\beta_c^{(b)}$

$\beta_{o_c}^{(b)}$

$\beta_{o_c}^{(a)}$

S

$S^{'(b)}$

$S^{''(b)}$

EDGE (b)

$S_c$

RECEIVER

$S^{''(a)}$

$Q_E^{(a)}$

$S^{'(a)}$

SOURCE

1st page Chapter end line
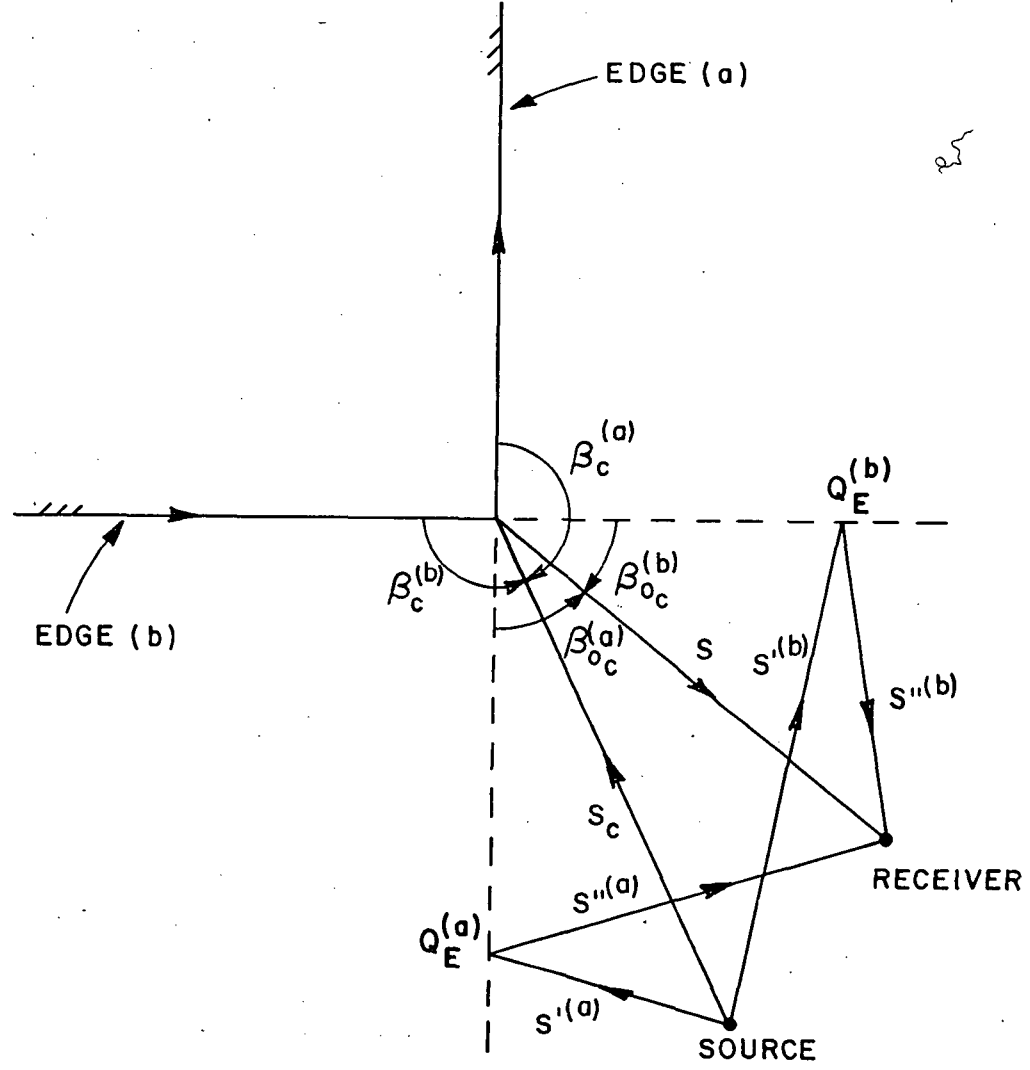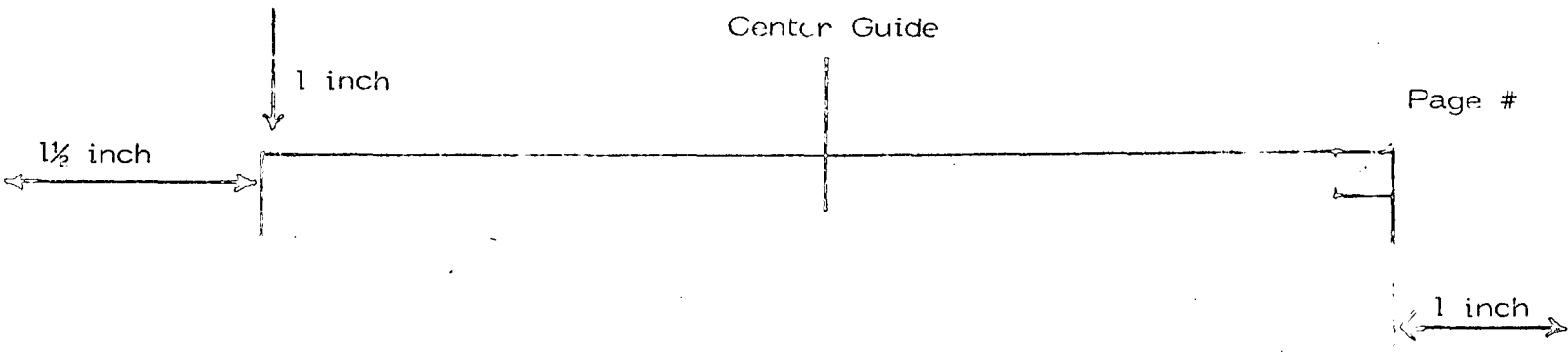
1st page Chapter end line

Figure 8.   Case where only corner fields are received by the receiver.

23

1 inch

JAB/80

Center Guide
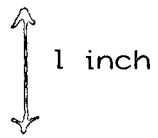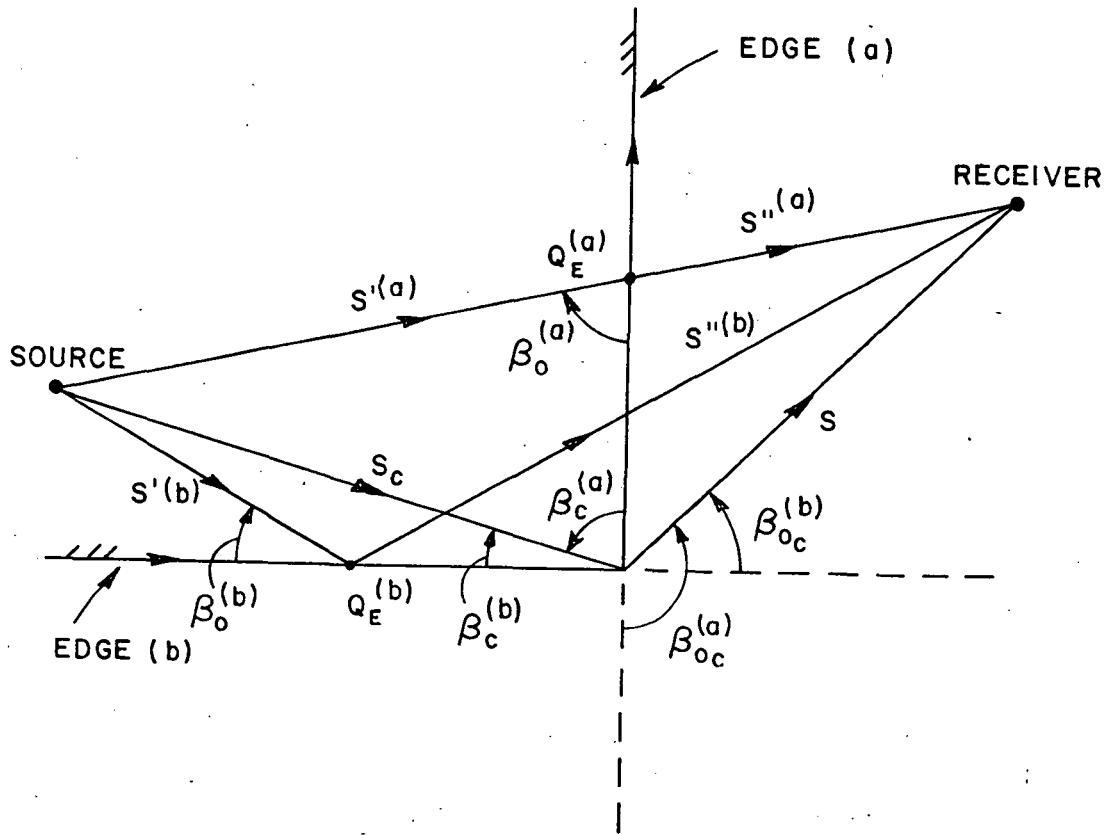
Page #

1 inch

1½ inch

inch

6 inch Chapter line

Figure 9. Case of all edge and corner diffracted fields are received by the receiver.

Center Guide

1 inch

Page #

1½ inch

Typing Guide Paper

1 inch

Careful examination of these prior studies leads one to a means of generating the fields in the direction of the shadow or reflection boundary as has been achieved by others but also over the main lobe that is formed in the vicinity of this caustic.

Consider the plate shown in Figure 10. To compute the scattered fields in the vicinity of the broadside, only the components of electric and magnetic currents perpendicular to the incident plane are used. This, in essence, is the same as representing the plate structure as being segmented into strips as is shown in Figure 11.

One must, however, inject a word of caution at this point. If the observation point from a straight edge is too far removed from the space occupied by the actual set of diffracted rays, then the Equivalent currents on that edge should not be expected to predict the fields at the observation point accurately. This has already been suggested and is now done with the corner diffraction.

The Equivalent current method will give results for the appropriate regions of space near broadside that are accurate to within a one dB which is acceptable in most RCS applications. However if a greater accuracy is desired, one has to include the higher order diffraction contributions. An example of such a case is the scattering from an elongated plate as shown in Figure 12. The double and triple diffracted field components should be included in this solution to improve the results. The above method of analysis is one of the reasons that the strip is to be reconsidered in some detail in Chapter III. Observe that this approach eliminates the need to use Physical Optics (PO) or the Physical Theory of Diffraction (PTD) for this type of scattering.

PLANE OF INCIDENCE IS
x – y PLANE

↑ : CURRENT COMPONENT
TO BE USED
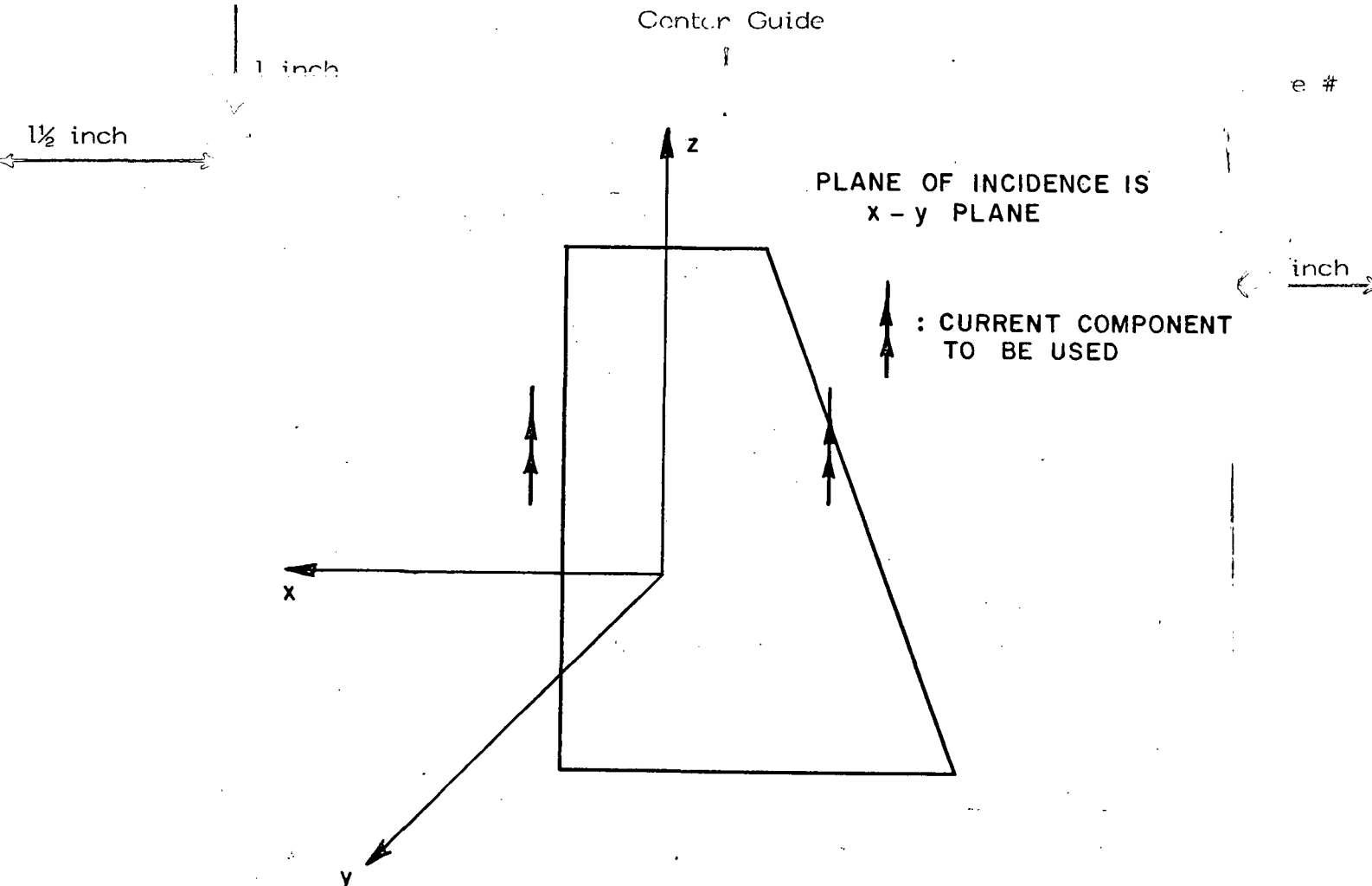
Figure 10. Equivalent Currents to be used in principle plane pattern computation.

Figure 11. Strip model.

JAB/80

1 inch

1½ inch

1 inch

**a**

**b**

FIRST ORDER
DIFFRACTION MECHANISM

THIRD ORDER
DIFFRACTION MECHANISM

SECOND ORDER
DIFFRACTION MECHANISM
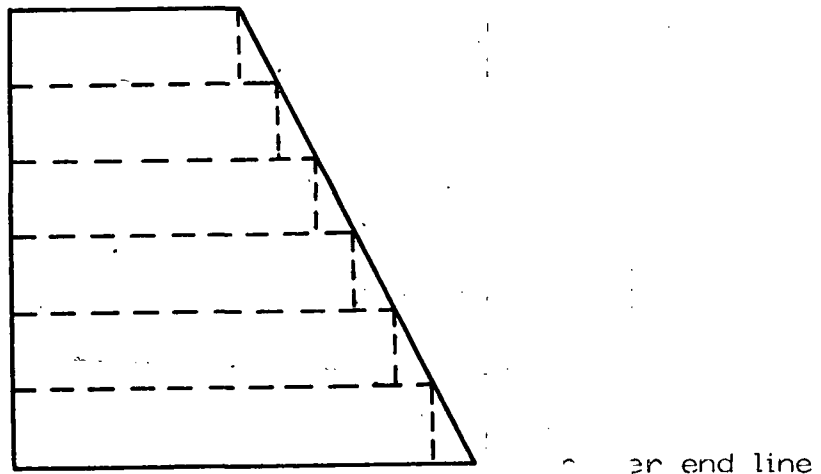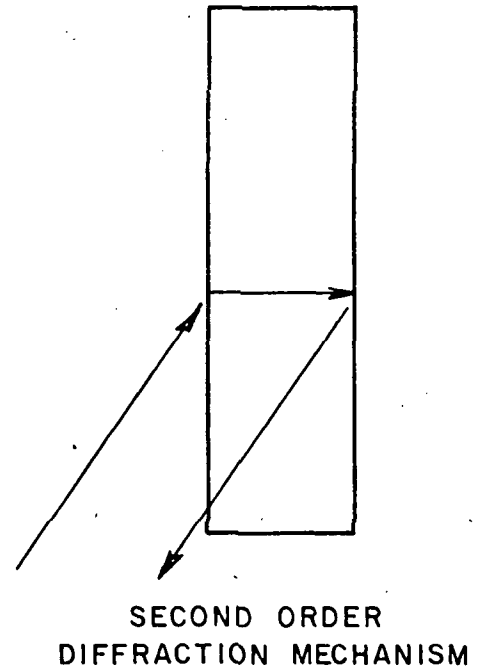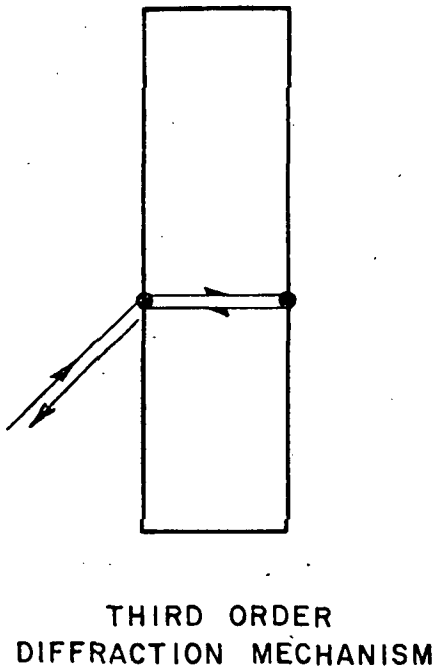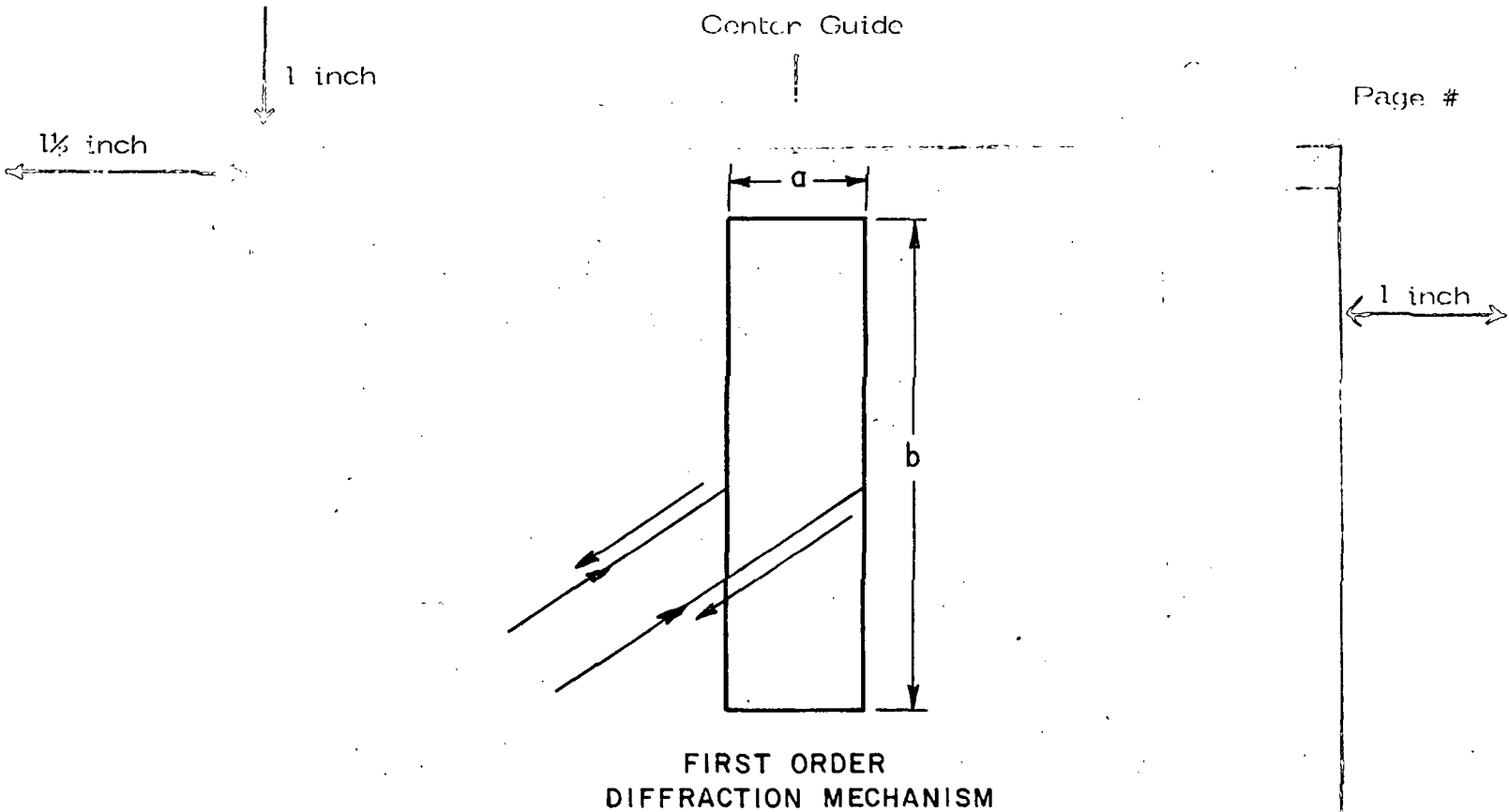
Figure 12.   Diffraction mechanism for a plate elongated in the transverse direction.

27

1 inch

1½ inch

## F. EDGE WAVE FORMULATION

If one considers a monopole on a perfectly conducting plate, the field diffracted by a corner on the plate is given by Equation (26). An interesting result is obtained if one considers the case when the monopole field is diffracted from the corner along the extension of the edge, as shown in Figure 13. In the following notation for $C_{ij}$ the first subscript indicates corner i and the second indicates edge j.

In this case, namely along the edge extension, the different parameters defined in Equation (26), i.e., s, s', s", all will approach infinity and $\beta_0$, $\beta_{oc}$ will approach zero. Using a limiting analysis [22], Equation (26) yields

$$\begin{Bmatrix} E_{\beta_0}^{(ew)} \\ \\ E_{\phi}^{(ew)} \end{Bmatrix} = \begin{Bmatrix} E_{\beta_0}^i(Q_c) \ D_s^{(ew)} \ (s_c,\phi,\phi',\beta_c) \\ \\ E_{\phi}^i(Q_c) \ D_h^{(ew)} \ (s_c,\phi,\phi',\beta_c) \end{Bmatrix} \sqrt{s_c} \ \frac{e^{-jks}}{s} \qquad (27a)$$

where

$$\begin{Bmatrix} D_s^{(ew)} \\ \\ D_h^{(ew)} \end{Bmatrix} = \frac{e^{-j\pi/4}}{2\sqrt{\pi k}} \ \frac{(1+\cos\beta_c)}{\sin(\beta_c/2)} \ F\left[2ks_c \ \sin^2\left(\frac{\beta_c}{2}\right)\right]$$

$$\begin{Bmatrix} \sin\frac{\phi}{2} \ \sin\frac{\phi'}{2} \\ \\ \cos\frac{\phi}{2} \ \cos\frac{\phi'}{2} \end{Bmatrix} \qquad (27b)$$

Equation (27) describes a non-decaying wave which propagates on the edge of the plate, hence, the name "edge-wave." This edge wave is excited by diffraction from the corner of this edge. This field satisfies the wave equation and the edge condition and therefore, is a valid solution for the fields propagating on an edge.

1 inch

JAB/80

1 inch

1½ inch

2 inch Chapter Line

1 inch

PERFECTLY CONDUCTING PLATE

#2        #1
s        $\beta_c$    (1)

$s_c$  ⊗

MONOPOLE    (4)

(2)

(3)

#3        #4
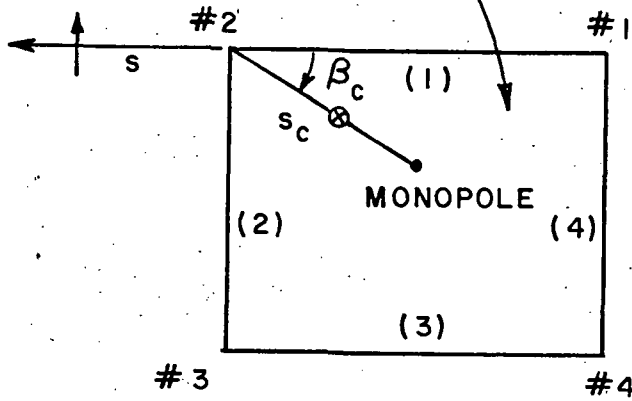
(a) FRONT VIEW          (b) SIDE VIEW
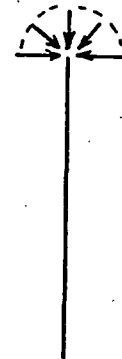
Figure 13.   Edge wave mechanism due to a monopole mounted on a plate.

LAST TEXT LINE

1 inch

JAB/80

1 inch

1½ inch

1 inch

The derivation of Equation (27) and a detailed discussion of the edge wave mechanism is shown in Appendix C. It is interesting to note that the diffracted field across the plate is cross polarized with respect to the field diffracted by the corner as is shown in Figure 13. This cross polarization effect is a consequence of the edge wave mechanism. It is one of the primary sources that contribute to the cross polarization field in scattering and antenna problems. This topic is going to be discussed in substantial detail in Chapters VI and VIII.

1st page Chapter end line

— — — — — — — 1st page Chapter end line

LAST TEXT LINE

1 inch

JAB/80

# CHAPTER III

## BACKSCATTERING FROM A PERFECTLY CONDUCTING STRIP

The infinite strip problem is a simple one, because the strip is the simplest shape which exhibits multiple diffraction from edges. The understanding of the different mechanisms that form the solution for the strip will help to understand and solve other related problems. The scattering of plane waves by a perfectly conducting strip has been treated extensively. J. Freeland, et. al, [23] found an approximate solution for the current on the strip and used it in conjunction with the radiation integral to find an approximate current pattern which is used with the GTD pattern to construct a pattern which is accurate at all aspects. J.S. Yu, et. al., [24], used Sommerfeld's exact solution [25] in conjunction with the reciprocity theorm and a self-consistent GTD formulation to account for higher order diffraction to obtain the required radiation patterns for the H-polarized plane wave case. Reference [26] lists some of the more significant papers on the scattering by a strip. The objective of this work is to compute the backscattered field pattern using the Kouyomjian-Pathak (K-P) form of the diffraction coefficient and compare the results with the exact Mathieu solution.

## A. STRIP GEOMETRY

The perfectly conducting strip is assumed to have infinite length, zero thickness and finite width. A homogeneous plane wave is

1st page Chapter end line

JAB/80

illuminating the strip with both the TE and TM polarization cases considered. Figure 14 shows the strip geometry in which an infinite strip is located in the X-Z plane where a/$\lambda$ is the strip width. The angles ($\phi$,$\phi'$) are the incident and scattering angles respectively and $\rho$, $\rho_2$ are the distances from edges (1) and (2) to the observation point. The phase is referred to edge (1).

2 inch Chapter Line

B.  TM$_z$ POLARIZED CASE

A homogeneous E-polarized plane wave is incident at an angle $\phi'$, assuming that the plane wave has unit amplitude, then the incident field can be written as:

Typing Guide Paper
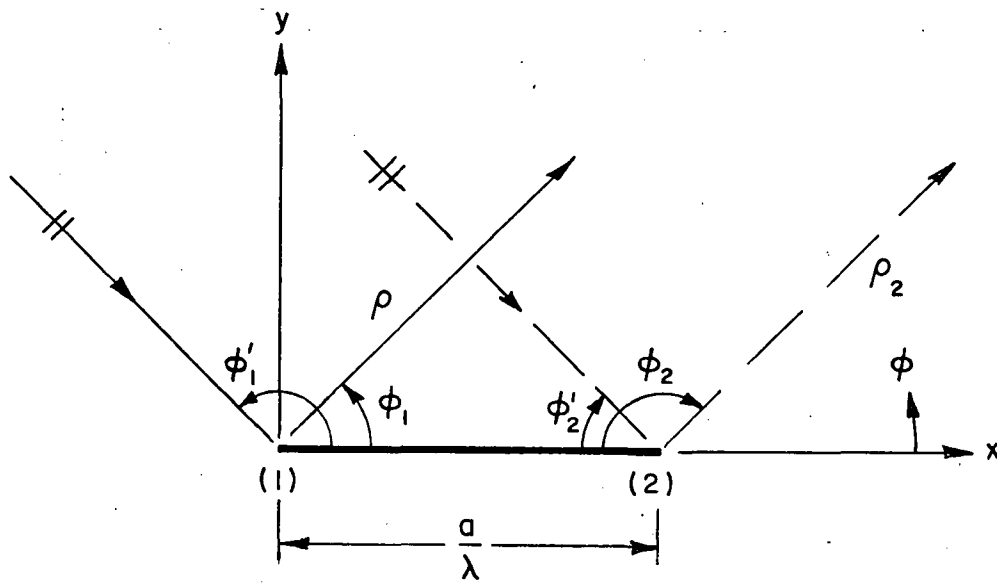


Figure 14.  Strip geometry.

1st page Chapter end line
— — — — — — — → 1st page Chapter end line

LAST TEXT LINE

JAB/80

$$\bar{E}^i = \hat{z}\; e^{jk(x\cos\phi_1' + y\sin\phi_1')} \tag{28}$$

For this case the only important diffraction component is the single diffracted one from edges 1 and 2. The double diffracted component is a slope diffracted wave which has a negligible contribution to the total back scattered field. The general expression for the two dimensional diffracted field from an edge is given by:

$$E^d = E^i(Q)\; D_s\; \frac{e^{-jks}}{\sqrt{s}}, \quad \text{where} \tag{29}$$

$D_s$ is the soft ordinary scalar diffraction coefficient given by:

$$D_s = \frac{-e^{-j\pi/4}}{2\sqrt{2\pi k}}\left\{\frac{1}{\cos\beta^-/2} - \frac{1}{\cos\beta^+/2}\right\} \tag{30}$$

where

$$\beta^{\pm} = \phi \pm \phi'$$

and s is the distance from the diffraction point to the receiver and $E^i(Q)$ is the value of the incident field at the diffraction point Q. The backscatter case $\phi=\phi'$ and Equation (30) reduces to

$$D_s = \frac{-e^{-j\pi/4}}{2\sqrt{2\pi k}}\left[1 - \frac{1}{\cos\phi'}\right] \tag{31}$$

the field diffracted from edges (1) and (2) are given by

$$E^d_{(1)} = D_s^{(1)}\frac{e^{-jk\rho}}{\sqrt{\rho}} \tag{32}$$

1st page Chapter end line

— — — — — — — 1st page Chapter end line

LAST TEXT LINE

JAB/80

$$E_{(2)}^d = D_s^{(2)} e^{j2ka \cos \phi_1'} \frac{e^{-jk\rho}}{\sqrt{\rho}} \tag{33}$$

where the subscripts (1) and (2) indicate edges (1) and (2) such that

$$D_s^{(1)} = \frac{-e^{-j\pi/4}}{2\sqrt{2\pi k}} \left(1 - \frac{1}{\cos \phi_1'}\right),$$

$$D_s^{(2)} = \frac{-e^{-j\pi/4}}{2\sqrt{2\pi k}} \left(1 - \frac{1}{\cos \phi_2'}\right), \text{ and}$$

$$\phi_2' = \pi - \phi_1'.$$

The total diffracted field is given by adding Equations (32) and (33) or

$$E_{total}^d = \frac{-e^{-j\pi/4}}{\sqrt{2\pi k}} \left[\cos(ka \cos \phi_1') + j\frac{\sin(ka \cos \phi_1')}{\cos \phi_1'}\right]$$

$$e^{jka \cos \phi_1'} \frac{e^{-jk\rho}}{\sqrt{\rho}} \tag{34}$$

The echo width is defined [27] by

$$L_e = \lim_{\rho \to \infty} \left[2\pi\rho \left|\frac{E^d}{E^i}\right|\right] \tag{35}$$

Note that while Equation (31) becomes infinite as $\phi' \to 90°$ (broadside). Equation (34) remains finite since the $\frac{1}{\cos \phi_1'}$ term and the $\frac{1}{\cos \phi_2'}$ term cancel in the limit as $\phi_1' \to 90°$. Equation (34) then reduces to

$$E_{total}^d (\phi' = 90) \simeq \frac{e^{j\pi/4}}{\sqrt{2\pi k}} ka \frac{e^{-jk\rho}}{\sqrt{\rho}} \tag{36}$$

substituting Equation (36) into (35) one gets:

$$L_e (\phi' = 90) \simeq ka^2 \tag{37}$$

which is the required value as given by physical optics approximation. It is the combination of the diffracted field from the two edges that cancels this singularity.

1 inch

1½ inch

C.    $TE_z$ POLARIZED CASE

For this case, the homogeneous plane wave incident field is given by

1 inch

$$\overline{H}^i = \hat{z}\, e^{jk\, (x\, \cos\, \phi_1' + y\, \sin\, \phi_1')} \tag{38}$$

For the TE case it is necessary to include higher order diffraction terms to obtain the required pattern.

The effect of these fields becomes important as the angle of incidence approaches grazing incidence. The single diffracted field is obtained in a similar manner as in the TM case with soft, ordinary diffraction coefficient $D_s$ replaced by the hard ordinary diffraction coefficient, i.e.,

$$D_h = \frac{-e^{-j\pi/4}}{2\sqrt{2\pi k}}\left[1 + \frac{1}{\cos\, \phi'}\right] \tag{39}$$

and the fields are given by:

$$H^d_{(1)} = D_h^{(1)}\frac{e^{-jk\rho}}{\sqrt{\rho}} \tag{40}$$

$$H^d_{(2)} = D_h^{(2)} e^{j2ka\, \cos\, \phi_1'}\, \frac{e^{-jk\rho}}{\sqrt{\rho}} \tag{41}$$

with

$$D_h^{(1)} = \frac{-e^{-j\pi/4}}{2\sqrt{2\pi k}}\,(1 + \frac{1}{\cos\, \phi_1'})\quad \text{and}$$

$$D_h^{(2)} = \frac{-e^{-j\pi/4}}{2\sqrt{2\pi k}}\,(1 + \frac{1}{\cos\, \phi_2'})$$

The total singly diffracted field is then given by the sum of (40) and (41), in the same manner as just discussed, i.e.,

35

1 inch

$$H^d = \frac{-e^{-j\pi/4}}{\sqrt{2\pi k}} \left[ \cos(ka \cos \phi_1'') - j \frac{\sin(ka \cos \phi_1')}{\cos \phi_1'} \right]$$

$$e^{jka \cos \phi_1'} \frac{e^{-jk\rho}}{\sqrt{\rho}} \tag{42}$$

The double diffraction mechanisms are illustrated by rays in Figure 15. The field diffracted from edge (1) give rise to two rays which are in turn diffracted from edge (2). The sum of the fields of these two rays give the double diffracted field from edge (2), i.e.,

$$H^d_{(21)} = R_1 + R_2 \tag{43}$$
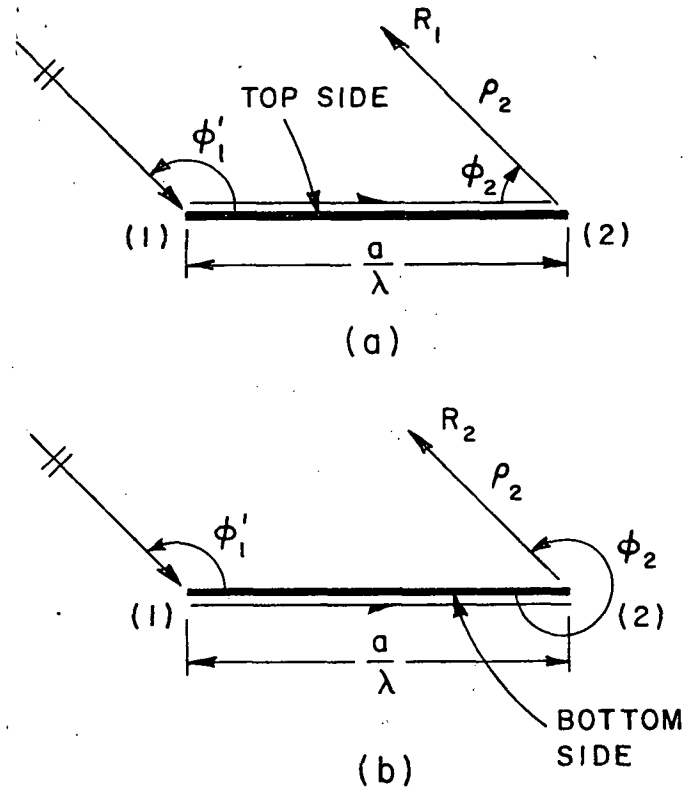
where



Figure 15. Double diffraction field components for a strip. (a) Top side; (b) Bottom side.

JAB/80
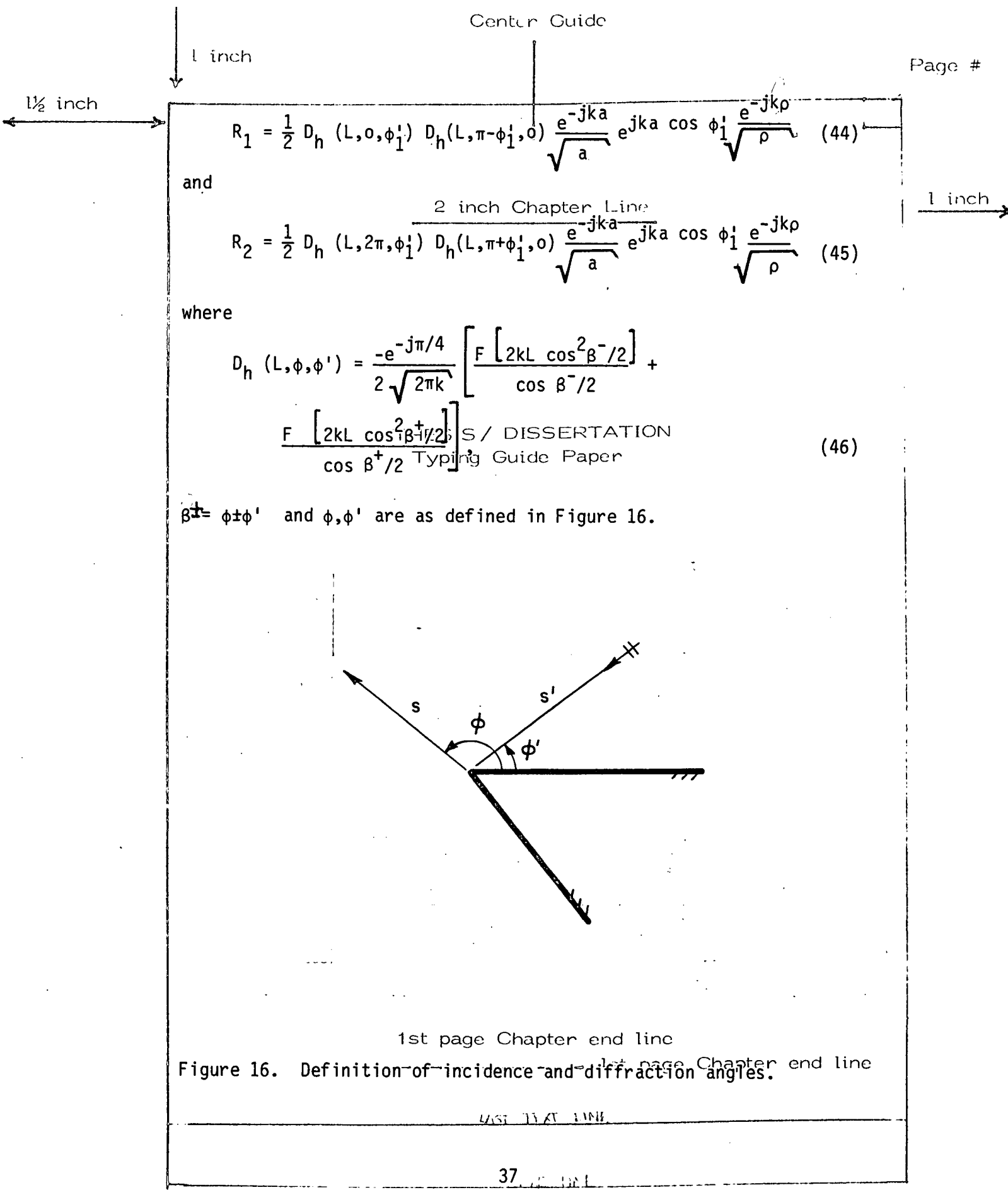
$$R_1 = \frac{1}{2} D_h (L,o,\phi_1') \, D_h(L,\pi-\phi_1',o) \frac{e^{-jka}}{\sqrt{a}} e^{jka \cos \phi_1'} \sqrt{\frac{e^{-jk\rho}}{\rho}} \qquad (44)$$

and

$$R_2 = \frac{1}{2} D_h (L,2\pi,\phi_1') \, D_h(L,\pi+\phi_1',o) \frac{e^{-jka}}{\sqrt{a}} e^{jka \cos \phi_1'} \sqrt{\frac{e^{-jk\rho}}{\rho}} \qquad (45)$$

where

$$D_h (L,\phi,\phi') = \frac{-e^{-j\pi/4}}{2\sqrt{2\pi k}} \left[ \frac{F\left[2kL \cos^2 \beta^-/2\right]}{\cos \beta^-/2} + \right.$$

$$\left. \frac{F\left[2kL \cos^2 \beta^+/2\right]}{\cos \beta^+/2} \right] \qquad (46)$$

$\beta^{\pm}= \phi\pm\phi'$ and $\phi,\phi'$ are as defined in Figure 16.

Figure 16.   Definition of incidence and diffraction angles.

1 inch

JAB/80

1 inch

1½ inch

$$L = \frac{s\,s'}{s+s'} = \frac{a\,s'}{a+s'} = a$$

since $s' = \infty$

2 inch Chapter Line

1 inch
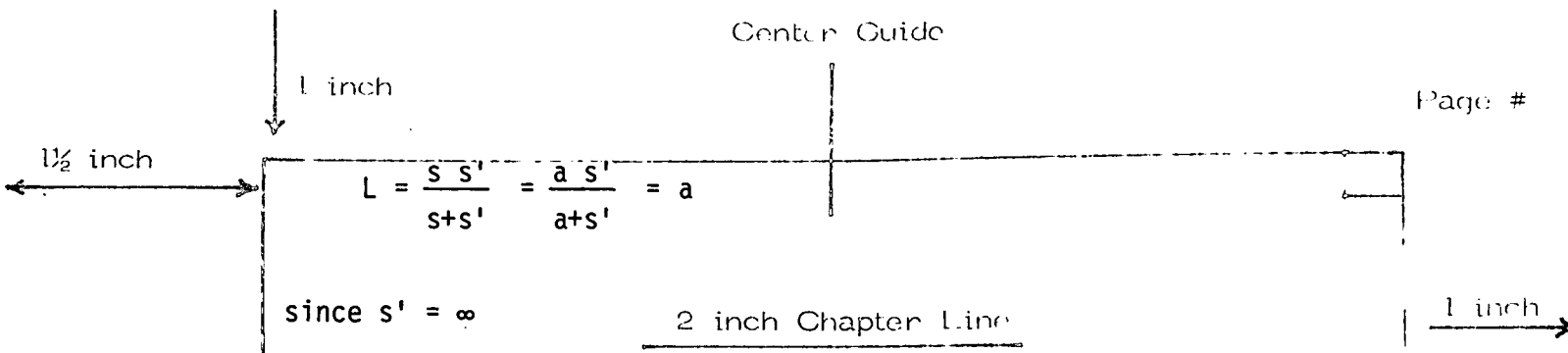
The ½ factor in Equations (44) and (45) is introduced since the ray along the surface is at grazing incidence. From Equation (46), one concludes that

$$R_1 \equiv R_2$$

then

THESIS / DISSERTATION
Typing Guide Paper

$$H^d_{(21)} = 2R_1 = 2R_2 \quad, \text{ and}$$

$$H^d_{(21)} = D_h\,(a,o,\phi_1')\,D_h\,(a,\pi-\phi_1',o)\,\frac{e^{-jka}}{\sqrt{a}}\,e^{jka\cos\phi_1'}\,\frac{e^{-jk\rho}}{\sqrt{\rho}} \qquad (47)$$

Since reciprocity must hold for the doubly diffracted field, the doubly diffracted field from edge (1), i.e., $H^d_{(12)}$ must be equivalent to Equation (47). The total doubly diffracted field is then givey by:

$$H^{2d} = 2\,D_h\,(a,o,\phi_1')\,D_h\,(a,\pi-\phi_1',o)\,\frac{e^{-jka}}{\sqrt{a}}\,e^{jka\cos\phi_1'}\,\frac{e^{-jk\rho}}{\sqrt{\rho}} \qquad (48)$$

where the superscript, 2d, indicates double diffraction.

Figure 17 illustrates the different diffraction mechanisms that combine to give the triple diffracted field from edge (1). In this case, the incident field on edge (1) is the doubly diffracted field from edge (2).

$$H_{(121)} = R_1 + R_2 + R_3 + R_4 \qquad (49)$$

1st page Chapter end line

— — — — — — — 1st page Chapter end line

38

1 inch

JAB/80

(a)

(b)
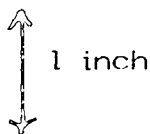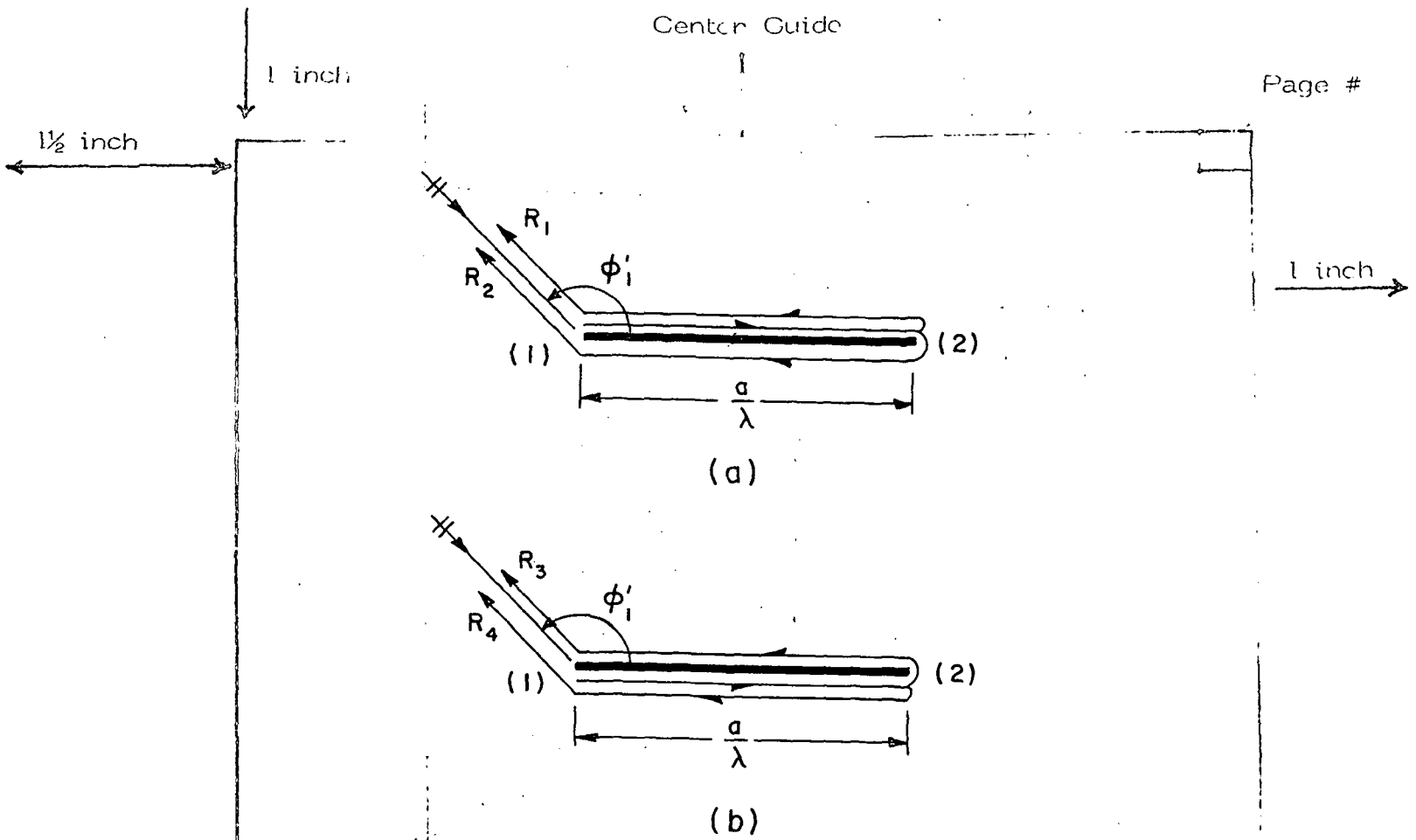
Figure 17.   Triple diffraction field components for a strip.

in a similar way, one finds that all 4 components are equal, i.e.,

$$H_{(121)} = 4 R_1 \tag{50}$$

where

$$R_1 = \tfrac{1}{4} D_h (a,o,\phi_1') \, D_h\left( \tfrac{a}{2},o,o\right) D_h(a,\phi_1',o) \, \frac{e^{-j2ka}}{a} \, \frac{e^{-jk\rho}}{\sqrt{\rho}} \tag{51}$$

or

$$H_{(121)} = D_h(a,o,\phi_1') \, D_h\left(\tfrac{a}{2},o,o\right) D_h(a,\phi_1',o) \, \frac{e^{-j2ka}}{a} \, \frac{e^{-jk\rho}}{\sqrt{\rho}} \tag{52}$$

The triple diffracted field from edge (2) is obtained by multiplying Equation (52) by
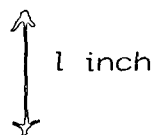
1½ inch

$e^{jka \cos \phi_1^-}$ with $\phi_1^-$ replaced by $\pi - \phi_1^-$.

So the total triple diffracted field is given by

$$H^{3d} = 2 j \sin (ka \cos \phi_1^!) D_h(a,o,\phi_1^!) D_h(\tfrac{a}{2},o,o) D_h(a,\phi_1^!,o)$$

$$\frac{e^{-j2ka}}{\sqrt{a}} \; e^{jka \cos \phi_1^!} \; \frac{e^{-jk\rho}}{\sqrt{\rho}} \qquad\qquad (53)$$

where the superscript 3d indicates triple diffraction. The sum of
Equations (42), (48), and (53) gives the total backscattered field for
the TE case. Note that at normal incidence, the total backscattered
field is dominated by the single diffraction term given by Equation
(42), which in turn, leads to the same value for the echo width given
by Equation (37).

The sum of the singly, doubly and triple diffracted field compo-
nent is sufficient for computing the backscattered field for strip length
of wavelength and above. For smaller lengths, higher order diffractions
must be included. Note that the fourth order diffraction term is
given by

$$H^{4d} = 2 D_h(a,o,\phi_1^!) \left[ D_h(\tfrac{a}{2},o,o) \right]^2 D_h(a,\pi-\phi_1^!,o) \; e^{jka \cos \phi_1^!}$$

$$\frac{e^{-j3ka}}{a\sqrt{a}} \; \frac{e^{-jk\rho}}{\sqrt{\rho}} \qquad\qquad (54)$$

The derivation of Equation (54) follows the same procedure used for
the doubly and triple diffracted fields. A self consistent UTD solu-
tion for the strip which accounts for all higher order diffraction
terms is presented in Appendix D.

1 inch

JAB/80

D.   DISCUSSION

The data computed using the above analysis is compared with the
exact solution for a strip. Figures 18-28 illustrate the accuracy of
this analysis for strip widths $3\lambda$ and $0.25\lambda$.  In all of these figures,
the data is normalized to broadside level.  Figures 18 and 19 show the
results for both TM and TE cases for a $3\lambda$ strip width.  The agreement
with the exact solution is quite good.  The results in Figure 19 are
obtained by using diffraction terms up to the third order.  Figures
20 and 21 show the TM and TE plane patterns for a strip width of $\frac{\lambda}{4}$.
The TE pattern remains in agreement with the exact solution while the
TM pattern deviates appreciably for angles of incidence less than $40^0$
from edge on.  This deviation is caused by the failure of our assumption
that the field diffracted from one edge to the other is a homogeneous
cylindrical wave.  As the strip size gets smaller, the nature of the
diffracted field on the surface of the strip becomes more complex than
a simple homogeneous cylindrical wave.  Figure 22 shows the effect of
adding the fourth order diffraction term to the results shown in Fig-
ure 21.  This indicates that adding more higher order diffraction terms
will not improve our result near edge on.

Comparing Figures 20 and 23, it is noted that the TM pattern is
computed very accurately by just using single diffraction.  This indi-
cates that even for smaller strip widths, the interaction between the
two edges is negligible and therefore, there is no need to include a
slope diffraction term to account for edge interactions.  On the other
hand, comparing Figures 25 and 26, illustrating the E-plane single
diffraction term with their counterparts in the H-plane as illustrated
in Figures 23 and 24, one observes the similarity between the two.
Accordingly, one concludes that it is the double and triple diffraction
terms in the E-plane pattern that create the difference between the
E and H-plane patterns.

JAB/80
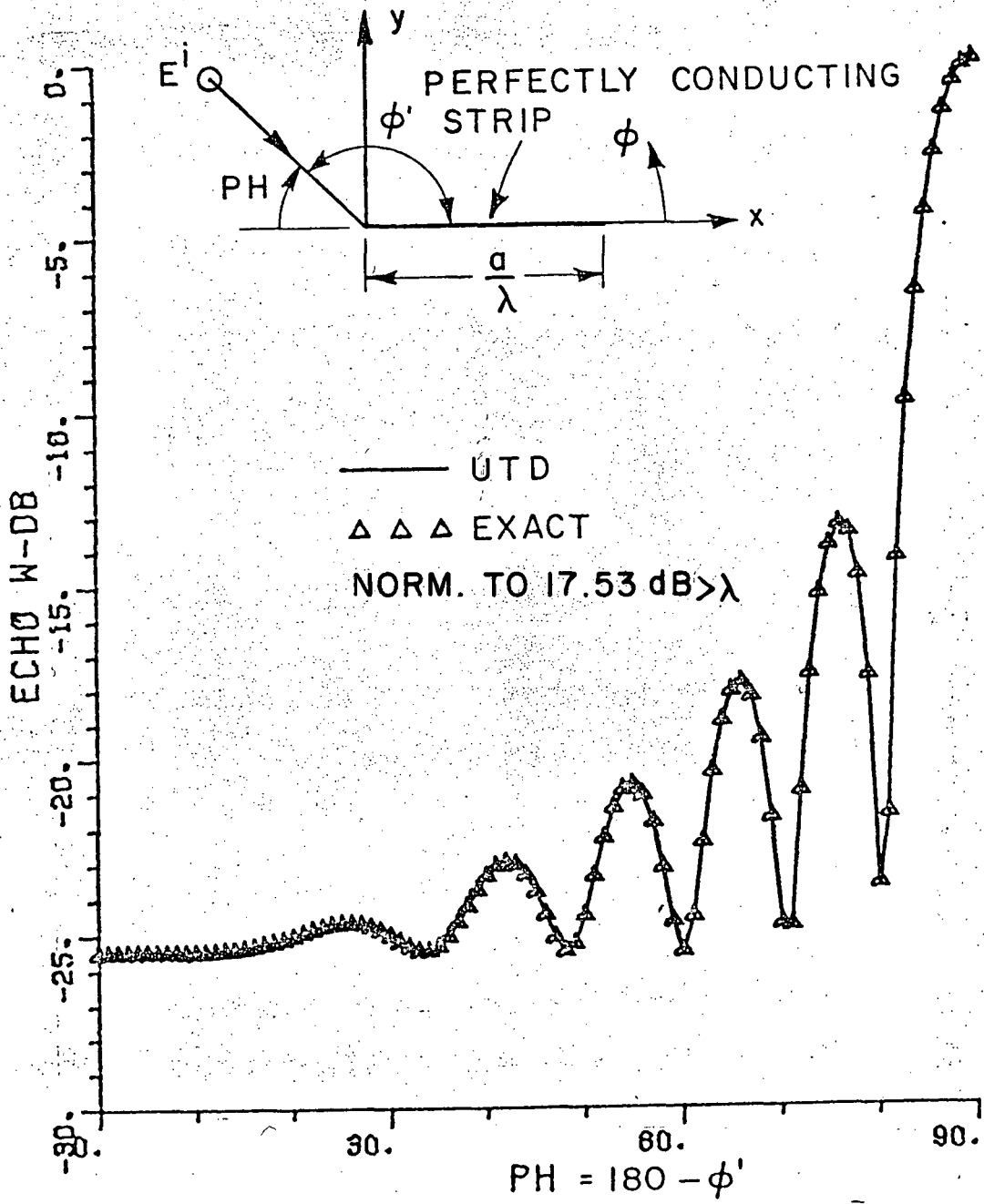
1 inch

1½ inch

1 inch



Figure 18. H-plane echo width pattern of a 3λ wide strip.

1st page Chapter end line

1 inch

JAB/80
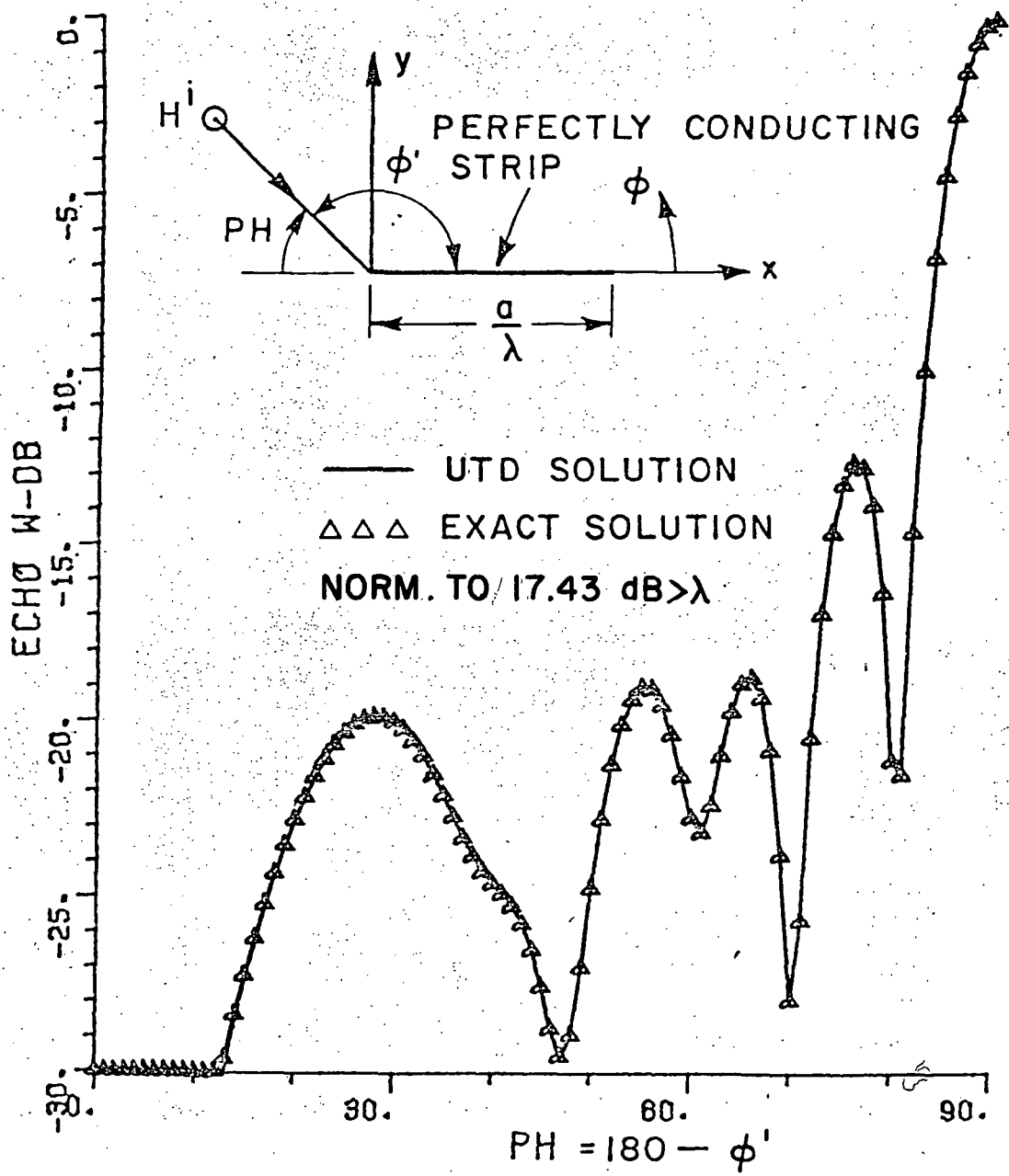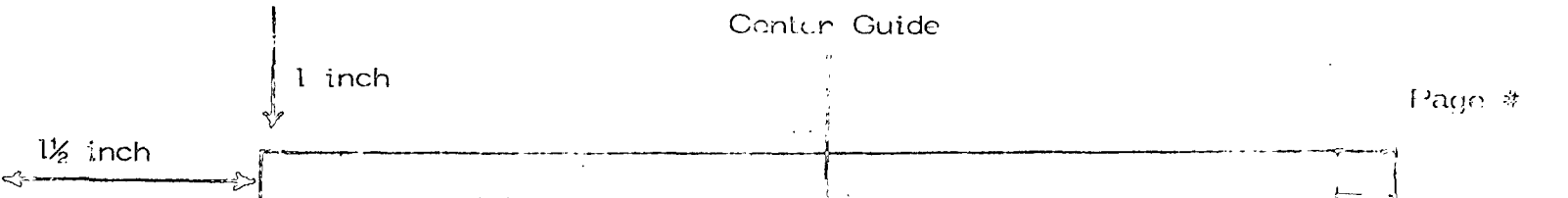
Figure 19.   E-plane echo width pattern of a 3λ wide strip.

1 inch

JAB/80

1 inch

1½ inch

inch



UTD
△ △ △ EXACT
NORM. TO −2.58 dB>λ

ECHO W-DB

$E^i$

PERFECTLY CONDUCTING
STRIP

PH

$\phi'$

$\phi$

y

x

$\frac{a}{\lambda}$

PH = 180 − $\phi'$
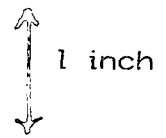
1st page Chapter end line
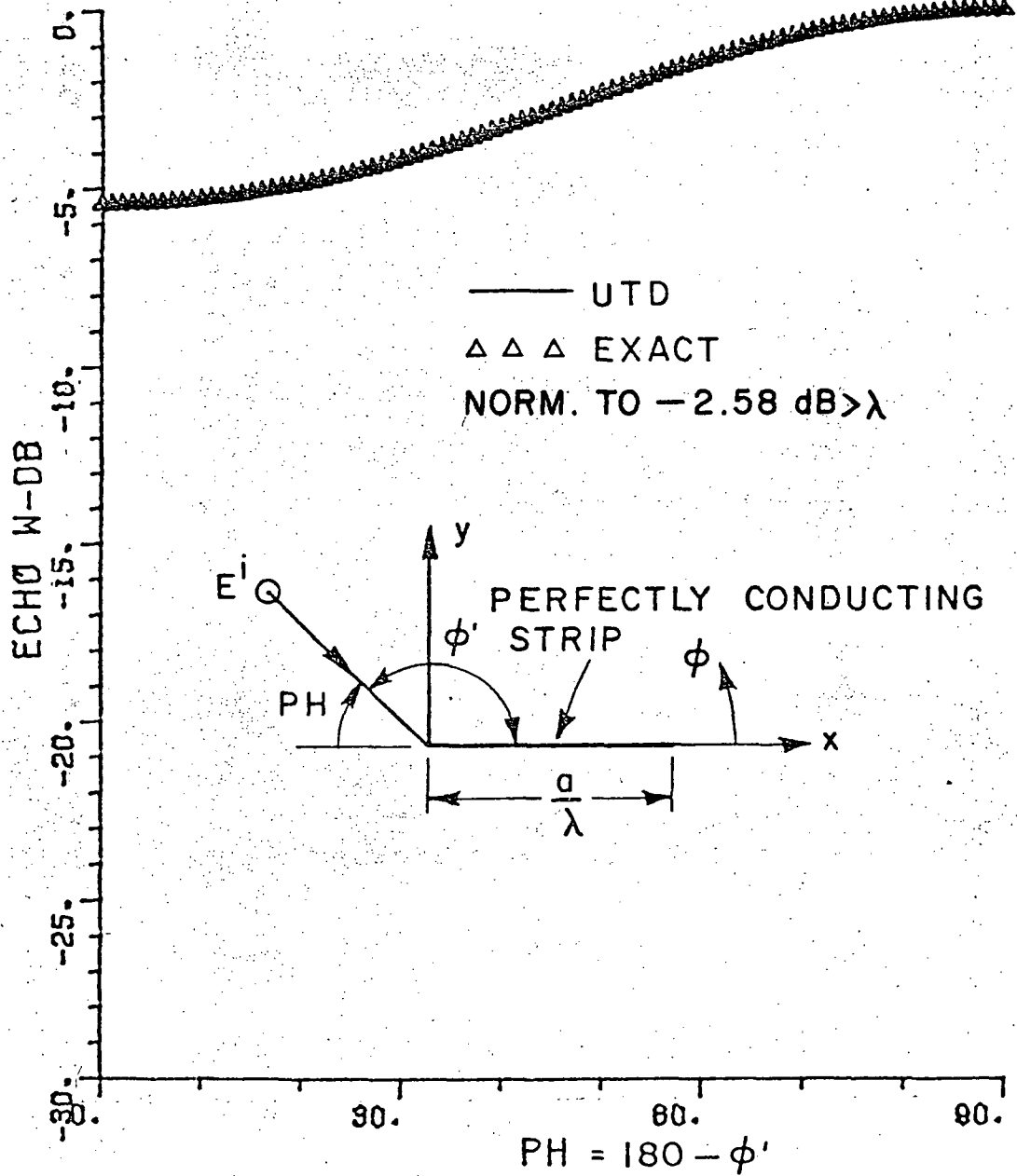
Figure 20.  H-plane echo width pattern of a λ/4 wide strip.

44

1 inch

JAB/60
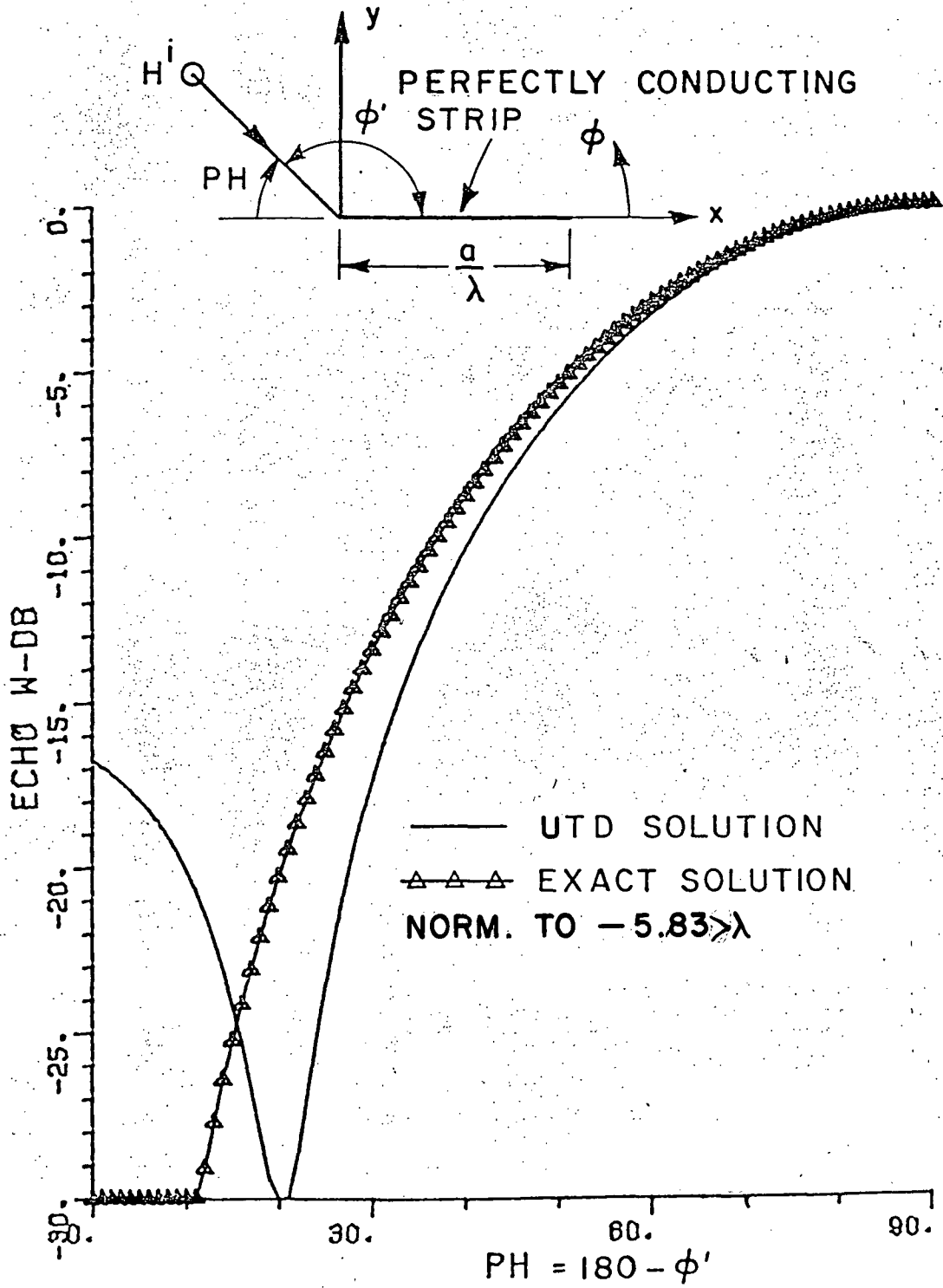
Figure 21.  E-plane echo width pattern of a λ/4 wide strip.

2 inch Chapter Line

PERFECTLY CONDUCTING STRIP

$H^i$

$\phi'$

PH

$\phi$

x

y

$\dfrac{a}{\lambda}$

ECHO W-DB

0.

-5.

-10.

-15.

-20.

-25.

-30.

——— GTD SOLUTION

△ △ △ △ EXACT SOLUTION

NORM. TO − 5.5 dB>λ

PH = 180 − $\phi'$
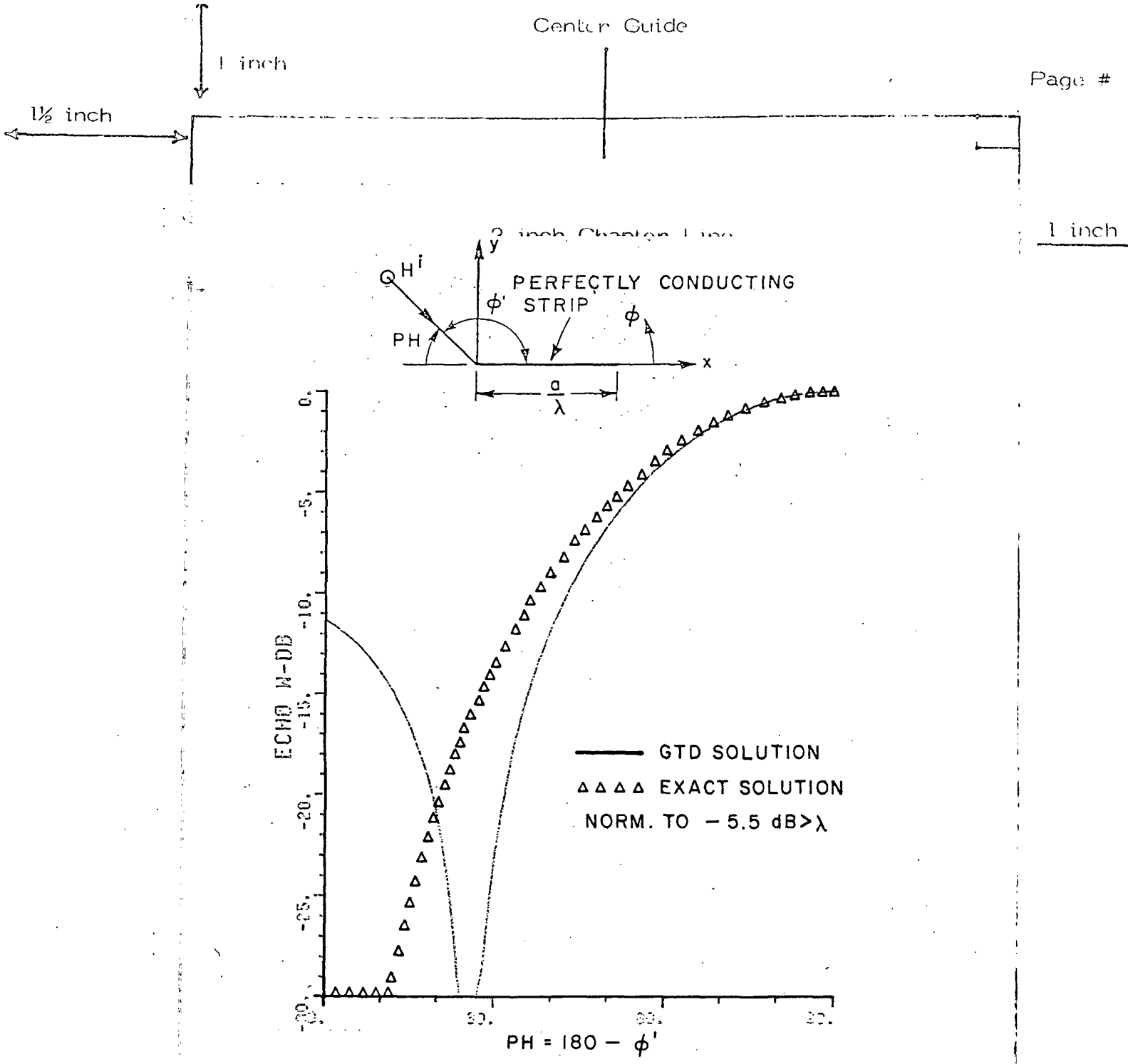
1st page Chapter end line

Figure 22. E-plane echo width pattern of a λ/4 wide strip with fourth order diffraction term included.

1 inch

JAB/80

1 inch

1½ inch

1 inch



PERFECTLY CONDUCTING STRIP

NORM. TO − 2.58 dB>λ

$$PH = 180 - \phi'$$
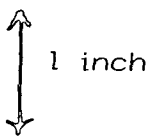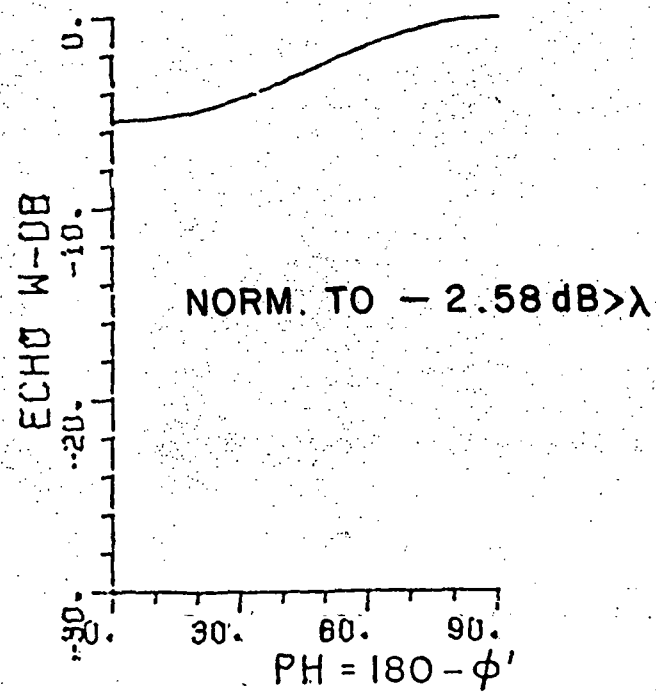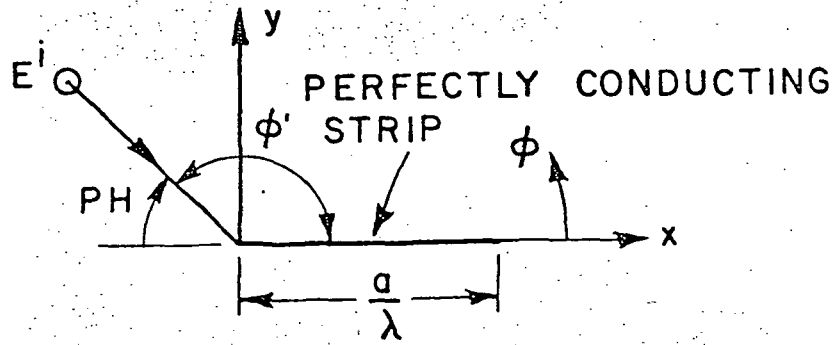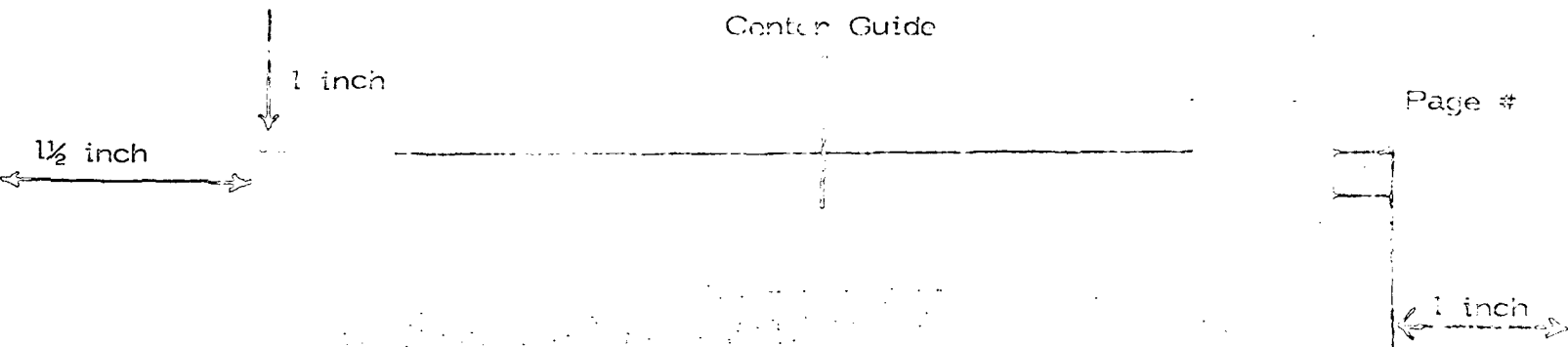
Figure 23.   Contribution to H-plane echo width pattern by single diffraction mechanism for λ/4 strip width.

1 inch

JAB/80

PERFECTLY CONDUCTING STRIP

$E^i$

$\phi'$

PH

$\phi$

x

y

$\dfrac{a}{\lambda}$

NORM. TO 17.53 dB>$\lambda$

ECHO/W-DB

0.

-10.

-20.

-30.

0.   30.   60.   90.

PH = 180 - $\phi'$
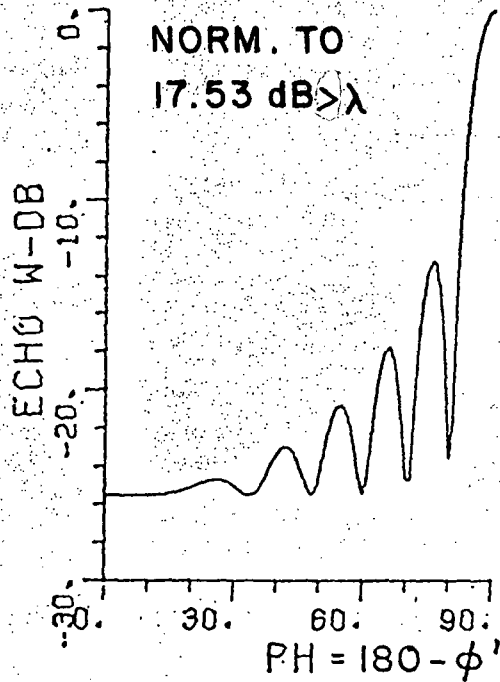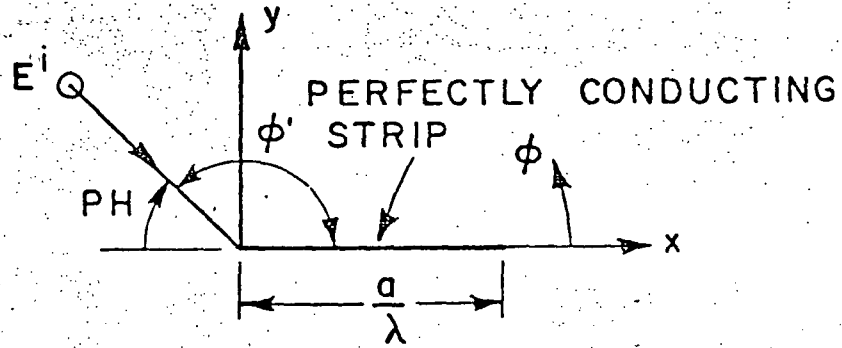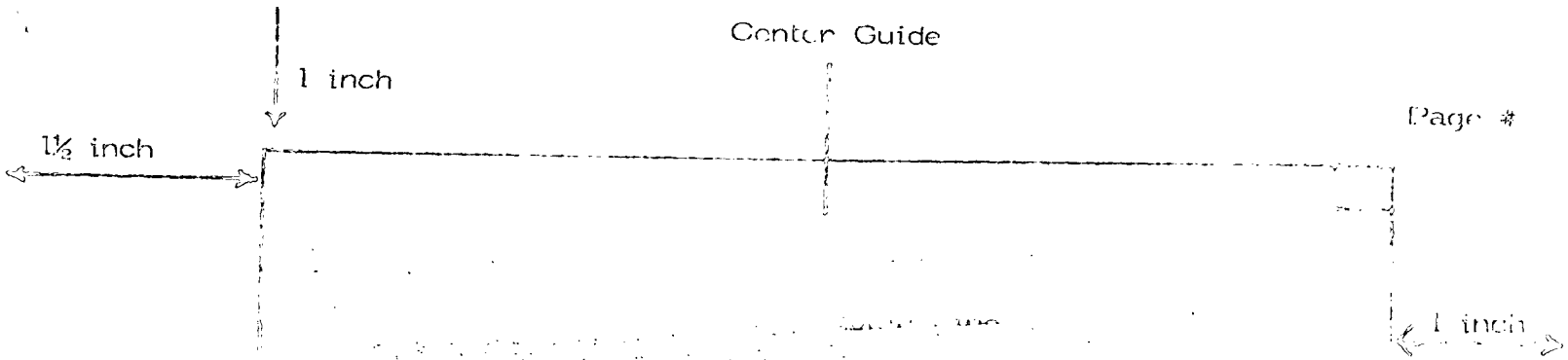
1st page Chapter end line

Figure 24.   Contribution to H-plane echo width pattern by single dif-
fraction mechanism for a 3$\lambda$ wide strip.

JAB/80
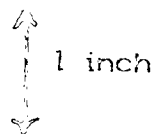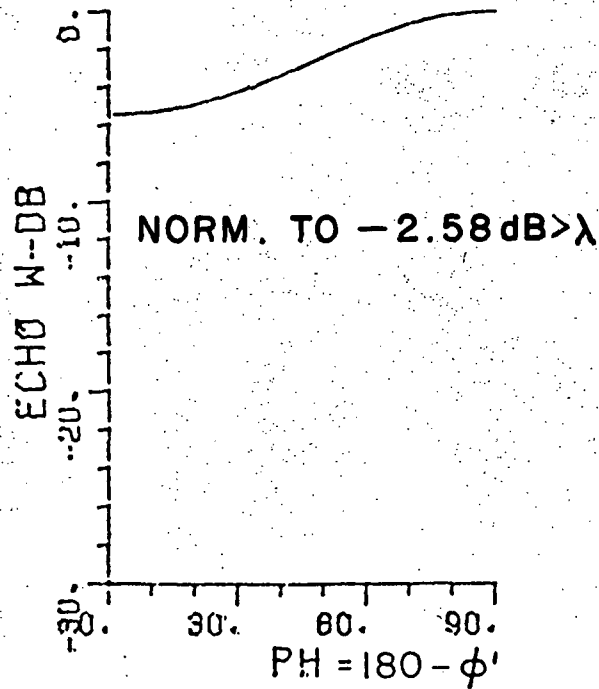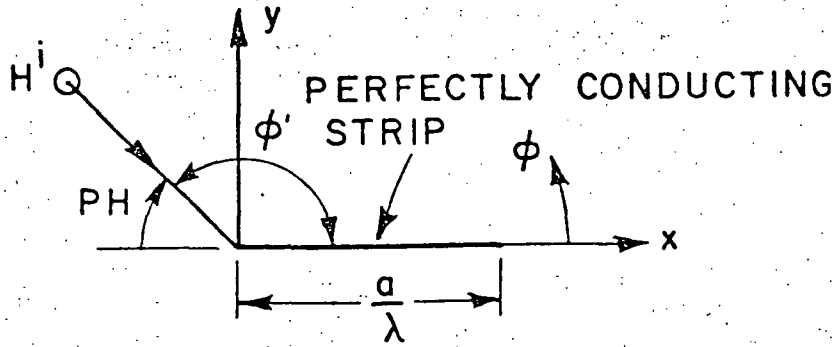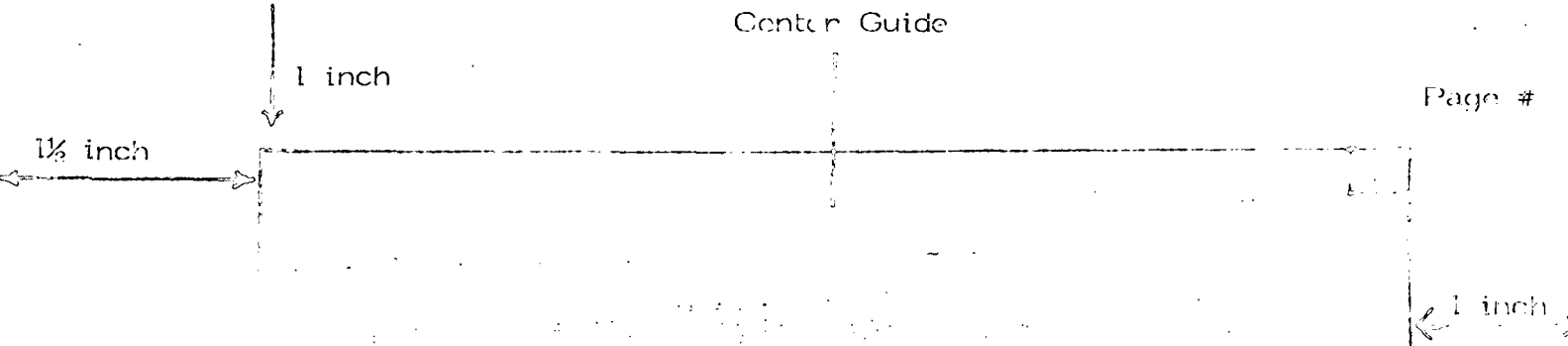
Figure 25.   Contribution to E-plane echo width pattern by single diffraction mechanisms for λ/4 strip width.

1 inch

JAB/80
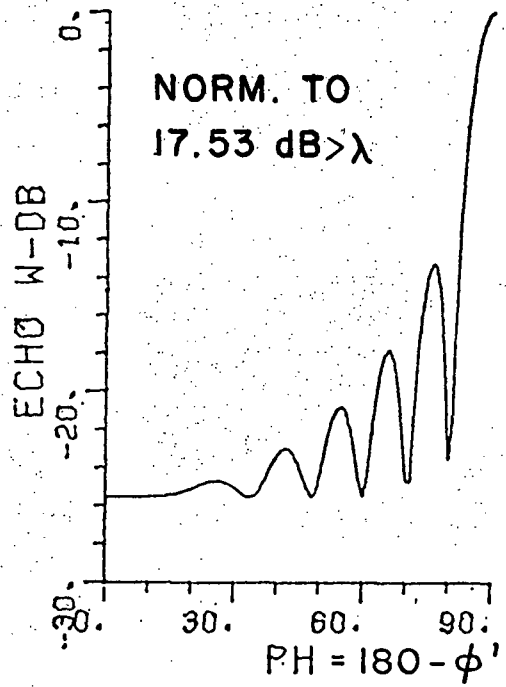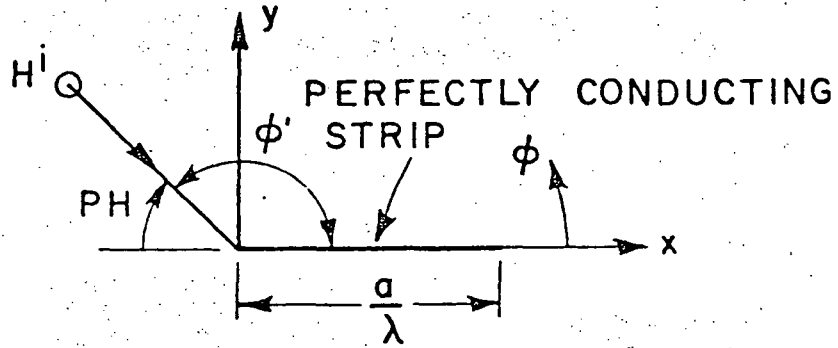
1½ inch

1 inch



Figure 26. Contribution to E-plane echo width pattern by single diffraction mechanisms for a 3λ wide strip.

1 inch

JA13/80

Figure 27. Contributions to E-plane echo width patterns by double diffraction mechanism.

JAB/80

1 inch

1½ inch

1 inch



PERFECTLY CONDUCTING STRIP

$---- \quad a/\lambda = 0.25$
$--- \quad a/\lambda = 0.5$
$--- \quad a/\lambda = 3$
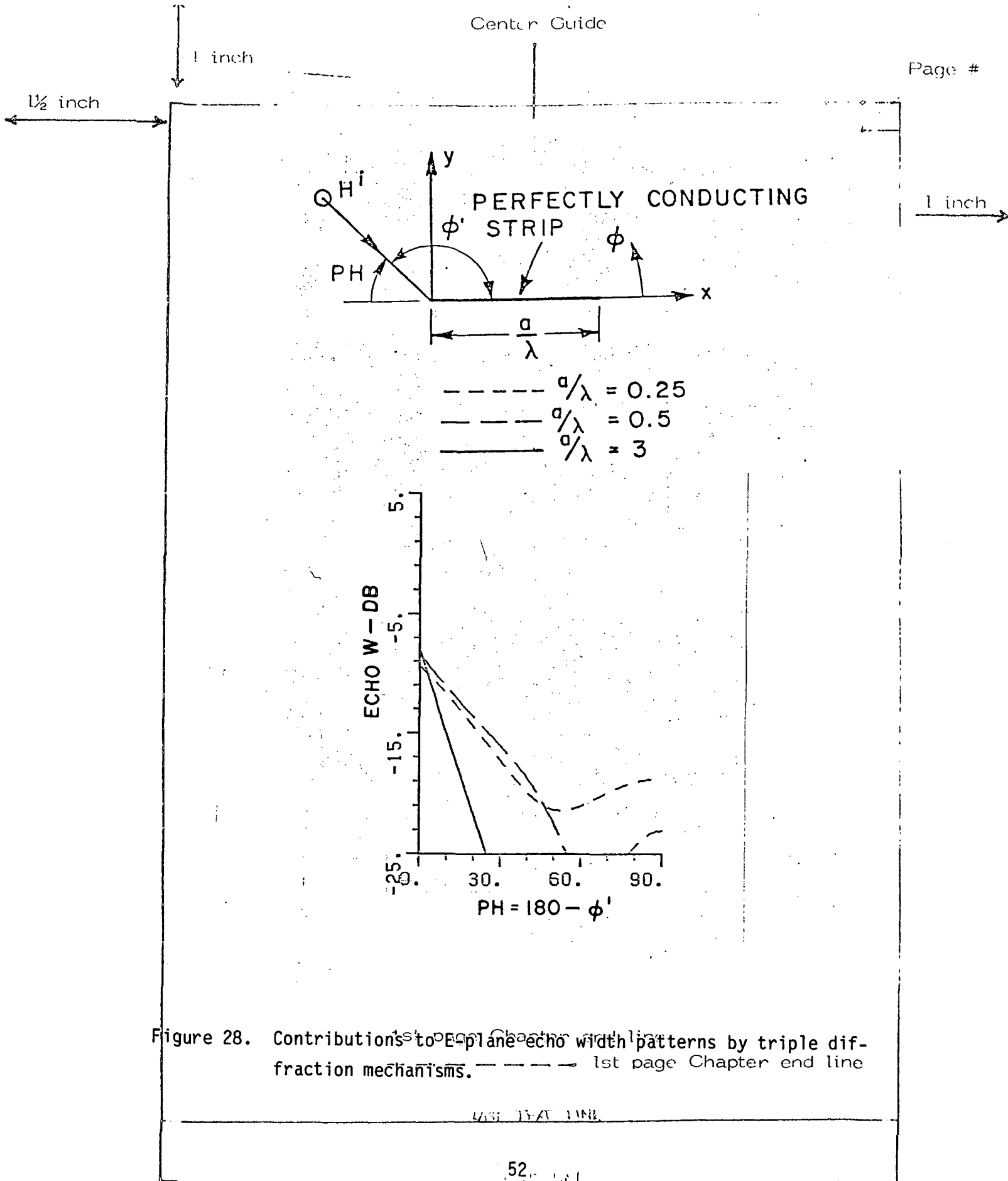
Figure 28.   Contributions to E-plane echo width patterns by triple diffraction mechanisms. — — — — 1st page Chapter end line

LAST TEXT LINE

1 inch

JAB/80
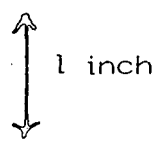
1½ inch

Figures 27 and 28 show the contributions to the E-plane pattern by the double and triple diffraction terms. For a 3λ strip, the double diffraction term is only needed for incidence angles up to 40° and triple diffraction to 10° from edge on. The high value obtained for these two terms for a 0.25λ strip makes it necessary to include higher order terms to offset this increase.

1 inch

THESIS / DISSERTATION
Typing Guide Paper

1st page Chapter end line
— — — — — — — 1st page Chapter end line

LAST TEXT LINE

53

1 inch

JAB/80

# CHAPTER IV

## H-PLANE BACKSCATTERING FROM PLATES

### A. PLATE GEOMETRY

Figure 29 illustrates the geometry used to define the plate which is assumed to be perfectly conducting and of zero thickness. The plate has N edges with the edge vectors given by

$$\bar{e}_p = x_p \,\hat{x} + y_p \,\hat{y} + z_p \,\hat{z} \quad , \quad p = 1, 2, \ldots, N \quad, \text{ and} \tag{55}$$

$$\bar{e}_p = \bar{c}_{p+1} - \bar{c}_p = \ell_p \hat{e}_p \tag{56}$$

where $\bar{c}_p$ is the position vector of the $p^{th}$ corner and $\ell_p$ is its length. The $p^{th}$ edge unit vector is then given by

$$\hat{e}_p = \frac{(x_{p+1}-x_p)}{\ell_p} \,\hat{x} + \frac{(y_{p+1}-y_p)}{\ell_p} \,\hat{y} + \frac{(z_{p+1}-z_p)}{\ell_p} \,\hat{z}$$

or

$$\hat{e}_p = \bar{x}_p \,\hat{x} + \bar{y}_p \,\hat{y} + \bar{z}_p \hat{z} \quad . \tag{57}$$

The plate normal unit vector and the binormal unit vector to the $p^{th}$ edge are defined, respectively, by

$$\hat{n} = \frac{\hat{e}_p \times \hat{e}_{p+1}}{|\hat{e}_p \times \hat{e}_{p+1}|} = n_x \,\hat{x} + n_y \hat{y} + n_z \hat{z} \tag{58}$$

54

1½ inch

2 inch Chapter Line

1 inch

PERFECTLY CONDUCTING
PLATE

$z$

$\hat{n}$

$\hat{b}_p$

$p$

$\hat{e}_p$

$\hat{e}_{p+2}$

$\bar{c}_p$

$p+1$

$\hat{e}_{p+1}$

$p+2$

$\bar{c}_{p+1}$

$y$

$x$
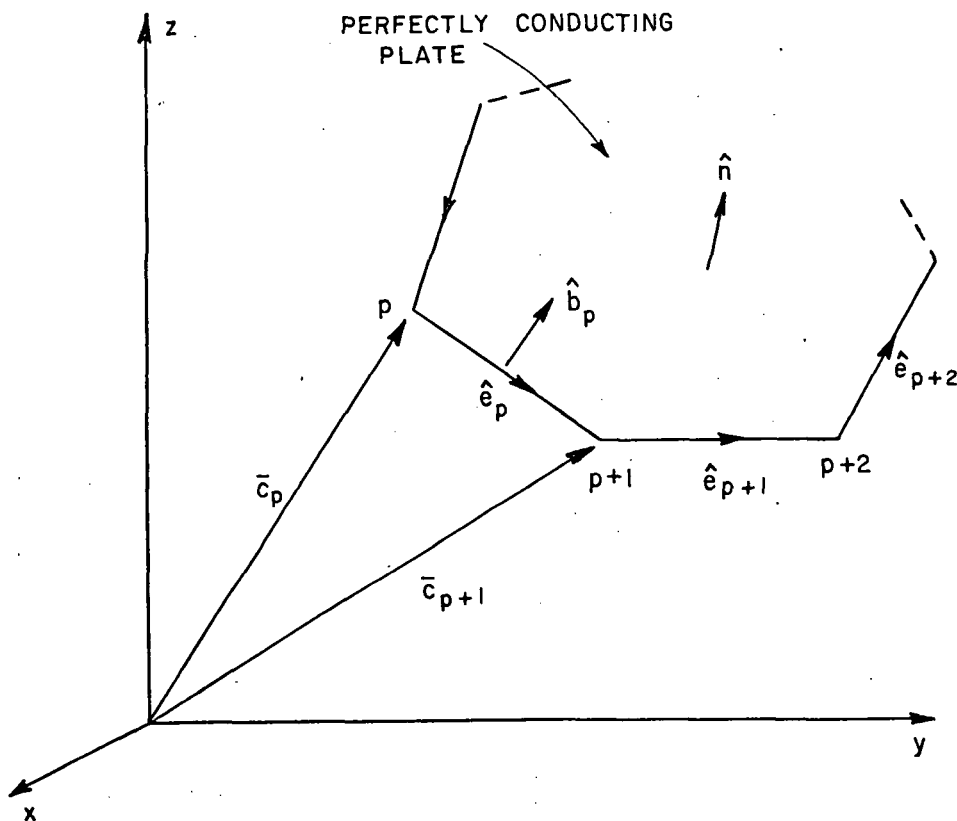
Figure 29.   Plate Geometry.

1st page Chapter end line

1st page Chapter end line

JAB/80

1½ inch

and
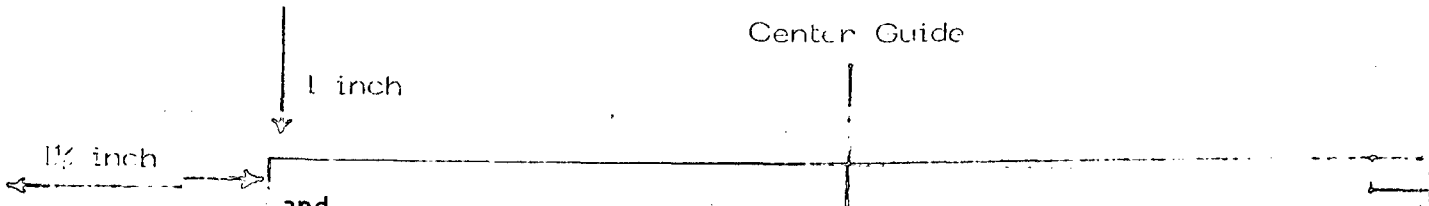
$$\hat{b}_p = \frac{\hat{n} \times \hat{e}_p}{|\hat{n} \times \hat{e}_p|} = b_x \hat{x} + b_y \hat{y} + b_{zp} \hat{z} \qquad (59)$$

## B. EQUIVALENT CURRENT FORMULATION

The analysis of backscattering in this chapter from plates is done using the Equivalent current principle discussed in Chapter II. The H-plane pattern is analyzed here by using the first order edge diffraction fields to formulate the Equivalent currents which are given by

$$I^e_{(1)} = \frac{2j}{Z_0 K} \frac{G^e(n,\phi,\phi')}{\sin^2\beta_o^{(p)}} (\bar{E}^i \cdot \hat{e}_p) \qquad \text{and} \qquad (60)$$

$$I^m_{(1)} = \frac{2j}{Y_0 K} \frac{G^m(n,\phi,\phi')}{\sin^2\beta_o^{(p)}} (\bar{H}^i \cdot \hat{e}_p) \qquad . \qquad (61)$$

The derivation of Equations (60) and (61), and the definition of the different parameters is shown in Appendix (B). In these equations the subscripts of $I^m_{(1)}$ indicate the order of diffraction and the superscripts indicate current type, i.e., the electric or magnetic currents.

The backscattered field is computed by substituting these currents into the radiation integral. The RCS is computed by using

$$\sigma = \lim_{r \to \infty} 4\pi r^2 \frac{|E^s|^2}{|E^i|^2} \qquad . \qquad (62)$$

It should be noted that Equations (60) and (61) are valid for computation of principle E and H plane patterns. For any other pattern cut, as the one shown in Figure 30, one has to use the components of the Equivalent currents perpendicular to the plane of incidence, accordingly Equations (60) and (61) are modified by replacing

56

JAB/80

1 inch

1½ inch

1 inch

θ

EQUIVALENT STRIP

$\hat{I}$

PH

$I^e, I^m$

y

PLANE OF INCIDENCE
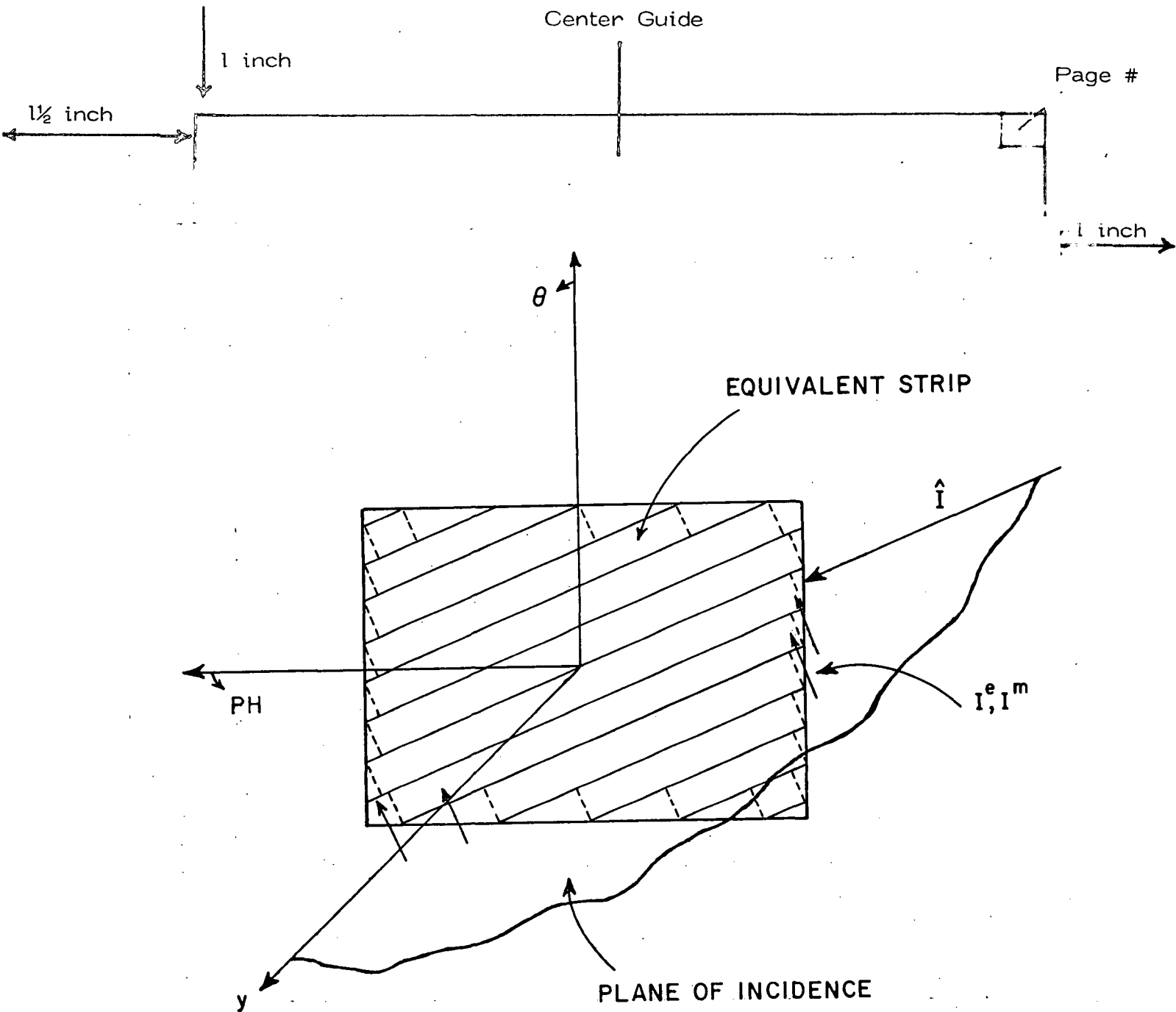
Figure 30.    Equivalent Current Components used for computation in a
pattern cut other than the principle planes.

1st page Chapter end line

end line

LAST TEXT LINE

57

PAGE NO. LINE

1 inch
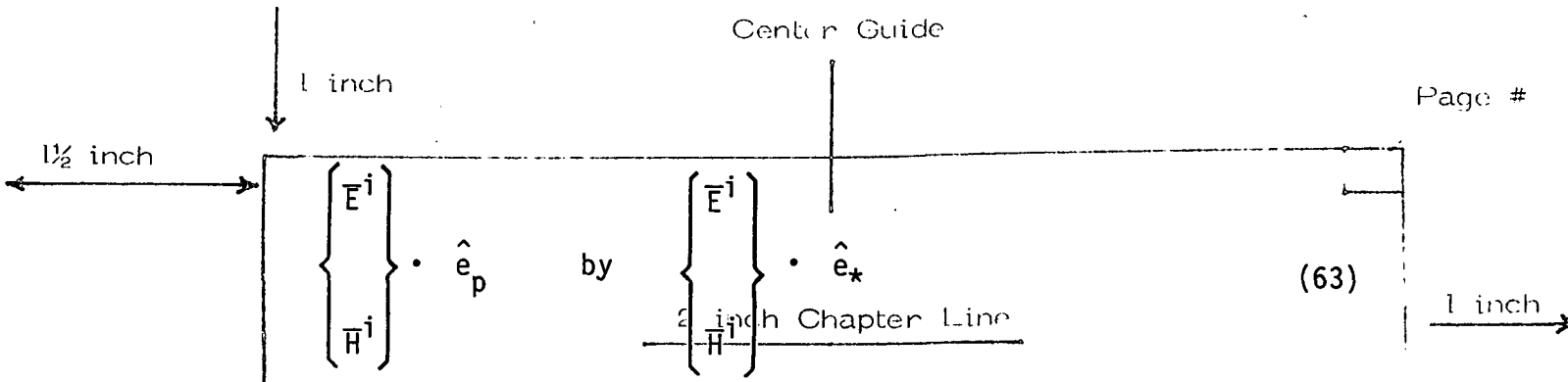
$$\left\{ \begin{array}{c} \overline{E}^i \\ \overline{H}^i \end{array} \right\} \cdot \hat{e}_p \quad \text{by} \quad \left\{ \begin{array}{c} \overline{E}^i \\ \overline{H}^i \end{array} \right\} \cdot \hat{e}_* \tag{63}$$

where the unit vector $\hat{e}_*$ is defined as a unit vector normal to the plane of incidence, i.e.,

$$\hat{e}_* = \frac{(\hat{I} \times \hat{n})}{|\hat{I} \times \hat{n}|} \tag{64}$$

where $\hat{I}$ is the incident unit vector and $\hat{n}$ is the plate normal unit vector defined in Equation (58).

This use of Equivalent currents is necessary since the far field diffraction coefficient of a single edge becomes singular as the observation point approaches a shadow or reflection boundary. A diffraction from a second point in the incident plane is required to remove this singularity as was done earlier for the strip (see Equation (36) ). A physical representation is that the plate takes the form of an array of strips parallel to the incidence plane.

Therefore, only the components of the Equivalent Currents perpendicular to the incidence plane need to be considered.

C. BACKSCATTERING FROM RECTANGULAR PLATE

Calculating the backscattered field from a perfectly conducting plate has been investigated by several authors. Ross [28] has applied the Geometrical Theory of Diffraction and physical optics methods to predict the RCS of a conducting rectangular plate. His results were in agreement with measured data except for regions near edge on incidence.
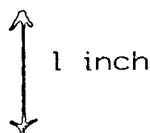
One of the reasons for the failure of his solution is the use of a plane wave diffraction coefficient for the higher order diffraction mechanisms. Yu [29] improved the result for a rectangular plate by using the technique developed by Ufimtsev [30], who used nonuniform cylindrical waves in conjunction with the reciprocity principle to describe the secondary diffraction. His solution also did not include a necessary edge wave mechanism. This problem is also to be discussed in this section for the RCS of thin rectangular plate at grazing incidence as a function of plate length and vertical polarization. Hey, et. al [31] and Knott, et. al [32] have reported measured data for flat plates two wave lengths in width and lengths as small as $0.05\lambda$ and as long as $7\lambda$. Ross [28] also provided an emperically derived equation to fit the measured data. Finally, a set of different shaped plates are studied. In several instances, the edge wave mechanisms have not been included and this will be noted as is appropriate.

### 1. RCS From Thin Rectangular Plate Illuminated At Edge On

The geometry of the problem is shown in Figure 31. A rectangular plate of length $\frac{a}{\lambda}$ and width $\frac{b}{\lambda}$ is located in the x-y plane, and is illuminated at edge on by a plane wave of unit amplitude and polarized parallel to edges 2 and 4. The term $C_{ij}$ defines corner i on edge j. The incident field is given by

$$\overline{E}^i = \hat{x} \, e^{jky} \qquad (66)$$

As this field is diffracted from corner $C_{11}$, it excites an edge wave. Over the surface of the plate, the field of this edge ray is, of course, polarized perpendicular to the plate. This field illuminates the back edge. The field diffracted back y this edge interacts with the front edge and corners $C_{11}$ and $C_{43}$ or Figure 32 illustrates the different interactions that contribute to the backscattered field. Observe that the second corner diffraction is required to convert the z-polarized field on the surface of the plate to the original x-polarized

1 inch

$C_{ij} \triangleq$ CORNER # i ON EDGE # j

PERFECTLY CONDUCTING
PLATE

#1

$\bar{E}^i$

(1)

(4)

(2)

$\dfrac{b}{\lambda}$

(3)

#2

#3

#4

y

x

$\dfrac{a}{\lambda}$
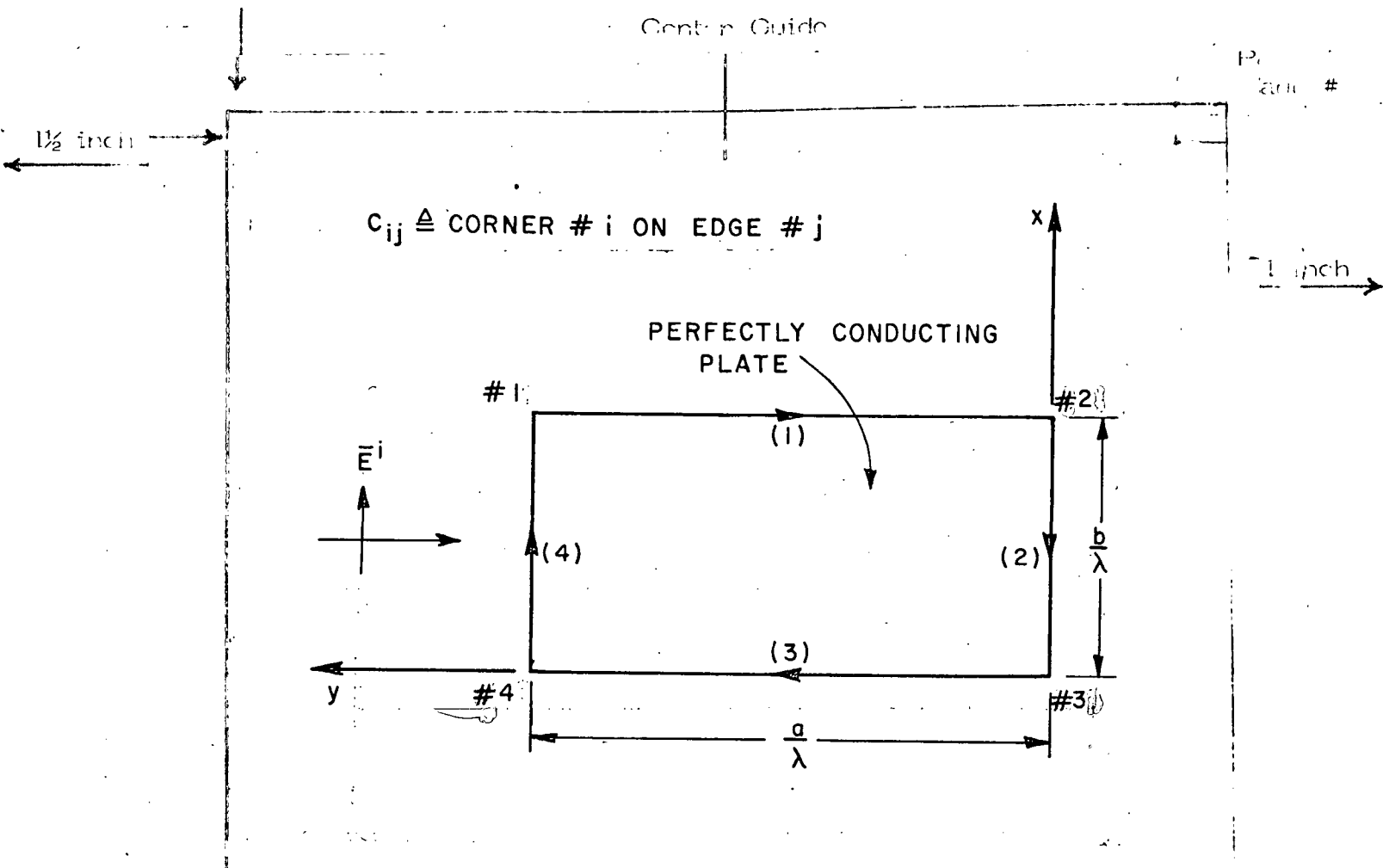
Figure 31. Edge on case geometry.

state. Also, these z-polarized fields on the surface of the plate will yield a strong cross polarized component for some non-grazing incidence and radiation angles. This cross-polarizing mechanism has not been studied in detail at this time but the techniques developed herein are directly applicable to it.

Figure 32-a illustrates the interaction between corner $C_{11}$ and itself. The different parameters shown in the figure are defined by

$$s_1 = \sqrt{a^2 + (b-x)^2}$$

$$\beta_{c_1} = \tan^{-1}\frac{(b-x)}{a}, \quad \text{and} \quad \beta_0 = \frac{\pi}{2} - \beta_{c_1}$$

JAB/80
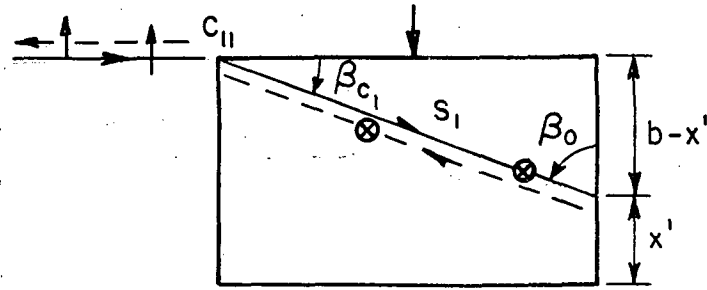
(a)  INTERACTION  $C_{11} - C_{11}$
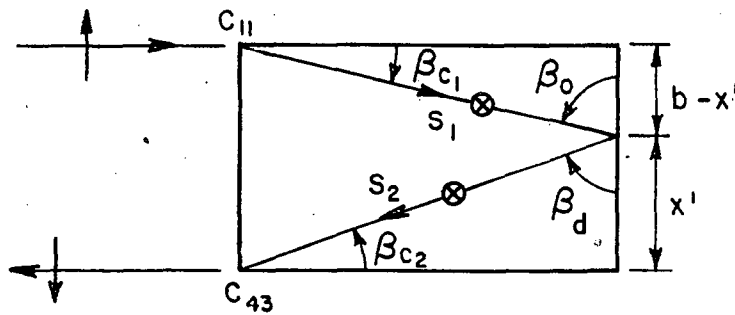


(b)  INTERACTION  $C_{11} - C_{43}$
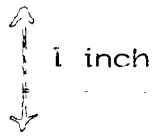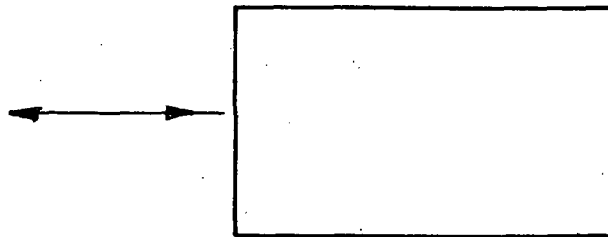


(c)  EDGE  DIFFRACTION  FROM  FRONT EDGE

Figure 32.  Edge on case interactions.  1st page Chapter end line

1 inch

JAB/80

The value of the edge wave field at the back edge due to corner $C_{11}$ is given by

$$E_z^{(ew)} = E^i(Q_{C_{11}}) \, D_h^{(ew)}(s_1, o, \frac{\pi}{2}, \beta_{c_1}) \frac{e^{-jks_1}}{\sqrt{s_1}} \quad , \qquad (67)$$

where $D_h^{(ew)}$ is defined in Equation (27). Using the Equivalent current concept, one can find the field due to the back edge. This field, in turn, diffracts from corner $C_{11}$ and radiates the desired x-polarized field component given by

$$E_x^d = - \frac{e^{j2ka}}{\pi \sin\beta_0} \frac{e^{-jky}}{y} \int_0^b \left\{ D_h^{(ew)}(s_1, o, \frac{\pi}{2}, \beta_{c_1}) \frac{e^{-jks_1}}{\sqrt{s_1}} \right\}^2 dx' \qquad (68)$$

The mechanism consisting of diffraction from corner $C_{11}$ to corner $C_{21}$ back to corner $C_{11}$ and hence to the source is inherent in Equation (68). Of course, there is a similar component that comes from corner $C_{43}$.

The interaction between $C_{11}$ and $C_{43}$, shown in Figure 32-b is found in a similar way. In this case the field diffracted by the back edge is diffracted also by the front edge. The necessary parameters shown in Figure 32-b are defined as follows:

$$s_2 = \sqrt{a^2 + x'^2}$$

$$\beta_{c_2} = \tan^{-1}\frac{x'}{a}$$

$$\beta_d = \frac{\pi}{2} - \beta_{c_2}$$

and $s_1$, $\beta_{c_1}$, $\beta_0$ are as defined before.

The backscattered field due to this interaction is given by

JAB/80

$$E_x^d = \frac{e^{j2ka}}{\pi} \frac{e^{-jky}}{y} \int_0^b \frac{D_h^{(ew)}(s_1,o,\frac{\pi}{2},\beta_{c_1}) \, D_h^{(ew)}(s_2,o,\frac{\pi}{2},\beta_{c_2})}{\sin \beta_0}$$

$$\frac{e^{-jks_1}}{\sqrt{s_1}} \frac{e^{-jks_2}}{\sqrt{s_2}} \, dx' . \tag{69}$$

A similar expression holds for the interaction between $C_{43}$ and $C_{11}$.

The third field component shown in Figure 32-c is the edge diffracted field from the front edge. It is evaluated by using the Equivalent current method and the field is given by

$$E_x^d = \frac{b}{2\pi} e^{j2ka} \frac{e^{-jky}}{y} . \tag{70}$$

The total backscattered field is obtained by summing up all the three different components.

2. Discussion

Figures 33-35 show the results for H-plane pattern ($E_\theta$-polarization) for three different square flat plate sizes. The results are compared to measurement data as well as results obtained by Ross [28]. His solution included higher order diffraction terms. His calculations are good everywhere except near grazing incidence. This error is caused by the use of plane wave diffraction coefficients which become singular near grazing incidence in the higher order diffraction terms formulation. The equivalent current solution as developed herein overcomes this difficulty as shown by the good agreement with the measured results. Figure 36 shows the H-plane RCS pattern for a $3\lambda \times 3\lambda$ plate. It is compared with a moment method solution using surface patches model developed by Newman [33]. For near edge on incidence, the two solutions give results which differ significantly. The reason is that higher order diffraction terms and the edge wave mechanisms discussed earlier

JAB/80

1½ inch



**CALCULATED**
o o o **MEASURED**
x x x **ROSS [28]**
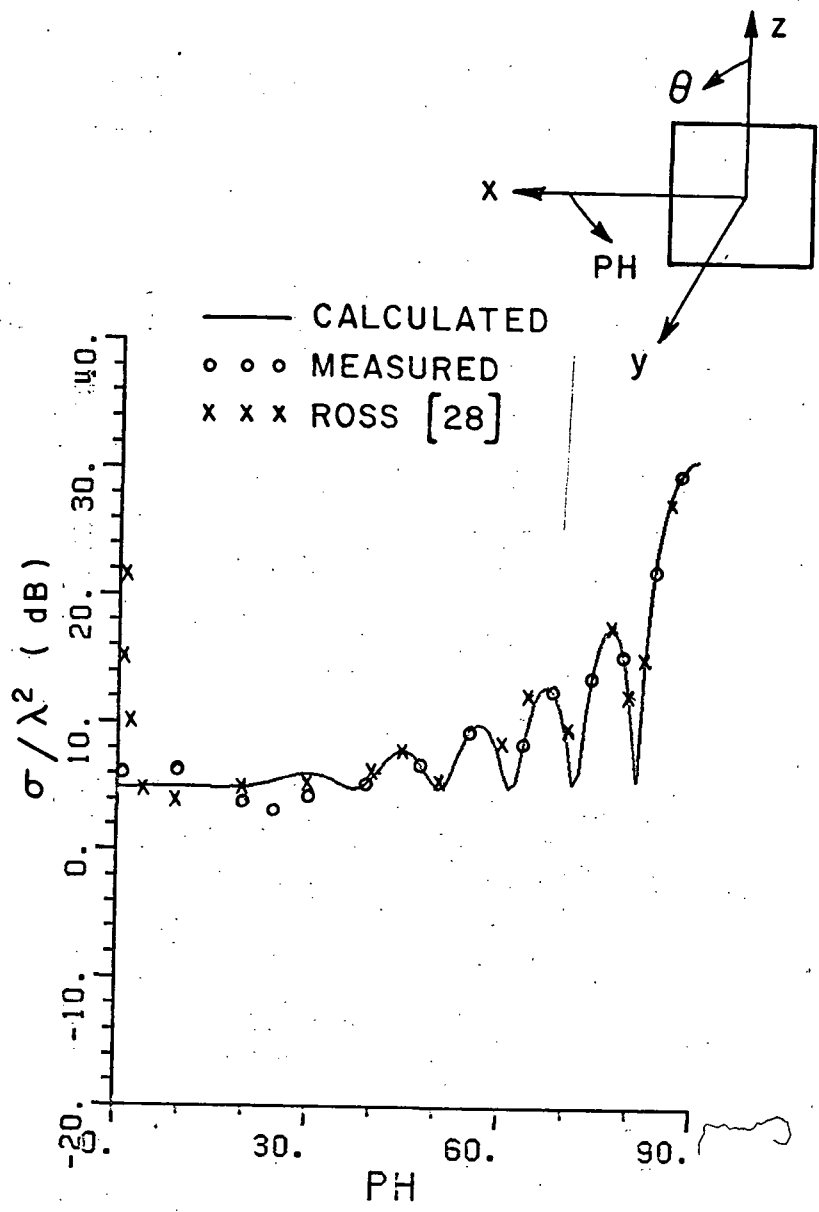
Figure 33. $E_\theta$, $\theta=90°$ RCS pattern for a 4 x 4 inch flat plate ($\lambda$ = 1.28 inch).

1 inch

JAB/80
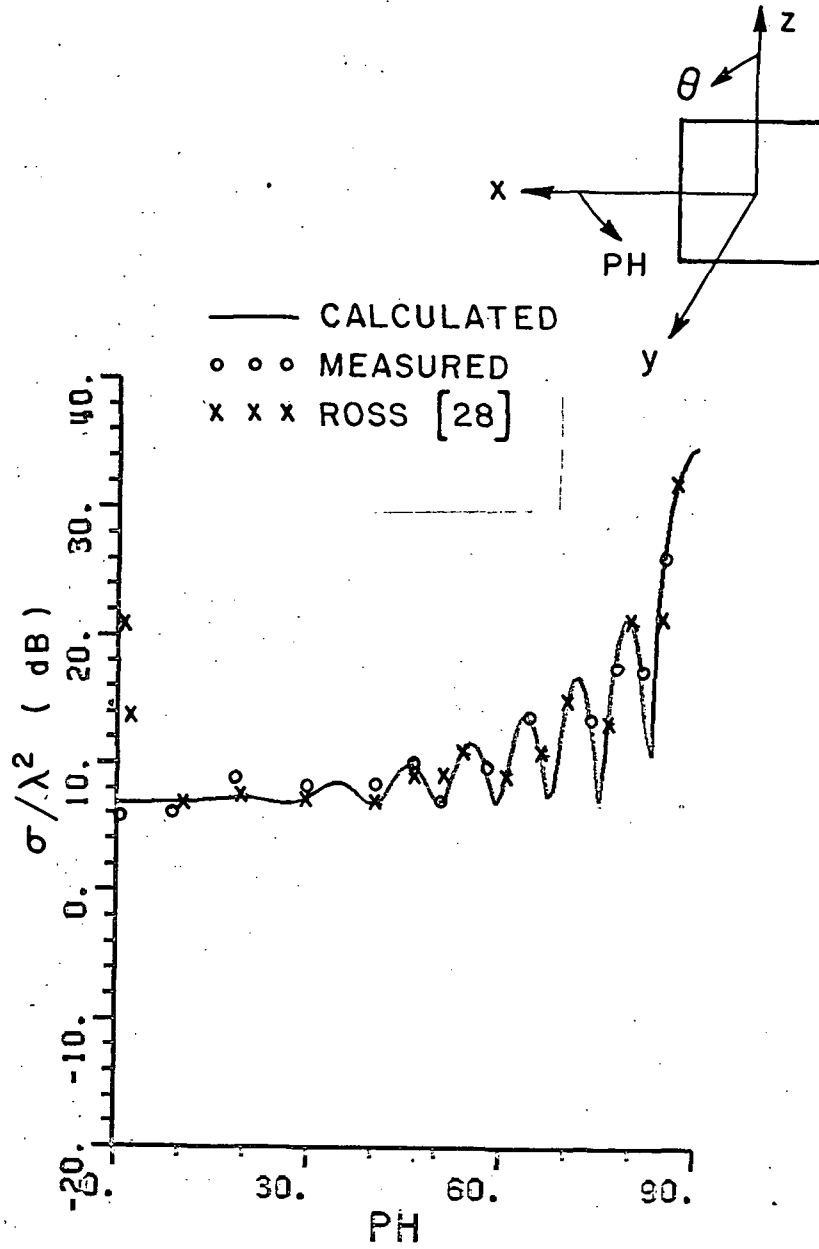
Figure 34. $E_\theta$, $\theta=90^0$ RCS pattern for a 5 x 5 inch flat plate ($\lambda=1.28$ inch)
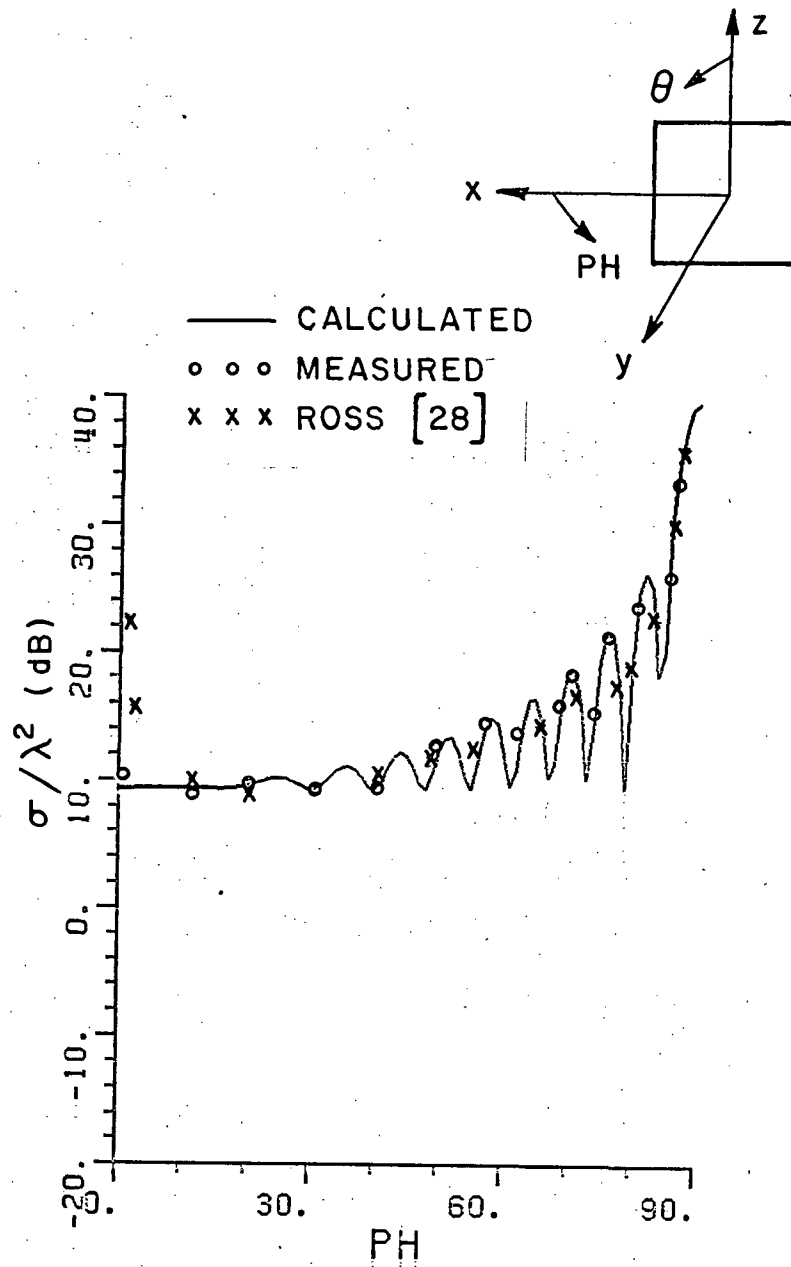
1½ inch

1 inch



Figure 35.  $E_\theta$, $\theta = 90°$ RCS pattern for a 6 x 6 inch flat plate ($\lambda$ = 1.28 inch).

1 inch

JAB/80

1 inch

1½ inch

1 inch

—— EQUIVALENT CURRENT SOL.
x x x MM PATCH METHOD

$\sigma_{max}=30.1dB$
$>\lambda^2$

1st page Chapter end line

Figure 36. $E_\theta$, $\theta=90^\circ$ RCS pattern for a $3\lambda$ x $3\lambda$ flat plate.

end line

1 inch

JAB/80
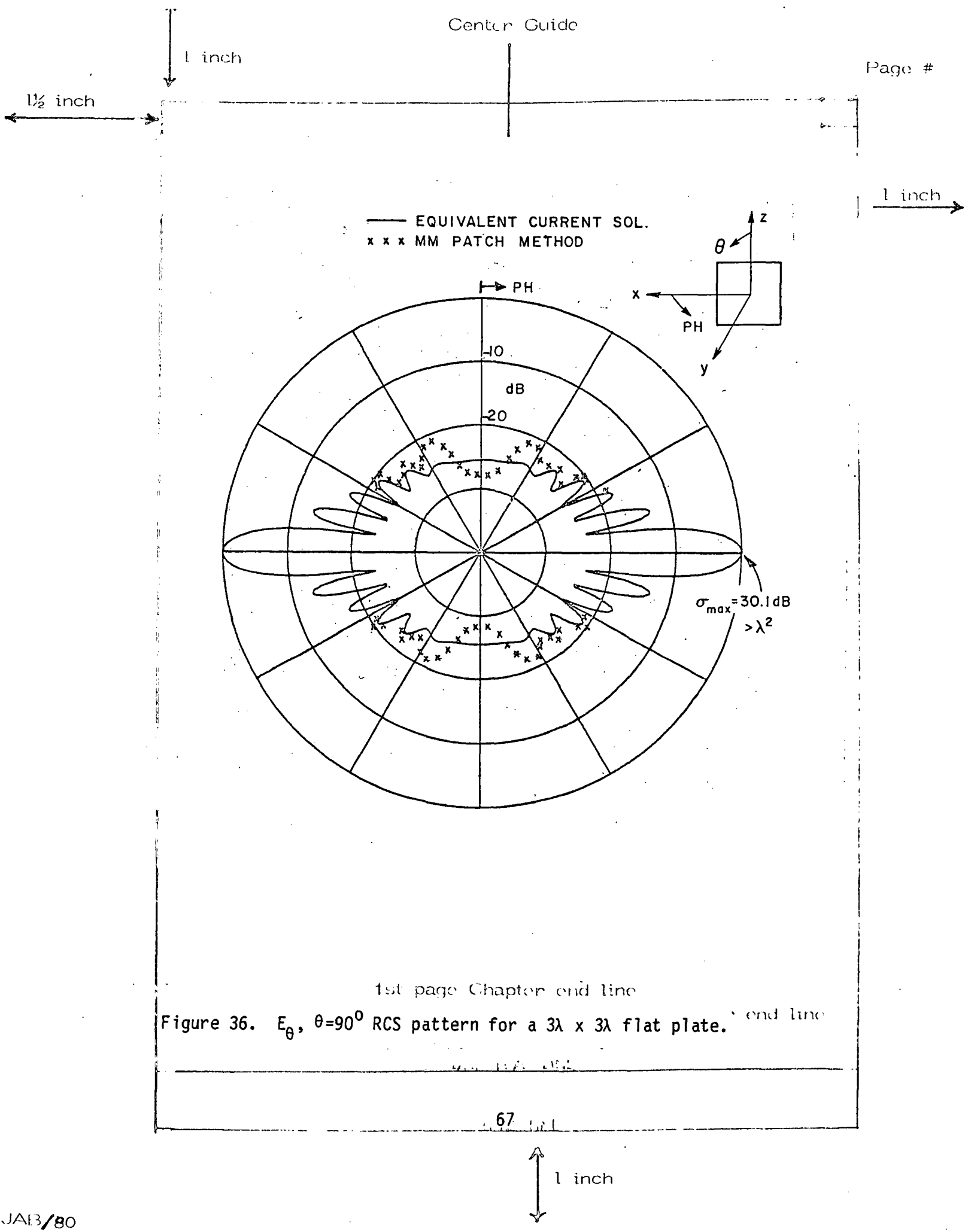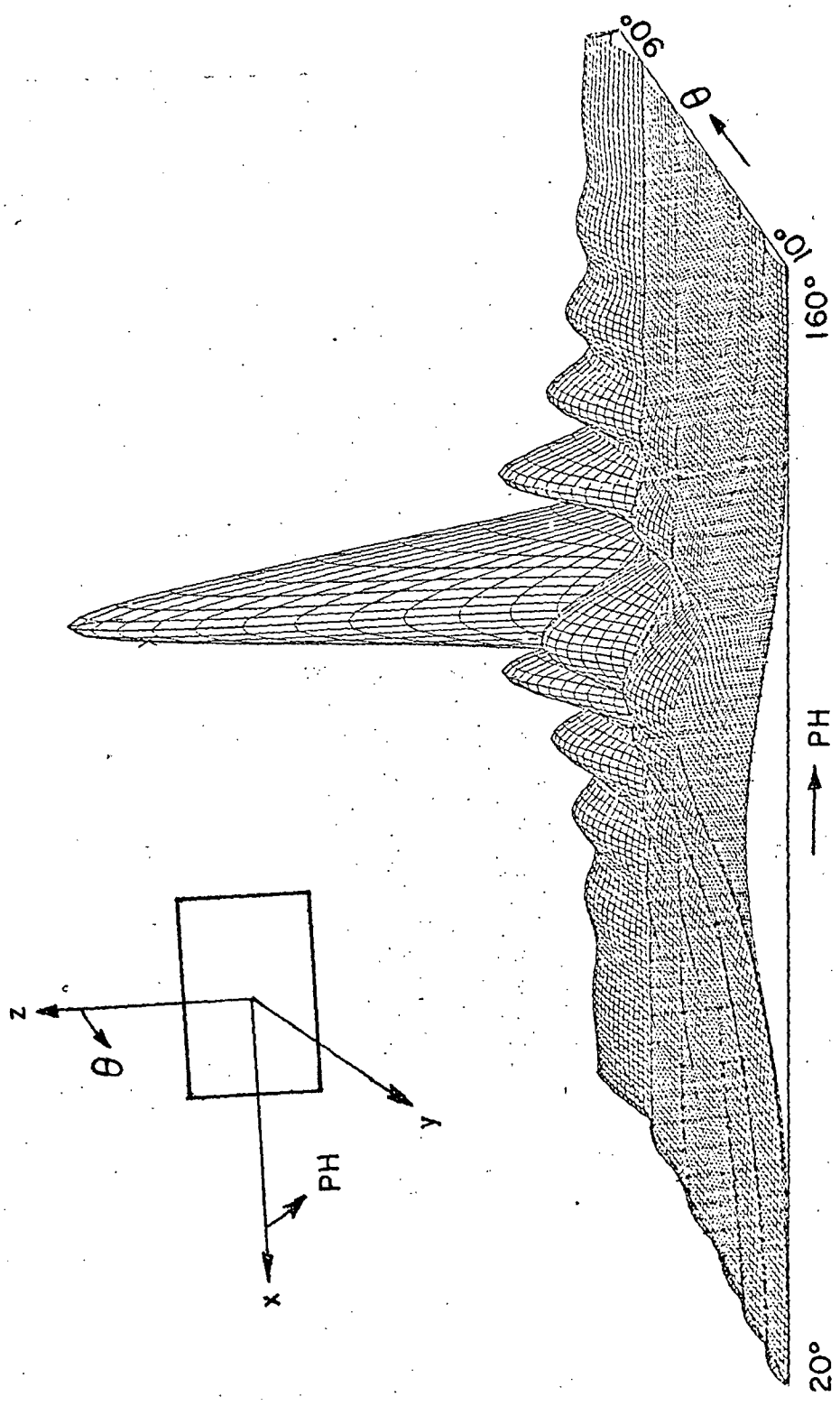
Figure 37. $E_\theta$, three-dimensional RCS pattern plot for a $2\lambda \times 3\lambda$ plate.
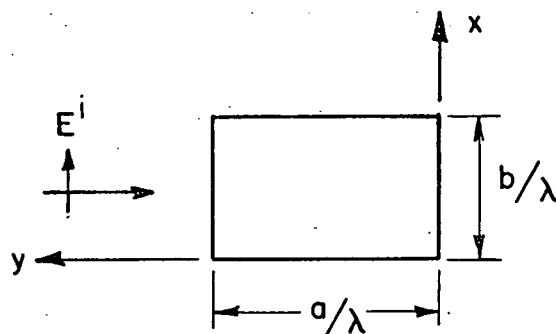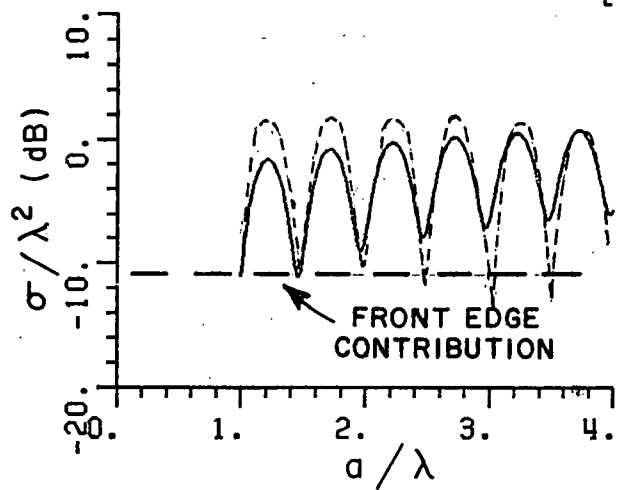
Figure 38.   Edge on RCS of a rectangular plate as a function of
             plate length (b/λ = 0.53).
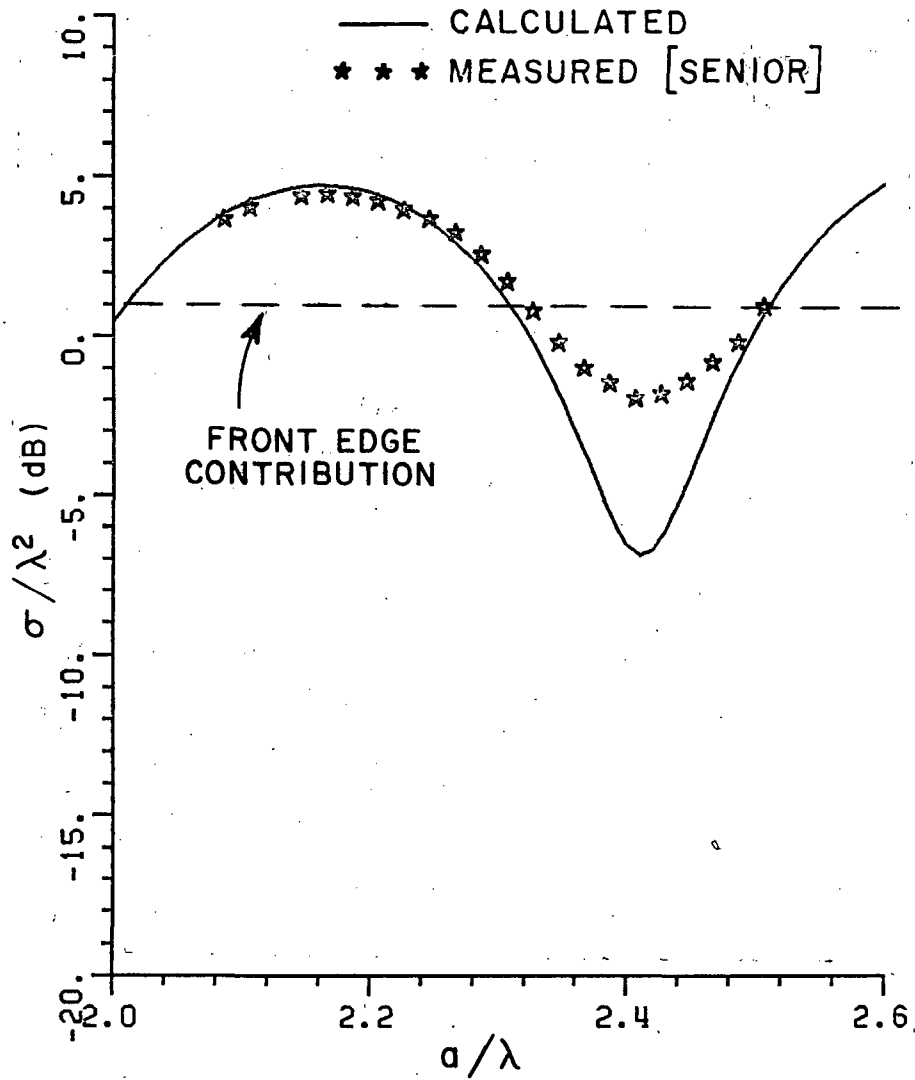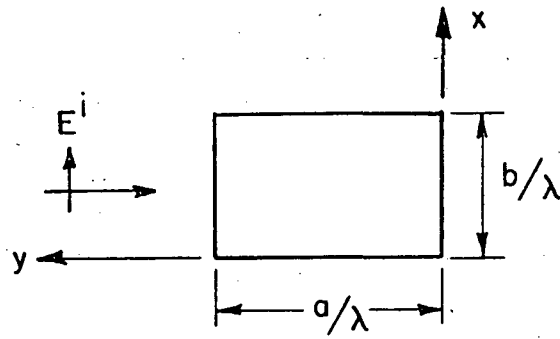
Figure 39. Edge on RCS of a rectangular plate as a function of plate length (b/λ = 2.).
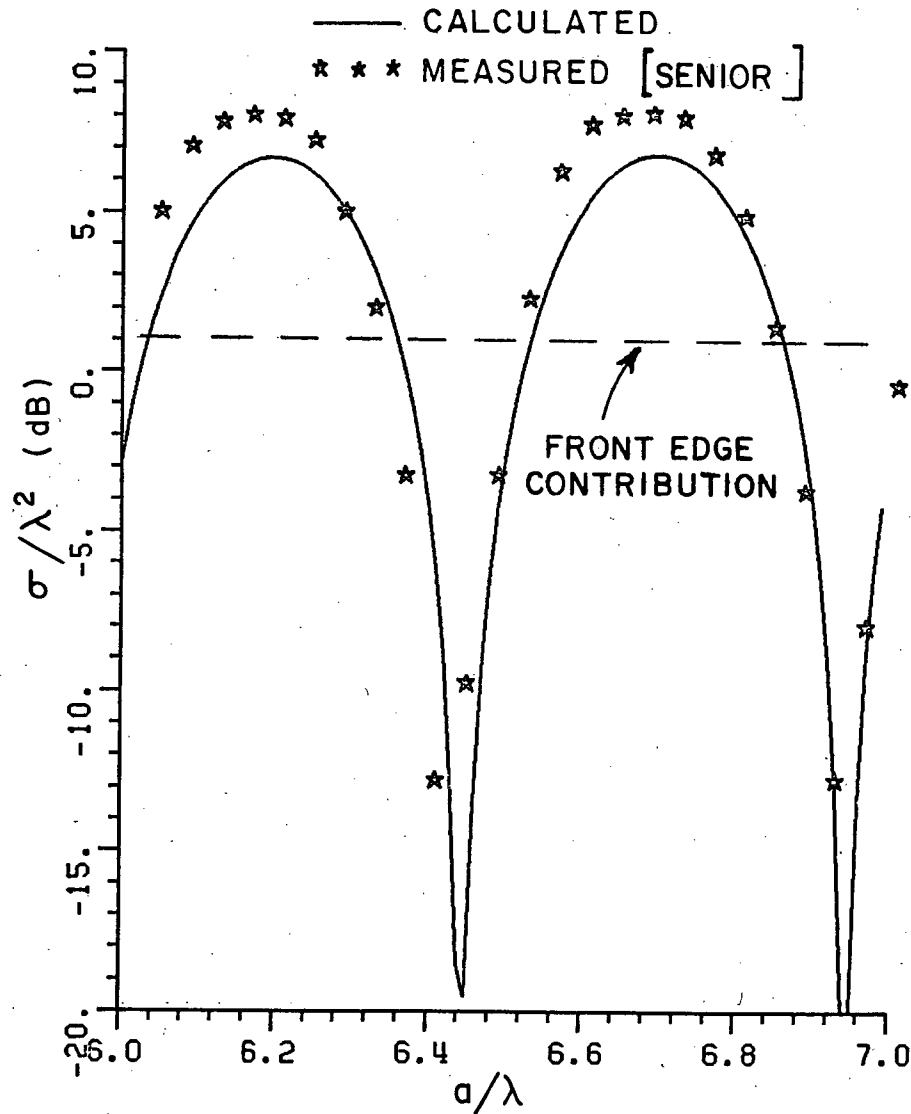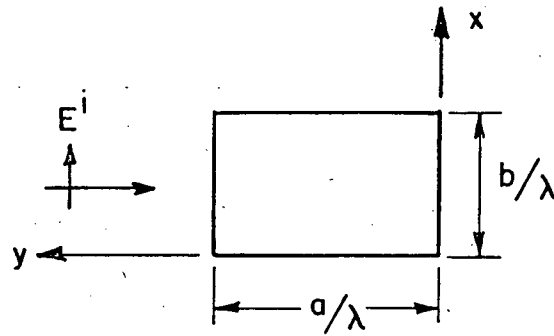
Figure 40. Edge on RCS of a rectangular plate as a function of plate length (b/λ = 2).

1½ inch

1 inch

have not been included in the solution. A three dimensional
plot for the RCS from a $2\lambda \times 3\lambda$ rectangular plate ($E_\theta$ polarization)
is shown in Figure 37. Again, only Equivalent currents corresponding
to first order interactions are used to generate the data shown.
As will be shown in Chapter VI, the higher order interactions play
a very important role in RCS computations in pattern cuts other than
the principal one. These interactions are not included in Figure
37. Figure 38 shows the RCS of a rectangular plate illuminated at
edge on. The plate width is $0.53\lambda$. The results are compared with
measured data obtained by [32], and the results are in good agreement
for plate lengths $3\lambda$ and above. At the lower sizes, the agreement
is in error by several decibles. This indicates that for small plate
widths and lengths, higher order interactions that involve other corners
become significant and should be included in the solution. This be-
comes clearer if one compares Figure 38 and Figure 39. Figure 39
shows the results compared to measured data obtained by [31] for a
$2\lambda$ plate width. Over the same plate lengths range, i.e., ($2\lambda$ - $2.6\lambda$),
the peak to peak deviation is about 0.5 dB in Figure 39, while it
is about 2.5 dB in Figure 38. By examining Figures 38 and 39, one
notices the rapid change of the fields near a pattern null. This
behavior makes the results more sensitive to measurement alignment er-
rors in that region of the pattern. The computed results for the
null value in both Figure 38 and 39 is in error by several decibles.
Note that the measured results span the computed results at $\frac{a}{\lambda} = 2.4$,
which indicates an alignment error in the measured results. In Fig-
ure 40, similar results are presented for a $2\lambda$ plate width. The agree-
ment is good which indicates that the dominant mechanisms for large
plate sizes are the ones discussed earlier.


D.  BACKSCATTERING FROM A GENERAL SHAPE PLATE

In this section, the RCS patterns of different types of plates are
analyzed. Northrop [34] analyzed the plate shown in Figure 41 by
subdividing it into a number of strips. The scattering from each

1 inch

JAB/80
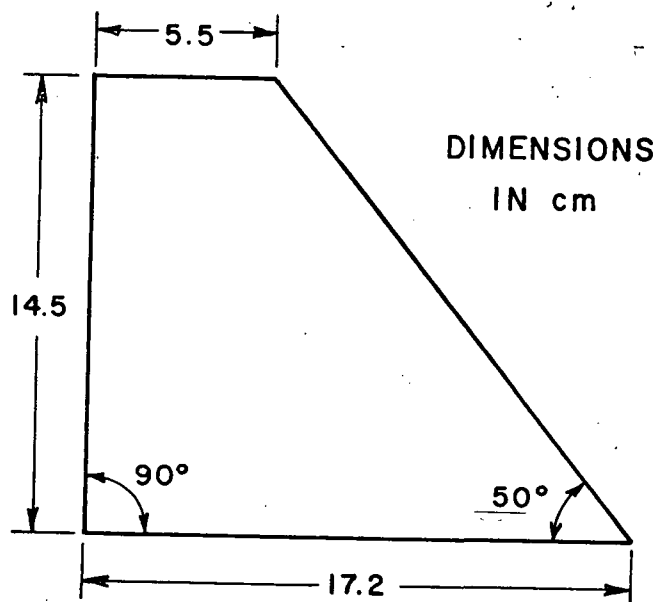
Figure 41. Northrop Fin.

of these strips was obtained using Ufimster's strip solution and then summing these to give the scattering from the plate. This model has two disadvantages:

1. As the plate geometry changes, one has to find the optimum number of strips that give satisfactory results.

2. If a pattern cut other than the principle plane cut is required, the modification of the strip model is not a simple task.

The Equivalent current method used to analyze the different types of plates overcomes all of these difficulties. While the Equivalent current model used in the region of the broadside lobe is in essence a modified version of the strip model, this model reduces to a much

simpler model for other regions of the pattern. It becomes a simple set of line currents around the perimeter of the plate which are used in conjunction with a free space Green's function. Thus, the RCS patterns of these Equivalent-currents-can-readily be computed for any observation point. The results obtained by this method for the H-plane pattern ($E_\theta$ polarization) is shown in Figure 42. The solution actually traces the solution obtained by Northrop and is in good agreement with their measurements. In the region near edge on, i.e., $0^o<PH<30^o$ and $150^o<PH<180^o$, the Equivalent current solution differs from measurements. This may require the use of the edge wave mechanism. It was found that at such high frequencies ($17.76$ GHz), the RCS patterns are extremely sensitive to orientation. In Figure 43, the results obtained by rotating the plate in the x-z plane by a mere $2.5^o$ are shown. A drop by 10 dB is obtained at $PH=0^o$.

The principal H-plane RCS pattern is dominated by the fields diffracted by the front edge. In regions near edge on, the Edge wave mechanism gives a significant contribution. This is seen in Figure 42 ($150^o<PH<180^o$ region) and also in Figure 44 which shows the principal H-plane RCS pattern for Northrop fin at 9.067 GHz compared to measured results obtained by Mr. Chu [35]. Good agreement is obtained and one notes the existance of ripple in the angular region $0^o-60^o$, which is caused by the edge wave mechanism that is not yet included in our solution. Figure 45 shows three different modifications to Northrop fin. The effect of these different modifications on the H-plane RCS pattern is clearly seen in Figure 46 which shows the H-plane pattern for these plates compared to that of the Northrop fin. One notices that a small change in the angles between edges results in more than 13 dB reduction in RCS in these planes. Of course, this reduction is achieved at the expense of an increase elsewhere.

1¼ inch



Figure 42.  $E_\theta$ ,  $\theta = 90^0$  RCS pattern of Northrop Fin at 17.76 GHz.

JAR/80
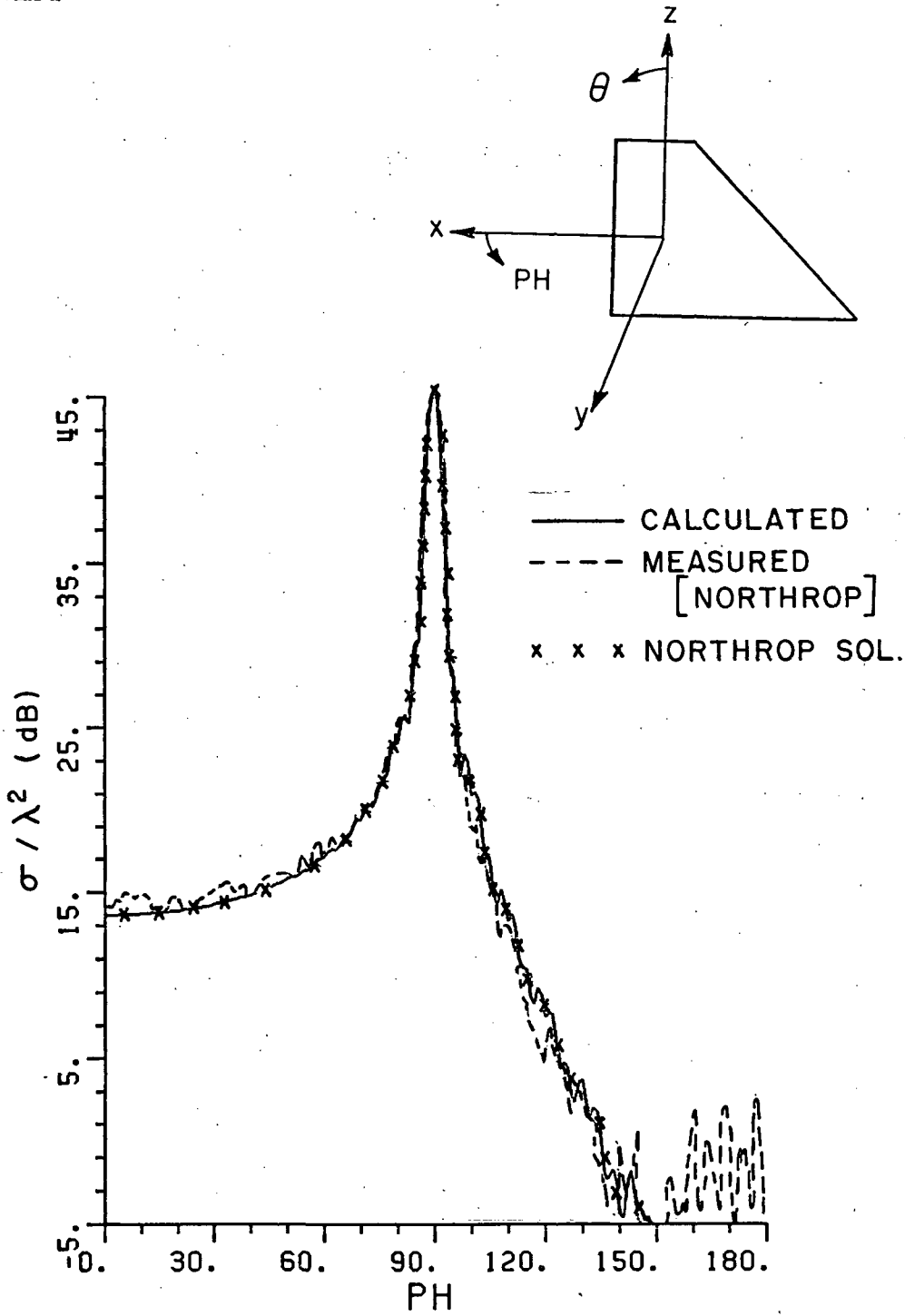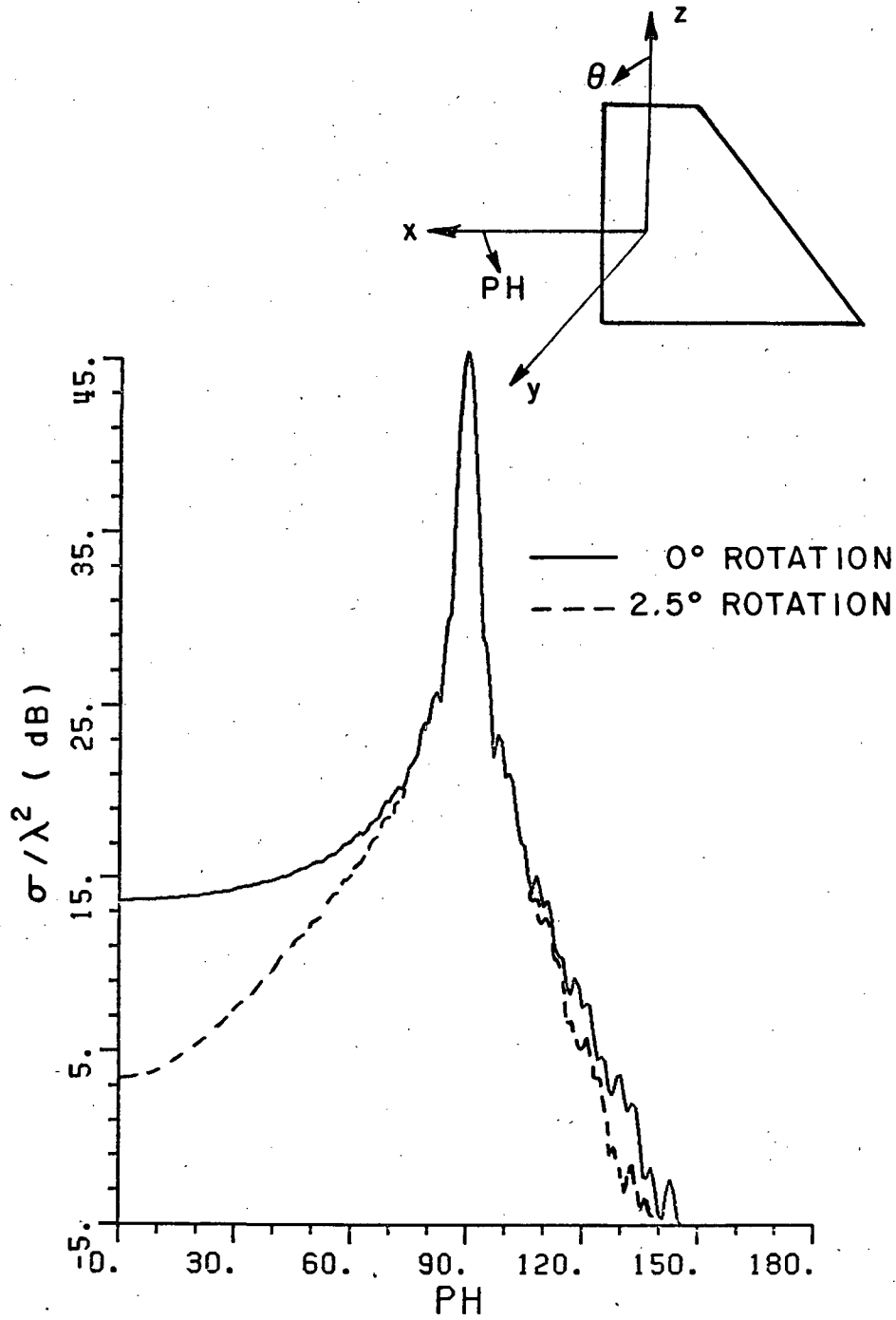
Figure 43. $E_\theta$, effect of plate rotation on $\theta = 90^0$ RCS pattern of Northrop fin at 17.76 GHz.

1 inch

Figure 44. $E_\theta$, $\theta = 90^\circ$ RCS pattern of Northrop fin at 9.067 GHz.
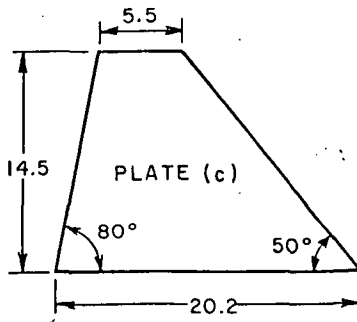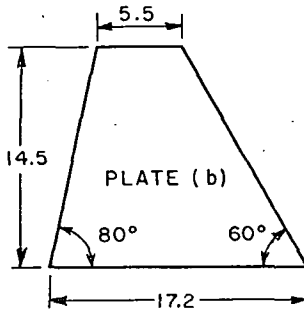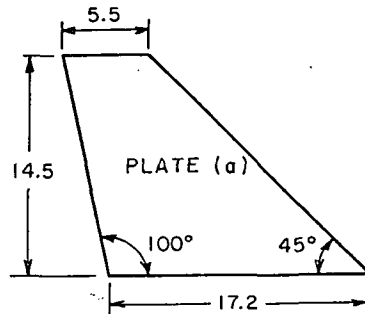
Figure 45. Plate modification of Northrop Fin. All dimensions are in CM.
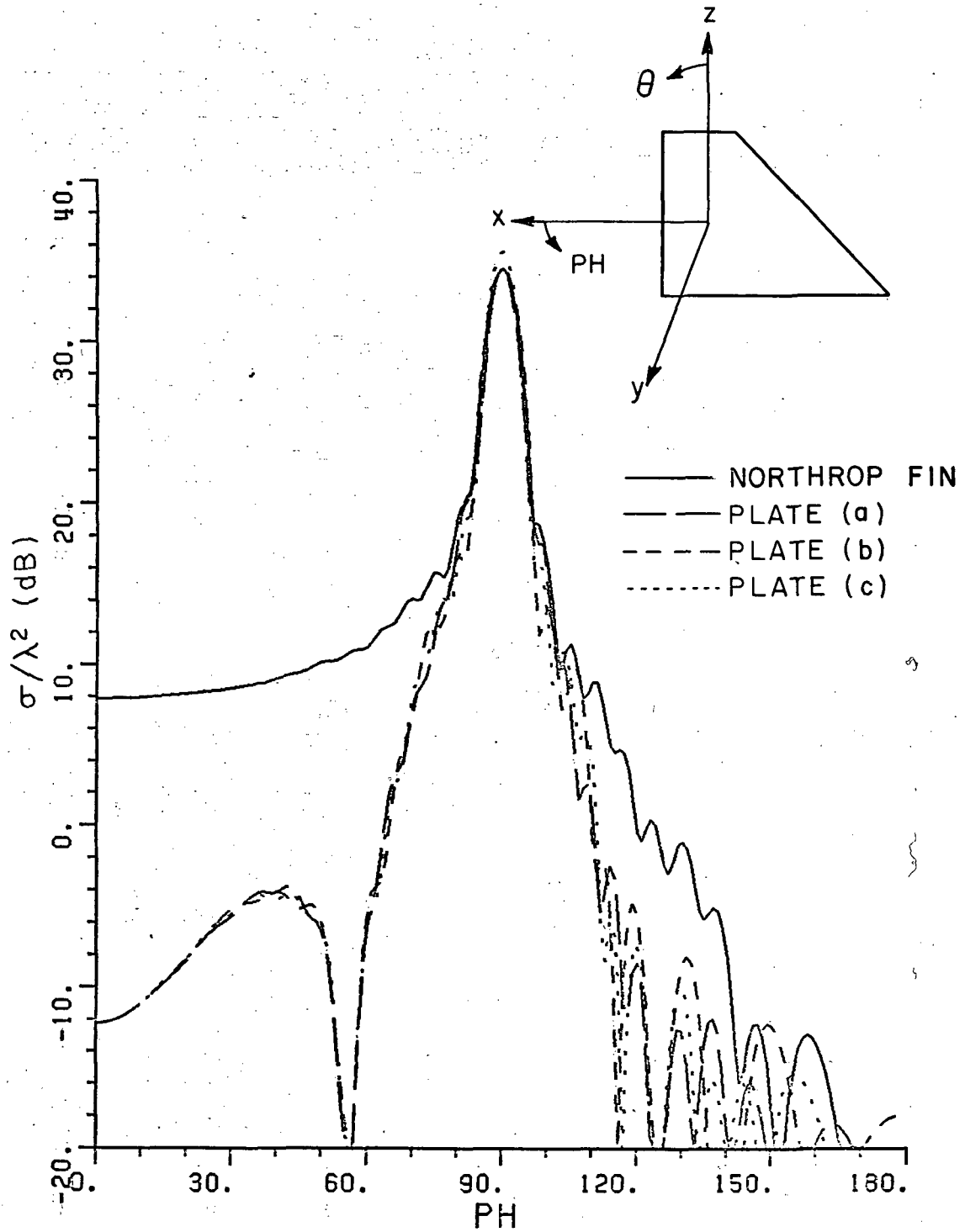
Figure 46. $E_{\theta}$, $\theta = 90^{\circ}$ RCS patterns for the plates shown in Figure (45) compared to Northrop Fin at 9.067 GHz.

The following results to be discussed demonstrate the versitility and power of the Equivalent current method. Only first order diffraction Equivalent currents are used to compute the results. All plates are located in the x-z plane and the H-plane RCS pattern is computed in the plane $\theta = 90^o$.

Figure 47 shows a plate with a curved edge smoothly connected to a straight edge which forms a triangular type junction. The model used in the analysis is shown in Figure 48. It uses three straight edges to model the curved part of the original plate. Figure 49 shows the H-plane RCS pattern ($E_\theta$ polarization) for this plate and the agreement between calculated and measured data is quite good. The deviation between the two results, especially as one approaches the edge on case, is due to several factors. The first is probably the effect of the finite curvature of the curved edge which is not accounted for in this particular model. The second factor is probably the higher order interactions such as edge wave mechanism and multiple diffractions between edges. Figure 50 shows a plate which has no straight edges. The plate model used in the computation is shown in Figure 51. It uses 18 edges to model the curved edges of the original plate. Figure 52 shows the computed H-plane pattern compared to measured data. In the region $90^o < PH < 180^o$, the computed results are quite good. It predicts quite closely the general behavior of the lobe structure. However, in the region $45^o < PH < 90^o$, our model does not predict the deep nulls shown in the measured data. It is our understanding that this lobe structure results from a creeping wave like mechanism associated with the edge curvature. Such mechanisms give rise to two waves which interact with each other to give the deep nulls observed in the measured data. Again the failure of this model to simulate the finite edge curvature is probably the cause of the deviation between the two results. As a first approximation, one can use the edge wave mechanism to simulate the effects of the finite curvature of an edge. Such a method has not yet been included in our solution.
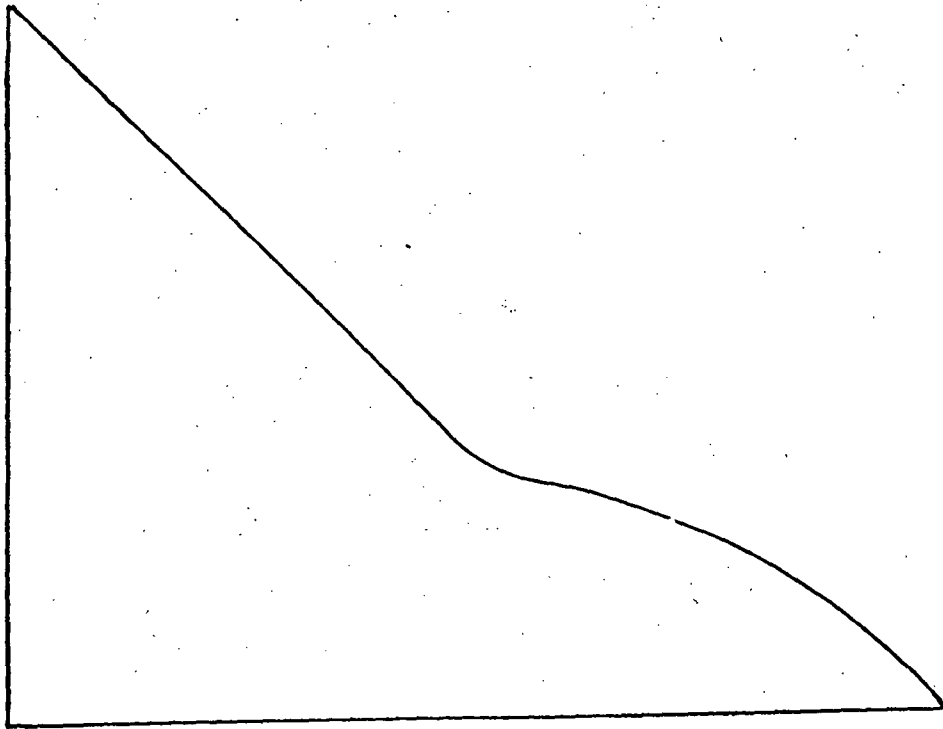
Figure 47. Plate geometry (Actual size).
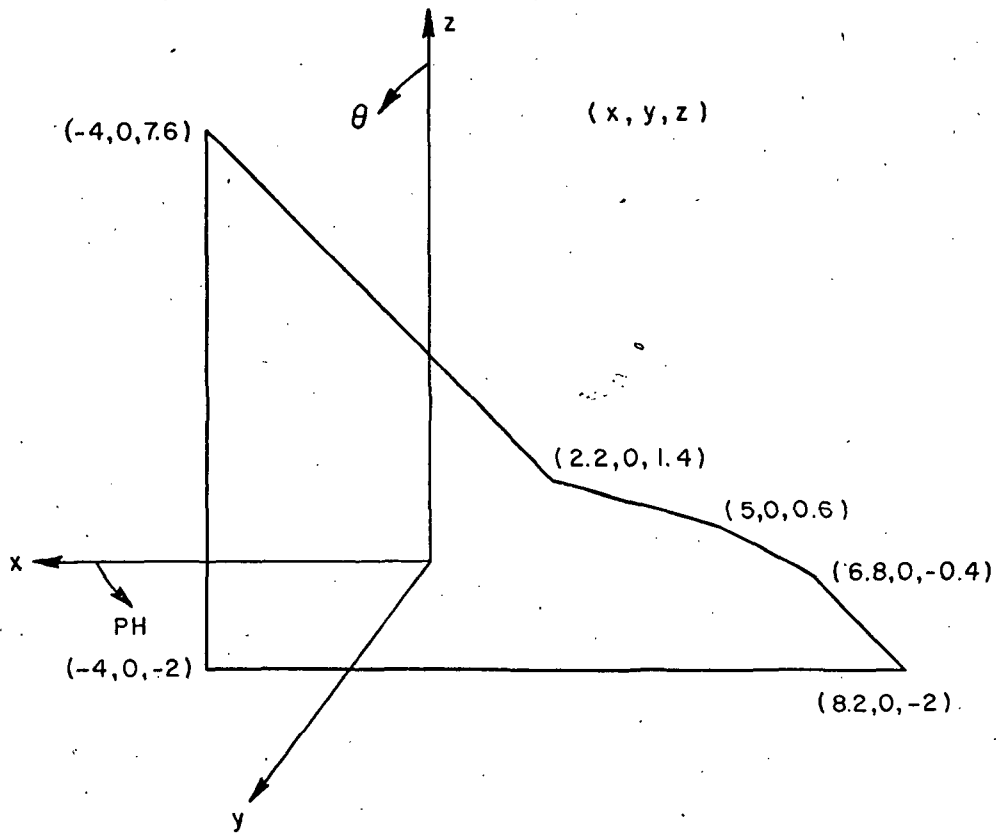
Figure 48.   Model used for the plate shown in Figure 47.
Dimensions in centimeters.

JAN/80
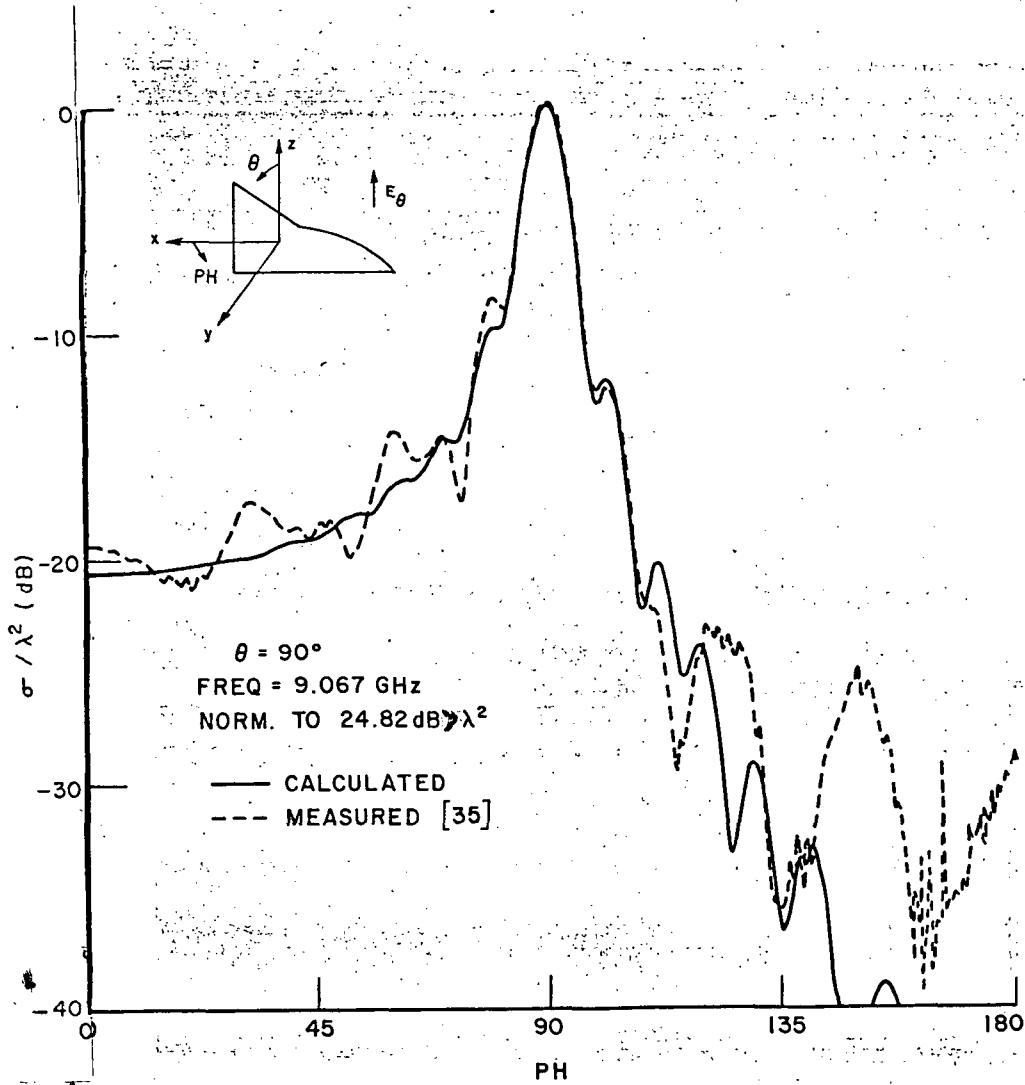
Figure 49.   $E_\theta$, $\theta = 90^\circ$ RCS pattern for the plate shown in Figure 48.

83
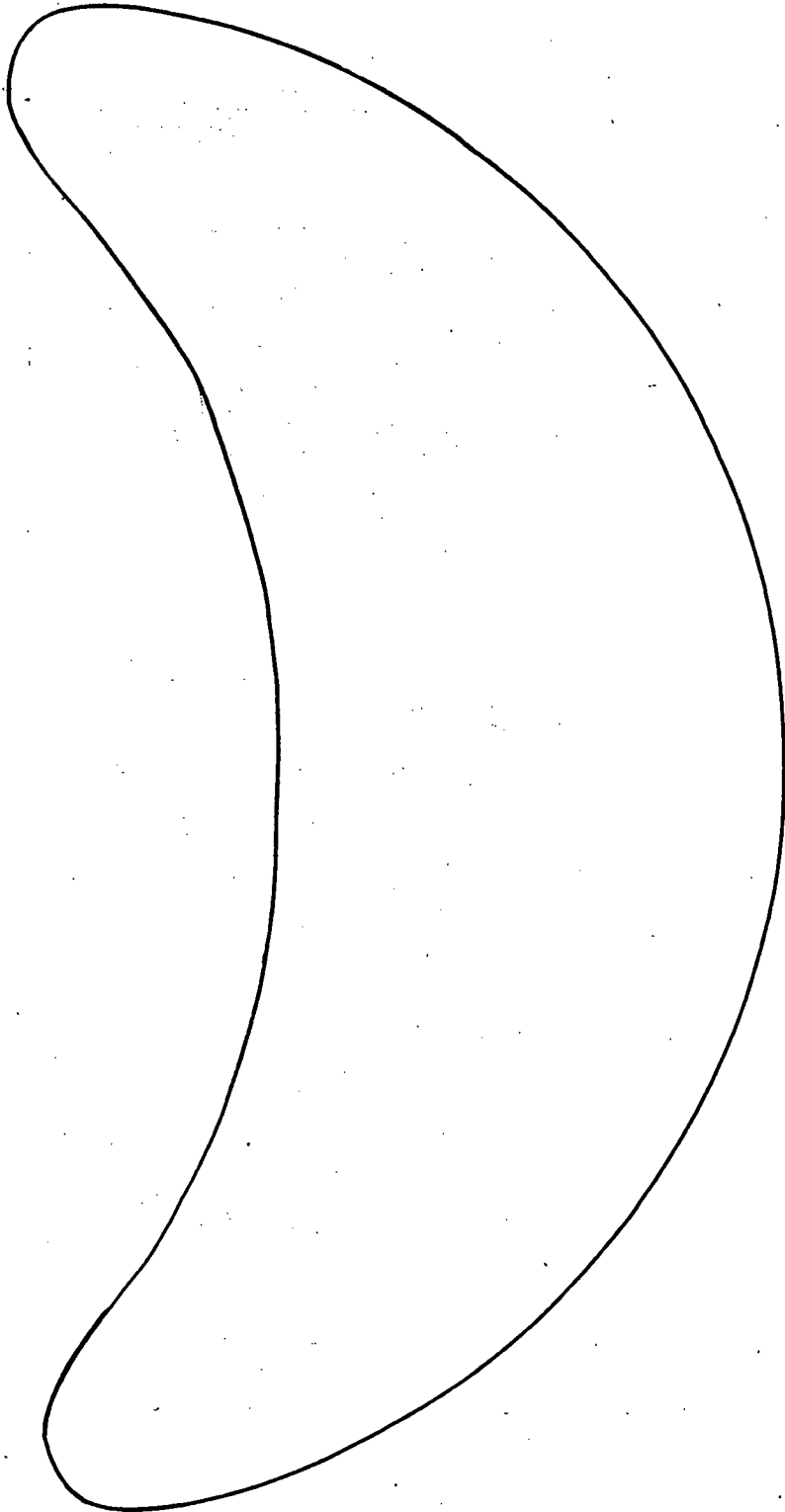
Figure 50. Geometry for a plate with no straight edges (Actual size).
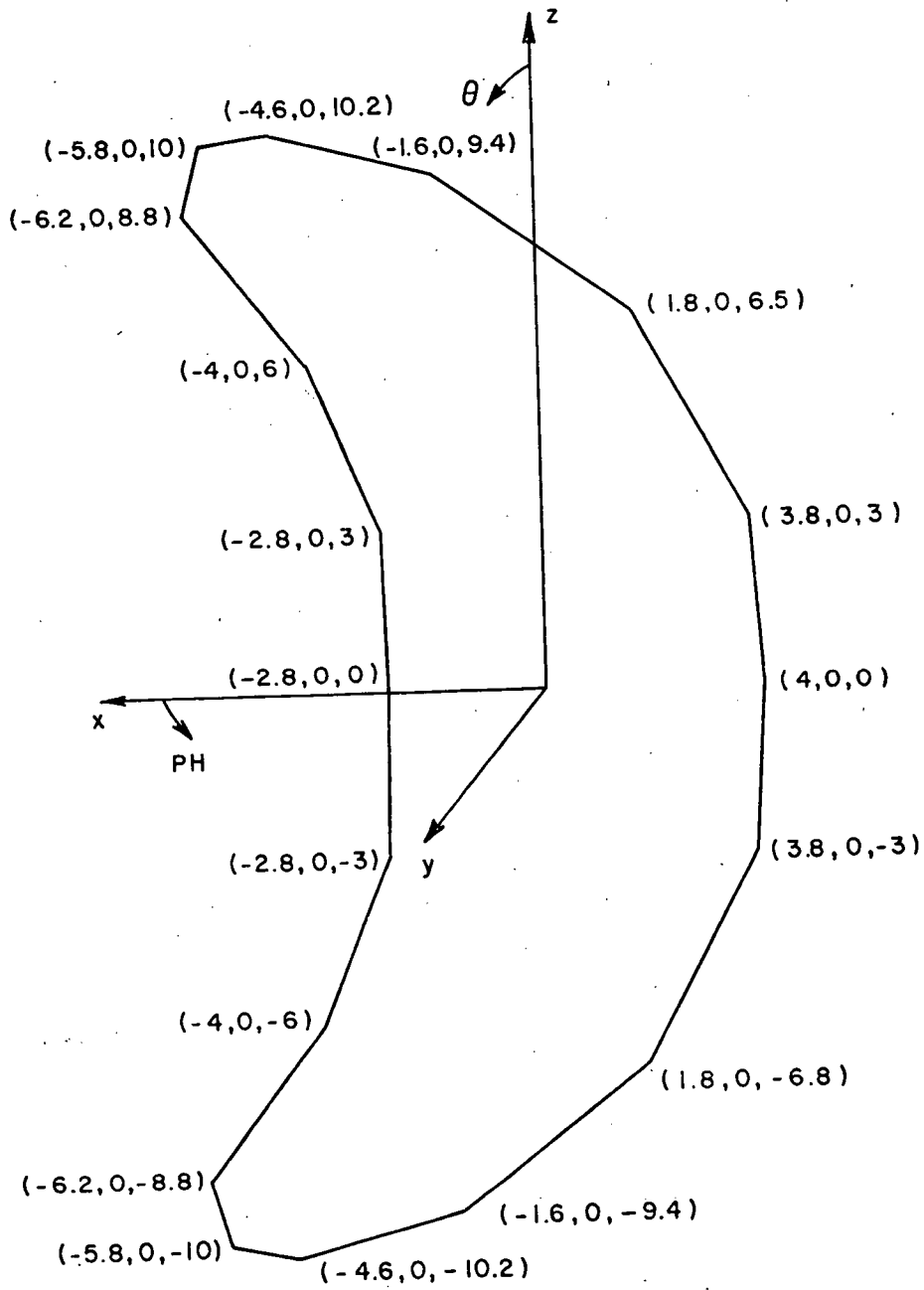
Figure 51.  Model used for the plate shown in Figure 50. Dimensions in centimeters.
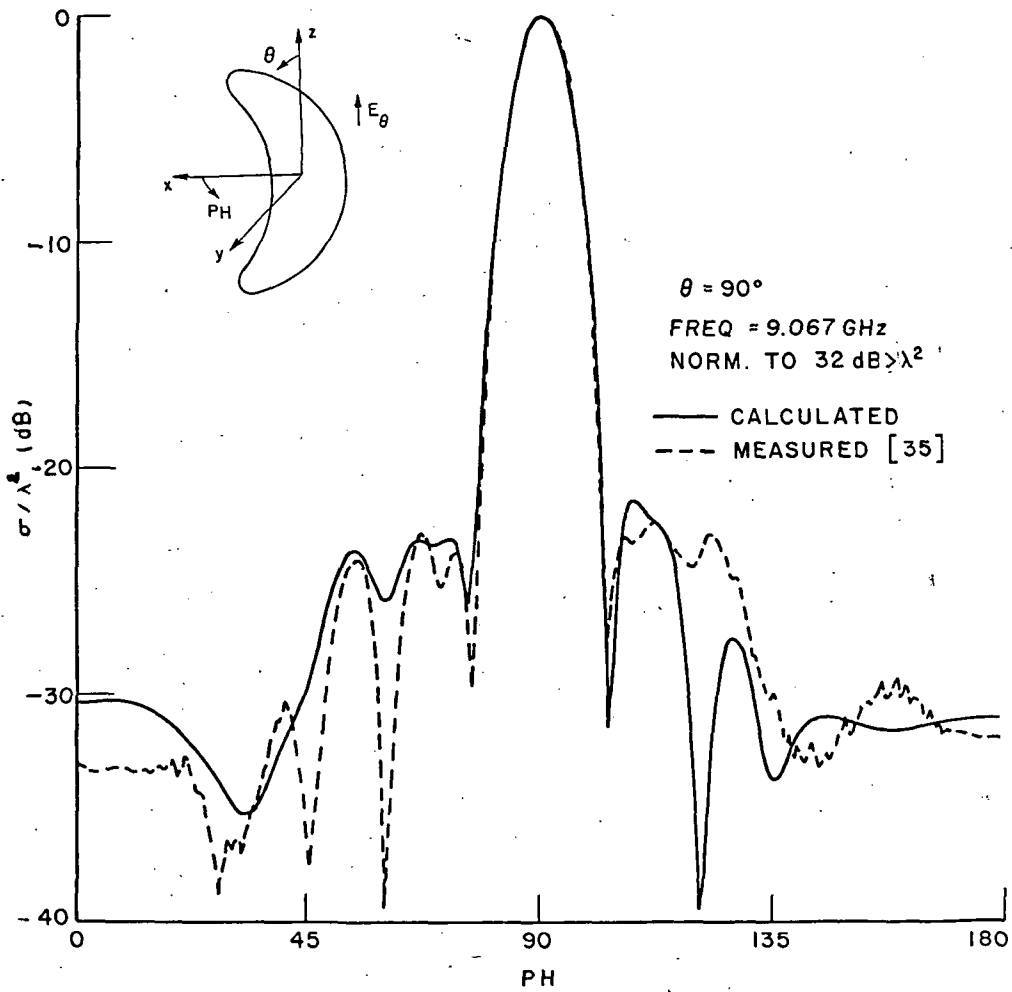
Figure 52.   $E_\theta$,   $\theta = 90^0$ RCS pattern for the plate shown in Figure 50.

JAB/80

The final plate analyzed is the one shown in Figure 53. This plate involves a large triangular section. The H-plane pattern is shown in Figure 54. The computed results are compared to measured data and good agreement is obtained. The deviation between the two results in the region $0^O < PH < 30^O$ is probably due to higher order inter-actions involving the edge wave mechanism. Such interactions are going to be discussed in the following chapters.

E.  BACKSCATTERING FROM A DISK

The closed form solutions for scattering from a perfectly conducting thin circular disk has been available for many years [36,37]. Several authors worked on a more efficient way to calculate the scattered field. DeVore, et. al., [38], succeeded in reducing the difficulty in obtaining the Eigenvalues for oblique incidence. Bechtel [39] used Keller Geometrical Theory of Diffraction to compute the disk RCS for both principal polarizations using first order diffraction. His results were in good agreement with measured data for angles less than $30^O$ from broadside. For angles greater than $30^O$, his E-plane patterns deviate considerably from measured data. This is due to neglecting the higher order interactions. The H-plane pattern, on the other hand, deviates from measured data due to neglecting the effect of creeping waves for near edge on incidence as discussed by Ryan, et. al [40]. A more detailed list of references concerning scattering from a disk is shown in [26].

In this section we use the Equivalent current method to compute the H-plane RCS pattern of a disk using the Equivalent currents corres-ponding to first order diffraction. The geometry of the problem is shown in Figure 55. A disk of radius a is located in the y-z plane. The pattern cut is taken in the x-y plane. The disk is modeled by a multi-sided plate. Figure 56 shows two plate models; one has 8 sides and the other has 12. The number of sides used is limited by its electrical length which should be of the order of a wavelength.
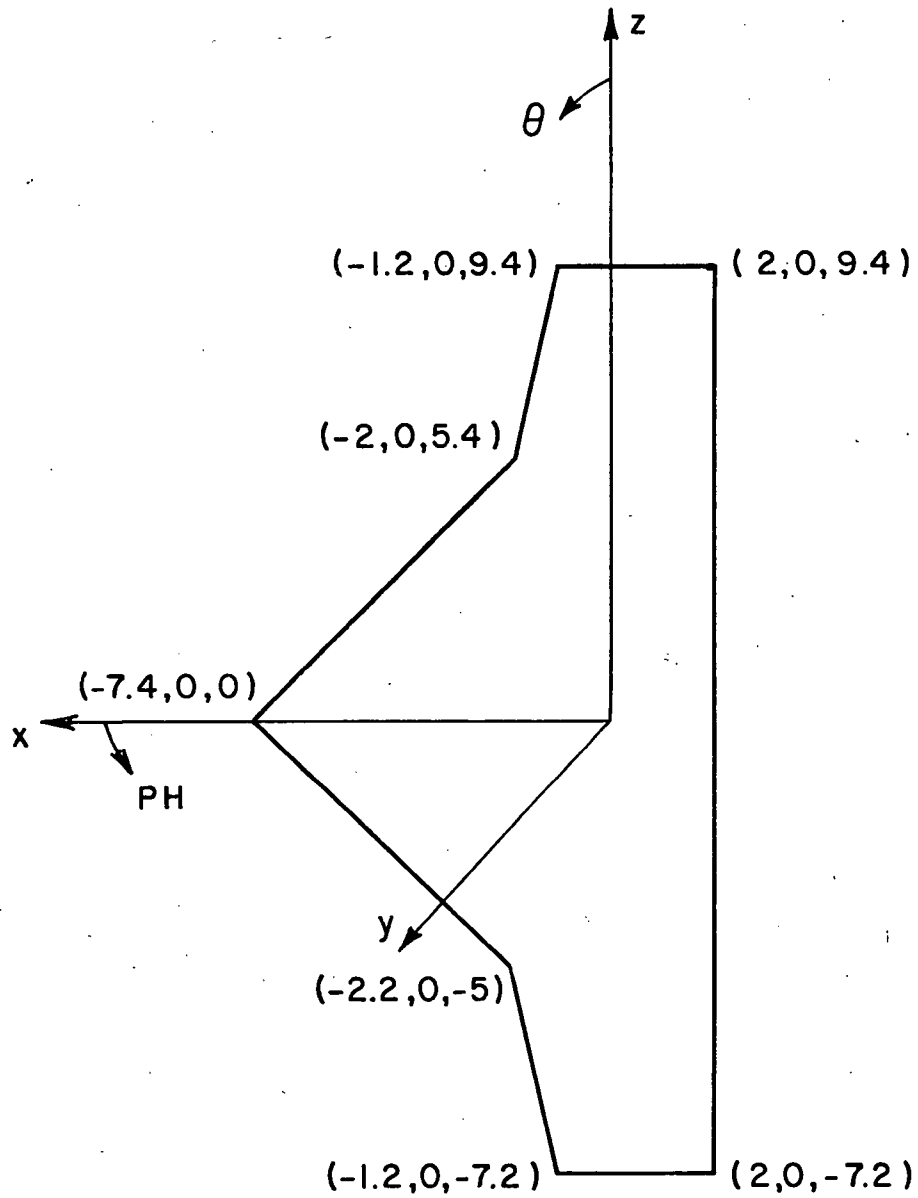
Figure 53.  Plate geometry.  Dimensions in centimeters.

Figure 54.  $E_\theta$,  $\theta = 90^0$ RCS pattern for the plate shown in Figure 53.

1 inch

1½ inch

2 inch Chapter Line
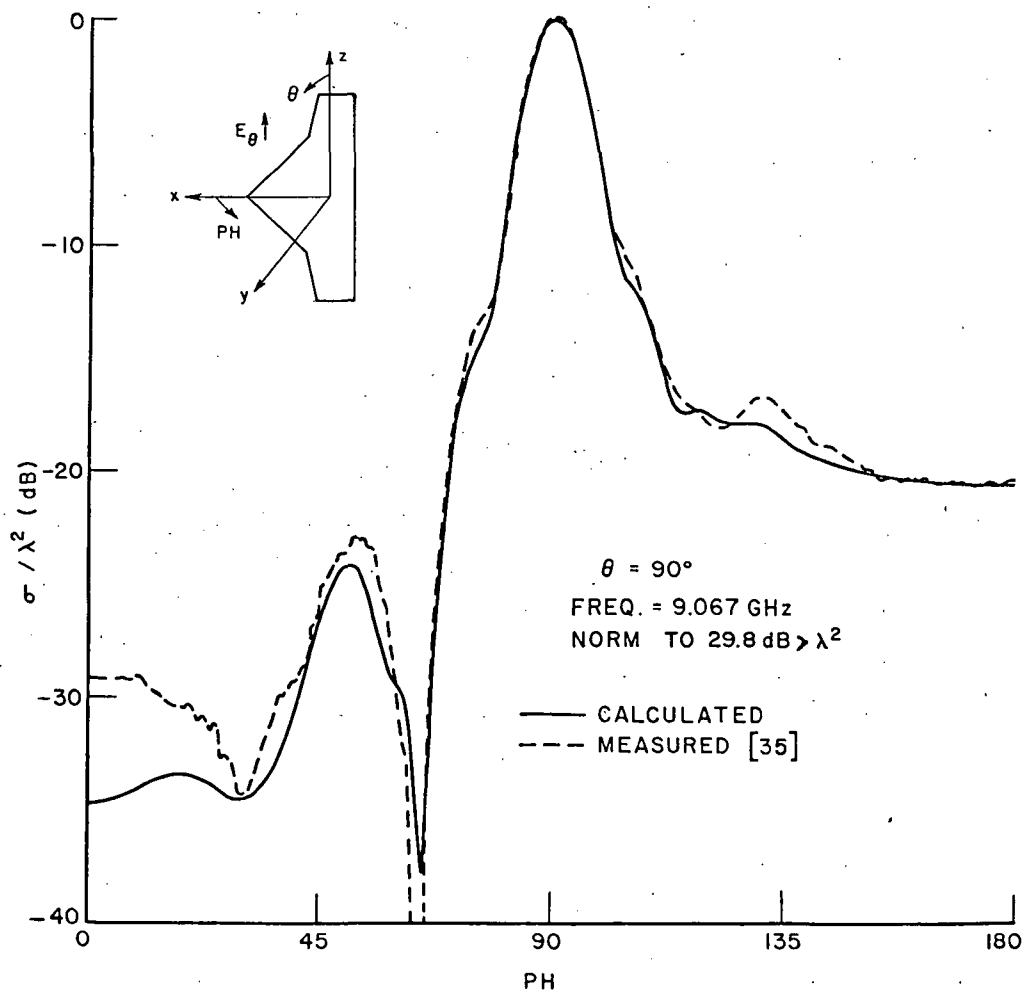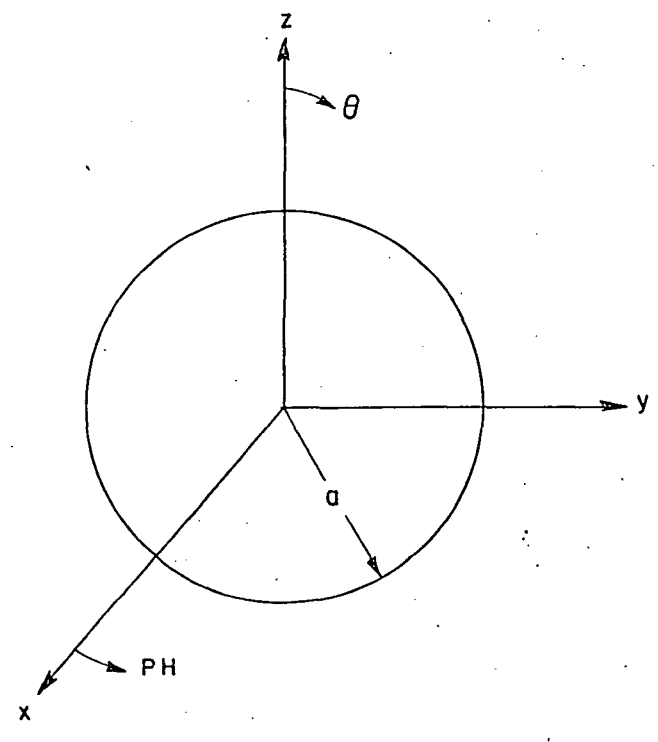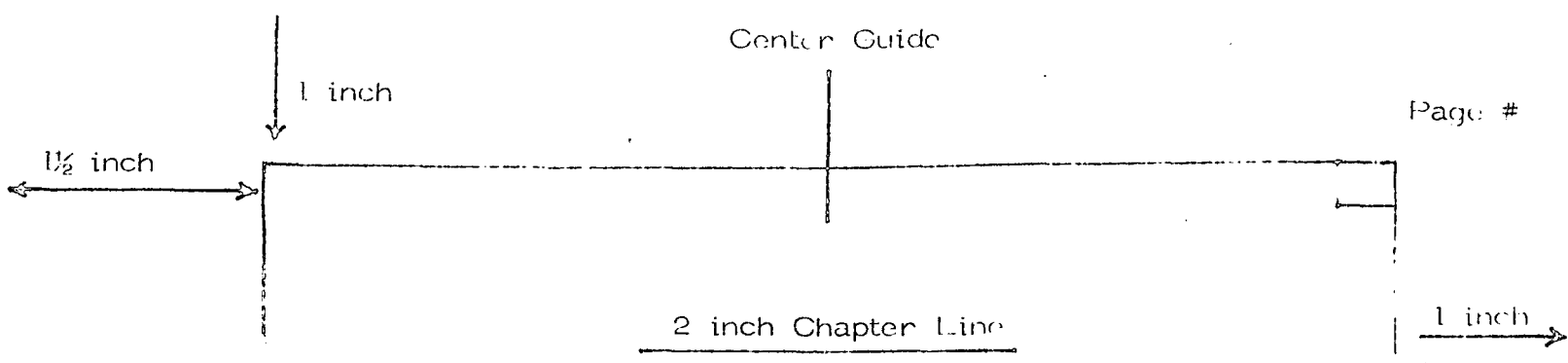
1 inch



Figure 55.  Disk geometry.

1st page Chapter end line

— — — — — — — —  1st page Chapter end line

4th TEXT LINE

1 inch

JAB/80
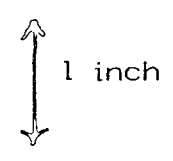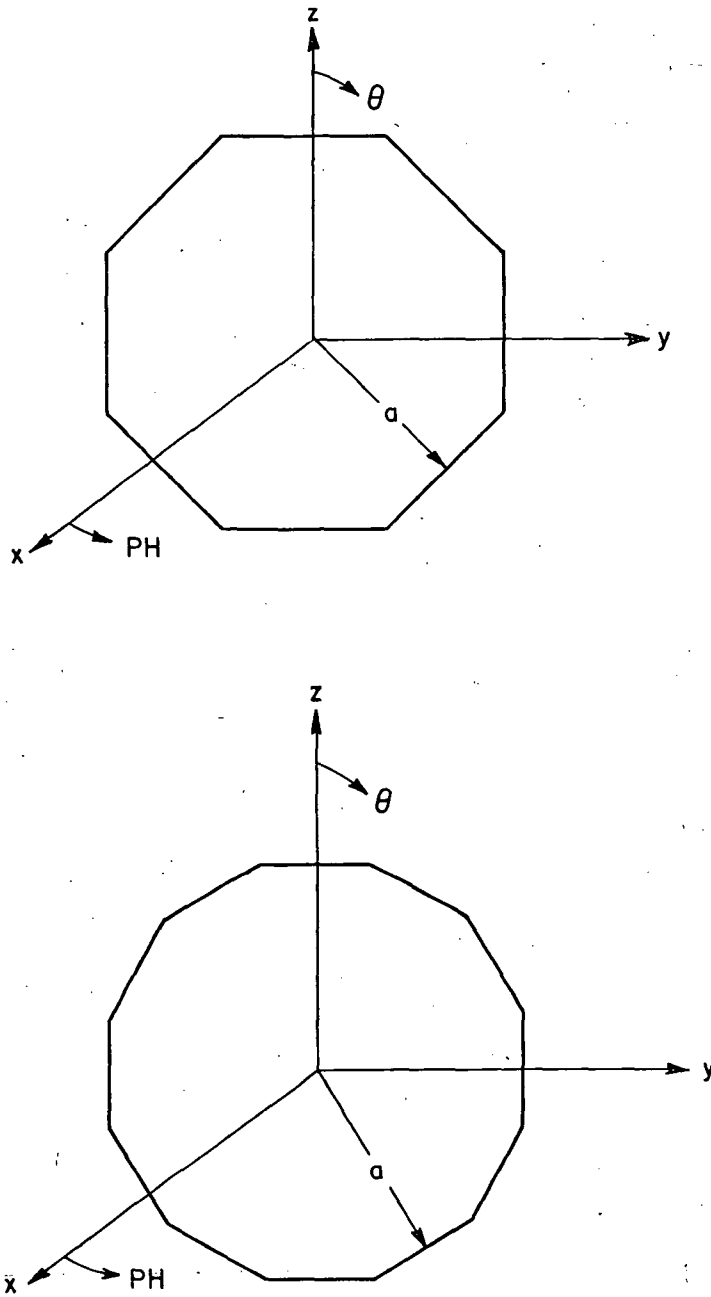
Figure 56.   Disk models geometry.

The results presented in this section are all compared with an exact solution obtained by using a computer code made available by Professor Hodge [41]. This exact solution is based on Andrejewski's rigorous eigenfunction solution to the disk scattering problem. The first order Electric Equivalent currents are used to compute the H-plane pattern from the two disk models shown in Figure 56 for different plate sizes. Due to the symmetry of the problem, the pattern is computed for pattern angles between zero and 90 degrees. Figures 57-58 show the H-plane RCS for the 8 and 12 sided plates respectively. The plate size is ka=8.28. The results are compared to Bechtel's solution [39] where he used Keller's Geometrical Theory of Diffraction to compute the disk RCS as well as the exact solution. Both solutions are in good agreement with the exact one in the main lobe region. As one moves the incidence angle toward edge on incidence, both solutions start to deviate from the exact case. This is due to the fact that in the region near edge on, the creeping wave mechanism [40] contributes extensively to the RCS pattern. Our solution does not include this mechanism. Hence, these results would indicate the angular extent for which the creeping wave is significant. One could use the forward scattering of the edge wave mechanism to simulate the creeping wave effect. However, the corner diffraction coefficient does not adequately treat this case as yet. Figures 59-66 show the H-plane pattern for different plate size and for both models. As the plate size is increased, the 12 sided plate model gives better results than the 8 sided plate model in the range $0^o < PH < 50^o$. This is because the 12 sided plate models the disk more closely than the 8 sided one, as the plate size is increased. Note also that the 12 sided plate always gives a lower level at edge on compared to that of the 8 sided plates. This is due to the edge size which is smaller in the 12 sided model. The results shown in Figures 57-66 are computed in a pattern cut that passes through the plate edges as shown in Figure 56. Figures 67-68 show the results obtained for two plate sizes, ka=8.28 and 20, for the case when the pattern cut is taken such that it passes through two plate corners in a symmetrical way. The region
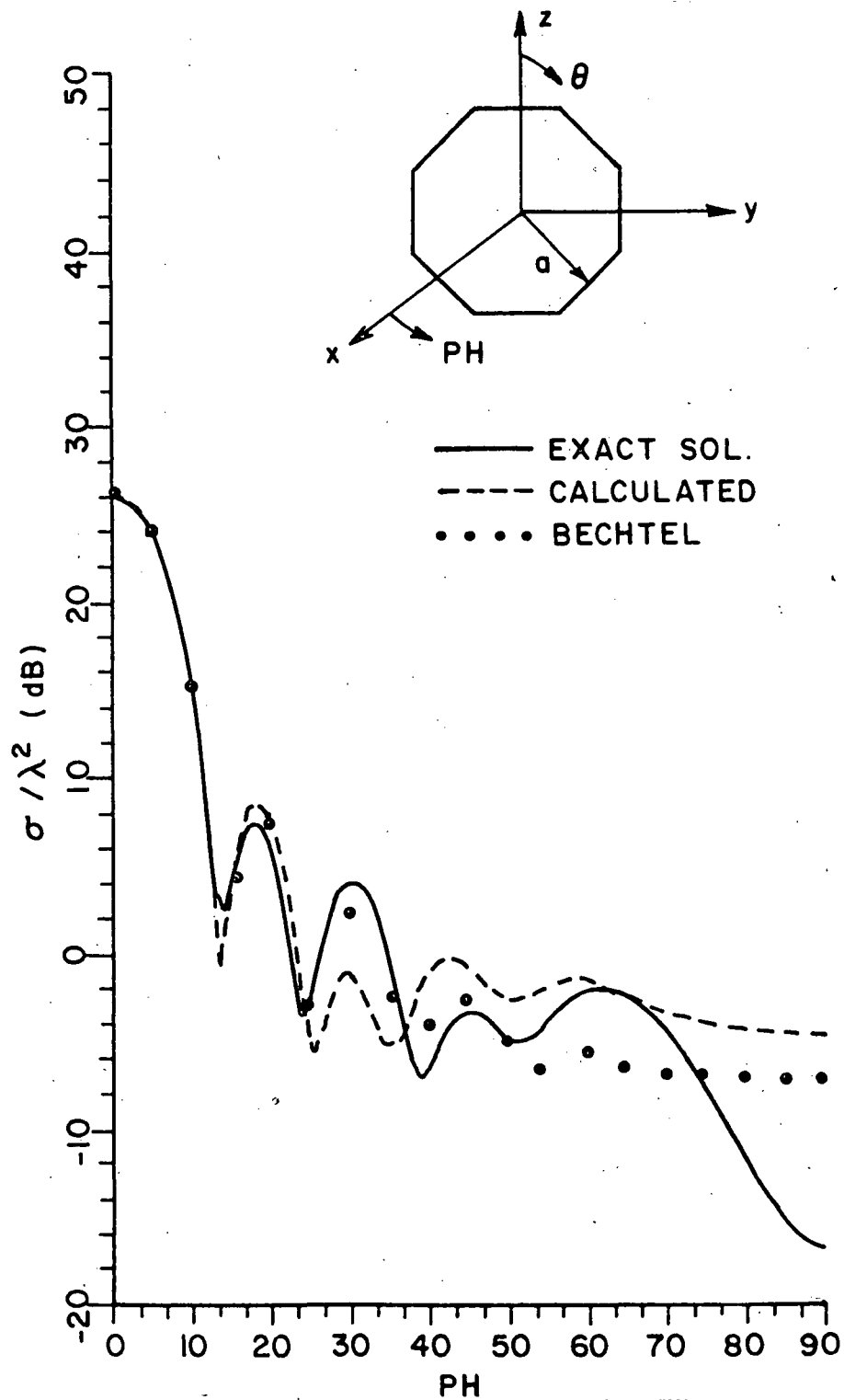
Figure 57. $E_\theta$, $\theta = 90^\circ$ RCS pattern for the 8 sided disk model. (ka = 8.28).
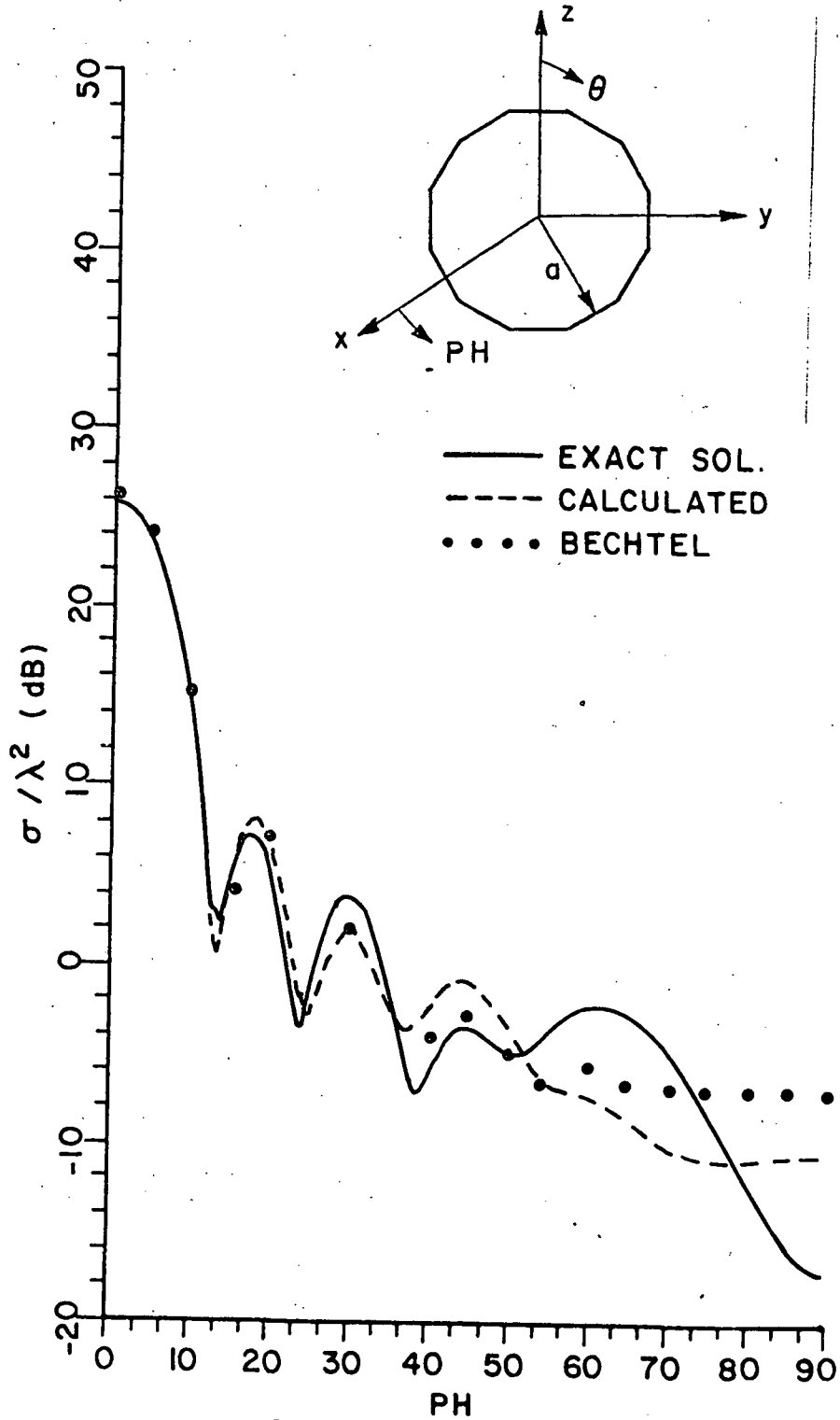
1½ inch

1 inch



Figure 58. $E_\theta$, $\theta = 90^\circ$ RCS pattern for the 12 sided disk model (ka = 8.28).

1 inch

JAB/80
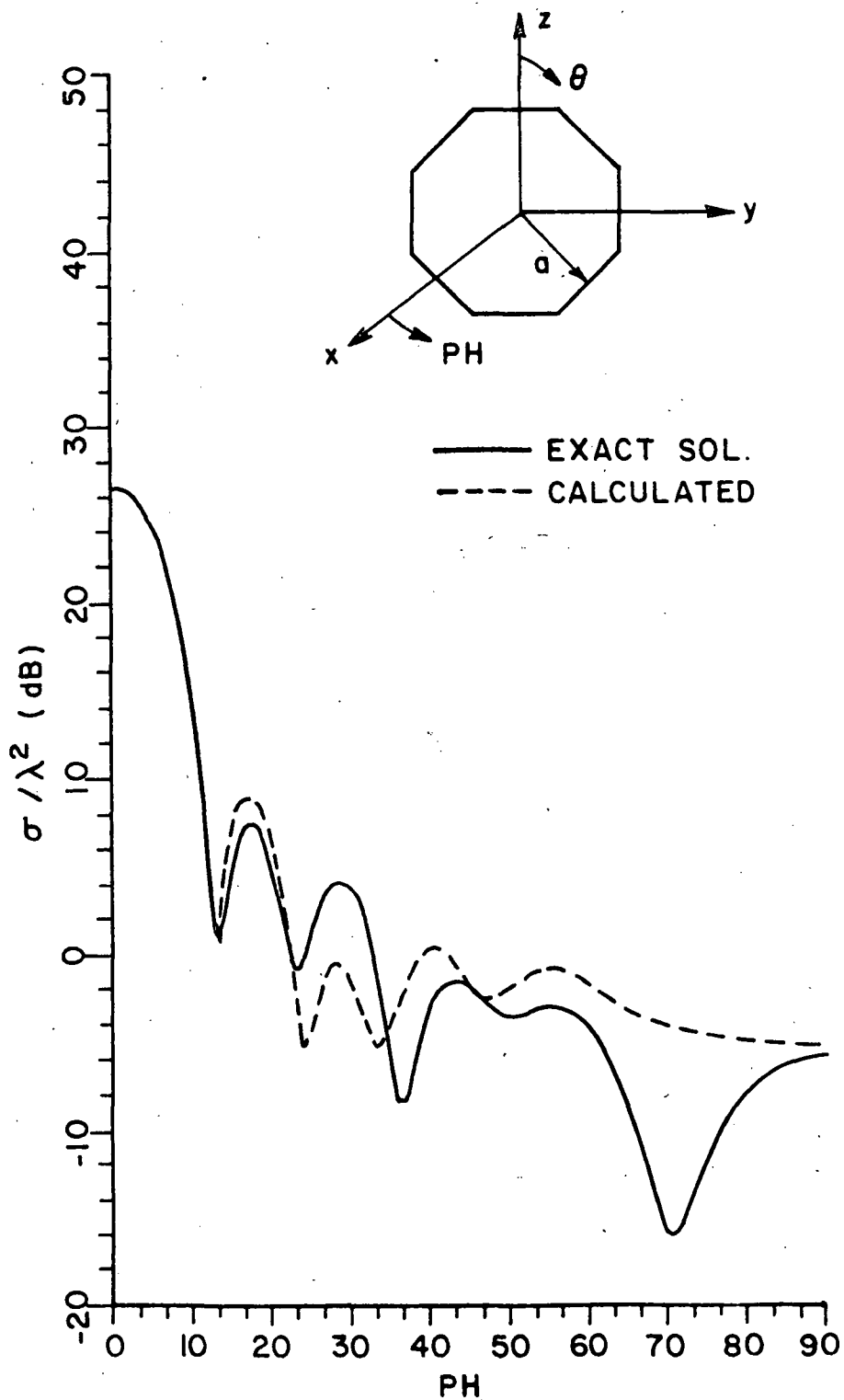
Figure 59.  $E_\theta$, $\theta = 90^\circ$ RCS pattern for the 8 sided disk model (ka = 8.59).
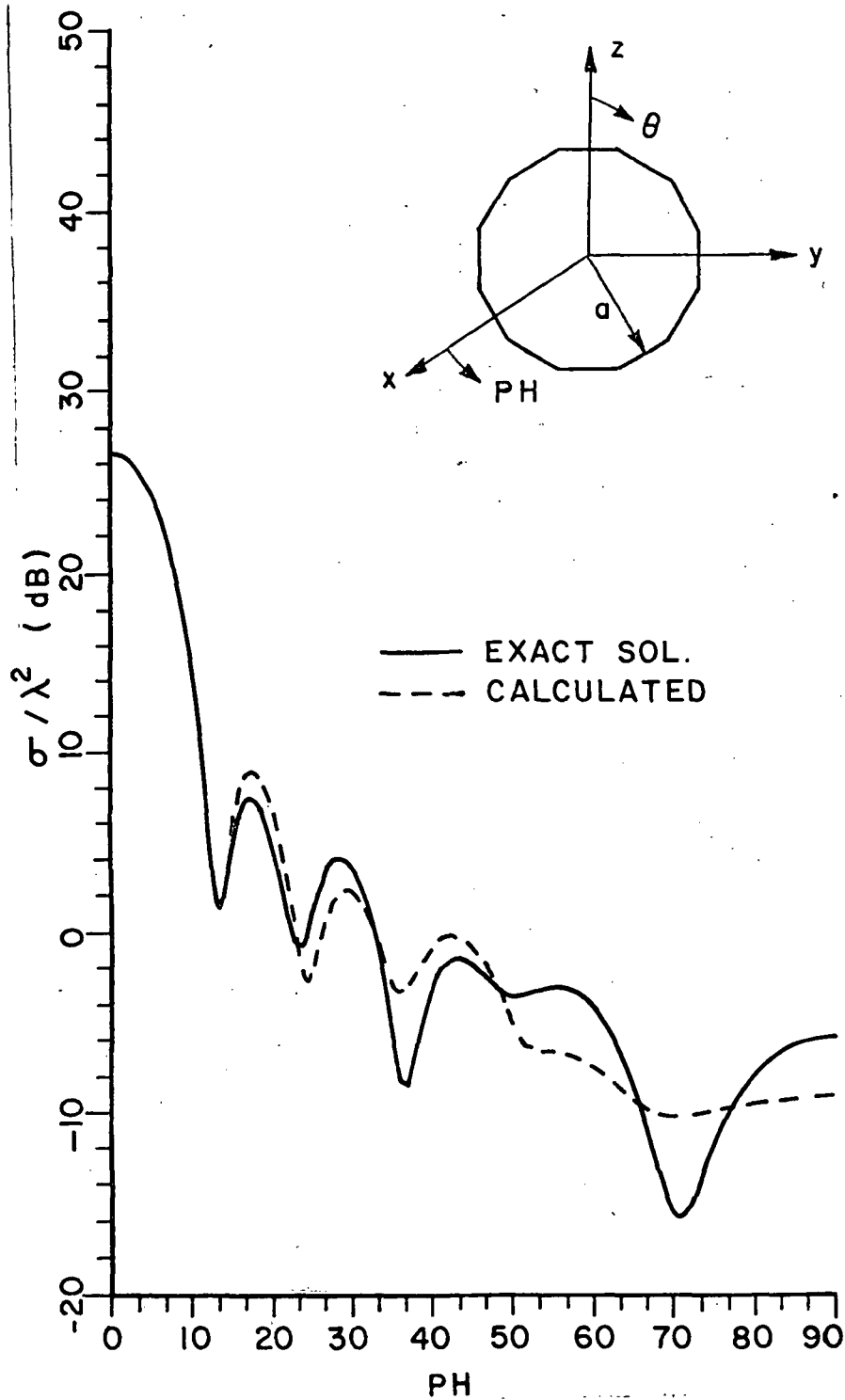
Figure 60. $E_\theta$, $\theta = 90^0$ RCS pattern for the 12 sided disk model (ka = 8.59).
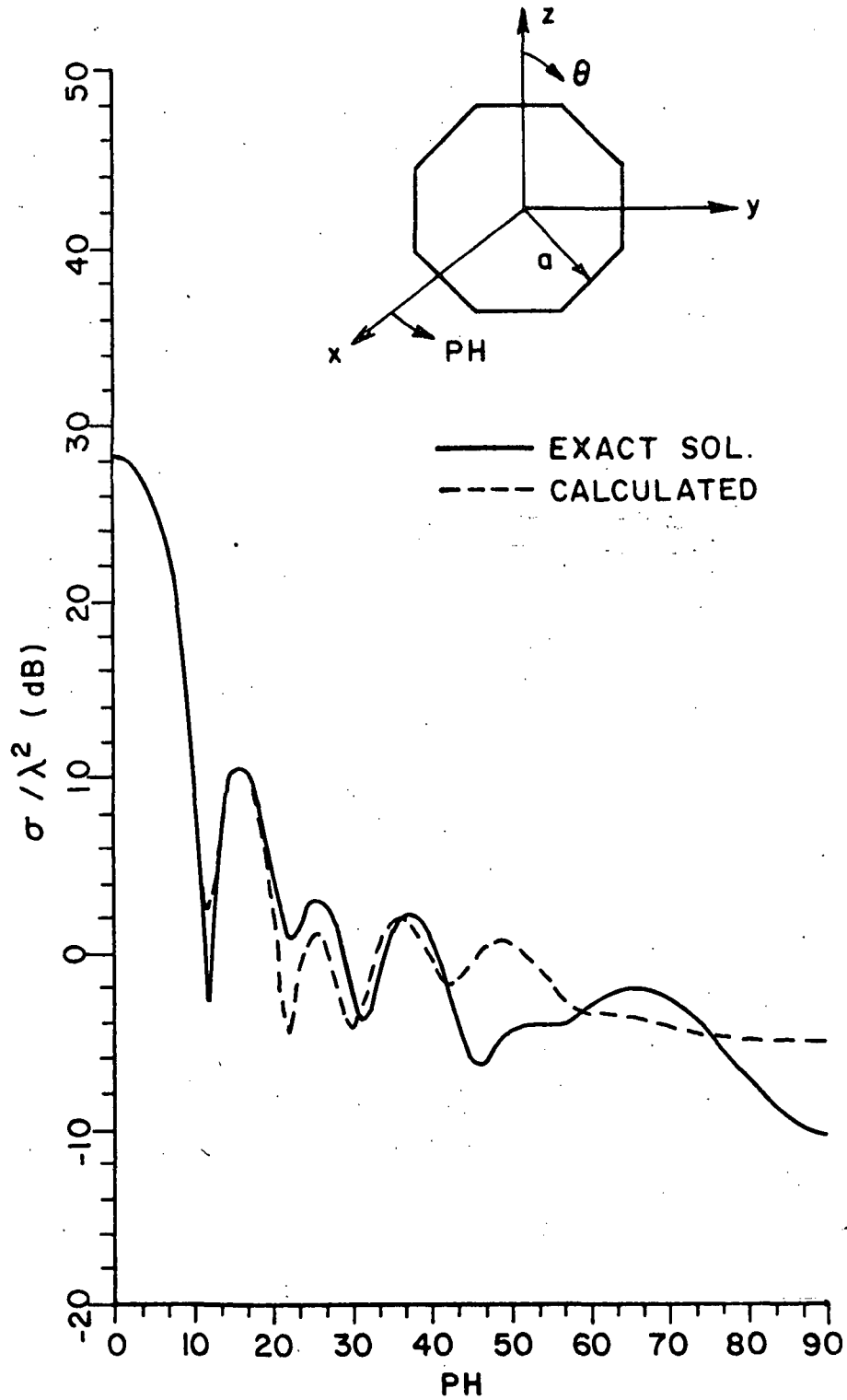
Figure 61. $E_\theta$, $\theta = 90^\circ$ RCS pattern for the 8 sided disk model ($ka = 9.45$).
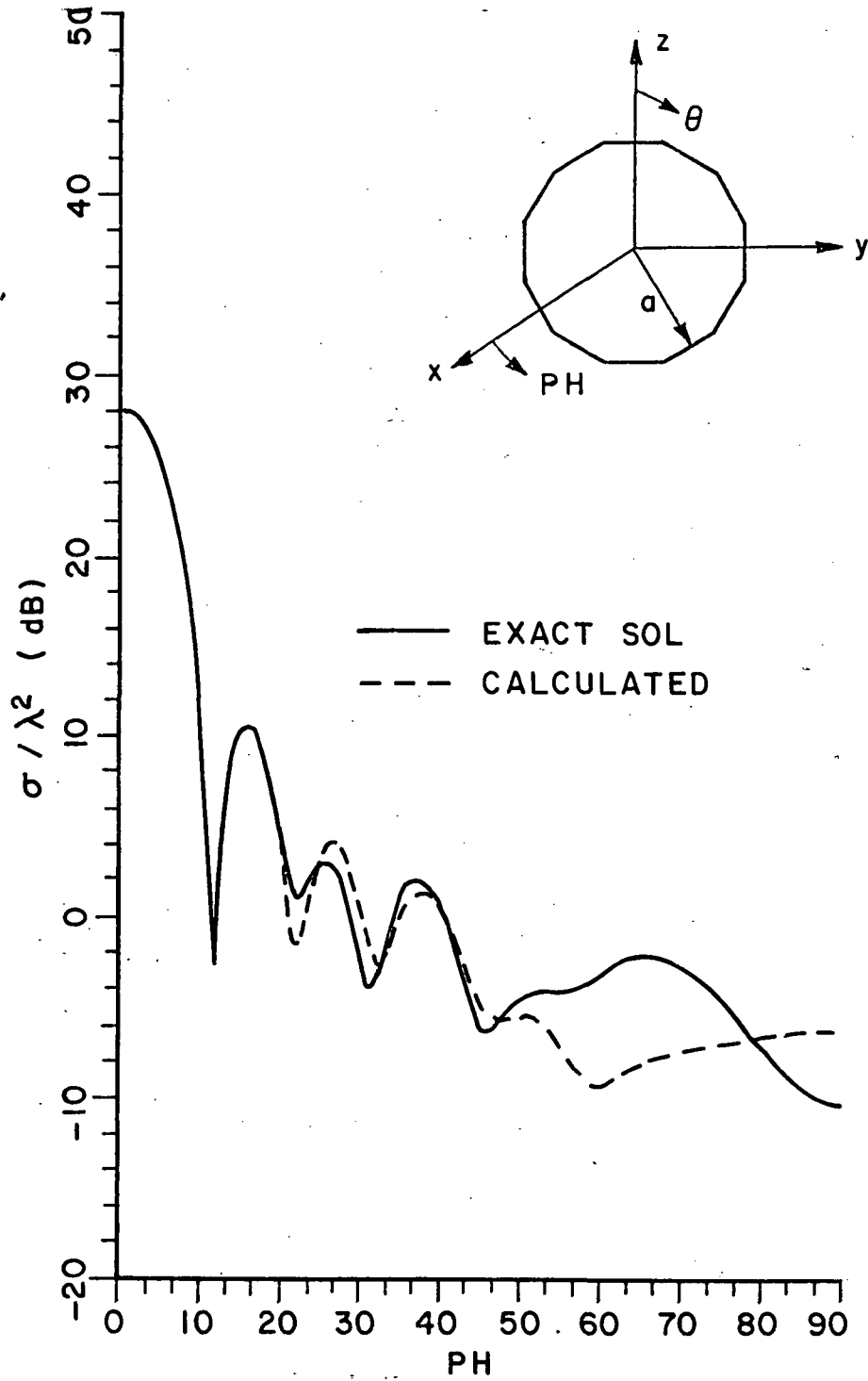
Figure 62. $E_\theta$, $\theta = 90^0$ RCS pattern for the 12 sided disk model (ka = 9.45).

JAB/80

Figure 63.  $E_\theta$, $\theta = 90^0$ RCS pattern for the 8 sided disk model (ka = 10).

JAB/80
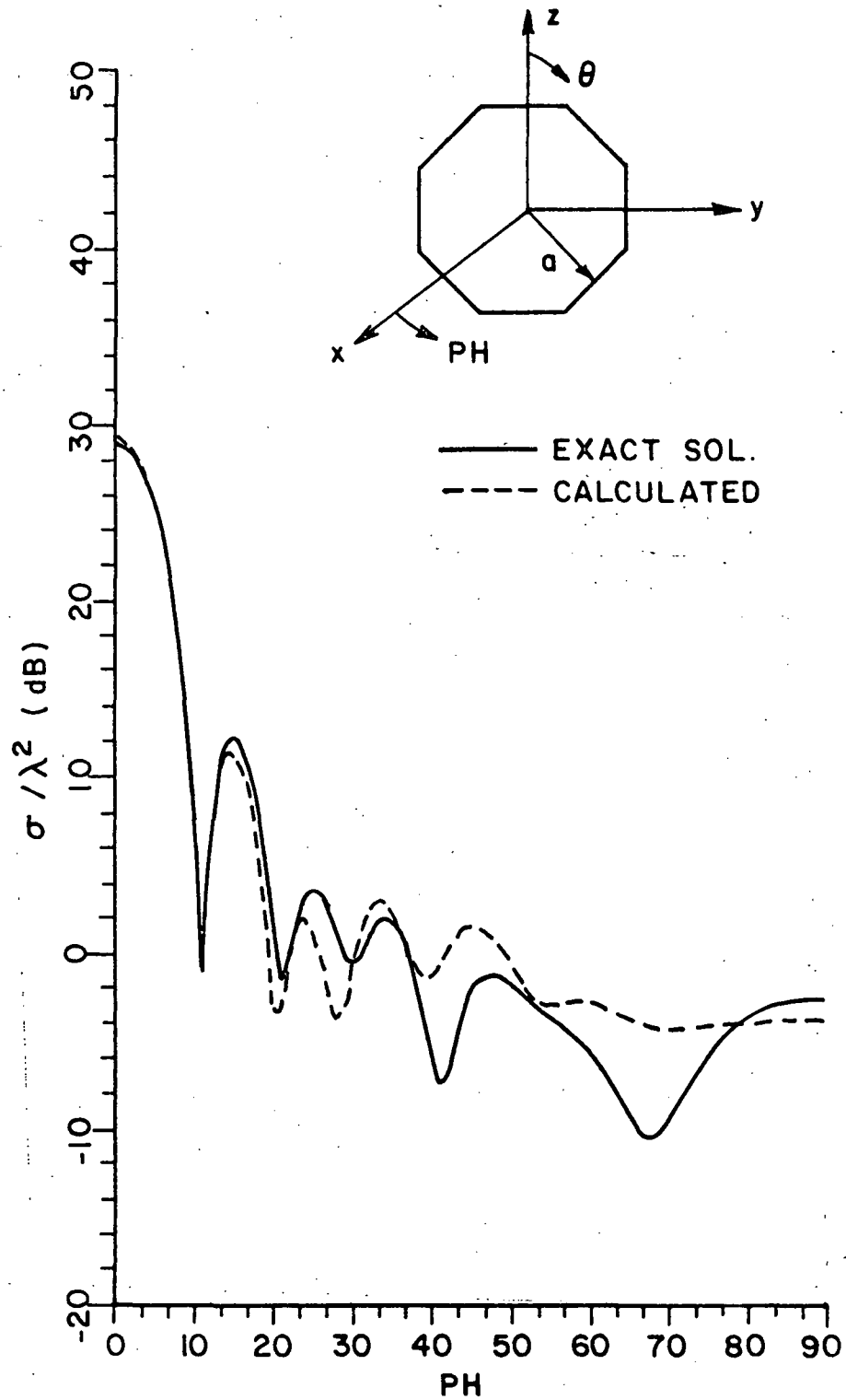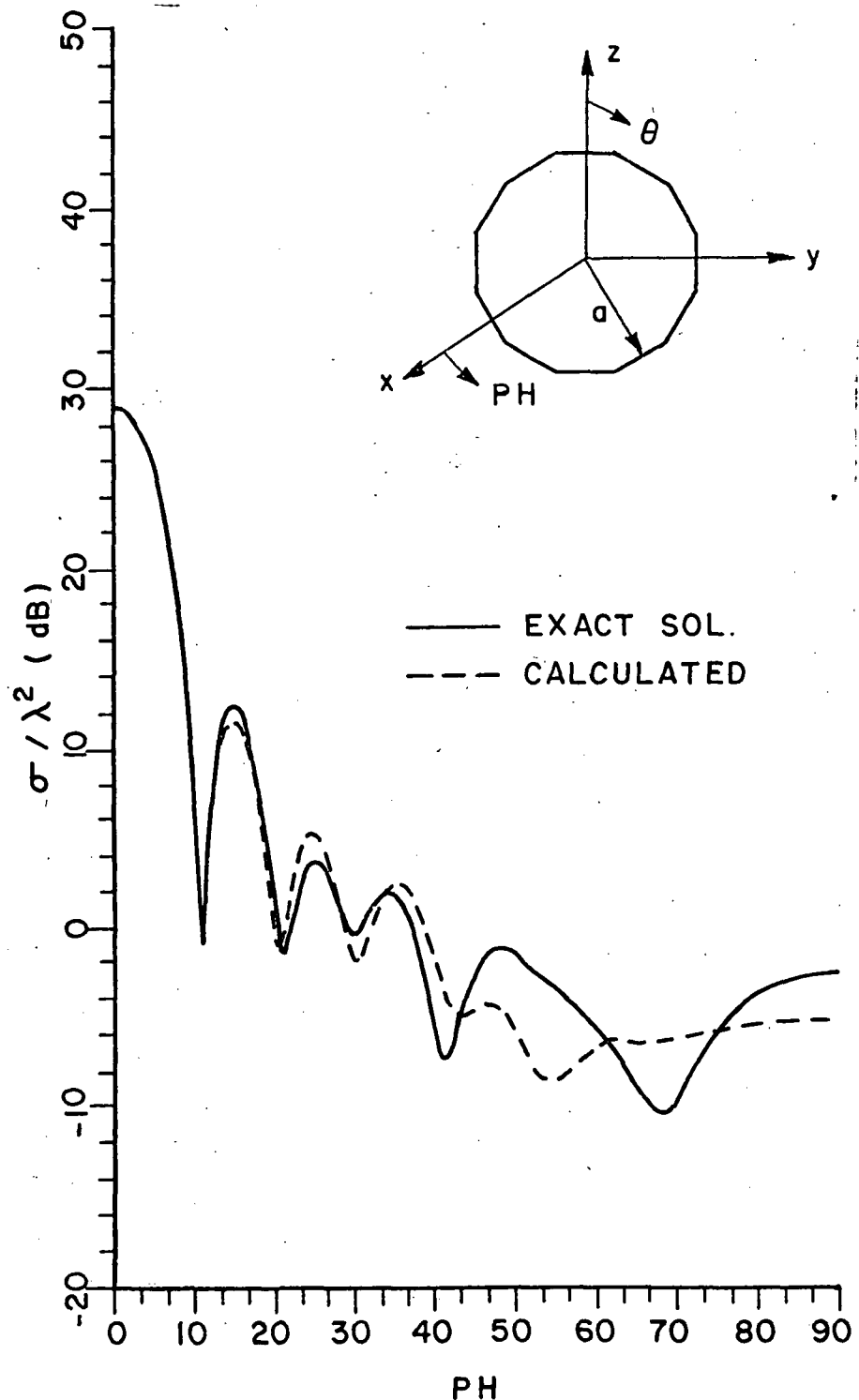
1½ inch

1 inch



Figure 64.  $E_\theta$, $\theta = 90^\circ$ RCS pattern for the 12 sided disk model (ka = 10).

1 inch
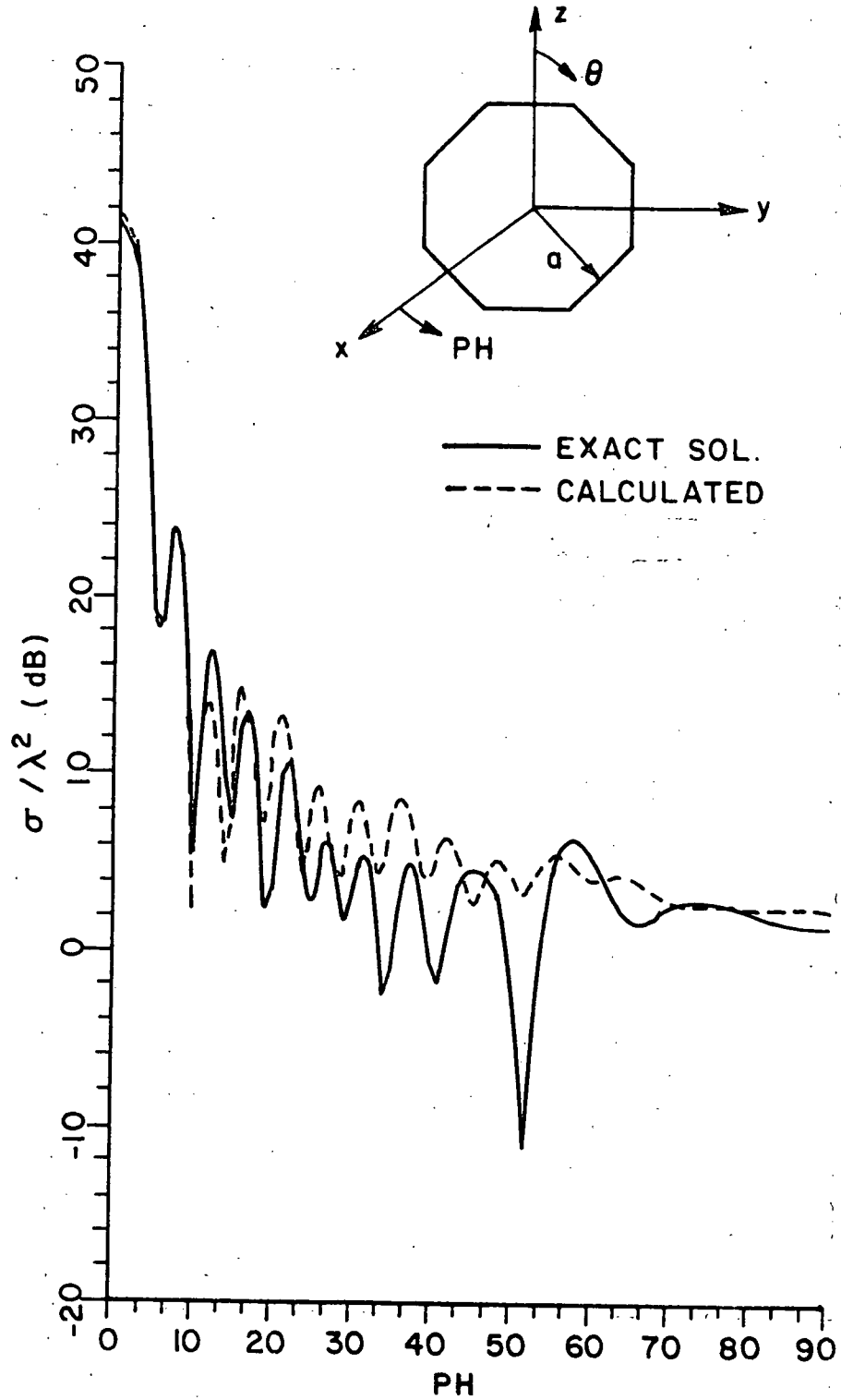
JAB/80

Figure 65. $E_\theta$, $\theta = 90^U$ RCS pattern for the 8 sided disk model $(ka = 20)$.

JAB/80

Figure 66.  $E_\theta$, $\theta = 90^0$ RCS pattern for the 12 sided disk model (ka = 20).

JAB/80
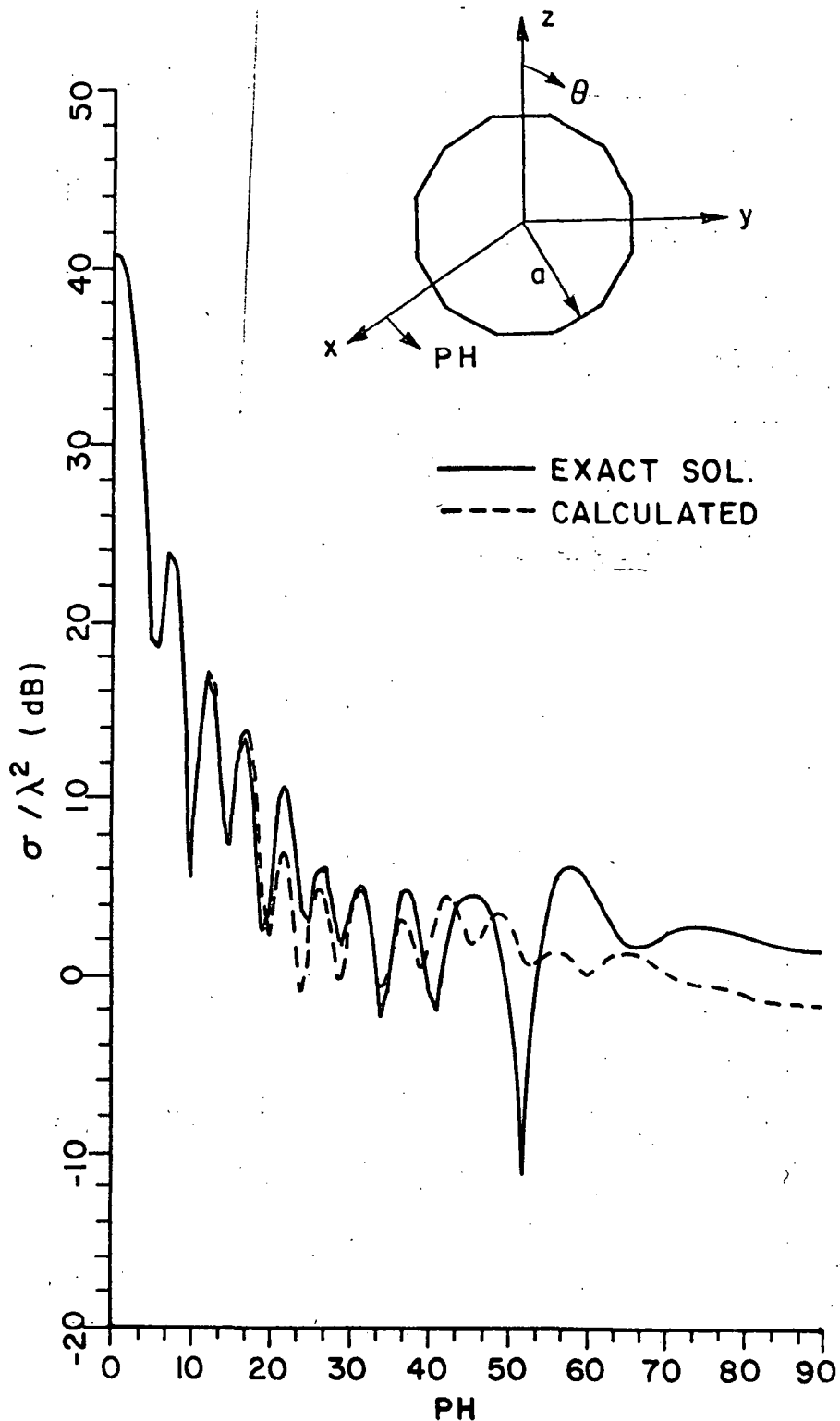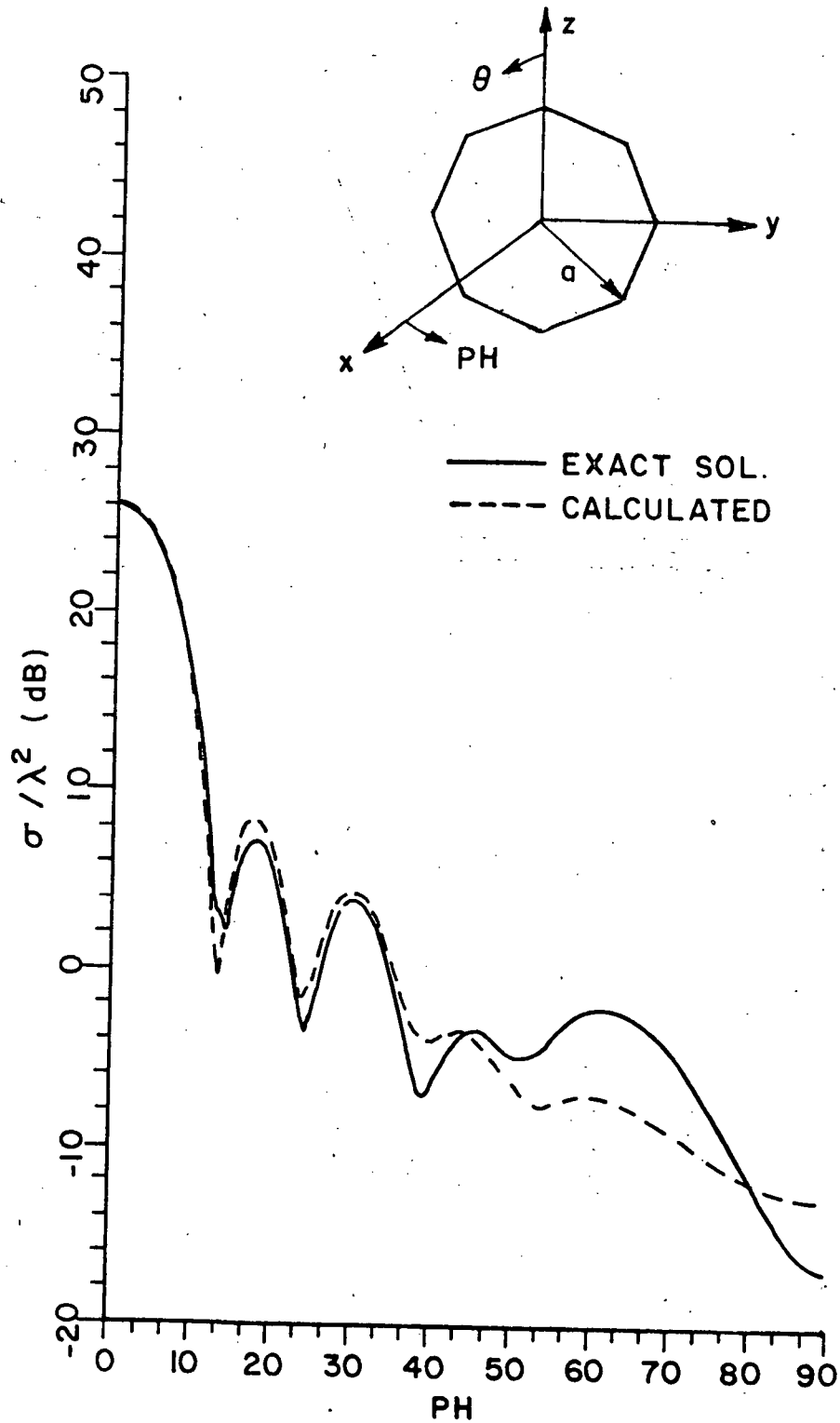
Figure 67.  $E_\theta$, $\theta = 90^\circ$ RCS pattern for the 8 sided disk model.  The pattern cut is taken through corners (ka = 8.28).

103

JAB/80
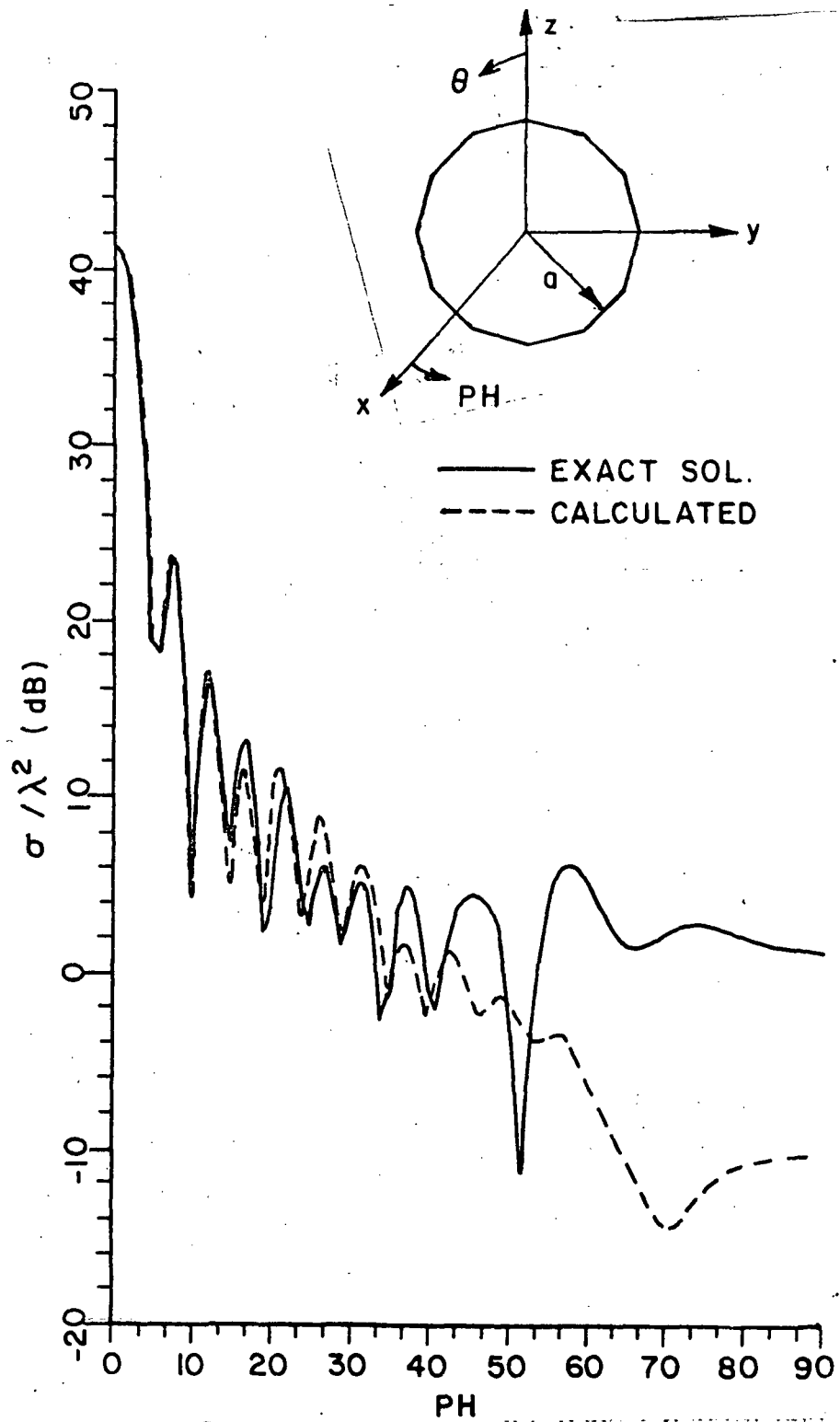
1½ inch

1 inch



Figure 68.  $E_\theta$, $\theta = 90^\circ$ RCS pattern for the 12 sided disk model.  The pattern cut is taken through corners (ka = 20).

1 inch

JAB/80

near edge on is still in error which indicates the importance of in-cluding the creeping wave contribution to complete the solution. Some slight improvement in the region away from edge on is noted. In Figure 69 and 70, our result computed using the 12 sided disk model is compared to a solution provided by Mr. Chu [42] , in which he used the Equivalent Current method to compute the RCS pattern by integrating numerically over the disk rim. His solution does not include the creeping wave contribution. Figure 69 shows the results for ka≈8.28. The Chu solution traces the GTD solution obtained by Bechtel while in Figure 70 the results for ka=10 are shown. The Chu solution gives better results in the region $40^{\circ} \leq PH \leq 60^{\circ}$ which indicates that using a disk model with more edges closer resembles the actual structure and provides better results.

F.  COMPARISON BETWEEN CORNER DIFFRACTION AND THE EQUIVALENT
    CURRENT METHOD

As was shown in the previous sections, the Equivalent current method gives adequate results for RCS computations. This method gives its most accurate results in the principal plane, since the radar lies on the cone of diffracted rays. As the radar is moved off the principal plane, its direction is moved away from the specular one, and accordingly, one would expect that the first order Equivalent current method results would become weaker as one moves further away from the principal plane and other mechanisms would become more significant.

In this section, the use of corner diffraction method is discussed as an alternative way to the Equivalent current approach to compute the contribution of first order diffraction to the RCS from plates.

The corner diffracted field [19] was discussed earlier in Chapter II. For the case of far field and plane wave incidence, Equation (26) reduces to give
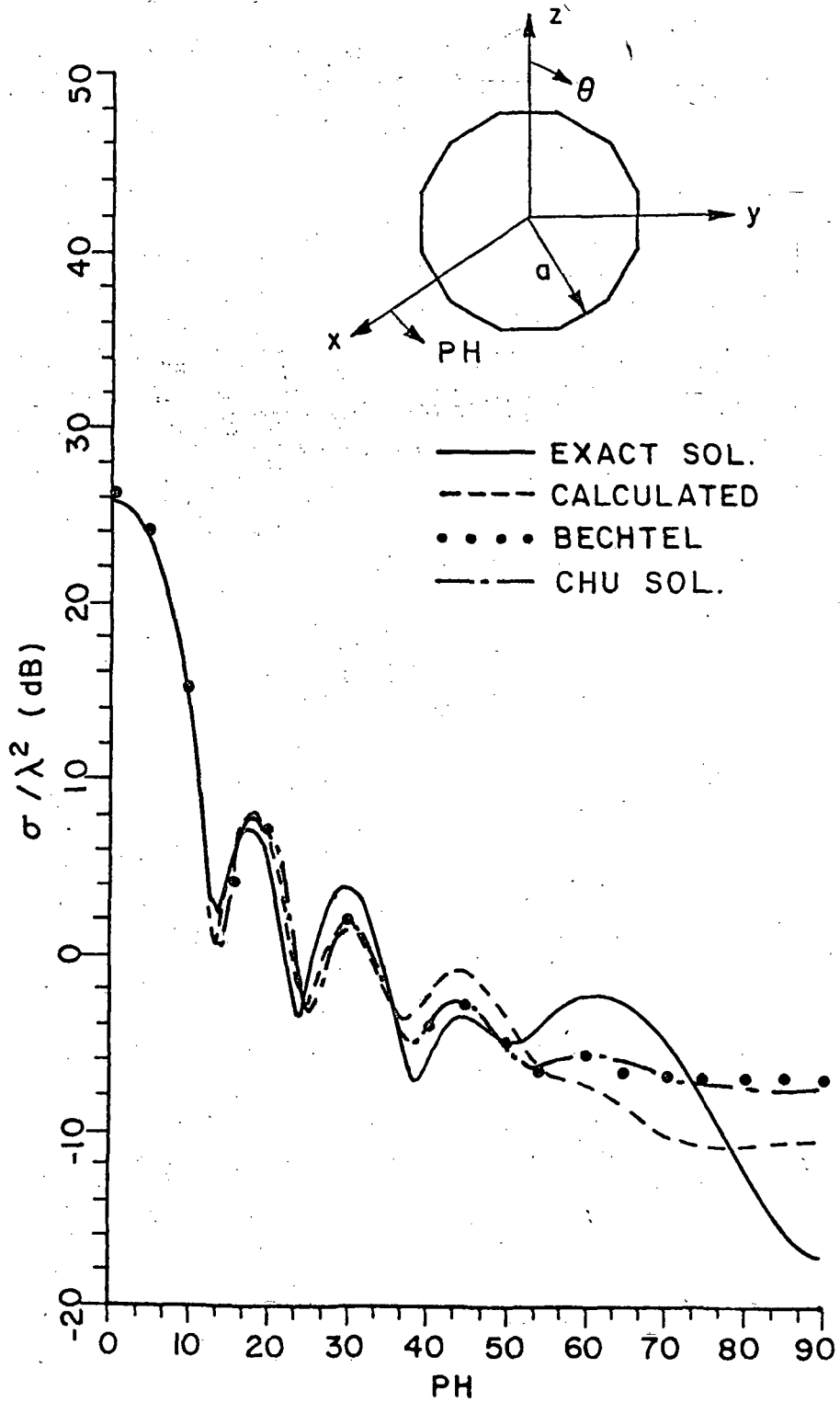
Figure 69.   $E_\theta$, $\theta = 90^\circ$ RCS pattern for the 12 sided disk model compared to rim integration method (ka = 8.28).
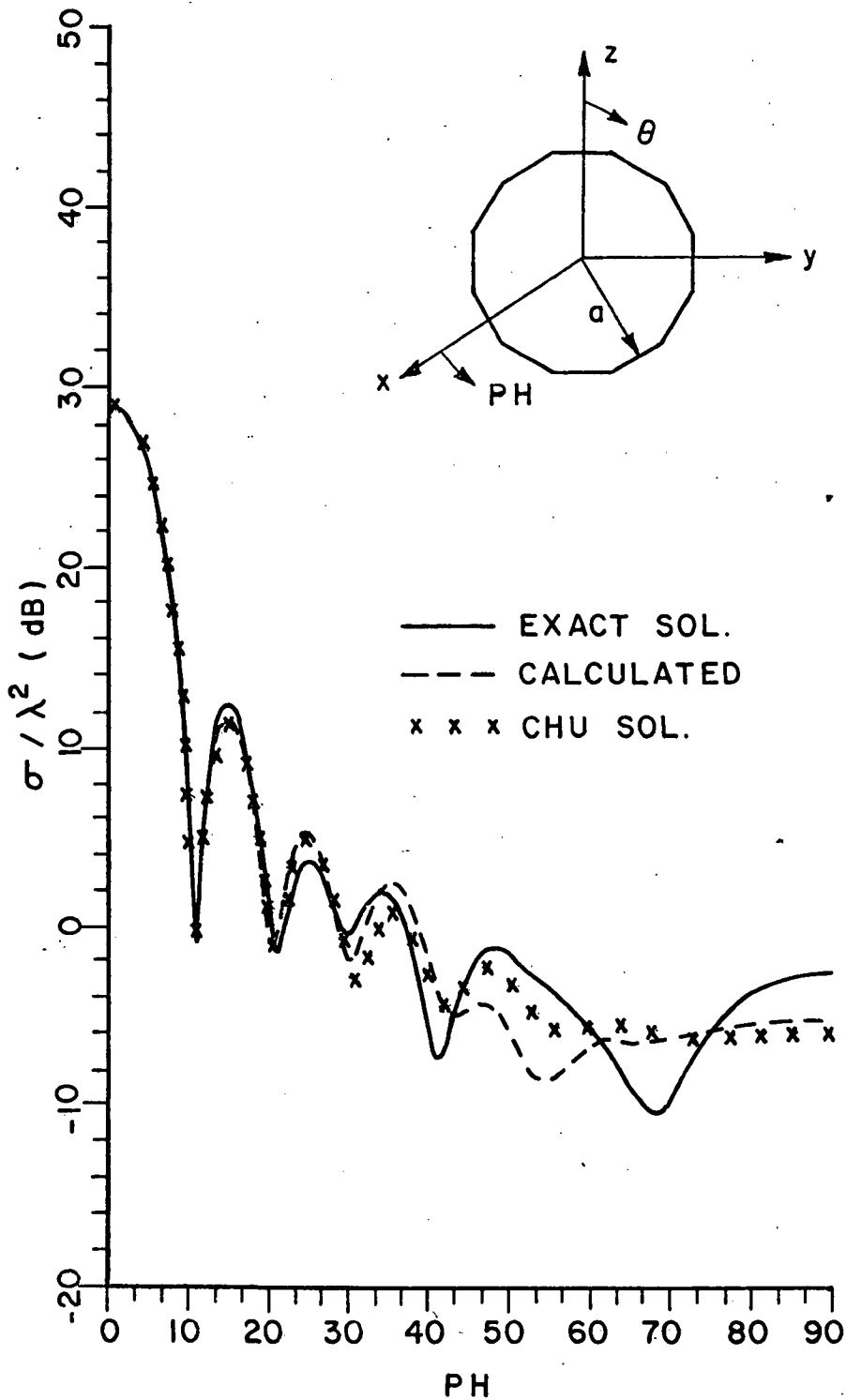
Figure 70.    $E_\theta$, $\theta = 90°$ RCS pattern for the 12 sided disk model compared to the rim integration method (ka = 10).

JAB/80

$$
\begin{bmatrix} E_{\beta_0}^c \\ \\ E_\phi^c \end{bmatrix} = - \begin{bmatrix} E_{\beta'_0}^i(Q_c) & D_s^c \\ \\ E_{\phi'}^i(Q_c) & D_h^c \end{bmatrix} \frac{e^{-jks}}{s}
\tag{71}
$$

where

$$
D_{\substack{s\\h}}^c = C_{\substack{s\\h}}(Q_E) \ \frac{\tan \beta_{0_c}}{8\pi} \sqrt{\frac{8\pi}{k}} \ e^{-j\pi/4}
\tag{72}
$$

and

$$
C_{\substack{s\\h}}(Q_E) = \frac{-e^{-j\pi/4}}{2\sqrt{2\pi k}} \left[ \left| F\left(\frac{1/\lambda}{k\,\cos^2\beta_{0_c}}\right) \right| \mp \frac{1}{\cos\phi} \left| F\left(\frac{\cos^2\phi/\lambda}{k\,\cos^2\beta_{0_c}}\right) \right| \right]
\tag{73}
$$

substituting Equation (73) into (72) one obtains

$$
D_{\substack{s\\h}}^c = \frac{j\tan\beta_{0_c}}{8\pi k} \left[ \left| F\left(\frac{1/\lambda}{k\,\cos^2\beta_{0_c}}\right) \right| \mp \frac{1}{\cos\phi} \left| F\left(\frac{\cos^2\phi/\lambda}{k\,\cos^2\beta_{0_c}}\right) \right| \right] \cdot
\tag{74}
$$

Equations (72-74) were obtained by substituting

$$L=\infty, \ L_c = \infty$$

$$\beta_c = \pi - \beta_{0_c} \qquad \beta_0 = \pi/2 \quad \text{and}$$

$$\phi = \phi'$$

The definition of all the different parameters can be found in Chapter II, Section D.

For the special case when $\beta_{o_c} = \frac{\pi}{2}$, Equation (74) reduces to give

$$D_{s_h}^c = \frac{-e^{-j\pi/4}}{4\sqrt{2\pi k}} \left(1 \mp \frac{1}{\cos\phi}\right) \tag{75}$$

The above Equations were used to compute the RCS for some of the plates discussed in sections D and E. The plates are located in the x-z plane. The H-plane ($E_\theta$ polarization) is computed in the x-y plane. The results are compared with those obtained by using the Equivalent current method. Figure 71 shows the RCS pattern for a $2\lambda$ square plate. The pattern is taken in the principal plane ($\theta=90^o$). The agreement between the two methods is excellent as one would expect. Figures 72 and 73 show the RCS conical patterns for the same plate. The patterns were taken for $\theta=60^o$ and $\theta=30^o$ respectively. The two methods agree well in the main lobe region. They start to deviate in the side lobes region especially as one approaches edge on incidence. The reason for this difference is that in the Equivalent current method, the three dimensional behavior of the scattered fields is computed through the radiation integral. One would question its accuracy in predicting the fields level as the receiving point is moved out from the main lobe region of the radiation integral pattern as is shown in Figure 74. In the corner diffraction method, the three dimensional effects are taken care of by the transition functions involving $\beta_c$ and $\beta_{o_c}$. Even though the two methods give two results that differ in the side lobe region, this difference is not going to affect the final results, since in this case, higher order interactions contribute significantly to all regions of the RCS pattern. This is to be discussed in more detail in Chapter V and VI.

Figure 75 shows the H-plane RCS pattern for the plate shown in Figure 56. The agreement between the two methods is good
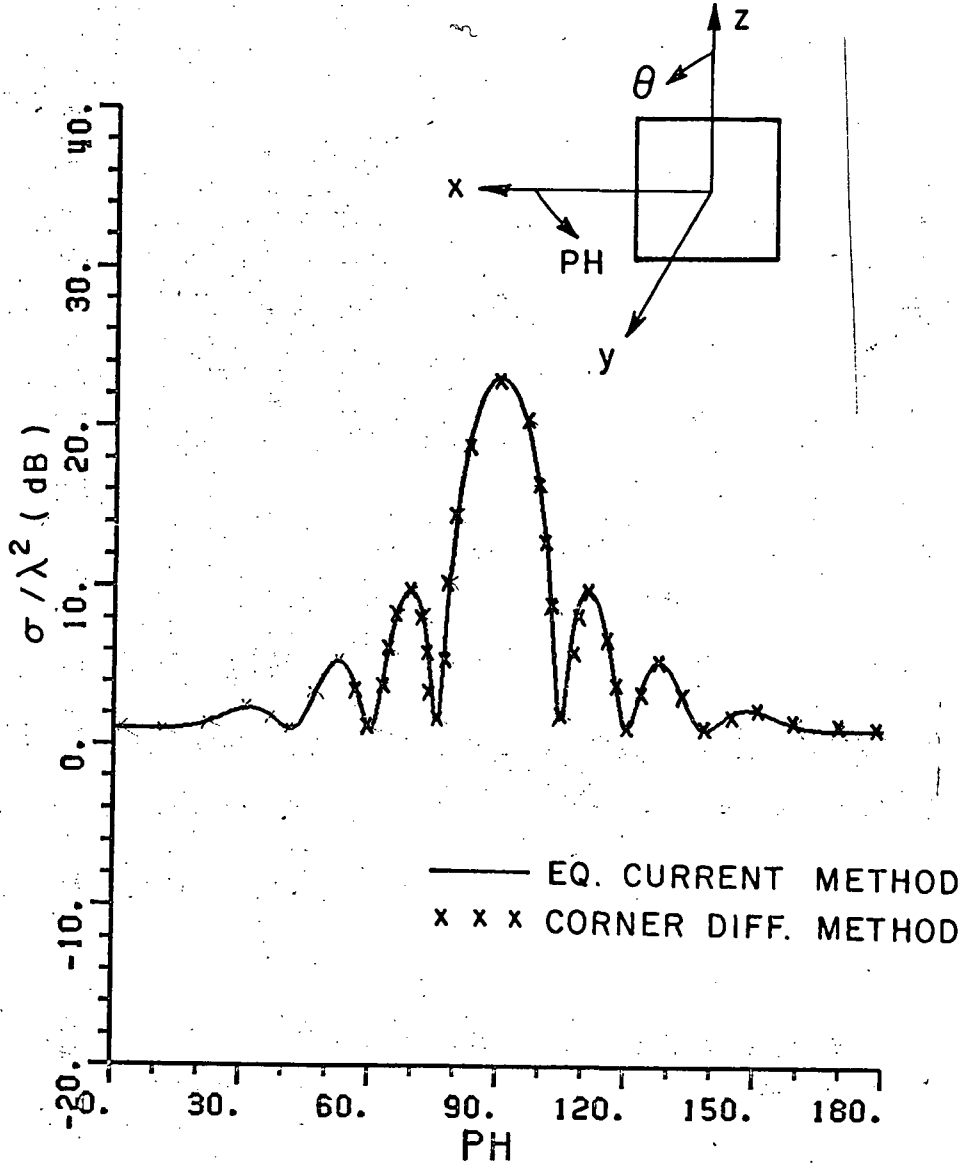
Figure 71.  $E_\theta$, $\theta = 90°$ RCS pattern for a $2\lambda \times 2\lambda$ flat plate.

Figure 72.  $E_\theta$,  $\theta = 60^0$ RCS pattern for a $2\lambda \times 2\lambda$ flat plate.

JAB/80
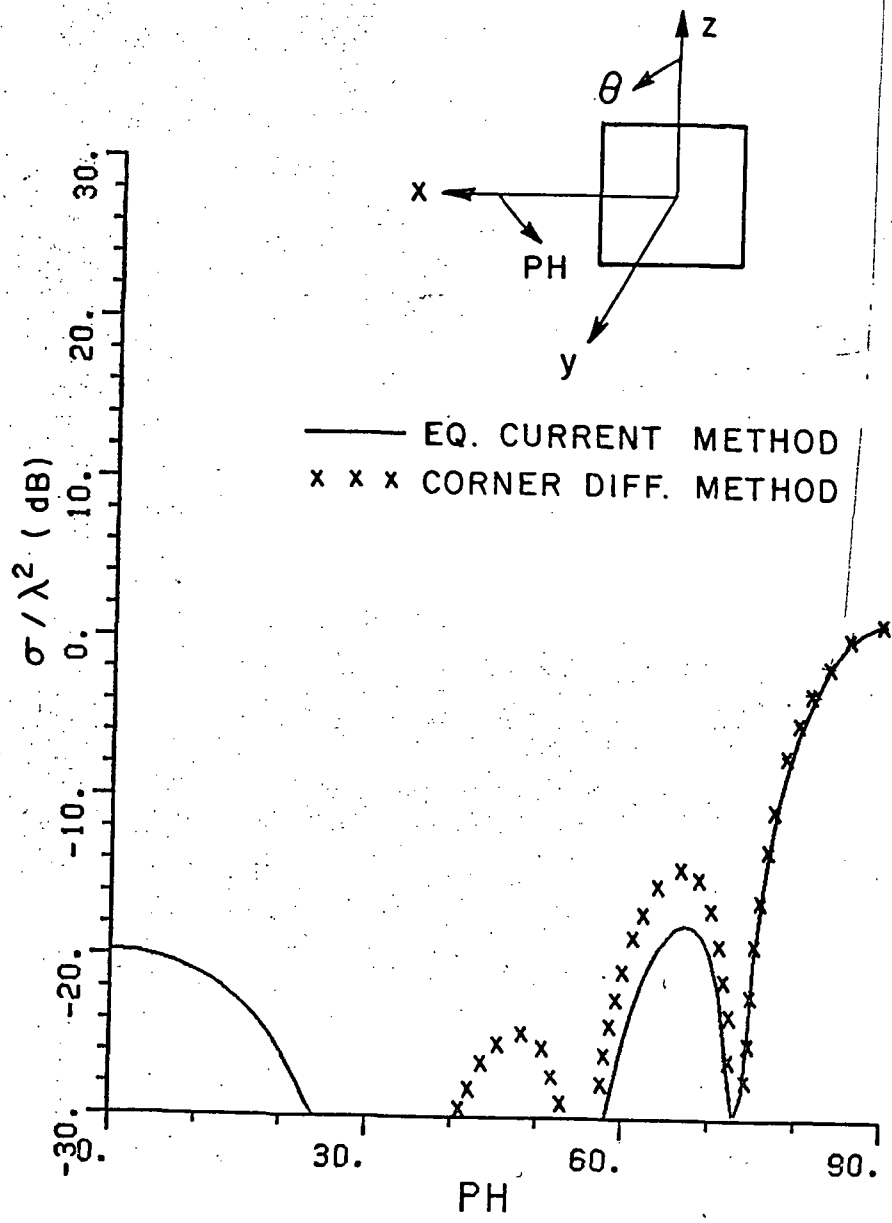
Figure 73. $E_\theta$, $\theta = 30°$ RCS pattern for a $2\lambda \times 2\lambda$ flat plate.

1st page Chapter end line

112

1 inch

JAB/80

RECEIVER
DIRECTION

PLATE

SPECULAR
DIRECTION
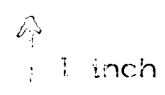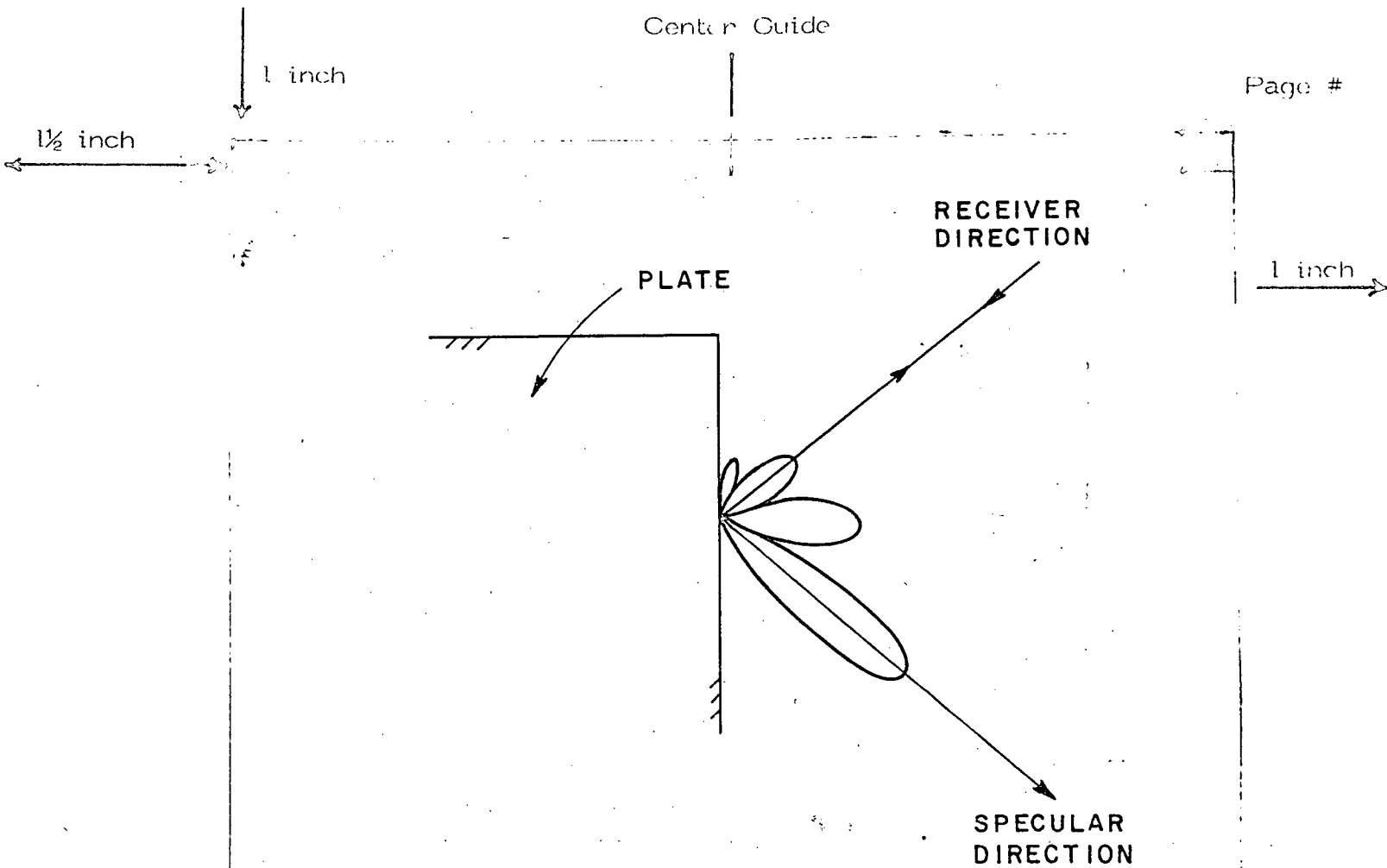
Figure 74. Radiation integral pattern.

for the entire pattern. Figures 76-77 show the H-plane RCS patterns for a disk for two sizes, ka-8.59 and 9.45. The pattern cut is taken through two corners in a symmetrical way. Figures 78 and 79 show the same data for the case when the pattern cut is taken through the edges as shown in Figure 56. The agreement is sufficient for engineering applications.

Finally, one should note that when using the corner diffraction method to compute the fields in the H-plane case, the pattern angles should be displaced by some small numbers, i.e., PH + $\varepsilon_1$ and $\theta$ + $\varepsilon_2$ where $\varepsilon_1$ and $\varepsilon_2$ are much less than one. This technique follows the same reasoning used in Chapter III to obtain the field value at broadside.
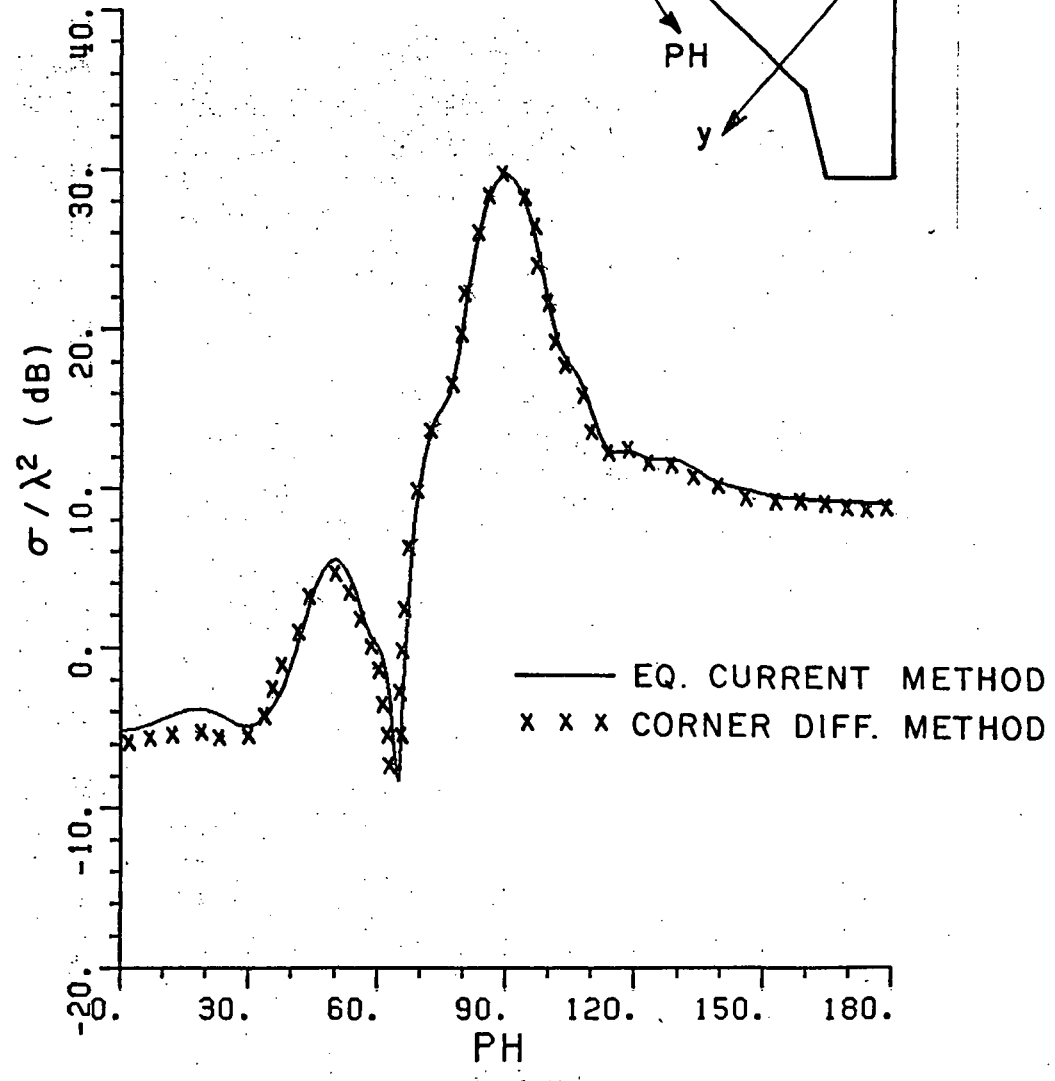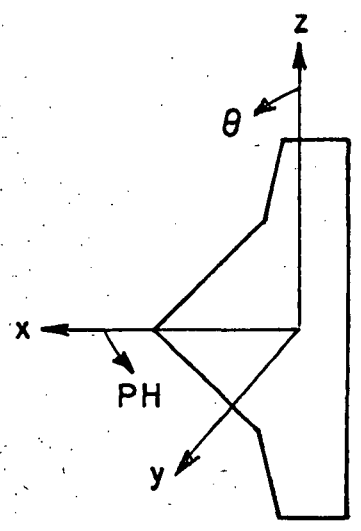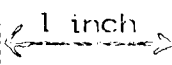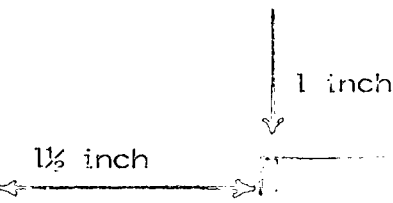
Figure 75.  $E_\theta$, $\theta = 90^o$ RCS pattern for the plate shown in Figure 53 at 9.067 GHz.
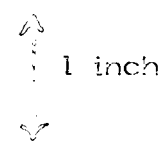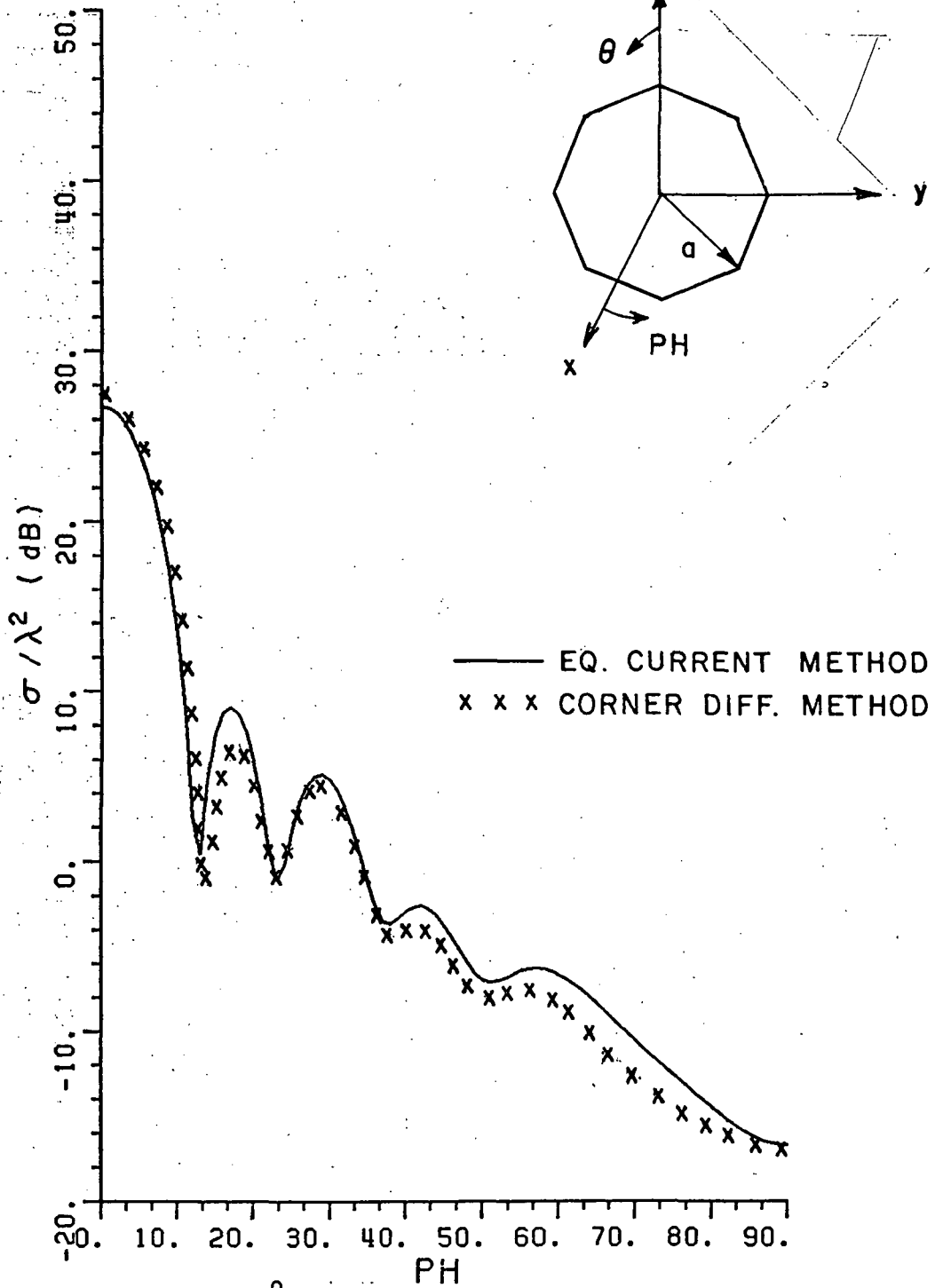
JAB/80

Figure 76. $E_\theta$, $\theta = 90^0$ RCS pattern for the 8 sided disk model. The pattern cut is taken through corners (ka = 8.59).
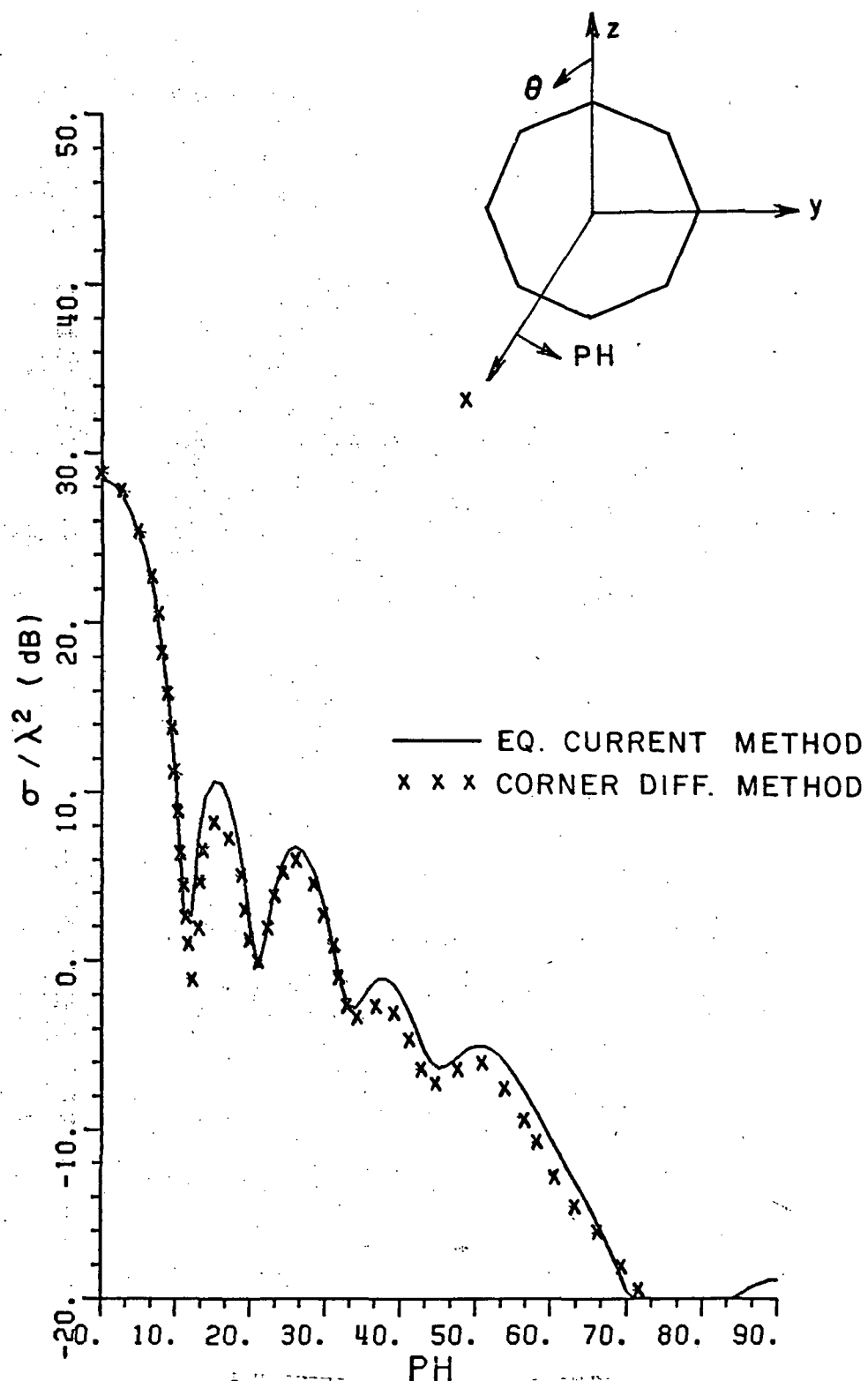
JAB/80

Figure 77. $E_\theta$, $\theta = 90^o$ RCS pattern for the 8 sided disk model. The pattern cut is taken through corners (ka= 9.45).

JAB/30
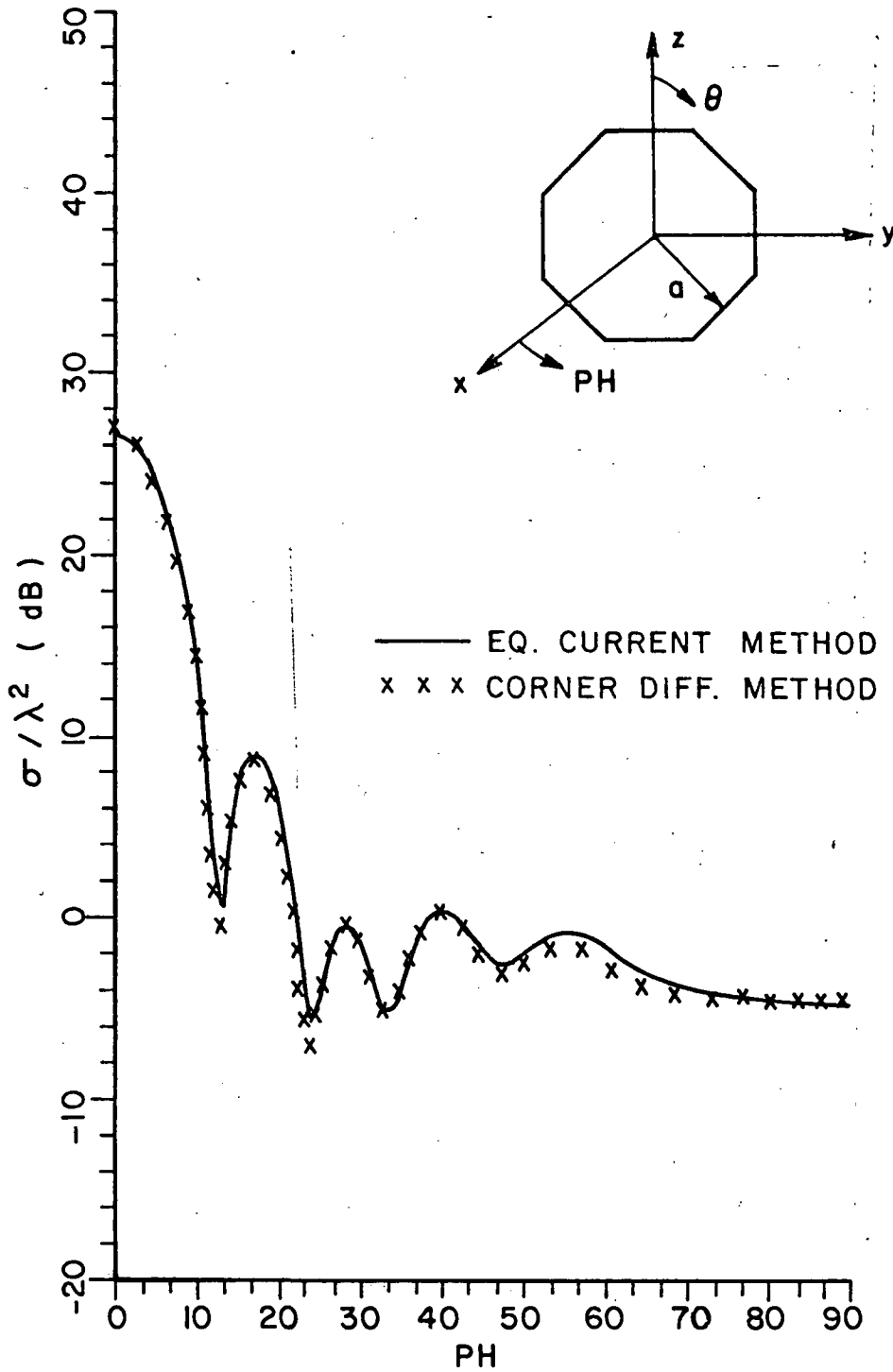
Figure 78. $E_\theta$, $\theta = 90^\circ$ RCS pattern for the 8 sided disk model. The pattern cut is taken through edges (ka = 8.59).

1 inch

JAB/80
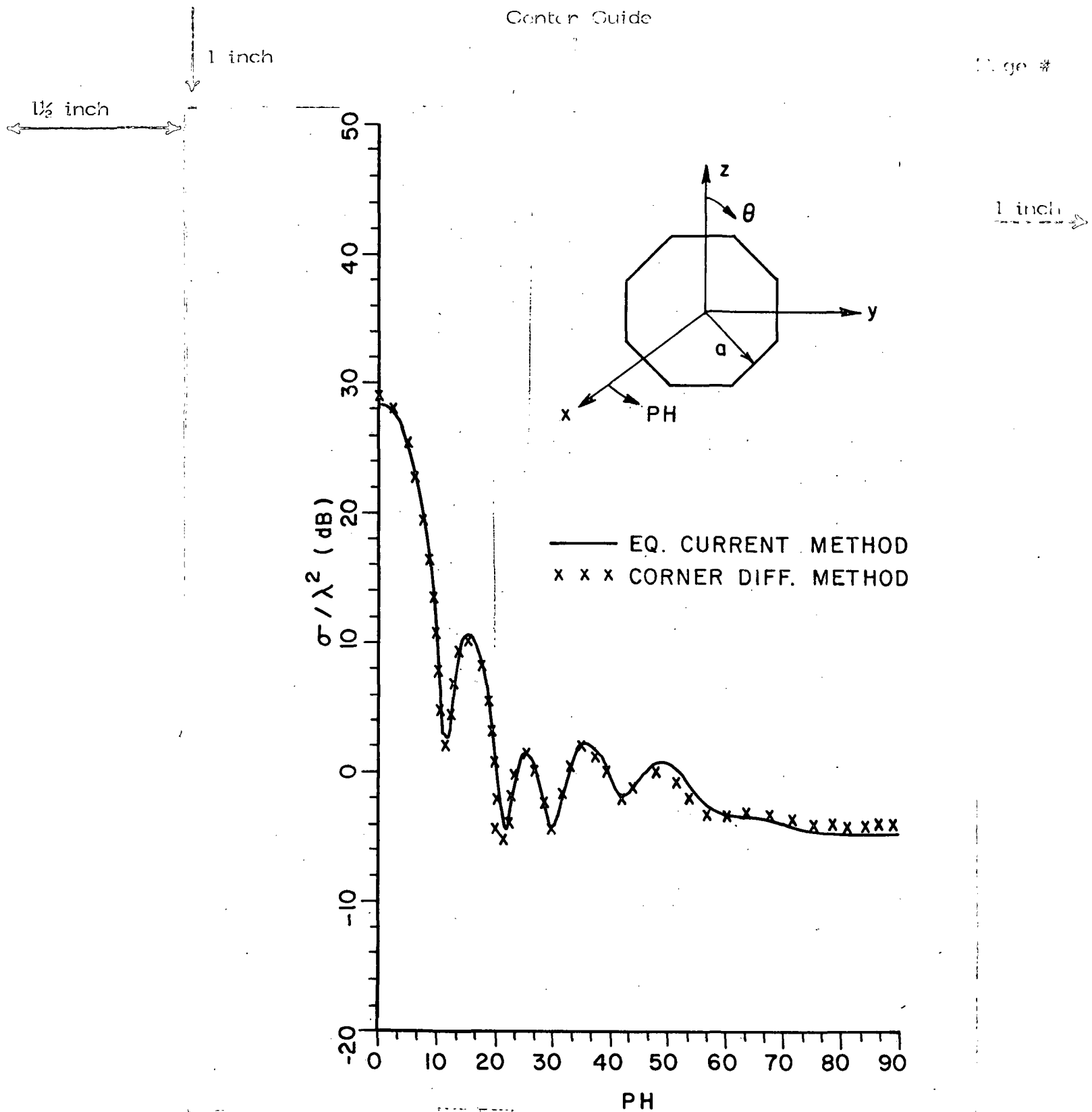
Figure 79. $E_\theta$, $\theta = 90^{\circ}$ RCS pattern for the 8 sided disk model. The pattern cut is taken through edges (ka = 9.45).

JAB/80

## G. SUMMARY OF H-PLANE BACKSCATTER ANALYSIS

The analysis in this dissertation is being introduced sequentially according to the complexity. This chapter focuses attention on the H-plane patterns where the Electric field vector is oriented perpendicular to the plane of incidence.

The techniques used to obtain the broadside RCS in the H-plane are in general applicable for any other plane. The major developments for this broadside RCS analysis being the orientation of first order Equivalent Currents taken perpendicular to the incidence plane and then simply using the accuracy of the computer to remove the singularity at near normal incidence. This makes it possible to approximate the broadside RCS with good accuracy.

It would be expected that the near edge on incidence RCS is dominated by the leading edge of the plate for this polarization and in general this is found to be true exclusive of creeping wave type of phenomena. The effect of such creeping waves are evident in the RCS patterns of the circular disks for PH near $90^o$. However, for rectangular plates whose leading edge is longer than the edge parallel to the direction of propagation, the leading edge diffraction is the dominant mechanism. Even here for smaller square plates whose dimensions are of the order of a few wavelengths, the multiple corner diffraction and edge diffraction mechanisms become significant but not dominant.

However, as the plate becomes elongated in the direction of propagation, these multiple corner diffraction mechanisms become dominant terms and must be incorporated in the analysis. A later chapter will discuss in detail the H-plane RCS patterns for a narrow triangular plate where some rather interesting features appear.

JAB/80

1 inch

1½ inch

1 inch

A set of rather general shaped plates have been treated using only the first order Equivalent Currents.  For this polarization, it is seen that in general this gives adequate results.  The curved edges of these plates have been modeled by straight line segments.  Variations from measured results, while small, appear since creeping waves, edge waves multiple corner diffractions have not been included in the analysis, primarily because they are not dominant mechanisms.  These more complex phenomena will be discussed in later chapters, particularly for the E-plane patterns.

2 inch Chapter Line

The one topic beyond the scope of this dissertation is the creeping wave analysis.  The effect of the creeping wave on the RCS is particularly evident in the RCS patterns for the circular disk for near edge on inci-dence.

Typing Guide Paper

The following chapter focuses attention on the higher order diffrac-tion mechanisms.  These are particularly important for the E-plane RCS patterns and become dominant mechanisms for non-principal plane patterns.

1st page Chapter end line

— — — — — — — 1st page Chapter end line

1 inch

1 inch

JAB/80

2 inch CHAPTER V Line

# E-PLANE BACKSCATTERING FROM PLATES USING HIGHER ORDER INTERACTIONS

## A.   INTRODUCTION

In Chapter IV, the effect of the first order interactions on RCS computation were discussed. These interactions generally involved only single edge diffraction terms.  The fields associated with these mechanisms were sufficient for computing the H-plane pattern.  The results obtained by using the Equivalent Current (EC) method or Corner diffraction were in good agreement with the measured results through out the pattern. Some deviation between the calculated and measured results were observed in the near edge on region.  These variations were due to the higher order interactions to be discussed here and in the following chapters.

In this chapter the interaction between plate edges shall be considered.  This involves double and triple diffracted rays between edges. The EC method is to be used to compute their contribution to the RCS. These two types of multiply diffracted interactions will be seen to be very important components in the computation of E-plane RCS patterns.

The incident field is assumed to be a homogeneous plane wave and is given by

1st page Chapter end line
— — — — — — — 1st page Chapter end line

1 inch

JAB/80

1 inch

1½ inch

1 inch
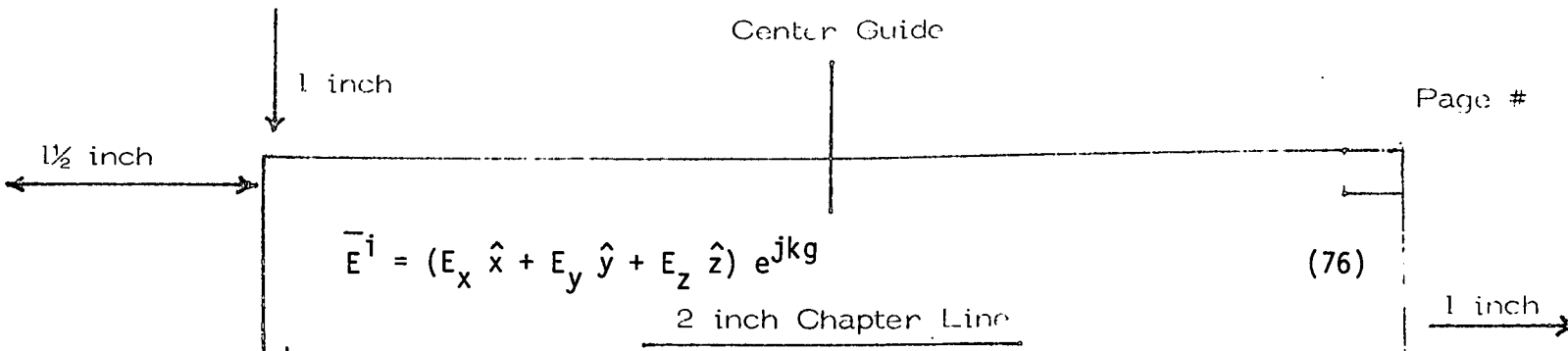
$$\overline{E}^i = (E_x \hat{x} + E_y \hat{y} + E_z \hat{z}) e^{jkg} \tag{76}$$

2 inch Chapter Line

where

$$g = x \sin\theta^i \cos PH^i + y \sin\theta^i \sin PH^i + z \cos\theta^i$$

Figure 80 shows the plate and radar geometry. The plate is located in the x-z plane. The E-plane RCS pattern is taken in the x-y plane.

## B. EQUIVALENT CURRENT FORMULATION

THESIS / DISSERTATION
Typing Guide Paper

The fields of the doubly and triply diffraction rays between plate edges are computed by constructing the corresponding magnetic Equivalent current and using it together with the radiation integral to compute the far backscattered field.

In the analysis of these two mechanisms, one has to consider the shadowing effect between edges. In Figure 81, an electromagnetic plane wave is incident on the $p^{th}$ edge, the diffracted field then illuminates a part of the $q^{th}$ edge and in turn the field diffracted from the $q^{th}$ edge illuminates part of the $v^{th}$ edge. The method used to determine the illuminated region on an edge is shown in Appendix A.

The Equivalent currents corresponding to the double and triple edge diffraction fields are given by

$$I^m_{(2)} = \frac{-2j}{y_o k} \frac{\sqrt{2\pi k}}{\sin \beta_o^{(q)}} e^{j\pi/4} \cdot \frac{(\overline{H}^{i(p)} (Q^{(p)}) \cdot \hat{e}_p)}{\sin \beta_o^{(p)}} D_h^{(p)}(s_1, o, \phi'^{(p)}, \beta_o^{(p)})$$

$$D_h^{(q)}(s_1, \phi^{(q)}, o, \beta_o^{(q)}) \frac{e^{-jks_1}}{\sqrt{s_1}} (\hat{\beta}_o^{(q)} \cdot \hat{e}_q) \quad \text{and} \tag{77}$$

1st page Chapter end line

LAST TEXT LINE

1 inch

JAB/80

1 inch

1½ inch

2 inch Chapter Line

1 inch



RADAR

z

$\theta^i$

x

PH$^i$

y

1st page Chapter end line

Figure 80.   Plate and radar geometry. ·—  1st page Chapter end line

LAST TEXT LINE

1 inch

JAB/80

$$I^m_{(3)} = \frac{-2j}{y_0 k} \frac{(\overline{H}^{i(p)}(Q^{(p)}) \cdot \hat{e}_p)}{\sin \beta_0^{(p)} \sin \beta_0^{(q)} \sin \beta_0^{(v)}} D_h^{(p)}(s_1, 0, \phi^{\prime(p)}, \beta_0^{(p)})$$

2 inch Chapter Line
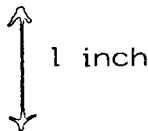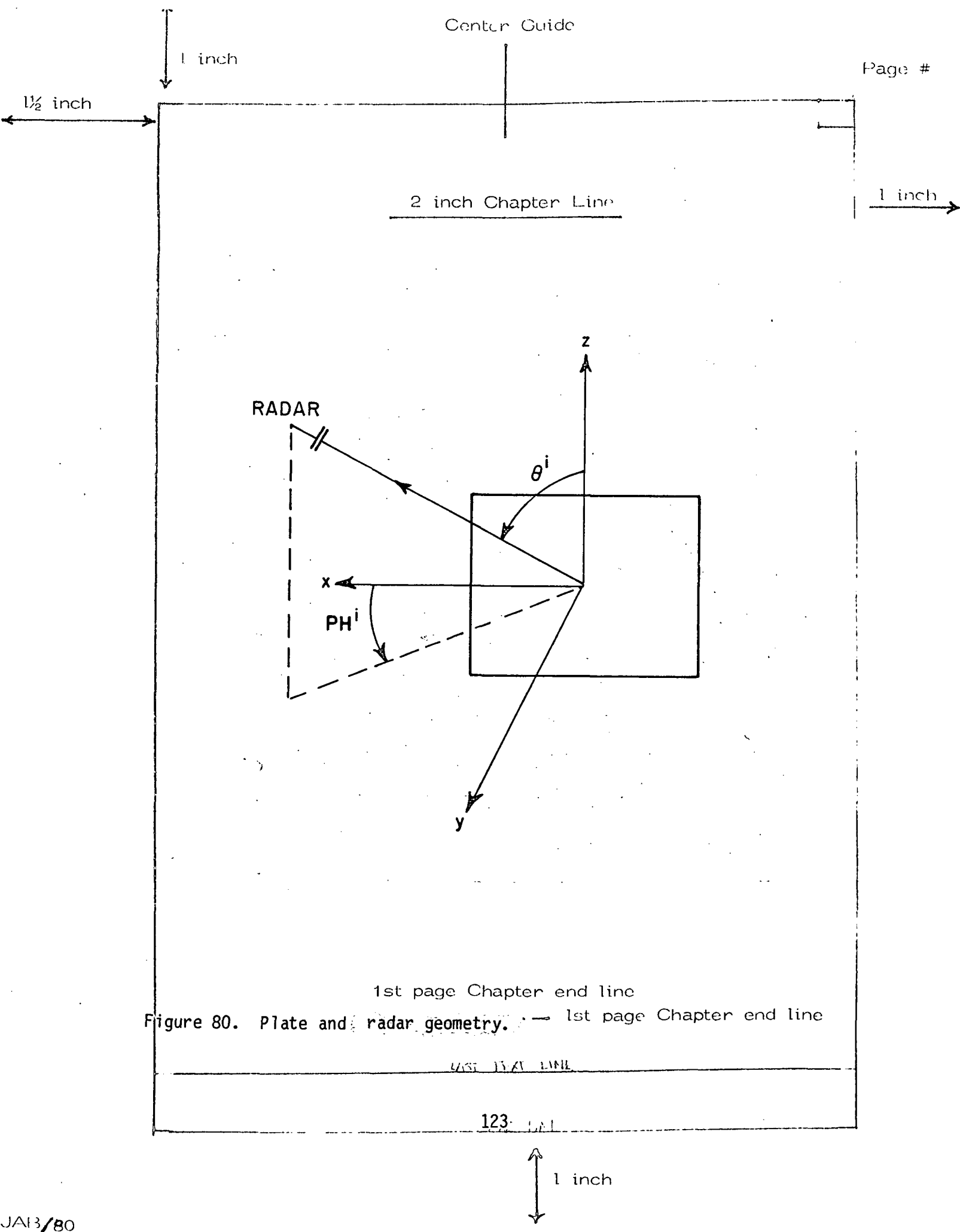
$$D_h^{(v)}(s_2, \phi^{(v)}, 0, \beta_0^{(v)}) \frac{e^{-jks_1}}{\sqrt{s_1}} \frac{e^{-jks_2}}{\sqrt{s_2}} (\hat{\beta}_0^{(v)} \cdot \hat{e}_v) \qquad (78)$$

The derivation of Equations (77-78) is shown in Appendix B. In these equations the subscripts of $I^m_{(2,3)}$ indicates the order of diffraction and the superscript indicates current type, i.e., the electric or magnetic currents. Figure 82 defines the different parameters used, where $Q^{(p)}$, $Q^{(q)}$, $Q^{(v)}$ defines the diffraction points on edges p, q, and v, respectively. The edge unit vectors are $\hat{e}_p$, $\hat{e}_q$, $\hat{e}_j$ for these edges and $s_1$, $s_2$ are the distances between these diffraction points. I and $\hat{d}$ are the incident and diffracted unit vectors.

When one substitutes these currents into the radiation integral, a numerical integration has to be used to evaluate it. The integration is carried out only over the illuminated part of the edge. Observe that there is a shadow boundary effect in the ray trajectories of Figure 81. This could be circumvented by adding corner diffracted fields to the fields incident on edge q (and subsequently to the field of edge v) as is shown in Figure 83 and including these results in the Equivalent Currents. A pulse type integration scheme was used in computing the data presented in this chapter.

One must observe that if the Equivalent Current is used only over the illuminated region, then the integration will approximate the fields from the diffraction caused by the resulting shadow boundary.

C. BACKSCATTERING FROM A GENERAL SHAPE PLATE

1st page Chapter end line

The E-plane pattern for an arbitrary shape plate is a more complex problem than the H-plane case. This is because the E-plane is dominated

1 inch

1 inch

1½ inch

1 inch



ILLUMINATED REGION ON EDGE v

ILLUMINATED REGION ON EDGE q

PERFECTLY CONDUCTING PLATE

$\hat{e}_q$

$\hat{d}$

$\hat{e}_v$

$\hat{e}_p$

$\hat{I}$

y

z

x
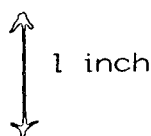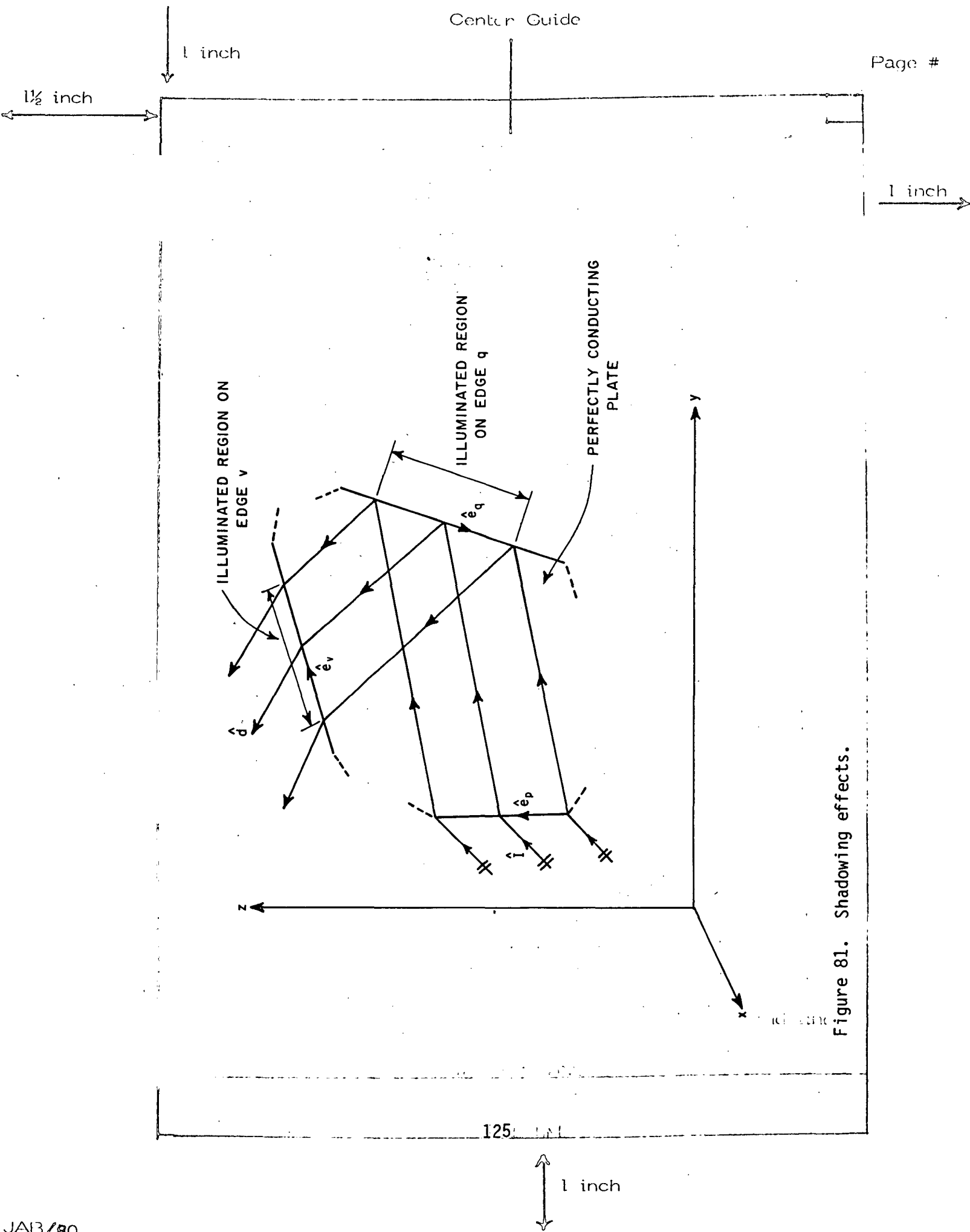
Figure 81. Shadowing effects.

1 inch

JAB/80
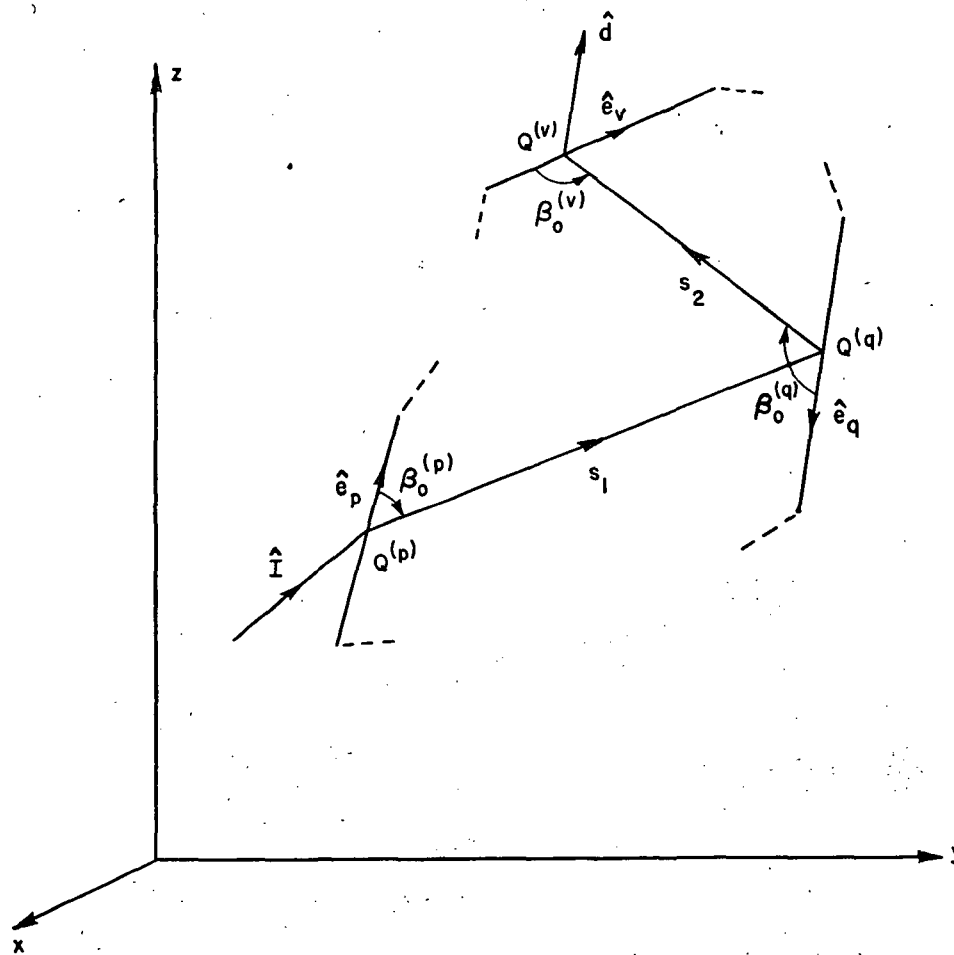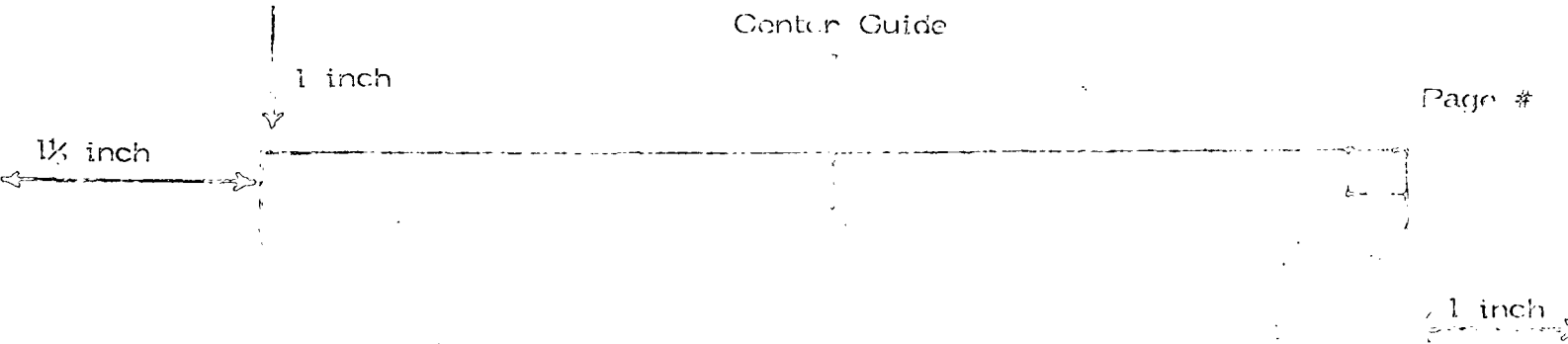
Figure 82.   Definition of parameters for higher order edge diffraction.

JAB/80

Center Guide

Page #

1 inch

1½ inch

1 inch

8 inch Chapter Line
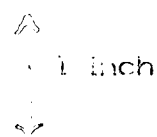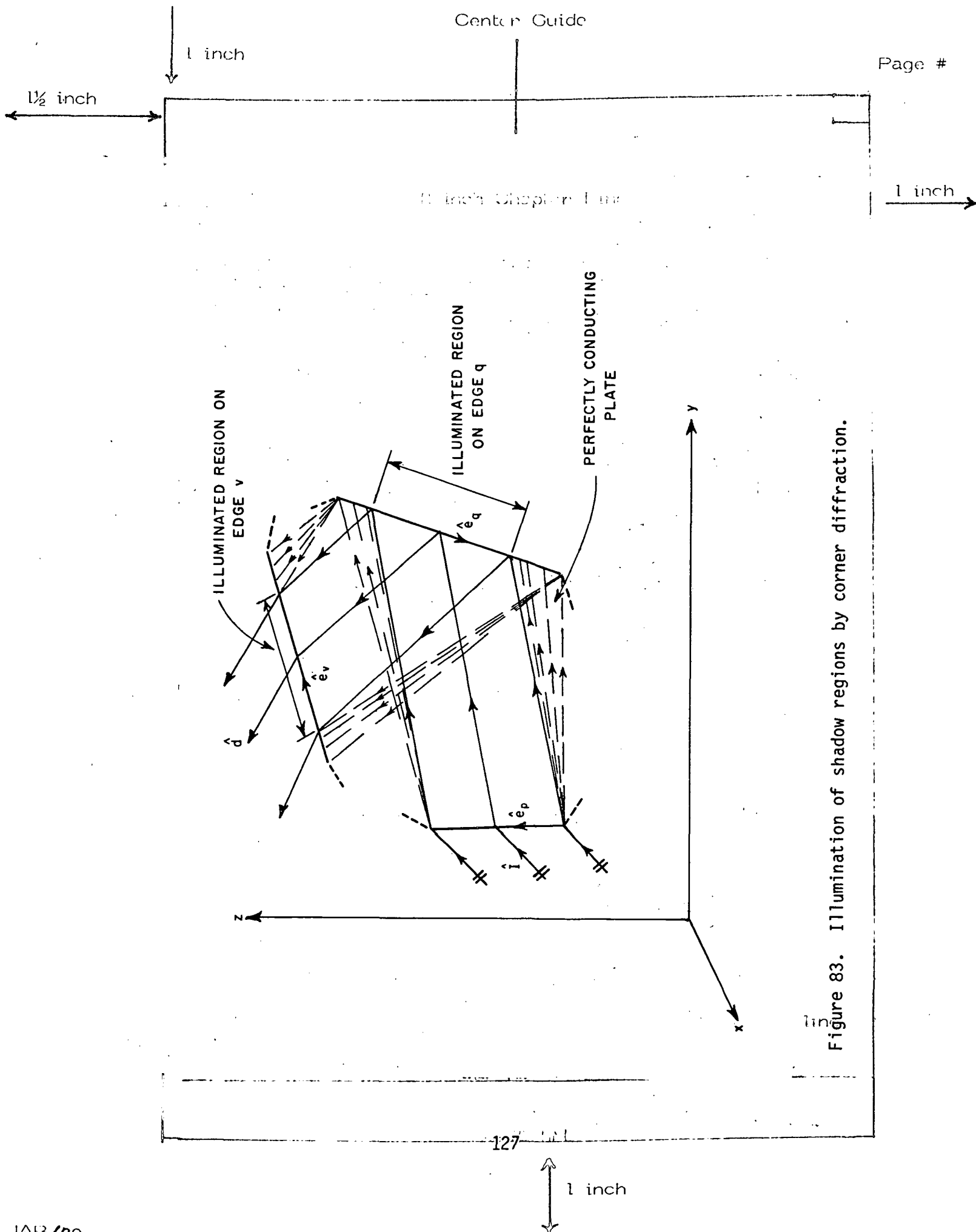
Figure 83. Illumination of shadow regions by corner diffraction.

1 inch

1½ inch

1 inch

by the back edge, accordingly interaction between the plate edges play
an important role in E-plane RCS pattern computations. These become
quite significant for near the edge on region as has been seen earlier
for the strip. Only single, double and triple edge diffracted fields
were considered, these were found to give adequate results for the geom-
etries used in our analysis, however, fourth order diffraction or even
higher may be included when dealing with smaller size geometries or when
considering patterns other than the principal E-plane. The EC method is
used in computing the contributions of all of these three mechanisms.
When computing the fields caused by the double and triple edge diffrac-
tion, ray tracing techniques must be used to determine the extent of the
illuminated region on an edge as needed for the numerical evaluation of
the radiation integrals associated with these interactions. The fields
diffracted from one edge to the other across the plate are assumed to be
plane waves.

Using these three mechanisms, the E-plane pattern for the Northrop
fin [34] shown in Figure 41 has been alanyzed. In Figure 84 our E-plane
RCS plane for the Northrop fin at 17.76 GHz is compared with their solu-
tion and also to their measured results. Northrop treated the problem
by breaking the plate into parallel strips. Our solution actually traces
the Northrop solution. But both solutions deviate from the measured
data near edge on regions. Considerable effort was directed to computing
the null value at PH=150$^O$. It was found that the E-plane pattern is
extremely sensitive to orientation at high frequencies (17.76). This is
clearly seen by examining Figure 85 which shows the results obtained by
rotating the plate in the X-Z plane by a mere 2.5$^O$, compared to the same
measured data. The calculated results in Figures 84, 85 span the experi-
mental results reported by Northrop. This explains the deviation between
measured and calculated results in the region 110$^O$<PH<180$^O$. However,
the deviation observed in the region 0$^O$<PH<50$^O$ is caused by not including
the edge wave contribution in our solution. Note that the notation $E_{PH}$
is used to indicate the PH component of the Electric field in the
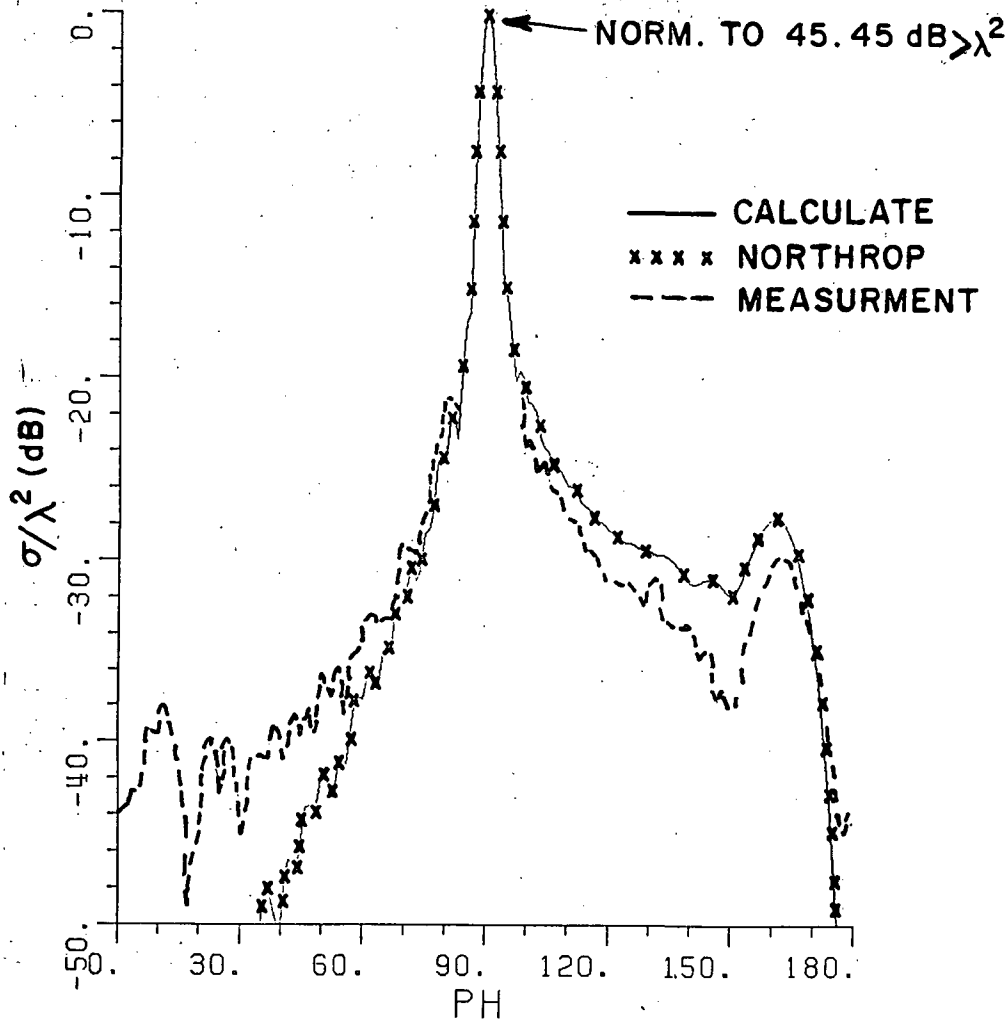
1 inch

JAB/80

1½ inc.



Figure 84. $E_{PH}$, $\theta = 90^0$ RCS pattern for Northrop fin at 17.76 GHz

1 inch

JAB/80

1½ inch

inch



NORM. TO 45.45 dB>$\lambda^2$

—— CALCULATE (ROTATION = 2.5°)

– – – MEASURED

$\sigma/\lambda^2$ (dB)

PH
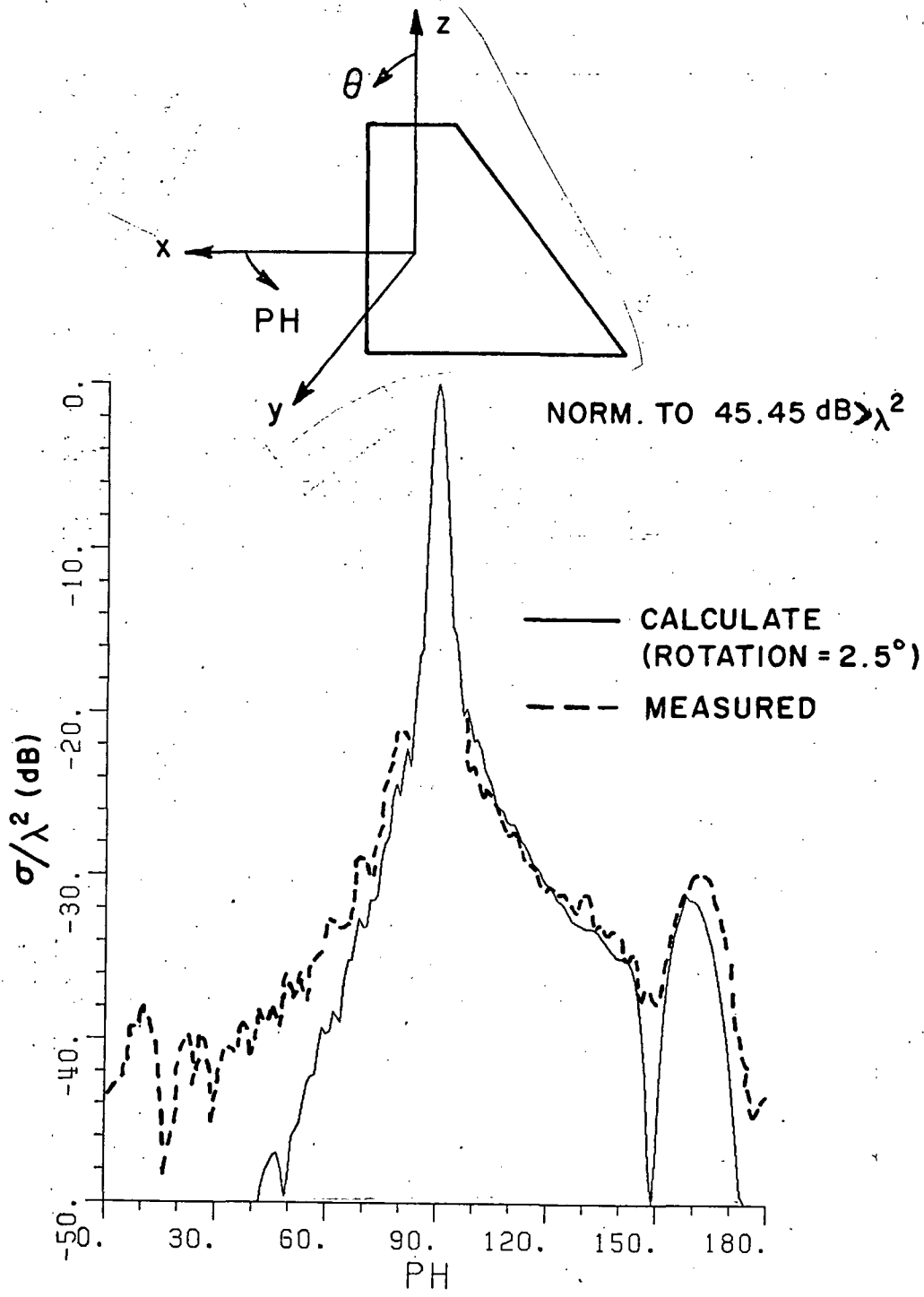
Figure 85.  $E_{PH}$,  $\theta = 90^0$ RCS pattern for Northrop fin at 17.76 GHz. Plate is rotated in x-z plane by 2.5°.

1 inch

JAB/80

1½ inch

1 inch

standard spherical coordinate system. Typical E-plane patterns ($E_{PH}$ polarization) for single, double and triple edge diffraction components for Northrop fin at 17.76 GHz are shown in Figures 86-88. In Figures

2 inch Chapter Line

87-88, one only observes the patterns for the range $90^o \leq PH \leq 180^o$ since the higher order terms are significant only in this region as is apparant by the comparison between Figure 84 and Figure 86. One also observes from Figures 87 and 88 that these terms, namely double and triple diffractions, are only needed for about $40^o$ from edge on. This becomes even clearer by examining Figure 89 which shows the sum of these two components.

THESIS / DISSERTATION
Typing Guide Paper

The ray mechanisms that were included in computing the double edge diffraction term are shown in Figure 90 where the incident ray is in the x-y plane. The ray diffracted from edge 4 (Figure 90-a) will illuminate part of edge 2. This illuminated region will or course depend on the angle of incidence on edge 4; however, the ray diffracted from edge 2 (Figure 90-b) will illuminate the entire edge 4. In Figure 91, one observes the component of the RCS pattern obtained using the EC associated with the double diffracted ray between edges 4 and 2 (ray 4-2), while that associated with the double diffracted ray between edges 2 and 4 (ray 2-4) is shown in Figure 92.

The EC method used to compute the field components shown in Figures 84-88 has an inherent error caused by the shadowing effect of an edge as is shown in Figure 93. To correct this inherent error, one has to include the corner diffracted fields which are the only ones that can illuminate the shadowed part of an edge. It should be noted that this source of error does not considerably affect our results since the double diffracted field is only needed in the region near edge on and by examining Figure 91 and Figure 92, it is clear that the difference between the two results is very small near edge on region; however, this difference could be large for a different plate geometry.

1st page Chapter center line

1st page Chapter end line

LAST TEXT LINE

1 inch

JAB/80

NORM. TO 45.45 dB/$\lambda^2$
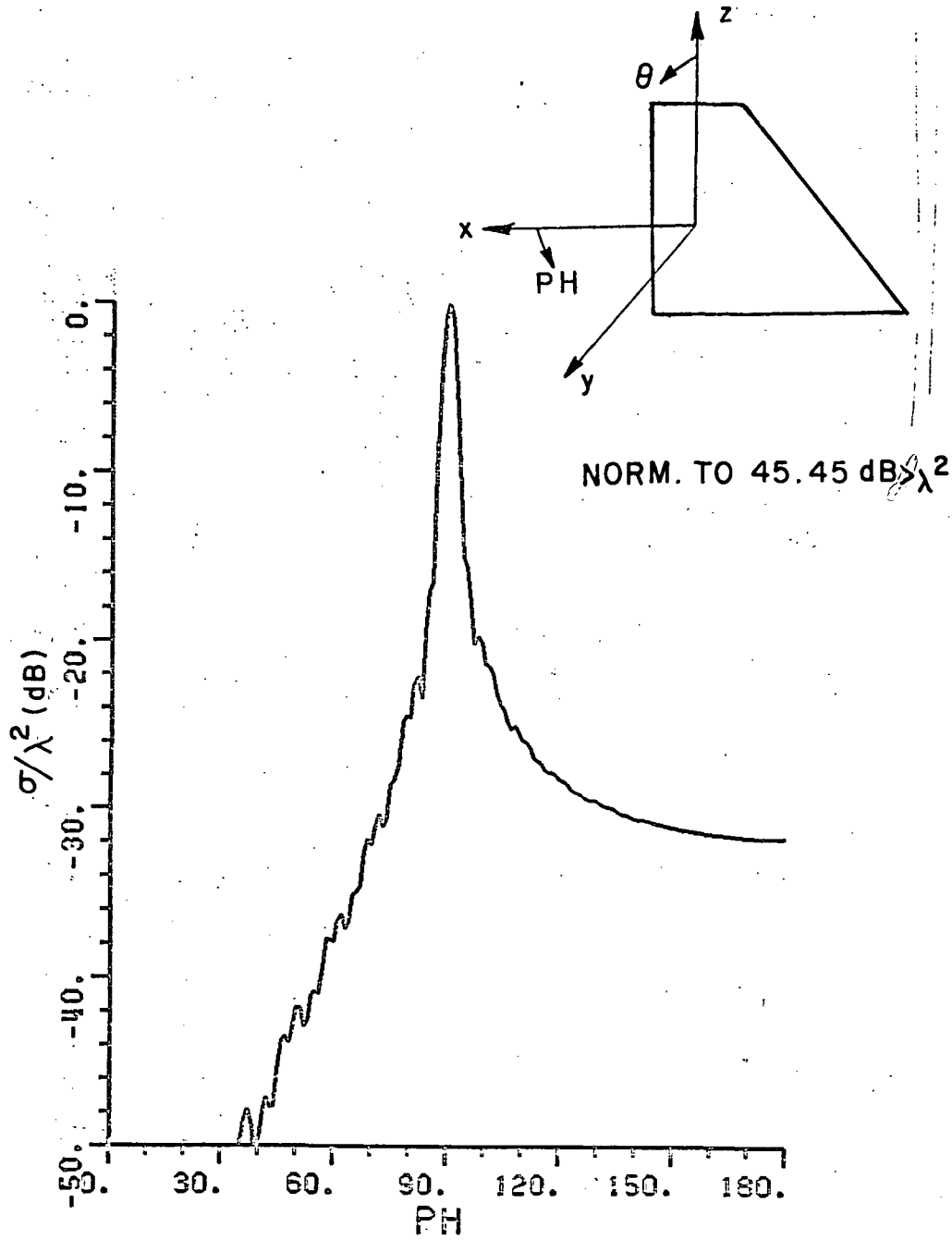
Figure 86. $E_{PH}$, single edge diffraction contribution to $\theta = 90^0$ RCS
pattern for Northrop fin at 17.76 GHz.

1 inch

JAB/80
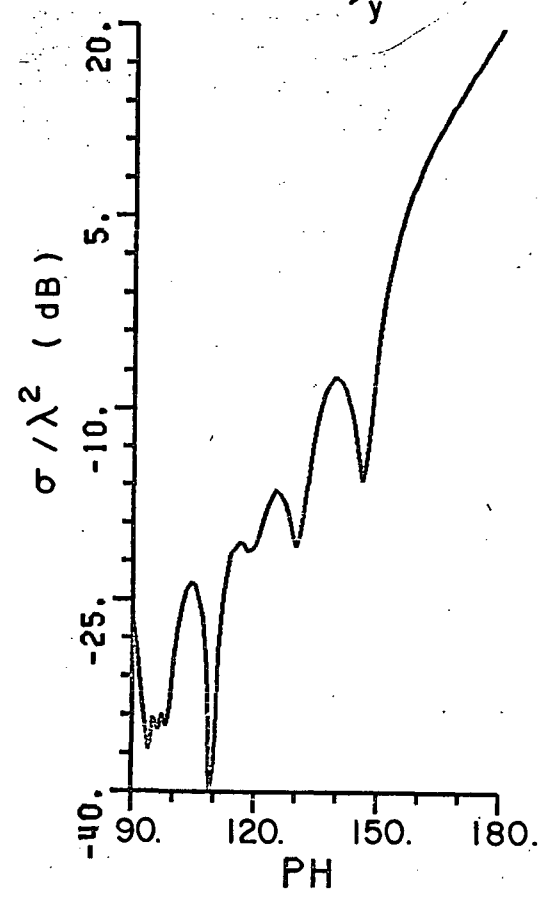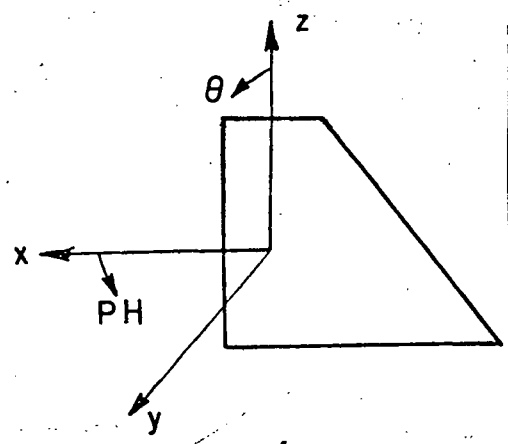
1½ inch

1 inch



Figure 87. $E_{PH}$, double edge diffraction contribution to $\theta = 90^\circ$ RCS pattern for Northrop fin at 17.76 GHz.

133

1 inch

JAB/30

1½ inch

1 inch

z

θ

x

PH

y

$\sigma/\lambda^2$ (dB)

20.

5.

-10.

-25.

-40.

90    120    150    180

PH
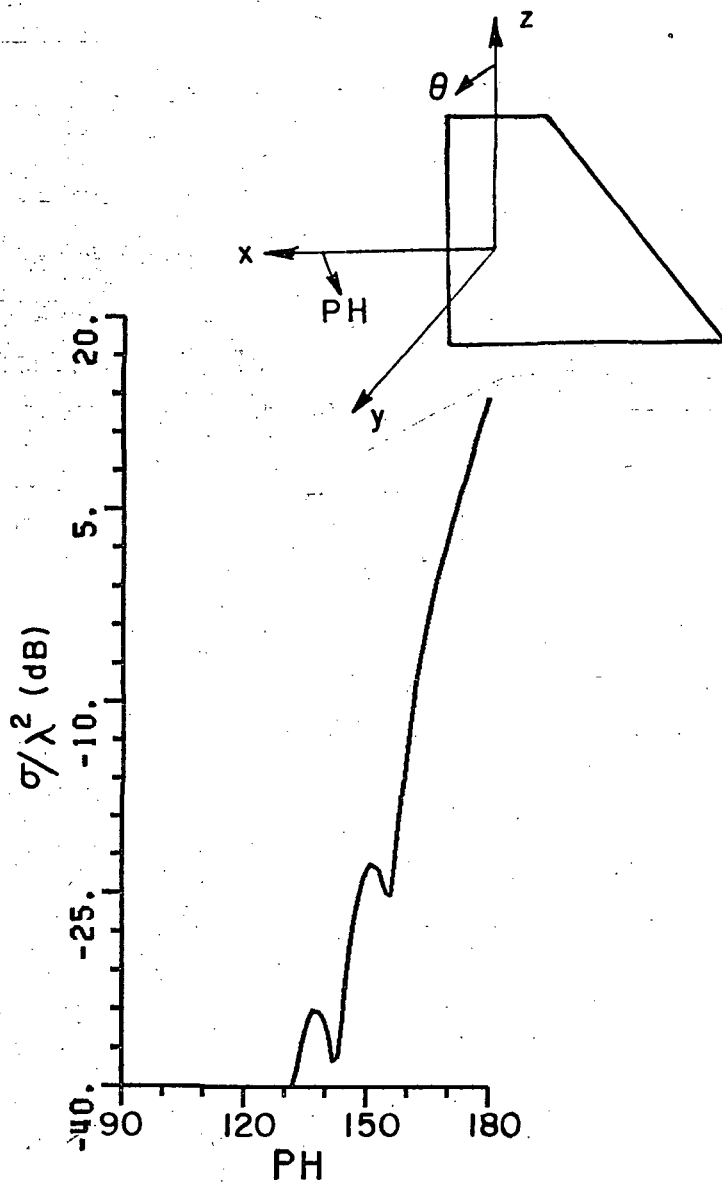
Figure 88.  $E_{PH}$, triple edge diffraction contribution to $\theta = 90^0$ RCS pattern for Northrop fin at 17.76 GHz.

1st page Chapter end line

1st page Chapter end line

JAB/80
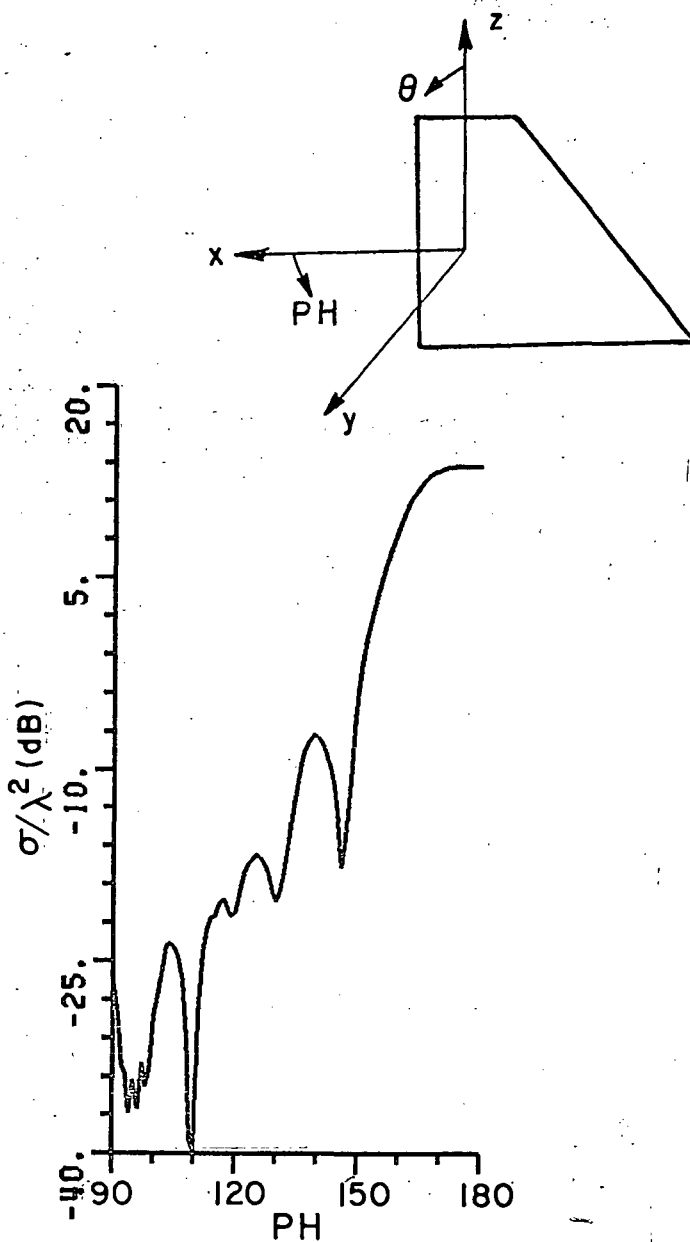
1 inch

1½ inch

1 inch



Figure 89. $E_{PH}$, sum of double and triple edge diffraction contributions to $\theta = 90^0$ RCS pattern for Northrop fin at 17.76 GHz.

135

1 inch

JAB/80

(a) RAY PATH 4—2

ILLUMINATED
REGION

(1)

(2)    (4)

(3)

Z

X

y

(b) RAY PATH 2—4

Z

X

(1)

(2)

ILLUMINATED
REGION

(4)

(3)

y
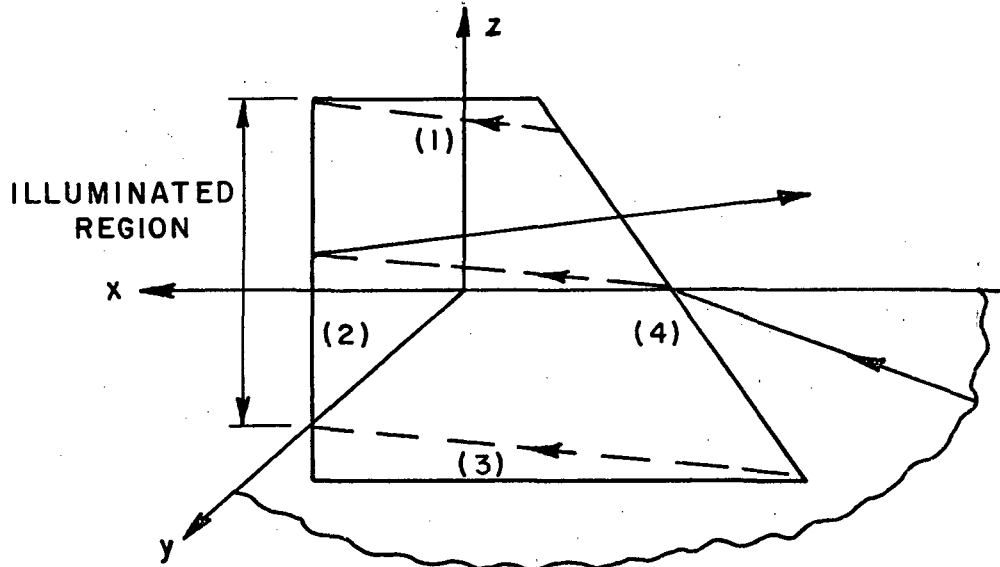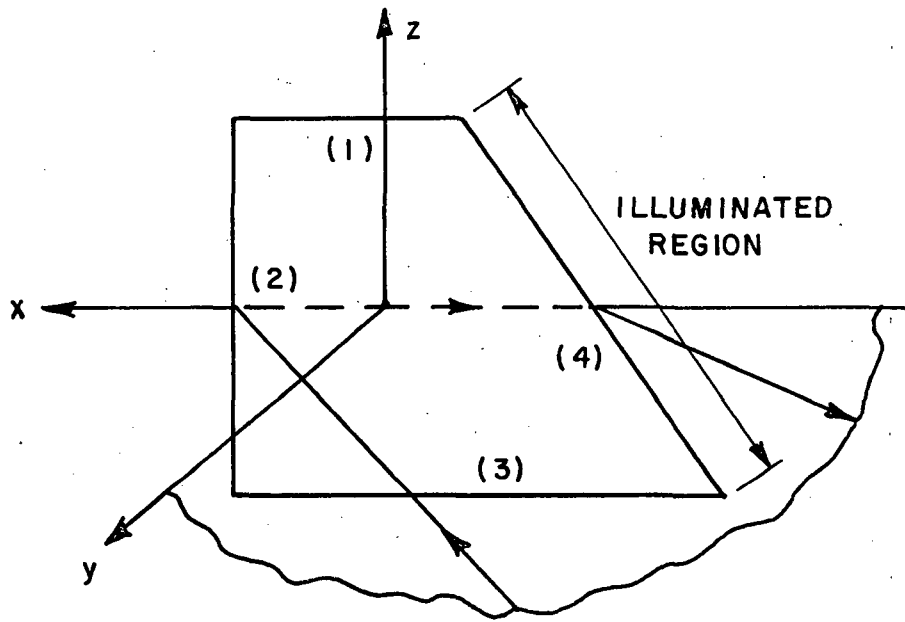
Figure 90.   Double edge diffraction ray paths.
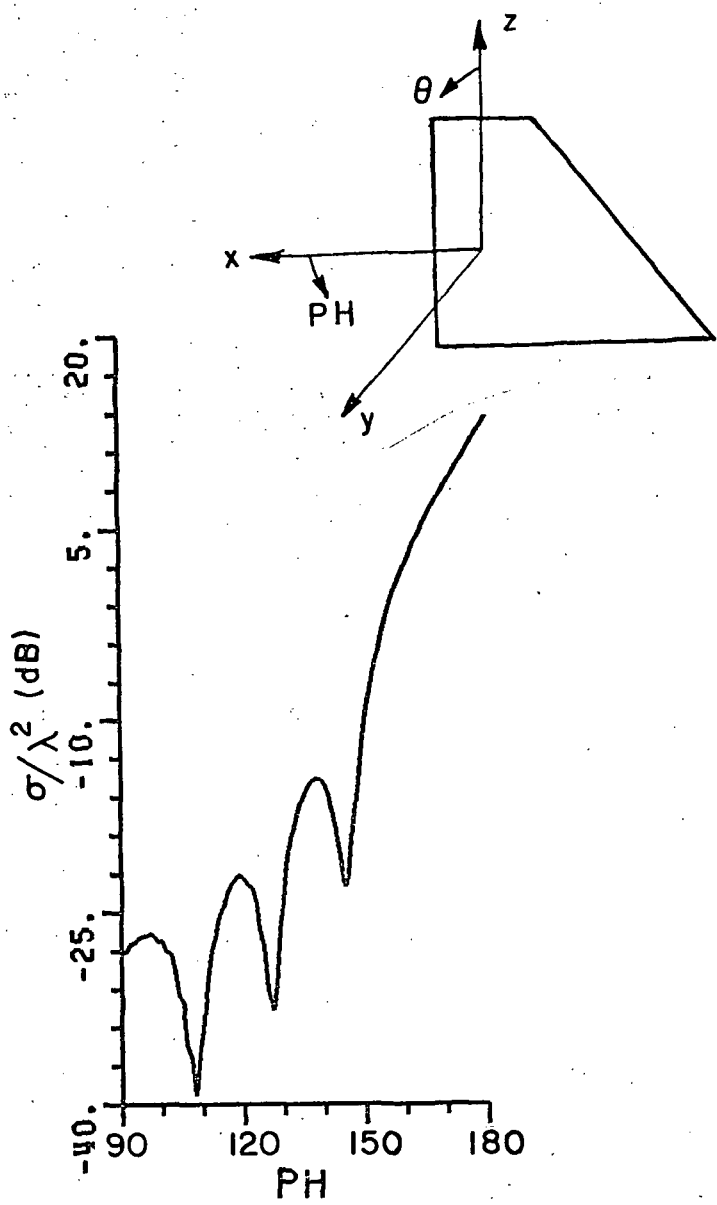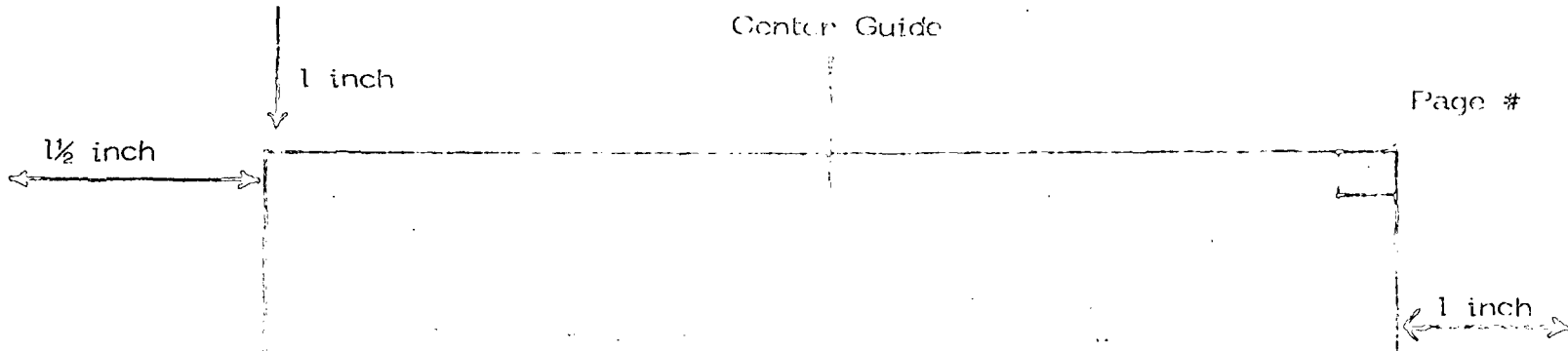
1 inch

Figure 91.   $E_{PH}$, double edge diffraction contribution to $\theta = 90^0$ fin
RCS pattern for Northrop fin due to ray (4-2) at 17.76 GHz.
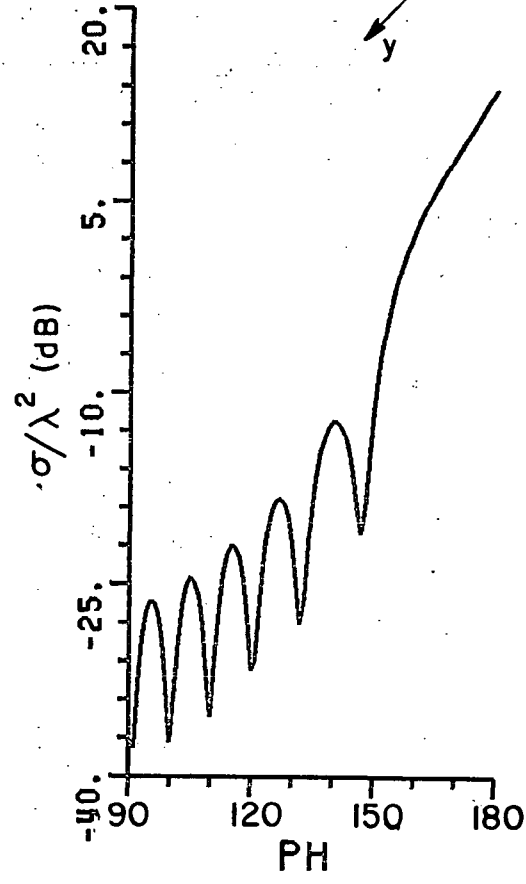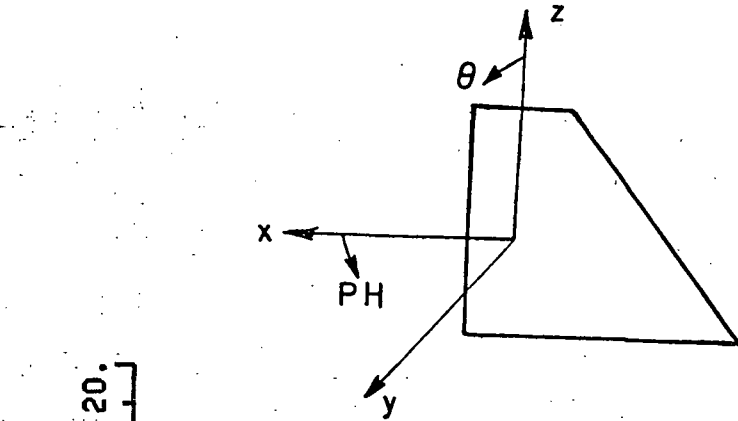
Figure 92. $E_{PH}$, double edge diffraction contribution to $\theta = 90^\circ$ RCS pattern for Northrop fin due to ray (2-4) at 17.76 GHz.

JAB/80

2 inch Chapter Line

**z**

ILLUMINATED
REGION

EDGE DIFFRACTED
RAYS

**x**

SHADOW
REGION

**y**

CORNER DIFFRACTED
RAYS

Figure 93.   Shadowing effects associated with Northrop fin.

1 inch

In Figure 94, the E-plane RCS pattern for the Northrop fin at 9.067 GHz is shown. The results are compared to measured results obtained by Mr. Chu [35]. Note the good agreement between the two results especially in the region $0 \leq PH \leq 90$ as compared to that in Figure 84. This indicates that at higher frequencies, the edge wave fields contribute more significantly to the lower levels of the RCS pattern.

In Figures 95 and 97 the individual contributions to the E-plane RCS pattern are shown due to single, double and triple diffraction mechanisms of Northrop fin at 9.067 GHz. The effect of modifying the Northrop fin geometry as shown in Figure 45 is seen in Figure 98. Again a small change in the plate angles results in more than 15 dB reduction in the E-plane RCS pattern. Of course this also implies the RCS has increased in some other regions of space. Table 1 shows the different edge diffracted rays associated with single, double and triple diffraction mechanisms which were used in our solution. It was found that double and

TABLE 1

SINGLE, DOUBLE AND TRIPLE EDGE DIFFRACTED RAYS
USED IN NORTHROP FIN ANALYSIS

| Single<br>edge # | Double<br>edge # - edge # | Triple<br>edge # - edge # - edge # |
|---|---|---|
| 2 | 2 - 4 | 2 - 4 - 2 |
| 4 | 4 - 2 | 4 - 2 - 4 |

$\theta = 90°$
FREQ = 9.067 GHz
NORM. TO 34.55 dB> $\lambda^2$

——— CALCULATED
- - - MEASURED [35]
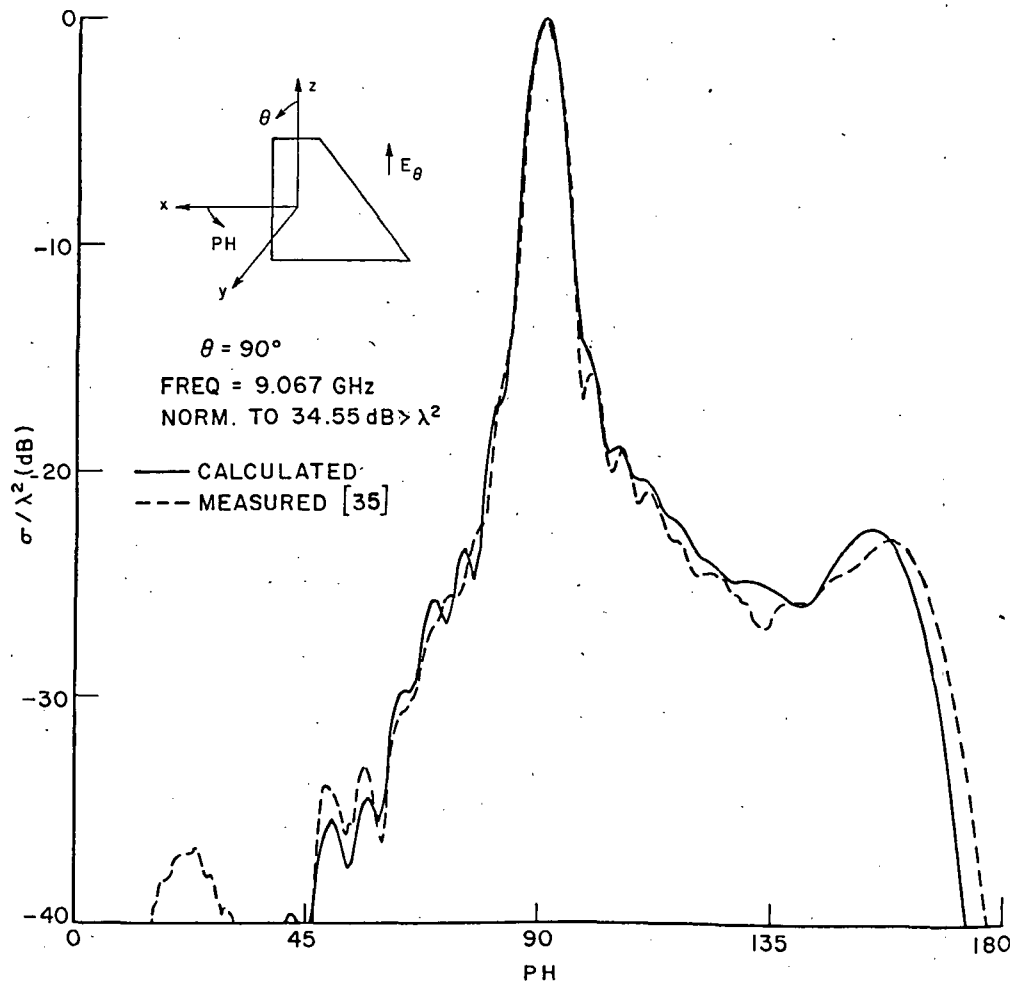
Figure 94. $E_{PH}$, $\theta = 90°$ RCS pattern for Northrop fin at 9.067 GHz.
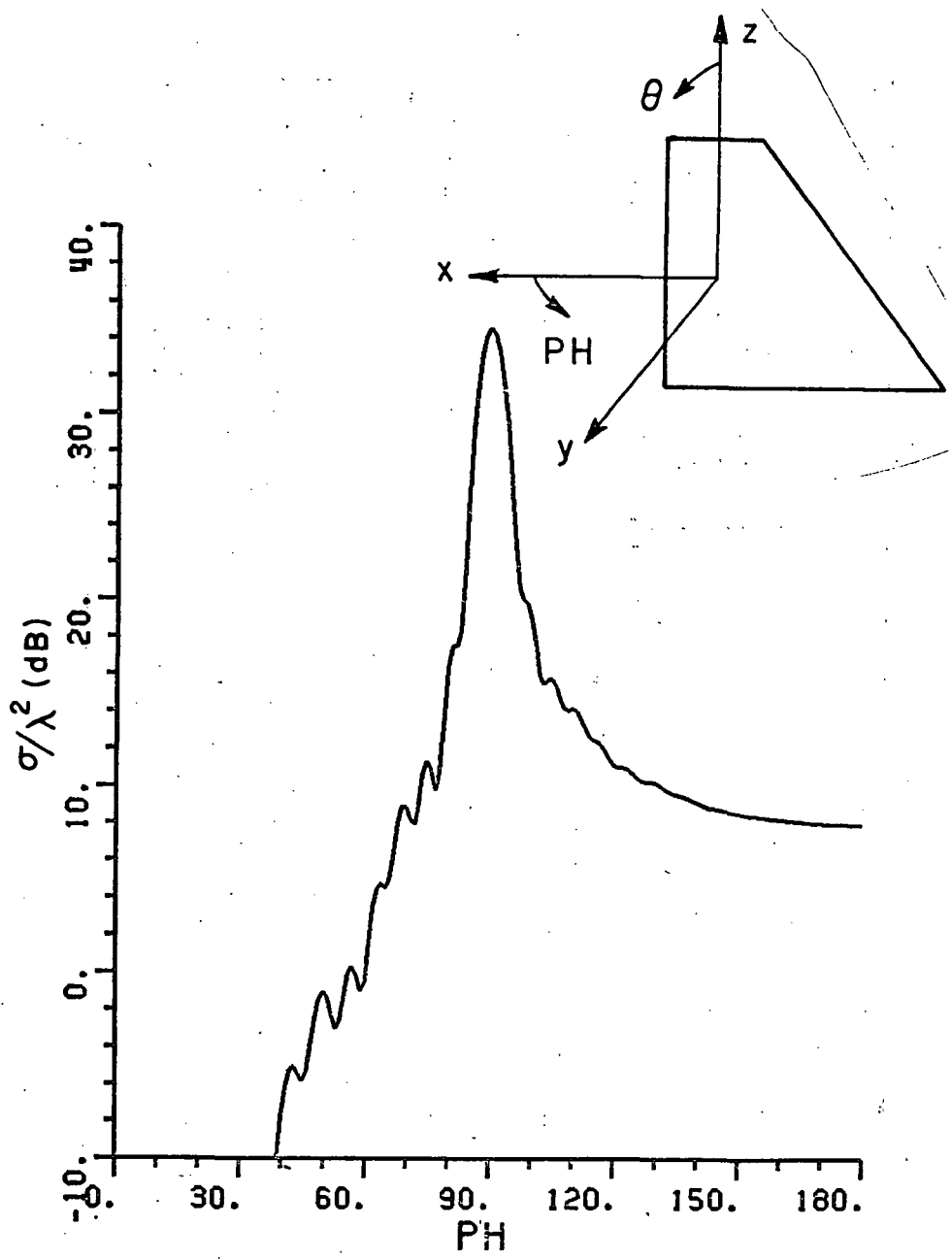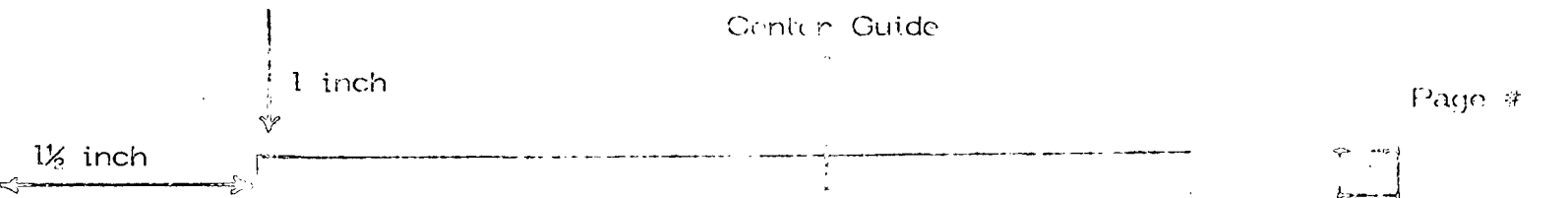
Figure 95. $E_{PH}$, single edge diffraction contribution to $\theta = 90^0$ RCS pattern for Northrop fin at 9.067 GHz.

JAB/80
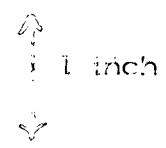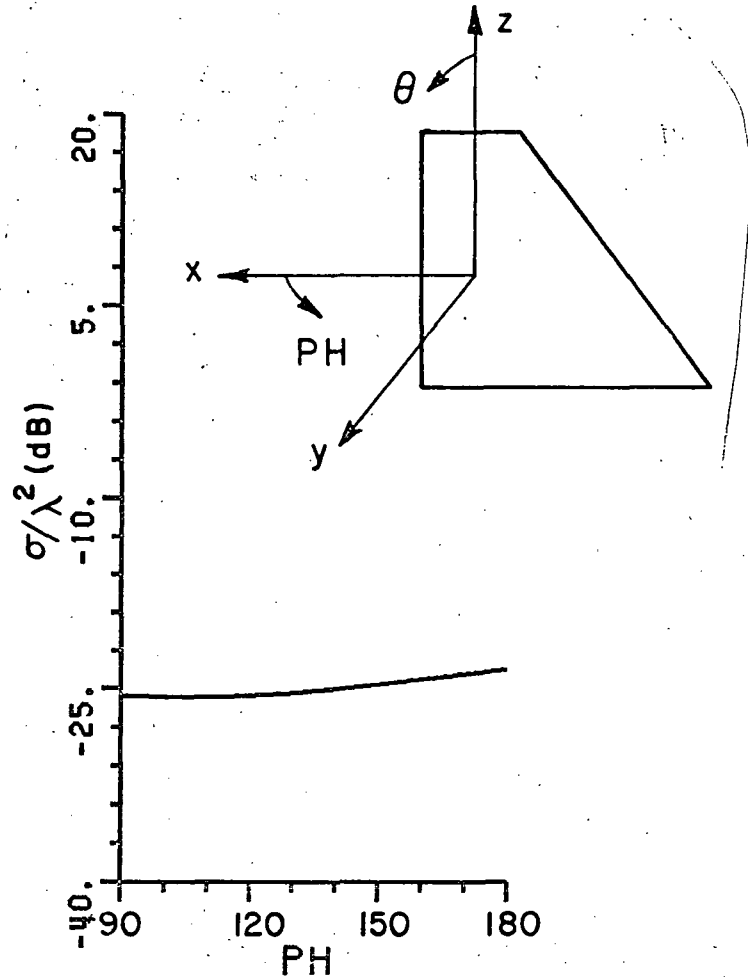
1 inch

1½ inch

1 inch



Figure 96.  $E_{PH}$, double edge diffraction contribution to $\theta = 90^\circ$ RCS pattern for Northrop fin at 9.067 GHz.

1 inch

JAB/80
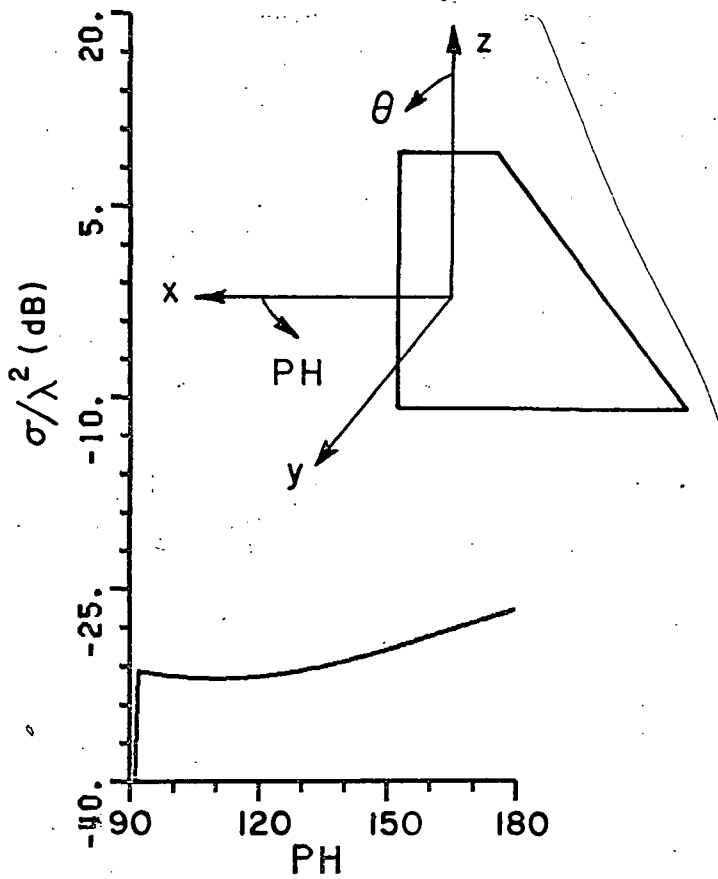
Figure 97. $E_{PH}$ triple edge diffraction contribution to $\theta = 90^0$ RCS pattern for Northrop fin at 9.067 GHz.

JAB/80

2 inch Chapter Line
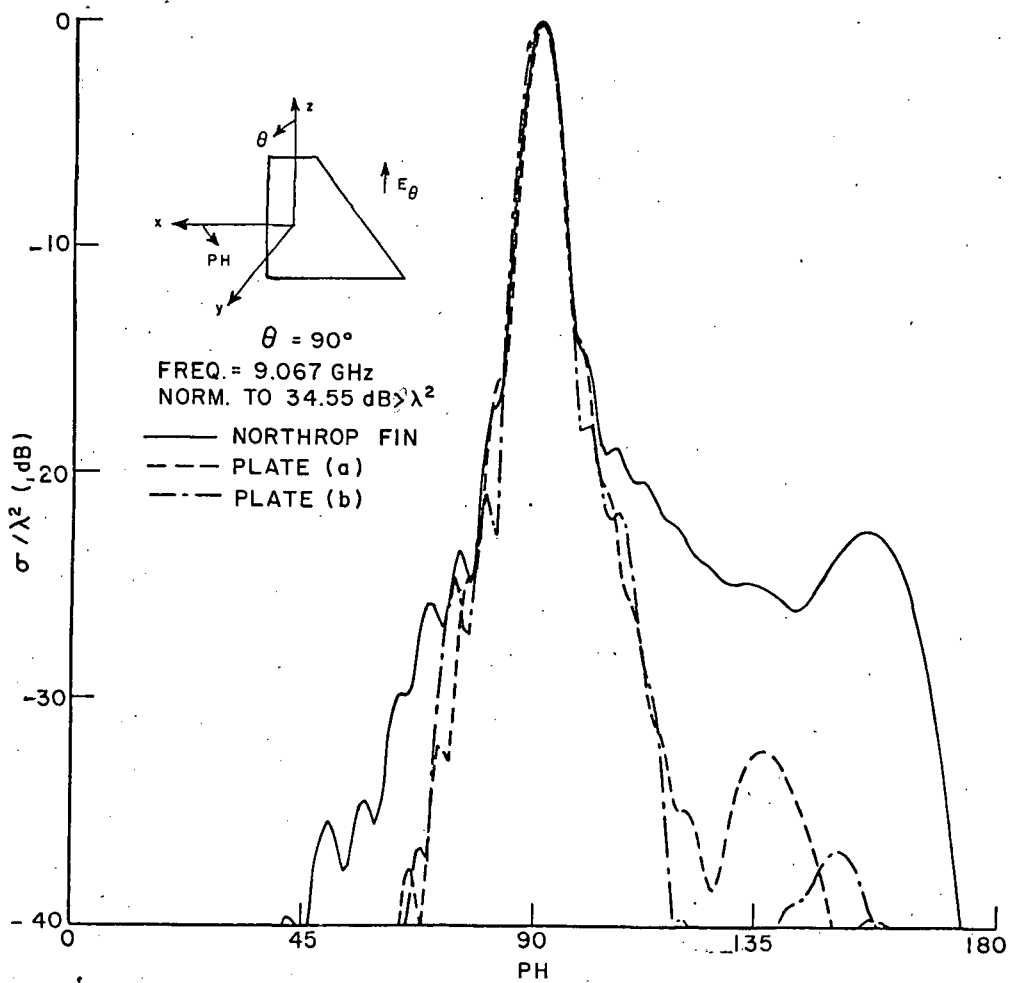


1st page Chapter end line

Figure 98. $E_{PH}$, $\theta = 90°$ RCS patterns for the plates shown in Figure 45 compared to that of Northrop fin at 9.067 GHz.

JAB/80

triple edge interactions between edges 2 and 4 are the ones that contri-bute significantly to the E-plane RCS pattern. The contribution of other edge interactions involving edges 1 and 3 were insignificant. However when computing the RCS pattern in a plane other than the principal E-plane these interactions should be included.

Finally the E-plane RCS pattern for the plate shown in Figure 47 is seen in Figure 99, it is compared to measured results [35]. The agreement between the two results is quite good. The deviation between them in the region $0^o$<PH<$45^o$ is probably caused by the finite curveture of the plate and also by not including the edge wave fields in our solution.

THESIS / DISSERTATION
Typing Guide Paper

D. BACKSCATTERING FROM A DISK

The E-plane RCS pattern for a disk is analyzed by using the Equiva-lent current method. The geometry used is shown in Figure 100. The disk of radius a is in the y-z plane and the pattern is taken in the x-y plane. The disk is modeled by a plate with finite number of edges. Figure 56 shows the two models used in our analysis, and the results presented here are compared with the exact solution [41]. Our solution includes the Equivalent currents associated with single, double and triple edge diffraction. Figure 101 shows typical ray paths for double and triple diffraction. Note that use of diffraction between straight line segments eliminates the need to consider caustics as would have been necessary if the diffraction by the circular rim were used.

Figures 102 and 103 show the E-plane ($E_{PH}$ polarization) pattern for ka=8.28 for both models, the 8 and 12 sided plates respectively. These results are compared with the exact solution and also to results obtained by Bechtel [39]. His results deviate considerably from the exact one in the range $45^o$<PH<$90^o$. This is because his solution does not include higher order diffraction contributions. The agreement be-tween our result and the exact solution is far superior. As one

JAB/80
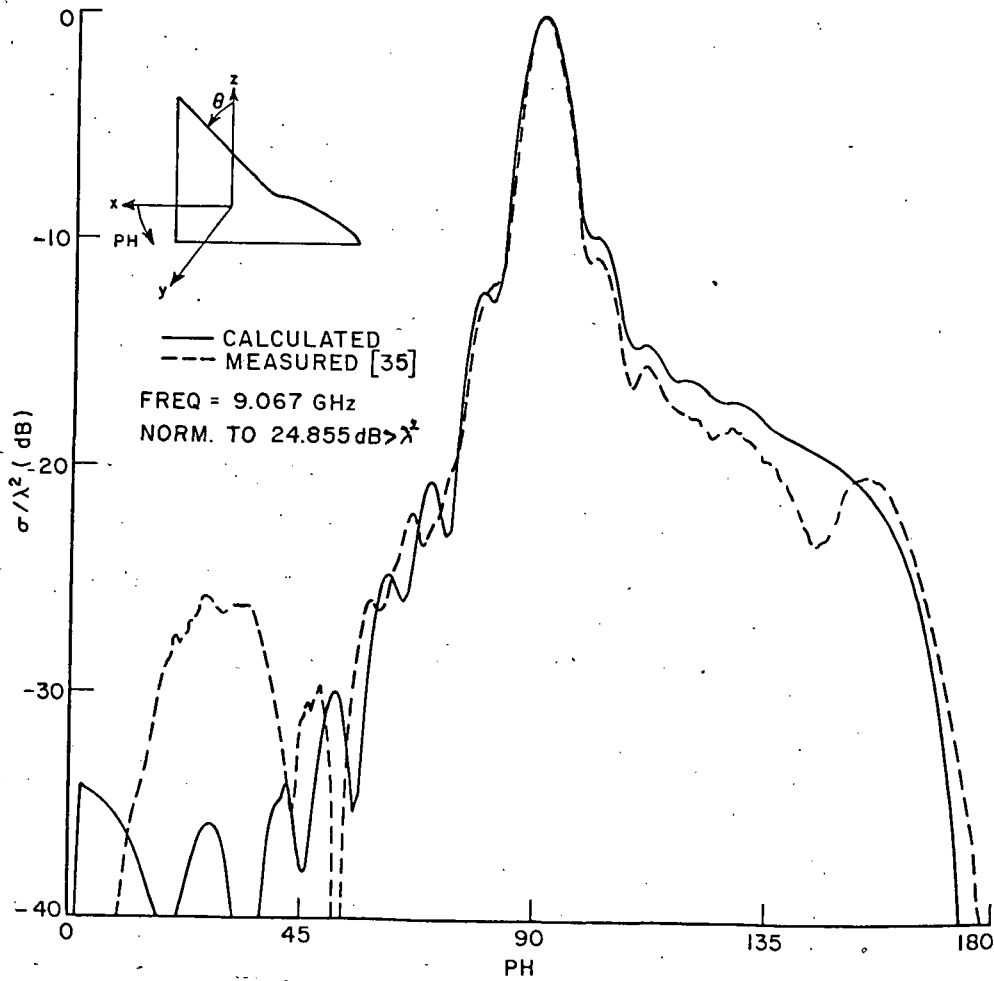
1 inch

1½ inch



Figure 99. $E_{PH}$, $\theta = 90^0$ RCS pattern for the plate shown in Figure 47, using first, second and third order Equivalent currents.

147

1½ inch

ch
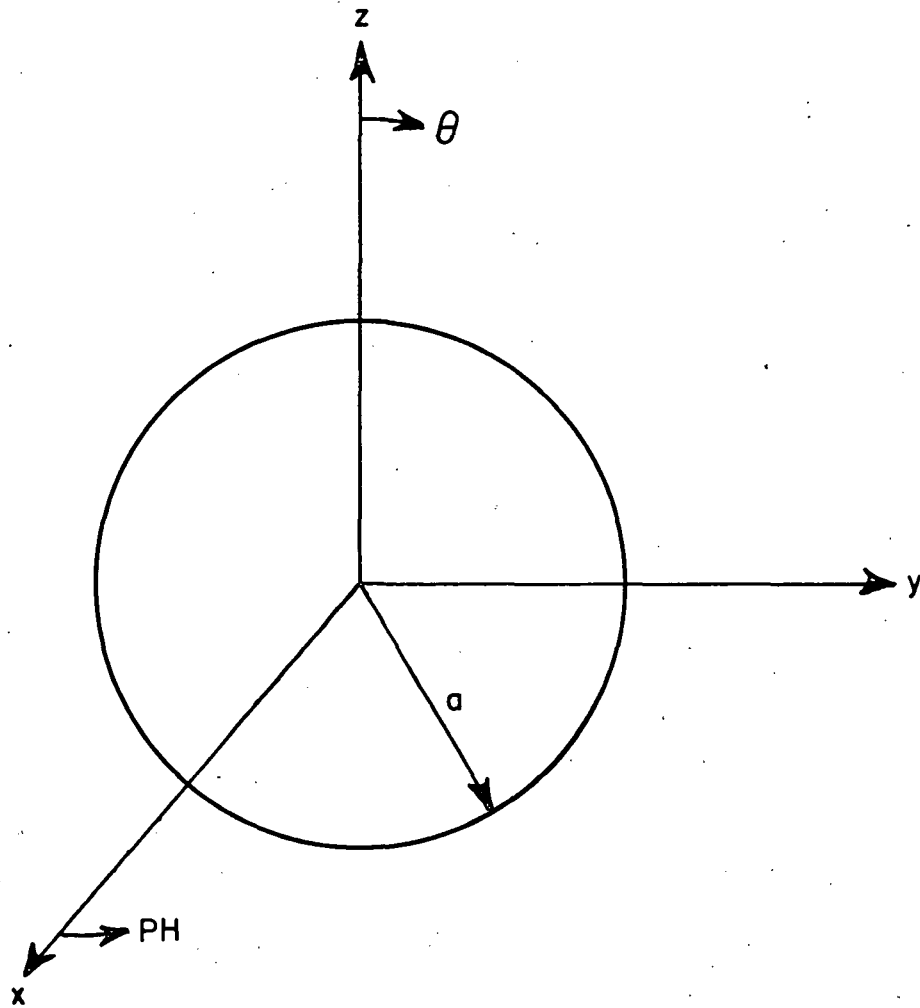


Figure 100. Disk geometry.

1 inch

JAB/80
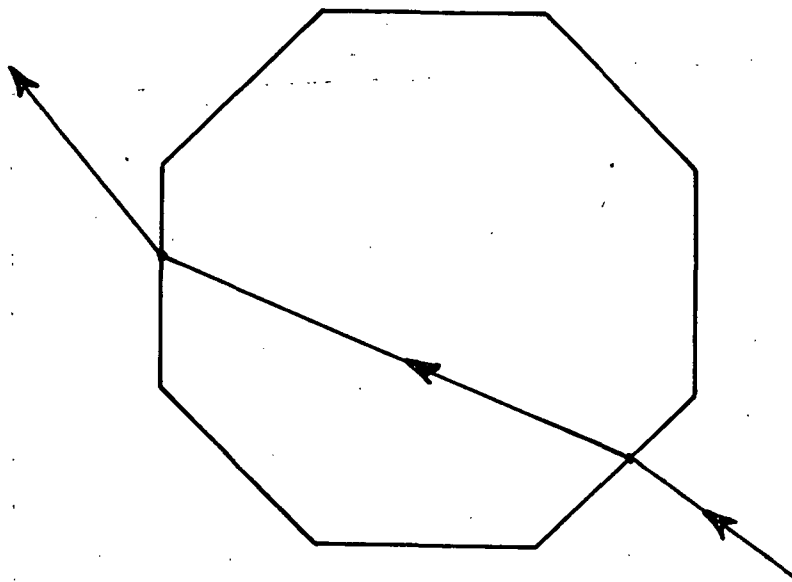
1½ inch

1 inch

**(a) DOUBLE DIFFRACTION**
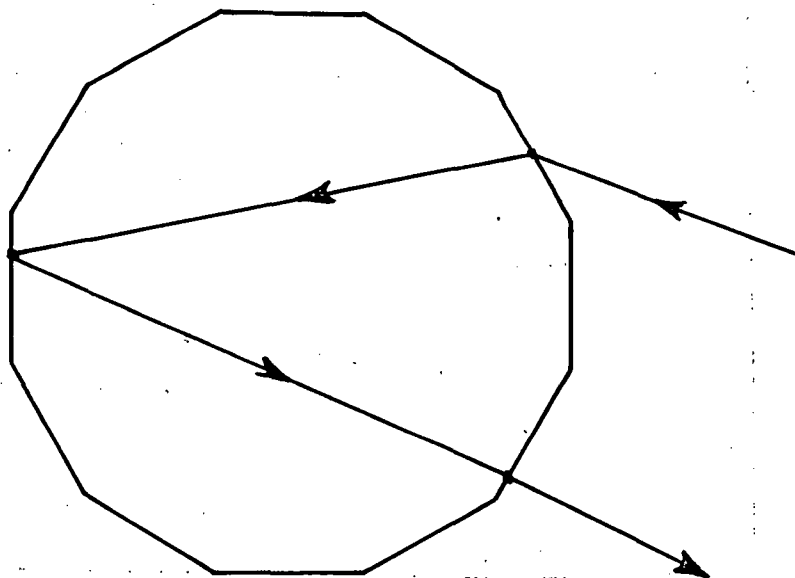
**(b) TRIPLE DIFFRACTION**

Figure 101. Ray paths for the double and triple edge diffraction mechanisms for the disk models.
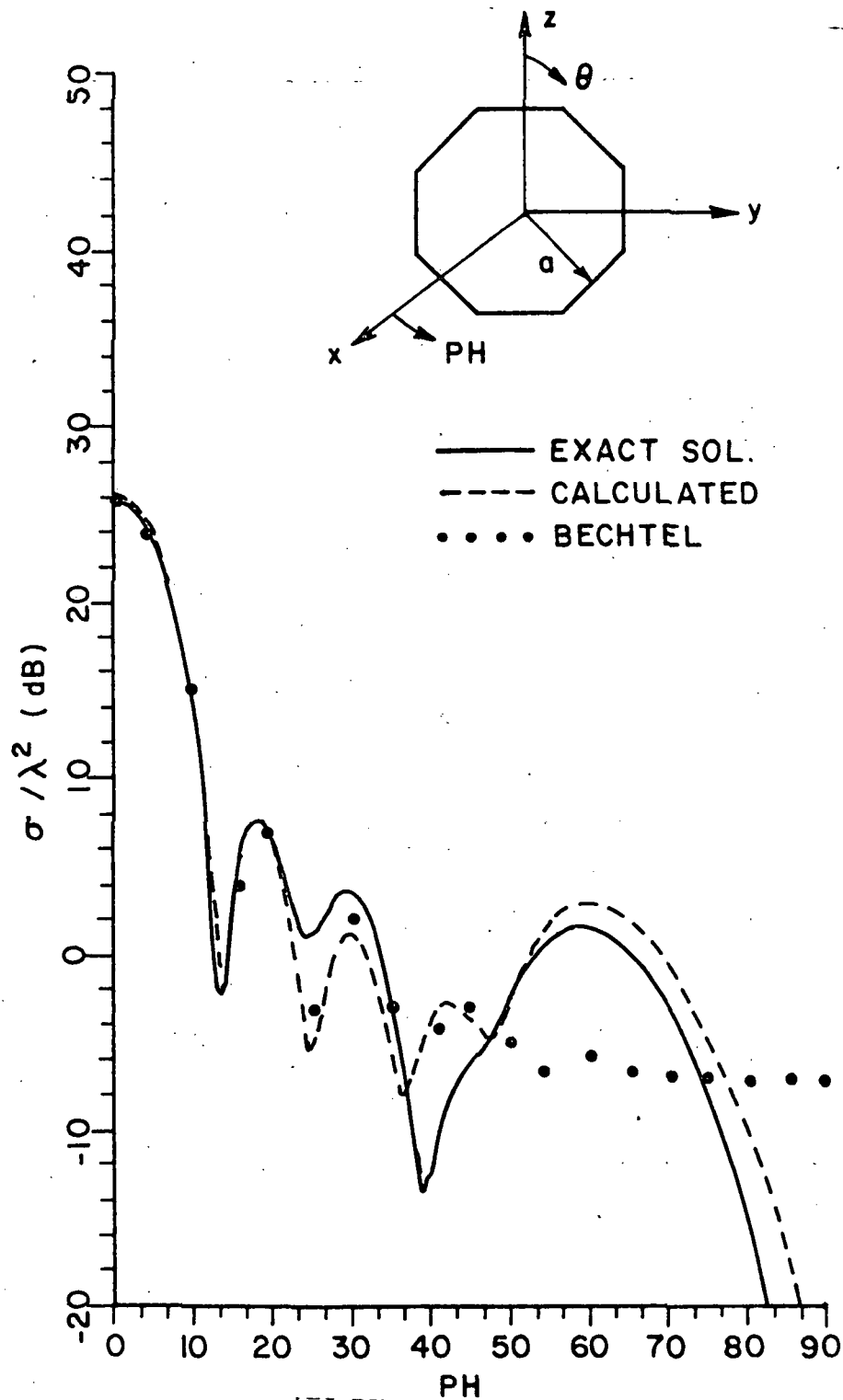
149

1 inch

JAB/80

Figure 102. $E_{PH}$, $\theta = 90^0$ RCS pattern for the 8 sided disk model line using first, second and third order Equivalent currents (ka = 8.28).

JAB/80

Figure 103. $E_{PH}$, $\theta = 90^{0}$ RCS pattern for the 12-sided disk model using first, second and third order Equivalent currents (ka = 8.28).

1½ inch
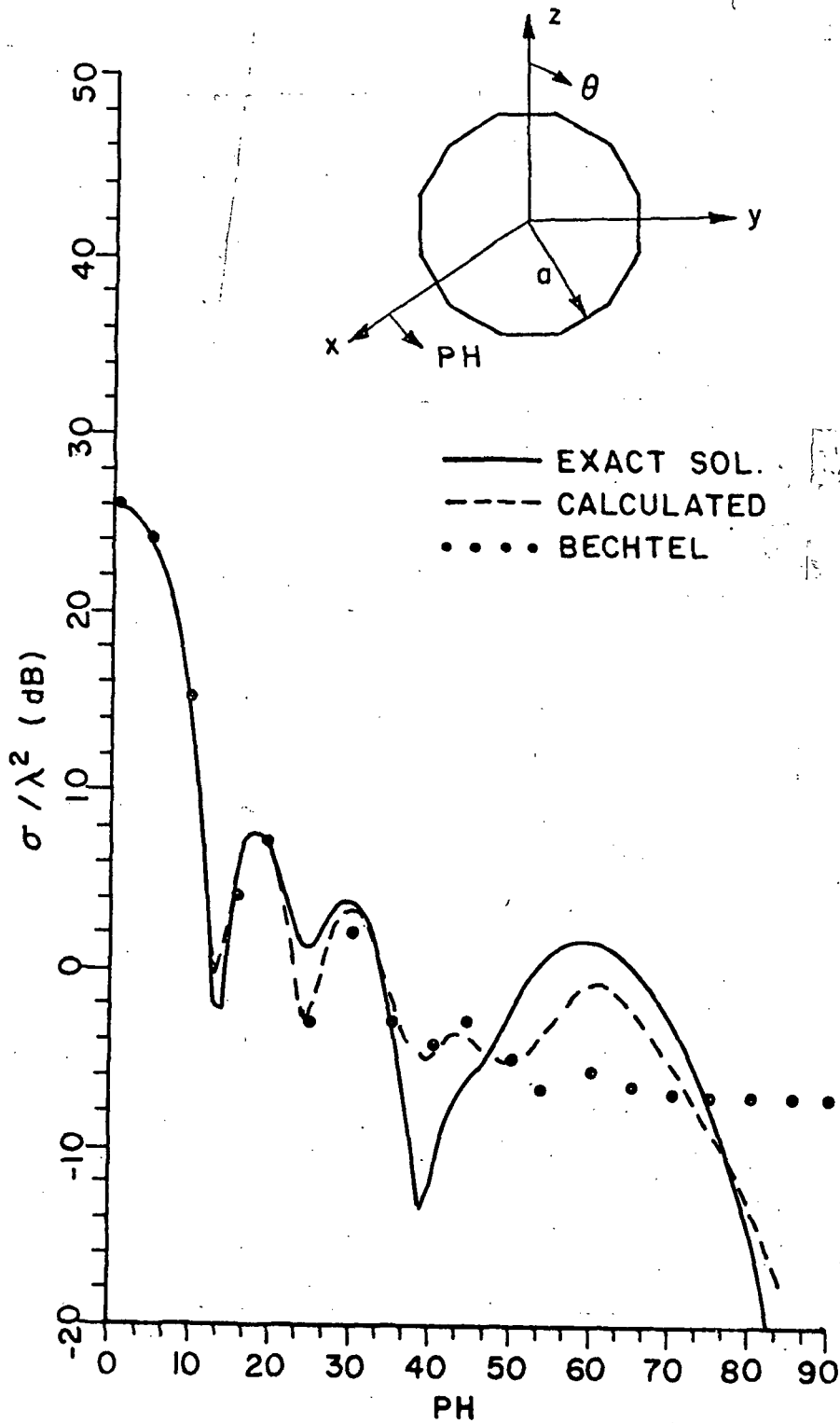
1 inch

1 inch

JAB/80

would expect the 12 sided model gives better agreement, particularly in the region near 30$^o$ since it better fits the disk.

1 inch

The deviations between the two solutions are obviously due to the finite curvature of the disk, accordingly as the number of edges is increased, better agreement is obtained. In Figures 104-109, we show the results for different disk sizes. As the size is increased, the 12 sided model gives better results than the 8 sided one. Again, our solution includes single, double and triple edge diffraction mechanisms and the EC method is used to compute their contributions to the E-plane RCS pattern. In Figures 110, 111, we show our result computed using the 12 sided disk model compared to the solution provided by Mr. Chu [42]. He used the EC method to compute the contribution of first order diffraction to the E-plane RCS pattern by integrating numerically over the disk rim. The deviation between his results and the exact solution is due to the fact that his solution does not include any higher order interactions. However, Burnside, et. al., [15] computed the contribution of double diffraction terms to the axial RCS of a finite cone using the EC method. A similar approach could be used to compute the contributions of the doubly and triply diffracted rays across the disk which is the limiting case of a finite cone. Note that when using this approach, one has to consider the line caustic located on the axis of symmetry. This introduces a phase shift of $+ \frac{\pi}{2}$ radians as the multiply diffracted rays cross the disk. The use of a multi-sided plate to model the disk circumvents the caustic problem. By using the approach shown in [15], one can compute the RCS of disks which have radii as small as 0.3$\lambda$. By using our method, the number of edges that can be used to model the disk is limited by the edge electrical length which should be of the order of a wavelength. Accordingly, one can handle disk sizes such that

$$ka \geq \frac{\pi}{\sin\alpha}$$
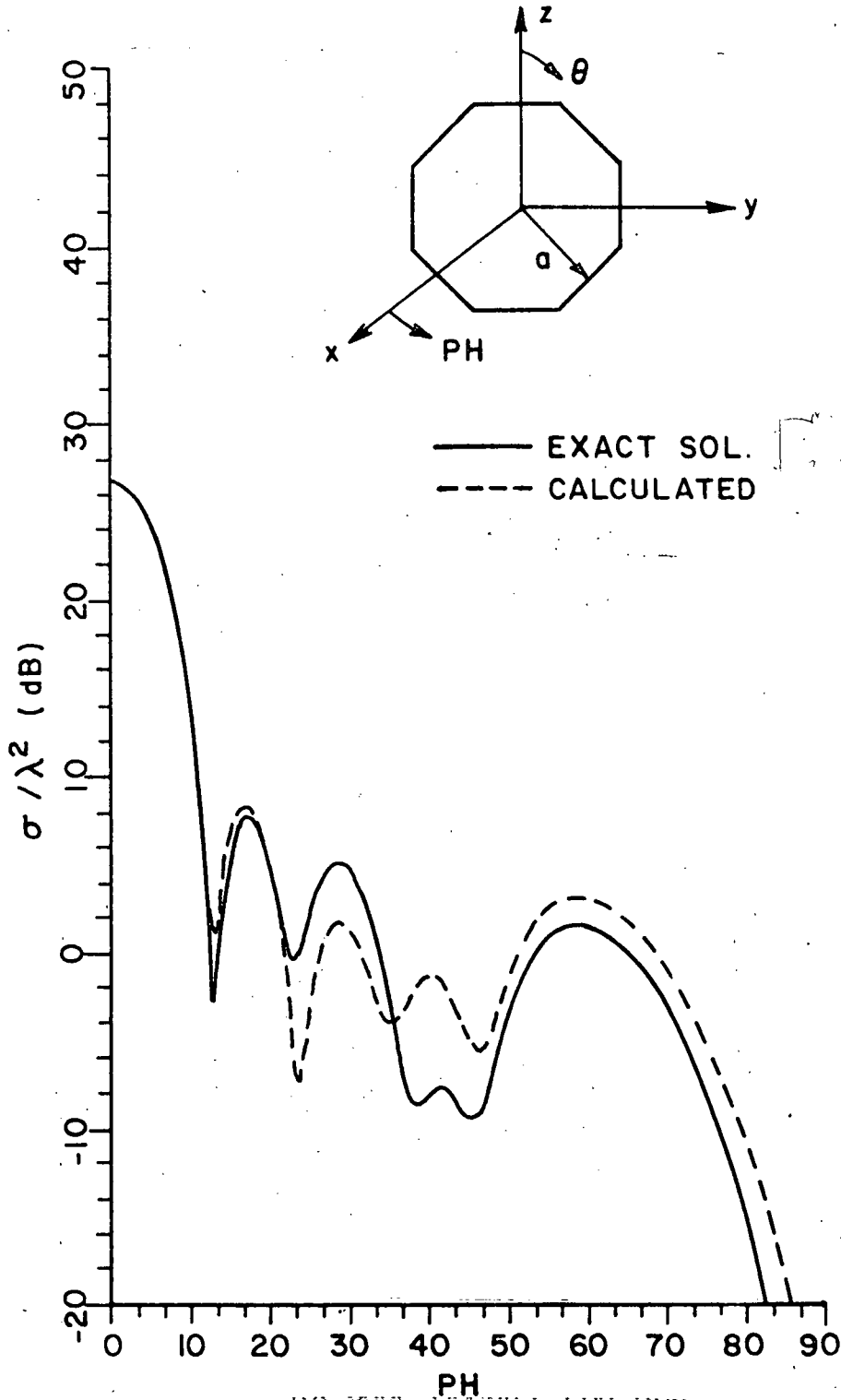
THESIS / DISSERTATION
Typing Guide Paper

1st page Chapter end line
— — — — — — — 1st page Chapter end line

LAST TEXT LINE

page 152, etc

1 inch

JAB/80

Figure 104. $E_{PH}$, $\theta = 90^0$ RCS pattern for the 8 sided disk model line using first, second and third order Equivalent currents (ka = 8.59).

JAB/80
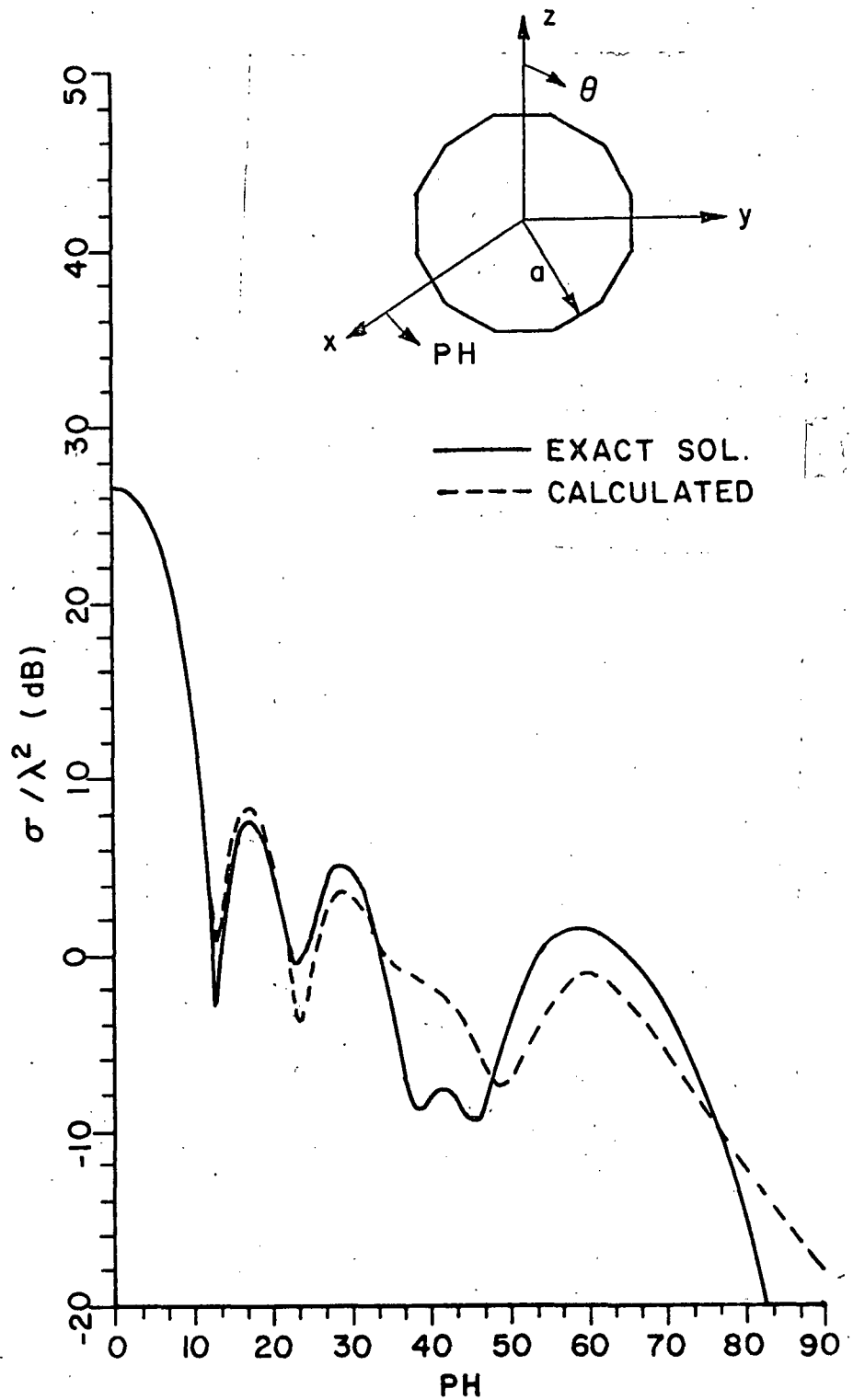
1 inch



Figure 105. $E_{PH}$, $\theta = 90^0$ RCS pattern for the 12 sided disk model using first, second and third order Equivalent currents $(ka = 8.59)$.

1 inch

JAB/30
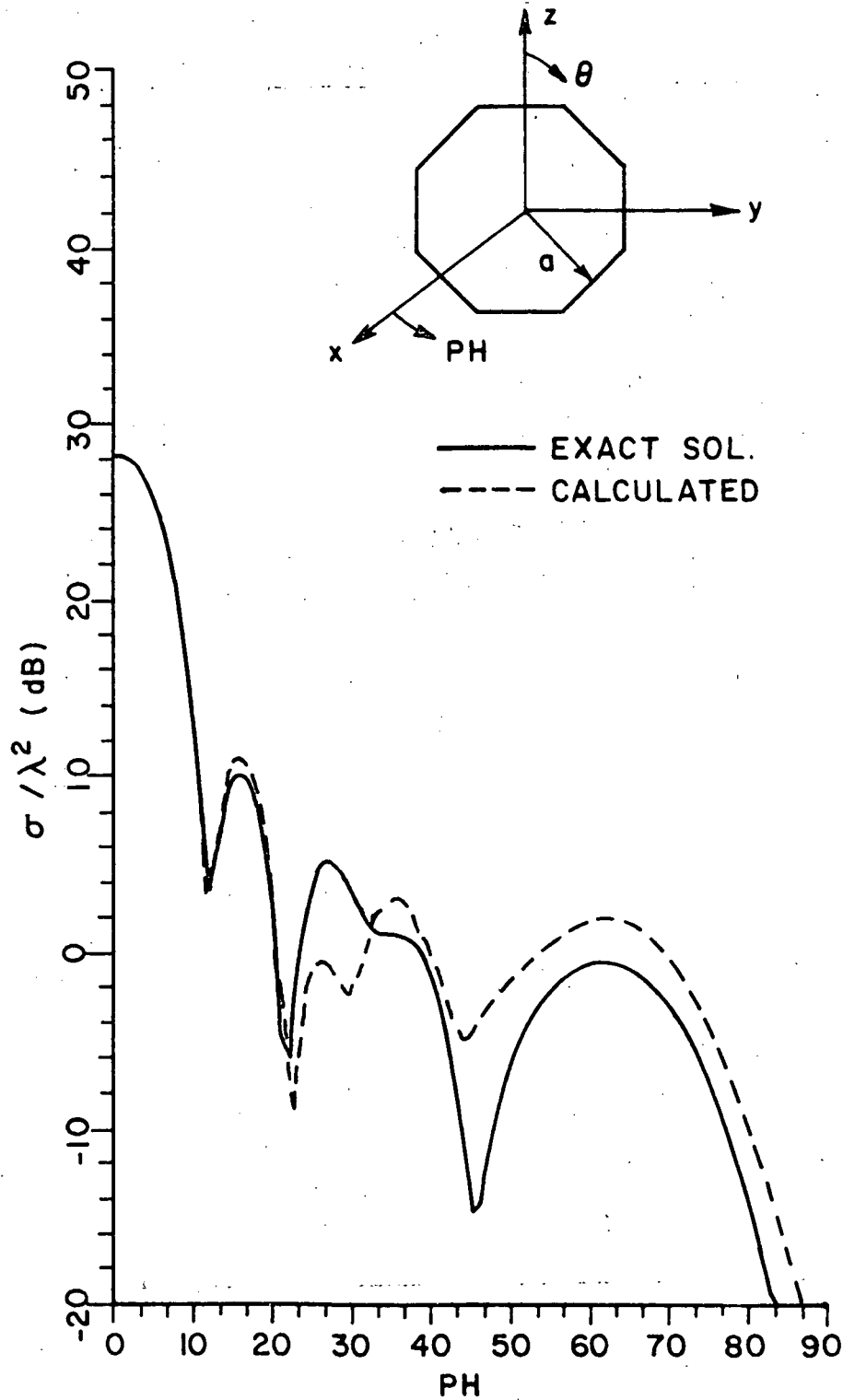
Figure 106. $E_{PH}$, $\theta = 90^\circ$ RCS pattern for the 8-sided disk model
using first, second and third order Equivalent currents
(ka = 9.45).

1½ inch

1 inch

1 inch

JAB/80

Figure 107.  $E_{PH}$,  $\theta = 90^{\circ}$ RCS pattern for the 12 sided disk model using first, second and third order Equivalent currents (ka = 9.45).

1 inch

1 inch

1½ inch

1 inch

1 inch

JAB/80
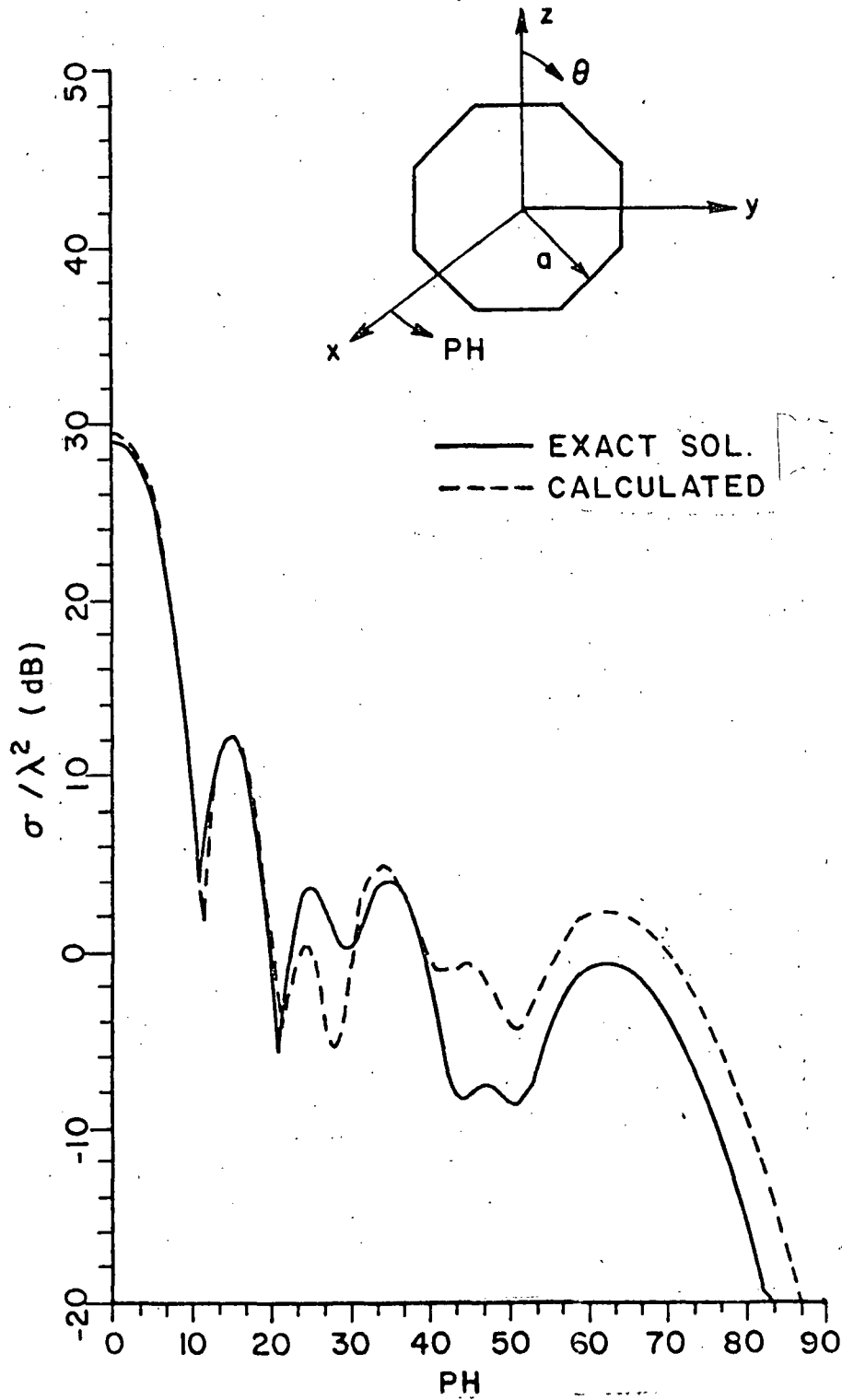
Figure 108. $E_{PH}$, $\theta = 90^\circ$ RCS pattern for the 8 sided disk model using first, second and third order Equivalent currents (ka = 10).

1 inch

1½ inch

1 inch

JAB/80

1½ inch

1 inch



Figure 109. $E_{PH}$, $\theta = 90^0$ RCS pattern for the 12 sided disk model using first, second and third order Equivalent currents (ka = 10).

1 inch

JAB/80
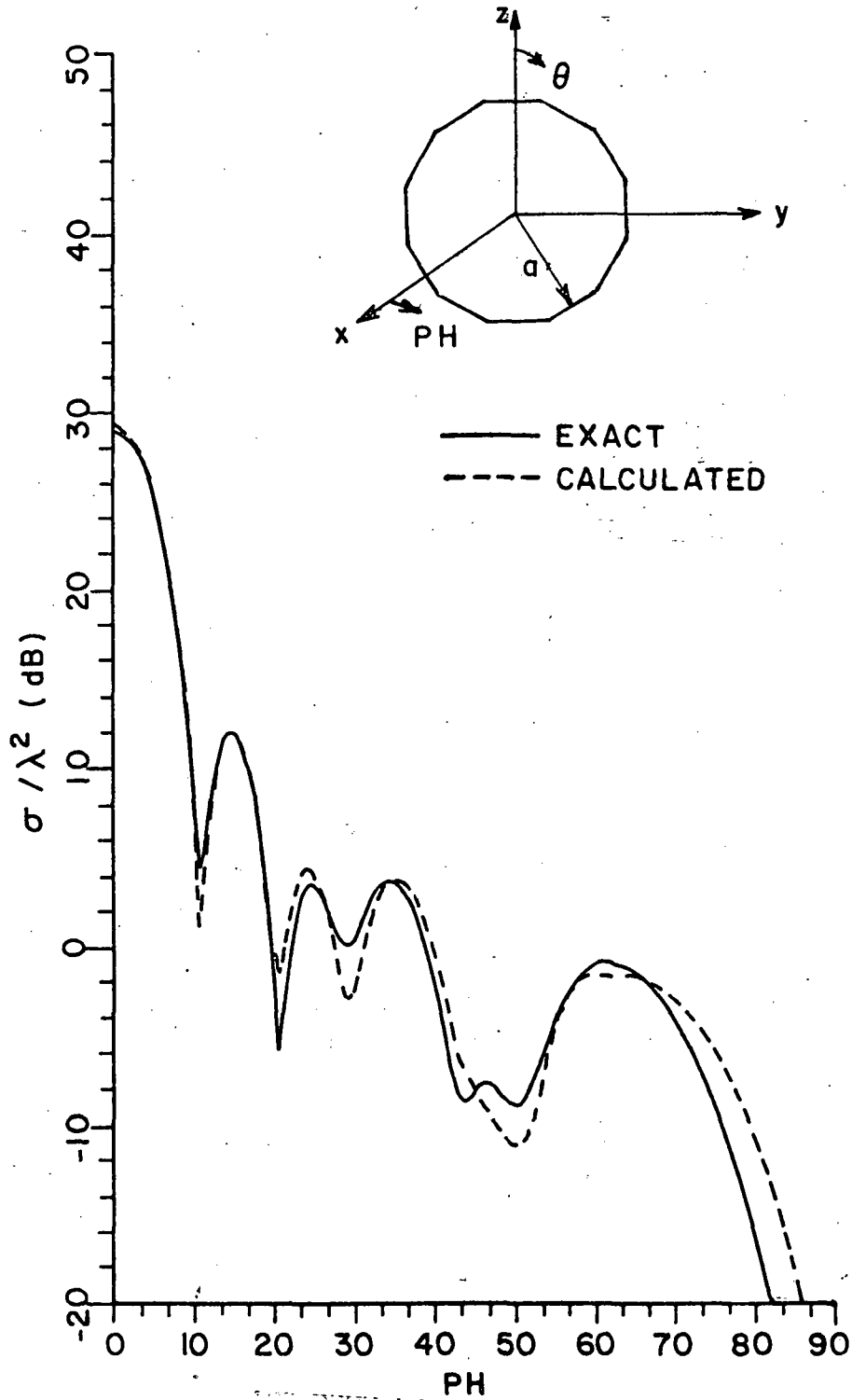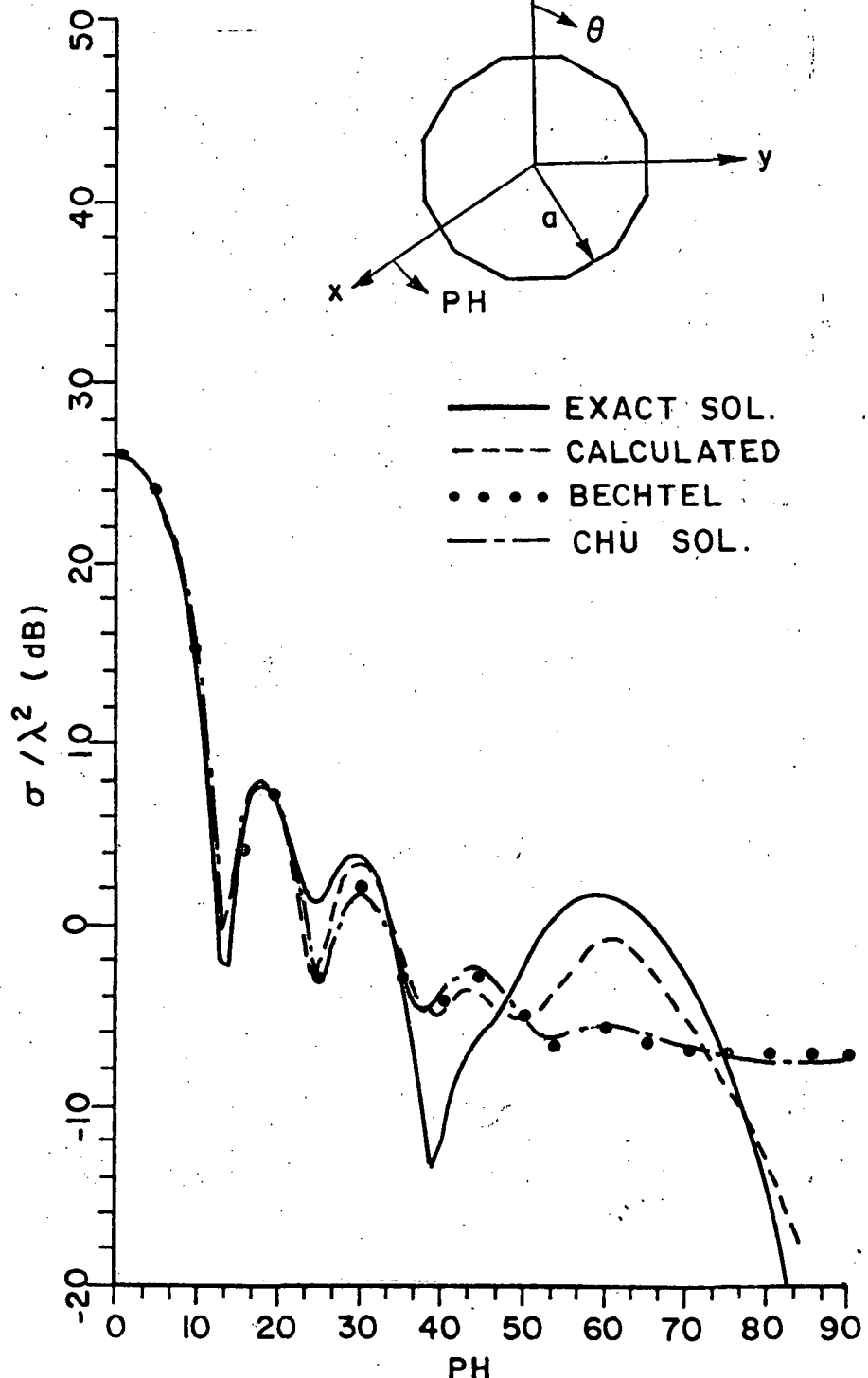
1½ inch

1 inch



Figure 110. $E_{PH}$, $\theta = 90^\circ$ RCS pattern, for the 12 sided disk model, using first, second and third order Equivalent currents, compared to the rim integration method ($ka = 8.28$).

1 inch
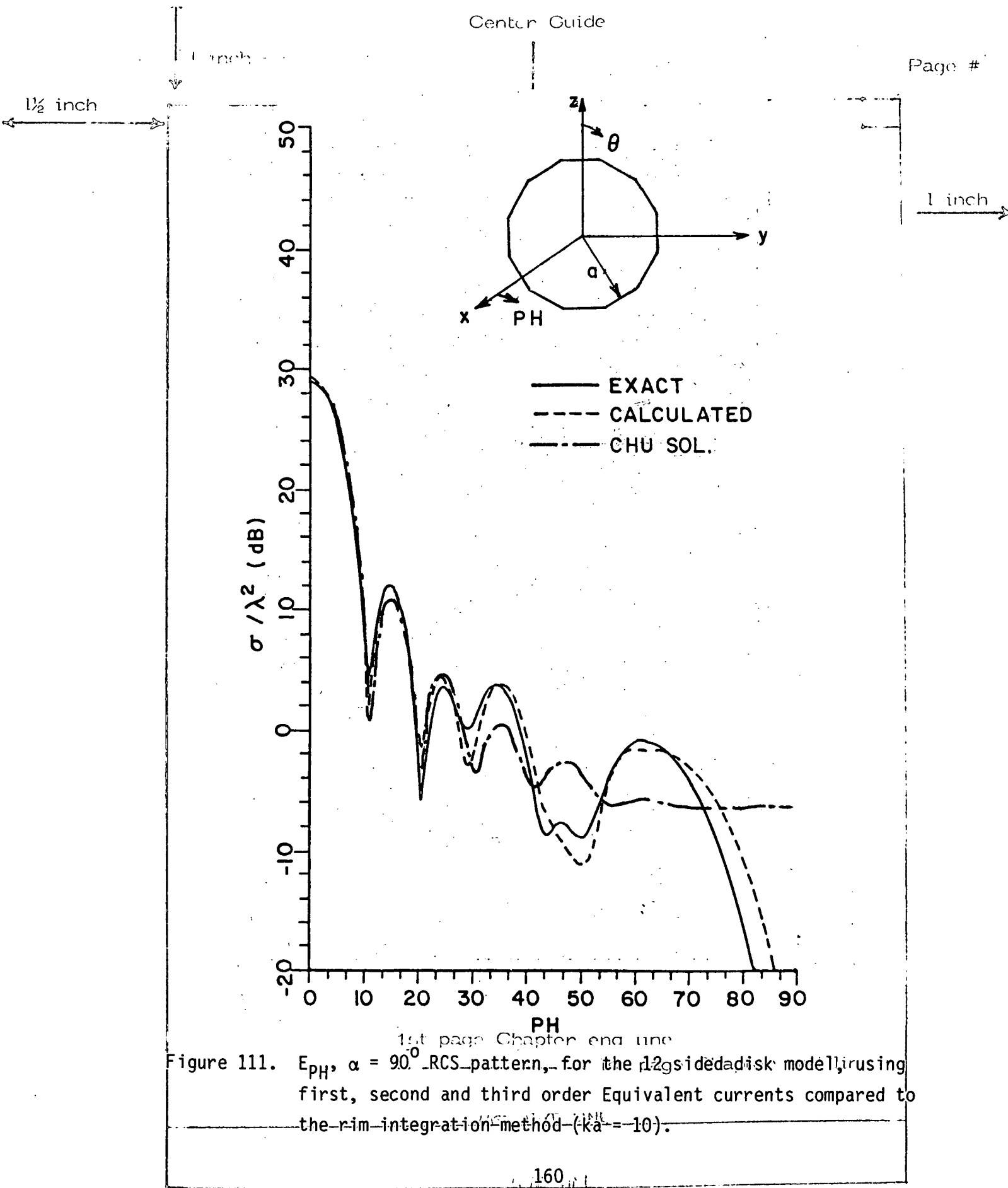
JAB/80

Figure 111. $E_{PH}$, $\alpha = 90.^0$ RCS pattern, for the 12 sided disk model, using first, second and third order Equivalent currents compared to the rim integration method (ka = 10).

JAB/80

where

$$\alpha = \frac{\pi}{n} \qquad \text{and}$$

n is the total number of edges used to model the disk.

## E.  SUMMARY OF E-PLANE BACKSCATTER ANALYSIS

In this chapter we analyzed the E-plane patterns where the Electric field vector is oriented parallel to the plane of incidence.

The techniques used to obtain the broadside RCS in the H-plane case were also used to compute the broadside RCS in the E-plane analysis.

The E-plane analysis is a more complex problem than the H-plane case since the RCS is dominated by diffractions from the back edge of the plate.  Therefore, multiple edge diffractions had to be included in the solution.  Together with first order diffractions, the effect of second and third order edge diffractions were considered.  The EC method was used to compute the contribution to the E-plane RCS pattern of these higher order interactions.  These mechanisms gave a significant contribution near the edge on region.  It was found that there is an inherent error associated with these higher order interactions due to the shadowing effect between the plate edges.  This error could be circumvented by including the corner diffracted fields in the EC formulation.

These edge diffraction mechanisms were also used to compute the E-plane pattern for a general shape plate.  The curved edges of this plate have been modeled by straight line segments.  Deviation from measured results in the region $45^0$ from edge on were observed since edge wave multiple corner diffractions have not been included in the analysis primarily because the edge wave diffraction coefficient is

not adequate to treat these interactions. The E-plane RCS pattern for a disk is also analyzed by using the EC corresponding to first, second and third order edge diffractions and adequate results were obtained. It was found that increasing the number of edges used to model the disk does improve the results, however, the number of edges is limited by the electrical length of an edge which should be of an order of a wavelength. One should point out that the disk problem could be analyzed using the approach shown in [15] which will allow one to analyze disk sizes smaller than that allowed by the straight line segment approach.

In the following chapters, we continue to discuss the effect of these higher order edge diffraction mechanisms together with that of the edge wave multiple corner diffraction. These mechanisms become dominant particularly for non-principle plane patterns.

1st page Chapter end line

— — — — — — — 1st page Chapter end line

LAST TEXT LINE

## 2 inch CHAPTER VI Line
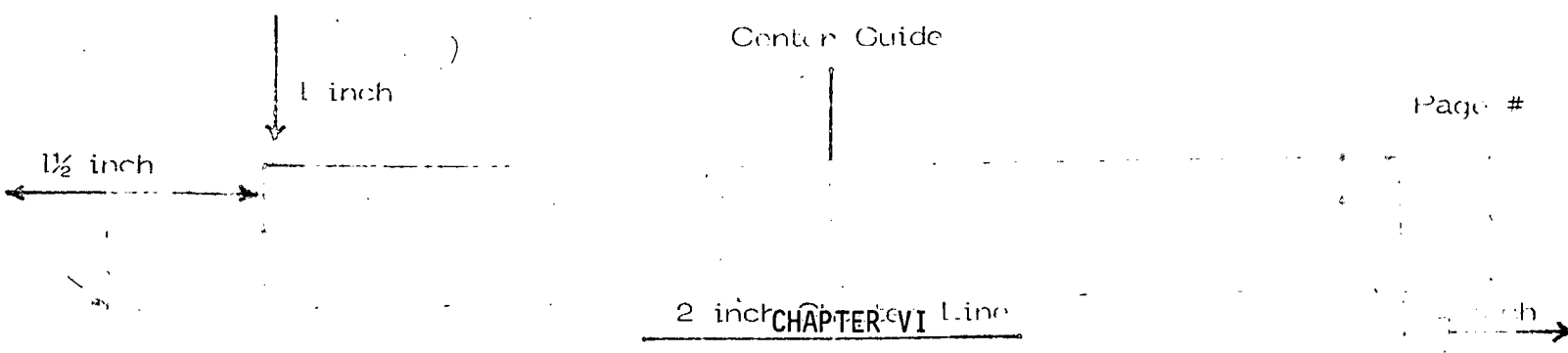
## BACKSCATTERING FROM RECTANGULAR PLATES USING HIGHER ORDER INTERACTIONS INCLUDING E-PLANE AND NON-PRINCIPAL PLANE PATTERNS

### A. INTRODUCTION

THESIS / DISSERTATION

In this chapter our discussion of the effect of higher order inter-actions on RCS pattern computations is continued. The geometry used in the analysis is a perfectly conducting rectangular plate. The E-plane RCS pattern and conical pattern planes for $\theta = 30^{\circ}$, $45^{\circ}$, and $60^{\circ}$ are analyzed. The single, double and triple edge diffraction mechanisms discussed in Chapter V are included.

In addition, another type of interaction now to be considered is the edge wave mechanism which is a degenerate form of the Corner dif-fraction mechanism. The goal of this chapter is to introduce and use these multiple diffraction mechanisms as needed. Again the incident field is a homogeneous plane wave and its electric field is given by Equation (76).

### B. E-PLANE CASE

In Chapter III, where the Echo Width of a strip was analyzed, it was noted that the multiply diffracted fields between the strip edges were the ones that create the difference between the E and H-plane pat-terns. In a similar way, these fields play the same role in the analysis of E-plane patterns for a rectangular plate. In Figure 112, the

1 inch

1½ inch

Center Guide

Page #

2 inch Chapter Line

1 inch

z

θ

#2      (1)      #1

PERFECTLY
CONDUCTING
PLATE

x

PH

(2)

(4)

#3      (3)      #4
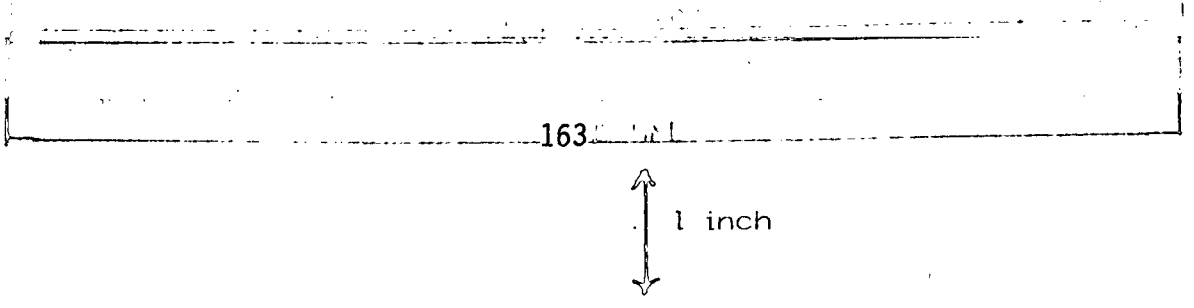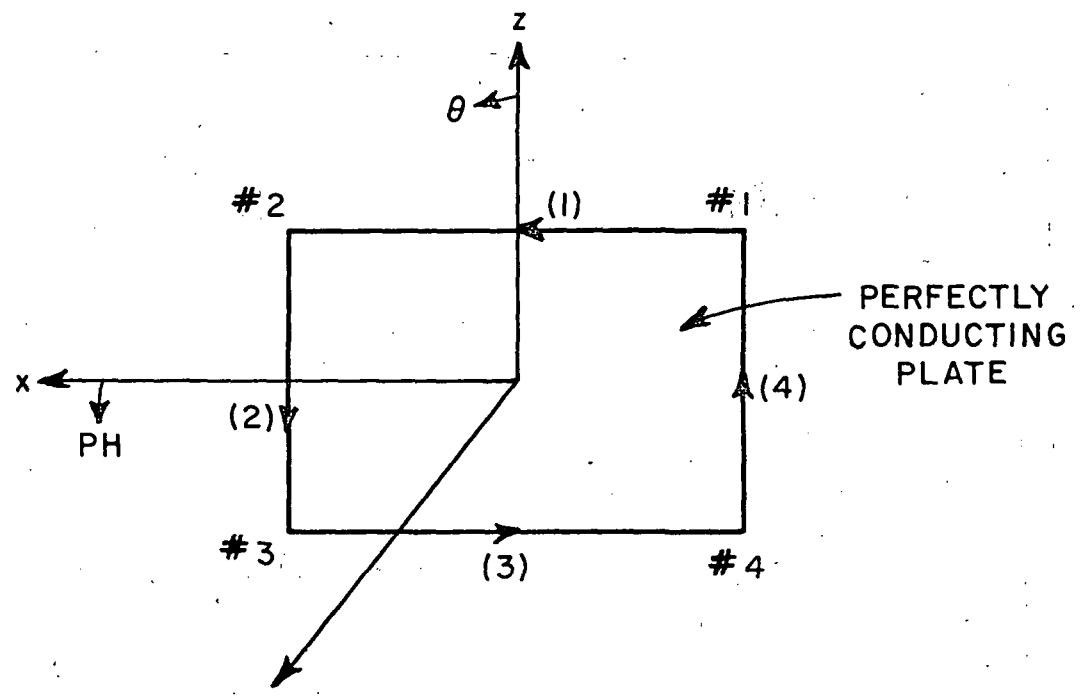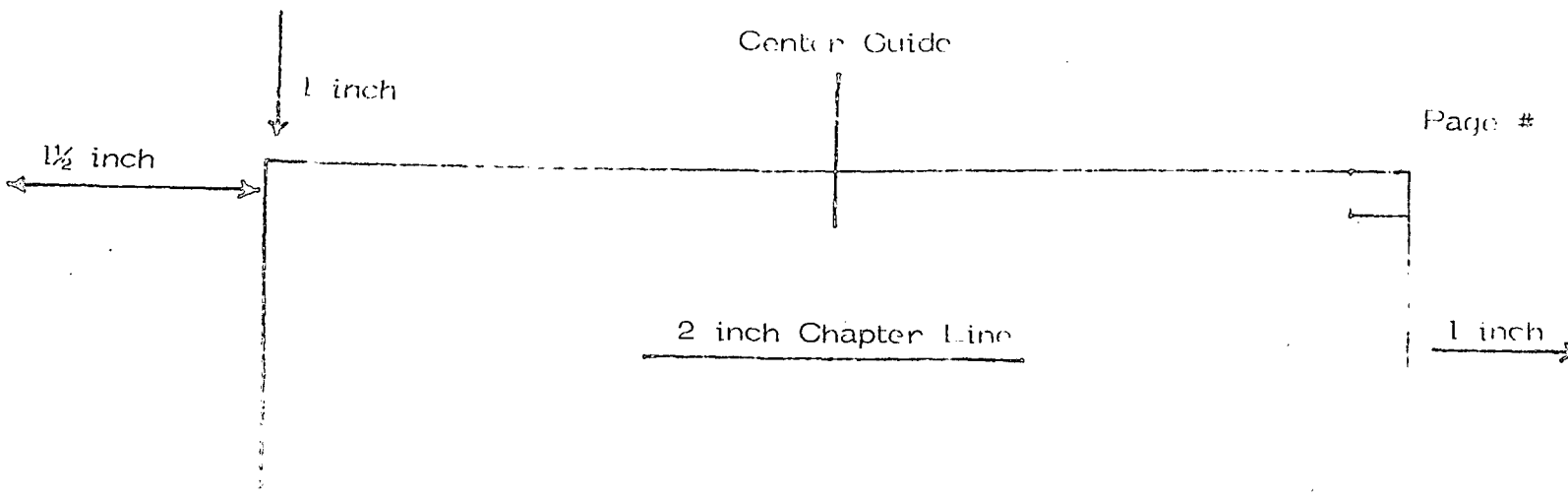
Figure 112. Rectangular plate geometry.

1 inch

JAB/80
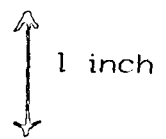
1½ inch

geometry of a rectangular plate is illustrated. The plate is in the x-z plane. The E-plane pattern is taken in the x-y plane, i.e., $\theta=90^\circ$ plane. Only magnetic Equivalent currents corresponding to the first, second and third order edge diffracted fields were used. They proved to be sufficient to produce satisfactory results for practical applications; however, fourth order diffraction terms or even higher may be needed when dealing with small plate sizes.

2 inch Chapter Line

1 inch

The results obtained using the Equivalent Current(EC) method for the E-plane RCS pattern ($E_{PH}$ polarization) for three different square flat plate sizes are shown in Figures 113-115. The results are compared to measurements and to results obtained by Ross [28]. Ross also used a normalization scheme to reduce the strip scattering solution to one applicable to the finite sized plates. This is not needed when the equivalent currents are introduced. His results are good everywhere except near grazing incidence. This error is caused by the use of the plane wave diffraction coefficients for the higher order interactions and was eliminated in our solution when the proper diffraction coefficients are used as shown by the good agreement with the measured results. An integration step of $0.1\lambda$ was used in evaluating the radiation integrals for the double and triple diffraction field components. The contribution of the double diffraction mechanism to the E-plane RCS pattern for the 3 different sized plates is shown in Figure 116. This field component contributes to the RCS throughout the pattern. Its magnitude increases gradually as one approaches edge on incidence. An increase of approximately $0.5\lambda^2$ in the plate area results in an increase of approximately 2 dB in RCS due to this component of the field at edge on incidence. Figure 117 shows the contribution of the triple diffraction mechanism for the same 3 plates. This field component is only needed for incidence angles up to $40^\circ$ from edge on. A similar increase of approximately

1st page Chapter end line

2 dB in RCS at edge on incidence is noticed when the area of the plate

1 inch

JAB/80
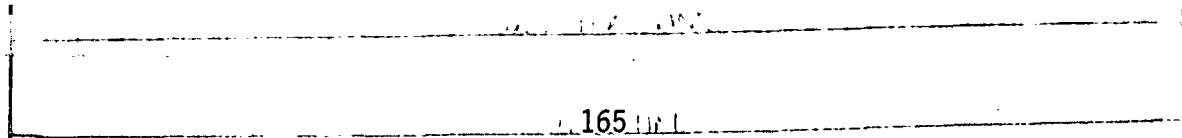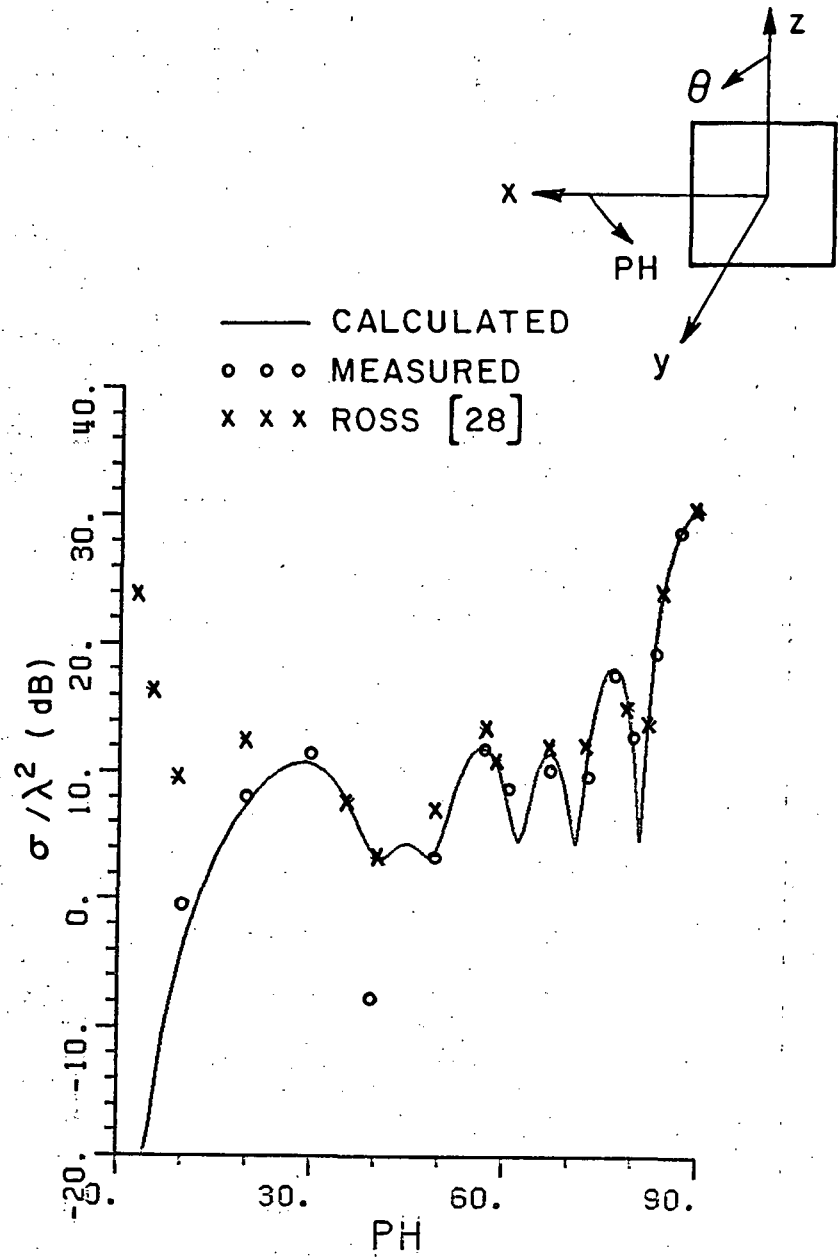
1½ inch

1 inch



Figure 113. $E_{PH}$, $\theta = 90^0$ RCS pattern for a 4 x 4 inch flat plate
using first, second and third order Equivalent currents
($\lambda = 1.28$ inch).

i inch

JAB/80
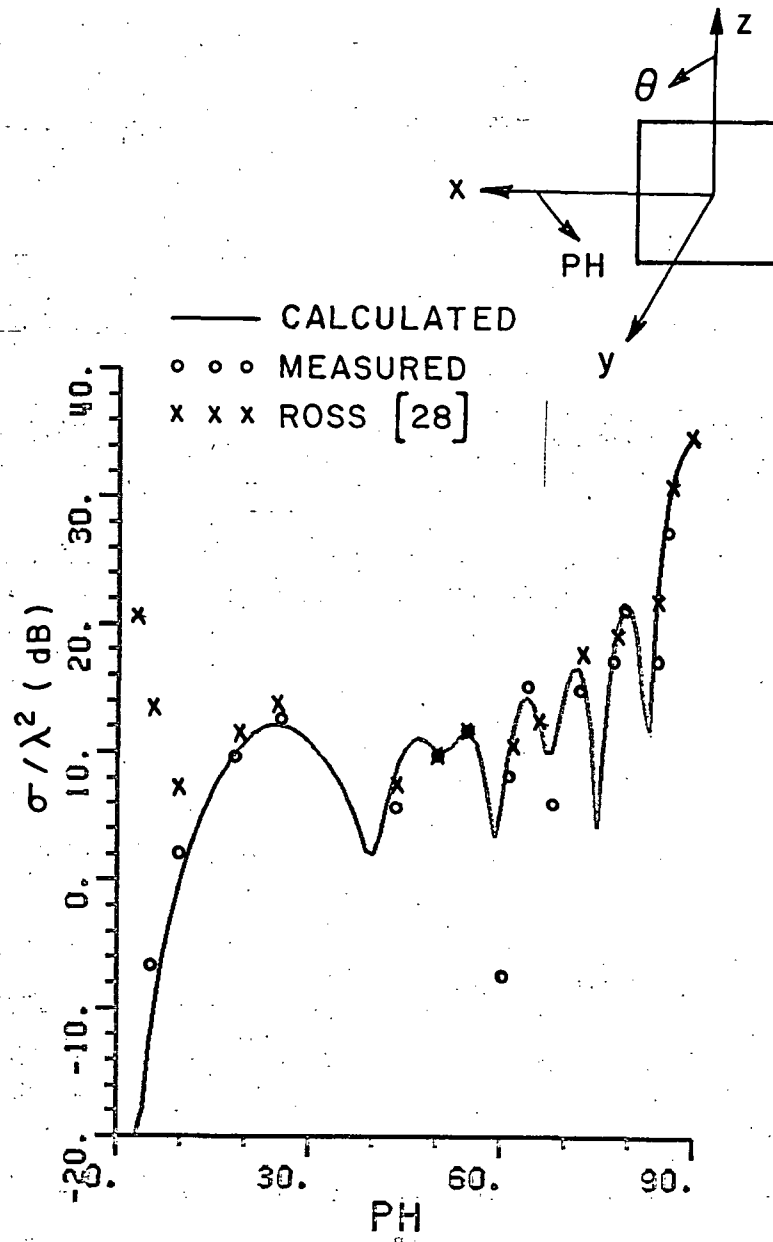
1½ inch



Figure 114. $E_{PH}$, $\theta = 90^{\circ}$ RCS pattern for a 5 x 5 inch flat plate
using first, second and third order Equivalent currents
($\lambda = 1.28$ inch).

1 inch

JAB/80
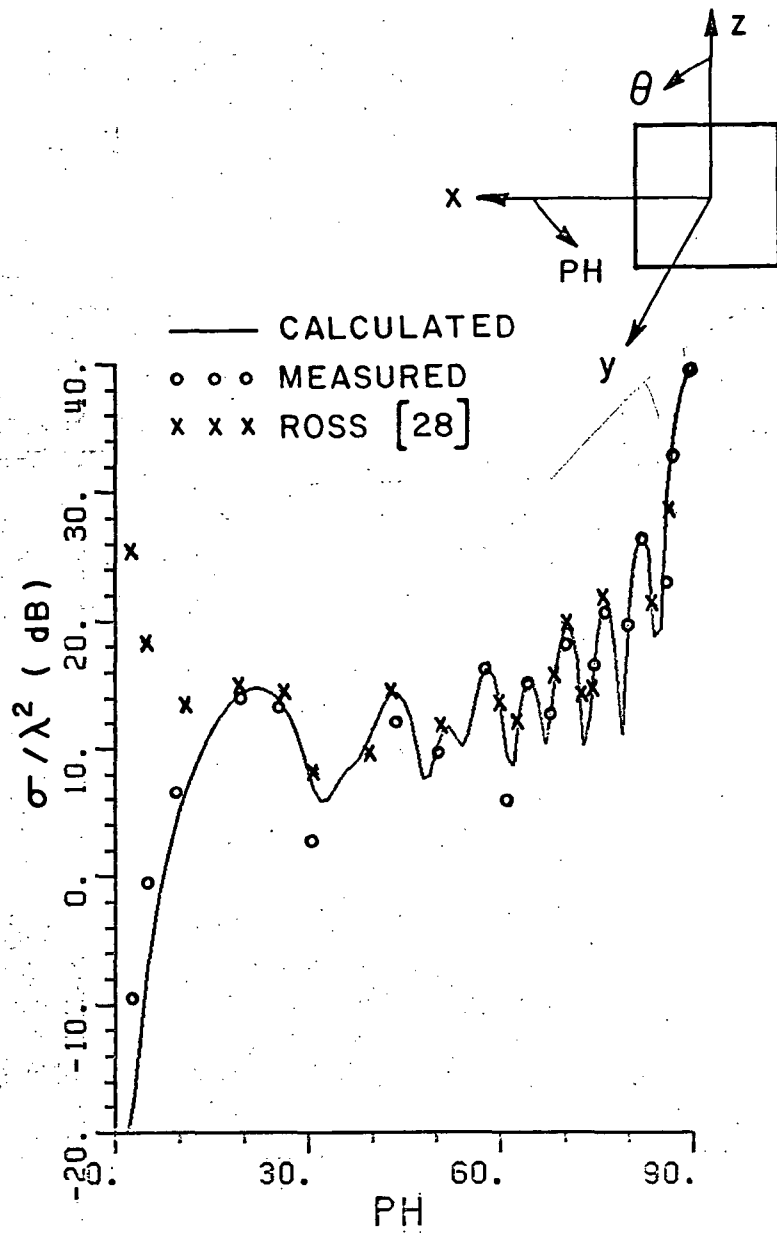
1½ inch

1 inch



Figure 115. $E_{PH}$, $\theta = 90^{\circ}$ RCS pattern for a 6 x 6 inch flat plate using first, second and third order Equivalent currents ($\lambda$ = 1.28 inch).

1st page Chapter end line

1st page Chapter end line

1 inch

JAB/80
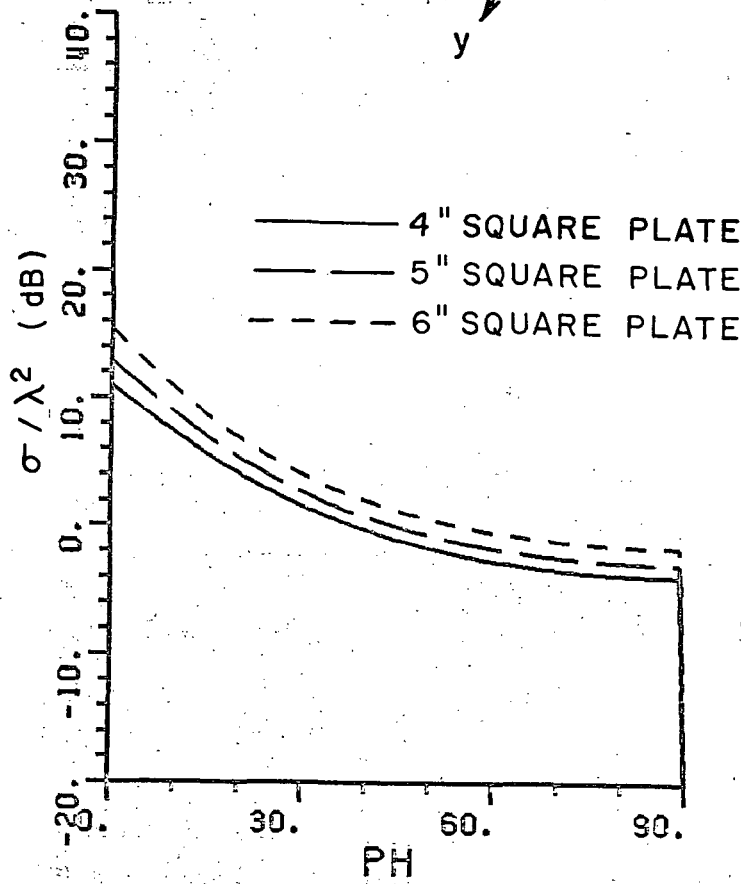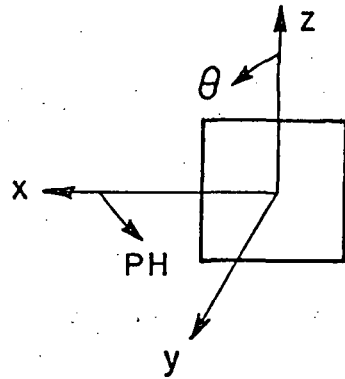
1 inch

1½ inch

1 inch

Figure 116. $E_{PH}$, contribution of double edge diffraction to $\theta = 90^\circ$ RCS pattern ($\lambda = 1.28$ inch).

1st page Chapter end line

1st page Chapter end line

1 inch

JAB/80

1 inch

1½ i

1 inch



σ/λ² ( dB )

——— 4" SQUARE PLATE
— — 5" SQUARE PLATE
— — — 6" SQUARE PLATE
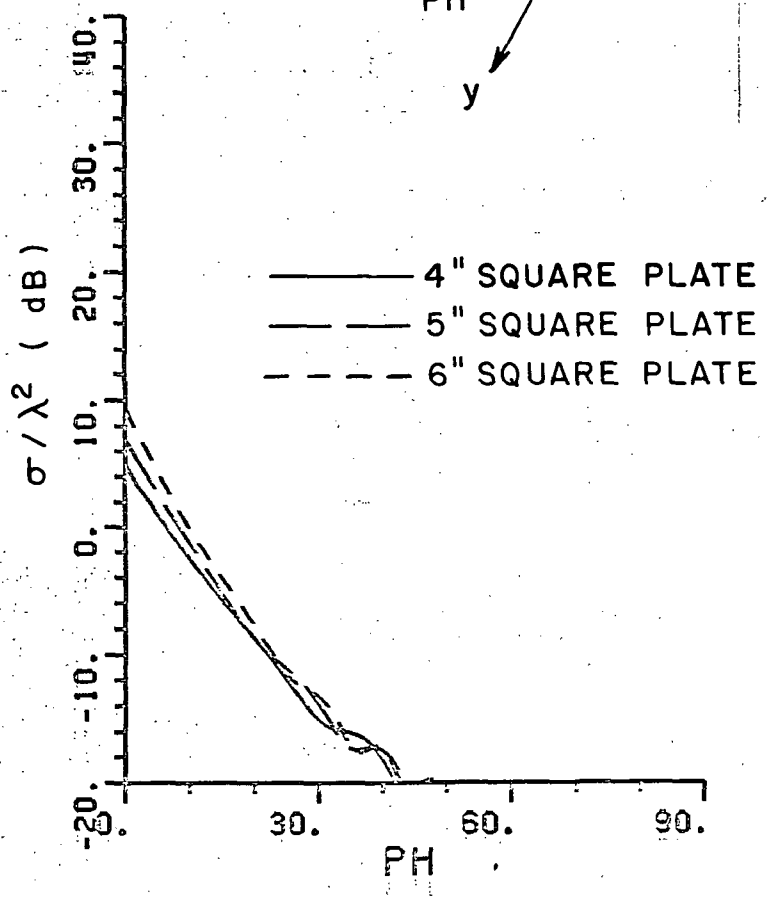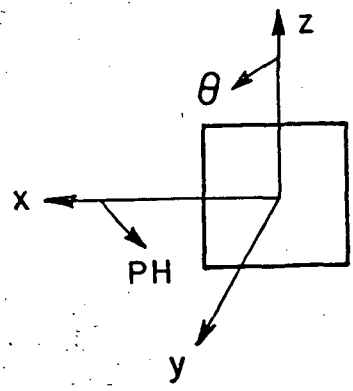
1st page Chapter end line

Figure 117. $E_{PH}$, contribution of triple-edge diffraction to $\theta = 90^{\circ}$ RCS pattern ($\lambda = 1.28$ inch).

1 inch

JAB/80

1 inch

1½ inch

is increased by approximately $0.5\lambda^2$. Because of the symmetry of the geometry, the contribution of the single diffracted fields is similar to the H-plane patterns shown in Figures 33-35.

2 inch Chapter Line

## C. OFF PRINCIPAL PLANE CASES

In this section the RCS pattern when $\theta \neq 90^\circ$ is analyzed. This conical pattern is a function of the azimuth angle $\varphi$ (PH) when $\theta=\theta_0$ is held constant. The incident field is polarized in the $\theta$-direction. Figure 118 defines the geometry used in our analysis. The symbol (PH) is used hereafter for this parameter to avoid confusing it with the parameter $\phi$ of Figure 1 used in edge diffraction.

THESIS/ DISSERTATION

1 inch

Paper

### 1. Analysis

The solution to this case is a complex one. The value of the RCS is lower by an order of magnitude and thus one has to consider many possible interactions that involve edges and corners of the plate. Some of these are, double and triple edge diffractions, edge to corner diffraction, multiple corner to corner diffractions and the newly developed edge wave . These higher order interactions were found to contribute significantly to the RCS pattern. As one moves further away from the principal plane, more interactions must be included to give satisfactory results. The edge wave mechanism contribution becomes very significant when the RCS pattern is taken in the plane of the plate, i.e., x-z plane. Furthermore, one has to consider the effect of each individual edge of the plate since different edges contribute different terms and these terms are now significant for one pattern and insignificant in another. This will be discussed in more detail later. The incident field can be written in the edge coordinate system as:

1st page Chapter end line

$$E^i = E^i \hat{\theta} = E^i_{\phi'}(p)\,-\hat{\phi}'(\bar{p}) \;+\; E^i_{\beta'}(\bar{p})\,-\hat{\beta}'(\bar{p}) \tag{79}$$

1st page Chapter end line

where

171

1 inch

$E^i_{\phi'(p)}$, $E^i_{\beta'(p)}$ are the incident $\phi$, $\beta$ field components defined in the $p^{th}$ edge coordinate system. The subscripts $\phi'(p)$ and $\beta'(p)$ indicate the $\phi'$, $\beta'$ field components for edge p, and $\hat{\phi}'(p)$, $\hat{\beta}'(p)$ are the corresponding $\phi'$ and $\beta'$ unit vectors.

Consider edge #1 shown in Figure 118. The incident field on this edge can be written as:

$$E^i_{(1)} = E^i_{\phi'(1)}\hat{\phi}'(1) + E^i_{\beta'(1)}\hat{\beta}'(1) = E_\theta(\sin(PH)\hat{\phi}'(1) + \cos(PH)\hat{\beta}'(1)). \tag{80}$$

When PH is equal to $0^o$ and $90^o$, Equation (80) reduces to:

$$E^i_{(1)}(PH=0) = E^i_{\beta'(1)}\hat{\beta}'(1) \quad \text{and} \quad E^i_{\phi'(1)} \equiv 0 \quad , \text{ and} \tag{81}$$

$$E^i_{(1)}(PH=90) = E^i_{\phi'(1)}\hat{\phi}'(1) \quad \text{and} \quad E^i_{\beta'(1)} \equiv 0 , \tag{82}$$

respectively.

From Equations (81, 82), there must be a transition region in space where both $\beta'$ and $\phi'$ exists.

The $\phi'$ component will be responsible for the following interactions:

1. Single, double and triple edge diffraction fields. The EC method is used to compute their contributions.

2. Edge wave fields that involve double and triple corner diffractions on the same edge.

3. Cross polarized edge wave fields, i.e., $\phi$ to $\beta$ field polarization conversion. This also requires double and triple corner diffractions on the same edge.

JAB/80
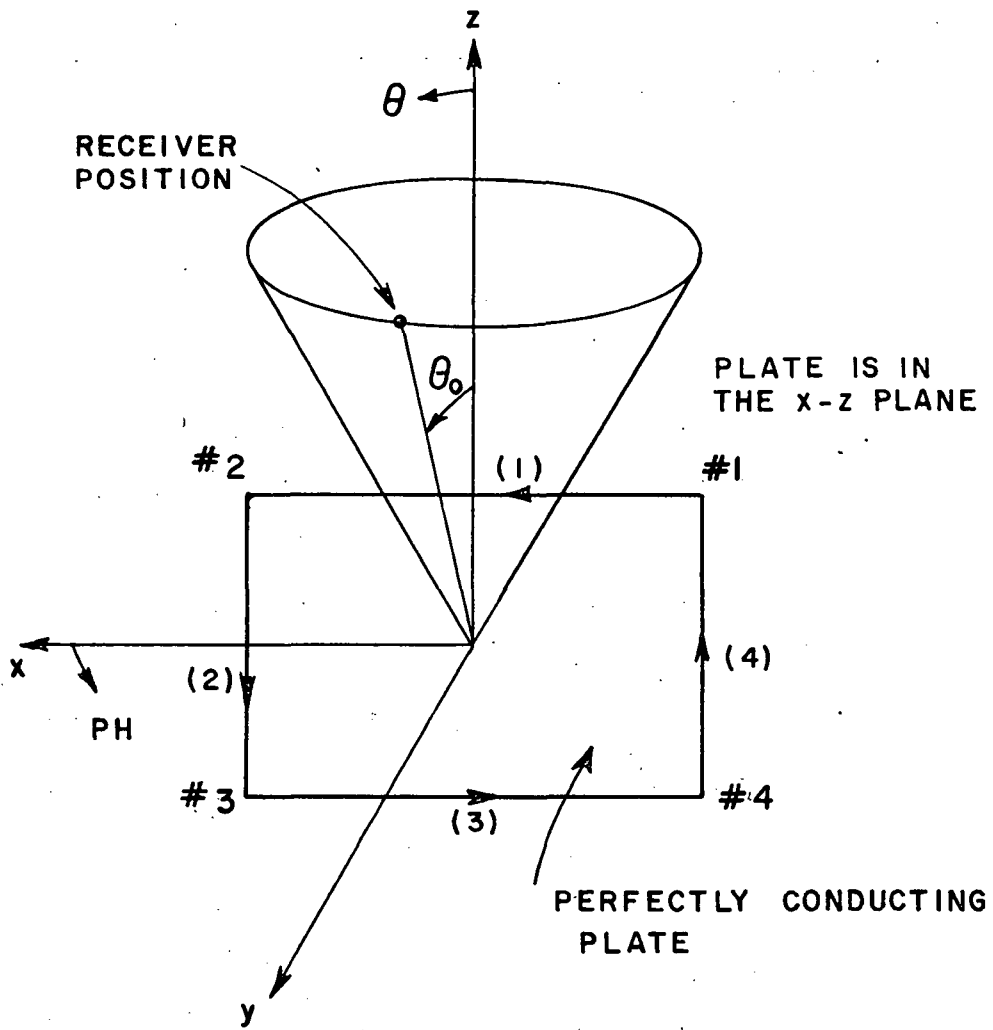
Figure 118. Conical pattern geometry.

There is a distinct possibility that multiple corner, and corner to edge contributions can contribute for rays that tend to propagate around the perimeter of the plate. Unfortunately the current diffraction coefficient is not adequate for evaluating these terms.

The $\beta'$ component will contribute to the RCS through single order edge diffraction and edge wave fields interactions similar to those discussed above in 2 and 3. Edge #3 will give similar interactions to the ones discussed above.

For edges #2 and #4, the incident field is polarized only in the $\beta'$ direction throughout the pattern, i.e.,

$$\overline{E}^i_{(2)} = E^i_{\beta'_{(2)}} \hat{\beta}'_{(2)} \quad \text{and} \quad E^i_{\phi'_{(2)}} \equiv 0 \quad , \text{ and} \tag{83}$$

$$\overline{E}^i_{(4)} = E^i_{\beta'_{(4)}} \hat{\beta}'_{(4)} \quad \text{and} \quad E^i_{\phi'_{(4)}} \equiv 0 \quad , \tag{84}$$

respectively.

Accordingly edges 2 and 4 will contribute to RCS pattern only through single edge diffractions and edge wave fields similar to those discussed above in 2 and 3.

In Figure 119, some of the different edge diffraction mechanisms associated with the contribution of edges 1 and 3 to the radar cross-section are illustrated. In evaluating the fields due to the double and triple diffraction mechanisms, all possible combinations of edge diffraction between any two or any three edges are considered. The evaluation of these fields follow the same procedure used above in part 1. Figure 120 shows the edge wave mechanism interactions. They involve double and triple corner diffractions on the same edge. Of course there are similar interactions on the other two edges of the plate.

JAB/80
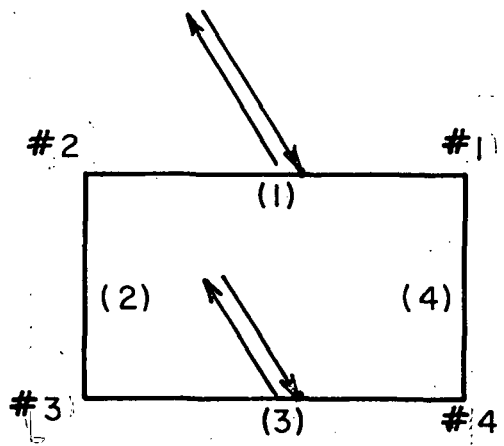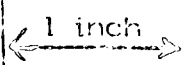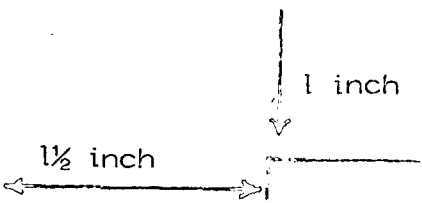
SINGLE EDGE DIFFRACTION
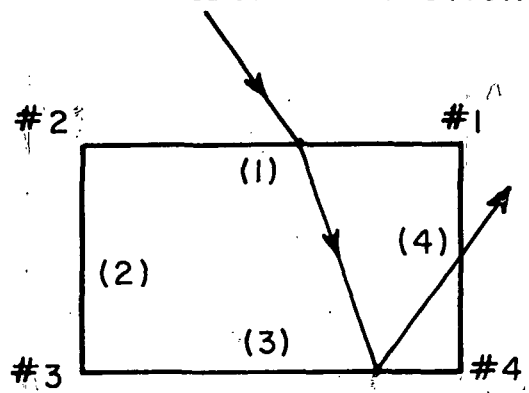
DOUBLE EDGE DIFFRACTIONS
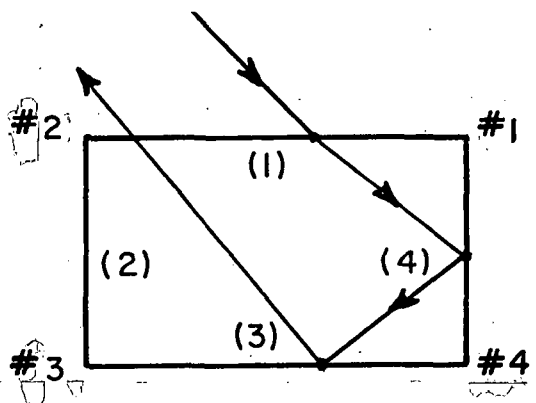
TRIPLE EDGE DIFFRACTIONS

Figure 119. Edge diffraction mechanisms contributing to the RCS due to edges #1 and 3.

JAB/80
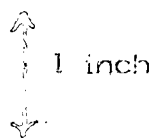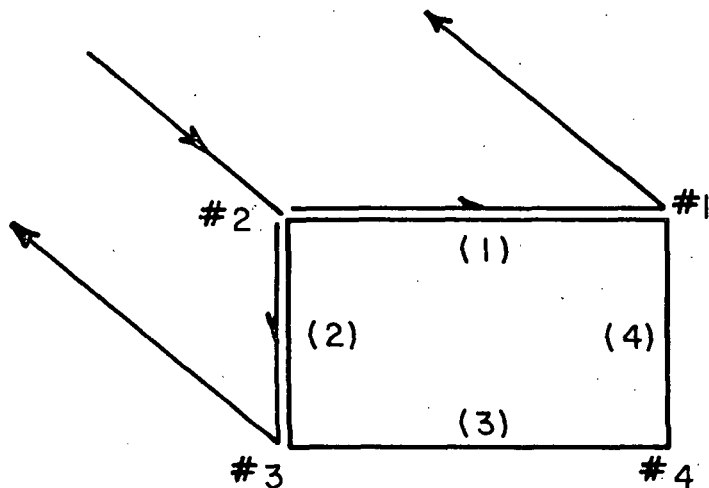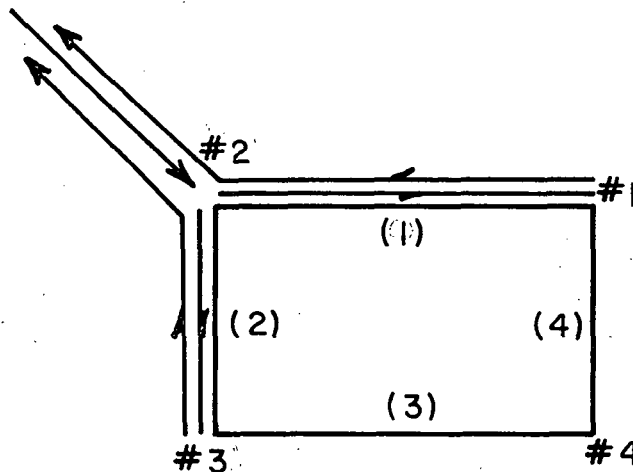
EDGE WAVE DOUBLE CORNER DIFFRACTION

EDGE WAVE TRIPLE CORNER DIFFRACTION

Figure 120.    Edge wave mechanisms contributing to the RCS.
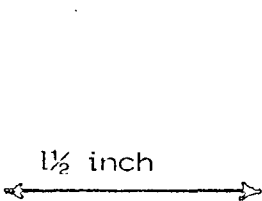
Again observe that we do not show any diffraction mechanism that encircles the plate in a manner similar to creeping waves.

a. Edge Wave Double Corner Interaction Mechanisms
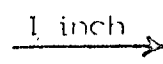
This mechanism is shown in Figure 121 where only the interaction due to edge #1 is illustrated. The same analysis holds for the other edges. Because of the cross polarization effect associated with the edge wave mechanism (see Appendix C), one has to consider the different possible combinations of incidence and diffracted fields, i.e., $\beta'\beta$, $\beta'\phi$, $\phi'\beta$, $\phi'\phi$ where the first letter indicates the polarization of the incident field and the second the polarization of the diffracted field.

The general form for the edge wave field is

$$
\begin{Bmatrix} E^d_\beta \\ E^d_\phi \end{Bmatrix} = \begin{Bmatrix} E^i_{\beta'}(Q_C) \; D^{(ew)}_s(L,\phi',\phi,\beta_C) \\ E^i_{\phi'}(Q_C) \; D^{(ew)}_h(L,\phi',\phi,\beta_C) \end{Bmatrix} \sqrt{\frac{s_C}{s(s_C+s)}} \; e^{-jks} \quad , \quad (85)
$$

where $s_C$ is the distance from the source to the corner, s is the distance from the corner to the receiver. The edge wave diffraction coefficient is given by

$$
D^{(ew)}_{s\,h}(L,\phi,\phi',\beta_C) = \frac{e^{-j\pi/4}}{2\sqrt{\pi k}} \; \frac{(1+\cos\beta_C)}{\sin\beta_C/2}
$$

$$
F(2kL \sin^2 \beta_C/2) \begin{Bmatrix} \sin\frac{\phi}{2} \; \sin\frac{\phi'}{2} \\ \cos\frac{\phi}{2} \; \sin\frac{\phi'}{2} \end{Bmatrix} \tag{86}
$$

where $L = \dfrac{ss_C}{s+s_C}$ ,

(a)



(b)
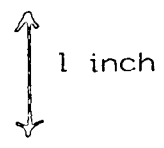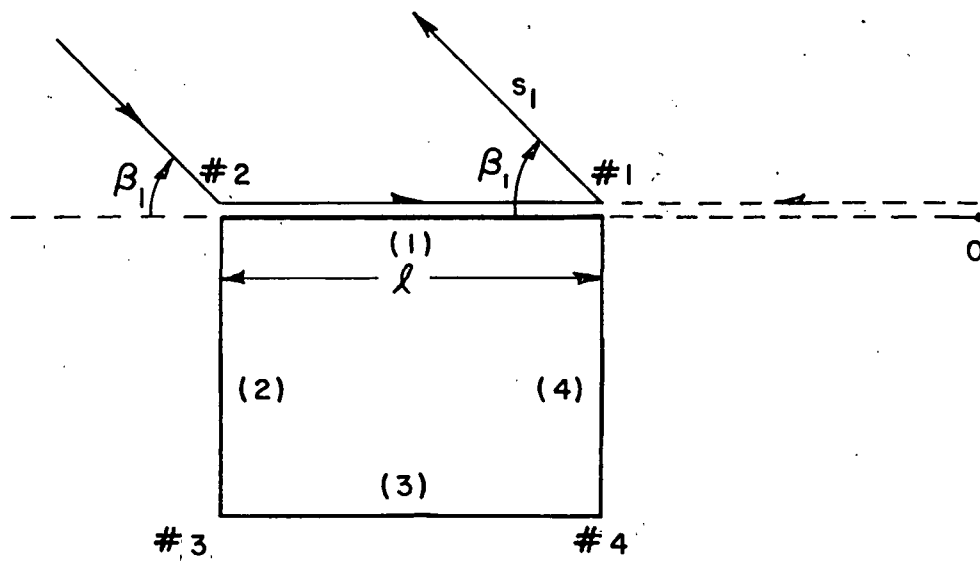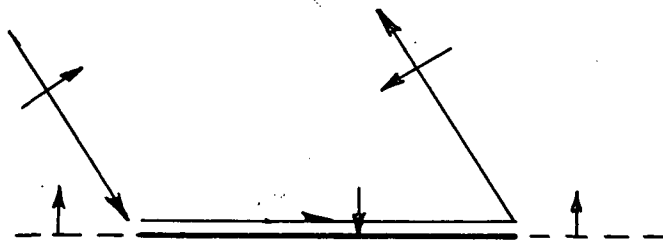
Figure 121. Edge wave double corner diffraction

JAB/80
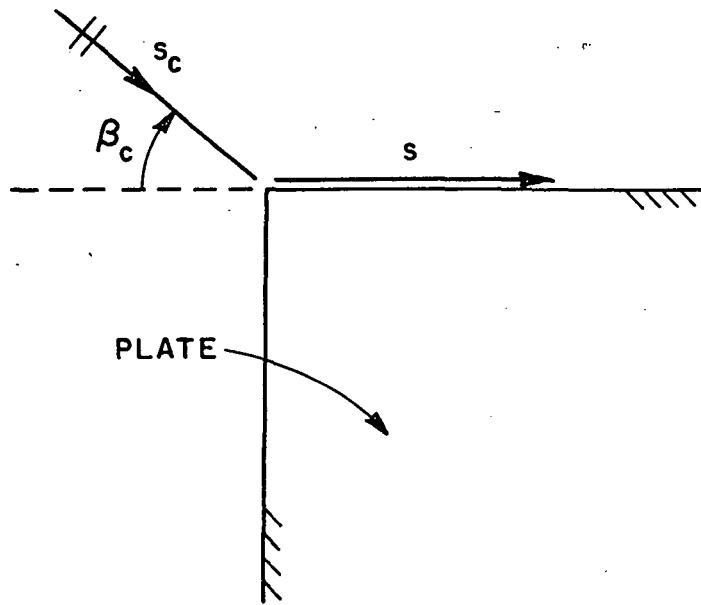
1½ inch

1 inch



(a)
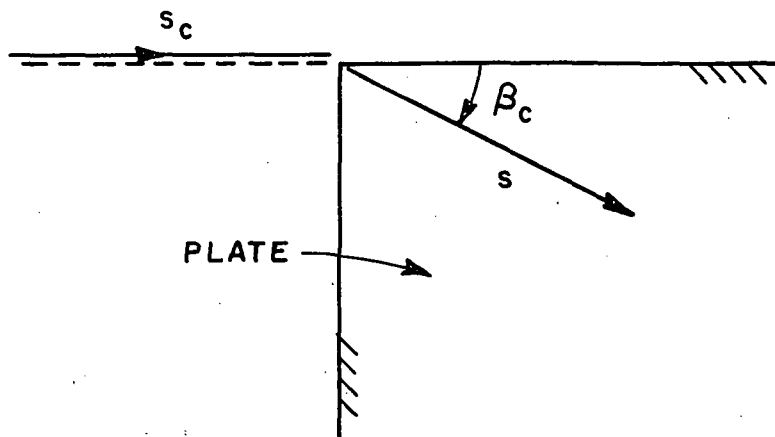


(b)

Figure 122. Edge wave diffraction cases. 1st page Chapter end line

179

1 inch

$\phi$, $\phi'$ are defined in Figure 16 and $\beta_{IC}$ is defined as in Figure 122. A detailed discussion of the edge wave mechanism and the derivation of Equation (85) is shown in Appendix C. Note that there are some limitations to the use of Equation (85) since this equation was derived from the imperically derived corner diffraction coefficient, it is valid only for the two diffraction mechanisms shown in Figure 122.

Let us consider first the case when both the incidence and diffracted fields are polarized in the $\beta$ direction, i.e., ($\beta'\beta$ case).

The field diffracted from corner #2 ($C_2$) along the edge and evaluated at corner #1 ($C_1$) is given by

$$E^d_{(1)} = E^i_{\beta'_{(1)}}(c_2) \; D_s^{(ew)}(\ell, \phi'_1, \tfrac{\pi}{2}, \beta_1) \; \frac{e^{-jk\ell}}{\sqrt{\ell}} \tag{87}$$

This incident field on $C_1$ appears to be coming from an image source located at point 0 shown in Figure 123. This source is created by the
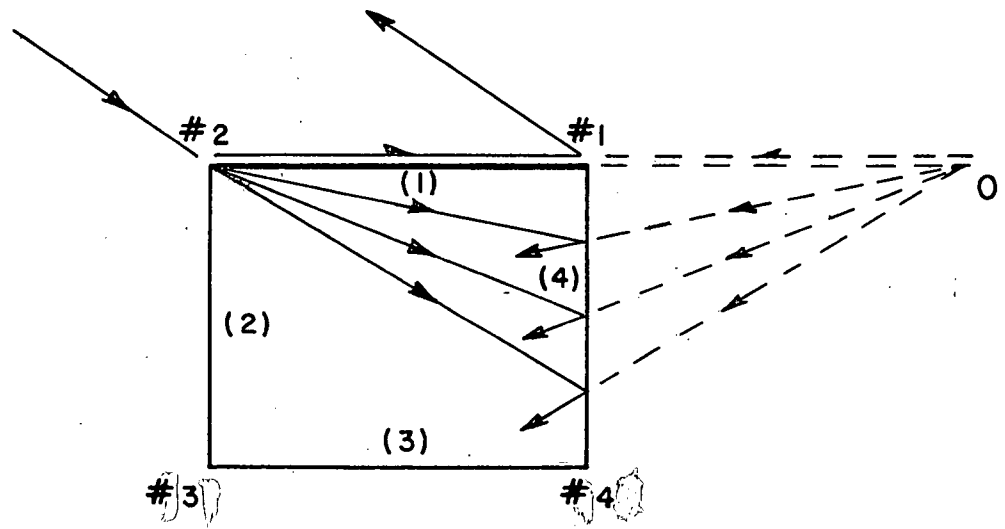


Figure 123. Effect of edge #4 on the edge wave field.

diffraction process due to edge #4. Due to this effect, the incident field on $C_1$ given by Equation (87) is modified by this reflection co-efficient, i.e., Equation (87) is modified as follows:

2 inch Chapter Line

$$E^d_{(1)} = E^i_{\beta'(1)}(c_2)\, D^{(ew)}_s(\ell, \phi'_1, \tfrac{\pi}{2}, \beta)\, R\, \frac{e^{-jk\ell}}{\sqrt{\ell}} \tag{88}$$

where $\qquad R = \dfrac{e^{-j\pi/4}}{\sqrt{2\pi k}}$ $\qquad\qquad$ . $\tag{89}$

The diffracted field to the receiver from $C_1$ is then given by

Typing Guide Paper

$$E^d_{\beta(1)} = E^d_{(1)} D^{(ew)}_s(\ell, \tfrac{\pi}{2}, \phi_1, \beta_1)\, \sqrt{\ell}\; \frac{e^{-jks_1}}{s_1} \tag{90}$$

substituting Equation (88) into (90) one gets

$$E^d_{\beta(1)} = E^i_{\beta'(1)}(c_2)\, D^{(ew)}_s(\ell, \phi'_1, \tfrac{\pi}{2}, \beta_1)R D^{(ew)}_s(\ell, \tfrac{\pi}{2}, \phi_1, \beta_1)$$

$$e^{-jk\ell}\; \frac{e^{-jks_1}}{s_1} \qquad\qquad . \tag{91}$$

There is another term due to diffraction from $C_1$ to $C_2$. The two terms are equal and both are given by Equation (91). So the total diffracted field for the $\beta'\beta$ interaction is given by

$$E^d_{\beta(1)} = 2E^i_{\beta'(1)}(c_2)\, D^{(ew)}_s(\ell, \phi'_1, \tfrac{\pi}{2}, \beta_1)R D^{(ew)}_s(\ell, \tfrac{\pi}{2}, \phi_1, \beta_1)$$

$$e^{-jk\ell}\; \frac{e^{-jks_1}}{s_1} \qquad\qquad . \tag{92}$$

1st page Chapter end line

— — — — — — → 1st page Chapter end line

LAST TEXT LINE

181

LAST LINE

1 inch

JAB/80

1 inch

1½ inc

1 inch

$$s_2$$

$$\beta_1$$

#2   (1)   #1

$\ell$

(2)   (4)

(3)

#3   #4

(a)

#2   (1)   #1

$$s_1$$

(2)   (4)

(3)

#3   #4

(b)
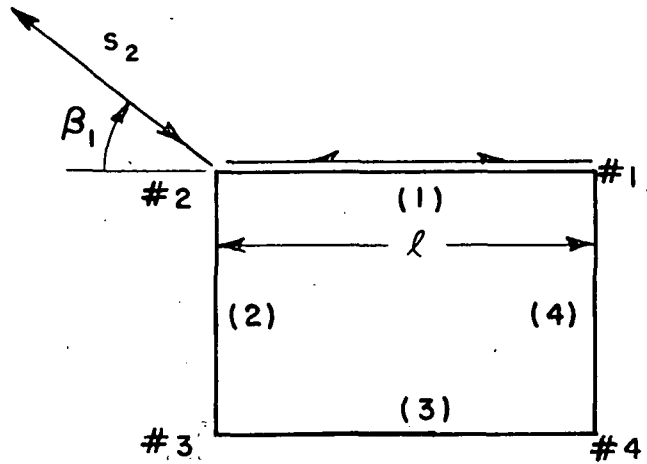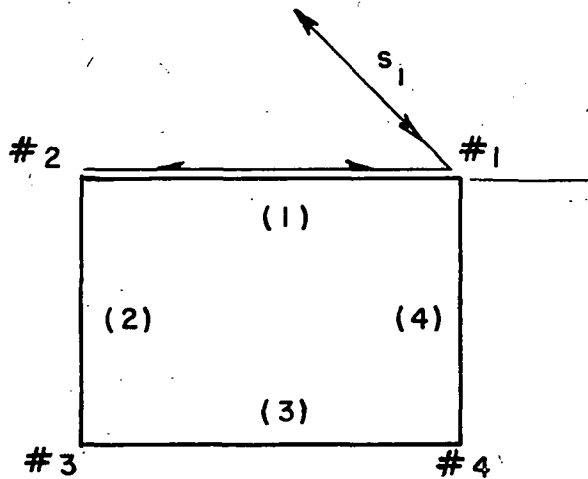
1st page Chapter end line

Figure 124. Edge wave triple-corner diffraction.

1 inch

JAB/80

and the $\phi$ polarized term is

$$E^d_{\phi(1)} = 2E^i_{\phi'(1)}(c_2)D^{(ew)}_h(\ell,\phi'_1,o,\beta_1)RD^{(ew)}_h(\ell,o,\phi_1,\beta_1)$$

$$e^{-j2k\ell} \frac{e^{-jks_2}}{s_2}$$

(100)

To compute the fields due to $C_1$ (Figure 124-b), one has to consider the effect of edge 4 on the incident field. This effect is shown in Figure 125. Again the incident field appears to be coming from an image source at infinity. The field components diffracted from $C_1$ are given by modifying Equations (98-100) such that

$$E^d_{\beta(1)} = -2E^i_{\beta'(1)}(c_1)D^{(ew)}_s(\ell,\phi'_1,\frac{\pi}{2},\beta_1)R^2D^{(ew)}_s(\ell,\frac{\pi}{2},\phi_1,\beta)$$

$$e^{-j2k\ell} \frac{e^{-jks_1}}{s_1} ,$$

(101)
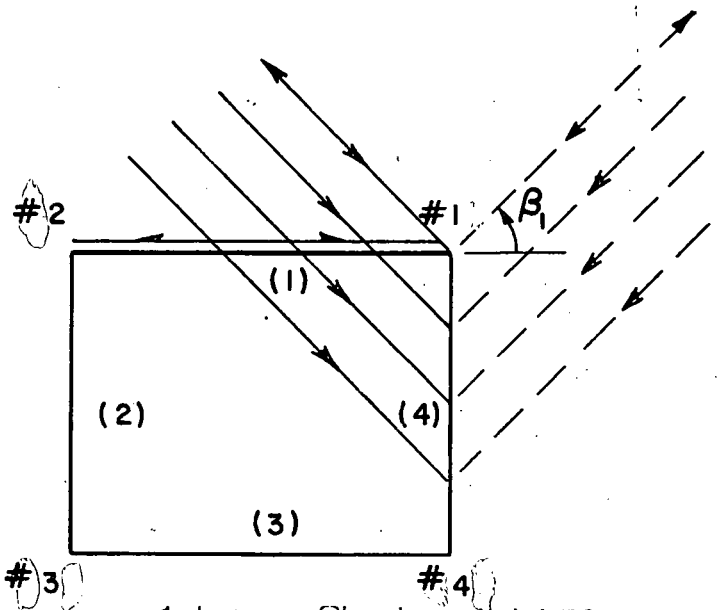
Figure 125. Effect of edge #4 on the incident field on corner #1 for the triple edge wave diffraction case.

1½ inch

1 inch →

Note that for backscatter $\phi_1 = \phi_1'$, also the cross polarization components, i.e., $\beta'\phi$ and $\phi'\beta$ are equivalent. Following the same procedure, the fields due to $\beta'\phi$ and $\phi'\beta$ combined together are given by

2 inch Chapter Line

$$E^d_{\beta(1)} = -4E^i_{\phi'(1)} (c_2) D^{(ew)}_h(\ell, \phi_1', o, \beta_1) RD^{(ew)}_s(\ell, \tfrac{\pi}{2}, \phi_1, \beta_1)$$

$$e^{-jk\ell} \frac{e^{-jks_1}}{s_1} \qquad , \tag{93}$$

and that for $\phi'\phi$ is given by

THESIS / DISSERTATION

$$E^d_{\phi(1)} = 2E^i_{\phi'(1)} (c_2) D^{(ew)}_h(\ell, \phi_1', o, \beta_1) RD^{(ew)}_h(\ell, o, \phi_1, \beta_1)$$

Guide Page

$$e^{-jk\ell} \frac{e^{-jks_1}}{s_1} \qquad . \tag{94}$$

## b. Edge Wave Triple Corner Interaction Mechanism

Figure 124 illustrates the triple edge wave diffracted fields from $C_1$ and $C_2$ on edge #1. Similar terms exist for each of the remaining edges.

Consider the field diffracted from $C_2$. In this case the double diffracted field from $C_1$ is incident on $C_2$. Since the edge wave formulation as developed here is valid when either the source or the receiver is in the far field region, we assume that the source of the incident field on $C_2$ is in the far field. Therefore the value of double diffracted field evaluated at $C_2$ is

1st page Chapter end line

$$E^d_{(2)} = E^i_{\beta'(1)} (c_2) D^{(ew)}_s(\ell, \phi_1', \tfrac{\pi}{2}, \beta_1) R \frac{e^{-jk\ell}}{\sqrt{\ell}} \qquad \text{1st page Chapter end line} \tag{95}$$

LAST TEXT LINE

1 inch

JAB/80
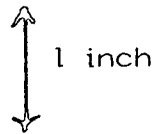
If one now considers the $\beta\beta$ interaction, then the diffracted field from $C_2$ to the receiver is given by

$$E^d_{\beta(1)} = -E^d_{(2)}D^{(ew)}_s(\ell, \frac{\pi}{2}, \phi_1, \beta_1) \sqrt{\ldots} \frac{e^{-jks_2}}{s_2} \quad , \tag{96}$$

where the negative sign is due to the fact that the edge wave field is polarized in the opposite direction to that of the $\beta$ polarization.

Substituting Equation (95) into (96), one obtains

$$E^d_{\beta(1)} = -E^i_{\beta'(1)}(c_2)D^{(ew)}_s(\ell, \phi_1', \frac{\pi}{2}, \beta_1)RD^{(ew)}_s(\ell, \frac{\pi}{2}, \phi_1, \beta_1)$$

$$e^{-j2k\ell} \frac{e^{-jks_2}}{s_2} \tag{97}$$

There are two possible combinations of $\beta$ polarized triple diffraction terms. These are due to the double diffraction terms discussed earlier, namely $\beta'\beta$ and $\phi'\beta$. These two possible combinations are $\beta'\phi'\beta$ and $\beta'\beta'\beta$. Therefore, the total $\beta$ polarized triple diffracted edge wave field from $C_2$ is given by

$$E^d_{\beta(1)} = -2E^i_{\beta'(1)}(c_2)D^{(ew)}_s(\ell, \phi_1', \frac{\pi}{2}, \beta_1)RD^{(ew)}_s(\ell, \frac{\pi}{2}, \phi_1, \beta_1)$$

$$e^{-j2k\ell} \frac{e^{-jks_2}}{s_2} \tag{98}$$

The cross polarized triple diffracted term can be written in a similar way

$$E^d_{\beta(1)} = 4E^i_{\phi'(1)}(c_2)D^{(ew)}_s(\ell, \phi_1', 0, \beta_1)RD^{(ew)}_s(\ell, \frac{\pi}{2}, \phi_1, \beta_1)$$

1st page Chapter end line

$$e^{-j2k\ell} \frac{e^{-jks_2}}{s_2} \tag{99}$$

LAST TEXT LINE

$$E^d_{\beta(1)} = 4E^i_{\phi'(1)}(c_1)\, D^{(ew)}_h(\ell,\phi_1^-,o,\beta_1)R^2 D^{(ew)}_S(\ell,\tfrac{\pi}{2},\phi_1,\beta_1)$$

$$e^{-j2k\ell}\ \frac{e^{-jks_1}}{s_1} \hspace{2em} (102)$$

$$E^d_{\phi(1)} = 2E^i_{\phi'(1)}(c_1)D^{(ew)}_h(\ell,\phi_1^-,o,\beta_1)R^2 D^{(ew)}_h(\ell,o,\phi_1,\beta_1)$$

$$e^{-j2k\ell}\ \frac{e^{-jks_1}}{s_1} \hspace{2em} (103)$$

## D. DISCUSSION

The above analysis is used to compute the RCS pattern for a $2\lambda \times 2\lambda$ plate. The incident field is polarized in the $\theta$-direction. The geometry used is shown in Figure 118. The notation $E_{PH}$ is used to indicate the backscattered field PH component defined with respect to the standard spherical coordinate system.

Figure 126 shows the E-plane RCS pattern. The results are compared with Moment Method (MM) solution provided by Dr. Newman [33]. Only single, double and triple edge diffraction mechanisms were used to compute the pattern by the EC method. The two results are in excellent general agreement throughout the pattern, however, they deviate slightly in the region $0^O < PH < 40^O$. The cause for this deviation is the edge wave field which was not included in the solution. If the edge wave field is included for just one point at $PH = 30^O$, as shown in Figure 126, then the value of the RCS agrees well with the MM solution.

1 it
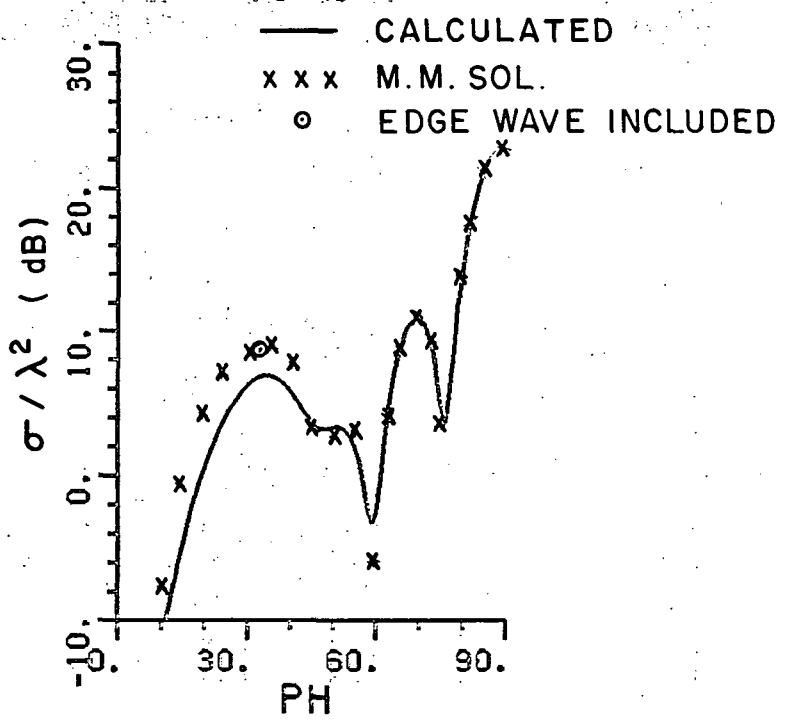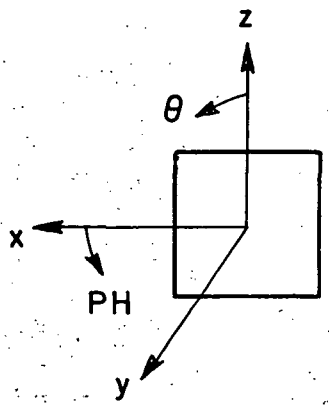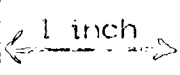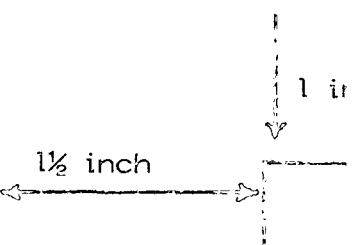
1½ inch

1 inch

Figure 126. $E_{PH}$, $\theta = 90^\circ$ RCS pattern for a $2\lambda$ x $2\lambda$ plate, using first, second and third order Equivalent currents.

1 inch

JAB/80
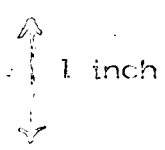
Let us now proceed to discuss the case when the plane wave is incident at an angle $\theta=60^O$. Figure 127 shows the individual edge diffraction contributions. Figure 127-d shows the sum of the single, double and triple edge diffraction terms. These field components contribute significantly in the main and first lobe region while the edge wave mechanism dominates the rest of the pattern. Again the EC method was used to compute the results shown in Figure 127. Table 2 shows the different single, double and triple edge diffraction mechanisms that were included in our solution for $\theta=60^O$ case.

| TABLE 2<br>SINGLE, DOUBLE AND TRIPLE EDGE DIFFRACTED RAYS USED IN<br>RCS COMPUTATION FOR $2\lambda$ SQUARE PLATE AND $\theta = 60^O$ | | |
| --- | --- | --- |
| Single<br>Edge # | Double<br>Edge #-Edge # | Triple<br>Edge #-Edge #-Edge # |
| 1 | 1-3 , 1-4 | 1-3-1, 1-3-2, 1-3-4 |
| 2 | 2-3 , 2-4 | 1-4-3, 1-4-2 |
| 3 | 3-4 , 3-1 | 2-3-4, 2-3-1 |
| 4 | 4-2 , 4-3 | 2-4-2, 2-4-3 |
| | | 3-4-1, 3-4-2 |
| | | 3-1-3, 3-1-4, 3-1-2 |
| | | 4-2-3, 4-3-2, 4-3-1 |

1st page Chapter end line

188
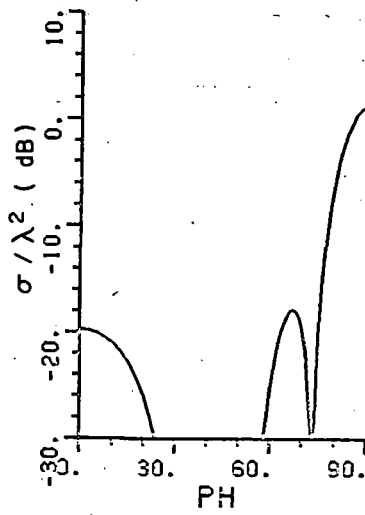
(a) SINGLE DIFFRACTION
COMPONENT
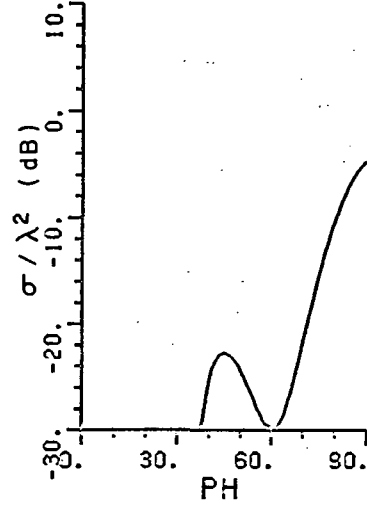
(b) DOUBLE DIFFRACTION
COMPONENT
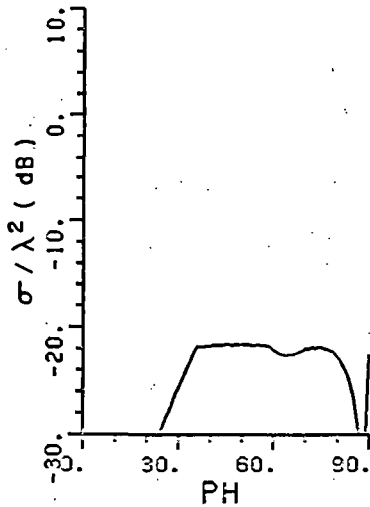
(c) TRIPLE DIFFRACTION
COMPONENT
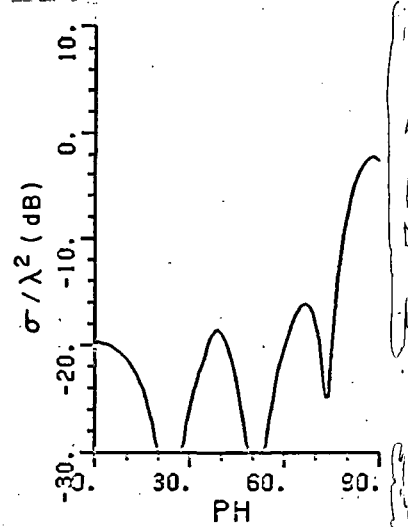
(d) SUM OF SINGLE, DOUBLE
AND TRIPLE DIFFRACTION
COMPONENTS

1st page Chapter end line

1st page Chapter end line

Figure 127. $E_{PH}$, individual contributions of edge diffraction mechanisms to $\theta = 60^{\circ}$ RCS pattern for a $2\lambda \times 2\lambda$ plate.

Center Guide

JAB/80

Figure 128 shows the individual contributions of the edge wave double diffraction mechanism, i.e., $\beta\acute{}\beta$, $\beta\acute{}\phi$, $\phi\acute{}\beta$ and $\phi\acute{}\phi$ components. Notice that the $\beta\acute{}\phi$ and $\phi\acute{}\beta$ components are equal. Their contribution is in the transition region as one expects. Figure 129 shows comparable field components for the edge wave triple diffraction mechanism. In both Figures 128 and 129 one notices that the $\beta\acute{}\beta$ field component contribute significantly in the edge on region while the $\beta\acute{}\phi$, $\phi\acute{}\beta$ and $\phi\acute{}\phi$ combine to contribute to the rest of the pattern. The total contribution of the edge wave mechanism (double and triple diffraction) is shown in Figure 130 where the importance of the edge wave mechanism is clearly seen. It dominates the pattern up to 60° from edge on, where the edge diffraction takes over. Table 3 shows the different double and triple corner diffractions used to compute the edge wave contribution.

TABLE 3

DOUBLE AND TRIPLE CORNER DIFFRACTIONS INCLUDED IN
EDGE WAVE SOLUTION FOR $\theta=60^{\circ}$ CASE

| Double<br>Corner #-Corner # | Triple<br>Corner #-Corner #-Corner # |
|---|---|
| 1-2 , 2-1 | 1-2-1 , 2-1-2 |
| 2-3 , 3-2 | 2-3-2 , 3-2-3 |
| 3-4 , 4-3 | 3-4-3 , 4-3-3 |
| 4-1 , 1-4 | 1-4-1 , 4-1-4 |

190
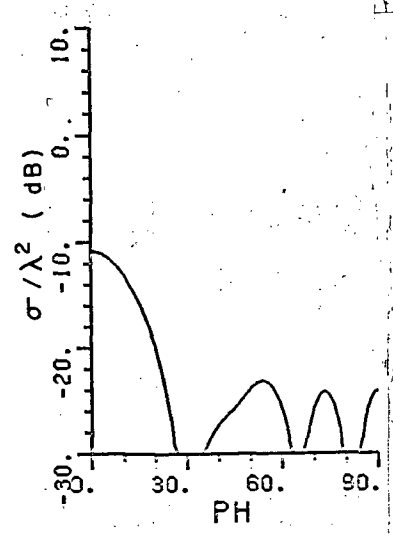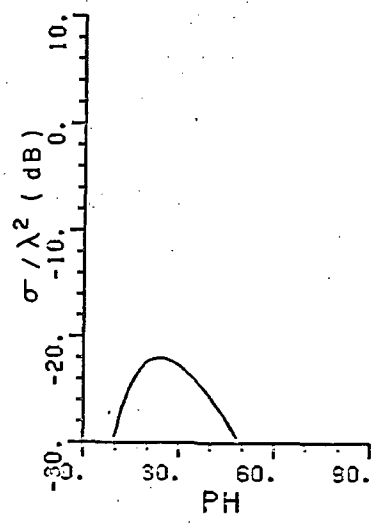
(a) $\beta'\beta$ COMPONENT
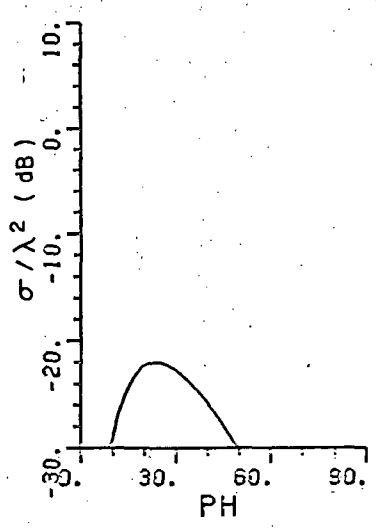
(d) $\beta'\phi$ COMPONENT
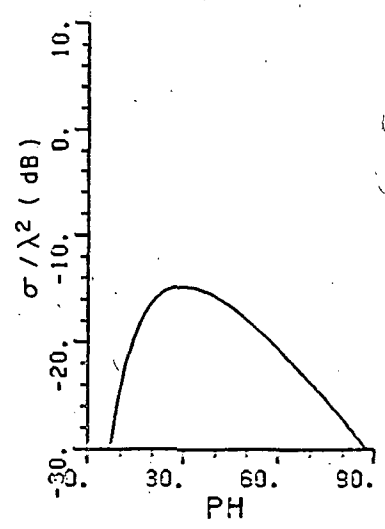
(c) $\phi'\beta$ COMPONENT

(d) $\phi'\phi$ COMPONENT

1st page Chapter end line

Figure 128. $E_\theta$, individual contributions of edge wave double corner diffraction mechanism to $\theta = 60^\circ$ RCS pattern for a 2λ x 2λ plate.

1 inch

JAB/80
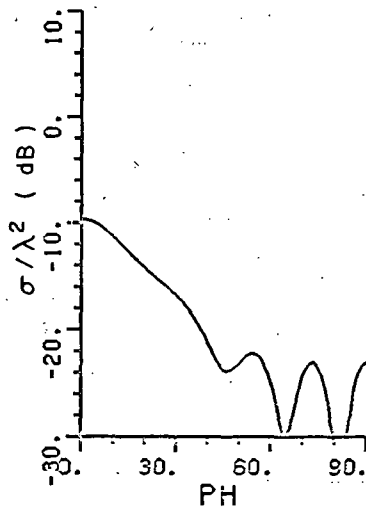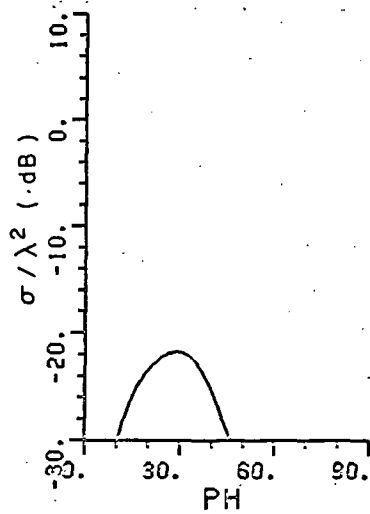
(a)  $\beta'\beta$  COMPONENT
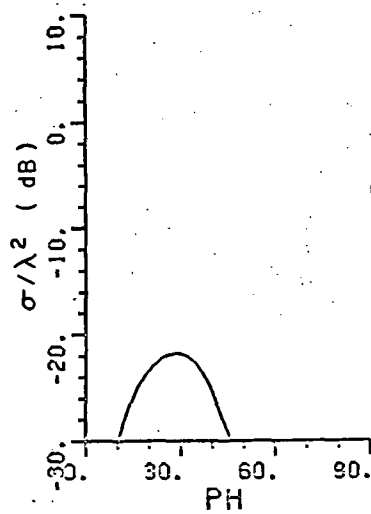
(b)  $\beta'\phi$  COMPONENT
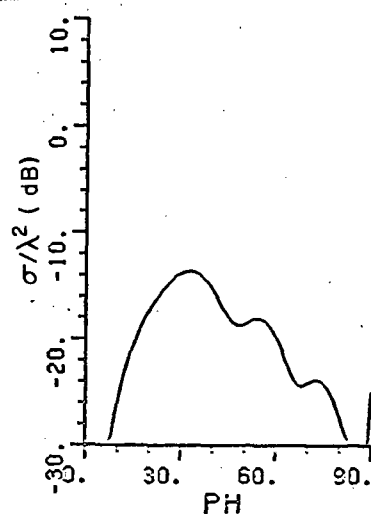
(c)  $\phi'\beta$  COMPONENT

(d)  $\phi'\phi$  COMPONENT

Figure 129. $E_\theta$, individual contributions of edge wave triple corner diffraction mechanism to $\theta = 60°$ RCS pattern for a $2\lambda \times 2\lambda$ plate.

JAB/80
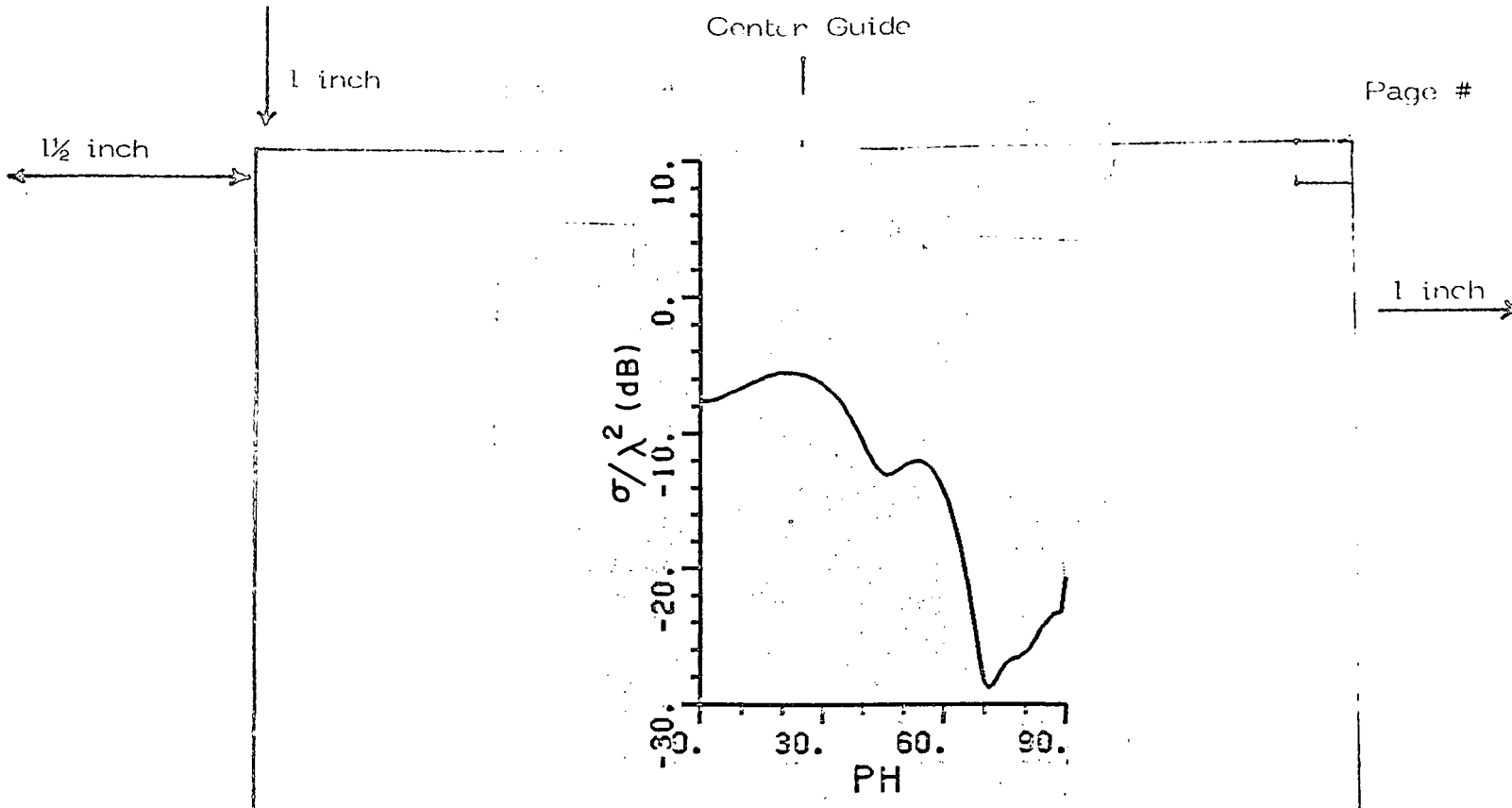
Figure 130. $E_\theta$, sum of all edge wave mechanisms contributing to $\theta = 60^o$ RCS pattern for a $2\lambda \times 2\lambda$ plate.



Figure 131. $E_\theta$, $\theta = 60^o$ RCS pattern for a $2\lambda \times 2\lambda$ plate.

193

JAB/80
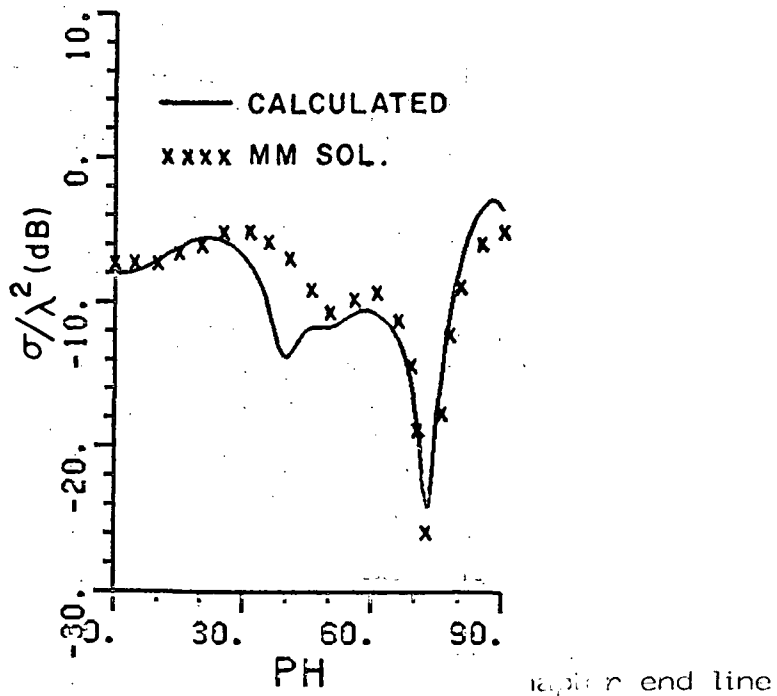
1½ inch

The final result as shown in Figure 131 is obtained by combining the patterns of Figures 127 and 130. This result is compared to MM solution with the agreement being quite good. However, the two solutions deviate in two regions. The first is in $80^O$<PH<$90^O$, where the deviation in this region becomes clear if we examine the point PH=$90^O$ in Figure 131 which corresponds to the point PH=$60^O$ in Figure 126 and noting the field is a null. In such a situation the phasing between the single, double and triple edge diffraction which determines the field value at this point becomes very critical when computing the fields numerically. The second region is $30^O$<PH<$50^O$, where other types of interactions involving the edge wave mechanism should be included and a more accurate edge wave diffraction coefficient should be developed. It is obvious that the two types of edge wave interaction discussed here are the dominant ones for the case $\theta$=$60^O$. However, the need for a more accurate diffraction coefficient as is discussed in Appendix C and the inclusion of other types of interactions becomes more clear as one moves further away from the principal plane.

In Figures 132-134, the effect of using the corner diffraction method is shown instead of the EC method for evaluating the first order diffraction fields. By comparing Figure 131 and Figure 134, one notices a slight improvement for $30^O$<PH<$60^O$. As indicated in Chapter IV, corner diffraction will give more accurate results as one moves off the principal plane.

The higher order interactions are one of the primary sources that contribute to the cross polarized field component ($E_{\theta PH}$). It is not our purpose here to present a study on cross polarization sources in scattering problems but rather to point out that a thorough investigation of this problem should include a complete study of all possible higher order interactions.

Figures 135 and 136 show the contributions of edge diffraction (single, double and triple) and the edge wave mechanism to the cross polarized field component ($E_{\theta PH}$), both mechanisms contribute

JAB/80

1 inch

1½ inch

1 inch
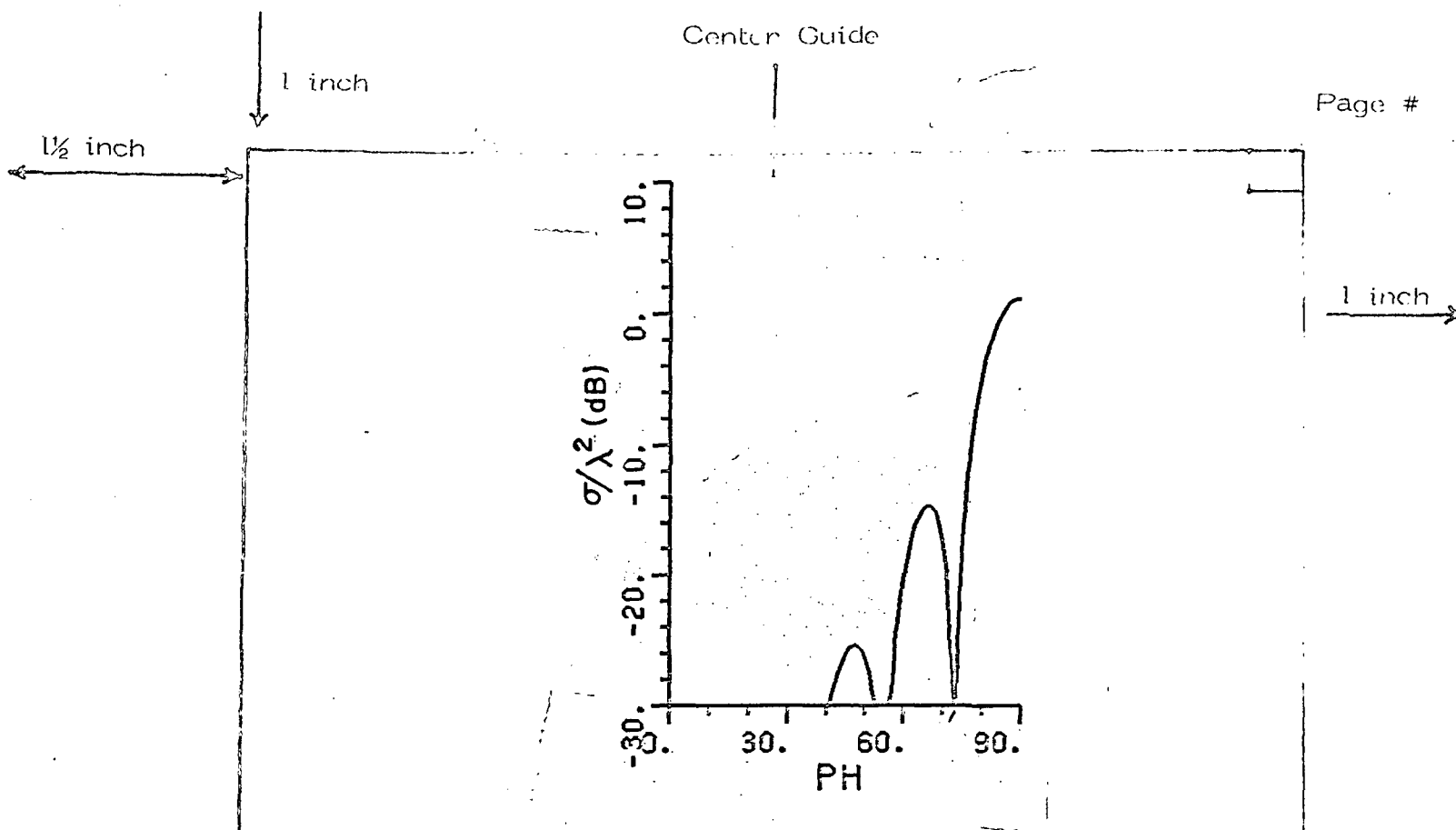


Figure 132. $E_\theta$, corner field due to single diffraction mechanism.
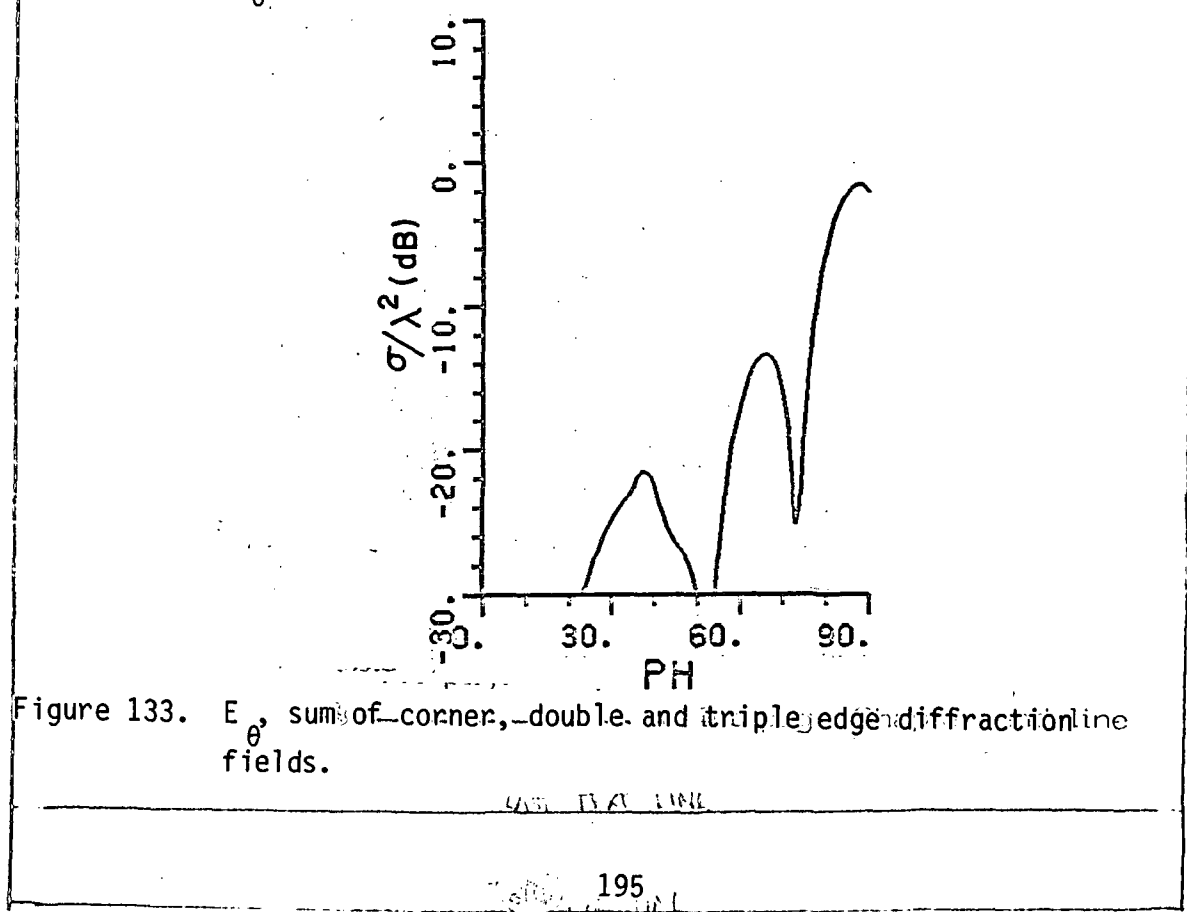


Figure 133. $E_\theta$, sum of corner, double and triple edge diffraction line fields.

195

1 inch

JAB/80

1 inch

1½ inch

1 inch
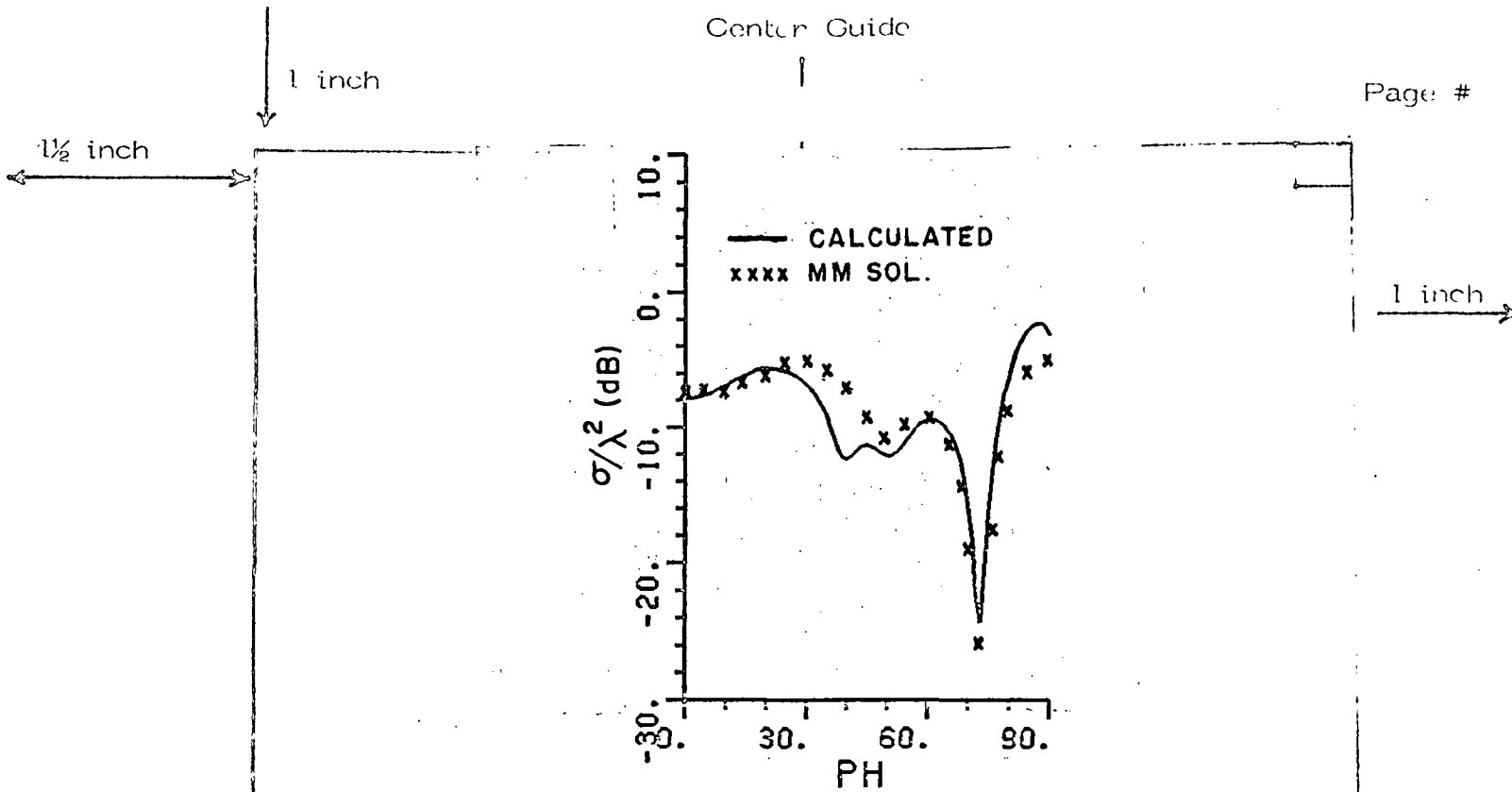


Figure 134.  $E_\theta$, $\theta = 60^o$ RCS pattern for a $2\lambda$ x $2\lambda$ plate.  Corner diffraction is used instead of EC single diffraction component.
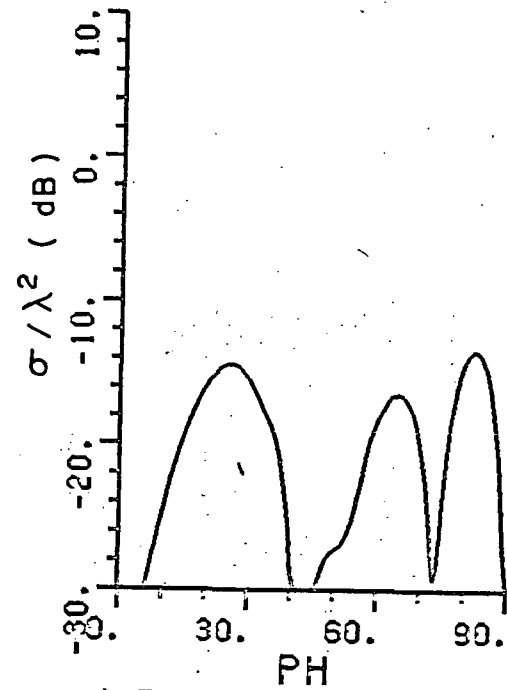


Figure 135.  $E_{\theta PH}$ edge diffraction contribution to cross-polarized RCS pattern for $\theta = 60^o$ case.

1 inch

JAB/80
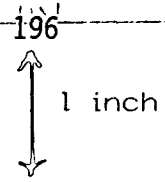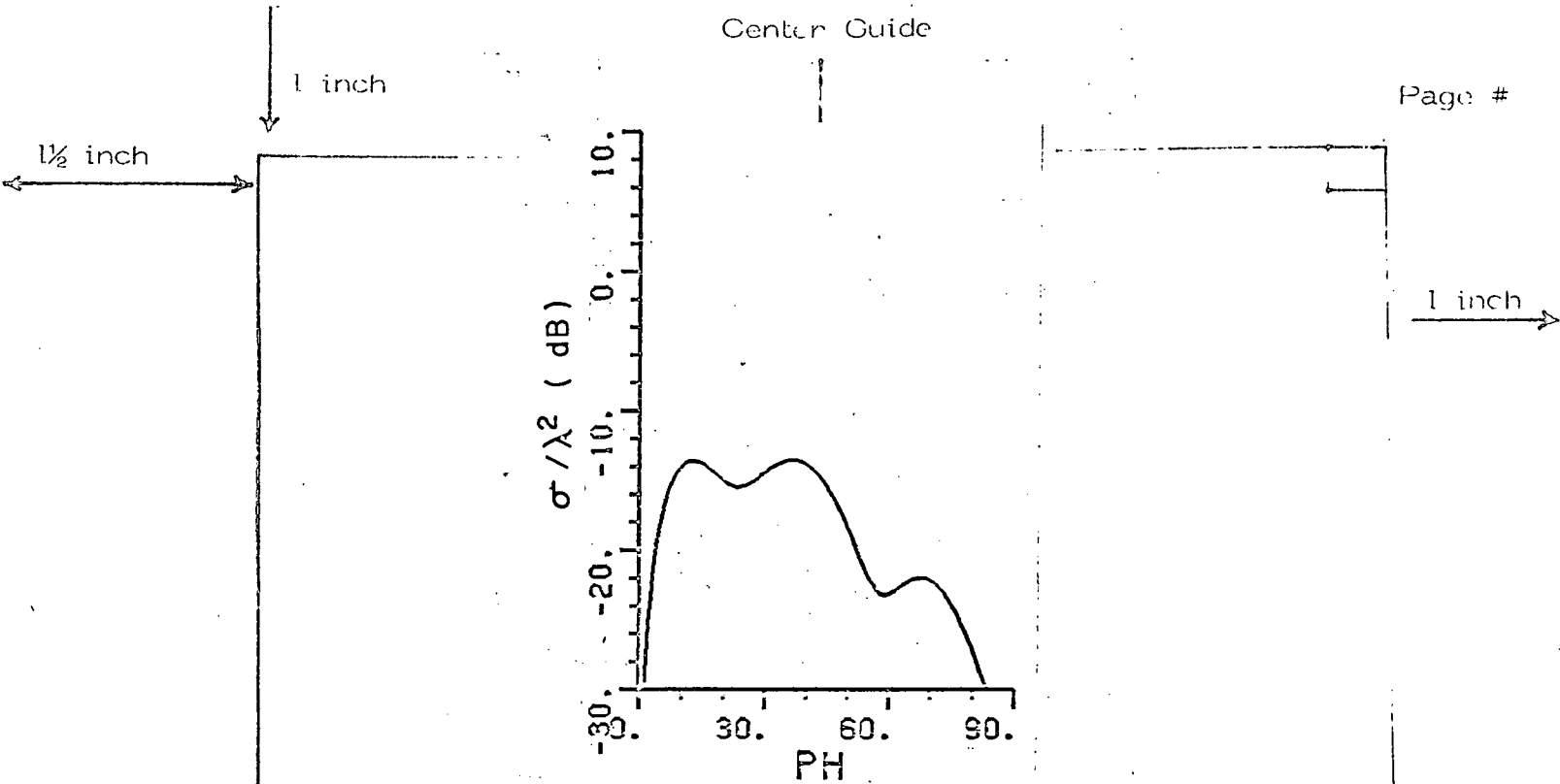
Figure 136.  $E_{\theta PH}$, edge wave contribution to cross polarized RCS pattern for $\theta = 60^0$ case.
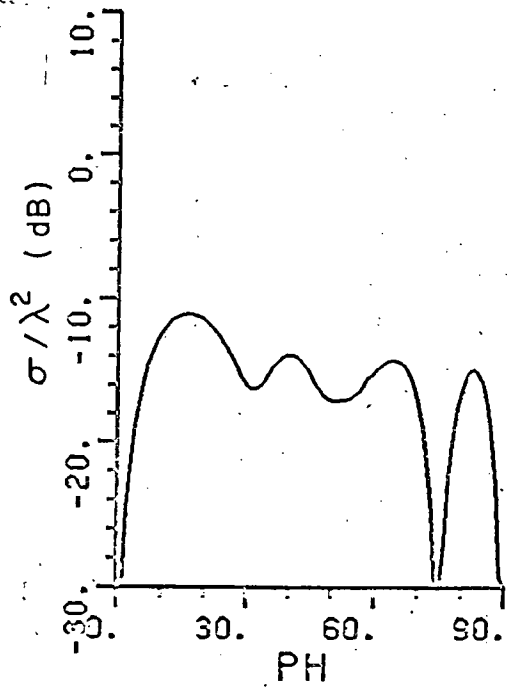


Figure 137.  $E_{\theta PH}$, $\theta = 60^0$ cross-polarized RCS pattern for a $2\lambda \times 2\lambda$ plate. All edge diffraction, and edge wave mechanism contributions are included.

JAB/80

significantly to the cross polarized RCS through out the pattern. The combined effect of both mechanisms is shown in Figure 137. Notice the high level of this field component compared to the principal polarization field component shown in Figure 134.

As was stated before, one would expect that more higher order interaction mechanisms involving edge waves become more significant and have to be included in the solution. As different pattern cuts are considered, edge waves on different edges contribute to the RCS by different interactions depending on how strongly it was excited. For instance, consider the $\theta=60^O$ pattern. Here the edge waves on edges #1 and 3 are more strongly excited than those on edges #2 and 4. However, the situation is reversed for the $\theta=30^O$ pattern and are equally excited when $\theta=45^O$. While the two edge wave mechanisms considered here namely the double and triple diffraction were sufficient to give satisfactory results for $\theta=60^O$ pattern cut, they do not appear to be completely adequate for the $\theta=45^O$ and $\theta=30^O$ patterns. Figures 138 and 139 show the RCS pattern for $\theta=45^O$ and $30^O$ respectively. The calculated results are compared to MM solutions, both results do not show as good agreement especially in the region $20^O<PH<70^O$. This is not too surprising since much effort was devoted to finding the appropriate mechanisms for the $\theta=60^O$ pattern, and then these were used to obtain the $\theta=45^O$ and $\theta=30^O$ patterns. No comparable study was performed to improve these latter patterns. Furthermore, the diffraction coefficients used herein are approximate and can be improved substantially. In Figures 140 and 141, the total RCS pattern is shown for $\theta=45^O$ and $30^O$ respectively but using Corner diffraction method to compute the contribution of first order diffraction. A slight improvement is noted near $PH = 30^O$ for $\theta = 30^O$ case. However, the deviation between our result and MM solution is still substantial in the region $20^O<PH<60^O$ which indicates that a higher order interactions are needed to correct for this deviation between the two solutions. Some of the different edge wave interactions that are still under investigation are shown in Figure 142.

JAB/80

1 inch

1½ inch

1 inch

z

θ

x

PH

y

—— CALCULATED

x x x   M.M. SOL

$\sigma / \lambda^2$ (dB)

10.

0.

-10.

-20.

-30.

30.   60.   90.

PH

1st page Chapter end line

Figure 138. $E_\theta$, $\theta = 45^0$ RCS pattern for a $2\lambda$ x $2\lambda$ plate.

LAST TEXT LINE

1 inch

JAB/80

1 inch

1½ inch

1 inch
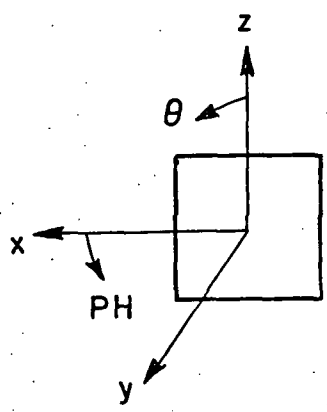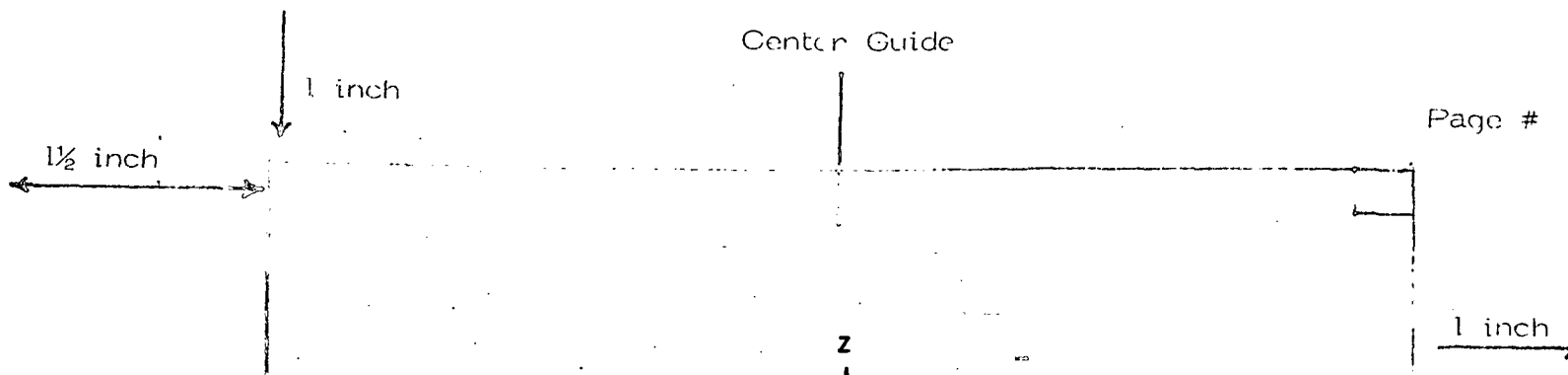


CALCULATED
x x x   M.M. SOL.
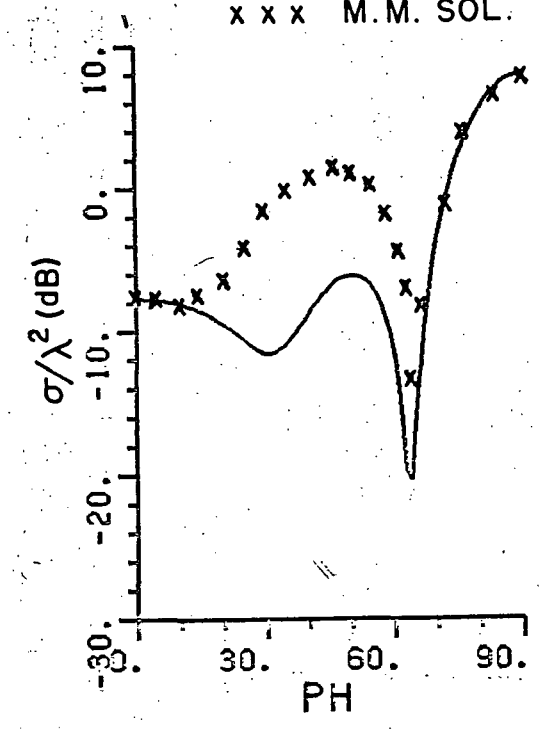
1st page Chapter end line

Figure 139. $E_\theta$, $\theta = 30^0$ RCS pattern for a $2\lambda \times 2\lambda$ plate. 1st page Chapter end line
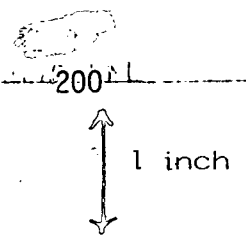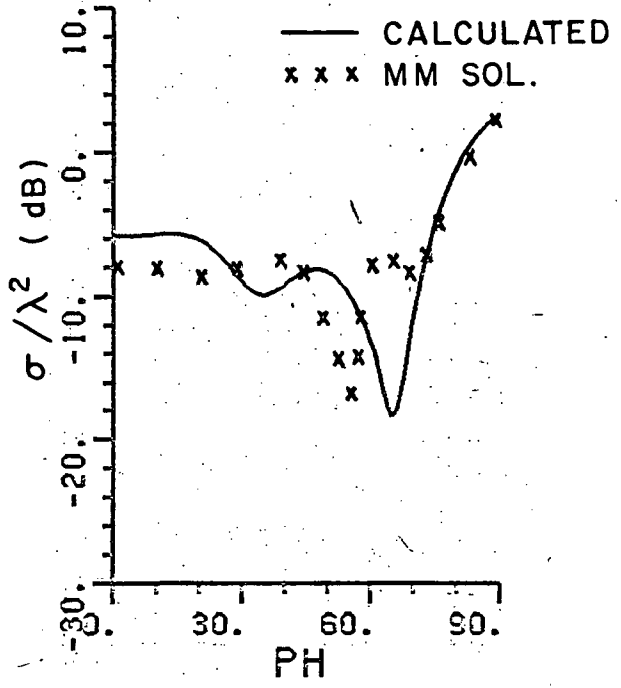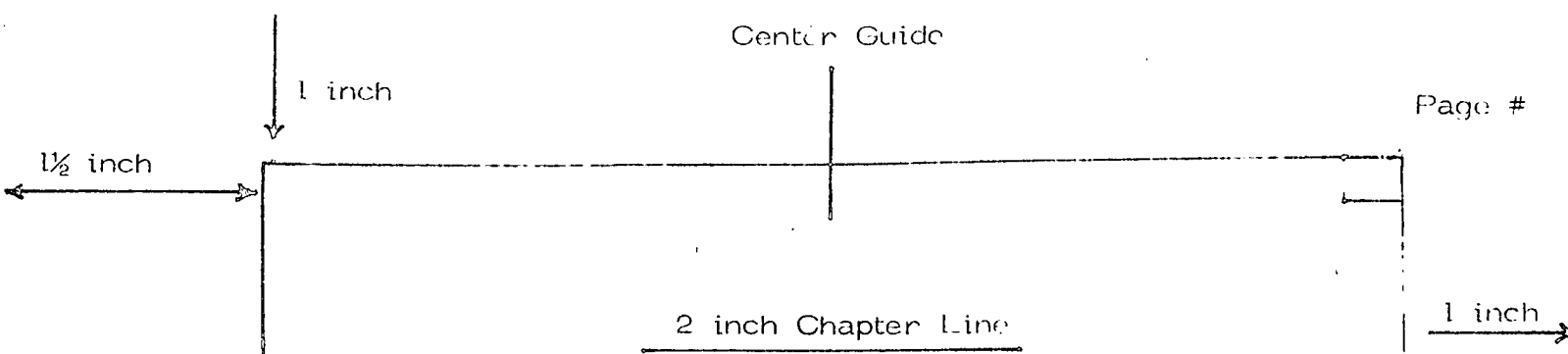
200

1 inch

JAB/80

2 inch Chapter Line

1st page Chapter end line

Figure 140. $E_\theta$, $\theta = 45^o$ RCS pattern for a $2\lambda$ x $2\lambda$ plate using corner diffraction method instead of EC single edge diffraction component.

1 inch

1½ inch

2 inch Chapter Line

1 inch

CALCULATED
x x x MM SOL.

$\sigma / \lambda^2$ (dB)

10.

0.

-10.

-20.

-30.

30.    60.    90.

PH
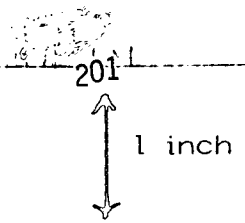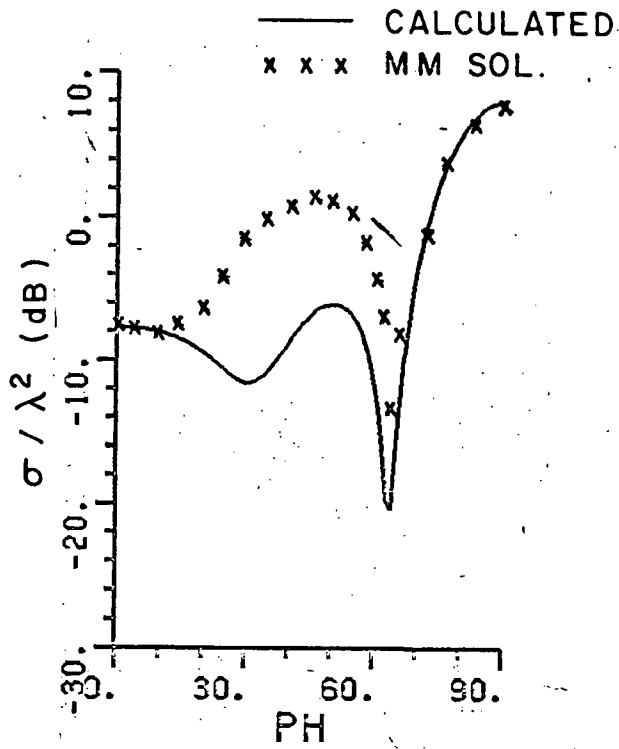
1st page Chapter end line

Figure 141. $E_\theta$, $\theta = 30^0$ RCS pattern for a $2\lambda$ x $2\lambda$ plate using corner diffraction method instead of EC single edge diffraction component.

1 inch

JAB/80
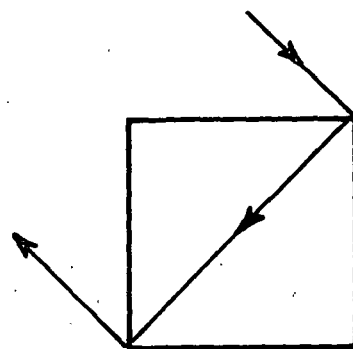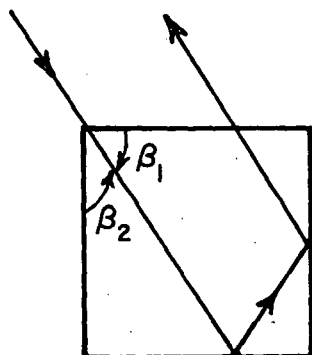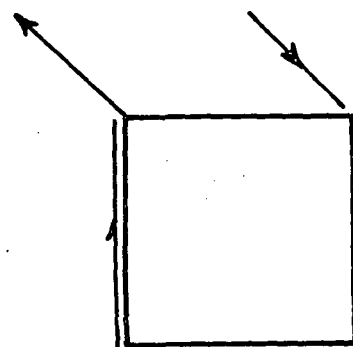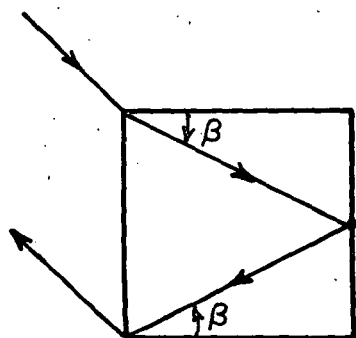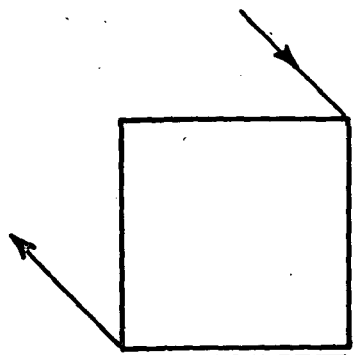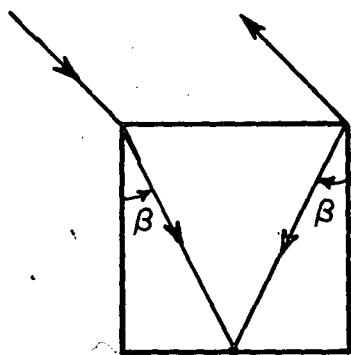
Figure 142. Possible edge wave mechanisms.

1st page Chapter end line

1 inch

JAB/80

1½ inch

1 inch

The individual contributions of edge diffraction and edge wave mechanisms are illustrated in Figures 143-145; whereas, in Figures 146 and 147 the total contribution of edge diffraction (single, double and triple) and that of edge wave (double and triple) diffraction mechanisms to $\theta=45^O$ RCS pattern are shown. Note that the edge wave fields contribute to the RCS throughout the pattern. In Figures 148-152 similar results are shown for $\theta=30^O$ RCS pattern. Note that for this case the $\beta^{\prime}\phi$ and $\phi^{\prime}\beta$ are negligible since the pattern is dominated by the edge waves on edges #2 and 4 where the incident field is polarized in the $\beta$ direction with respect to these two edges. Edges 1 and 3 contribute slightly through the $\phi^{\prime}\phi$ component. The different edge diffraction and corner to corner diffraction terms used to compute the edge diffraction and Edge wave contributions for $\theta=45^O$ and $\theta=30^O$ are similar to those used for $\theta=60^O$ case and are shown in Tables 2 and 3 above.

Finally a word should be said on the contribution of the edge wave fields to the E-plane pattern. If one examines Figure 139 specifically at PH=$90^O$, he notices the good agreement between the two solutions. However if one examines Figure 126 at PH=$30^O$ which corresponds to the same observation point as PH=$90^O$ in Figure 139, he notices the difference between the MM solution and our solution which does not include the edge wave fields. As was noted before, the RCS value at PH=$90^O$ in Figure 139 is also plotted in Figure 126 at PH=$30^O$. This leads one to conclude that it is the edge wave field that makes the difference between the two solutions in Figure 126 in the region $0^O<PH<40^O$.

In evaluating the double and triple edge diffraction fields for these different patterns, it was found that the integrals converge slowly and an integration step of $0.01\lambda$ was needed to get a convergent solution.

1st page Chapter end line
— — — — — — — 1st page Chapter end line

1 inch

JAB/80
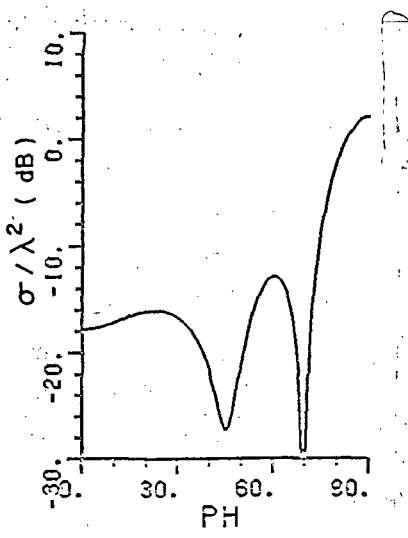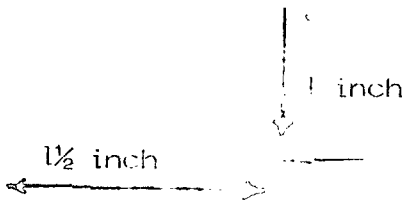
(a)  SINGLE DIFFRACTION
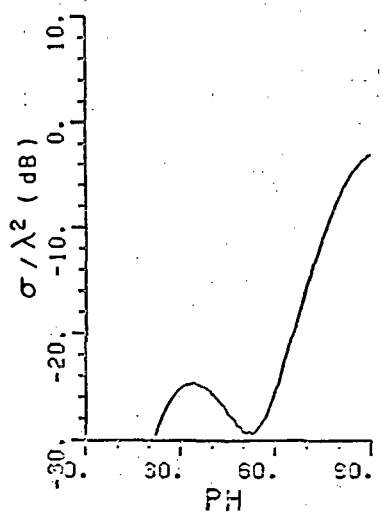
(b)  DOUBLE DIFFRACTION
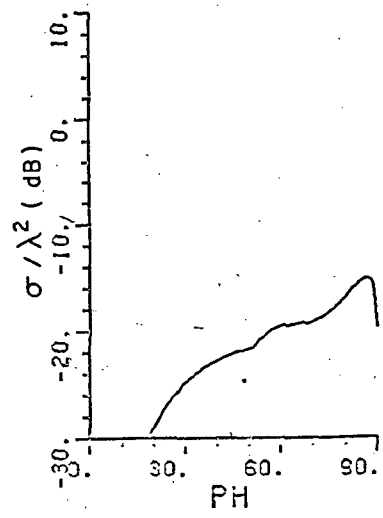
(c)  TRIPLE DIFFRACTION

1st page Chapter end line

Figure 143. $E_\theta$, individual contributions of edge diffraction mechanisms to $\theta = 45^o$ RCS pattern for a $2\lambda \times 2\lambda$ plate.

JAB/80
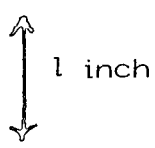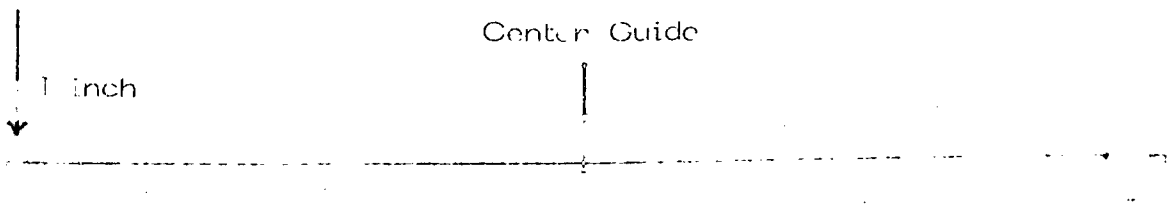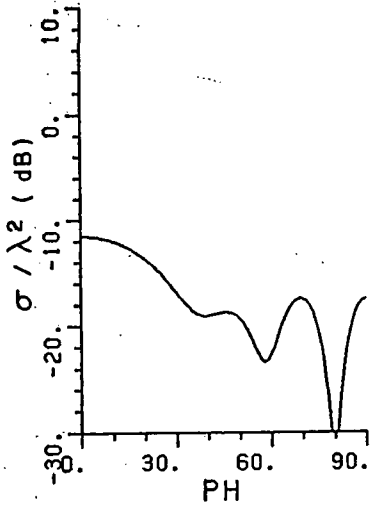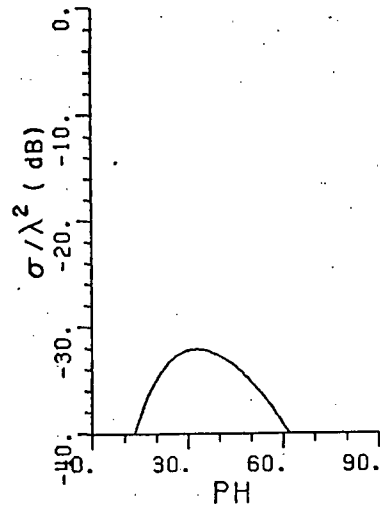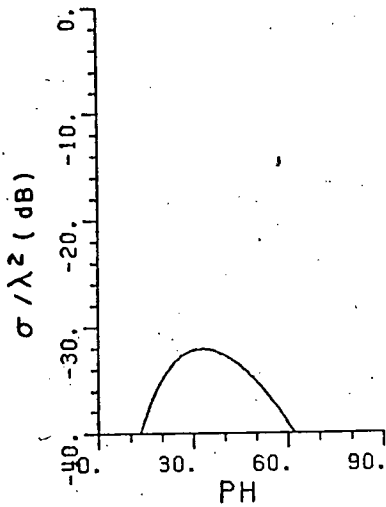
1 inch

1½ inch
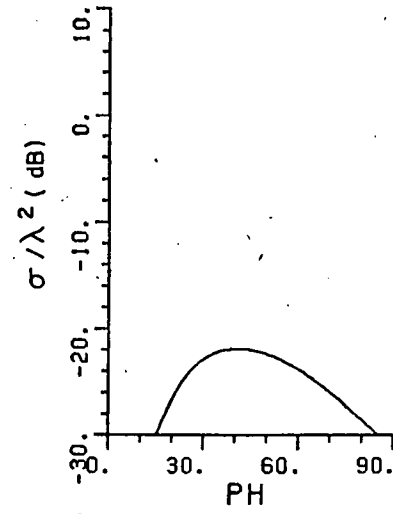
1 inch



(a) $\beta'\beta$ COMPONENT

(b) $\beta'\phi$ COMPONENT

(c) $\phi'\beta$ COMPONENT

(d) $\phi'\phi$ COMPONENT

1st page Chapter end line

Figure 144. $E_\theta$, individual contributions of edge-wave double corner diffraction mechanism to $\theta = 45^\circ$ RCs pattern for a $2\lambda \times 2\lambda$ plate.

1st page Chapter end line

1 inch

JAB/80
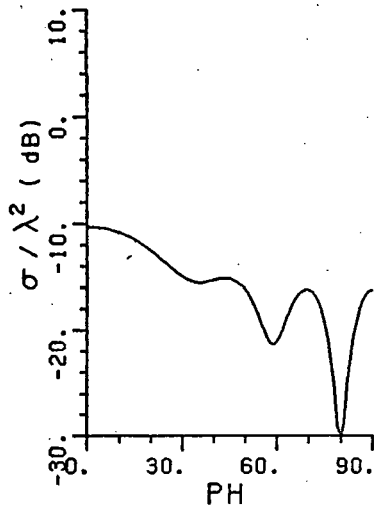
1½ inch
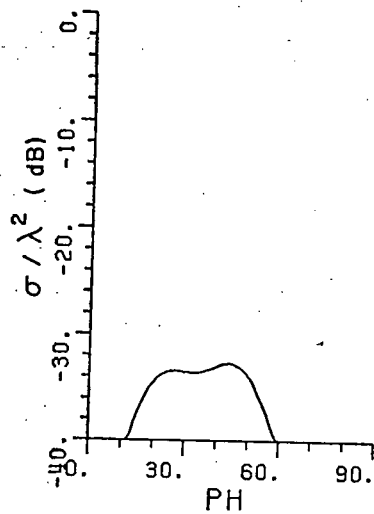
1 inch



(a) $\beta'\beta$ COMPONENT
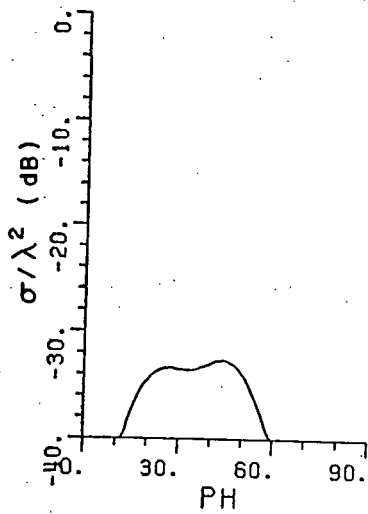
(b) $\beta'\phi$ COMPONENT
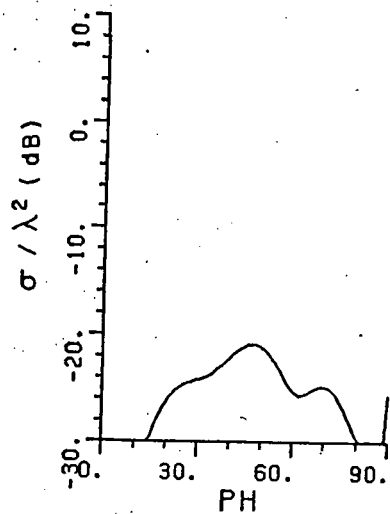
(c) $\phi'\beta$ COMPONENT

(d) $\phi'\phi$ COMPONENT

Figure 145. $E_\theta$, individual contributions of edge wave triple corner diffraction mechanism to $\theta = 45^0$ RCS pattern for $2\lambda \times 2\lambda$ plate.

207

1 inch
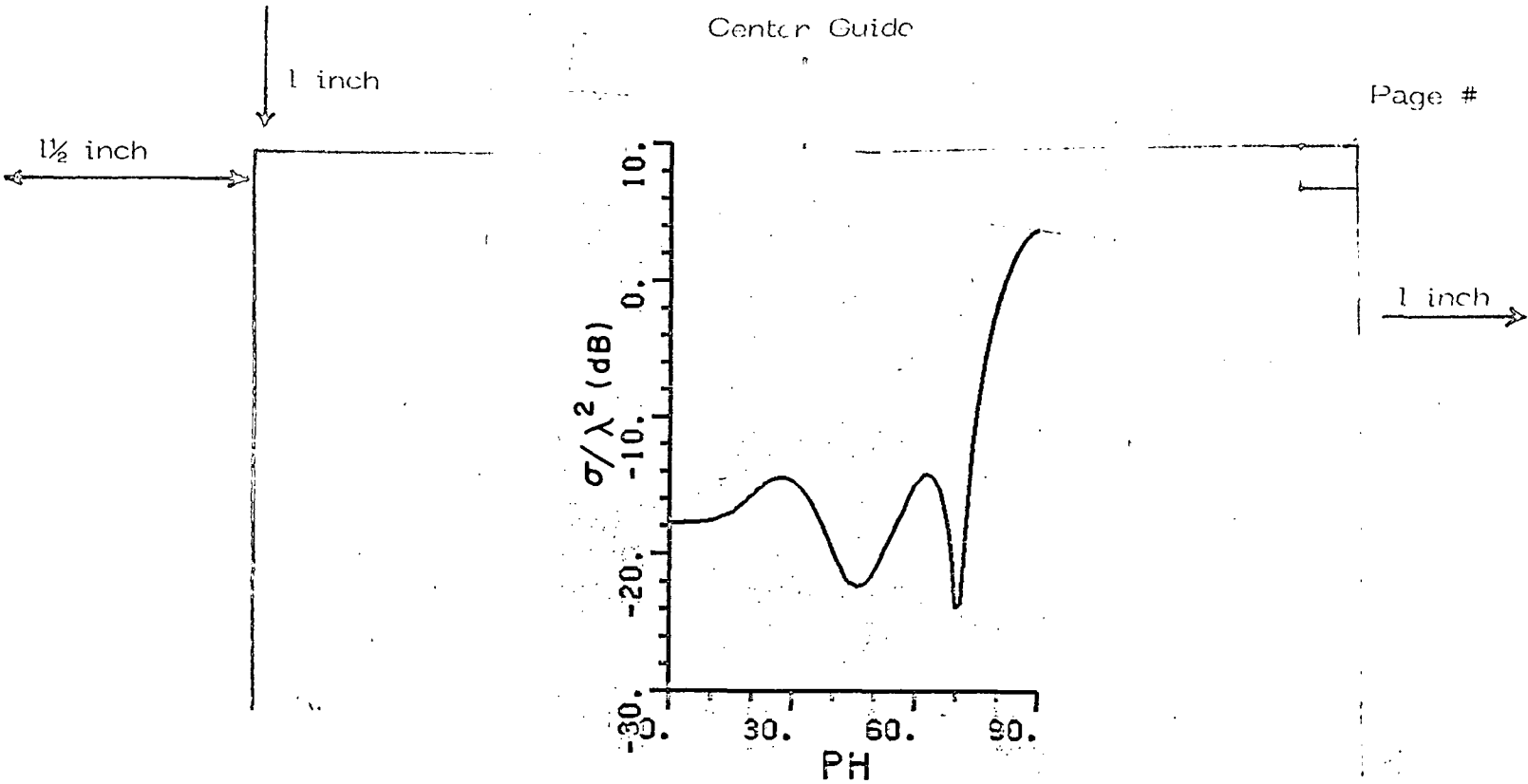
1 inch

1½ inch

1 inch



Figure 146. E$_\theta$, sum of edge diffraction mechanisms (single, double and triple) contributing to θ = 45° RCS pattern for a 2λ x 2λ plate.
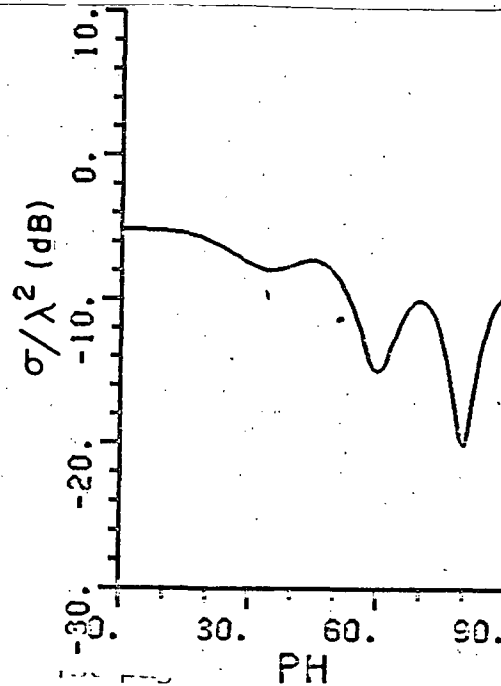


Figure 147. E$_\theta$, sum of edge wave mechanisms contributing to θ=45° RCS pattern for a 2λ x 2λ plate.

208
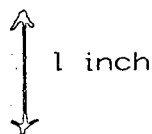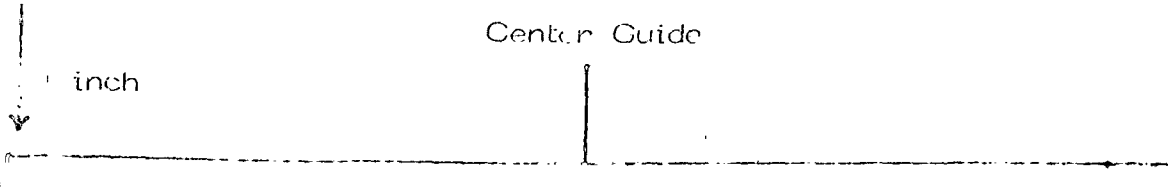
1 inch

(a) SINGLE DIFFRACTION
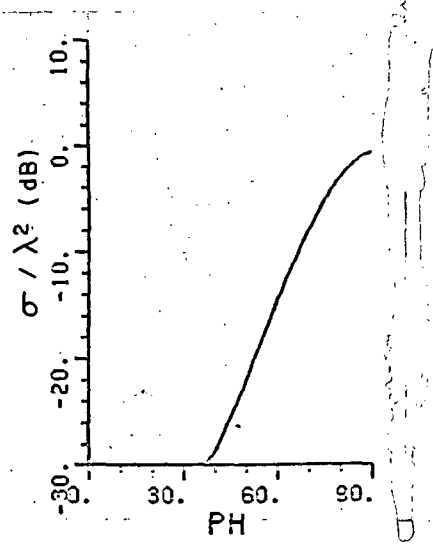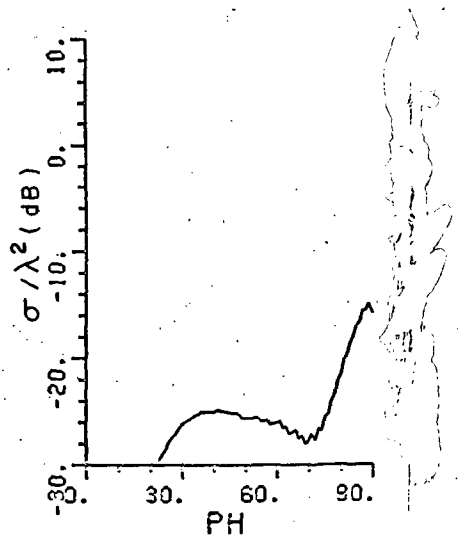
(b) DOUBLE DIFFRACTION

(c) TRIPLE DIFFRACTION

Figure 148. $E_\theta$, individual contributions of edge diffraction mechanisms to $\theta = 30^o$ RCS pattern for a $2\lambda \times 2\lambda$ plate.

1 inch

1½ inch

1 inch



(a) $\beta'\beta$ COMPONENT

(b) $\phi'\phi$ COMPONENT
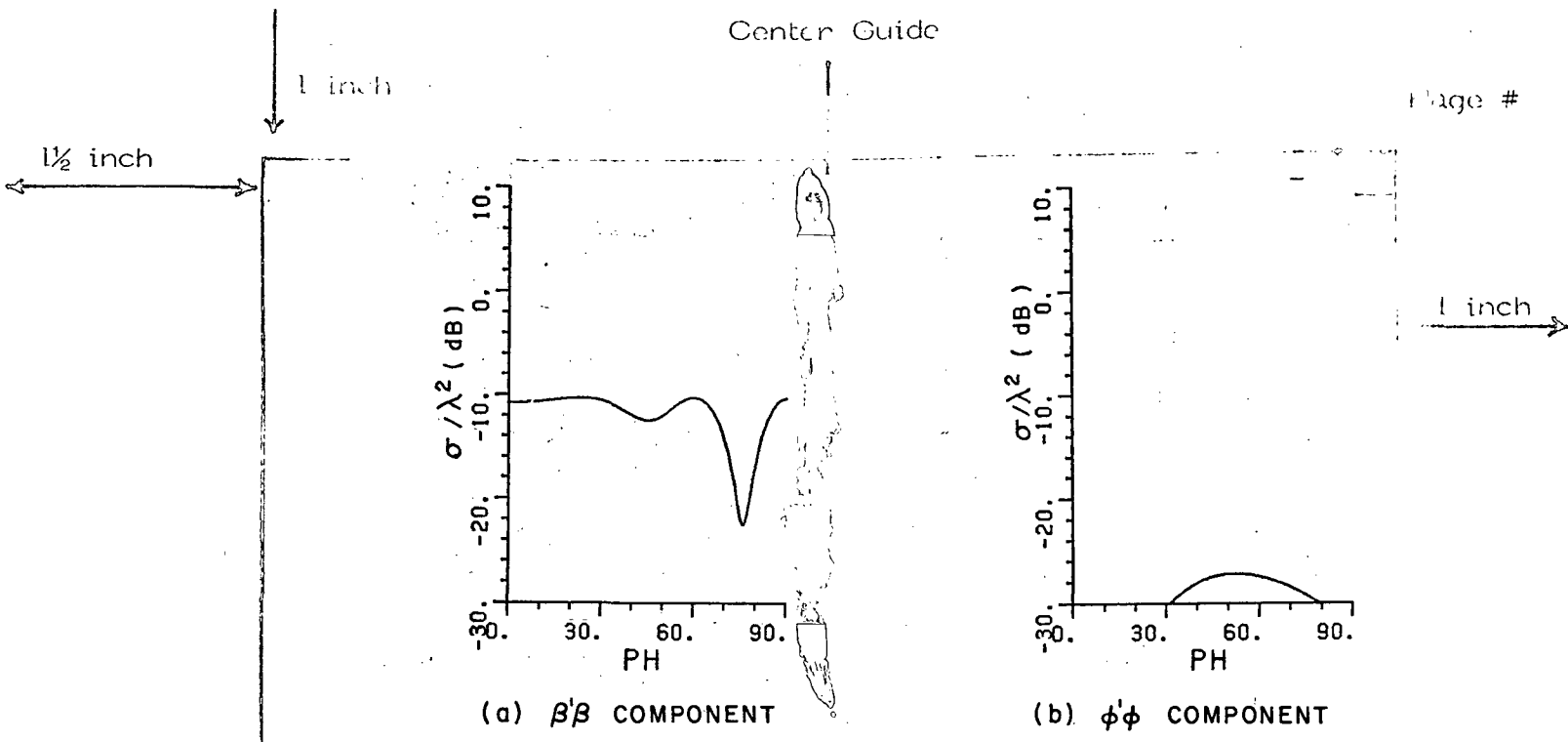
Figure 149.  $E_\theta$, individual contributions of edge wave double corner dif-
fraction mechanism to $\theta = 30^\circ$ RCS pattern for a $2\lambda \times 2\lambda$
plate.



(a) $\beta'\beta$ COMPONENT

(b) $\phi'\phi$ COMPONENT

1st page Chapter end line
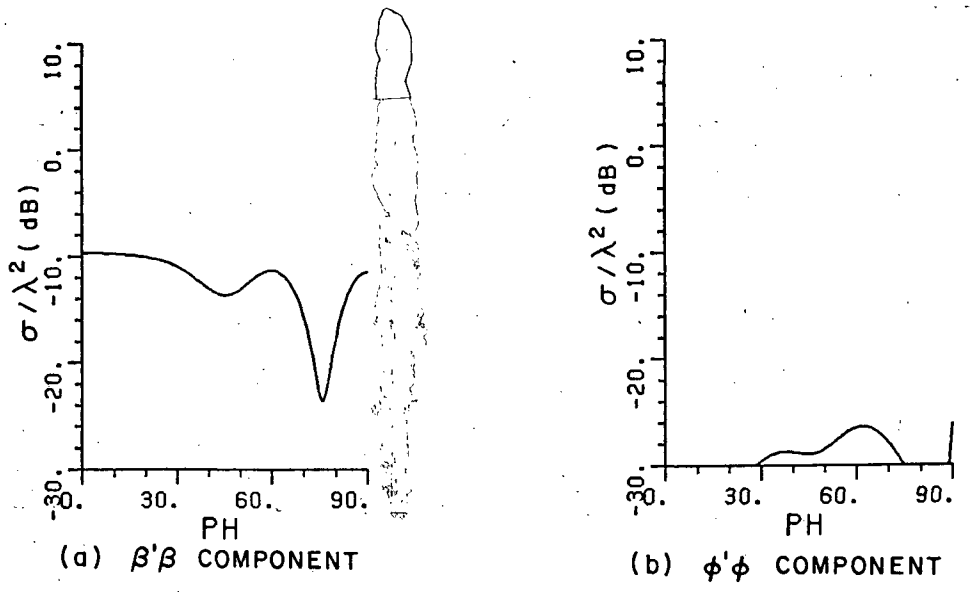
Figure 150.  $E_\theta$, individual contributions of edge wave triple corner dif-
fraction mechanism to $\theta = 30^\circ$ RCS pattern for a $2\lambda \times 2\lambda$
plate.

1 inch

JAB/80
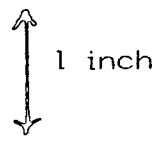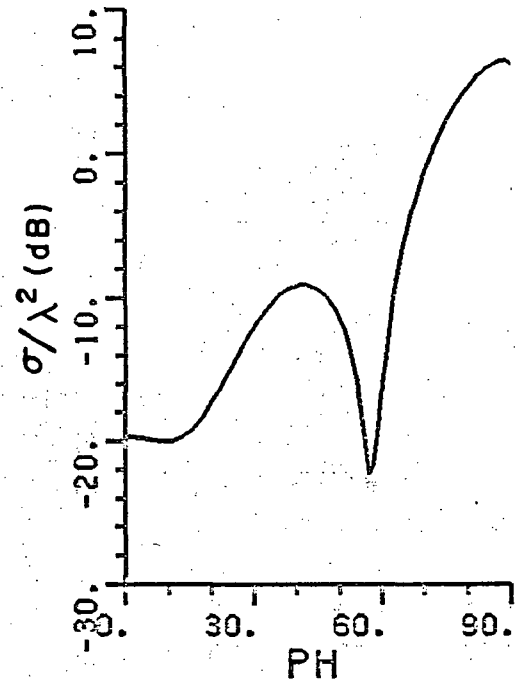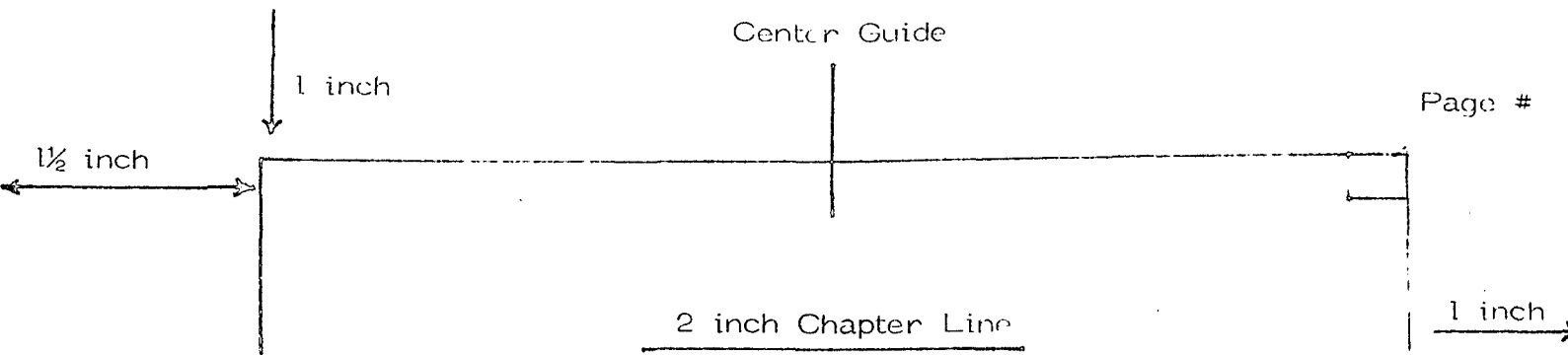
Figure 151. $E_\theta$, sum of edge diffraction mechanism (single, double, and triple) contributing to $\theta = 30^\circ$ RCS pattern for a $2\lambda \times 2\lambda$ plate.

1½ inch

2 inch Chapter Line
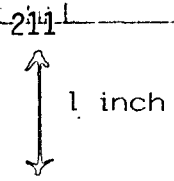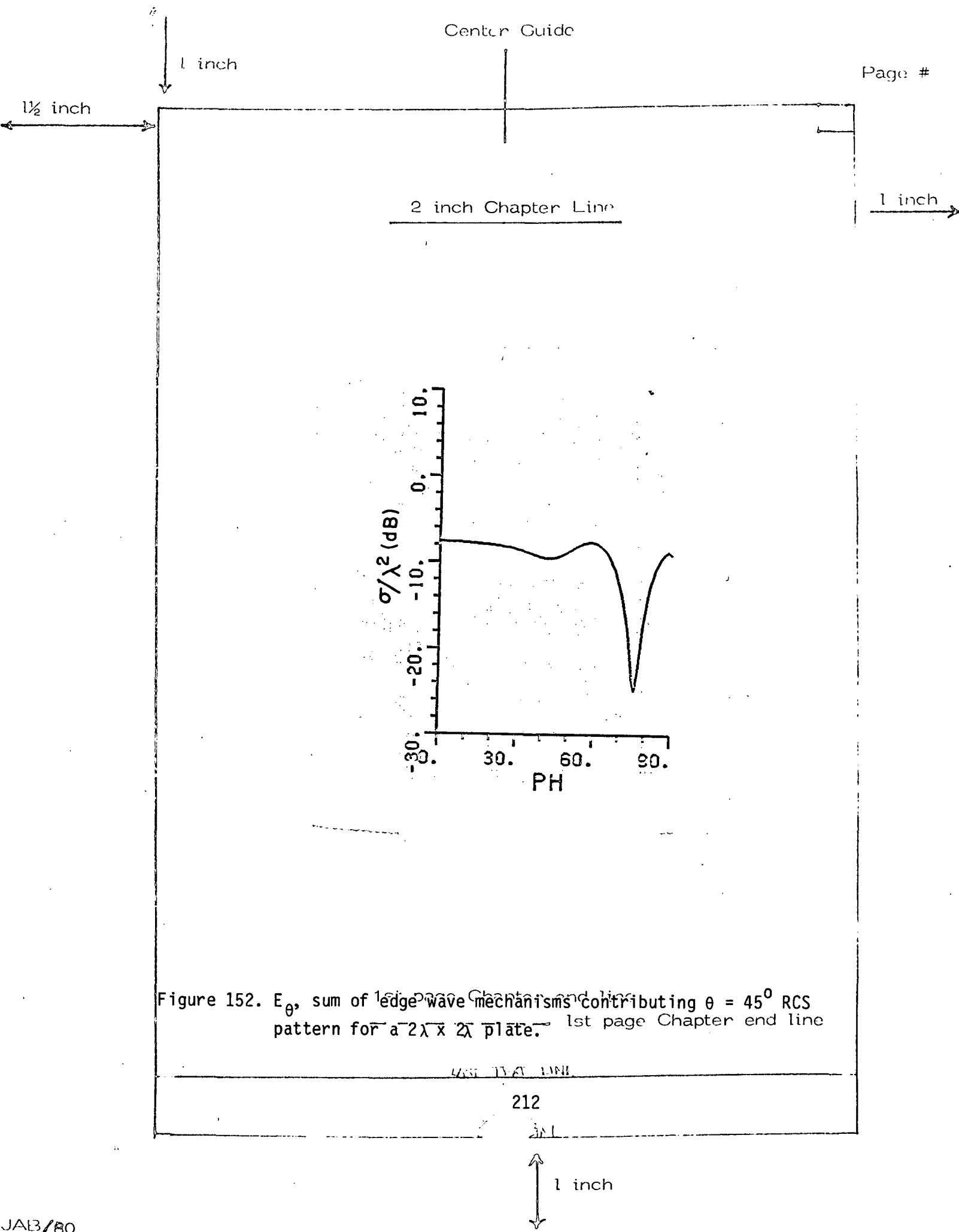
1 inch



Figure 152. $E_\theta$, sum of edge wave mechanisms contributing $\theta = 45^0$ RCS
pattern for a $2\lambda \times 2\lambda$ plate.

1st page Chapter end line

1 inch

JAB/80
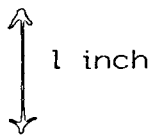
E.  SUMMARY OF E-PLANE AND NON-PRINCIPAL PLANE PATTERNS FOR A
RECTANGULAR PLATE

In this chapter the discussion on the effect of higher order inter-
actions on RCS was continued. The analysis focuses on treating the E-
plane and non-principal plane RCS patterns for a rectangular plate.

For the E-plane patterns of a 2λ square plate, the single, double
and triple edge diffraction terms were included in the solution, and
the EC method was used to compute their contributions.  As was noted
in Chapter V, the double and triple edge diffraction terms become sig-
nificant near the edge-on region.  However, the edge wave contribution
is needed to obtain good agreement with results obtained using the
Moment Method.  For a 3λ square plate or larger, the single, double
and triple edge diffraction terms are sufficient to obtain good agree-
ment with measured results.

For a non-principal plane case, where the incidence electric field
vector is oriented in the θ-direction, the single and multiple edge
diffraction terms and the interactions associated with the edge wave
mechanism were found to be dominant terms in the region outside the
main beam.  Two types of edge wave interactions were considered in our
analysis -- the double and triple corner diffractions.  They proved
to be sufficient for θ=60$^0$ case while for θ=45$^0$ and 30$^0$, they do not
appear to be completely adequate.  The solution could be further improved
if a more accurate corner diffraction coefficient is developed which
will permit the addition of more edge wave interactions, such as the
ones shown in Figure 142, to be included in the solution.

These higher order interactions were found to be one of the primary
sources of cross polarized field components which is of a comparable
level compared to that of the principal polarization.
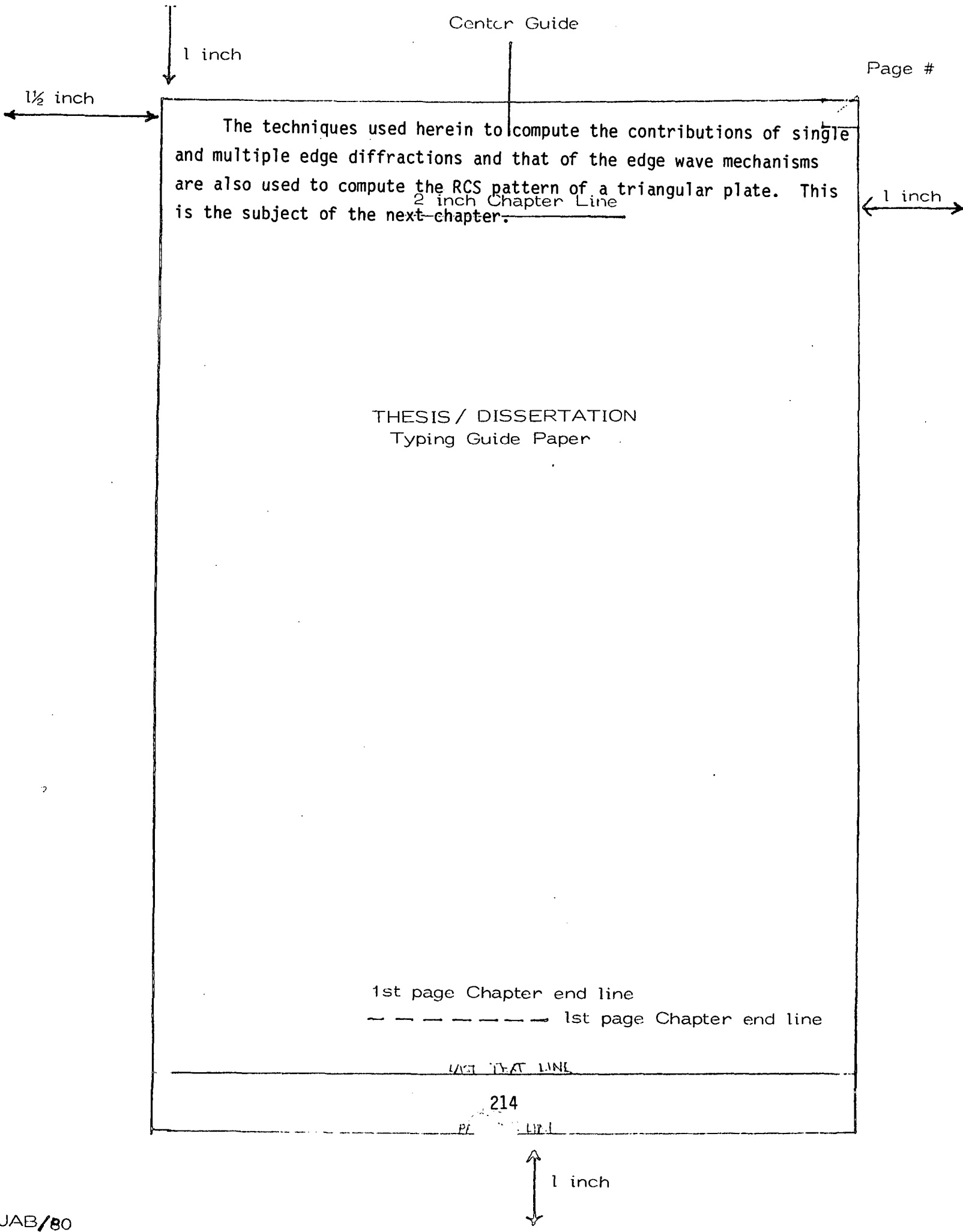
The techniques used herein to compute the contributions of single and multiple edge diffractions and that of the edge wave mechanisms are also used to compute the RCS pattern of a triangular plate. This is the subject of the next chapter.

2 inch Chapter Line

THESIS / DISSERTATION
Typing Guide Paper

1st page Chapter end line

— — — — — — — 1st page Chapter end line

LAST TEXT LINE

214

PAGE LINE

1 inch

JAB/80

2 inch CHAPTER VII Line

# H AND E-PLANE BACKSCATTERING FROM A TRIANGULAR PLATE

## A. INTRODUCTION

In this chapter, we analyze the backscattering in the principal planes of triangular plates. The incentive for this part of the study is the previous lack of theoretical values that agree with measured results [31], [43] for an incident y polarized wave (see Figure 153). Our original solution at tip on incidence agreed reasonably well with the measured data as shall be seen later. However, when the angle $\theta$ increased from zero (in the x-z plane) for the H-plane case, the results deteriorated significantly for $\frac{a}{\lambda}$ small and $\alpha = 30^o$, also, when $\theta$ is close to $180^o$ for the E-plane case, the results were not in good agreement with the measured data. Since this topic was essentially suggested as a final step in this dissertation by a curious advisor, it has not been carried to completion (with his consent). It remains as a sign post to show that there is still significant research to be considered on this topic in the future.

Here again, the Equivalent Current method and the Edge Wave formulation are also used in our analysis. The plate geometry is defined in Figure 153, the plate is located in the y-z plane, and the pattern is taken in the x-z plane. The incident field is a linearly polarized homogeneous plane wave whose field is given by

1st page Chapter end line

1st page Chapter end line

1 inch

JAB/80
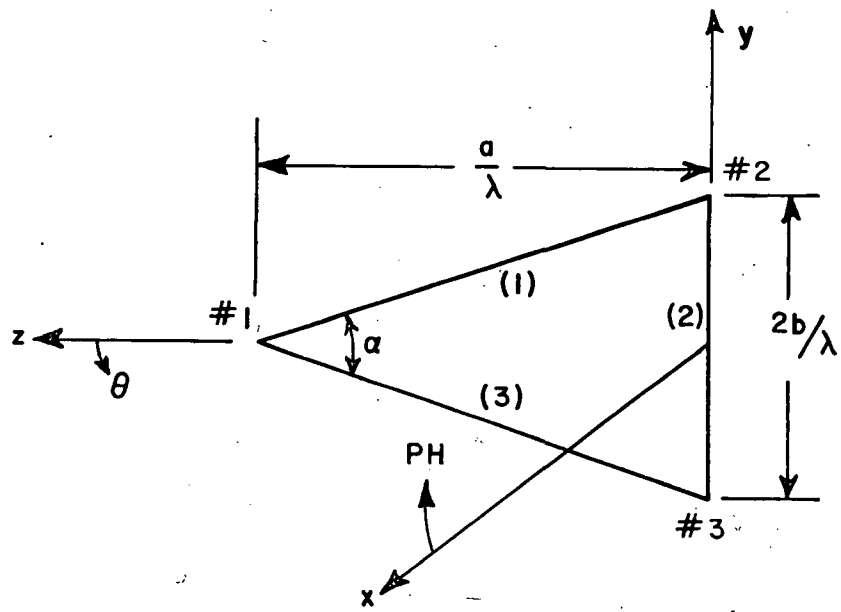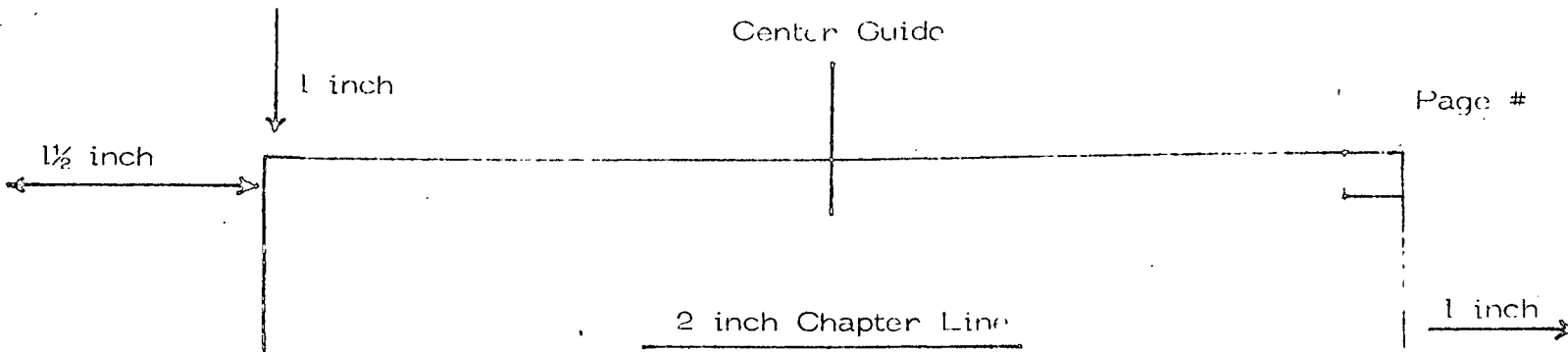
2 inch Chapter Line



Figure 153. Triangular plate geometry.

JAB/80

1 inch

1½ inch
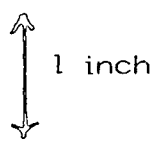
$$\overline{E}^i = \hat{y}\, E_y\, e^{jkg} \text{ , for H-plane case and,}$$

$$\overline{H}^i = \hat{y}\, H_y\, e^{jkg} \text{ , for E-plane case.}$$

(104)

1 inch

2 inch Chapter Line

where $g = x \sin\theta^i + z \cos\theta^i$.

The ray mechanisms to be used to compute the E-plane and the H-plane patterns are discussed. At this time either the set of rays or the Corner diffraction coefficients are not quite complete. As we shall see, something is amiss for small values of $\theta$ other than $\theta = 0$ in the H-plane. The H-plane results are presented first primarily because this represents a region where more work is necessary. The E-plane results, while not complete, are such that straight forward applications of existing techniques should eliminate deviations from measured data.

THESIS / DISSERTATION
Typing Guide Paper

B.   ANALYSIS

The E-plane pattern for the triangular plate is analyzed, using the EC method technique discussed in Chapters IV and V, to compute the contributions of single, double and triple edge diffraction to the RCS pattern. Here again, the shadowing effect associated with multiple edge diffraction mechanisms is also present in this problem and is handled by the same technique discussed in Appendix A. The equivalent current corresponding to the first order edge diffraction is given by Equation (60) and that corresponding to the second and third order edge diffractions are respectively given by Equations (77, 78). Figure 154 shows the single, double and triple edge diffraction ray mechanisms associated with the triangular plate. Table 4 lists the different edge diffractions that have been included in our solution for E-plane RCS pattern. Note that the doubly diffracted rays 1 - 3 and 3 - 1, also the triple diffracted ray 1 - 3 - 1, 1 - 3 - 2, 3 - 1 - 2 and 3 - 1 - 3, were not included. Their contributions were found to be insignificant.

1st page Chapter end line
1st page Chapter end line

LAST TEXT LINE

Center Guide

1 inch

JAB/80
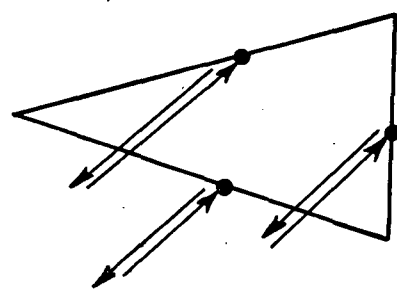
1 inch

1½ inch

1 inch

**(a) SINGLE EDGE DIFFRACTION**
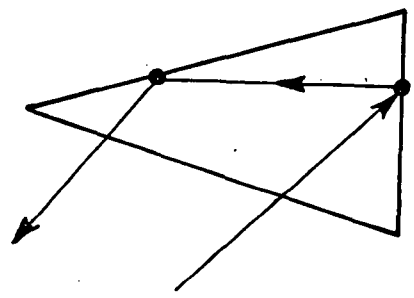
**(b) DOUBLE EDGE DIFFRACTION**
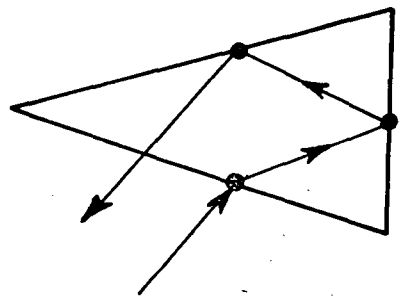
**(C) TRIPLE EDGE DIFFRACTION**

1st page Chapter end line

Figure 154.   Edge diffraction mechanisms for triangular plate problem.

1st page Chapter end line

LAST TEXT LINE

Center Guide

1 inch

JAB/80

**TABLE 4**

**SINGLE, DOUBLE AND TRIPLE EDGE DIFFRACTION TERMS INCLUDED
IN E-PLANE RCS PATTERN ANALYSIS FOR TRIANGULAR PLATE PROBLEMS**

| SINGLE | DOUBLE | TRIPLE |
|--------|--------|--------|
| Edge # | Edge #-to-Edge # | Edge #-to-Edge #-to-Edge # |
| 1 | 1 - 2 | 1 - 2 - 1 |
|   | 2 - 1 | 1 - 2 - 3 |
| 2 | 2 - 3 | 2 - 3 - 1 |
|   | 3 - 2 | 2 - 1 - 3 |
| 3 |   | 3 - 2 - 3 |
|   |   | 3 - 2 - 1 |

The H-plane RCS pattern is also studied by computing the contri-
butions of edge diffraction using the EC method and the edge wave mech-
anism. In this case, namely H-plane pattern, only the first and third
order edge diffraction are included in the solution. The second order
edge diffraction terms were not included in our solution because of
the symmetry of the problem, where, the doubly diffracted rays between
edge 1 and 2 are canceled by those rays diffracted between edge 3 and
2, while the rays diffracted between edge 1 and 3 had insignificant
contribution. The steps involved in this analysis are given in the
following section. Table 5 lists the different edge diffractions that
have been included in our solution for H-plane RCS pattern.

The incident field on edges 1 and 3 can be written in terms of
the edge coordinate system component as

1 inch

JAB/80

1 inch

1½ inch ←

1 inch →

| TABLE 5 |||||
| SINGLE AND TRIPLE-EDGE DIFFRACTION TERMS INCLUDED IN H-PLANE RCS PATTERN ANALYSIS FOR TRIANGULAR PLATE PROBLEMS |||||
| SINGLE | TRIPLE ||||
| Edge # | Edge # | - | Edge # | - | Edge # |
| 1 | 1 | - | 2 | - | 1 |
| 2 | 1 | - | 2 | - | 3 |
| 3 | 3 | - | 2 | - | 3 |
|   | 3 | - | 2 | - | 1 |

$$\overline{E}^i_{(1)} = E^i_{\phi'(1)} \; \hat{\phi}'_{(1)} + E^i_{\beta'(1)} \; \hat{\beta}'_{(1)} \tag{105}$$

and

$$\overline{E}^i_{(3)} = E^i_{\phi'(3)} \; \hat{\phi}'_{(3)} + E^i_{\beta'(3)} \; \hat{\beta}'_{(3)} \tag{106}$$

where $\hat{\phi}'$, $\hat{\beta}'$ are the unit vectors in the edge fixed coordinate frame.

When $\theta = 0^o$ or $90^o$, Equation (105) reduces to

$$\overline{E}^i_{(1)}(\theta=0^o) = E^i_{\beta'(1)} \; \hat{\beta}'_{(1)} \tag{107}$$

JAB/80

1½ in:

and

$$\bar{E}^i_{(1)}(\theta=90^o) = E^i_{\phi'(1)} \hat{\phi}'_{(1)} + E^i_{\beta'_{(1)}} \hat{\beta}'_{(1)} \quad . \qquad (108)$$

ε inch

Equation (106) gives similar results for $\theta=0^o$ and $90^o$. The $\phi$ component of the incident field associated with edges 1 and 3 is the one that gives rise to all higher order edge interactions involving the plate edges which will contribute to both the principal polarization and the cross polarization RCS patterns.

The edge wave mechanisms, namely double and triple corner diffractions discussed in Chapter VI, are also included in our solution.

1.    Edge Wave Double Corner Interaction Mechanism

This mechanism is shown in Figure 155, where the field diffracted from $C_1$ is then diffracted from corners $C_2$ and $C_3$ on edges 1 and 3, respectively.  Note that the edge wave field associated with edge 1 and propagating on the surface of the plate is oppositely polarized to that associated with edge 3.  Figure 156 shows the effect of edge 2 on the edge wave field incident on $C_2$.  The field diffracted from edge 2 will appear to be coming from an image like source located at 0'.  This affects the incident field on $C_2$ by introducing a reflection coefficient to account for the energy reflected by edge 2.

In Figure 157, the double corner diffraction case is shown for the interaction between corners $C_1$ and $C_2$.  Again, one has to consider the different combinations of incident and diffracted fields, i.e., $\beta'\beta$, $\beta'\phi$, $\phi'\beta$, and $\phi'\phi$, where the first letter indicates the polarization of the incident field and the second the polarization of the diffracted field.

1st page Chapter end line

1st page Chapter end line

LAST TEXT LINE

JAB/80

1 inch

1½ inch

2 inch Chapter Line

1 inch



#2

(1)

$s_2$

#1

(2)

(3)

#3

$s_3$
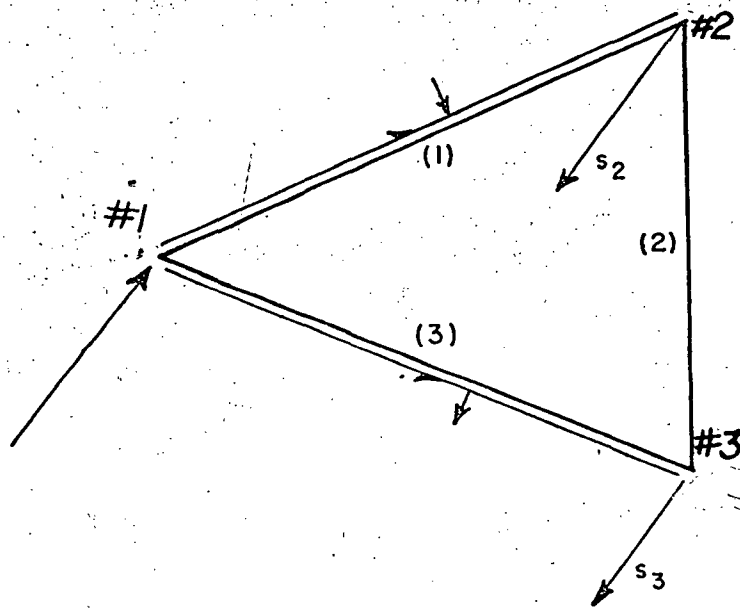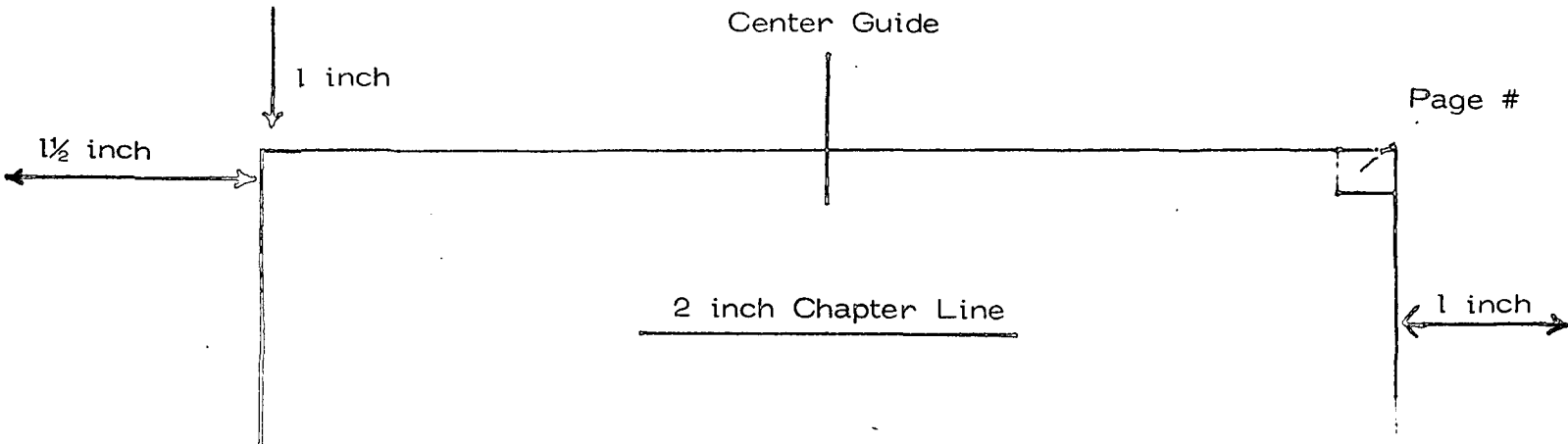
Figure 155.    Edge wave double corner diffraction mechanism for a triangular plate. Chapter end line

— — — — — — — — ➔  1st page Chapter end line

LAST TEXT LINE

PAGE LINE

1 inch

JAB/80

1 inch

1½ inch

1 inch

(1)

(2)

(3)

O'
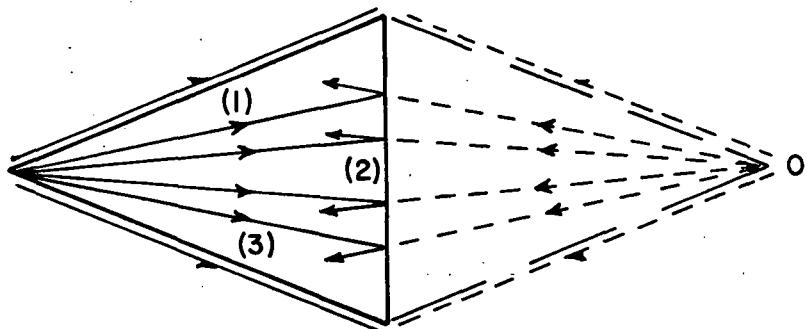
THESIS / DISSERTATION
Typing Guide Paper

Figure 156. Effect of edge #2 on edge wave fields.

#2

$\ell$

$\beta_1$

(1) ⊗

$s_2$

#1

$\alpha$

(2)

$\beta_1$

(3)

$\gamma$

#3
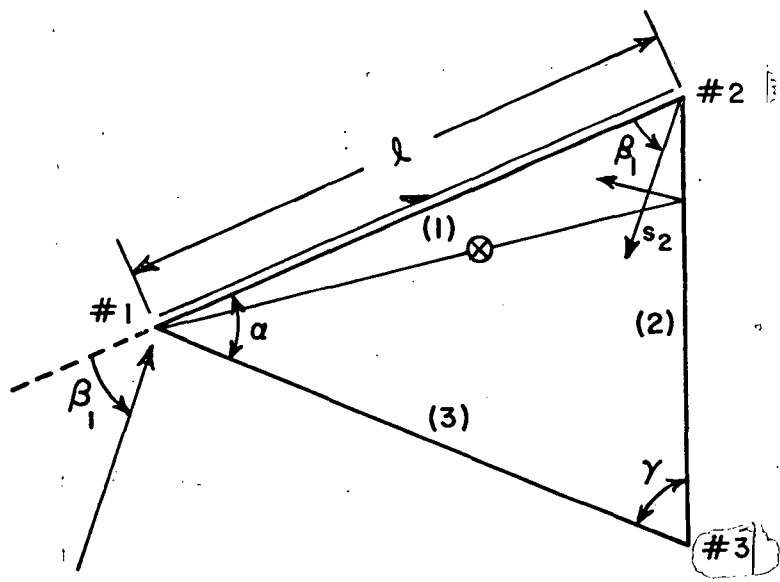
Figure 157. Edge wave field due to interaction $C_1$ $C_2$
1st page Chapter end line

1 inch

JAB/80

1 inch

1½ inch

Let us consider first the case when both the incident and diffracted fields are polarized in the $\beta$ direction, i.e., ($\beta'\beta$ case). The incident field on $C_2$ is given by

2 inch Chapter Line

$$E^d_{(2)} = E^i_{\beta'(1)} \ (C_1) \ D^{(ew)}_s \ (\ell, \ \phi'_1, \ \frac{\pi}{2}, \ \beta_1) \ R \ \frac{e^{-jk\ell}}{\sqrt{\ell}} \ , \qquad (109)$$

where R is the reflection coefficient due to edge 2 and is given by

THESIS / DISSERTATION
Typing Guide Paper

$$R = \frac{e^{-j\frac{\pi}{4}}}{\sqrt{2\pi k} \ \sin \gamma} \ .$$

Because of the limitation of the edge wave formulation as is discussed in Appendix C, one had to assume that the field incident on $C_2$ is incident along the extention of edge 1 rather than at an angle $\alpha$ as is dictated by the reflection process due to edge 2. This is shown in Figure 158.

The diffracted field from $C_2$ to the radar is then given by

$$E^d_{\beta(1)} = E^d_{(2)} \ D^{(ew)}_s \ (\ell, \ \frac{\pi}{2}, \ \phi_1, \ \beta_1) \sqrt{\ell} \ \frac{e^{-jks_2}}{s_2} \ . \qquad (110)$$

1st page Chapter end line

Substituting Equation (109) into (110), we get page Chapter end line

LAST TEXT LINE

1 inch

JAB/80
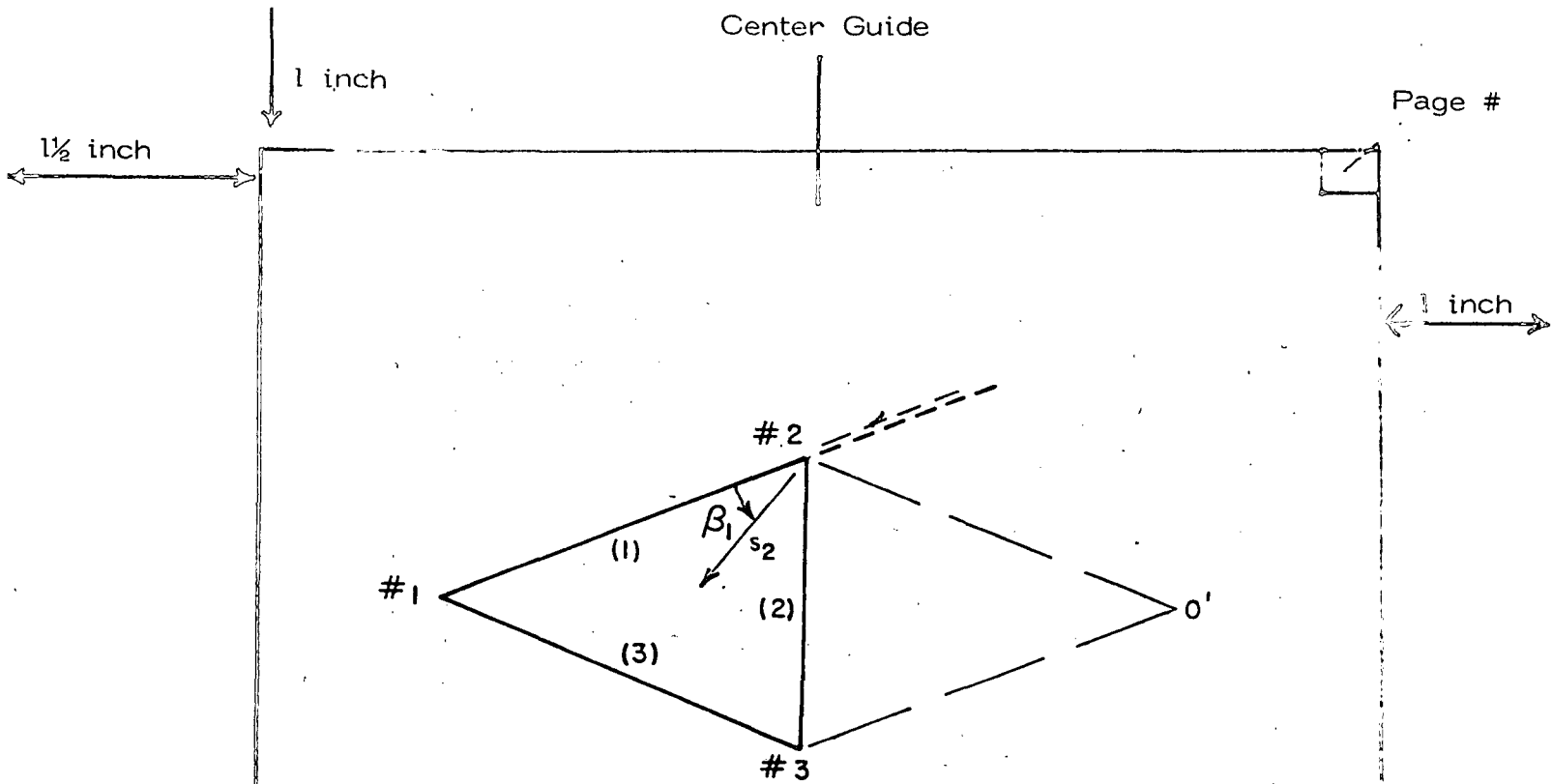
Figure 158.     Modification of incident field diffraction on $C_2$.

$$E^d_{\beta(1)} = E^i_{\beta'(1)}\ (C_1)\ D^{(ew)}_s\ (\ell,\phi'_1,\tfrac{\pi}{2},\beta_1)\ R\ D^{(ew)}_s\ (\ell,\tfrac{\pi}{2},\phi_1,\beta_1)$$

$$e^{-jk\ell}\ \frac{e^{-jks_2}}{s_2}\ .\tag{111}$$

There is another term due to diffraction from $C_2$ to $C_1$, i.e., (Interaction $C_2$-$C_1$), the two terms are equal and both are given by Equation (111), so the total diffracted field for the $\beta'\beta$ interaction on edge 1 is given by

1st page Chapter end line

— — — — — — — → 1st page Chapter end line

LAST TEXT LINE

PAGE LINE

225

1 inch

1 inch

1½ inch

1 inch

$$E^d_{\beta(1)} = 2E^i_{\beta'(1)} (C_1) D^{(ew)}_s (\ell, \phi'_1, \frac{\pi}{2}, \beta_1) R D^{(ew)}_s (\ell, \frac{\pi}{2}, \phi_1, \beta_1)$$

2 inch Chapter Line

$$e^{-jk\ell} \frac{e^{-jks_2}}{s_2} . \tag{112}$$

Note that for backscatter $\phi_1 = \phi'_1$ and the cross-polarization components, i.e., $\beta'\phi$ and $\phi'\beta$, are equivalent. Following the same procedure, the fields due to the $\beta'\phi$ and $\phi'\beta$ combined together are given by

THESIS / DISSERTATION
Typing Guide Paper

$$E^d_{\beta(1)} = -4E^i_{\phi'(1)} (C_1) D^{(ew)}_h (\ell, \phi'_1, 0, \beta_1) R D^{(ew)}_s (\ell, \frac{\pi}{2}, \phi_1, \beta_1)$$

$$e^{-jk\ell} \frac{e^{-jks_2}}{s_2} , \tag{113}$$

and that for the $\phi'\phi$ component is given by

$$E^d_{\phi(1)} = 2E^i_{\phi'(1)} (C_1) D^{(ew)}_h (\ell, \phi'_1, 0, \beta_1) R D^{(ew)}_h (\ell, 0, \phi_1, \beta_1)$$

$$e^{-jk\ell} \frac{e^{-jks_2}}{s_2} . \tag{114}$$

1st page Chapter end line

1st page Chapter end line

Note that there are similar terms due to interactions between corners $C_1$ and $C_3$. In the principal plane and because of the symmetry of the problem

Center Guide

1 inch

JAB/80

these terms are equivalent to those due to interactions between corners $C_1$ and $C_2$. Therefore, their contribution is given by Equations (112-114). Table 6 shows the different edge wave double corner diffractions that have been included in our solution. Note that double diffraction $C_2$ to $C_3$ and back are not included, primarily because they are currently beyond the state of the art.

2. <u>Edge Wave Triple Corner Interaction Mechanism</u>

This mechanism is shown in Figure 159, and in Figure 160 we show the term associated with edge 1 where the doubly diffracted field from $C_2$ is now incident on $C_1$ and is diffracted back to the radar. The value of this field at $C_1$ for the $\beta'\beta$ term is given by

$$E^d_{(1)} = E^i_{\beta'\ (1)}\ (C_1)\ D^{(ew)}_s\ (\ell, \phi'_1, \frac{\pi}{2}, \beta_1)\ R\ \frac{e^{-j2k\ell}}{\sqrt{\ell}} \tag{115}$$

| | TABLE 6 |
|---|---|

EDGEWAVE DOUBLE CORNER DIFFRACTION TERMS FOR TRIANGULAR
PLATE PROBLEM

| EDGE # | DOUBLY DIFFRACTED TERMS |
|---|---|
| | Corner #  -  Corner # |
| 1 | 1-2    and    2-1 |
| 3 | 1-3    and    3-1 |

227

JAB/80
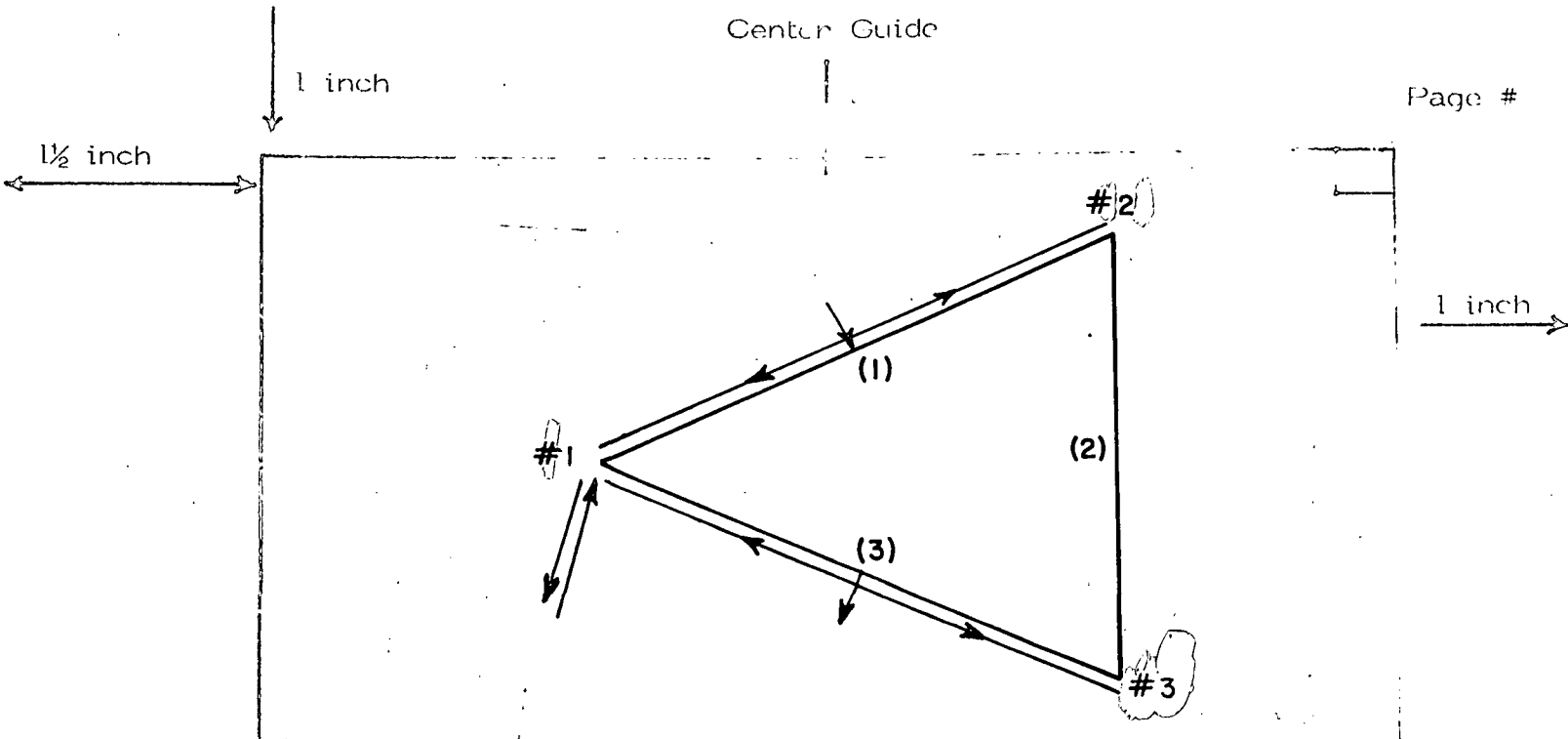
Figure 159. Edge wave triple corner diffraction mechanism for triangular plate.
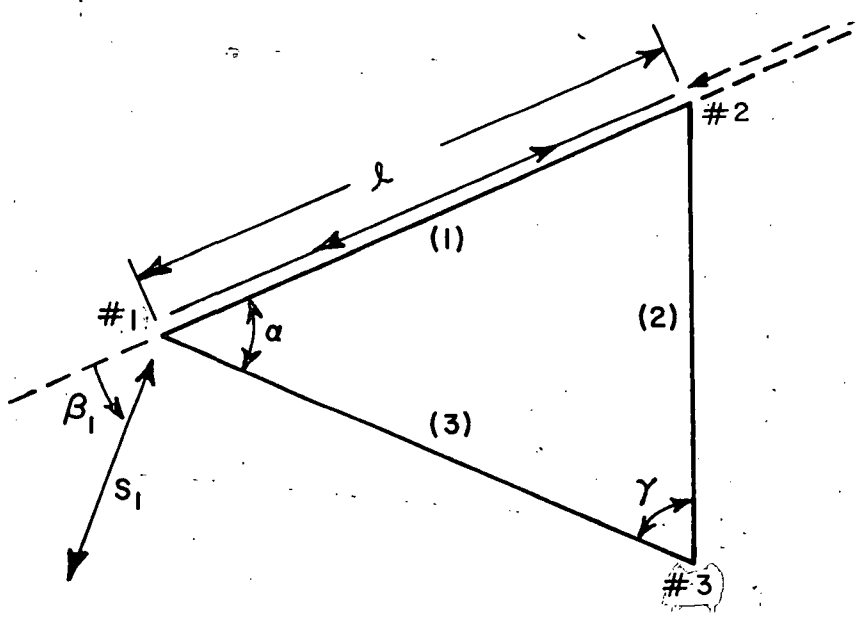
Figure 160. Edge wave field due to interaction $C_1 - C_2 - C_1$

1st page Chapter end line

1st page Chapter end line

LAST TEXT LINE

228

Center Guide
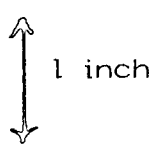
1 inch

where again R accounts for the effect of edge 2 on the field incident on $C_2$ and is given by

$$R = \frac{e^{-j\frac{\pi}{4}}}{\sqrt{2\pi k \sin \gamma}} \; .$$

The diffracted field from $C_1$ to the receiver is then given by

$$E^d_{\beta(1)} = -E^d_{(1)} \; D^{(ew)}_s (\ell, \tfrac{\pi}{2}, \phi_1, \beta_1) \sqrt{\ell} \; \frac{e^{-jks_1}}{s_1} \qquad (116)$$

where the negative sign is introduced since the diffracted edge wave field is polarized in opposite direction to the $\beta$ polarization.

Substituting Equation (115) into (116), one gets

$$E^d_{\beta(1)} = -E^i_{\beta'(1)} \; (C_1) \; D^{(ew)}_s (\ell, \phi'_1, \tfrac{\pi}{2}, \beta_1) \; R \; D^{(ew)}_s (\ell, \tfrac{\pi}{2}, \phi_1, \beta_1)$$

$$e^{-j2k\ell} \; \frac{e^{-jks_1}}{s_1} \; . \qquad (117)$$

As was indicated in Chapter VI, there are two possible combinations of $\beta$-polarized triple diffraction terms. These are due to the double diffraction terms, namely $\beta'\beta$ and $\phi'\beta$. These two possible combinations

229

1½ inch

are $\beta'\phi'\beta$ and $\beta'\beta'\beta$. Therefore, the total $\beta$-polarized triple diffracted edge wave field associated with edge 1 is given by

$$E^d_{\beta(1)} = -2E^i_{\beta'(1)} \; (C_1) \; D^{(ew)}_s (\ell, \phi'_1, \frac{\pi}{2}, \beta_1) \; R \; D^{(ew)}_s (\ell, \frac{\pi}{2}, \phi_1, \beta_1)$$

$$e^{-j2k\ell} \; \frac{e^{-jks_1}}{s_1} \; . \tag{118}$$

THESIS / DISSERTATION

The combined cross polarized triple corner diffracted term is given by

$$E^d_{\beta(1)} = 4E^i_{\phi'(1)} \; (C_1) \; D^{(ew)}_h (\ell, \phi'_1, 0, \beta_1) \; R \; D^{(ew)}_s (\ell, \frac{\pi}{2}, \phi_1, \beta_1)$$

$$e^{-j2k\ell} \; \frac{e^{-jks_1}}{s_1} \tag{119}$$

and that for the $\phi$-polarized term is

$$E^d_{\phi(1)} = 2E^i_{\phi'(1)} \; (C_1) \; D^{(ew)}_h (\ell, \phi'_1, 0, \beta_1) \; R \; D^{(ew)}_h (\ell, 0, \phi_1, \beta_1)$$

$$e^{-j2k\ell} \; \frac{e^{-jks_1}}{s_1} \; . \tag{120}$$

1st page Chapter end line

1 inch

JAB/80
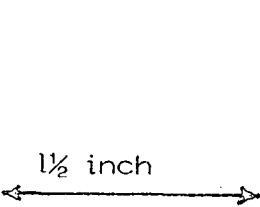
In a similar way, the triple corner diffracted field associated with edge 3, i.e., interaction $C_1$-$C_3$-$C_1$ can be obtained. In the principal plane and because of the problem symmetry, the field due to this term is equivalent to that associated with edge 1 and is given by Equations (118-120). Table 7 shows the different triply diffracted terms that have been included in our solution.

## C. DISCUSSION

The above analysis is used to compute the H-plane RCS pattern for different plate sizes. The calculated results are compared to measured data provided by Mr. Chu [35]. In Figures 161-163, the results for three different size plates ($\frac{a}{\lambda}$ = 2, 3 and 9) are shown. The three plates have tip angle $\alpha = 30^0$. Some deviation between the calculated and measured results is observed especially in the region $0^0 < \theta < 45^0$. This indicates that the solution is not valid in this region for $\alpha = 30^0$ and $\frac{a}{\lambda} < 3$ except for $\theta$ near zero. It also suggests that a more accurate corner diffraction coefficient is needed, and probably, one has to

TABLE 7

EDGE WAVE TRIPLE CORNER DIFFRACTION TERMS FOR TRIANGULAR
PLATE PROBLEM

| Edge # | TRIPLE DIFFRACTED TERMS | | | | |
|--------|----------|---|----------|---|----------|
|        | Corner # | - | Corner # | - | Corner # |
| 1      | 1        | - | 2        | - | 1        |
| 3      | 1        | - | 3        | - | 1        |

2 inch Chapter Line



CALCULATED
MEASURED [35]

$\sigma / \lambda^2$ (dB)

PH = 0

$\alpha$ = 30°

$\frac{a}{\lambda}$ = 2

NORM. TO 12.6 dB > $\lambda^2$

$\theta$
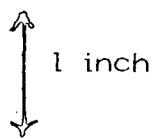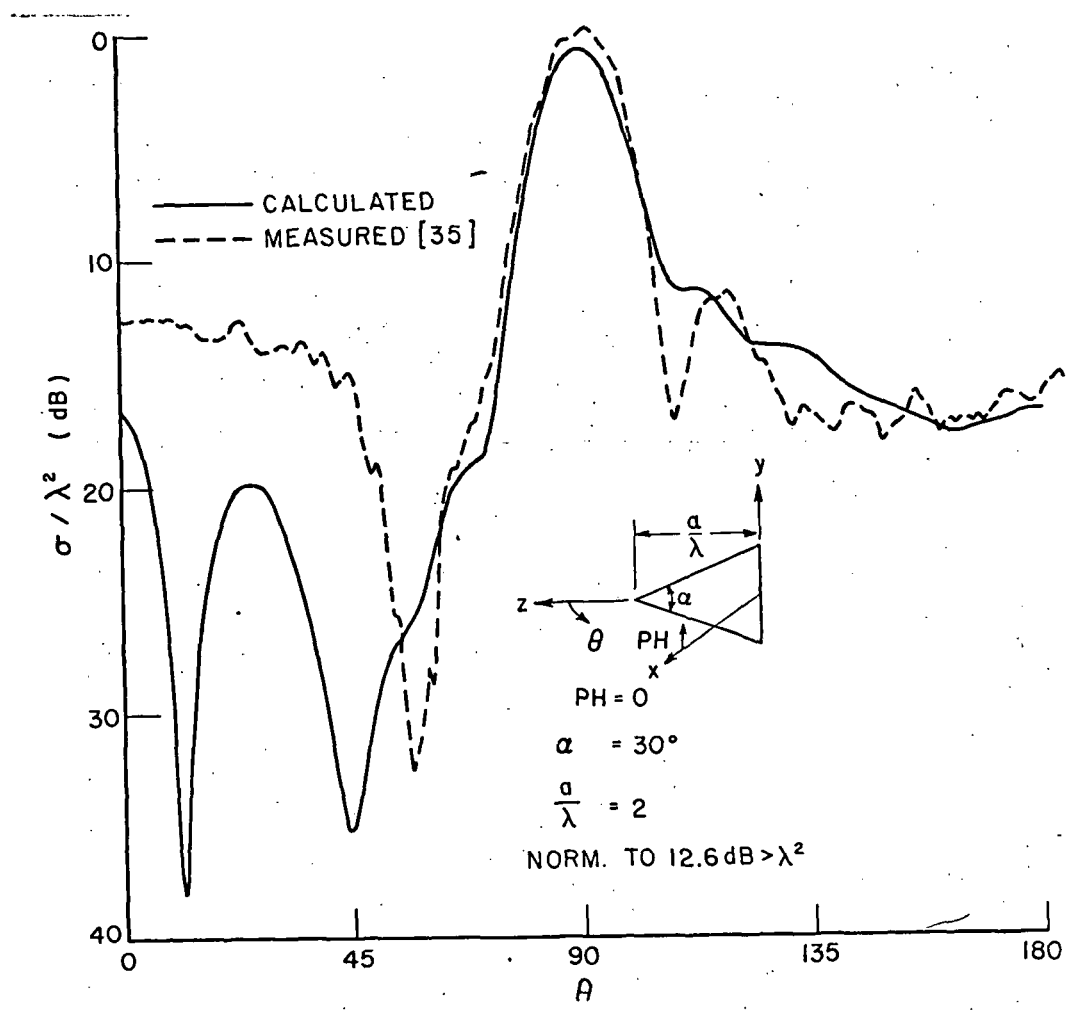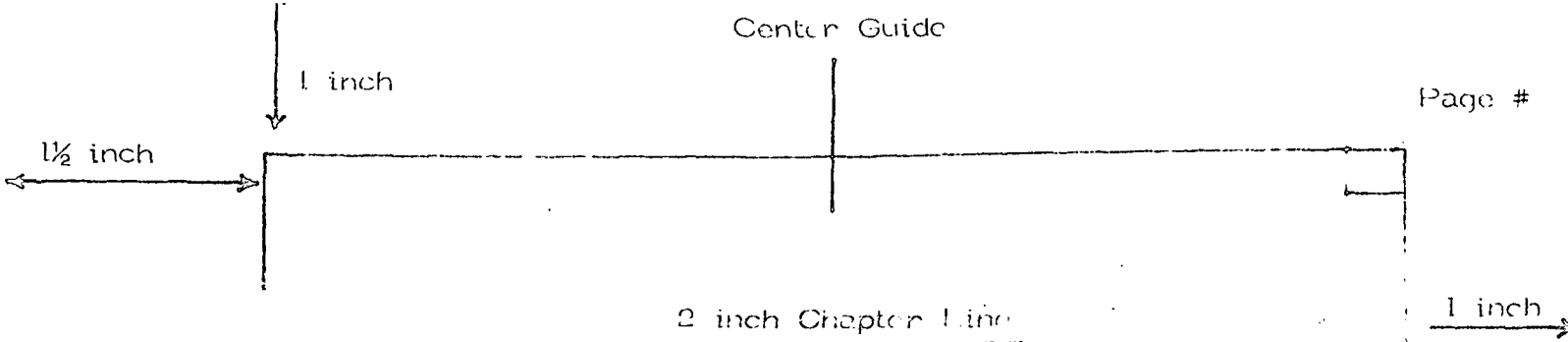
Figure 161. $E_{PH}$, PH = 0 RCS pattern for a triangular plate ($\alpha$ = 30°, $a/\lambda$ = 2).

JAB/80

1 inch →



PH = 0
$\alpha = 30°$
$\frac{a}{\lambda} = 3$
NORM. TO 18.7 dB $> \lambda^2$

—— CALCULATED
— — — MEASURED [35]
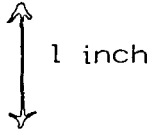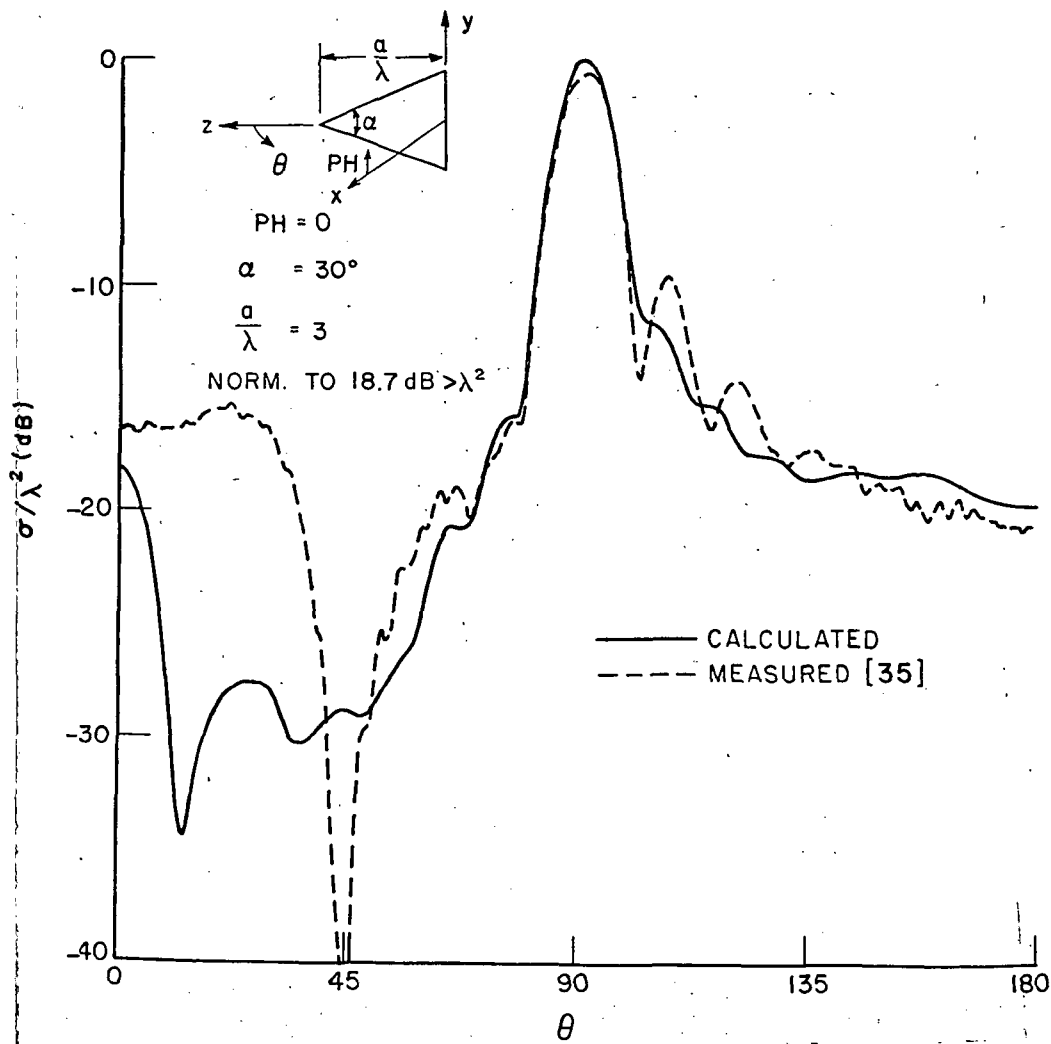
Figure 162. $E_{PH}$, PH = 0 RCS pattern for a triangular plate ($\alpha = 30°$, $\overline{a/\lambda = 3}$).
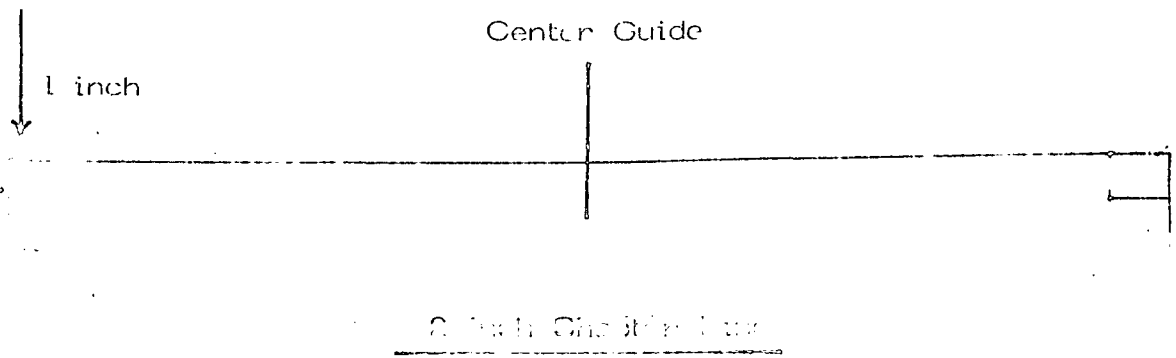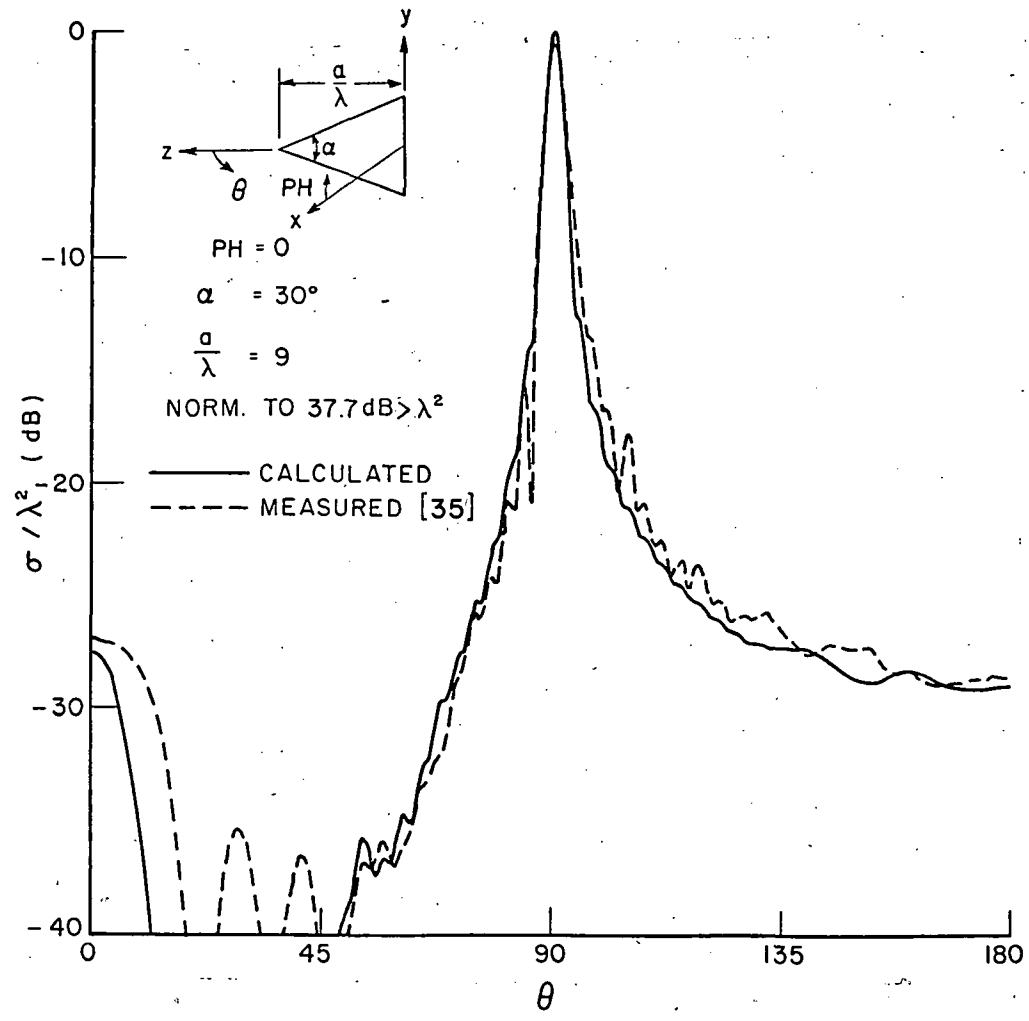
1st page Chapter end line

1 inch

Figure 163. $E_{PH}$, PH = 0 RCS pattern for a triangular plate ($\alpha$ = 30, a/$\lambda$ = 9).

JAB/80
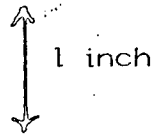
include more higher order diffraction mechanisms whose contributions become more significant as the plate size is decreased. Some of these higher order interactions that are still under investigation are shown in Figure 164. The individual contributions to the H-plane RCS pattern of single, triple edge diffraction and that due to edge wave double and triple corner diffraction are respectively shown in Figures 165-167 for $\alpha = 30^O$ and $\frac{a}{\lambda} = 2$, 3, and 9. The slope discontinuity observed near $\alpha = 30^O$ in Figure 166 is due to the effect of edge shadowing. Figure 168, illustrates the case when $\frac{\alpha}{2} < \beta_0 < \alpha$, where the double diffracted field from edge 2 illuminates both edges 1 and 3, as shown by the ray trajectories due to the incident rays 1 and 2. When $\beta_0 < \frac{\alpha}{2}$, the double diffracted field illuminates only edge 3 while edge 1 is shadowed. However, when $\beta_0 < \alpha$, the situation is reversed and edge 3 is shadowed while edge 1 is illuminated. The results for three plates with $\frac{a}{\lambda} = 4$ and $\alpha = 45^O$, $60^O$ and $90^O$ are shown in Figures 169-171 respectively. From these figures, one notices that it is the higher order interactions which involve edges 1 and 3, which are the ones most likely responsible for the deviation between the calculated and measured results. As $\alpha$ is increased from $45^O$ to $90^O$, edges 1 and 3 get further apart and an improvement between the two results is noticed, especially in the region $100^O < \theta < 180^O$. Observe that in Figure 171 the prediction of the general behavior of the pattern is quite good except in the region $0^O < \theta < 20^O$ where an error in measurement or the inaccuracy of the edge wave diffraction coefficient are probably the cause of the deviation between the two results. The individual contributions of single, triple edge diffraction mechanisms and that of edge wave double, triple corner diffraction are respectively shown in Figures 172-174 for $\frac{a}{\lambda} = 4$ and $\alpha = 45^O$, $60^O$, and $90^O$. The results for the RCS when the field is incident at edge on the tip side and $\alpha = 30^O$ compared to measured data obtained by Hey, et. al., [31] is shown in Figure 175. Observe that as $\frac{a}{\lambda}$ is increased, the agreement between the two results improves. Since for this case, namely edge on incidence, the edge wave mechanism is the only contributor to the RCS, the deviation between

1½ inch

1 inch
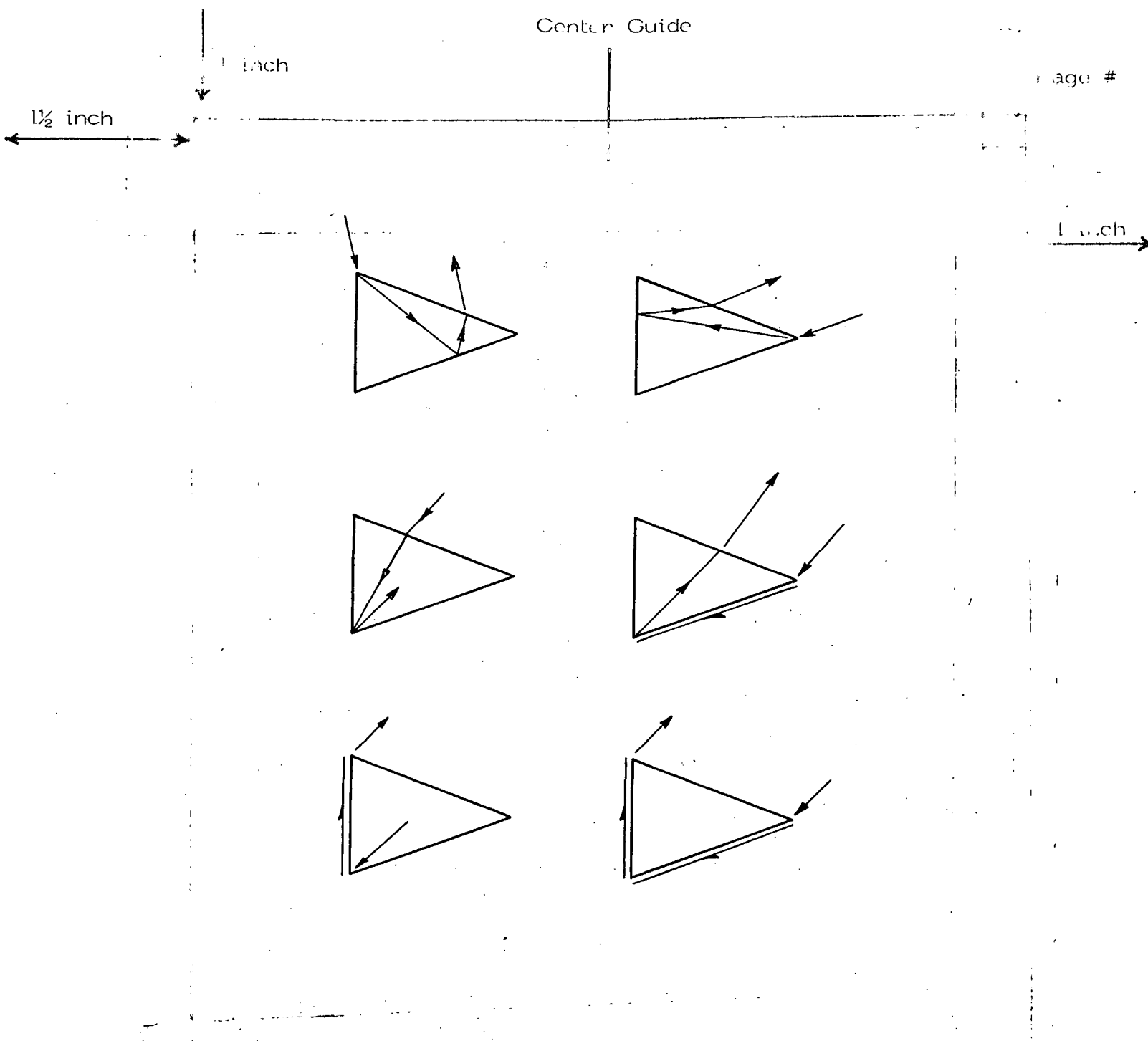
Figure 164. Possible higher order interactions for triangular plate problems.

JAB/80

1 inch

1½ inch

1 inch

$\frac{a}{\lambda} = 2$

$\alpha = 30°$

$\sigma/\lambda^2$ (dB)

$\theta$

(a)

$\frac{a}{\lambda}$

$\alpha$

PH

(b)

$\frac{a}{\lambda} = 3$

$\alpha = 30°$

$\sigma/\lambda^2$ (dB)

$\theta$

(c)

$\frac{a}{\lambda} = 9$

$\alpha = 30°$

$\sigma/\lambda^2$ (dB)

$\theta$
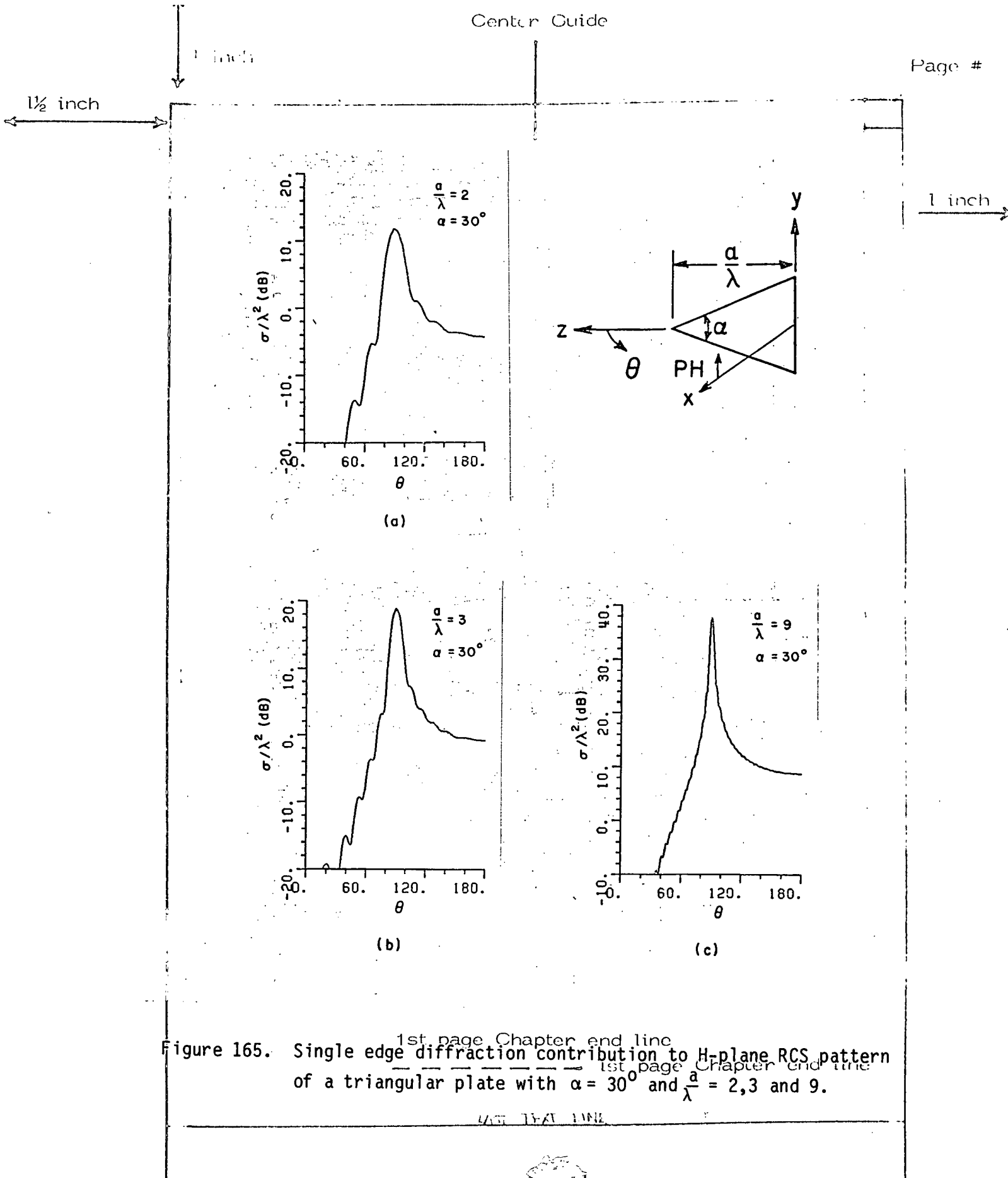
Figure 165.  Single edge diffraction contribution to H-plane RCS pattern of a triangular plate with $\alpha = 30°$ and $\frac{a}{\lambda} = 2, 3$ and 9.

1st page Chapter end line

1st page Chapter end line

LAST TEXT LINE

1 inch

JAB/80

1 inch

1½ inch

1 inch

$\frac{a}{\lambda} = 2$

$\alpha = 30°$

$\sigma/\lambda^2$ (dB)

20.

10.

0.

-10.

-20.

0.   30.   60.   90.

$\theta$

(a)

$\frac{a}{\lambda} = 3$

$\alpha = 30°$

$\sigma/\lambda^2$ (dB)

20.

10.

0.

-10.

-20.

0.   30.   60.   90.

$\theta$

(b)

$\frac{a}{\lambda} = 9$

$\alpha = 30°$

$\sigma/\lambda^2$ (dB)

20.

10.

0.

-10.

-20.

0.   30.   60.   90.

$\theta$

(c)

y

$\frac{a}{\lambda}$

z

$\alpha$

$\theta$

PH

x
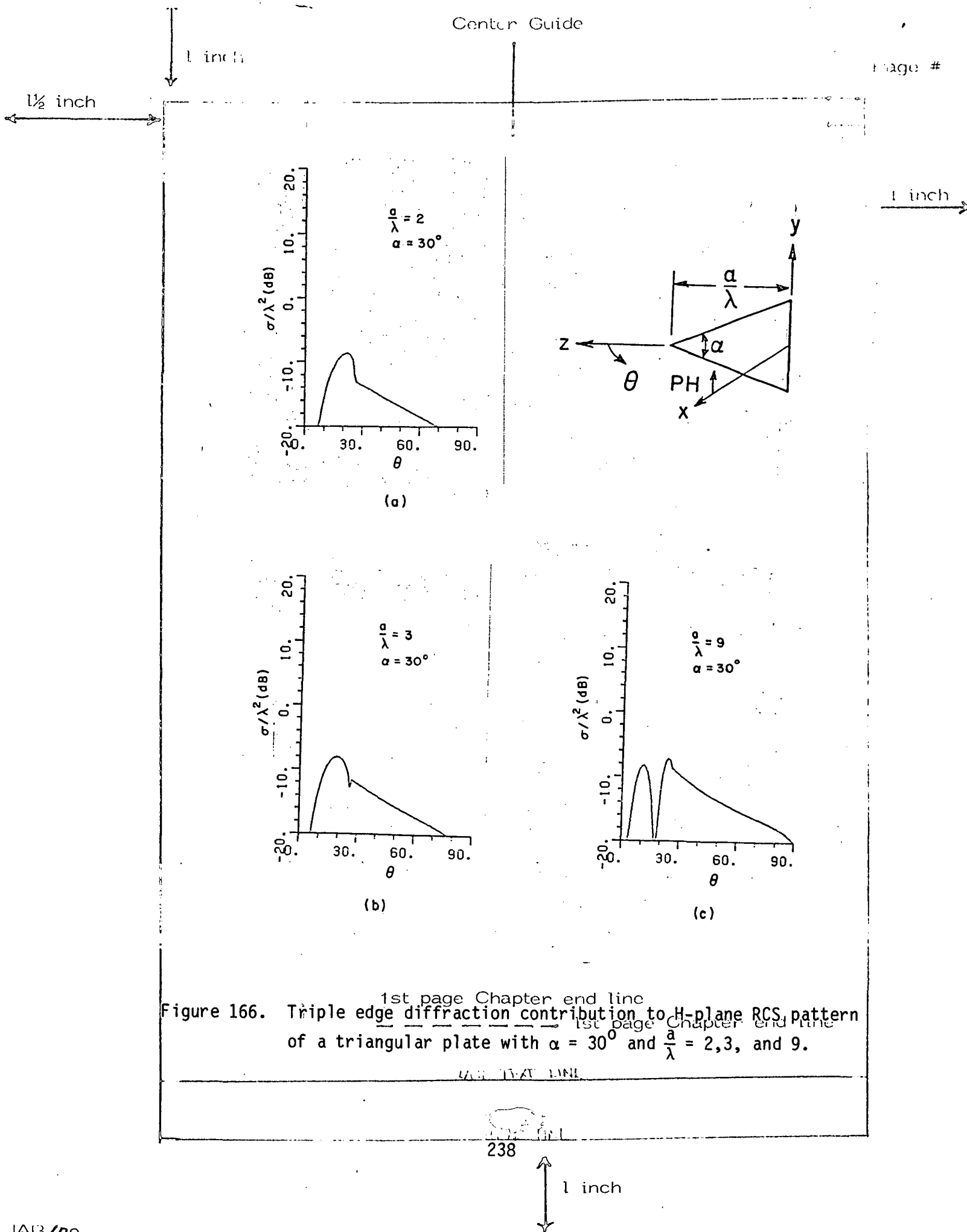
1st page Chapter end line

Figure 166.   Triple edge diffraction contribution to H-plane RCS pattern of a triangular plate with $\alpha = 30°$ and $\frac{a}{\lambda} = 2, 3,$ and 9.

1st page Chapter end line

LAST TEXT LINE

1 inch

JAB/80

Figure 167.   Total edge wave diffraction contribution to H-plane RCS pattern of a triangular plate with $\alpha = 30°$ and $\frac{a}{\lambda} = 2, 3,$ and 9.

239

JAB/80

1 inch

1½ inch

2 inch Chapter Line

1 inch



#2

(1)

#1  α

(2)

$\beta_0$

(3)

RAY 2

RAY 1

#3

Figure 168.   Shadowing effects due to triple edge diffraction term for triangular plate problem.

1st page Chapter end line

LAST TEXT LINE

1 inch

JAB/80

Figure 169. $E_{PH}$, PH = 0 RCS pattern for a triangular plate ($\alpha$ = 45°, a/$\lambda$ = 4).

JAB/80

1 inch

1½ inch

PH = 0

$\alpha = 60°$

$\dfrac{a}{\lambda} = 4$

NORM. TO 30.3 dB > $\lambda^2$

—— CALCULATED
- - - MEASURED [35]

$\theta$

$\sigma / \lambda^2$ (dB)
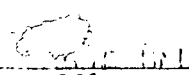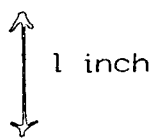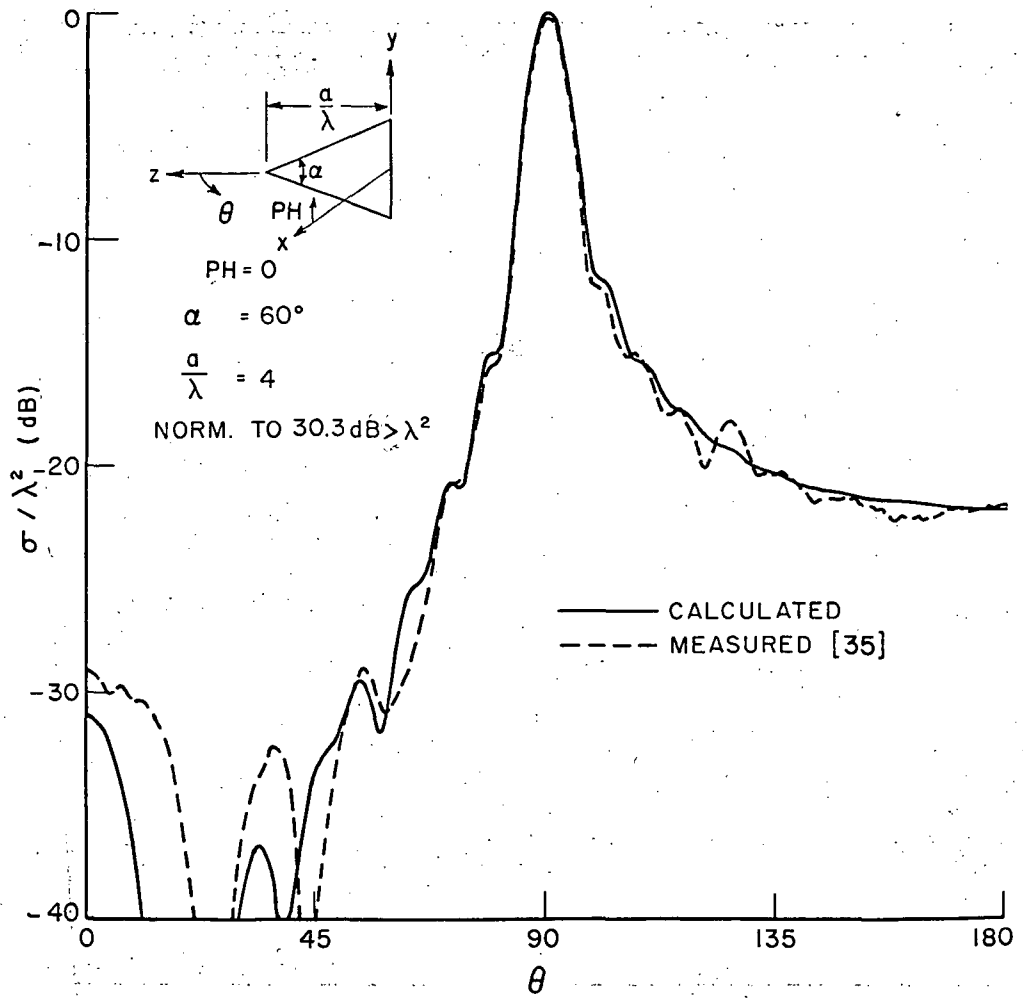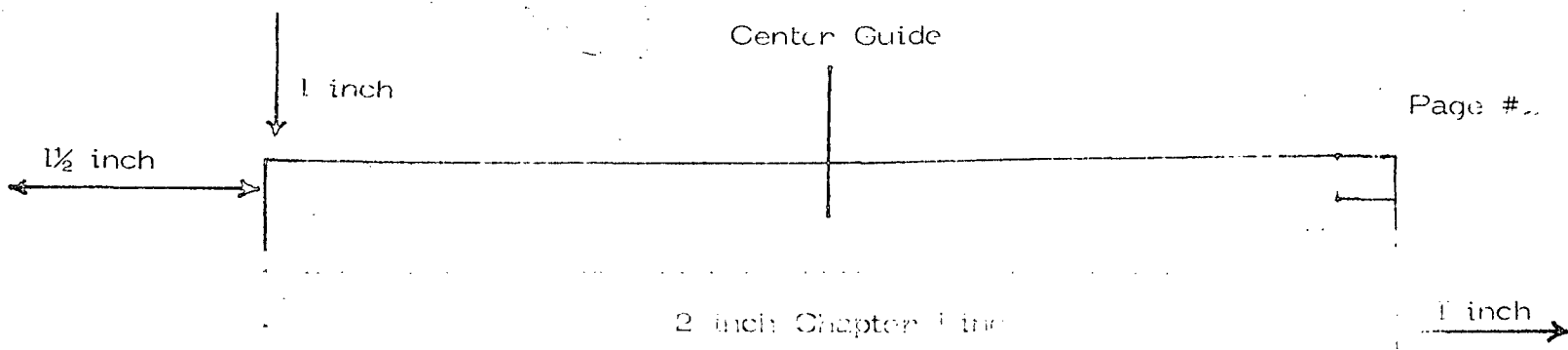
Figure 170. $E_{PH}$, PH = 0 RCS pattern for a triangular plate ($\alpha = 60°$, $a/\lambda = 4$).

JAB/80

1 inch

1½ inch

2 inch Chapter Line
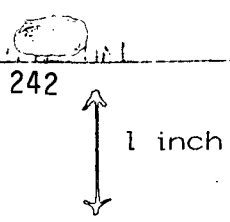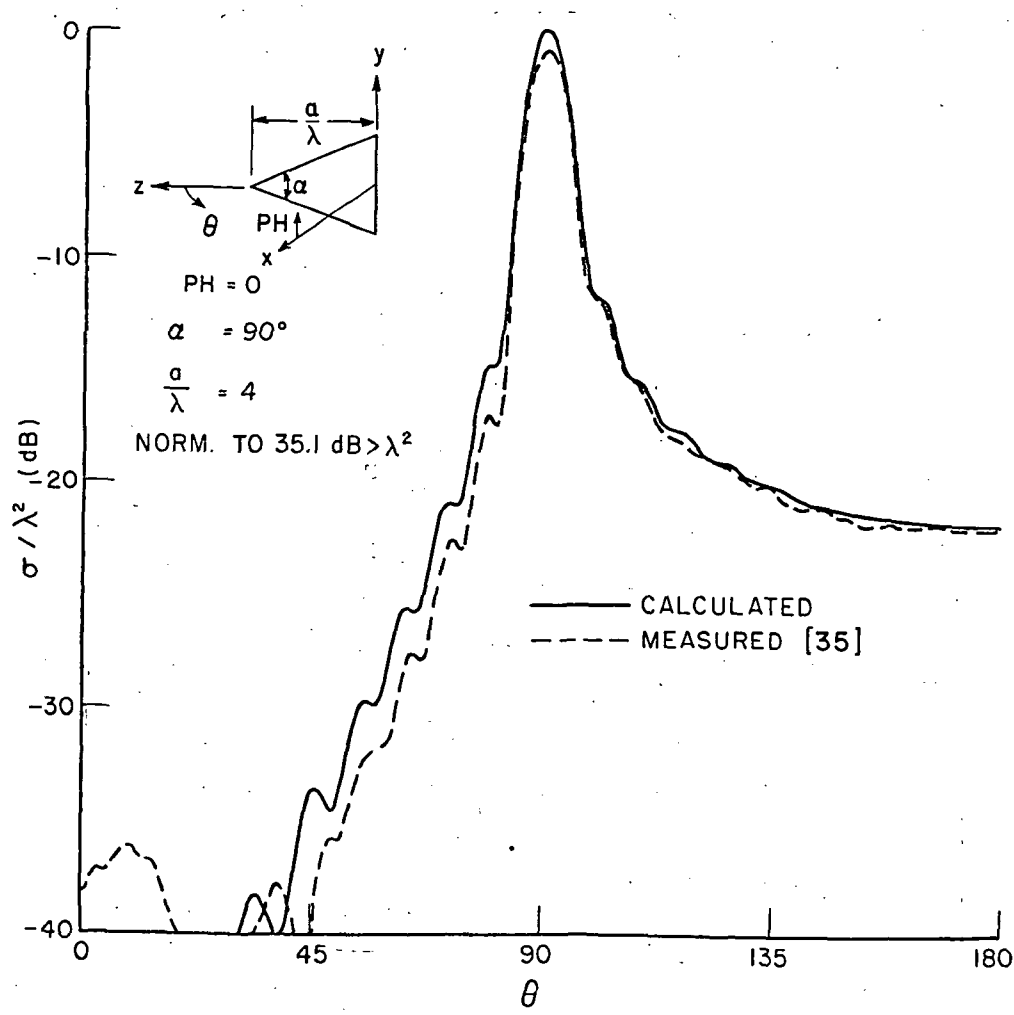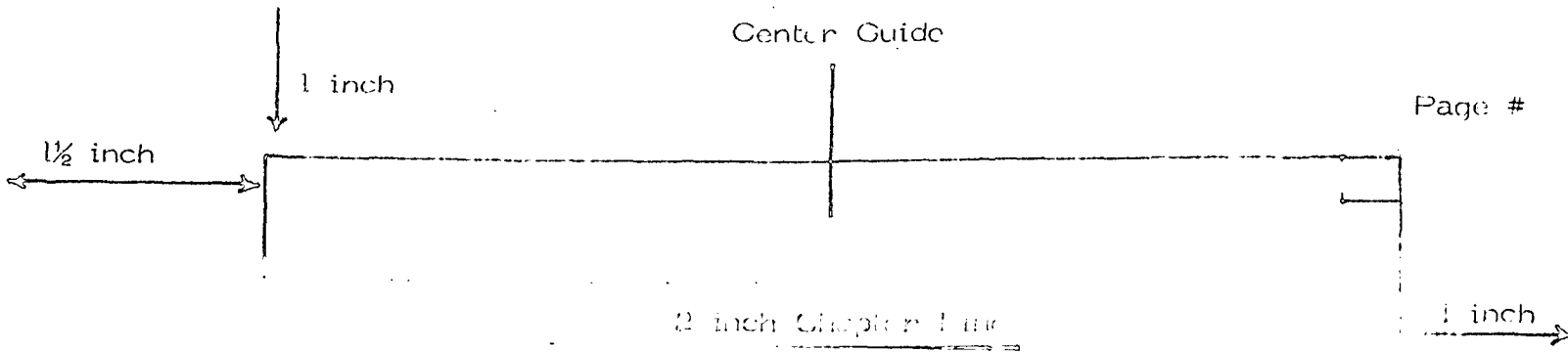
1 inch

Figure 171. $E_{PH}$, PH = 0 RCS pattern for a triangular plate ($\alpha$ = 90°, $a/\lambda$ = 4).

1 inch

JAB/80

Figure 172. Single edge diffraction contribution to H-plane RCS pattern of a triangular plate with a/λ = 4 and α = 45°, 60° and 90°.

JAB/80
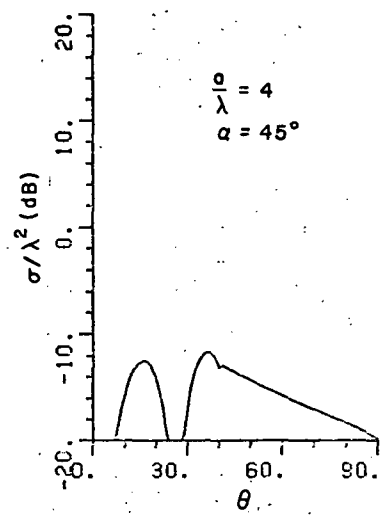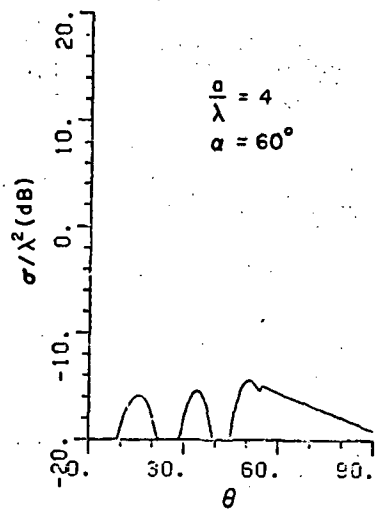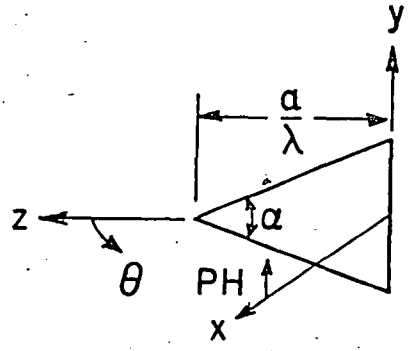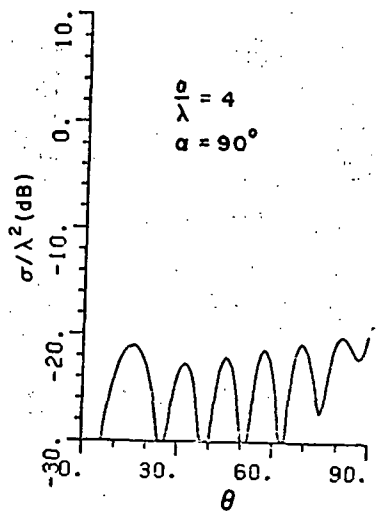
Figure 173. Triple edge diffraction contribution to H-plane RCS pattern of a triangular plate with a/λ = 4 and α = 45°, 60° and 90°.

$\frac{a}{\lambda} = 4$

$\alpha = 45°$

(a)

$\frac{a}{\lambda} = 4$

$\alpha = 60°$

(b)

$\frac{a}{\lambda} = 4$

$\alpha = 90°$

(c)

Figure 174. Total edge wave diffraction contribution to H-plane RCS pattern of a triangular plate with $a/\lambda = 4$ and $\alpha = 45°$, $60°$ and $90°$.

JAB/80
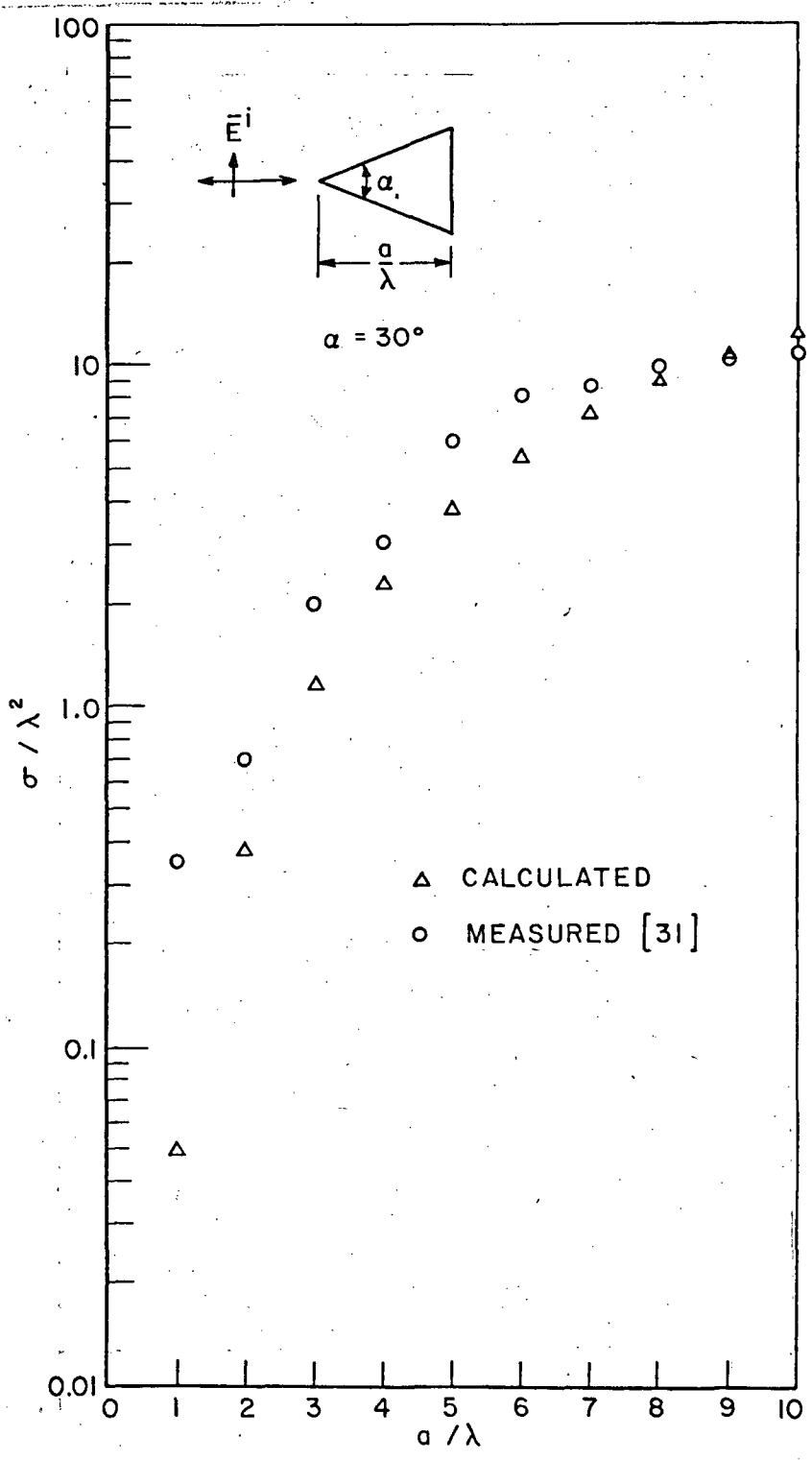
Figure 175.   Edge on RCS for a triangular plate as a function of its length ($\alpha$ = 30°).

1½ inch

1 inch

the two results is due to the inaccuracy of the edge wave diffraction coefficient. In Figures 176-178, the computed results for the E-plane RCS pattern compared to measured data [43] are shown for three triangular plates with $\alpha = 30^O$ and $\frac{a}{\lambda} = 2, 3, 9$. The solution includes the contributions of single, double, and triple edge diffraction. In Figures 176 and 177, one notices that the two results deviate in two regions, $0^O < \theta < 60^O$ and $120^O < \theta < 180^O$. This deviation indicates that there is another mechanism which is significant for these plate sizes especially in the region $120^O < \theta < 180^O$. Peters [44], showed that a traveling wave mode could be considered in treating the RCS of thin bodies in near edge on regions. Techniques developed in this dissertation could be applied to obtain a solution for the RCS in this region. And it is expected that good results would be obtainable. This, however, has not been done at this time. As the plate length $\frac{a}{\lambda}$ is increased from 2 to 9, an improvement between the two results is noticed in the region $0^O < \theta < 60^O$ as is shown in Figure 178. However, one should not rule out the effect of measurements errors. The contribution of single edge diffraction mechanism to the E-plane RCS pattern for these three plates is shown in Figure 179. Similar results for double and triple edge diffraction mechanisms are shown in Figures 180 and 181, respectively. Note that the higher order interactions have their significant contribution in the region $0^O < \theta < 90^O$. The E-plane RCS pattern for triangular plates with $\frac{a}{\lambda} = 4$ and $\alpha = 45^O$, $60^O$ and $90^O$, are shown in Figures 182-184. Good agreement between the two results is obtained except in the region $160^O < \theta < 180^O$, where the higher order diffractions have not been included as discussed earlier. This contribution, namely the edge wave, becomes weaker as $\alpha$ is increased. The contributions of single, double, and triple edge diffraction mechanisms to the E-plane RCS pattern of these plates are shown in Figures 185-187.

D. SUMMARY OF BACKSCATTERING FROM A TRIANGULAR PLATE

1st page Chapter end line

In this chapter, the H and E plane RCS patterns for a triangular plate were analyzed for a plane wave incidence.

1 inch

JAB/80

1 inch

1½ inch

2 inch Chapter Line

1 inch



$\frac{\sigma}{\lambda^2}$ (dB)

—— CALCULATED
— — MEASURED
NORM. TO 11.76 dB>$\lambda^2$
$\frac{a}{\lambda}$ = 2 ,  $\alpha$ = 30°

$\theta$
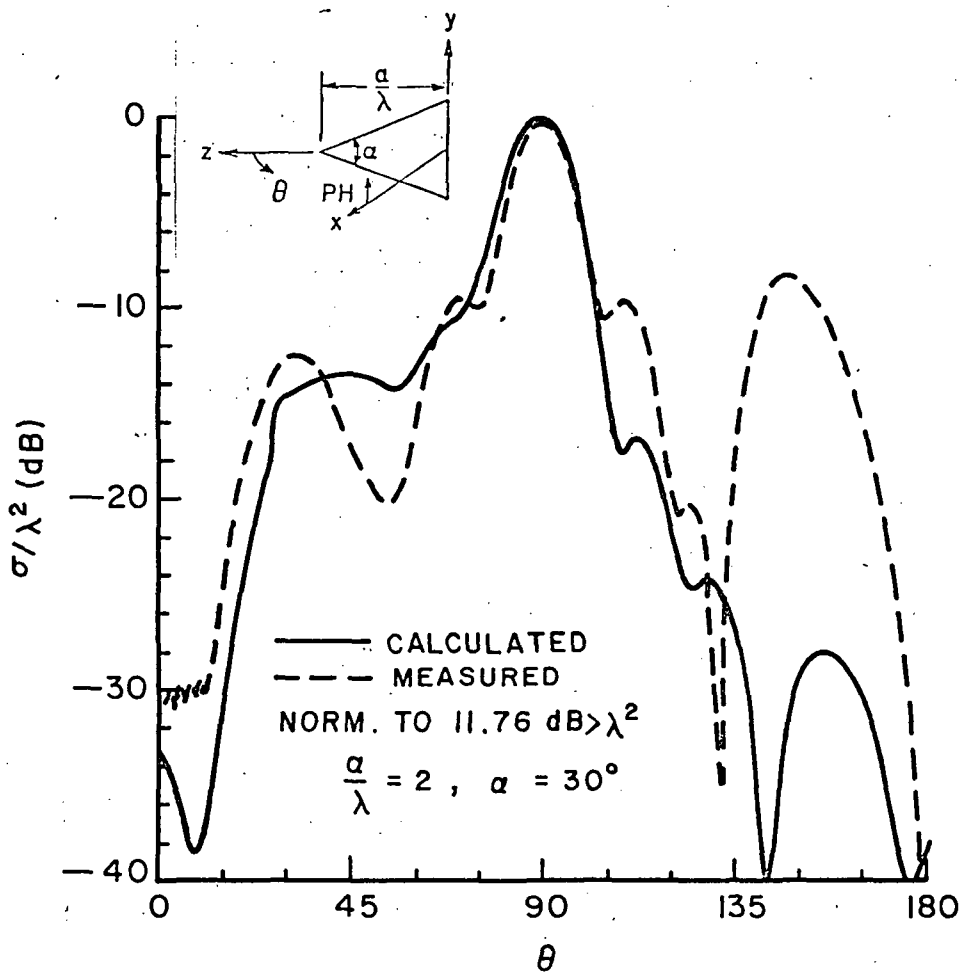
1st page Chapter end line

Figure 176.  $E_\theta$, PH=0 RCS pattern for a triangular plate ($\alpha_r$ = 30°
$\frac{a}{\lambda}$ = 2).  Only single, double and triple edge diffraction
are included.

1 inch

JAB/80

1 inch

1½ inch

2 inch Chapter Line

1 inch



1st page Chapter end line

Figure 177. $E_\theta$, PH = 0 RCS pattern for a triangular plate ($\alpha$ = 30°, $\frac{a}{\lambda}$ = 3). Only single, double and triple edge diffraction are included.

250

1 inch

1 inch

1½ inch

1 inch



CALCULATED
MEASURED
NORM. TO 36.67 dB>$\lambda^2$
$\frac{a}{\lambda} = 9$ , $\alpha = 30°$
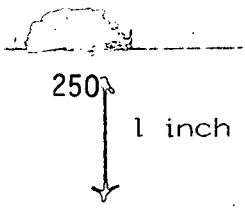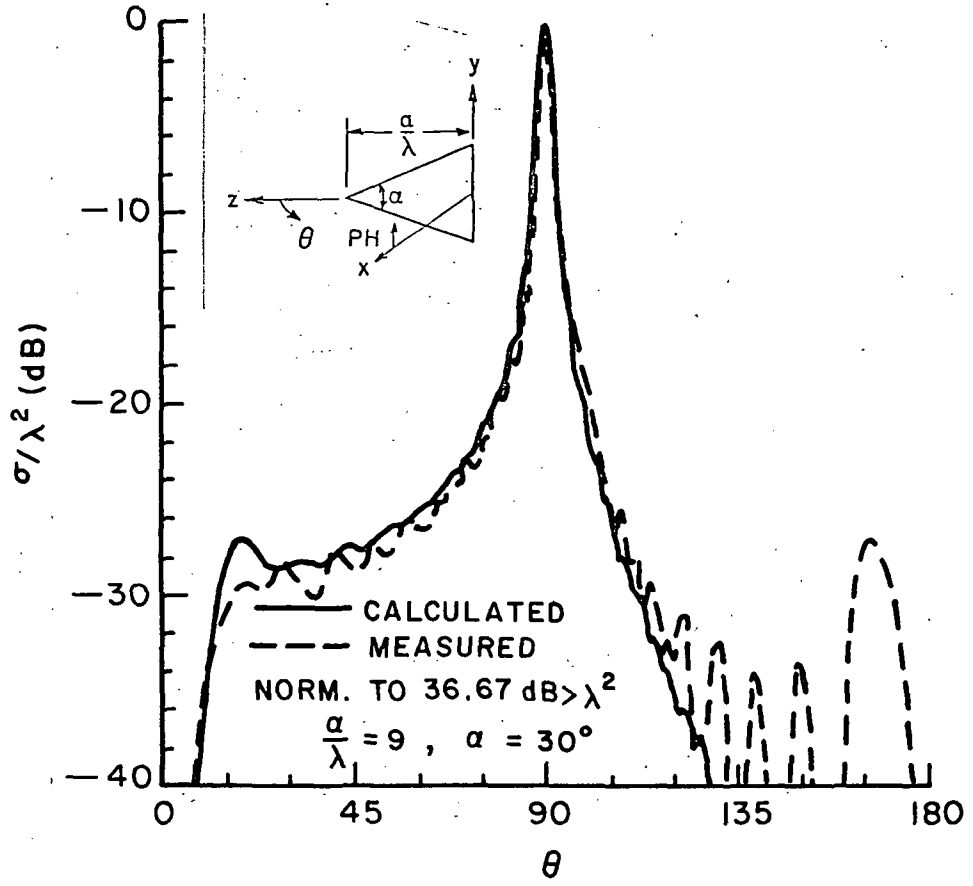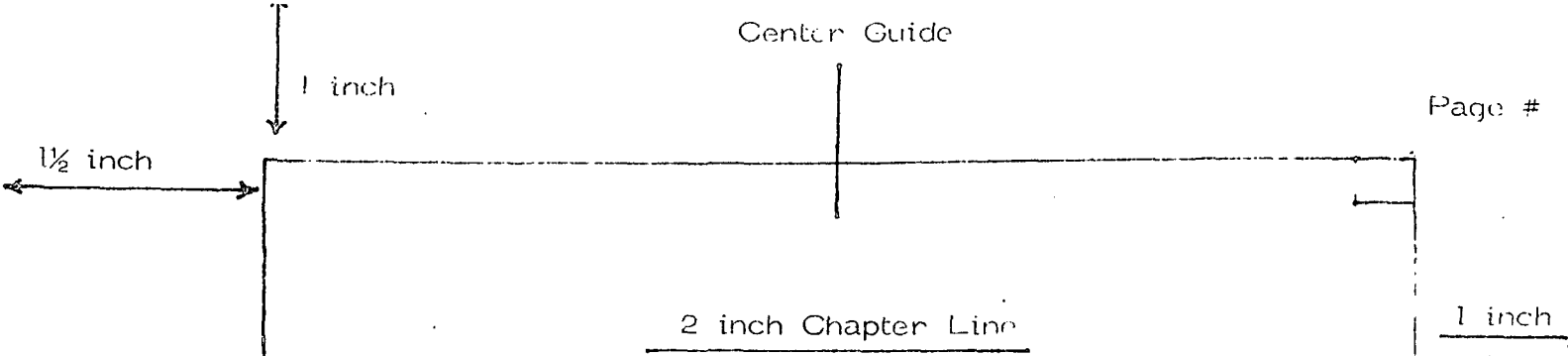
1st page Chapter end line

Figure 178. $E_\theta$, PH = 0 RCS pattern for a triangular plate ($\alpha = 30°$, $\frac{a}{\lambda} = 3$).
Only single, double and triple edge diffraction are included.

1 inch

JAB/80
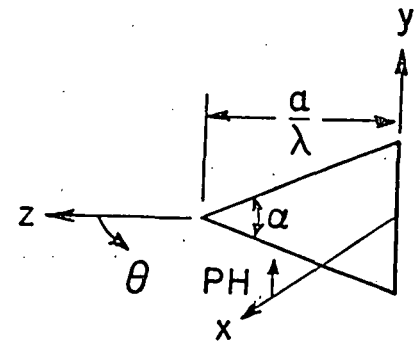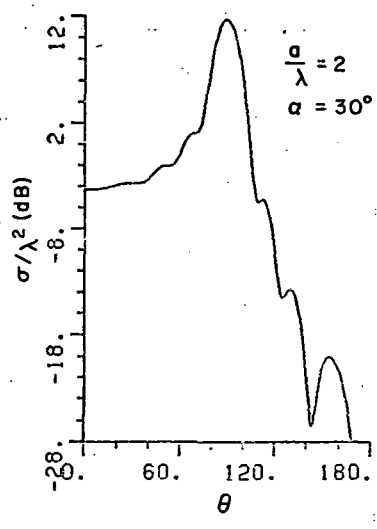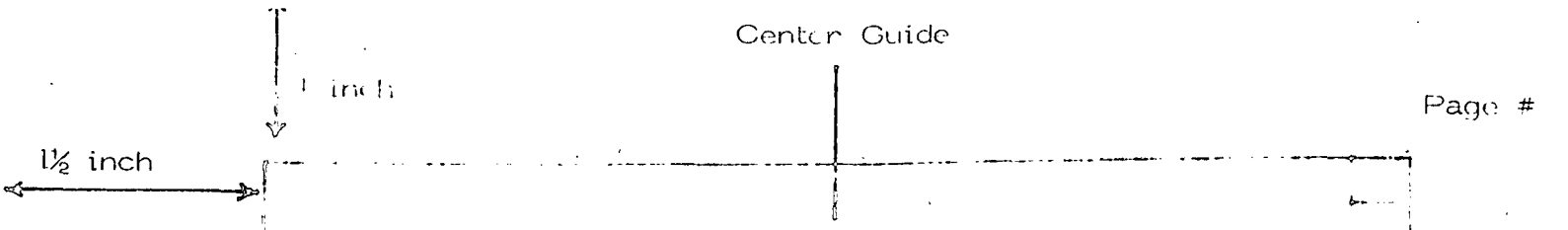
1 inch

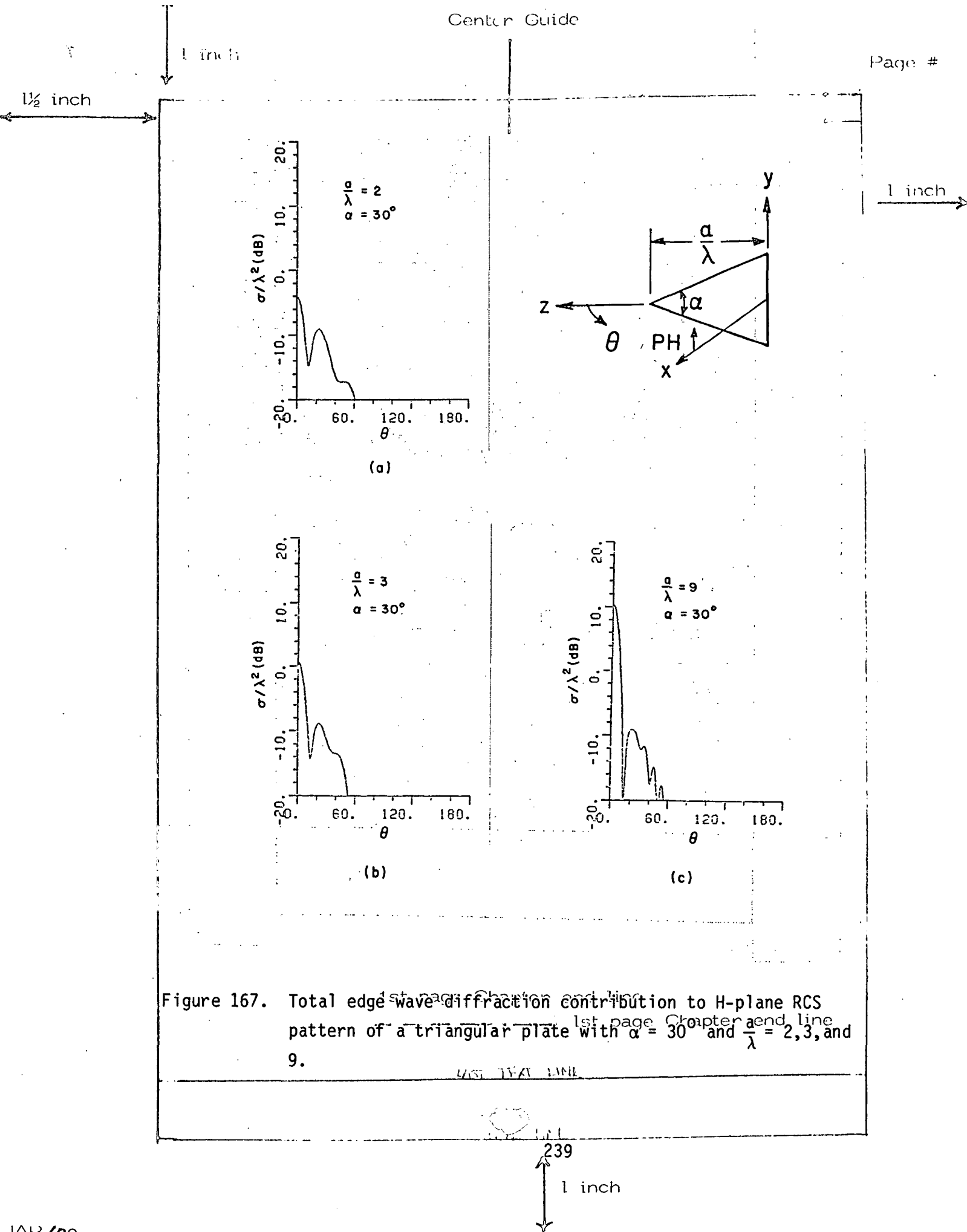1½ inch

1 inch



(a)
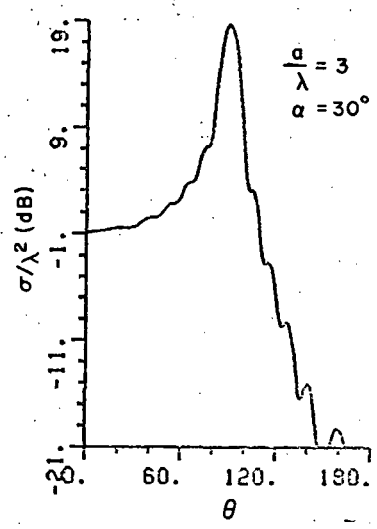
(b)

(c)
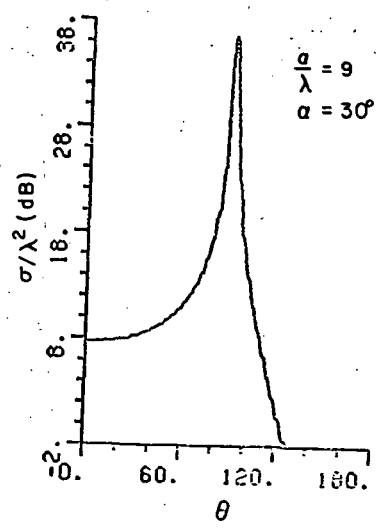
1st page Chapter end line

Figure 179.   Single edge diffraction contribution to the E-plane RCS pattern of a triangular plate with $\alpha = 30^O$ and $\frac{a}{\lambda} = 2$, 3 and 9.

1 inch

JAB/80

1 inch

1½ inch

1 inch



(a)
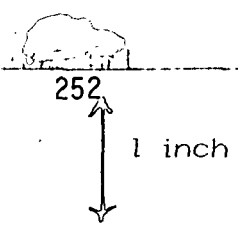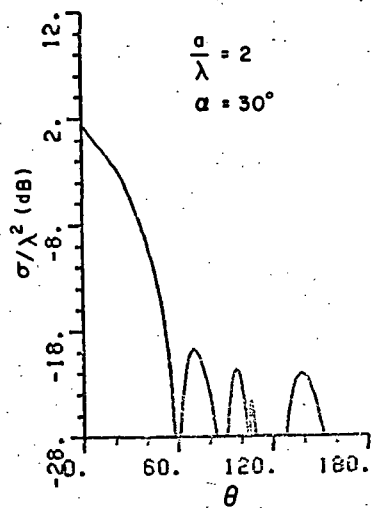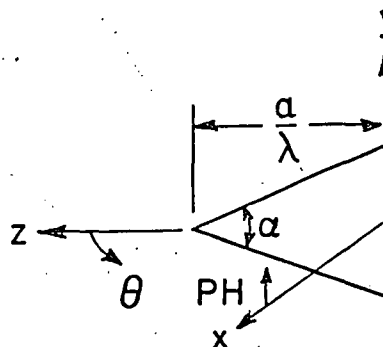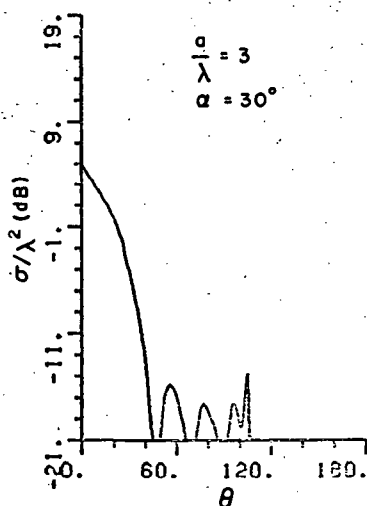
(b)
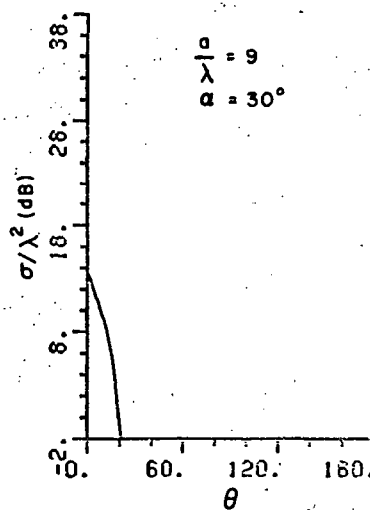
(c)

Figure 180. Double edge diffraction contribution to the E-plane RCS pattern of a triangular plate with $\alpha = 30^\circ$ and $\frac{a}{\lambda} = 2, 3$ and 9.

253

1 inch

1 inch

1½ inch
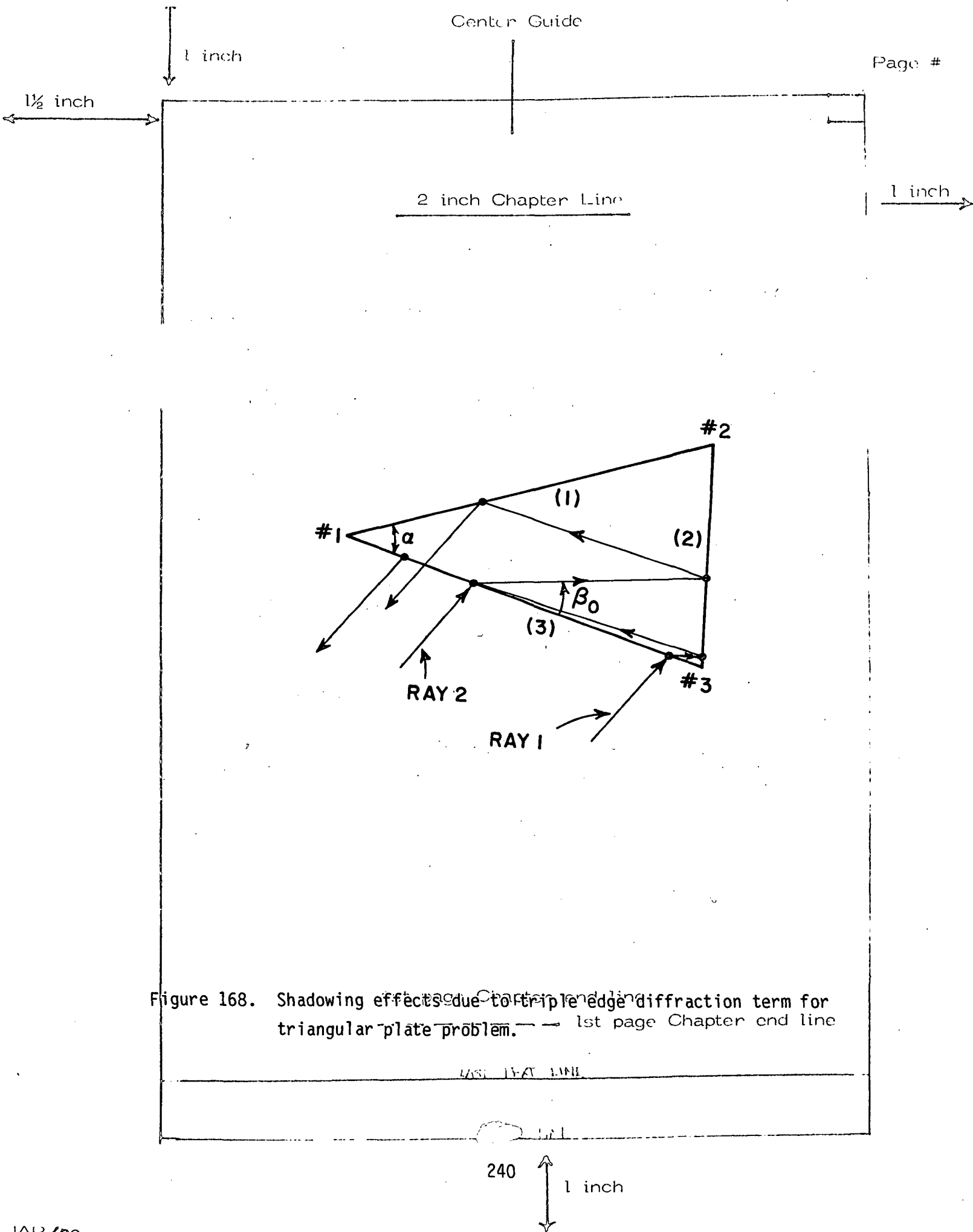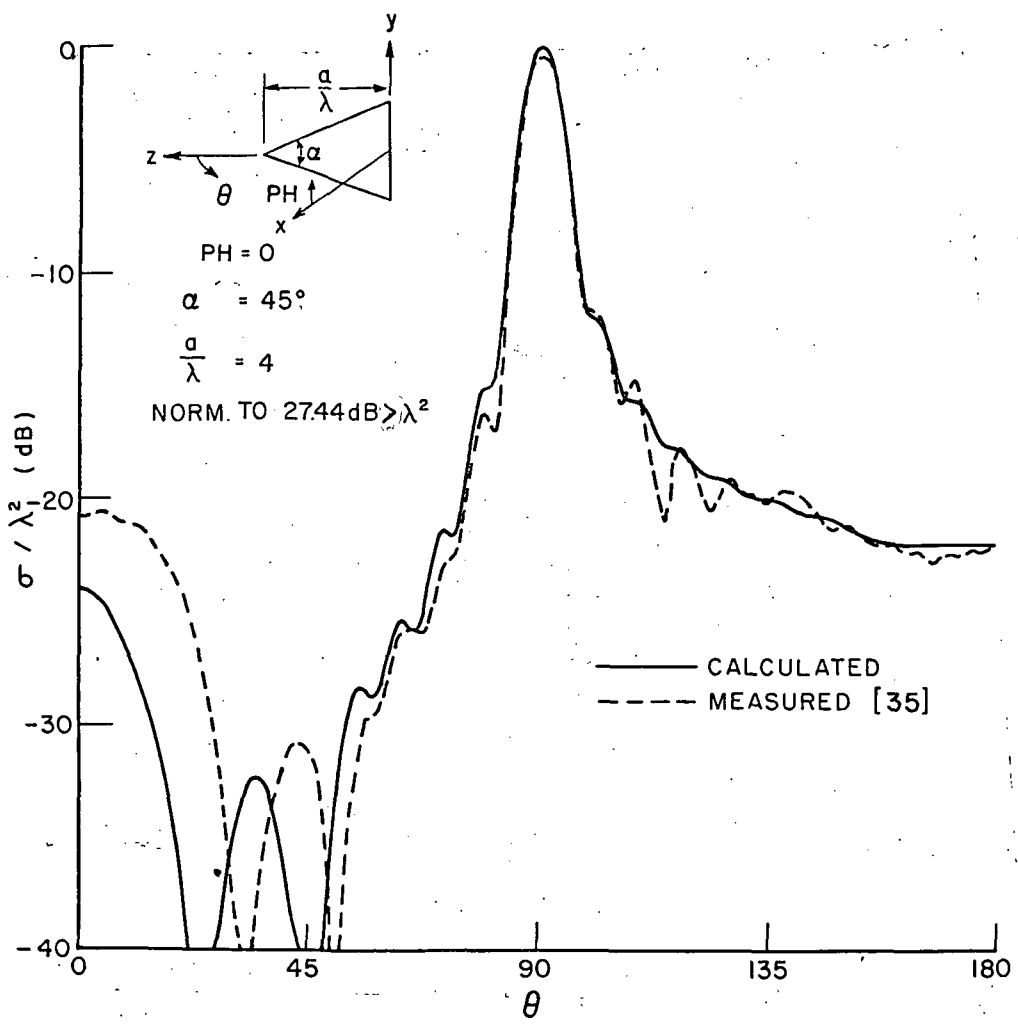
1 inch



(a)

(b)

(c)
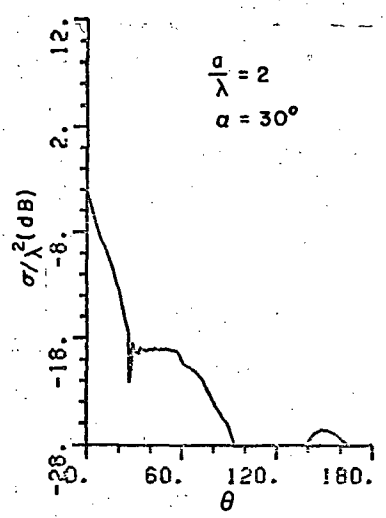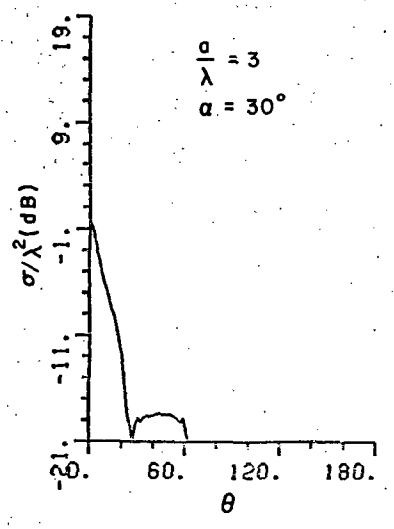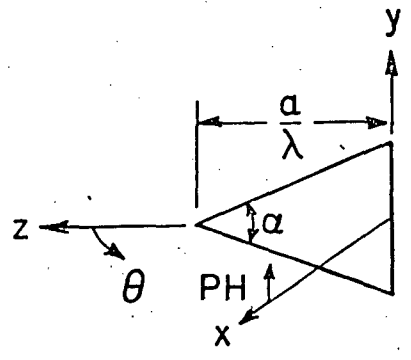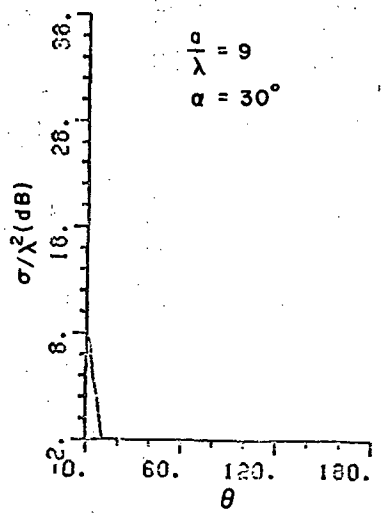
Figure 181.  Triple edge diffraction contribution to the E-plane RCS pattern of a triangular plate with $\alpha = 30^o$ and $\frac{a}{\lambda} = 2$, 3 and 9.

1st page Chapter end line

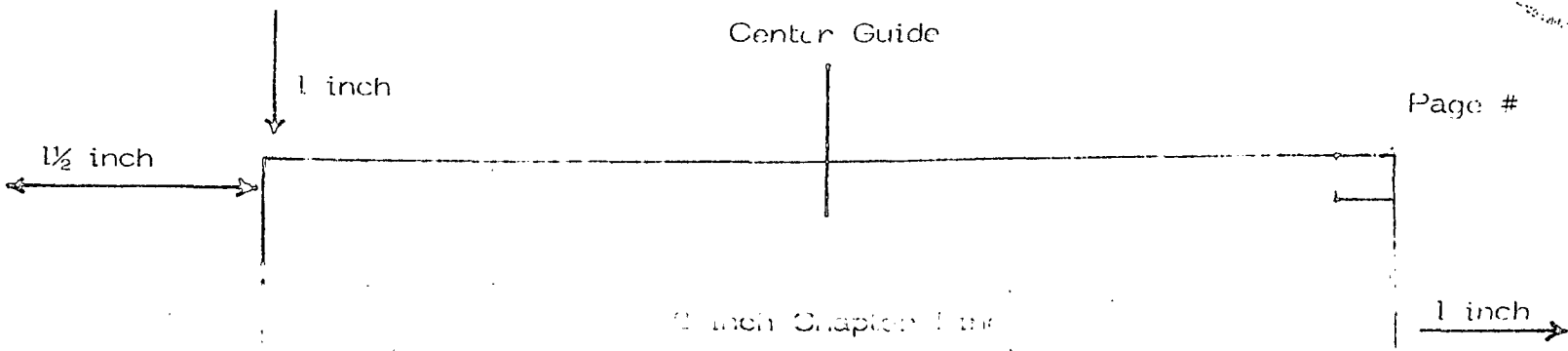1st page Chapter end line

LAST TEXT LINE

1 inch

JAB/80

Center Guide

1 inch

Page #

1½ inch

2 inch Chapter Line

1 inch



$$\frac{\sigma}{\lambda^2} \text{ (dB)}$$

CALCULATED
MEASURED
NORM. TO 27.43 dB>$\lambda^2$
$\frac{a}{\lambda} = 4$ , $\alpha = 45°$

$\theta$
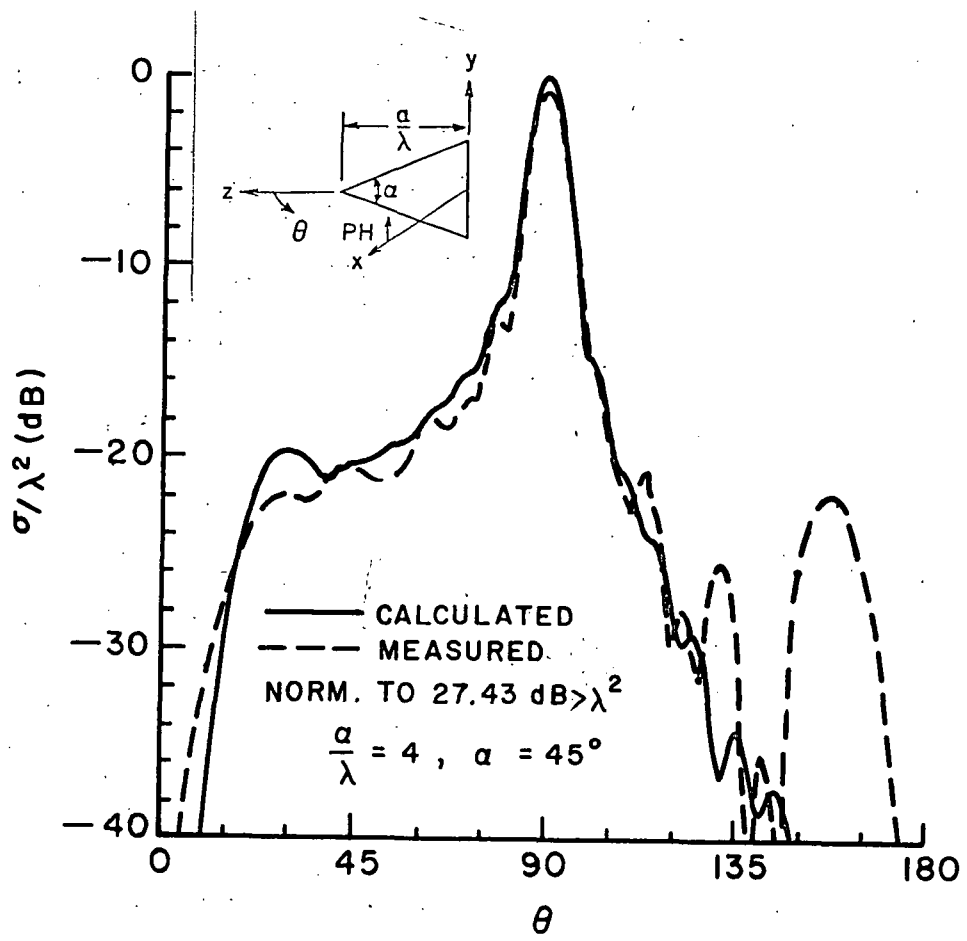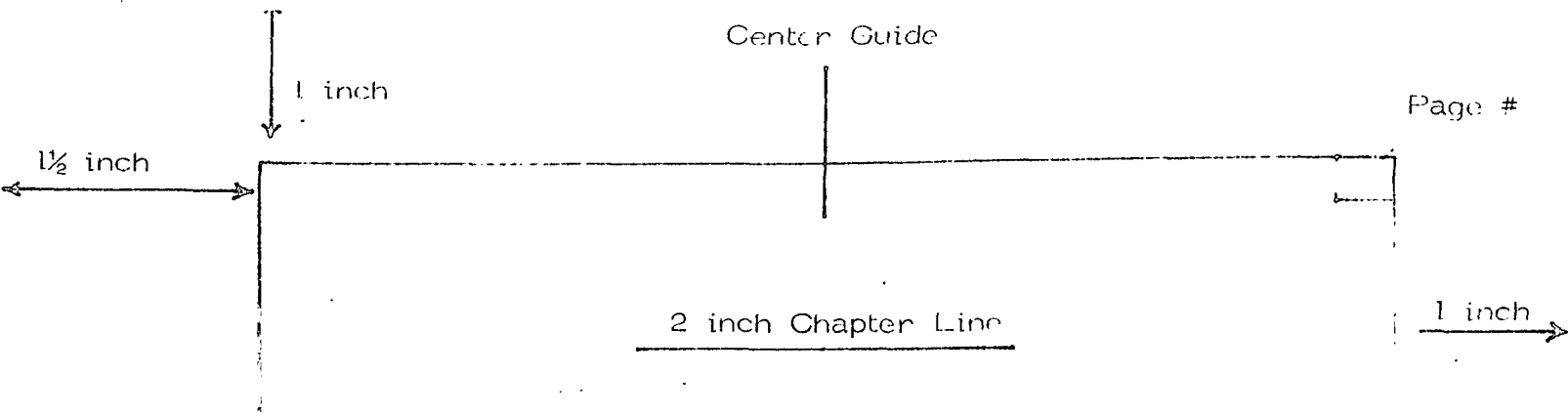
Figure 182. $E_\theta$, PH = 0 RCS pattern for a triangular plate ($\frac{a}{\lambda} = 4$, $\alpha = 45°$).
Only single, double and triple edge diffraction are included.

1st page Chapter end line
1st page Chapter end line

LAST TEXT LINE

1 inch

JAB/80
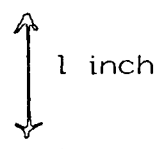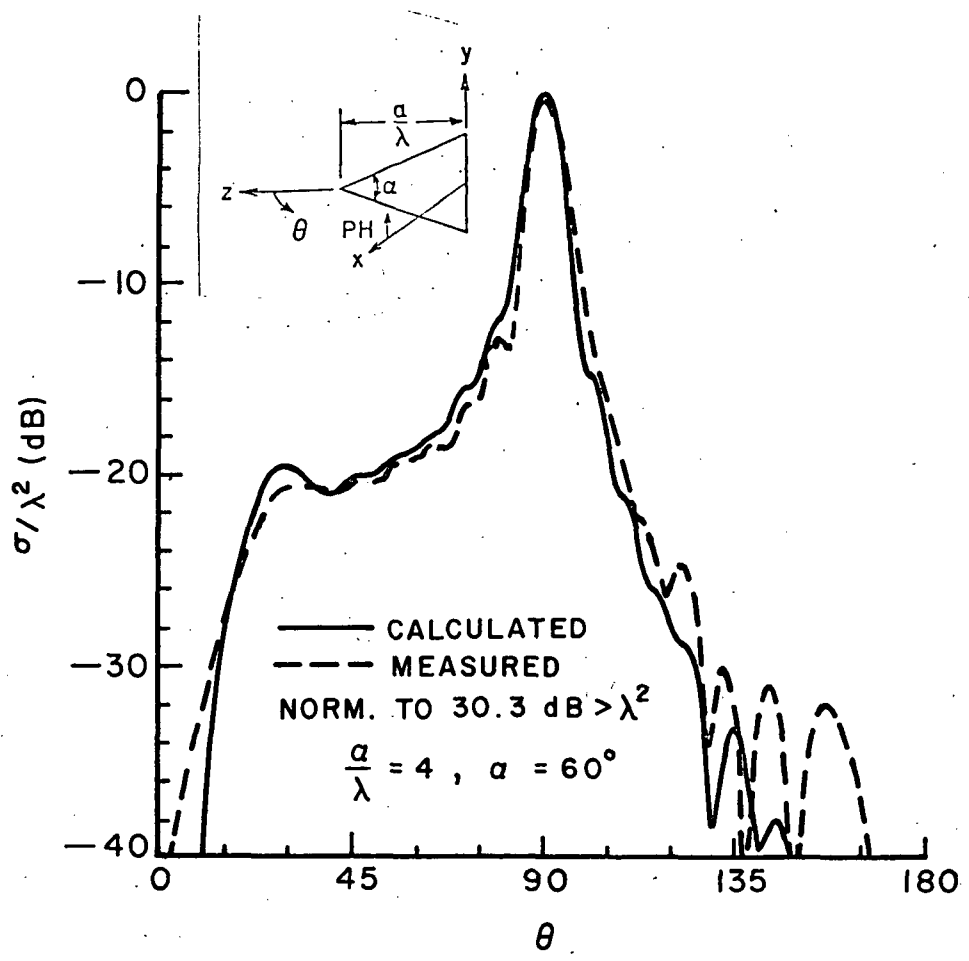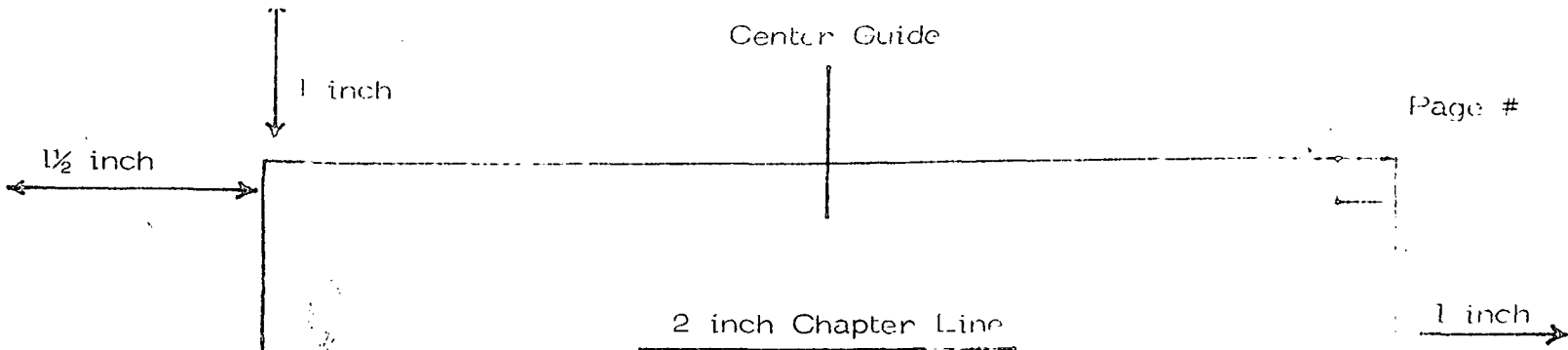
Figure 183. $E_\theta$, PH = 0 RCS pattern for a triangular plate ($\frac{a}{\lambda} = 4$, $\alpha = 60°$). Only single, double and triple edge diffraction are included.

JAB/80

2 inch Chapter Line
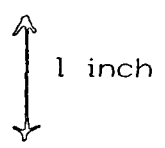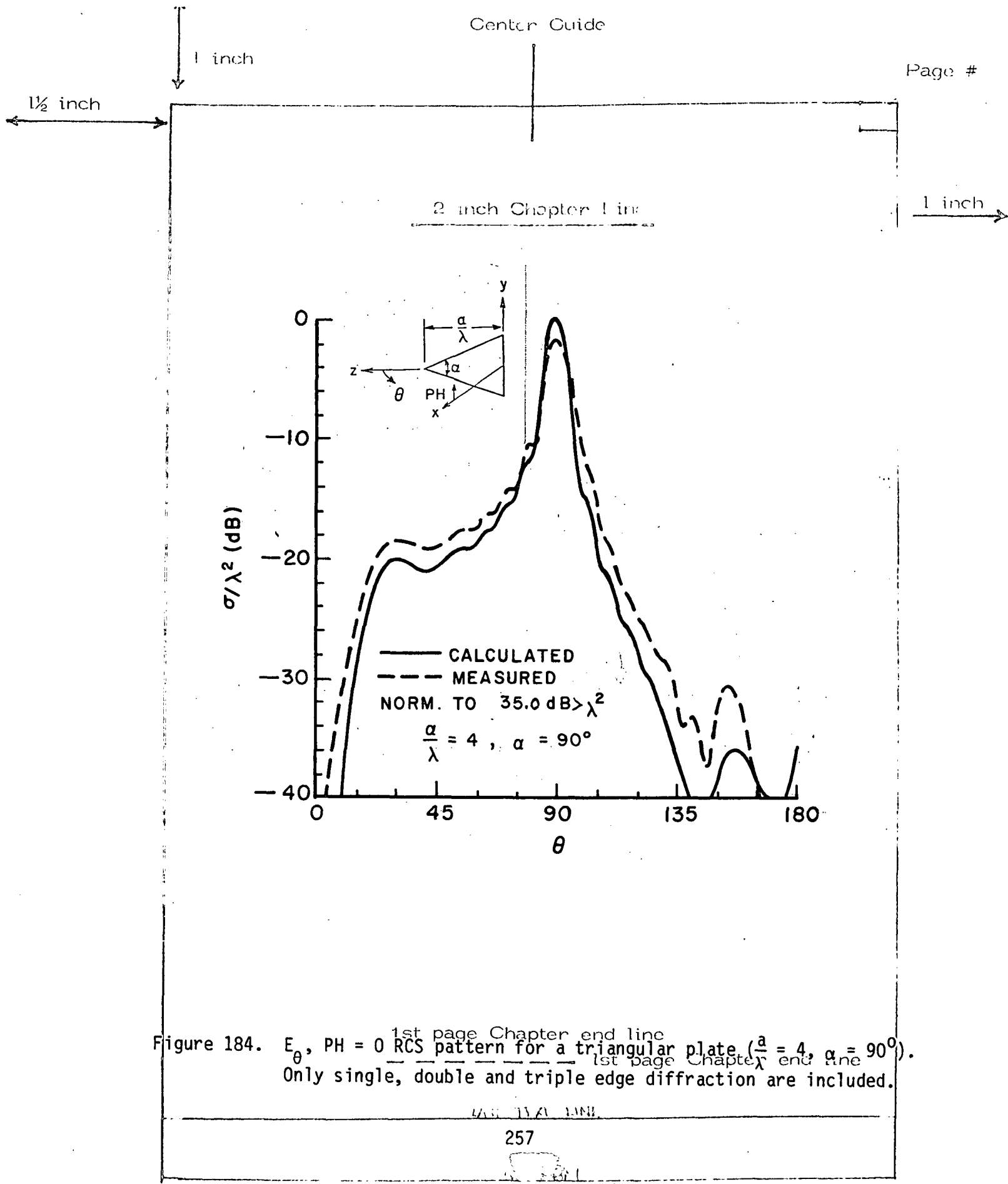


Figure 184. $E_\theta$, PH = 0 RCS pattern for a triangular plate ($\frac{a}{\lambda}$ = 4, $\alpha$ = 90°). Only single, double and triple edge diffraction are included.

JAB/80
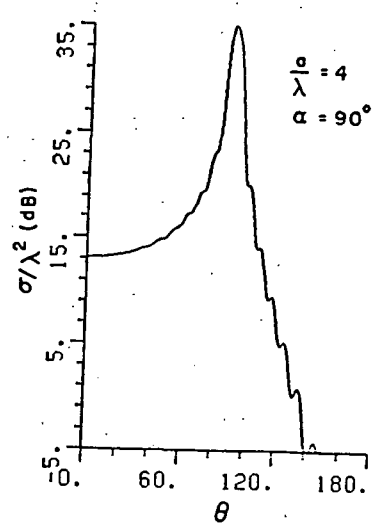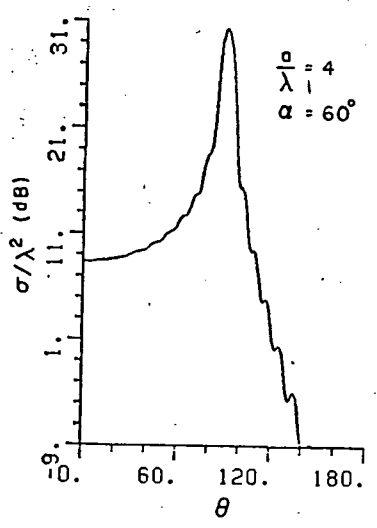
Figure 185.  Single edge diffraction contribution to the E-plane RCS pattern of a triangular plate with $\frac{a}{\lambda}$ = 4 and $\alpha$ = 45°, 60° and 90°.

JAB/80

(a)
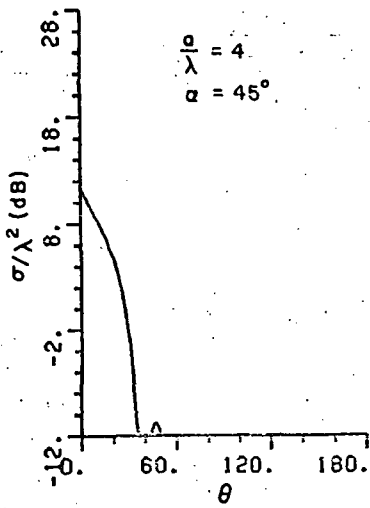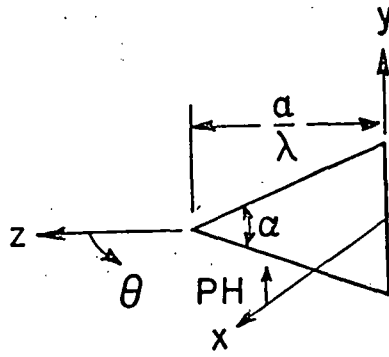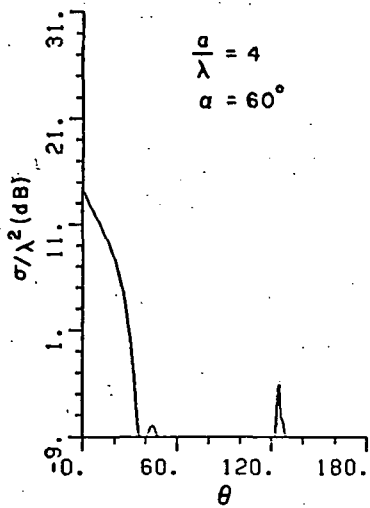
(b)
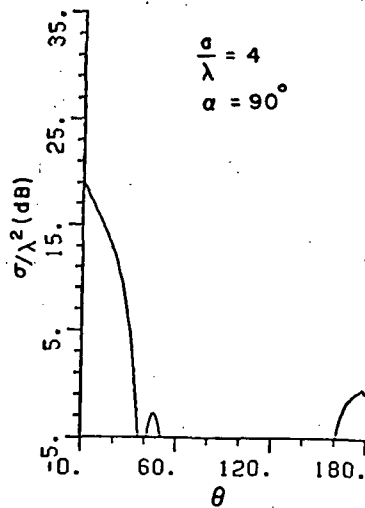
(c)
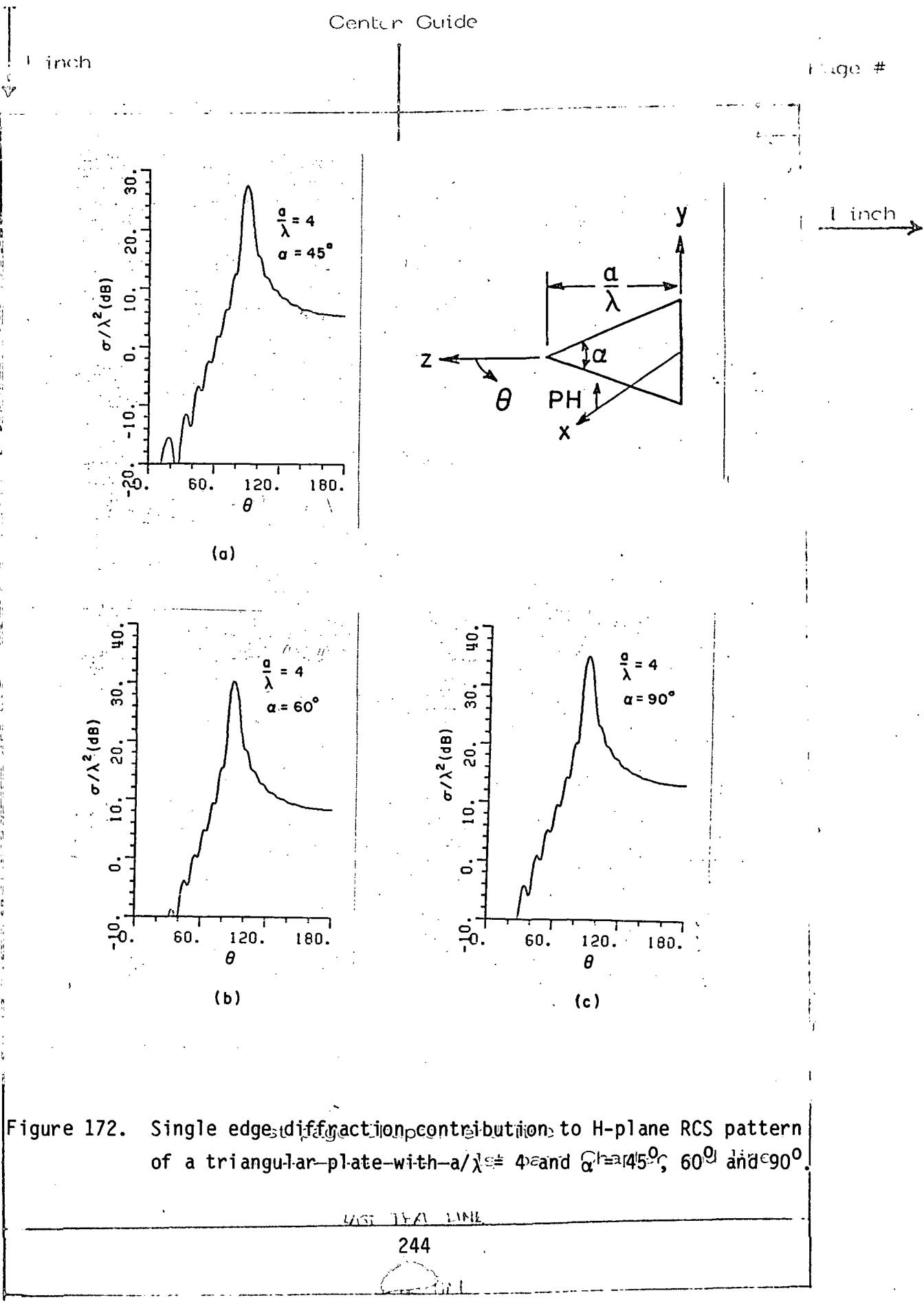
Figure 186. Double edge diffraction contribution to the E-plane RCS pattern of a triangular plate with $\frac{a}{\lambda} = 4$ and $\alpha = 45^0$, $60^0$ and $90^0$

259

JAB/80

$\frac{a}{\lambda} = 4$

$\alpha = 45°$

(a)

$\frac{a}{\lambda} = 4$

$\alpha = 60°$

(b)

$\frac{a}{\lambda} = 4$

$\alpha = 90°$
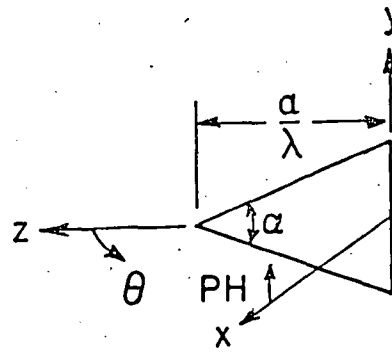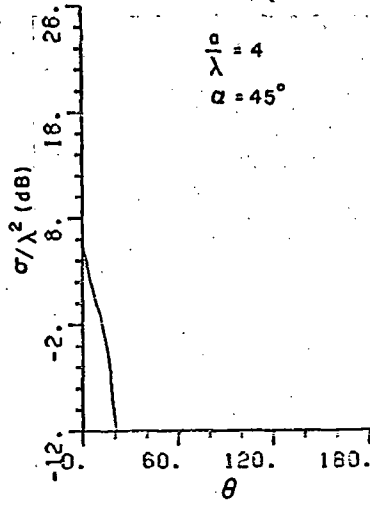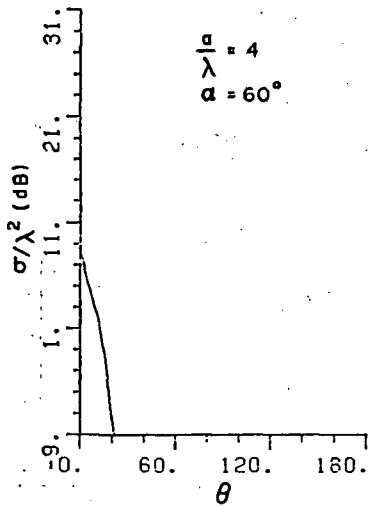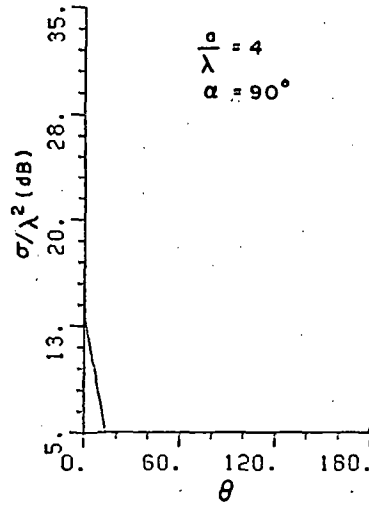
(c)

Figure 187. Triple edge diffraction contribution to the E-plane RCS pattern of a triangular plate with $\frac{a}{\lambda} = 4$ and $\alpha = 45°$, $60°$ and $90°$.
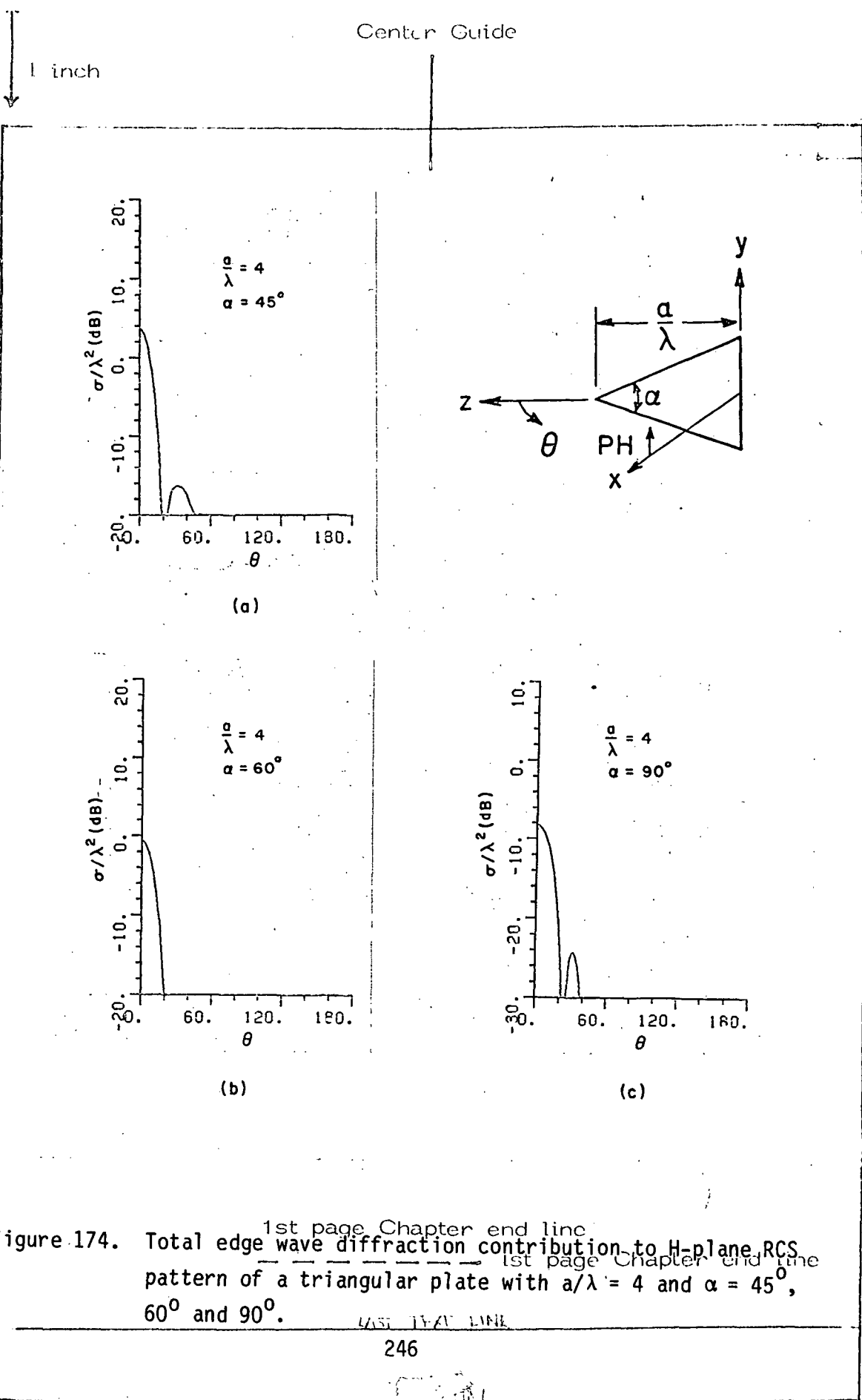
JAB/80

The H-plane pattern was analyzed by using the EC method to compute the contributions of single and triple edge diffraction mechanisms, also the Edge wave concept was extended to compute the contributions of double and triple edge wave corner diffraction mechanisms. The computed results were compared to measured data where it was found that for $\alpha = 30^0$ and $\frac{a}{\lambda} < 3$, our solution does not agree well with the measurements in the region near edge on, the tip side. Better agreement could be obtained if a more accurate corner diffraction coefficient is developed and probably more higher order interactions involving the edge waves are included in the solution. As the plate size is increased, better agreement is obtained between calculated and measured data.

The E-plane was also analyzed by using the EC method to compute the contributions of single, double, and triple edge diffraction mechanisms. The results are compared to measured data where some deviation is observed especially in the region $0^0 < \theta < 60^0$ and $120^0 < \theta < 180^0$ for $\alpha = 30^0$ and $\frac{a}{\lambda} \le 3$. This deviation is caused by neglecting to include the contribution of certain mechanisms not yet included in our solution. As the plate size is increased, better agreement is obtained in the region $0^0 < \theta < 60^0$ while some deviation in the region $120^0 < \theta < 180^0$ still remains.

As was stated earlier, the work presented in this chapter has not been carried to completion (with the consent of the advisor). The methods used in our analysis will serve as a guide for further work.

2 inch Chapter Line

This concludes our study on RCS from plate structures. We have successfully and clearly shown the important role of higher order interactions which includes the newly developed Edge wave concept in RCS pattern analysis.

A study on the cross polarization field for a monopole mounted on a rectangular plate is presented in the next chapter. The analysis is based on the Edge wave concept.

JAB/80

CHAPTER VIII

CROSS POLARIZATION STUDY FOR A
MONOPOLE MOUNTED ON A RECTANGULAR PLATE

A. INTRODUCTION

When an electromagnetic plane wave illuminates an object, the scattered field usually includes both direct and cross polarized components. The direct component has been widely studied in the literature since it is the component typically sensed by the receiver and it tends to be the larger of the two. The cross-polarized component on the other hand is produced as a result of the discontinuities and the finer details of the scatterer. It could also be produced as a result of the asymmetry of the object. The dependence of the cross-polarized component of the scattered field on the scattering object characteristics should be of value in evaluating the inverse scattering properties of the target. Such information may not be as readily obtainable from the direct return.

B. MONOPOLE ON A RECTANGULAR PLATE

The far zone radiated field of a monopole mounted on a rectangular perfectly conducting plate is analyzed by using GTD, corner diffraction and edge wave diffraction. Figure 188 illustrates the problem geometry. The monopole could be located anywhere on the plate. The following convension is used throughout this chapter:

The component $C_{ij}$ defines corner $i$ on edge $j$ where

$j = 1,2,\ldots\ldots,N$ and $i = j, j+1$

JAB/80
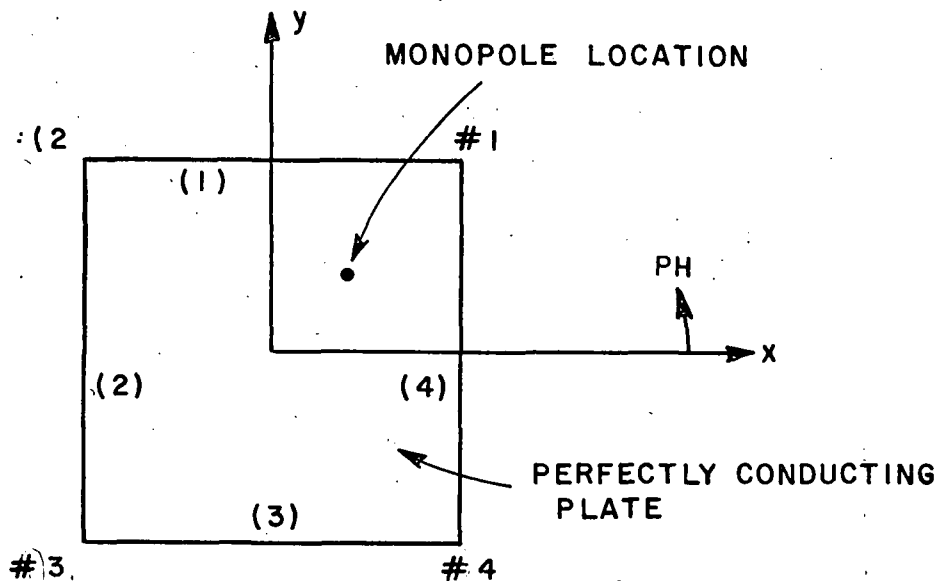
(a) TOP VIEW
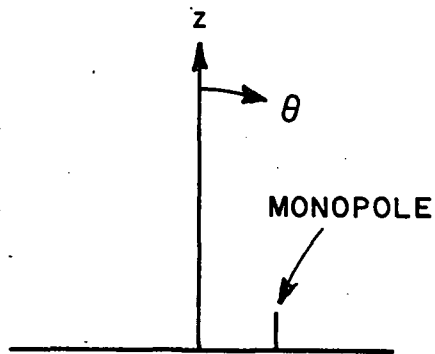
(b) SIDE VIEW

Figure 188. Monopole geometry.

JAB/80

and N is the total number of edges. $C_j$ defines corner j formed by edge-number j and (j-1).

### 1. <u>Analysis</u>

The principal polarization component of the scattered field, i.e., $E_\theta$ is obtained by summing up the fields due to the different components illustrated in Figures 189-191. In these figures, the field components due to only one edge are shown. The fields associated with the other edges are computed in a similar way. Figure 189 shows the field components due to direct illumination of the source. The different parameters shown are defined below:

$\bar{s}$ defines the position vector of the monopole, i. e.,

$$\bar{s} = x_s \hat{x} + y_s \hat{y} + z_s \hat{z}$$

$$\bar{s}_{c_1} = \bar{c}_1 - \bar{s} \qquad\qquad , \text{ and}$$

$$\bar{s}_{c_2} = \bar{c}_2 - \bar{s} \qquad\qquad .$$

Note that $\bar{c}_1$ and $\bar{c}_2$ are vectors that specify the positions of corners 1 and 2, and

$$\beta_{oc_1} = \cos^{-1}(-\hat{e}_1 \cdot \hat{d}) \qquad ,$$

$$\beta_{oc_2} = \pi - \beta_{oc_1} \qquad ,$$

$$\beta_o = \beta_{oc_1} \qquad ,$$

$$\beta_{c_1} = \cos^{-1}\left[-\hat{e}_1 \cdot \bar{s}_{c_1}\right] \qquad ,$$

$$\beta_{c_2} = \cos^{-1}\left[\hat{e}_1 \cdot (\bar{c}_2 - \bar{s})\right]$$

JAB/80
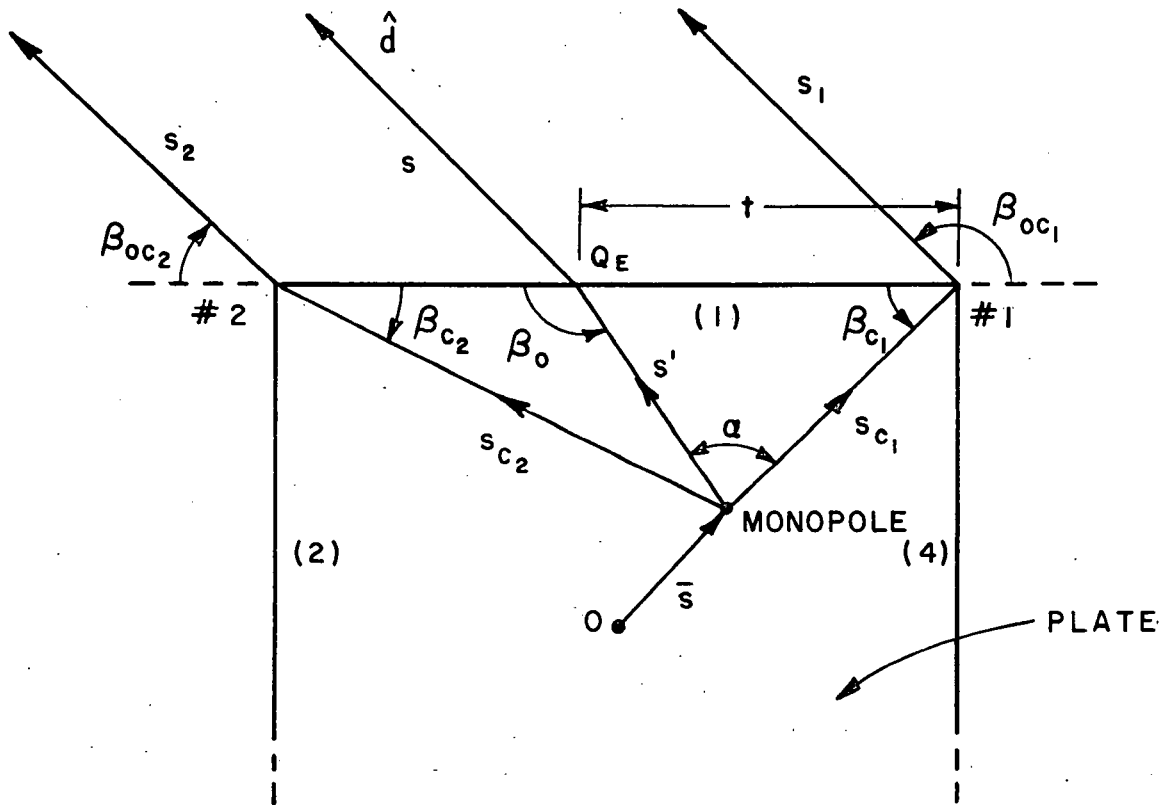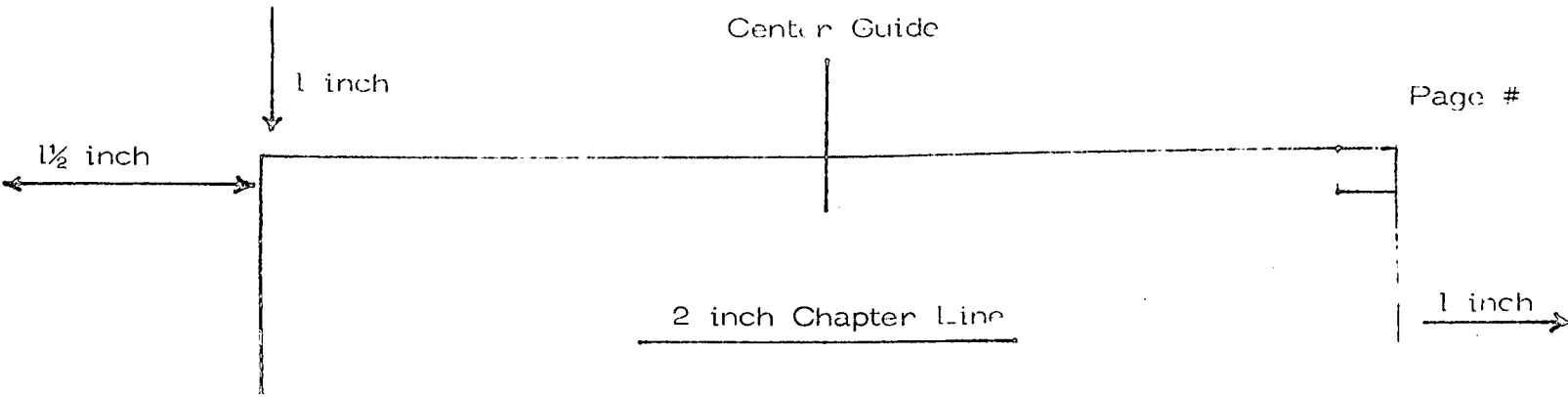
1 inch

1½ inch

2 inch Chapter Line

1 inch

Figure 189. Scattered field components due to monopole

1 inch

JAB/80

1 inch

1½ inch

1  ch



#2

#1

(1)

MONOPOLE

$I_1$

IMAGE
MONOPOLE

(2)

(4)

O

PLATE

(3)

#3

#4

1st page Chapter end line
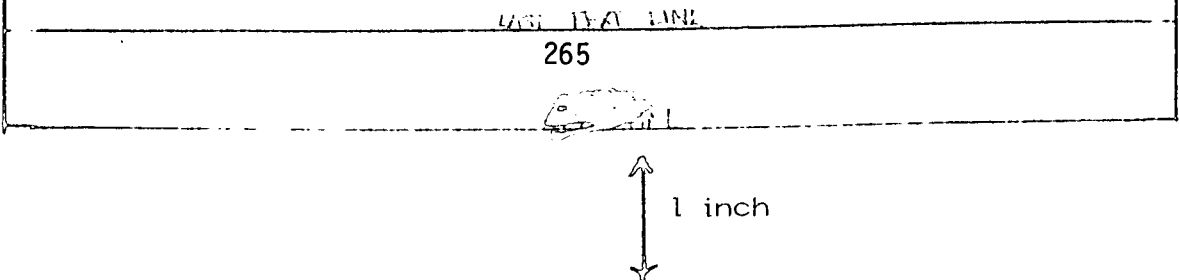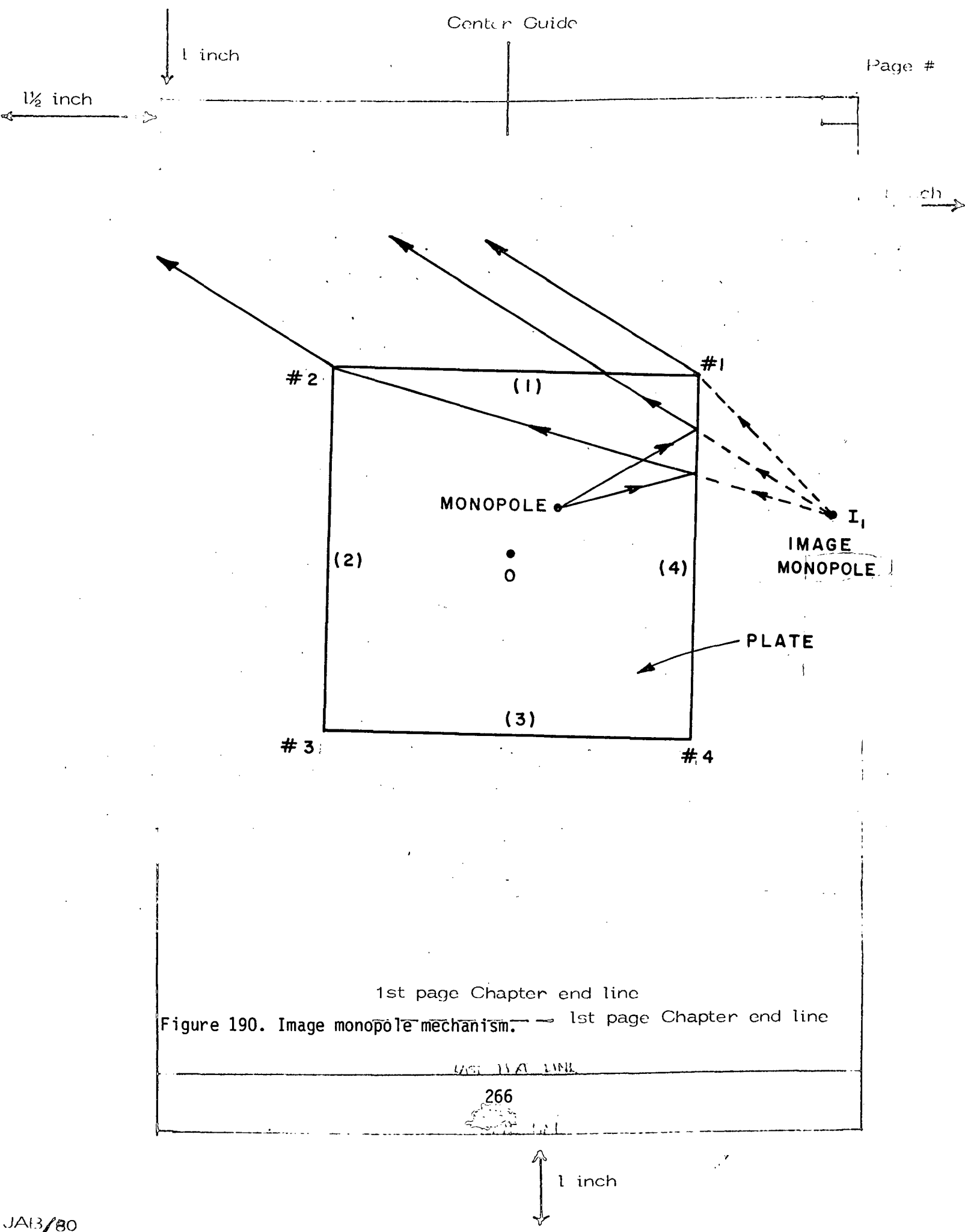
Figure 190. Image monopole mechanism.       1st page Chapter end line

266
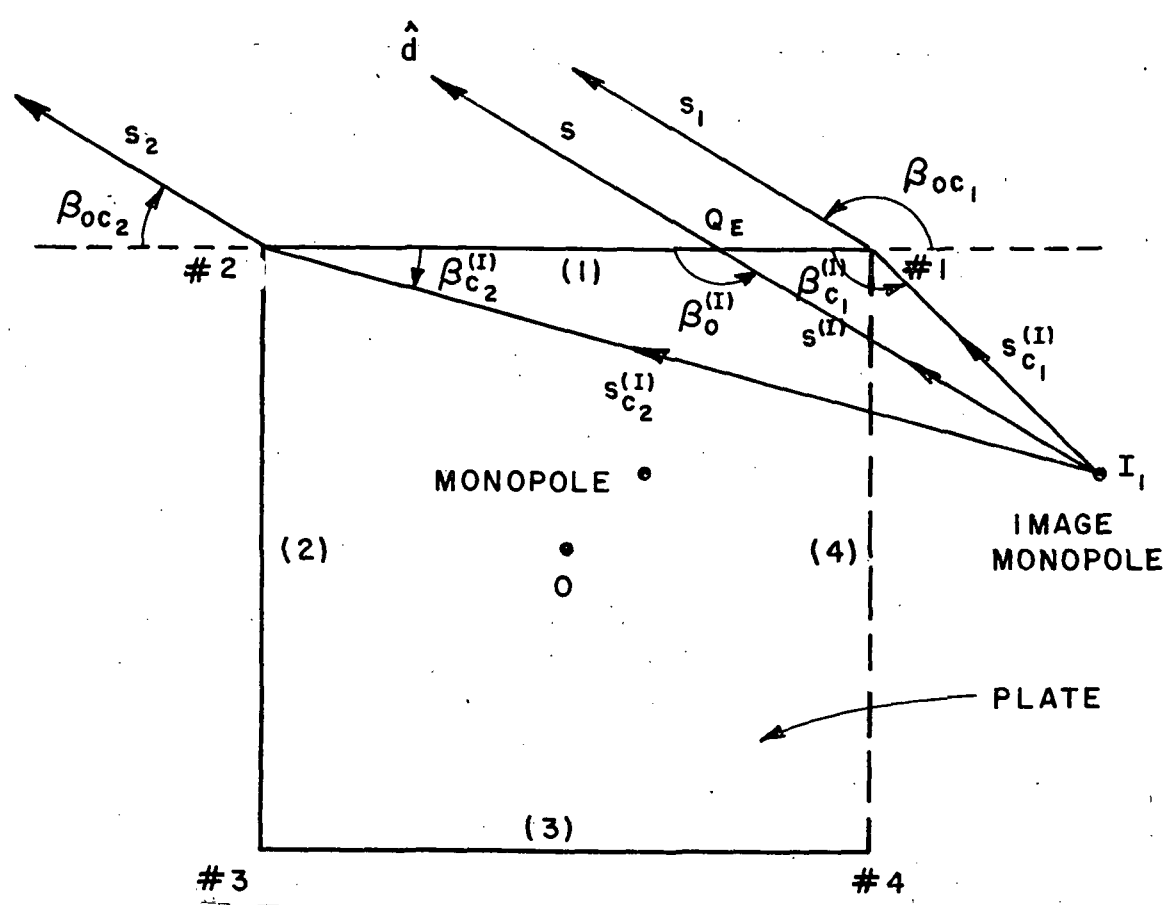
1 inch

Figure 191. Image monopole fields.

1 inch

JAB/80

1 inch

1½ inch

1 inch

$$\alpha = \beta_0 - \beta_{c_1} \qquad \text{and}$$

$$t = \frac{s_{c_1}}{\sin \beta_0} \sin \alpha \qquad \text{2 inch Chapter Line}$$
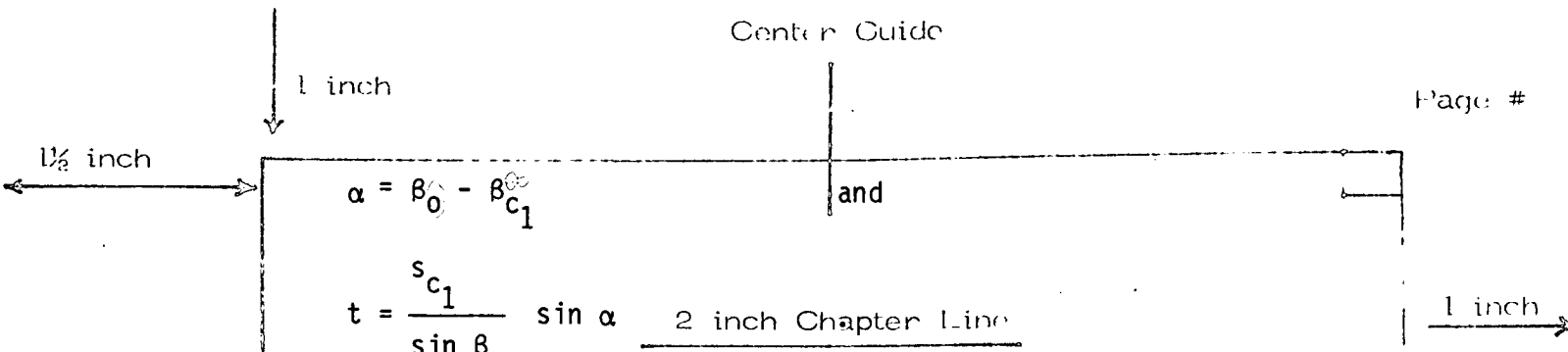
The diffraction point $Q_E$ position vector is then given by

$$\overline{Q}_E = \overline{c}_1 + t\,\hat{e}_1 \quad,$$

with $s$, $s_1$, $s_2$ being the distances to the receiver from the edge diffraction point, corner #1 and corner #2 on edge #1 respectively. The field diffracted from the edge is then given by

$$E_{\phi(1)} = -\,E^i_{\phi'(1)}(Q_E)\,D_h(L,\phi_1,0,\beta_0)\,\sqrt{s'}\ \frac{e^{-jks}}{s} \qquad (121)$$

where

$$E^i_{\phi'(1)}(Q_E) = j\,\sin\theta_s\,\frac{e^{-jks'}}{s'}\,(\hat{z}\cdot\hat{\phi}'_{(1)})$$

and

$$L = s'\,\sin^2\beta_0$$

Note that $\theta_s$ is the angle between the monopole axis and the line joining the monopole position and the diffraction point on the edge. For the case considered here, $\theta_s = \frac{\pi}{2}$. The field diffracted from $C_1$ is given by

$$E^{c_1}_{\phi(1)} = -\,E^i_{\phi'(1)}(c_1)\,D^{c_1}_h(L,\,L_{c_1},\phi_1,0,\beta_0,\beta_{c_1},\beta_{oc_1})$$

1st page Chapter end line

$$\sqrt{\frac{s'}{s_{c_1}}}\ \frac{e^{-jks_1}}{s_1} \qquad\qquad \text{1st page Chapter end line} \qquad (122)$$

1 inch

JAB/80
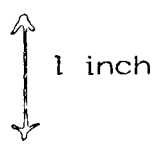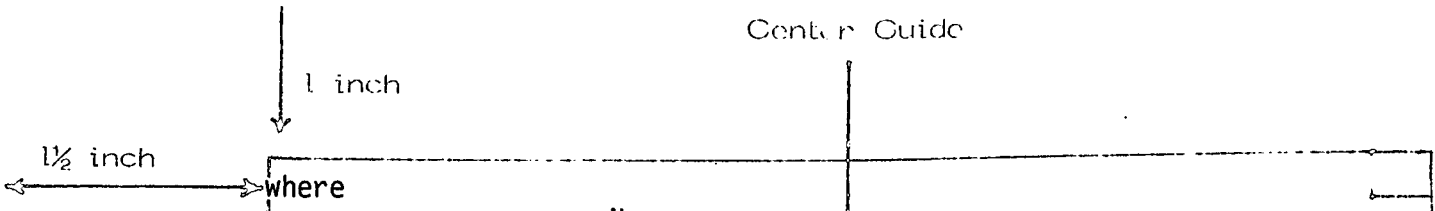
where

$$E^i_{\phi'(1)}(c_1) = j\frac{e^{-jks_{c_1}}}{s_{c_1}}(\hat{z}\cdot\hat{\phi}'_{(1)}) \quad, \quad L_{c_1} = s_{c_1}$$

and $D^{c_1}_h(L, L_{c_1}, \phi_1, 0, \beta_0, \beta_{c_1}, \beta_{oc_1})$ is defined by Equation (26).

The field diffracted from $C_2$ is given by

$$E^{c_2}_{\phi(1)} = -E^i_{\phi'(1)}(c_2)\, D^{c_2}_h(L, L_{c_2}, \phi_1, 0, \beta_0, \beta_{c_2}, \beta_{oc_2})\sqrt{\frac{s'}{s_{c_2}}}\frac{e^{-jks_2}}{s_2} \qquad (123)$$

where

$$E^i_{\phi'(1)}(c_2) = j\frac{e^{-jks_{c_2}}}{s_{c_2}}(\hat{z}\cdot\hat{\phi}'_{(1)}) \quad \text{and} \quad L_{c_2} = s_{c_2} \quad .$$

It should be noted that when

$$\beta_{c_2} < \beta_0 < \beta_{c_1} \qquad \text{no edge diffraction occurs.}$$

Figure 190 illustrates the effect of edge 4 on the fields due to edge 1. The field radiated by the monopole diffracts from edge 4 and in turn, illuminates edge 1. This diffracted field appears to emanate from an image monopole located at point $I_1$. Of course, there is another image monopole due to diffraction from edge 2, i.e., for each edge on the plate there are two image monopoles that illuminate the edge and significantly contribute to the far scattered field. Figure 191 defines

1½ inch

$$E^i_{\phi'(1)}(c_1) = j \frac{e^{-jks^{(I)}_{c_1}}}{s^{(I)}_{c_1}} (\hat{z} \cdot \hat{\phi}'_{(1)}) \quad .$$

2 inch Chapter Line
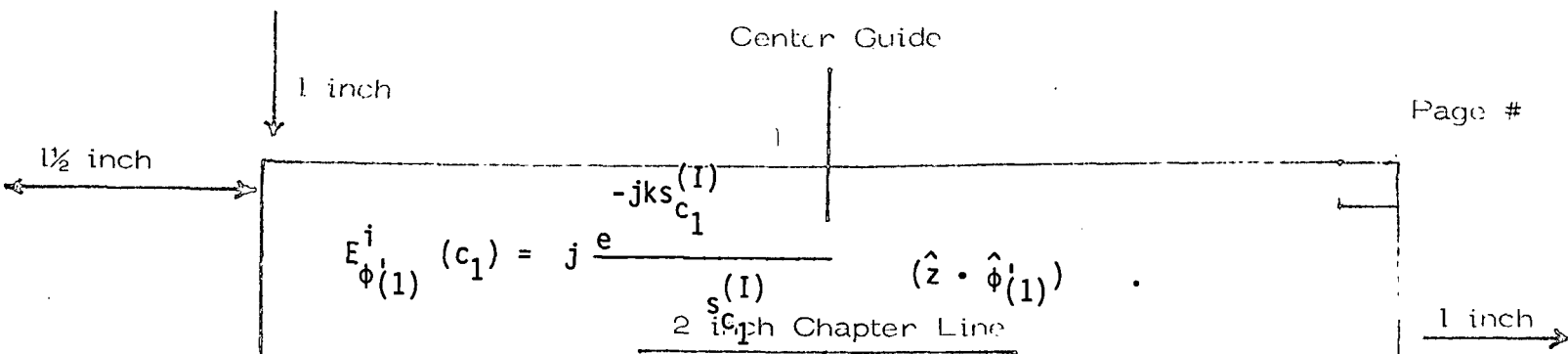
Similarly, the field due to corner 2 is given by.

$$E^{c_2}_{\phi(1)} = - E^i_{\phi'(1)}(c_1) D^{c_2}_h (L^{(I)}, L^{(I)}_{c_2}, \phi_1, 0, \beta^{(I)}_0, \beta^{(I)}_{c_2}, \beta_{oc_2}) \sqrt{\frac{s'^{(I)}}{s^{(I)}_{c_2}}}$$

$$R^{c_2} \frac{e^{-jks_2}}{s_2} \tag{126}$$

THESIS / DISSERTATION
Typing Guide Paper

where

$$R^{c_2} = \frac{e^{-j\pi/4}}{\sqrt{2\pi k} \cos \beta^{(I)}_{c_2}} \quad , \text{ and}$$

$$E^i_{\phi'(1)}(c_2) = j \frac{e^{-jks^{(I)}_{c_2}}}{s^{(I)}_{c_2}} (\hat{z} \cdot \hat{\phi}'_{(1)}) \quad .$$

Note that when $\beta^{(I)}_{c_2} < \beta^{(I)}_0 < \beta^{(I)}_{c_1}$ no edge diffraction occurs.

In a pattern plane cut very close to the plane of the plate, the fields due to Equations (121-126) contribute very little to the cross-polarized field components. The major contribution comes from the edge wave mechanism discussed in Chapter II. In a similar way, there are edge wave fields due to the monopole and its images.

1st page Chapter end line

Figure 192 illustrates the edge wave mechanisms associated with the monopole itself. If one considers the case shown in Figure 192-a and

LAST TEXT LINE

1 inch

JAB/80
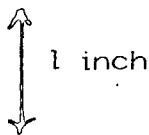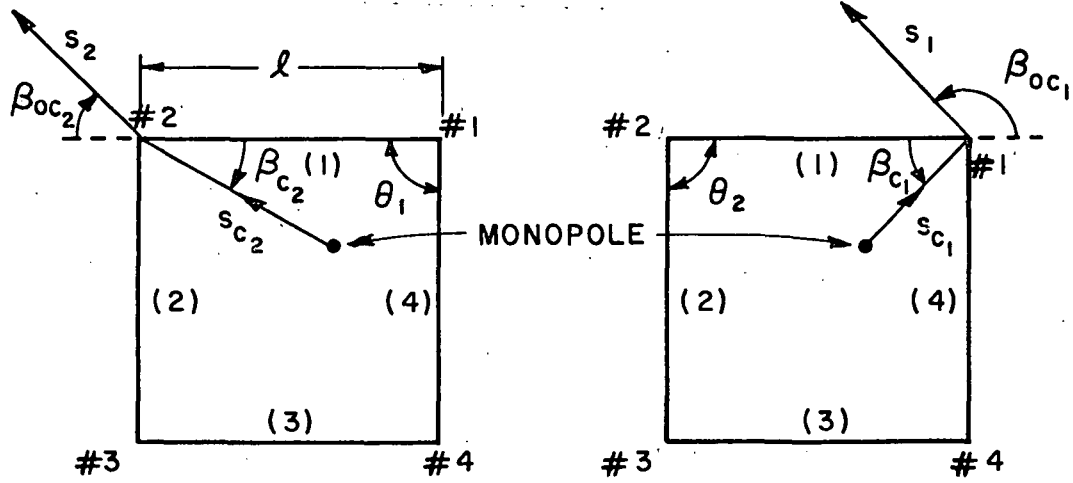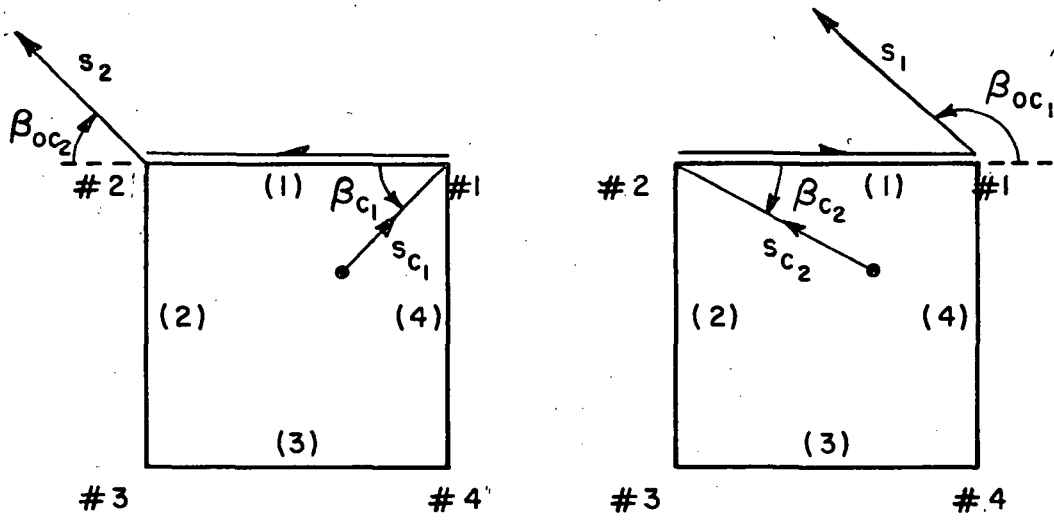
Figure 192. Edge wave mechanisms due to monopole.

271

1½ inch

1 inch

the different parameters associated with the image monopole. The edge diffracted field due to this monopole is given by

2 inch Chapter Line

$$E_{\phi(1)}^{(I)} = - E_{\phi'(1)}^{i} (Q_E) \, D_h(L^{(I)}, \phi_1, 0, \beta_0^{(I)}) \, \sqrt{s'^{(I)}} \; R \, \frac{e^{-jks}}{s} \qquad (124)$$

where the super script (I) indicates image monopole and

$$L^{(I)} = s'^{(I)} \sin^2 \beta_0^{(I)}$$

THESIS / DISSERTATION
Typing Guide Paper

$$R = - \frac{e^{-j\pi/4}}{\sqrt{2\pi k} \, \cos \beta_0^{(I)}} \qquad , \text{ and}$$

$$E_{\phi'(1)}^{i} (Q_E) = j \, \frac{e^{-jks'^{(I)}}}{s'^{(I)}} \quad (\hat{z} \cdot \hat{\phi}'_{(1)}) \qquad .$$

For the corner fields one writes

$$E_{\phi(1)}^{c_1} = - E_{\phi'(1)}^{i} (c_1) \, D_h^{c_1} (L^{(I)}, L_{c_1}^{(I)}, \phi_1, 0, \beta_0^{(I)}, \beta_{c_1}^{(I)}, \beta_{0c_1}) \sqrt{\frac{s'^{(I)}}{s_{c_1}^{(I)}}}$$

$$R^{c_1} \, \frac{e^{-jks_1}}{s_1} \qquad (125)$$

where

$$L_{c_1}^{(I)} = s_{c_1}^{(I)} \qquad , \qquad R_1^{c_1} = - \frac{e^{-j\pi/4}}{\sqrt{2\pi k} \, \cos \beta_{c_1}^{(I)}} \qquad , \text{ and}$$

1st page Chapter end line

1st page Chapter end line

1 inch

JAB/80
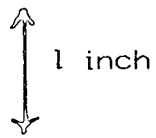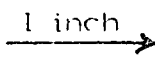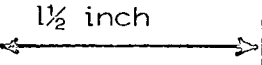
examine it as a reciprocal problem i.e., a plane wave being incident on the plate and the field strength received by the monopole. The plane wave is diffracted by $C_2$. This diffracted field excites an edge wave whose field is received by the monopole. By reciprocity, the cross-polarized far field is then given by

$$E_{\beta(1)} = E^i_{\phi'(1)}(c_2) \, D_s^{(ew)}(\epsilon,\pi,\pi,\beta_{oc_2}) D_h^{(ew)}(s_{c_2},o,\tfrac{\pi}{2},\beta_{c_2}) \, F(\gamma)$$

$$\frac{e^{-jks_2}}{s_2} \tag{127}$$

where

$D_s^{(ew)}_h$ is defined by Equation (27) and

$$E^i_{\phi'(1)}(c_2) = j \, \frac{e^{-jks_{c_2}}}{\sqrt{\epsilon \times s_{c_2}}} \, (\hat{z} \cdot \hat{\phi}'_{(1)})$$

and

$\epsilon$ is a very small number ~0.01.

$F(\gamma)$ is a heuristic pattern function which is needed to account for the presence of the adjacent edges and to satisfy the boundary condition over the plate. It is given by

$$F(\gamma) = \begin{cases} 0 & \text{, over the plate} \\ \dfrac{\sin\left(\frac{\pi\gamma}{\theta}\right)}{\sqrt{2} \; \sin\left(\frac{2\pi}{3}\right)} & \text{, otherwise.} \end{cases} \tag{128}$$

where γ is an angle defined with respect to the diffracting edge and

$$\theta' = 2\pi - \theta$$ , where
θ is the interior angle between two adjacent edges forming the corner. These parameters are shown in Figure 193. Figure 194 shows two plots of $F(\gamma)$ for $\theta = 90^\circ$ and $120^\circ$.

The field from $C_1$ is found by a similar expression with $\beta_{oc_2}$, $\beta_{c_2}$, $S_{c_2}$ and $S_2$ replaced by $\beta_{oc_1}$, $\beta_{c_1}$, $S_{c_1}$ and $S_1$ which are defined in Figure 192-b.
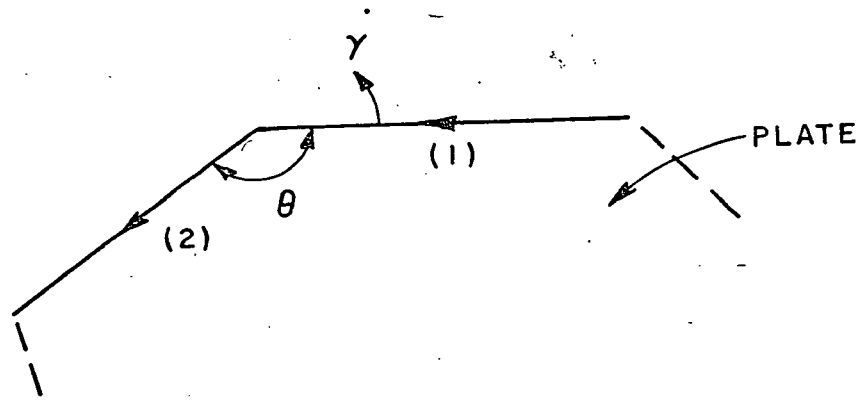
Figure 193. Parameter definition for pattern function.

JAB/80

1½ inch

1 inch

PLATE

90°

**(a)**

PLATE

120°
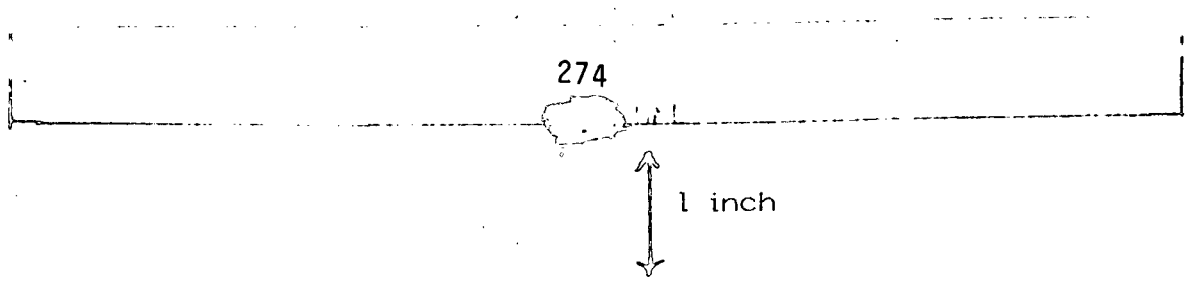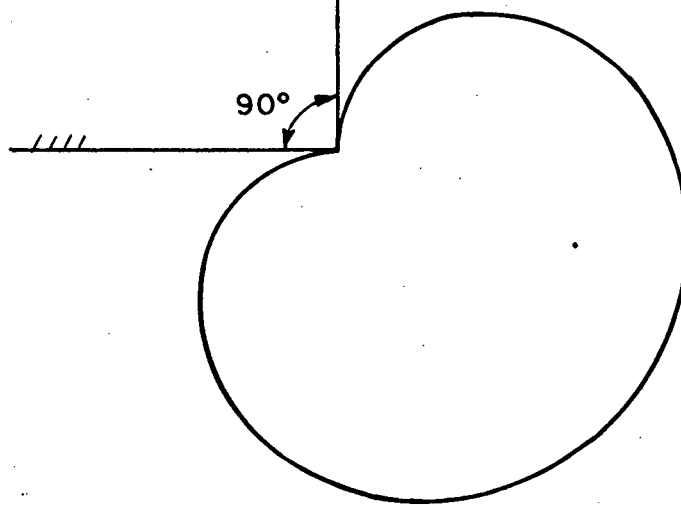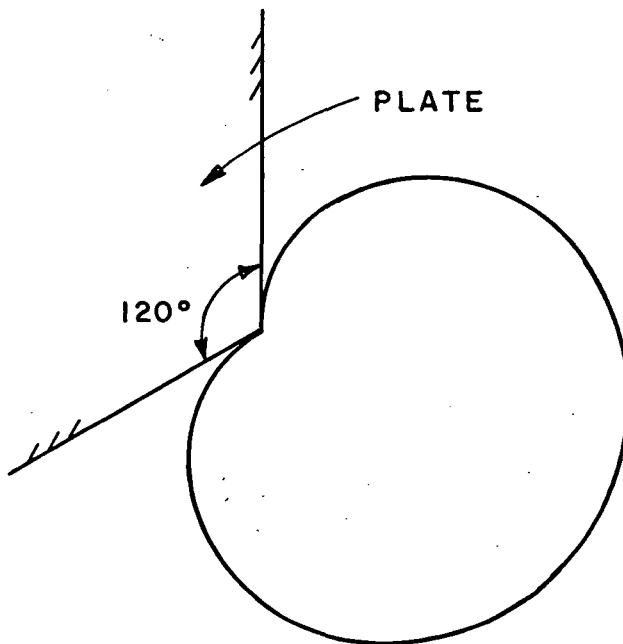
**(b)**

Figure 194. Plot of pattern function for plate corner angles 90° and 120°.

275

1 inch

JAB/80
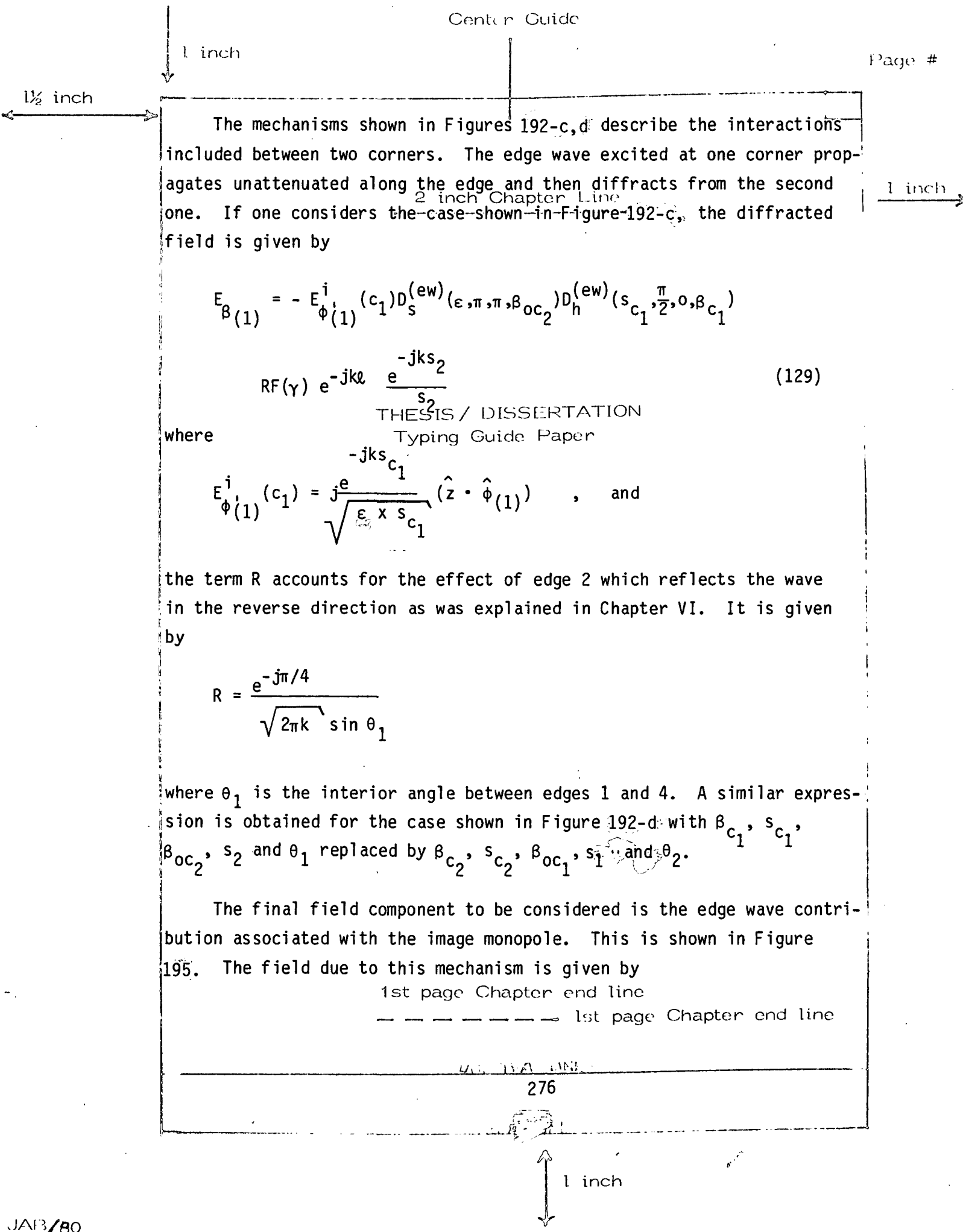
The mechanisms shown in Figures 192-c,d describe the interactions included between two corners. The edge wave excited at one corner propagates unattenuated along the edge and then diffracts from the second one. If one considers the case shown in Figure 192-c, the diffracted field is given by

$$E_{\beta(1)} = - E_{\phi(1)}^i (c_1) D_s^{(ew)}(\varepsilon, \pi, \pi, \beta_{oc_2}) D_h^{(ew)}(s_{c_1}, \tfrac{\pi}{2}, o, \beta_{c_1})$$

$$RF(\gamma)\, e^{-jk\ell}\, \frac{e^{-jks_2}}{s_2} \qquad\qquad (129)$$

where

$$E_{\phi(1)}^i (c_1) = j \frac{e^{-jks_{c_1}}}{\sqrt{\varepsilon \times s_{c_1}}} (\hat{z} \cdot \hat{\phi}_{(1)}) \quad , \quad \text{and}$$

the term R accounts for the effect of edge 2 which reflects the wave in the reverse direction as was explained in Chapter VI. It is given by

$$R = \frac{e^{-j\pi/4}}{\sqrt{2\pi k}\, \sin\theta_1}$$

where $\theta_1$ is the interior angle between edges 1 and 4. A similar expression is obtained for the case shown in Figure 192-d with $\beta_{c_1}$, $s_{c_1}$, $\beta_{oc_2}$, $s_2$ and $\theta_1$ replaced by $\beta_{c_2}$, $s_{c_2}$, $\beta_{oc_1}$, $s_1$ and $\theta_2$.

The final field component to be considered is the edge wave contribution associated with the image monopole. This is shown in Figure 195. The field due to this mechanism is given by
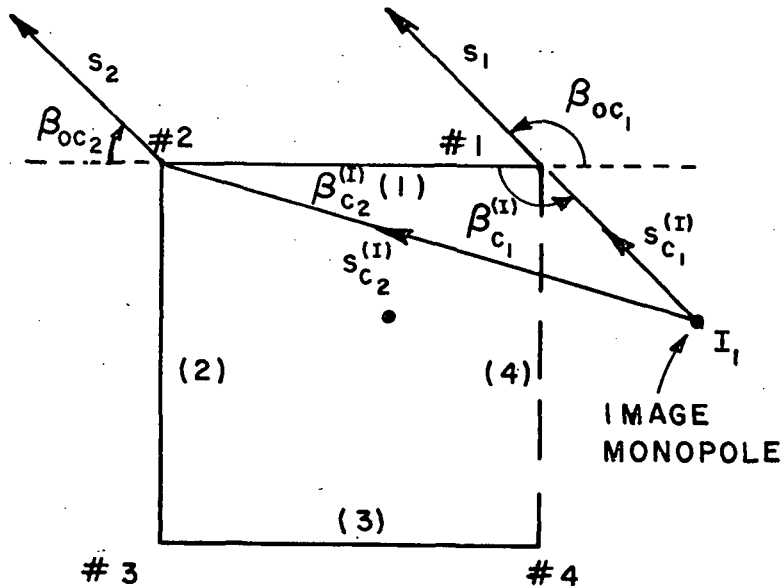
(a)
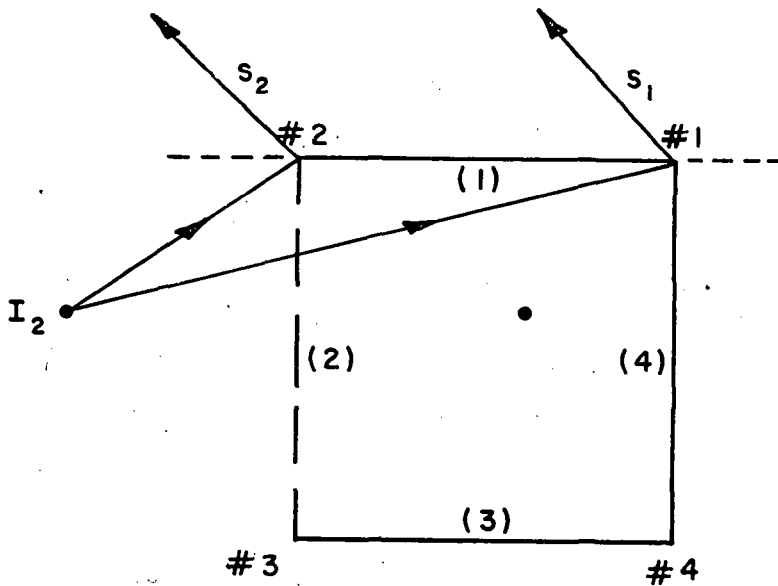
(b)

Figure 195. Edge wave mechanism due to image monopole.

$$E_{\beta_{(1)}} = E^i_{\phi_{(1)}}(c_1)\ D_s^{(ew)}(\epsilon,\pi,\pi,\beta_{o\,c_1})D_h^{(ew)}(s_{c_1}^{(I)},\tfrac{\pi}{2},o,\beta_{c_1}^{(I)})$$

$$R_1^{(I)}F(\gamma)\ \frac{e^{-jks_1}}{s_1} \tag{130}$$

where

$$E^i_{\phi_{(1)}}(c_1) = j\ \frac{e^{-jks_{c_1}^{(I)}}}{\sqrt{\epsilon \times s_{c_1}^{(I)}}}\quad (\hat{z}\cdot\hat{\phi}_{(1)})$$

and

$$R_1^{(I)} = -\ \frac{e^{-j\pi/4}}{\sqrt{2\pi k}\ \cos\beta_{c_1}^{(I)}}$$

and from $C_2$, one gets

$$E_{\beta_{(1)}} = E^i_{\phi_{(1)}}(c_2)\ D_s^{(ew)}(\epsilon,\pi,\pi,\beta_{o\,c_2})\ D_h^{(ew)}(s_{c_2}^{(I)},\tfrac{\pi}{2},o,\beta_{c_2}^{(I)})\ R_2^{(I)}$$

$$F(\gamma)\ \frac{e^{-jks_2}}{s_2} \tag{131}$$

where

1½ inch

$$E^i_{\phi(1)}(c_2) = j \; \frac{e^{-jks^{(I)}_{c_2}}}{\sqrt{\epsilon \times s^{(I)}_{c_2}}} \; (\hat{z} \cdot \hat{\phi}_{(1)})$$

and

2 inch Chapter Line

$$R^{(I)}_2 = \frac{e^{-j\pi/4}}{\sqrt{2\pi k} \; \cos \beta^{(I)}_{c_2}}$$

Two similar expressions exist due to the second image monopole shown in Figure 195-b.

THESIS / DISSERTATION

If one defines $E_\theta$ and $E_{\theta PH}$ as the principal and cross-polarized far field components defined in the spherical coordinate system, then the contribution of the $E_\beta$ and $E_\phi$ field component defined with respect to the $p^{th}$ edge coordinate system to the principal and cross-polarized field components are given by

$$E_\theta = (E_\phi \; \hat{\phi}_{(p)} + E_\beta \; \hat{\beta}_{(p)}) \cdot \hat{\theta} \qquad (132)$$

$$E_{\theta PH} = (E_\phi \; \hat{\phi}_{(p)} + E_\beta \; \hat{\beta}_{(p)}) \cdot \hat{PH} \qquad (133)$$

where $\hat{\theta}$ and $\hat{PH}$ are the $\theta$ and PH unit vectors defined in the spherical coordinate system. Note that $E_\beta$, $E_\phi$ in Equations (132, 133) define the total $\beta$ and $\phi$ field components due to all of the above diffraction mechanisms discussed above associated with edge p.

2. Discussion

The above analysis is used to compute data for different plate sizes and different monopole locations. The calculated results are compared to measured data provided by NASA Langly Laboratory and also to Moment

1 inch

Method (MM) patch mode solutions provided by Dr. Newman [33].

In Figure 196, the calculated results for the cross-polarized field component for a 1$\lambda$ square plate with a monopole mounted at the center is shown.  It is compared with measured results and the agreement between the two results is quite good.  The general behavior of the pattern is well predicted by our solution.  It was found that the contribution of the principal polarization edge and corner diffracted fields to the cross-polarized field component is minimal.  Most of the cross-polarized field is due to the edge wave mechanisms discussed earlier. Thus one would expect that when an antenna is mounted on a finite structure with several surface discontinuities such as corners, a strong cross-polarized field component will result due to the different edge wave mechanisms created by these surface discontinuities.  Note that as the surface structure is changed, one may have to consider other edge wave interactions other than the ones discussed and used in our work.  These interactions proved to be adequate for the problems and geometries analyzed here.  In Figure 197, a typical field plot is shown from a single corner on a single edge ($C_{11}$) for a 2$\lambda$ square plate with the monopole mounted at the center.  Figure 197-a shows the field due to direct monopole illumination while Figure 197-b shows that due to the image monopole illumination, even though the field due to the image monopole is approximately 12 dB lower than that of the direct monopole excitation, the combined effect of the image monopole contribution changes the final result by 1.5 to 2 dB depending on the size and location of the monopole on the plate.  The field due to two edge corners, i.e., $C_1$ is shown in Figure 198.  The deep null at PH = $45^0$ is created by the perfect cancellation of the two edge waves on the two edges forming the corner.  For a symmetric geometry, the null created by this corner lines up with that of the final pattern result.  In Figure 199, the field pattern is shown for two corners ($C_1$ and $C_4$) due to a monopole mounted at the center of a 2$\lambda$ square plate.  The pattern maxima is created by such an interaction.  The total cross polarized field due to

1 inch

1 inch

1½ inch

1 inch



PH
CALCULATED
--- MEASURED

MONOPOLE LOCATED AT
(0, 0)

−10

−20

−30
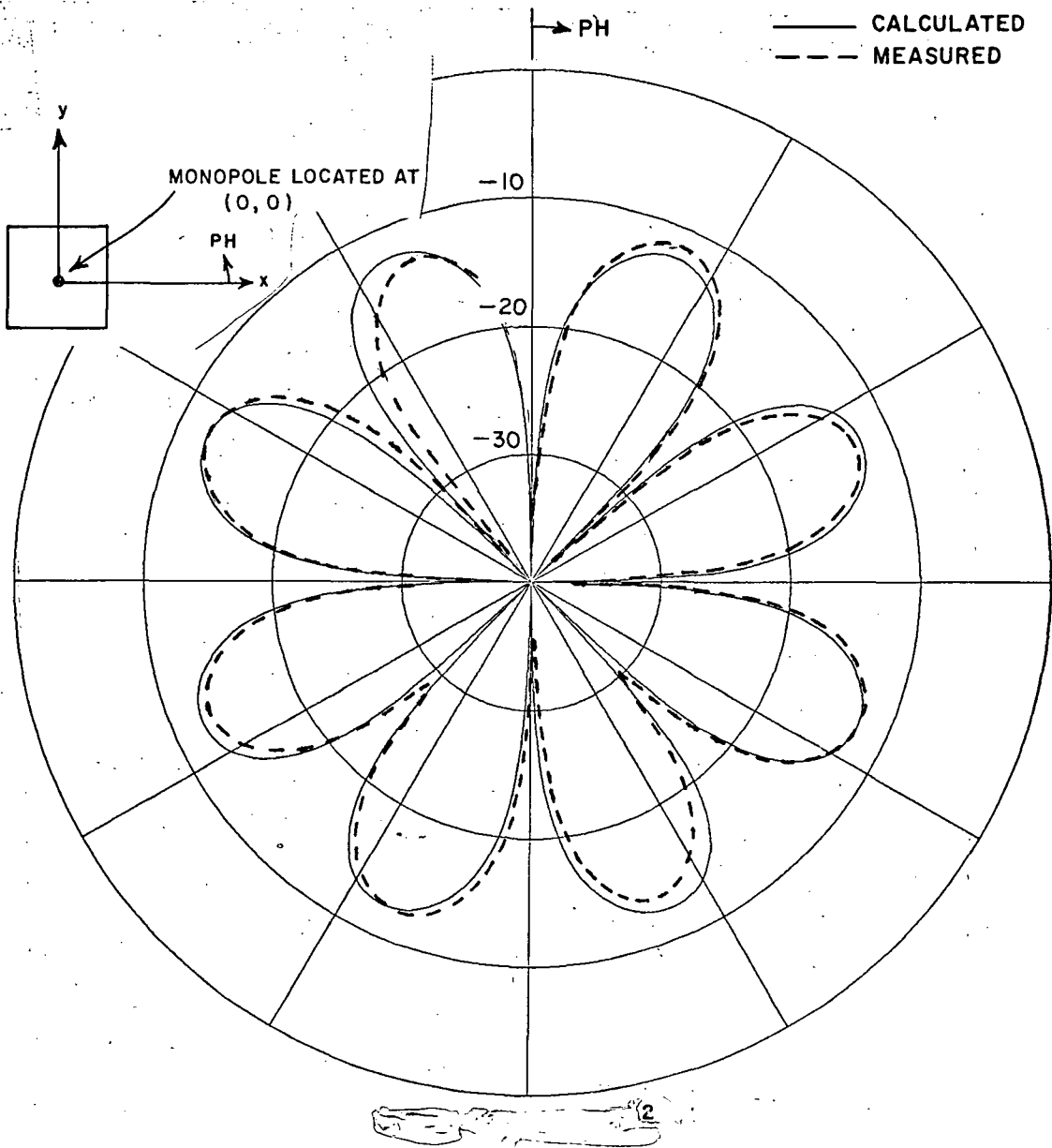
1st page Chapter end line

1st page Chapter end line

Figure 196. $E_{\theta PH}$, $\theta = 90^o$ field pattern in dB for a 1λ x 1λ plate. Pattern maxima is 8.7 dB below principal polarization.

281

1 inch

JAB/80

1½ inch

1 inch

**y**

$C_{||}$

MONOPOLE LOCATED AT
(0,0)

PH

PH

**x**
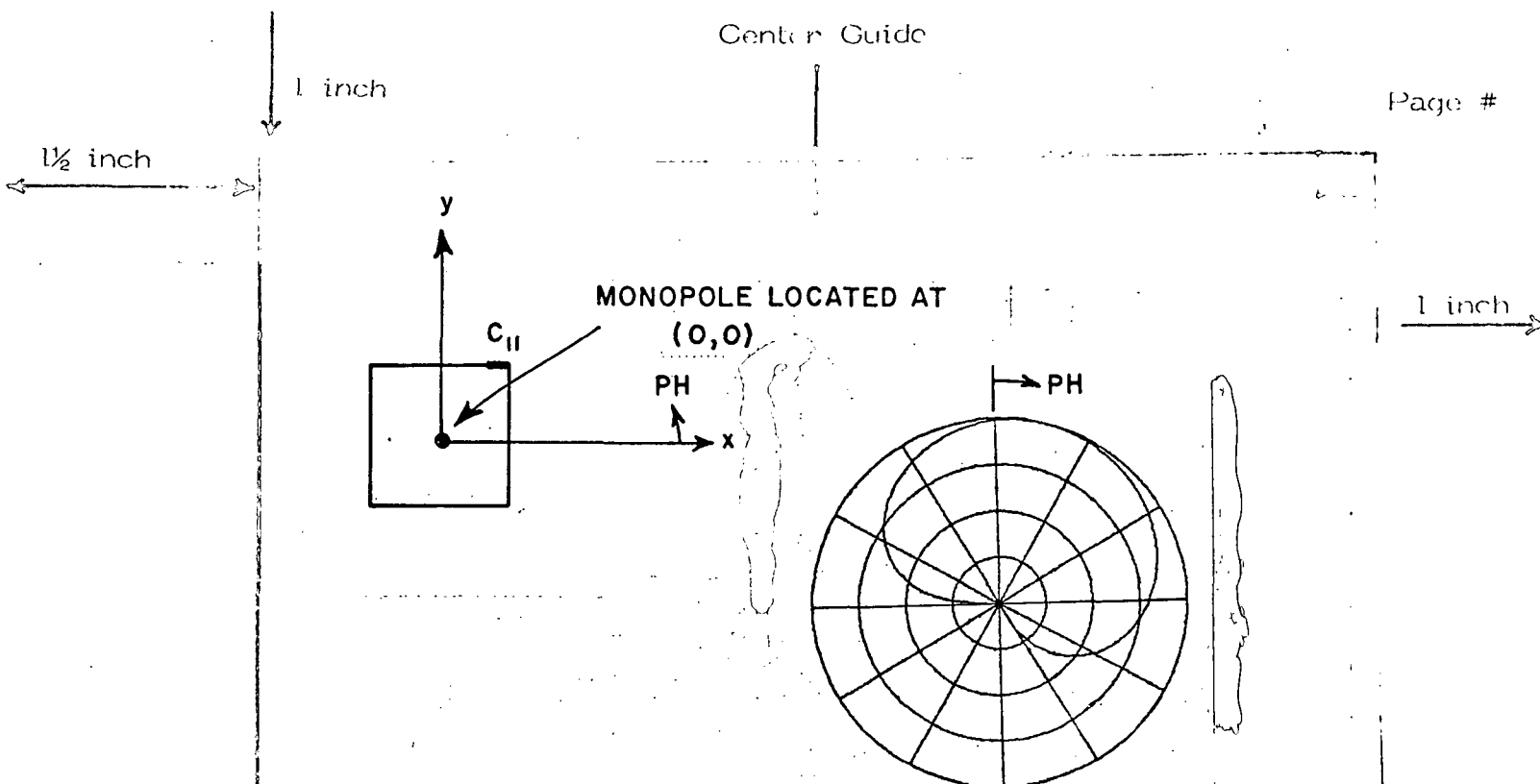
**(a) DIRECT MONOPOLE ILLUMINTION**

PH
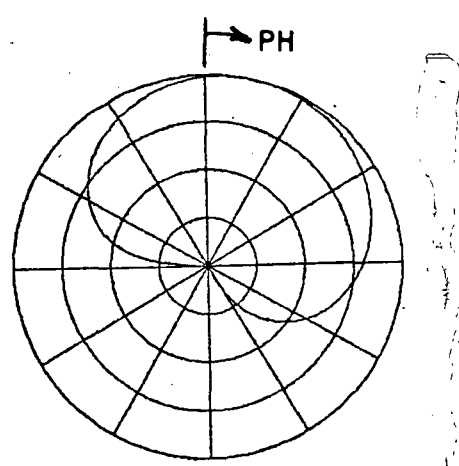
**(b) IMAGE MONOPOLE ILLUMINATION**

Figure 197. $E_{\theta PH}$, $\theta = 90^{0}$ field pattern in dB due to corner $C_{||}$ for a
2λ × 2λ plate.

11

JAB/80

1 inch

1½ inch

1 inch



y

MONOPOLE LOCATED AT
(0,0)

$C_1$

PH

x

PH
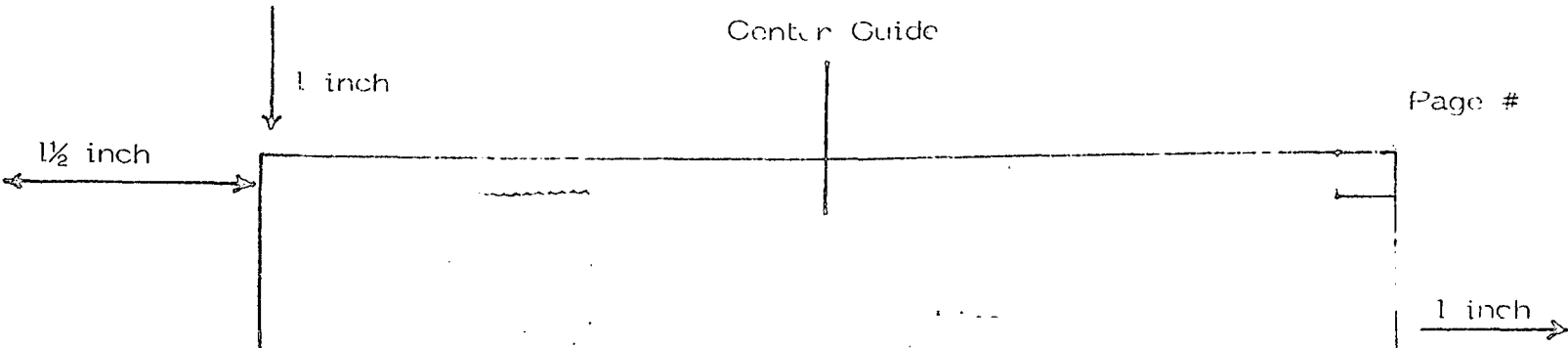
1st page Chapter end line

Figure 198. $E_{\theta PH}$, $\theta = 90^0$ field pattern in dB due to corner $C_1$ and direct
monopole illumination for a $2\lambda \times 2\lambda$ plate.

1 inch

JAB/80

1 inch

1½ inch

1 inch

2 inch Chapter Line



y

MONOPOLE LOCATED AT
(0,0)

$C_1$

PH

x

$C_4$

PH
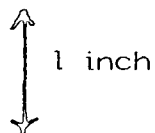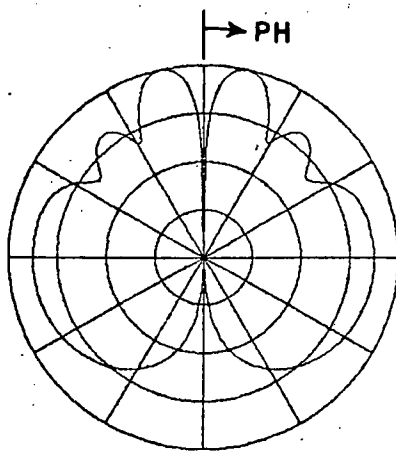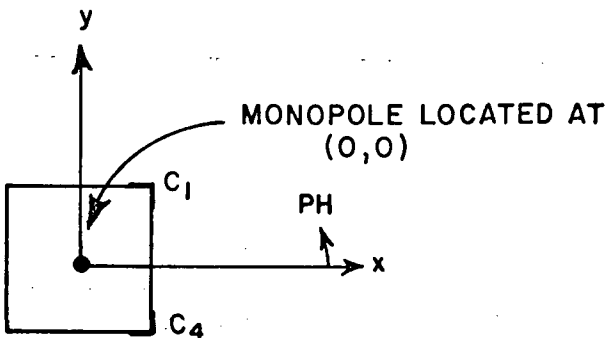
1st page Chapter end line

Figure 199. $E_{\theta PH}$, $\theta = 90^O$ field pattern in dB due to corners $C_1$, $C_4$ and direct monopole illumination for a $2\lambda \times 2\lambda$ plate.

1 inch

JAB/80

1½ inch

1 inch

a monopole mounted at the center of a 2λ square plate is shown in Figure 200. This is compared to a MM solution shown in Figure 201. The same calculated pattern is compared to measured results in Figure 202 which show good agreement between the two patterns. The MM solution which is obtained by using a 15 x 15 patch modes differs by a 1.5 dB with respect to our solution. The MM solution could be improved by either increasing the number of modes or using a non-even mode distribution, i.e., increase the number of modes around the corners since the cross-polarized field pattern structure is controlled by the surface currents near these corners. Figures 203-206 illustrate the effect of the monopole position variation. The results are compared to MM solutions.

THESIS / DISSERTATION
Typing Guide Paper

Both methods predict nearly the same pattern structure. The difference is due to the fact that one or two corners are strongly excited by the monopole. In such cases, the MM solution using 15 x 15 patch mode, is not sufficient to predict the fine details of the lobe structure. By comparing Figure 200 with Figures 203 and 205, one can notice the sensitivity of the cross-polarized field component to variations in monopole location on the plate. Figure 207 shows the results for a monopole at the center of a 3λ square plate and in Figure 208, the MM solution is shown for the same geometry. Both solutions predict nearly the same level with respect to the principal polarization ($E_\theta$) but the details of the lobe structure in the MM solution are not as good. Again the 15 x 15 patch modes used to compute the result are not sufficient to predict these details. In Figures 209 and 210, the effect of varying the monopole location on the 3λ square plate is illustrated. Similar comments hold for this case, too. In Figures 211 and 212, the computed results are shown for a monopole located at the center of a 4λ and 6λ square plate, respectively. And in Figures 213 and 214, the same results are compared to measured data. Note the non-symmetrical behavior in the measured data which indicate the sensitivity to alignment which become critical as the plate size is increased.

1st page Chapter end line
1st page Chapter end line

285
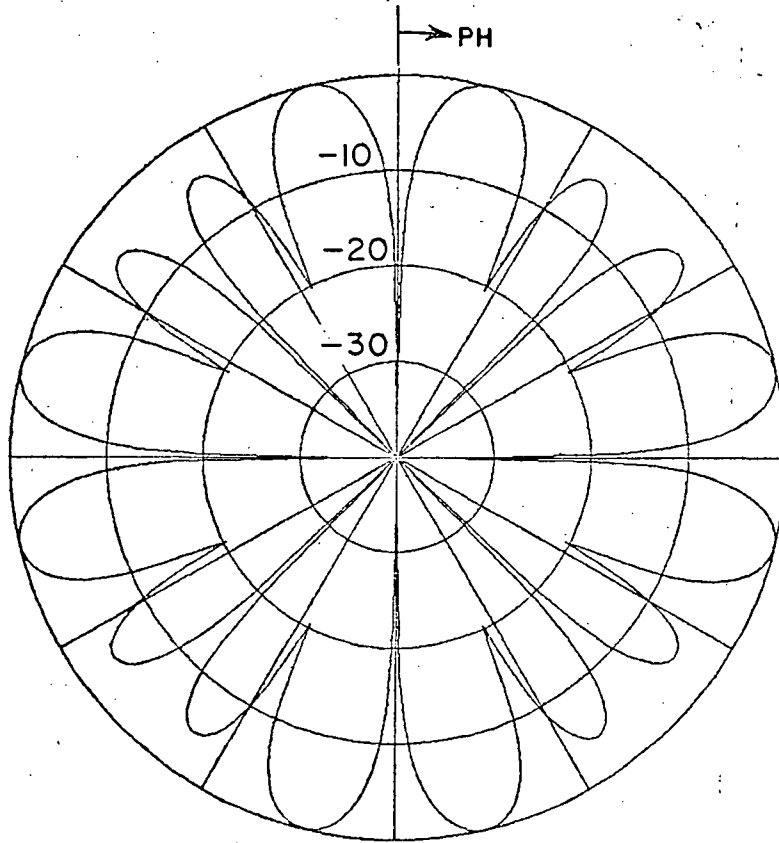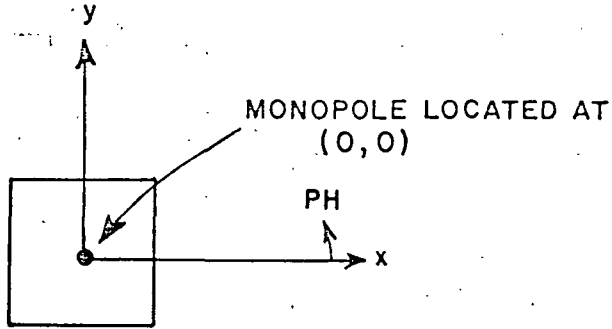
1 inch

Figure 200. $E_{\theta PH}$, $\theta = 190^0$ total field pattern in dB for a $2\lambda \times 2\lambda$ plate. Pattern maxima is 10.58 dB below principal polarization.

JAB/80

y

MONOPOLE LOCATED AT
(O, O)

PH

x

PH

−10

−20

−30
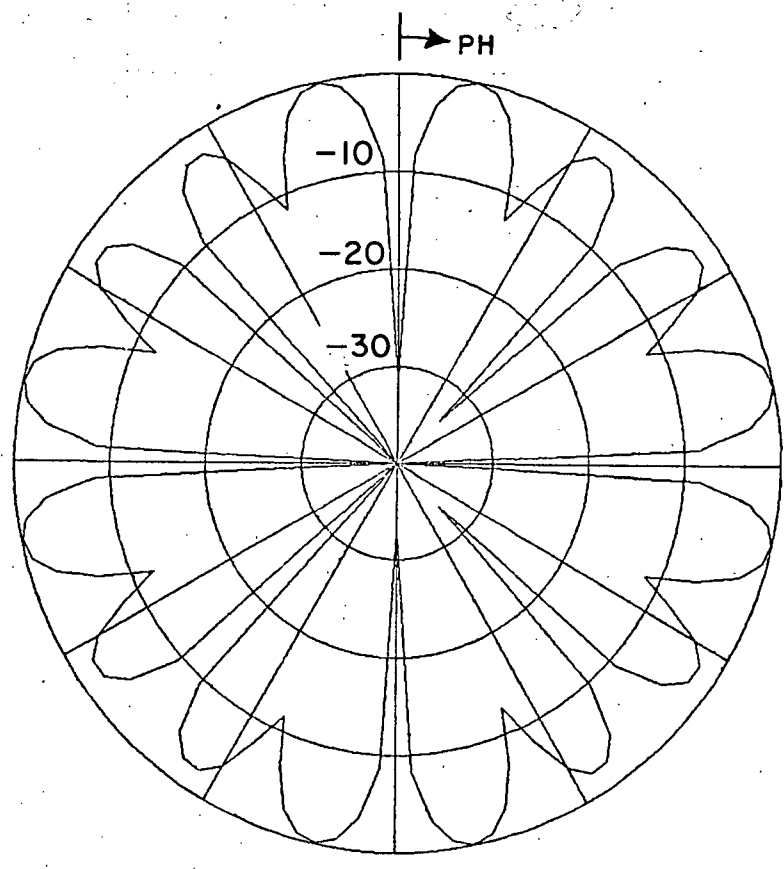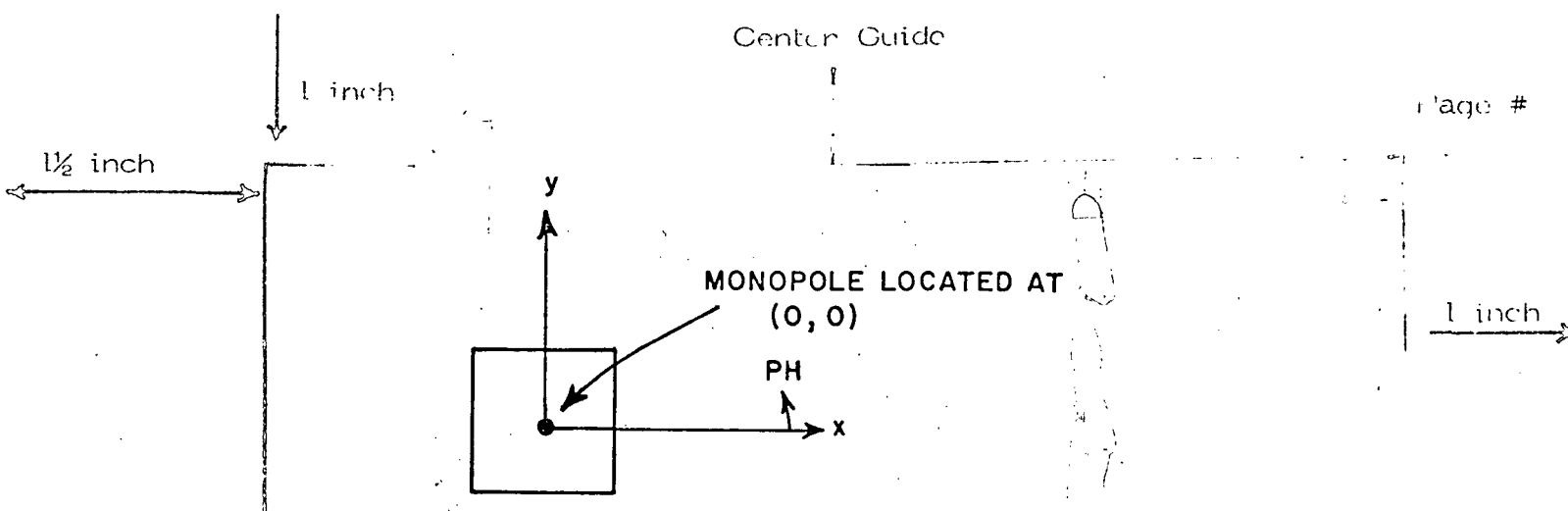
Figure 201. MM solution for $E_{\theta PH}$, $\theta = 90^0$ field pattern in dB for lane
$2\lambda \times 2\lambda$ plate. Pattern maxima is 8.81 dB below principal
polarization.

287

JAB/80

1 inch

1½ inch

inch



y

MONOPOLE LOCATED AT
(0,0)

PH

x

PH

———— CALCULATED
— — — MEASURED

−10

−20

−30
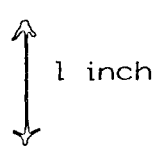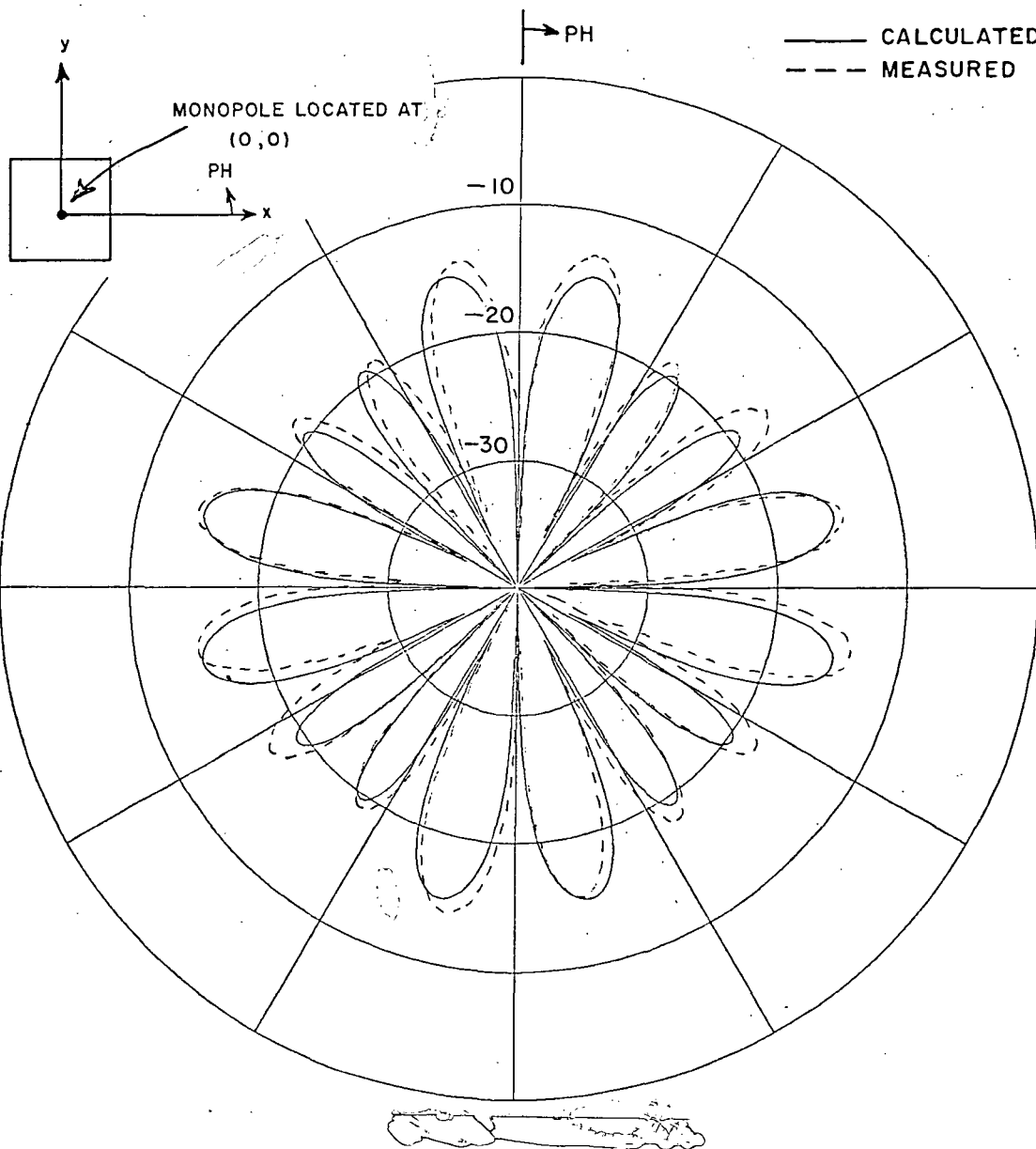
Figure 202. $E_{\theta PH}$, $\theta = 190^0$ Total field pattern in dB compared to measurement for a $2\lambda \times 2\lambda$ plate.

1st page Chapter end line

LAST TEXT LINE

288

PAGE NO.

1 inch

JAB/80

1 inch

1½ inch

1 inch

y

MONOPOLE LOCATED AT
(0.5, 0.5)

PH

x

→ PH

-10

-20

-30
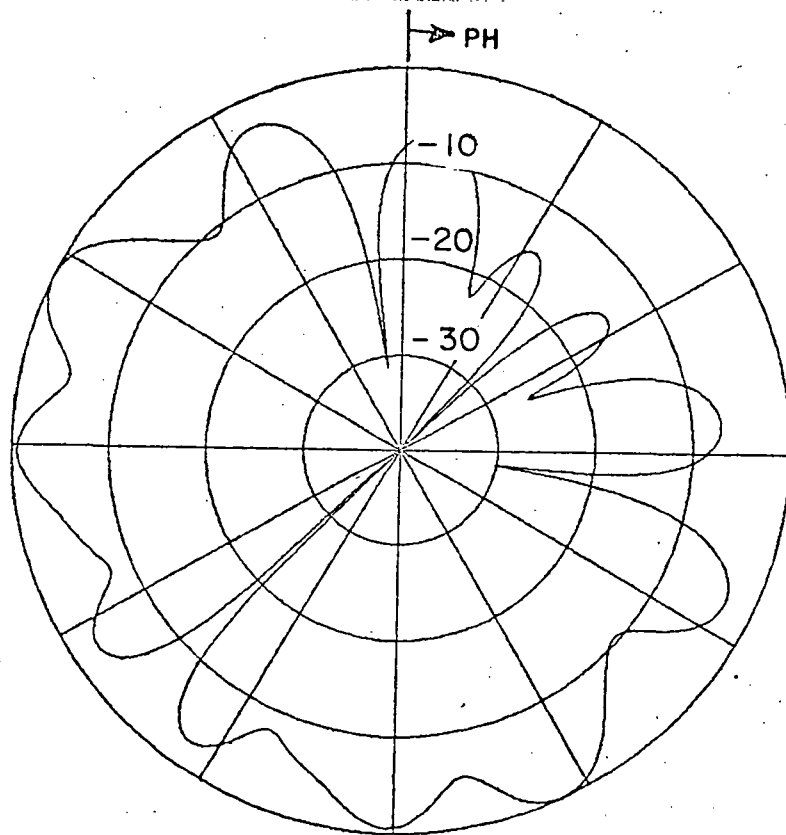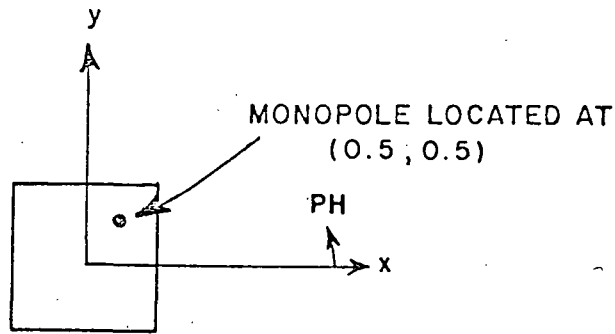
1st page Chapter end line

Figure 203. $E_{\theta PH}$, $\theta = -90^{O}$ total-field pattern in dB for a $2\lambda \times d2\lambda$ plate.
Pattern maxima is 5.75 dB below principal polarization
and the monopole is located at x = 0.5, y = 0.5.

PAGE LINE

1 inch

JAB/80
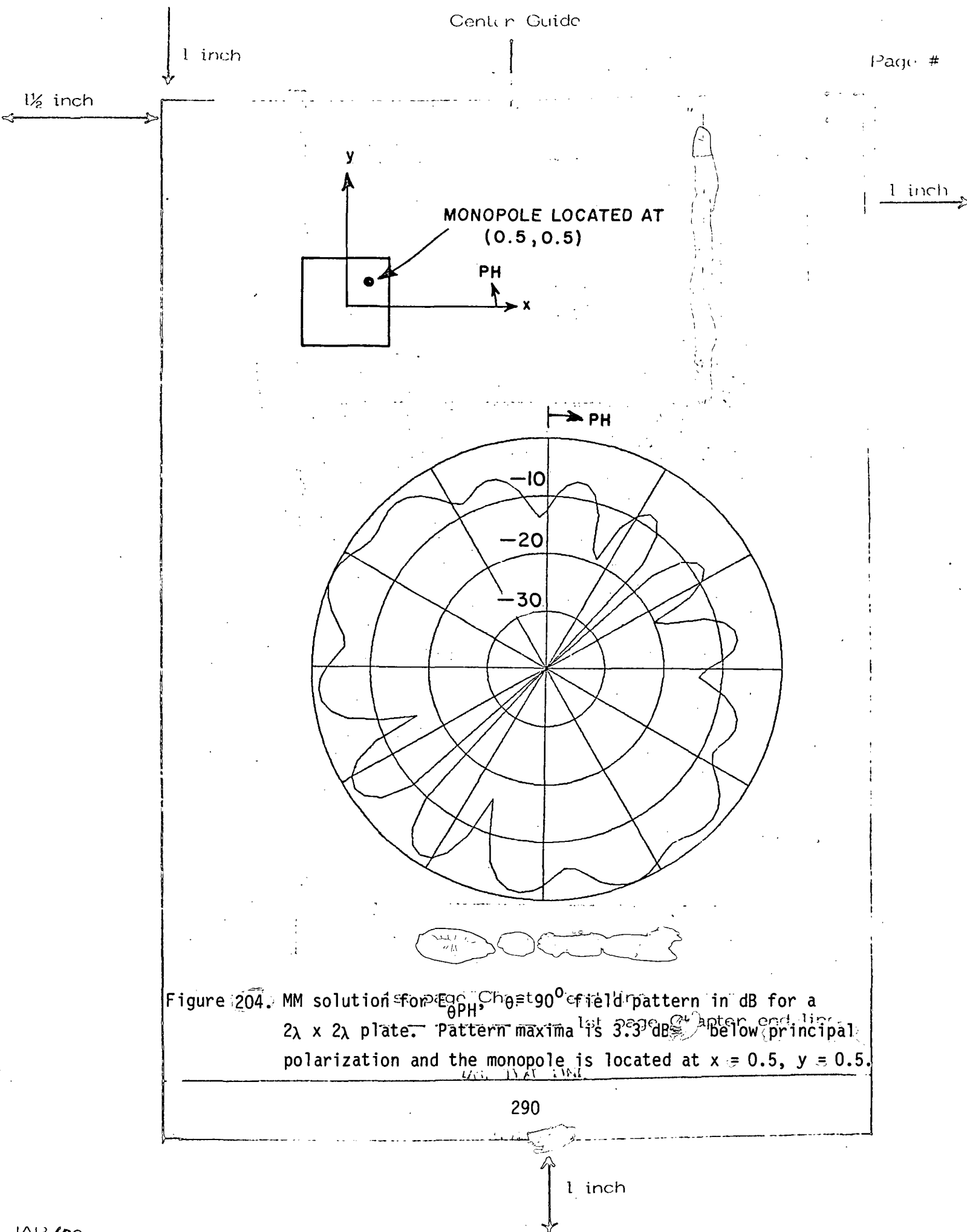
Figure 204. MM solution for $E_{\theta\varphi}$, $\theta = 90°$ field pattern in dB for a $2\lambda \times 2\lambda$ plate. Pattern maxima is 3.3 dB below principal polarization and the monopole is located at $x = 0.5$, $y = 0.5$.

JAB/80

1½ inch

1 inch

y

MONOPOLE LOCATED AT
(0, 0.5)

PH

x

PH

−10

−20

−30
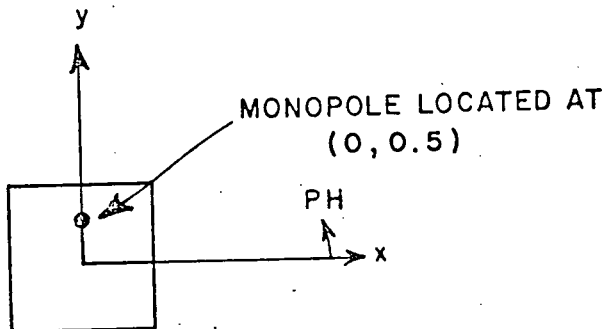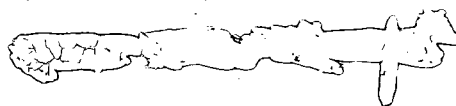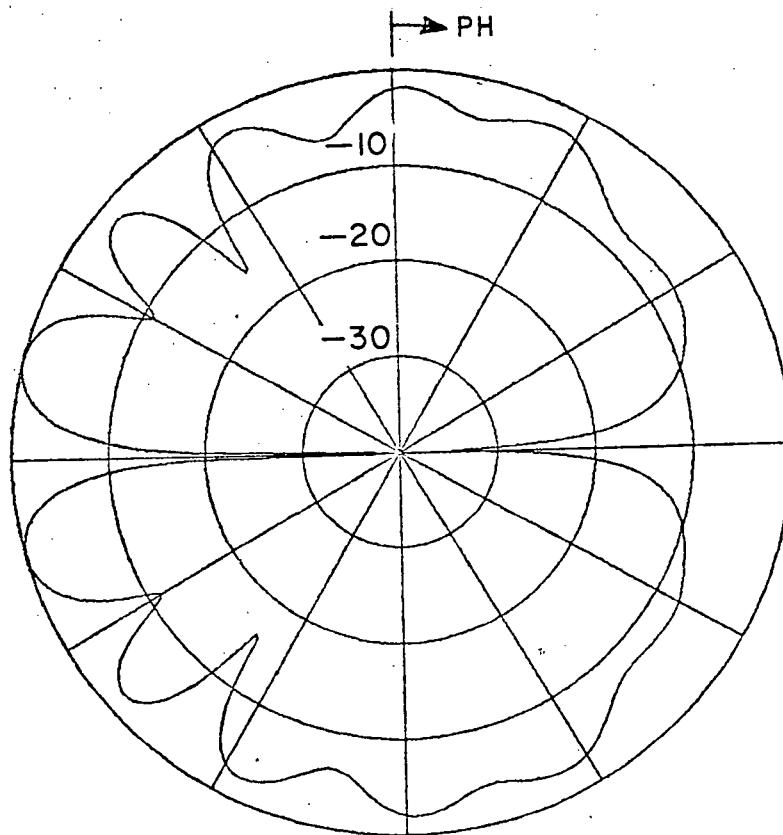
Figure 205. $E_{PH}$, $\theta = 90°$ total field pattern in dB for a $2\lambda \times 2\lambda$ plate.
1st page Chapter end line
Pattern maxima is 5.791 dB below principal polarization
1st page Chapter end line
and the monopole is located at x = 0, y = 0.5.

LAST TEXT LINE

1 inch

JAB/80

MONOPOLE LOCATED AT
(0,0.5)

PH

y

x



→ PH

−10

−20

−30
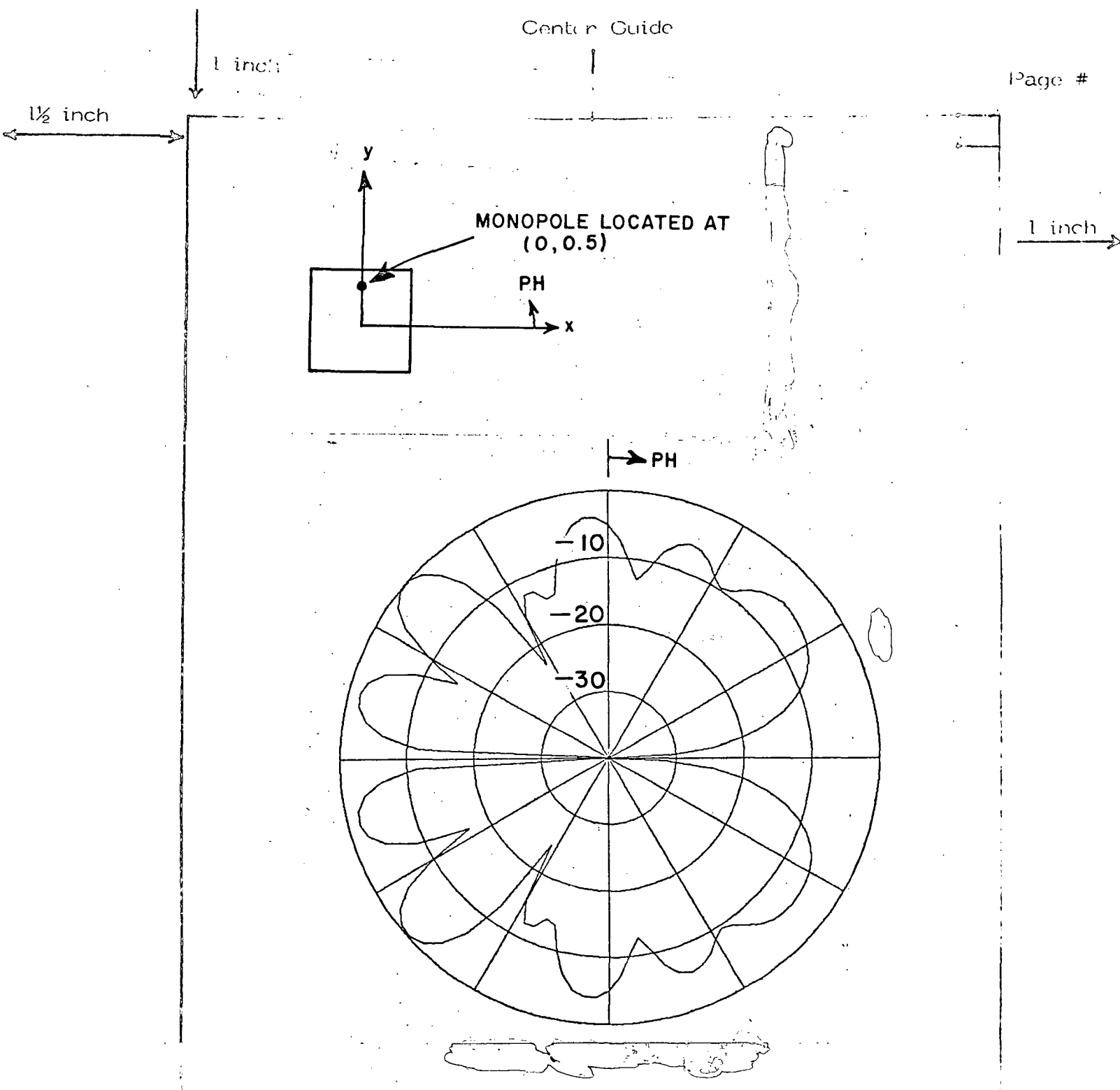
Figure 206. MM solution for $E_{\theta PH}$, $\theta = 90^0$ field pattern in dB for a 2λ x 2λ plate. Pattern maxima is 3.12 dB below principal polarization and the monopole is located at x = 0, y = 0.5.

JAB/80

1½ inch

1 inch

y

MONOPOLE LOCATED AT
(0,0)

PH

x

→ PH

-10

-20

-30
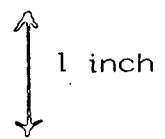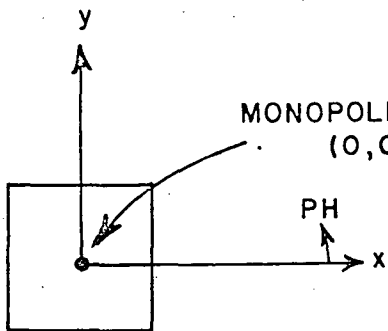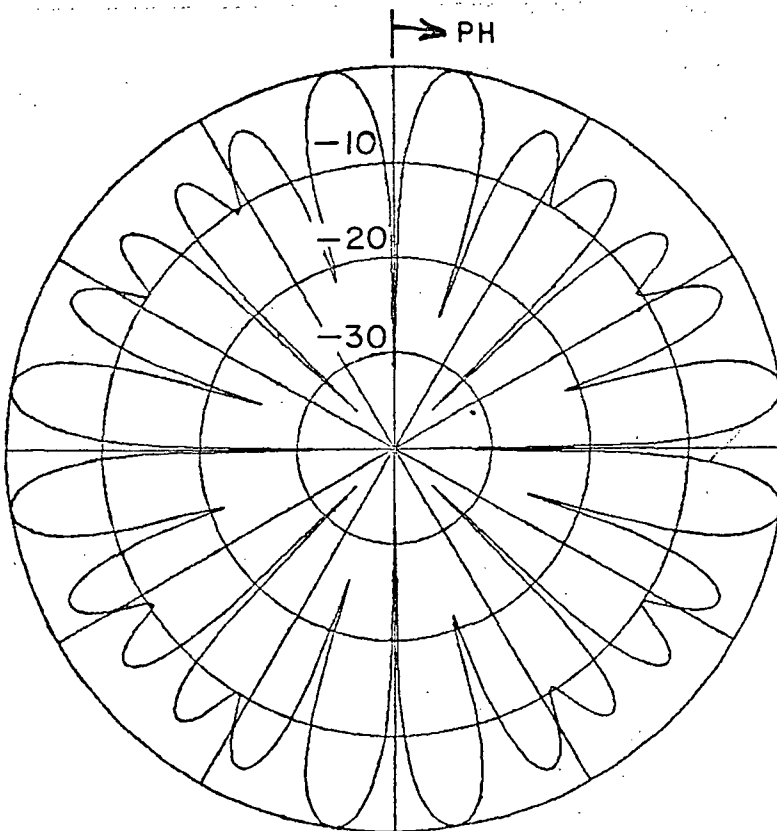
Figure 207. $E_{\theta PH}$, $\theta = 90^{\circ}$ total field pattern in dB for a $3\lambda \times 3\lambda$ plate.
1st page Chapter end line
Pattern maxima is 13.254 dB below principal polarization.
1st page Chapter end line

LAST TEXT LINE

PAGE NUMBER

1 inch

JAB/80
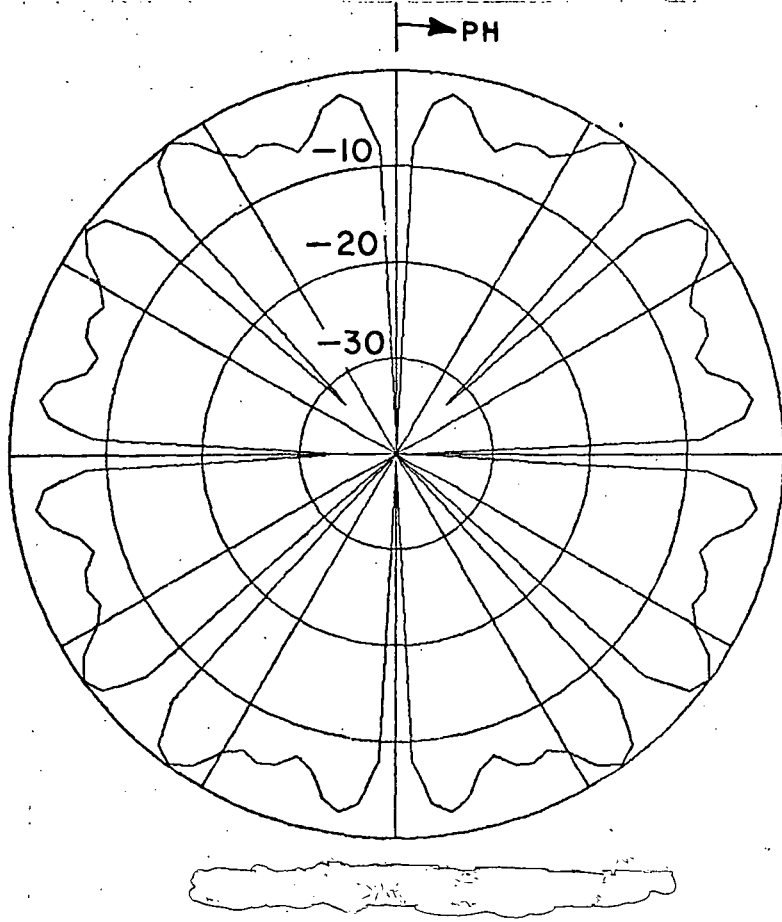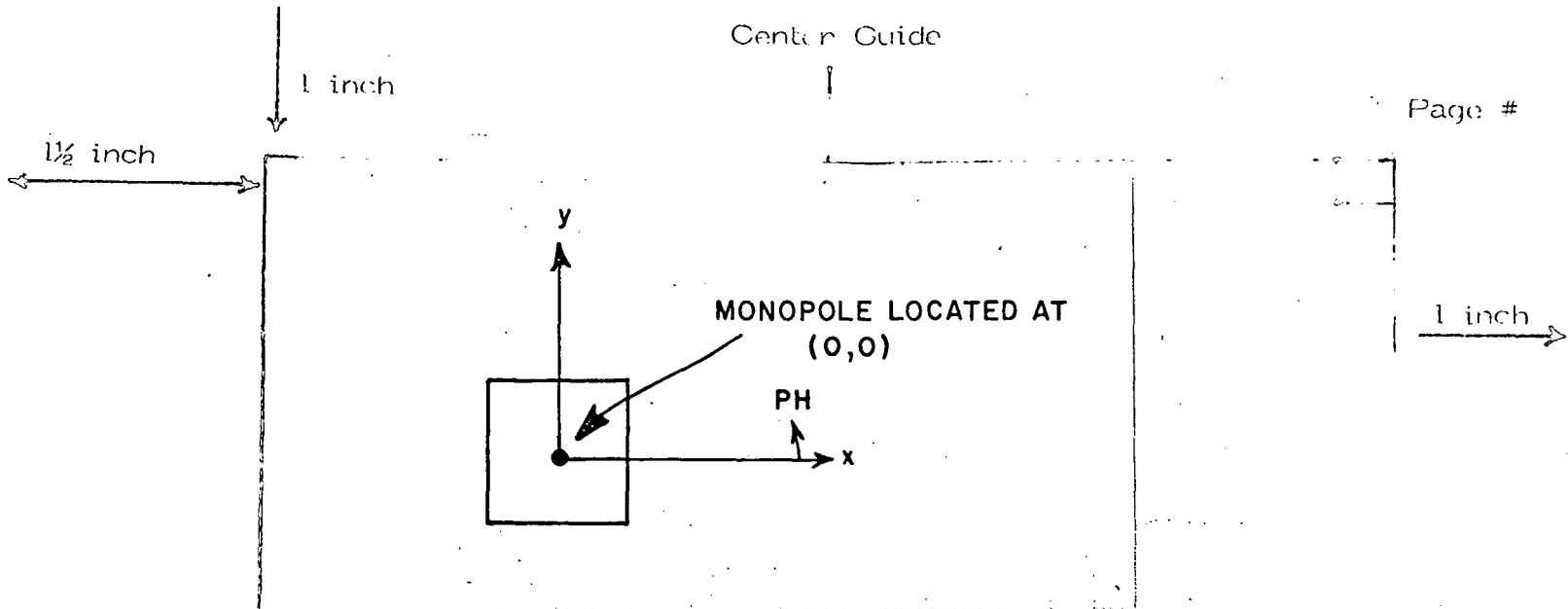
Figure 208. MM solution for $E_{\theta PH}$, $\theta = 90°$ field pattern in dB for a 3λ x 3λ plate. Pattern maxima is 13.63 dB below principal polarization.

JAB/80

1½ inch

↕ inch

y

MONOPOLE LOCATED AT
(0, 0.75)

PH

x

PH

−10

−20

−30
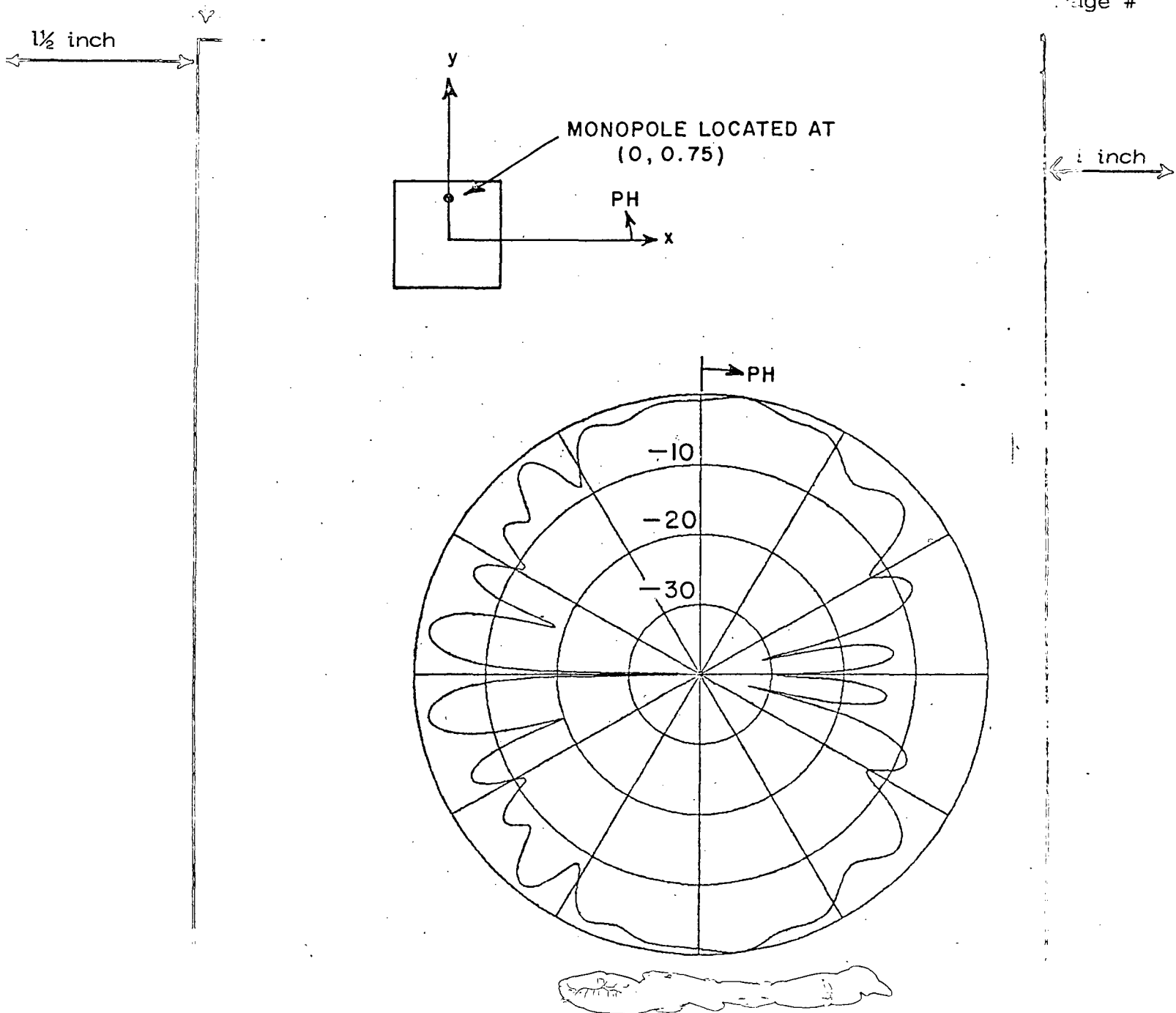
Figure 209.  $E_{\theta PH}$, $\theta = 90^0$ total field pattern in dB for a $3\lambda \times 3\lambda$ plate.
Pattern maxima is 8.89 dB below principal polarization
1st page Chapter end line
and the monopole is located at $x = 0$, $y = 0.75$.
1st page Chapter end line

LAST TEXT LINE

295

PAGE LINE

1 inch

JAB/80

y

MONOPOLE LOCATED AT
(0, 0.75)

PH

x

PH

-10

-20

-30
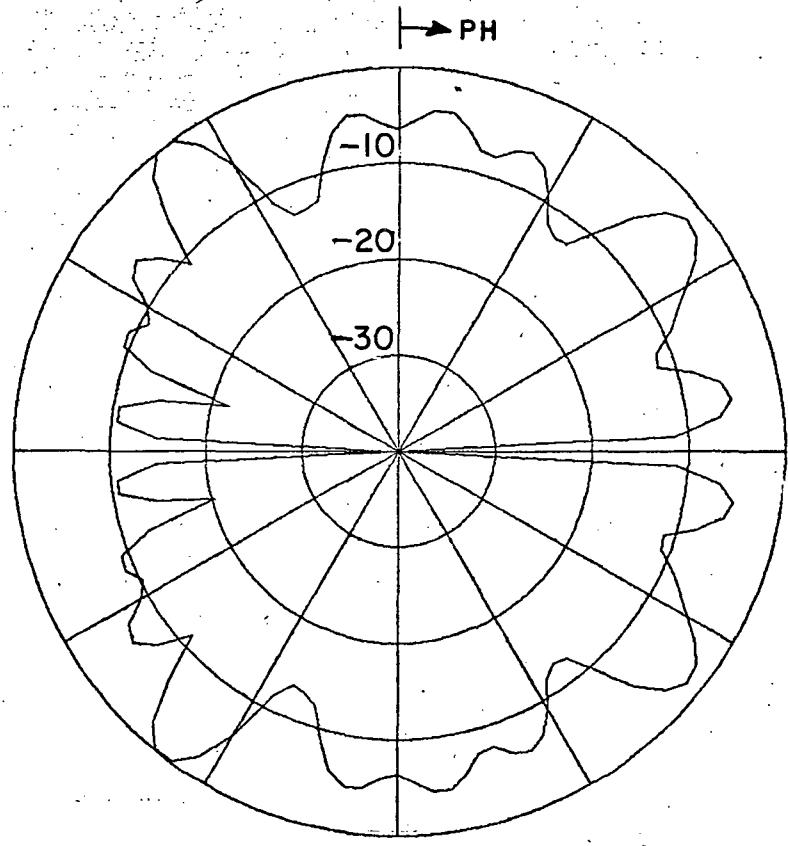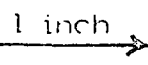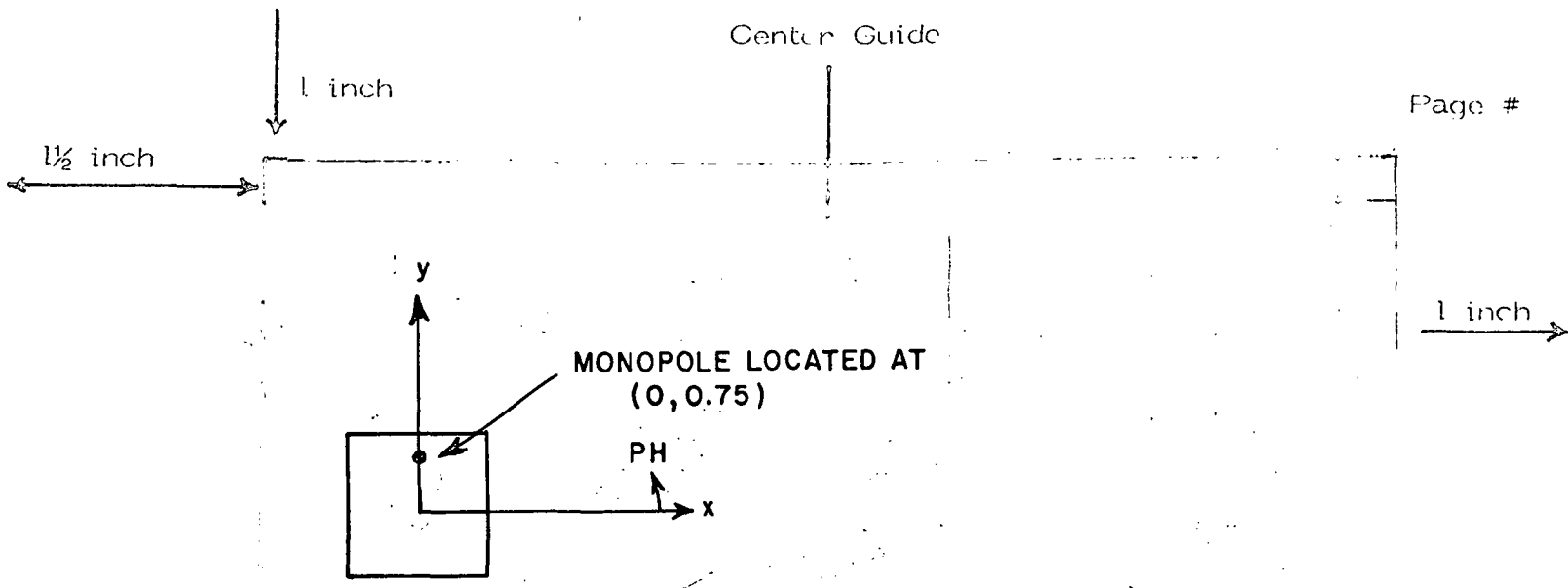
Figure 210. MM solution for $E_{\theta PH}$, $\theta = 90^{\circ}$ field pattern in dB for a
$3\lambda \times 3\lambda$ plate. Pattern maxima is 6.71 dB below principal
polarization and monopole is located at x = 0, y = 0.75.

1 inch

1½ inch

1 inch

y

MONOPOLE LOCATED AT
(0,0)

PH

x

PH

-10

-20

-30

Figure 211.  $E_{\theta PH}$, $\theta = 90^0$ total field pattern in dB for a $4\lambda$ x $4\lambda$ plate.
Pattern maxima is 16.27 dB below principal polarization.

LAST TEXT LINE

PAGE LINE

1 inch

JAB/80

1 inch

1½ inch

1 inch

y

MONOPOLE LOCATED AT
(0,0)

PH

x

PH

-10

-20

-30

1st page Chapter end line

Figure 212. $E_{PH}$, $\theta = 90^0$ total field pattern in dB for a 6 $\lambda$ x 6 $\lambda$ plate.
Pattern maxima is 17.78 dB below principal polarization.

LAST TEXT LINE

PAGE LINE

1 inch

JAB/80

Figure 213. $E_{\theta PH}$, $\theta = 90^{O}$ field pattern in dB for a $4\lambda \times 4\lambda$ plate. Calculated pattern maxima is 16.27 dB below principal polarization.
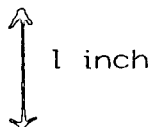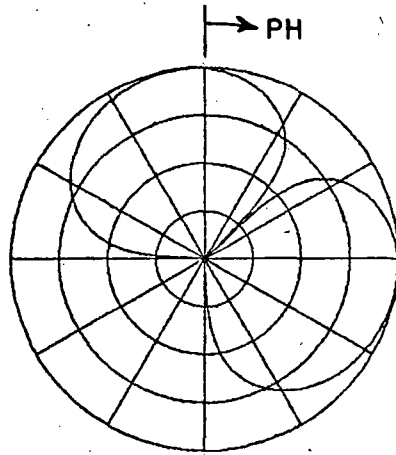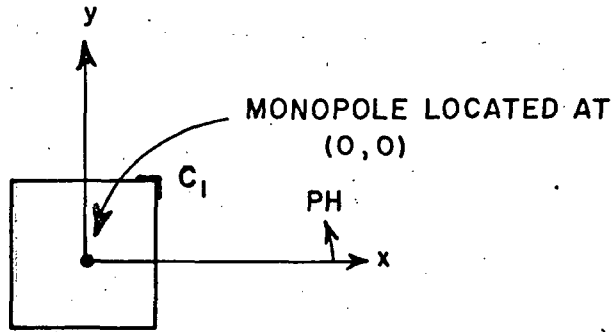
JAB/80
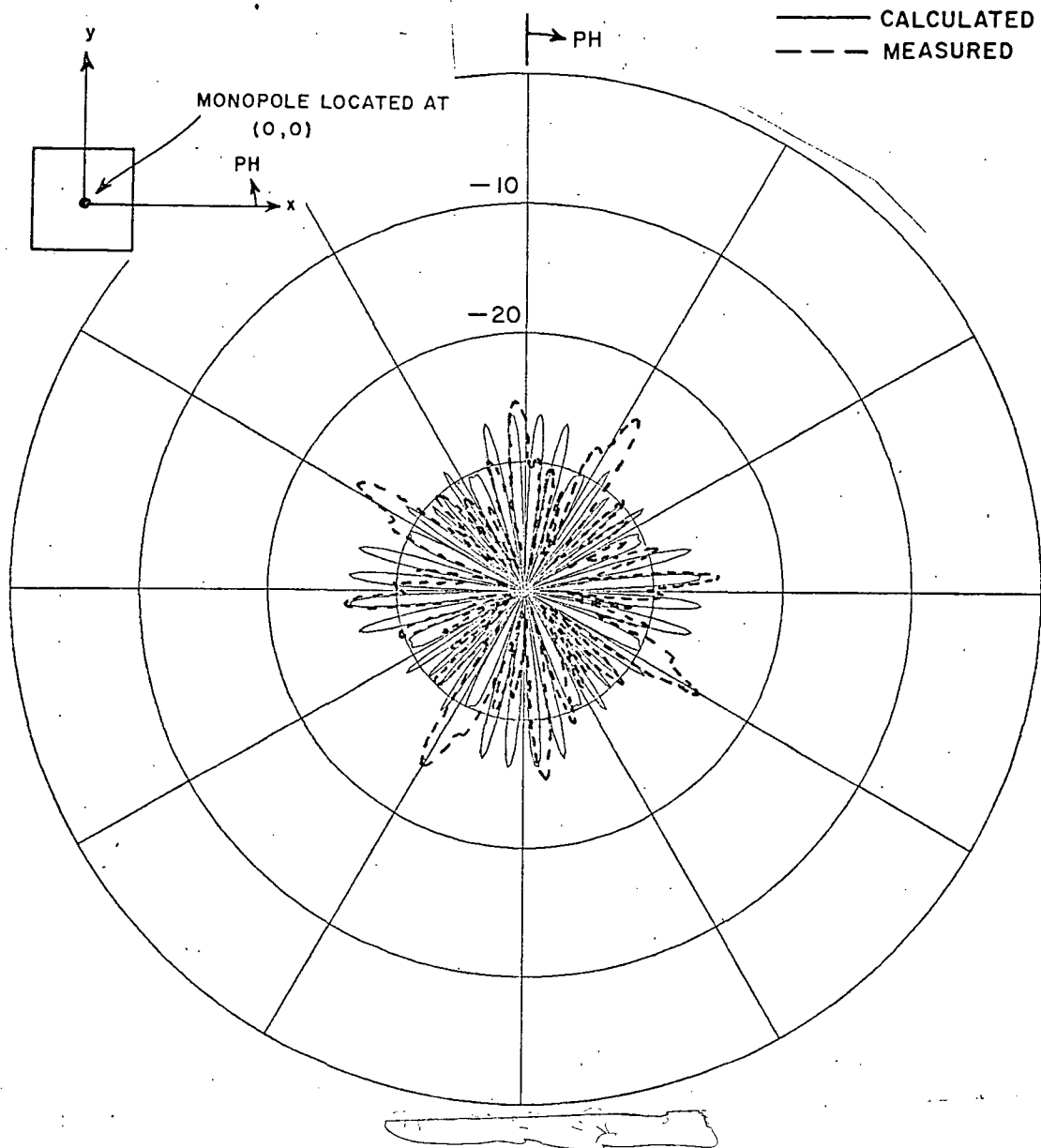
Figure 214. $E_{\theta PH}$, $\theta = 90^{\circ}$ field pattern in dB for a 6λ x 6λ plate. Calculated pattern maxima is 17.78 dB below principal polarization.

JAB/80

2 inch CHAPTER IX Line

## SUMMARY

In this work we extended the analysis presented in Chapter III
which was used to analyze the Echo width for a perfectly conducting
strip illuminated by a homogeneous plane wave to analyze the RCS pat-
terns for perfectly conducting plates of general shapes.

The Equivalent Current concept was used to compute the contributions
of edge diffraction mechanisms that involve single and multiply diffracted
rays.  The Kouyoumjian-Pathak (K-P) form of the diffraction coefficient
was used in conjunction with the Equivalent Currents when the higher
order edge interactions are involved.  This procedure made it possible
to compute the RCS of several finite plate geometries in the near edge
on region more accurately in a manner comparable to the computations
for the infinite strip.

The broadside scattered fields for flat plates has in the past re-
quired the use of a surface integral type of solution such as Physical
Optics or the Physical Theory of Diffraction.  Also the forward scattering
theorm has also been invoked to obtain a single point in the specular
direction.  The present solution uses the accuracy of present day digital
computers to obtain accurate RCS patterns in the region sufficiently
near the specular direction such that there is no need to use any of
these special procedures.

There has been considerable discussion of edge wave mechanisms in
the RCS community.  In this dissertation, we have generated a new line

1 inch

JAB/80

1½ inch

1 inch

solution involving the relatively new corner diffraction coefficient. We have successfully shown that such ray mechanisms interact with the plate edges and corners to give a very significant contribution to the RCS patterns. We have pointed out in our discussions presented earlier that these ray mechanisms interact differently with the plate structure depending on its geometry and have applied these techniques to analyze the scattering from several geometries for which no adequate prior analytic solution exists. Also these mechanisms become dominant when angles of incidence do not lie in the principal planes. Specific cases involving these general concepts are noted in the following paragraphs.

### THESIS / DISSERTATION

The H-plane RCS pattern for a general shape plate illuminated by a plane wave was analyzed in Chapter IV. The Equivalent Current method was used to compute the contribution of the first order edge diffraction to the RCS patterns. This proved to be sufficient to give good agreement between calculated and measured results. However, at high frequencies a recently understood edge wave mechanism gives a significant contribution near the edge on region as was seen in the analysis of Northrop fin. A comparison between using the EC method or the Corner diffraction method to compute the contribution of the first order diffraction mechanism was also presented. The two methods gave comparable results; a slight deviation was observed near the edge on region for some more complicated plate geometries. However, this deviation increases more when computing the RCS in a pattern plane other than the principal ones. The Corner diffraction method is a more accurate method due to the inherent error associated with the EC concept as was discussed in Chapter IV.

The H-plane RCS pattern for a disk was also considered. Our results were compared to the exact solution and good agreement was obtained near the main lobe region. However, the two results deviate considerably near edge on region where the creeping wave mechanism dominate the pattern. This mechanism was not included in our solution one

1 inch

JAB/80

In Chapter V, the E-plane patterns for a general shape plate were analyzed. This is a more complex problem since one has to include the effects of higher order diffraction mechanisms. Together with first order edge diffraction, the effect of second and third order edge diffractions were considered. The EC method was used to compute their contributions to the E-plane RCS patterns. These interactions were found to be sufficient to produce good agreement between calculated and measured data for the plate size greater than a wavelength on a side. However, for smaller size plates, fourth order edge diffraction terms or even higher may be needed to produce satisfactory results. These edge diffraction mechanisms namely single, double and triple diffraction, were also used to compute the E-plane RCS pattern for a disk. The agreement between the calculated and the exact solutions was quite good.

A more detailed analysis of the effects of the higher order interactions on the RCS pattern for a rectangular plate was presented in Chapter VI where two cases were considered. The first was the E-plane pattern where the EC method was again used to compute the contributions of the single, double and triple edge diffraction mechanisms. Good agreement between calculated and measured data was obtained throughout the pattern for square plate sizes $4\lambda$ and above. However, for $2\lambda$ square plate, slight deviation in the region of $30^\circ$ from edge on was observed. It was shown that an edge wave mechanism had to be included to compensate for this deviation. In the second case, the computation of the RCS pattern for a $2\lambda$ square plate in a plane other than the principal ones and for a vertically polarized incident plane wave was considered. Together with the single, double and triple edge diffraction mechanisms, the contributions from the newly developed edge wave diffraction coefficient were included in the RCS pattern. The effects of double and triple corner edge wave diffractions were analyzed and included in our solution. The results were compared to Moment Method patch mode solutions [33] and good agreement was obtained for the $30^\circ$ off the principal plane cases. However, not as good agreement was obtained for the $45^\circ$

and 60$^{0}$ of the principle plane cases. These higher order interactions were also found to contribute considerably to the cross-polarized RCS patterns.

The same mechanisms discussed in Chapter VI were also used in Chapter VII to analyze the E and H-plane RCS pattern for a triangular plate. The calculated results were compared to measured data and the need for a more accurate edge wave diffraction coefficient was clearly seen from this comparison. Finally, the cross-polarized field patterns for a monopole mounted on a square plate is analyzed. The edge wave mechanism was found to be the principle source of this cross-polarized field component. The calculated results were compared to MM solutions and also to measured data when available for different plate sizes and different monopole locations. Quite good agreement was obtained for many cases.

A. TOPICS FOR FURTHER WORK

There are several research points that are available for further work associated with the method presented here to analyze the RCS patterns of plates. Some of these are:

1. The use of the Corner diffraction method to compute the contributions of the double and triple or even higher order edge diffraction mechanisms to the RCS patterns: This will eliminate the problems associated with the geometry and accordingly will save considerable computer time and also correct for the errors introduced by the shadowing effects discussed in Chapter V.

2. The development of a more accurate edge wave diffraction coefficient: This should be done by first solving the basic corner diffraction problem which should lead to a more accurate corner diffraction coefficient which is still at this point in time a heuristically derived expression.

304

JAB/80

1½ inch

The availability of such diffraction coefficients will enable us
to compute the contributions of the many higher order interactions
involving the edge wave mechanism and the plate's edges and corners.
One such interaction is the simulation of the Creeping wave mechanism
by the successive edge wave forward diffraction around the plate.  Also
one could study the cross-polarization RCS patterns from plates more
accurately since the edge wave mechanism and the interactions associated
with it are one of the major sources of the cross-polarization effects
in RCS studies as was seen in Chapter VI.  In addition, one could in-
vestigate the effect of the higher order diffraction mechanisms on RCS
pattern computations in a plane other than the principal ones but with
a PH-polarized incident plane wave field.  Such a problem is more complex
than the one analyzed in Chapter VI.  This will help to improve the re-
sults presented in Chapter VII for the H-plane RCS pattern for a tri-
angular plate.

3.   The study presented in Chapter VIII on the cross-polarized
field of a monopole mounted on a square plate should be extended to
a multi-sided plate and arbitrary pattern cuts.

1st page Chapter end line
1st page Chapter end line

1 inch

JAB/80

## APPENDIX A

# DETERMINATION OF ILLUMINATED REGION OF AN EDGE

In this section, we discuss the methods used to determine the extent of the illumination of a second edge by the field diffracted from the first edge.. In Figure (215) we show two arbitrary edges, i and j, on a flat plate. The field diffracted from edge i is assumed to be a plane wave. This field illuminates part of edge j. The position vectors $\bar{P}^i_{\binom{1}{2}}$ define the location of the diffraction points $Q^i_{\binom{1}{2}}$ which define the (lower/upper) bounds of the illuminated region on edge i. Similarly, the vectors $\bar{P}^j_{\binom{1}{2}}$ define the (lower/upper) bounds of the illuminated region on edge j. The unit vector $\hat{I}$ which defines the direction of the ray diffracted from edge i to edge j makes an angle $\beta_i$ with edge unit vector $\hat{e}_i$ and is given by

$$\beta_i = \cos^{-1}\left[\hat{e}_i \cdot \hat{I}\right] \tag{134}$$

As was stated in Chapter IV, the position vectors $\bar{C}_i$, $\bar{C}_{i+1}$, $\bar{C}_j$ and $\bar{C}_{j+1}$ defines the corner locations of edges i and j respectively.

If we define the vectors, $\bar{h}_1$ and $\bar{h}_2$ as

306

JAB/80
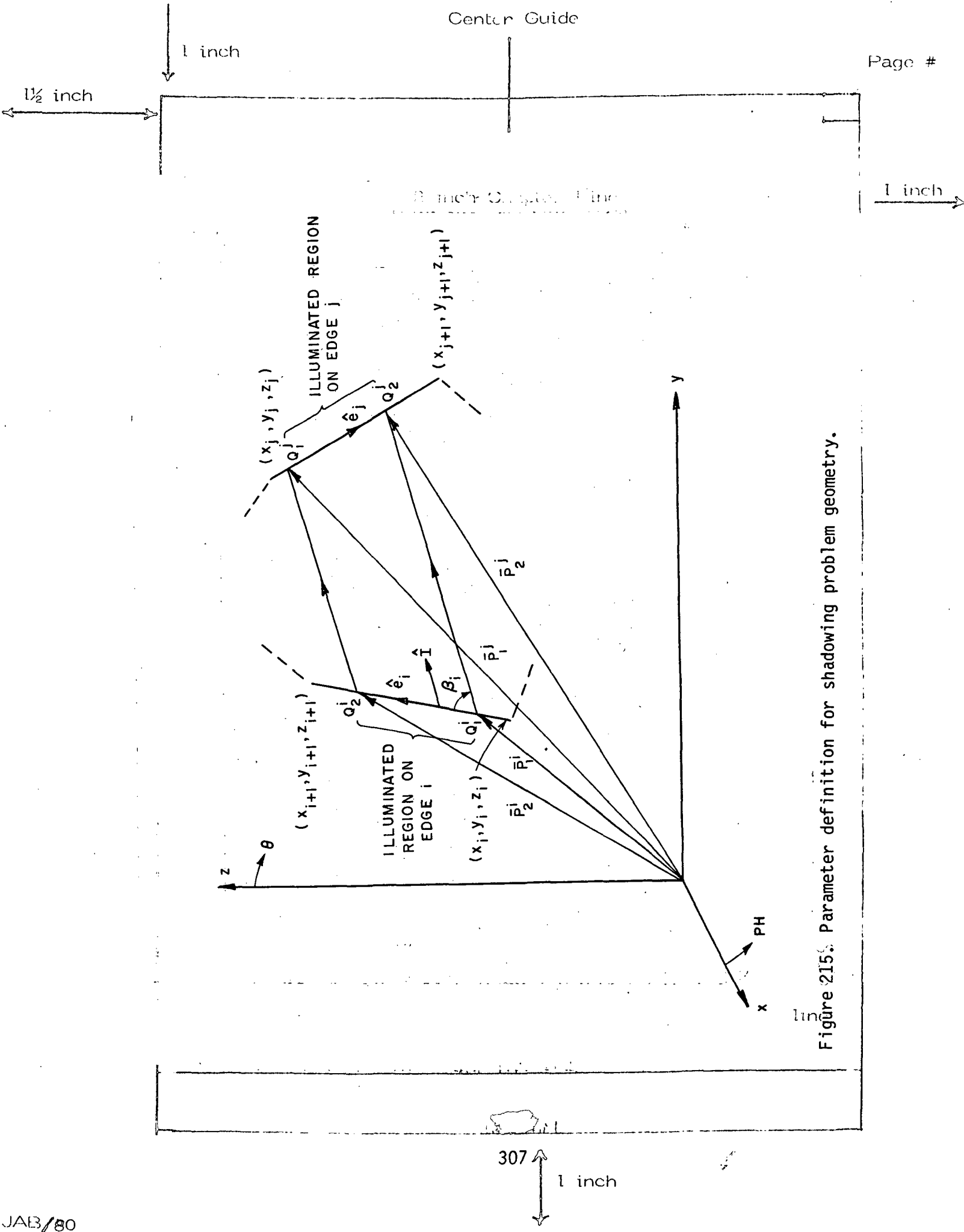
Figure 215. Parameter definition for shadowing problem geometry.
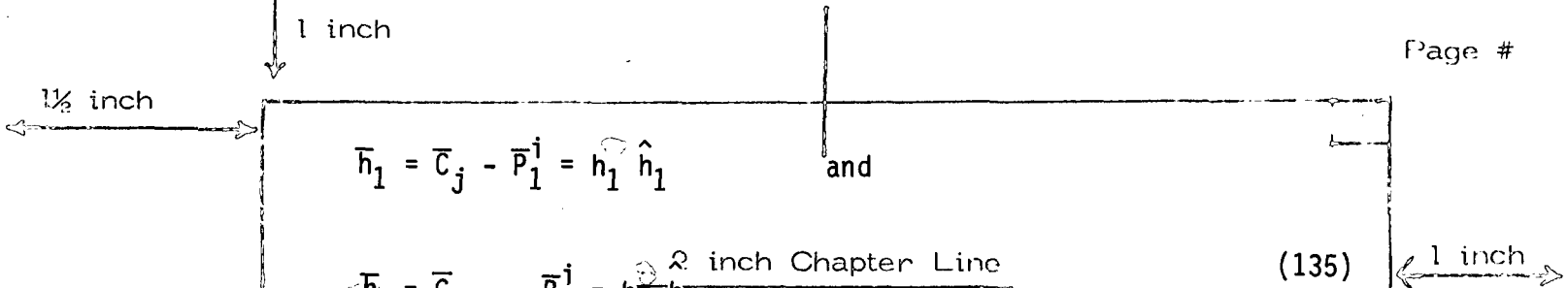
$$\overline{h}_1 = \overline{C}_j - \overline{P}_1^i = h_1 \hat{h}_1 \qquad \text{and}$$

$$\overline{h}_2 = \overline{C}_{j+1} - \overline{P}_2^i = h_2 \hat{h}_2 \tag{135}$$

where $h_{1 \atop 2}$ and $\hat{h}_{1 \atop 2}$ are the magnitude and unit vectors of $\overline{h}_{1 \atop 2}$.

## A.   CASE OF INTERSECTING VECTORS $\overline{h}_1$ AND $\overline{h}_2$

This case is illustrated in Figure 216 where the angles $\beta_1$ and $\beta_2$ are defined by

$$\beta_1 = \cos^{-1}\left[\hat{e}_i \cdot \hat{h}_1\right] \qquad \text{and}$$

$$\beta_2 = \cos^{-1}\left[-\hat{e}_i \cdot \hat{h}_2\right] \qquad . \tag{136}$$

The diffracted rays from edge i will not illuminate edge j if

$$\beta_i \leq \beta_1 \quad \text{or} \quad \beta_i \leq \beta_2$$

Once the fact that edge i illuminates edge j is established, one can proceed to find the illuminated portion of edge j.

First, let us consider finding the lower bound of the illuminated region on edge j.  Figure 217 defines the following variables

$$\overline{U}_1 = \overline{C}_j - \overline{P}_2^i = U_1 \hat{U}_1 \qquad ,$$

$$\alpha_1 = \cos^{-1}\left[\hat{e}_i \cdot \hat{U}_1\right] \qquad \text{and} \tag{137}$$

$$\alpha_2 = \pi - \beta_2$$

308

JAB/80

1 inch

1½ inch

2 inch Chapter Line

1 inch
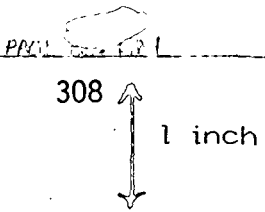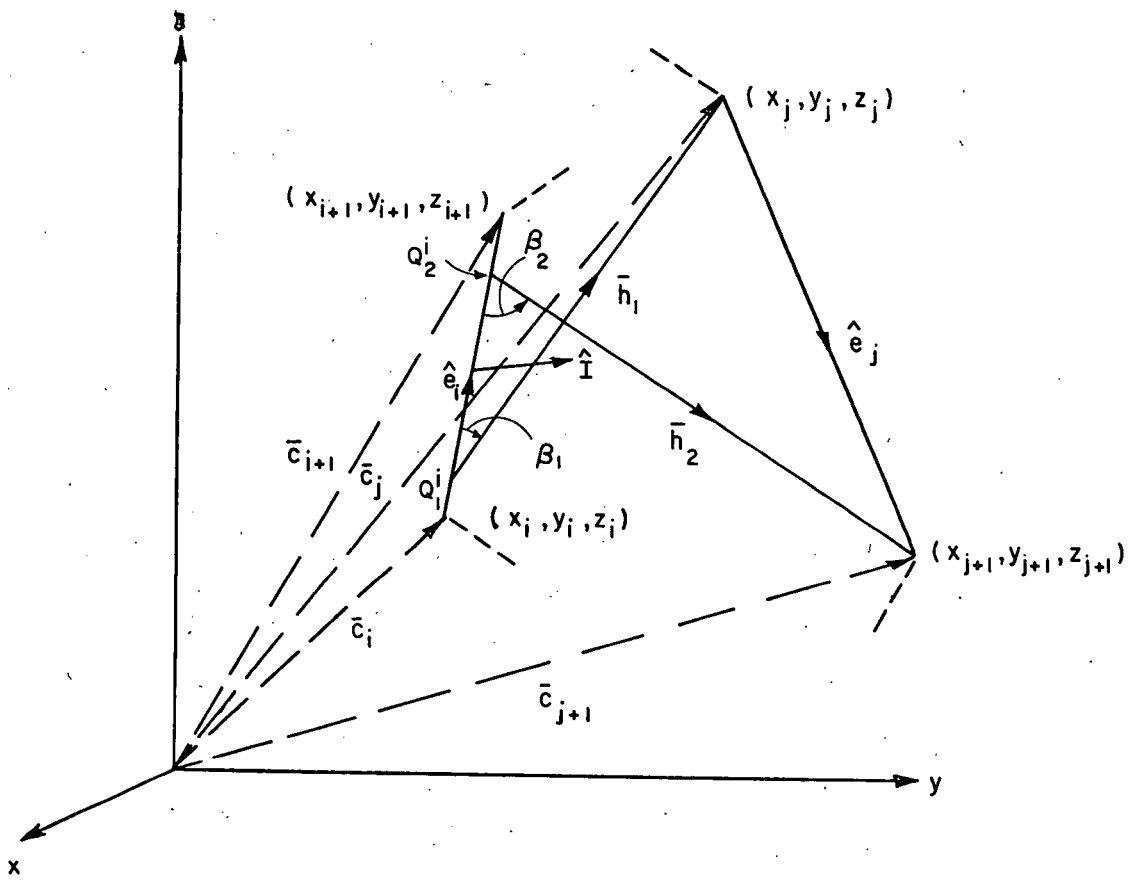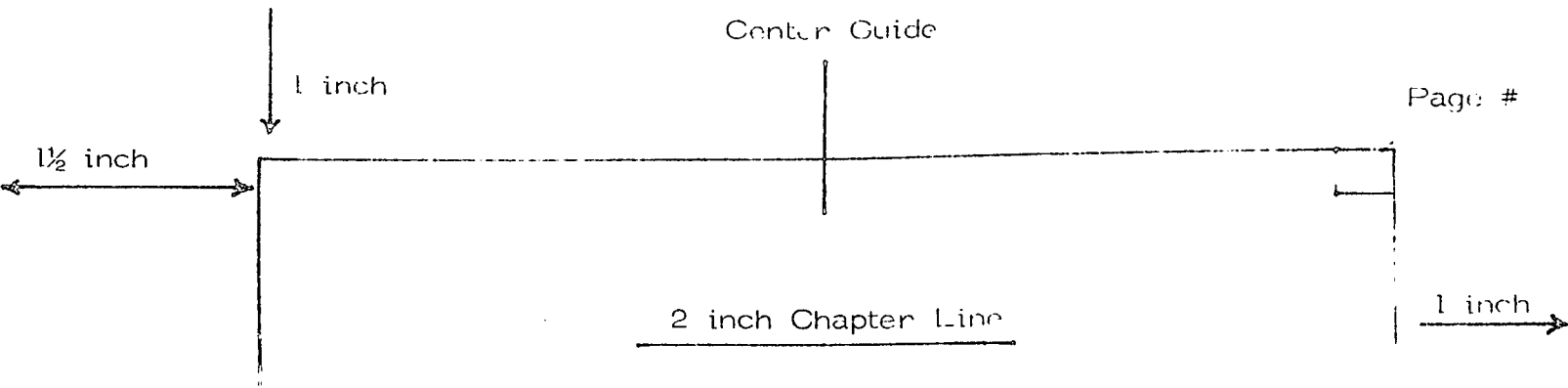
Figure 216.  Case of intersecting vectors $\bar{h}_1$ and $\bar{h}_2$.

JAB/80
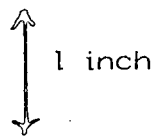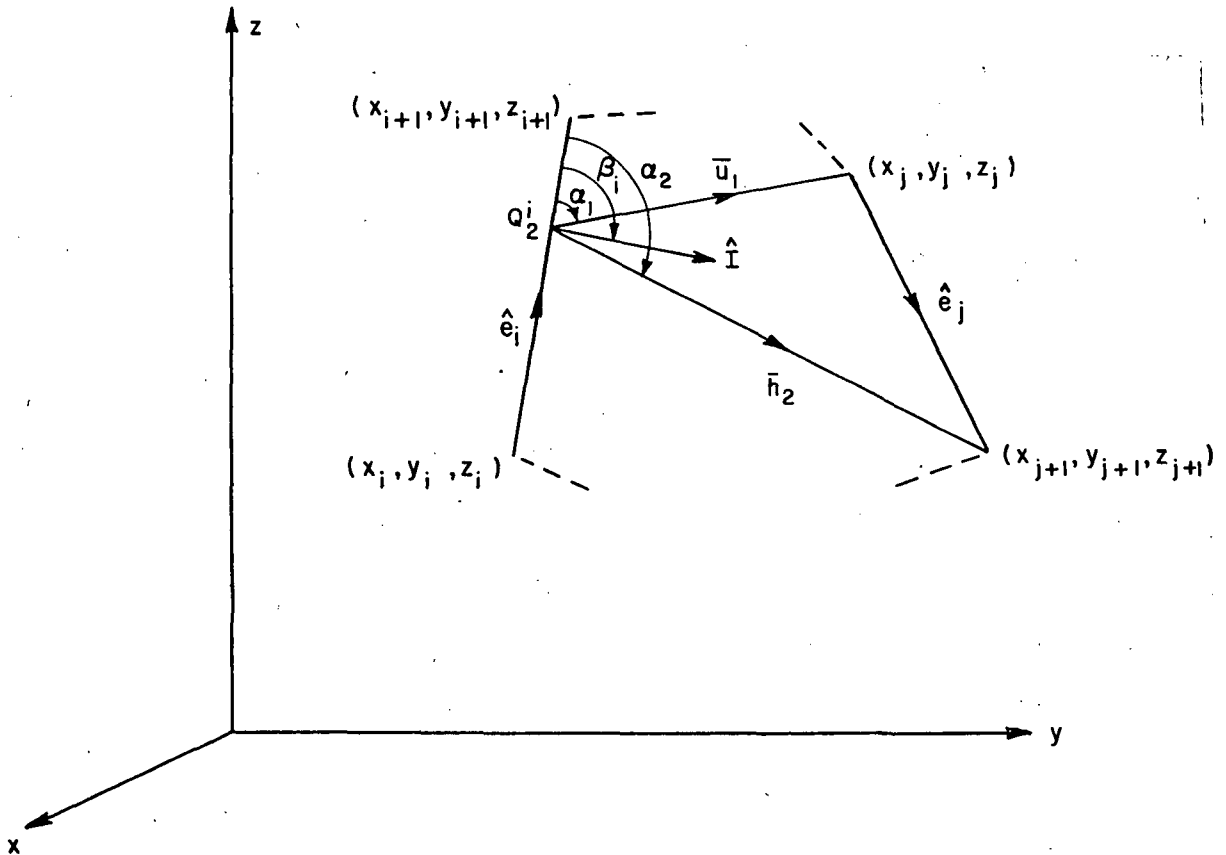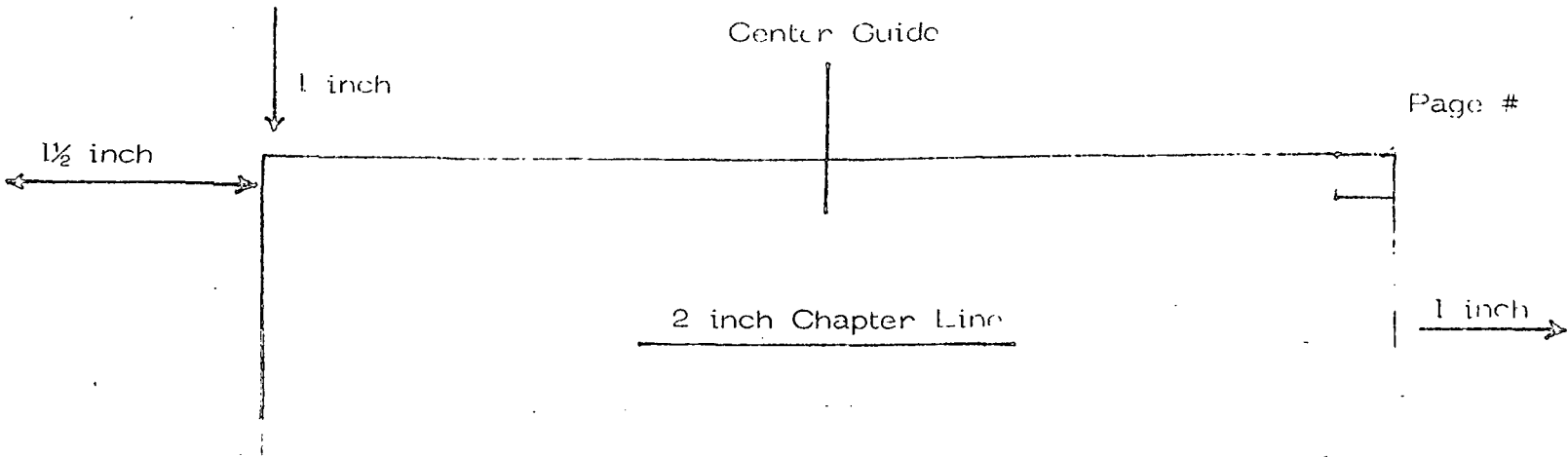
2 inch Chapter Line



Figure 217. Parameter definition for the determination of the illuminated region upper bound on edge i and lower bound on edge j.

JAB/80
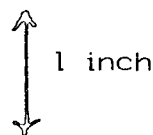
where $U_1$ and $\hat{U}_1$ are the magnitude and unit vectors of $\overline{U}_1$.

Based on the values of $\beta_i$, $\alpha_1$, and $\alpha_2$, one has to consider the following cases.

Case a:    $\alpha_1 < \beta_i < \alpha_2$

Figure 218 defines the geometry for this case. The different parameters are defined as follows:

$$\theta_j = \cos^{-1}\left[-\hat{e}_j \cdot \hat{U}_1\right]$$

$$\beta_j = \cos^{-1}\left[\hat{e}_j \cdot \hat{I}\right] \qquad , \qquad (138)$$

$$r = \frac{U_1}{\sin \beta_j} \sin \theta_j \qquad \text{and}$$

$$\overline{r} = r\,\hat{I} \qquad .$$

The illuminated region upper bound location on edge i is given by the vector $\overline{P}_2^i$, and that of the lower bound on edge j is given by

$$\overline{P}_1^j = \overline{P}_2^i + \overline{r} \qquad .$$

Case b:    $\beta_i < \alpha_1$

The geometry for this case is shown in Figure 219. The parameters shown are defined as follows

311

Center Guide

1 inch

Page #

1½ inch

2 inch Chapter Line

1 inch
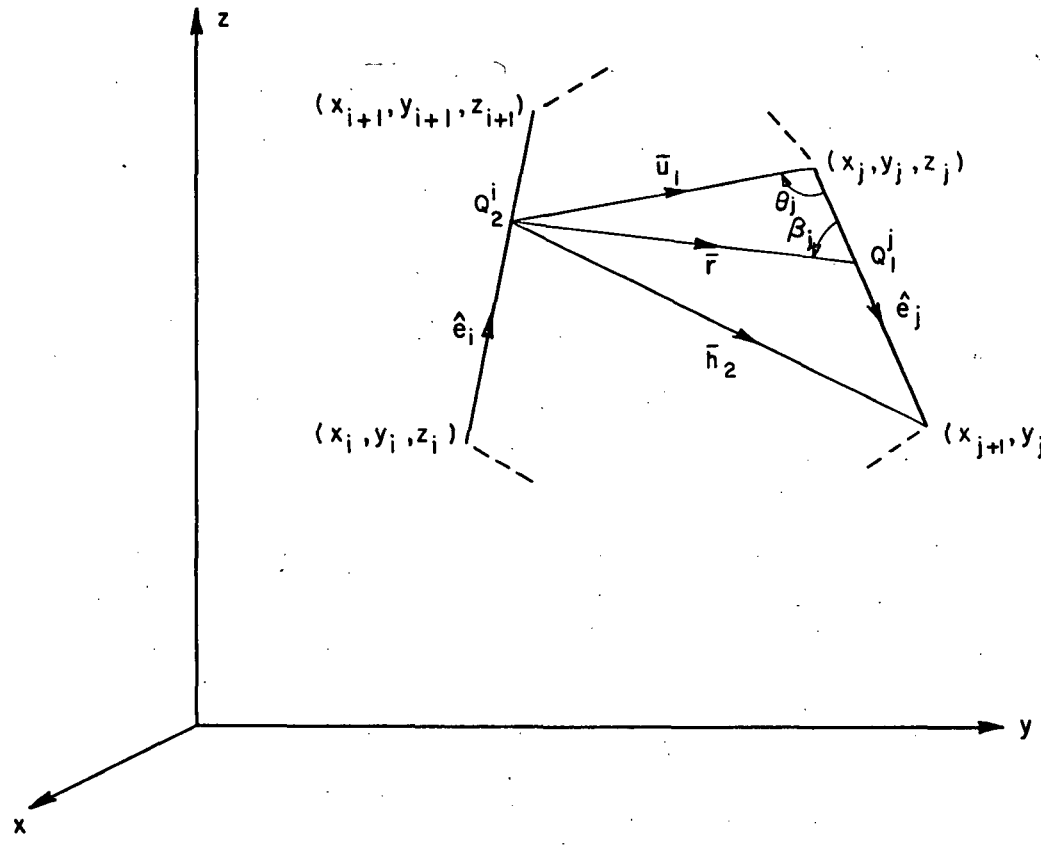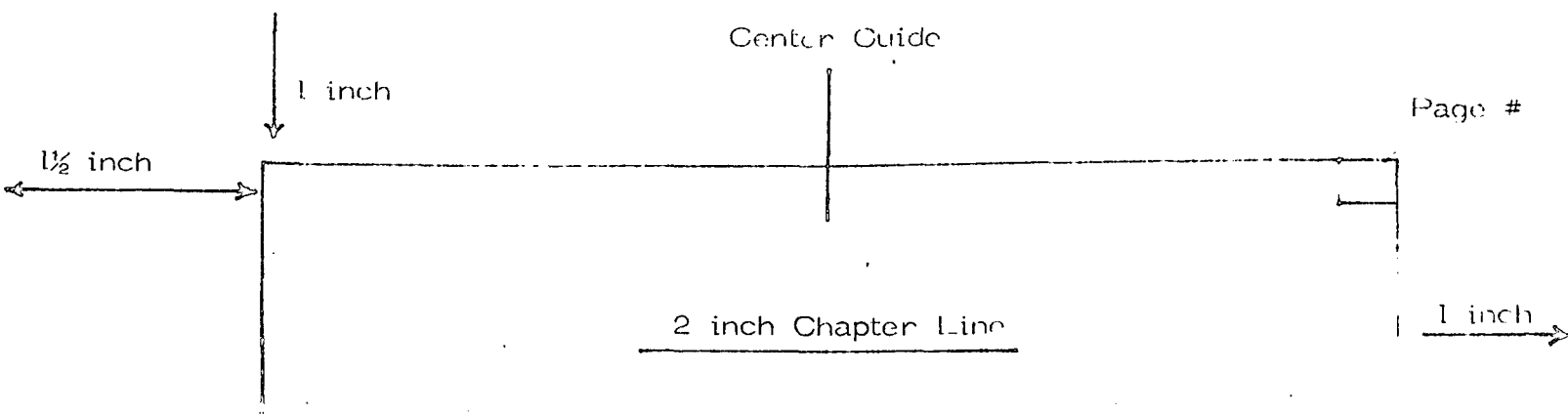
Figure 218. Determination of illuminated region upper bound on edge i
and the lower bound on edge j for case a.

JAB/80

Cent r Guide

1 inch

1½ inch

Page: #

2 inch Chapter Line

1 inch



$(x_{i+1}, y_{i+1}, z_{i+1})$

$Q_2^i$

$\hat{1}$

$\bar{u}_l$

$\theta_{i+1}$

MODIFIED POSITION
OF UPPER BOUND

$(x_j, y_j, z_j)$

$\bar{r}$

$\hat{e}_i$

$\beta_i$

$\bar{h}_2$

$\hat{e}_j$

$(x_i, y_i, z_i)$

$(x_{j+1}, y_{j+1}, z_{j+1})$

z

x

y
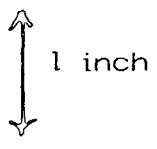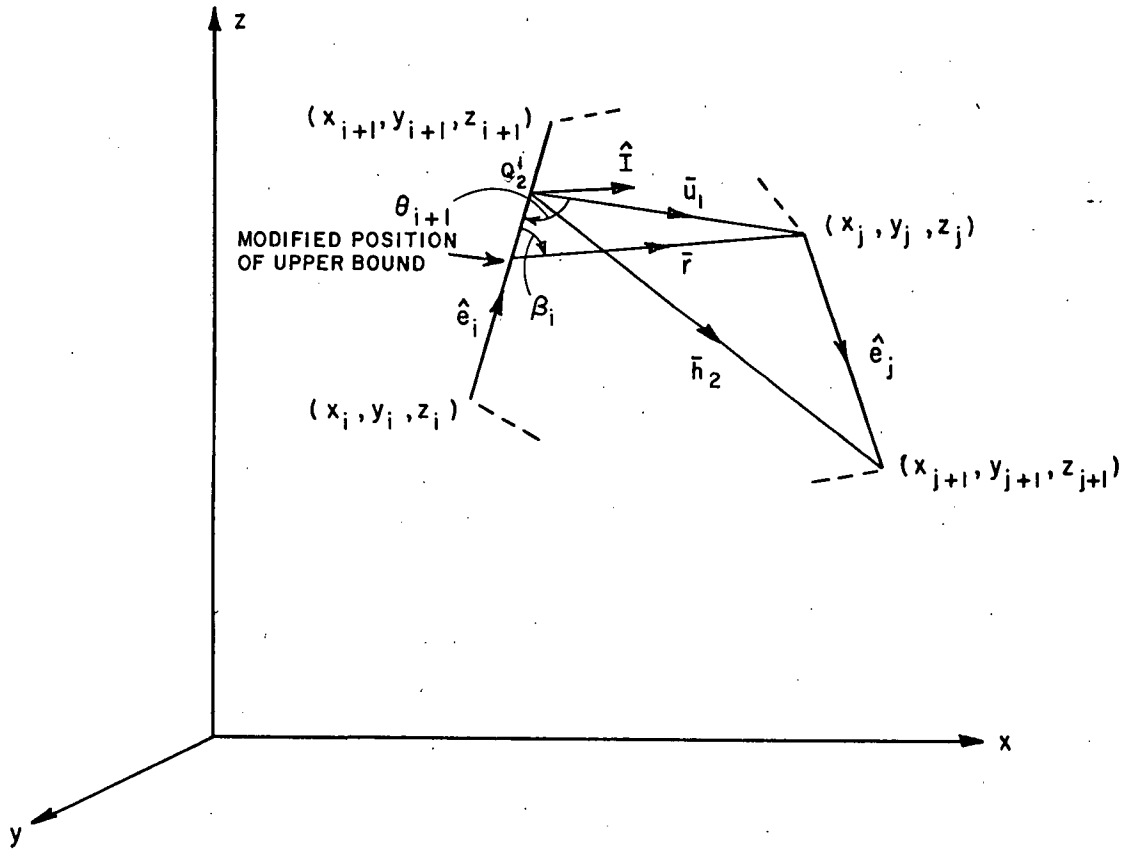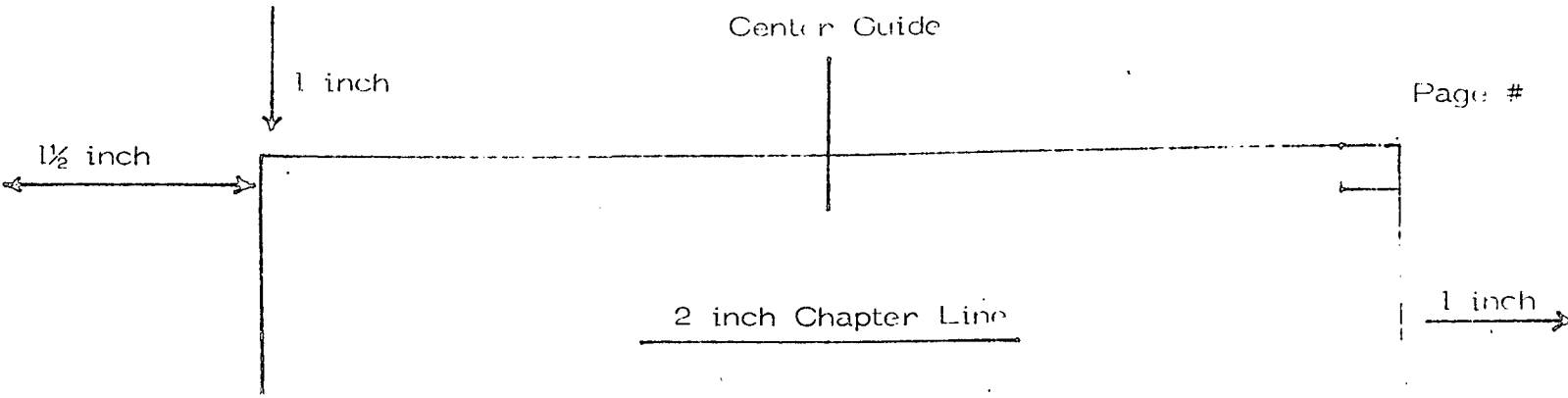
Figure 219. Determination of illuminated region upper bound on edge i
and the lower bound on edge j for case b.

1½ inch

$$\theta_{i+1} = \pi - \alpha_1 \qquad ,$$

$$r = \frac{U_1}{\sin \beta_i} \sin \theta_{i+1} \quad \text{and} \tag{139}$$

2 inch Chapter Line

$$\bar{r} = r \, \hat{I} \qquad .$$

In this case, the location of the illuminated region lower bound on edge j is given by

$$\bar{P}_1^j = \bar{C}_j \tag{140}$$

and that of the upper bound on edge i is modified to be

$$\bar{P}_2^i = \bar{P}_1^j - \bar{r} \qquad .$$

For the special case $\beta_i = \alpha_1$, the location of the upper bound on edge i is not modified and that of the lower bound on edge j is given by Equation (140).

To find the location of the illuminated region upper bound on edge j, one proceeds in a similar manner as above. Figure 220 defines the geometry involved where

$$\bar{V}_1 = \bar{C}_{j+1} - \bar{P}_1^i = V_1 \, \hat{V}_1 \qquad \text{and}$$

$$\gamma_1 = \cos^{-1} \left[ \hat{e}_i \cdot \hat{V}_1 \right] \qquad . \tag{141}$$

where $V_1$ and $\hat{V}_1$ are the magnitude and unit vectors of $\bar{V}_1$. Depending on the values of $\beta_1$, $\beta_i$ and $\gamma_1$ one has to consider the following cases:

1st page Chapter end line

1st page Chapter end line

LAST TEXT LINE

314

PAGE #

JAB/80

Center Guide
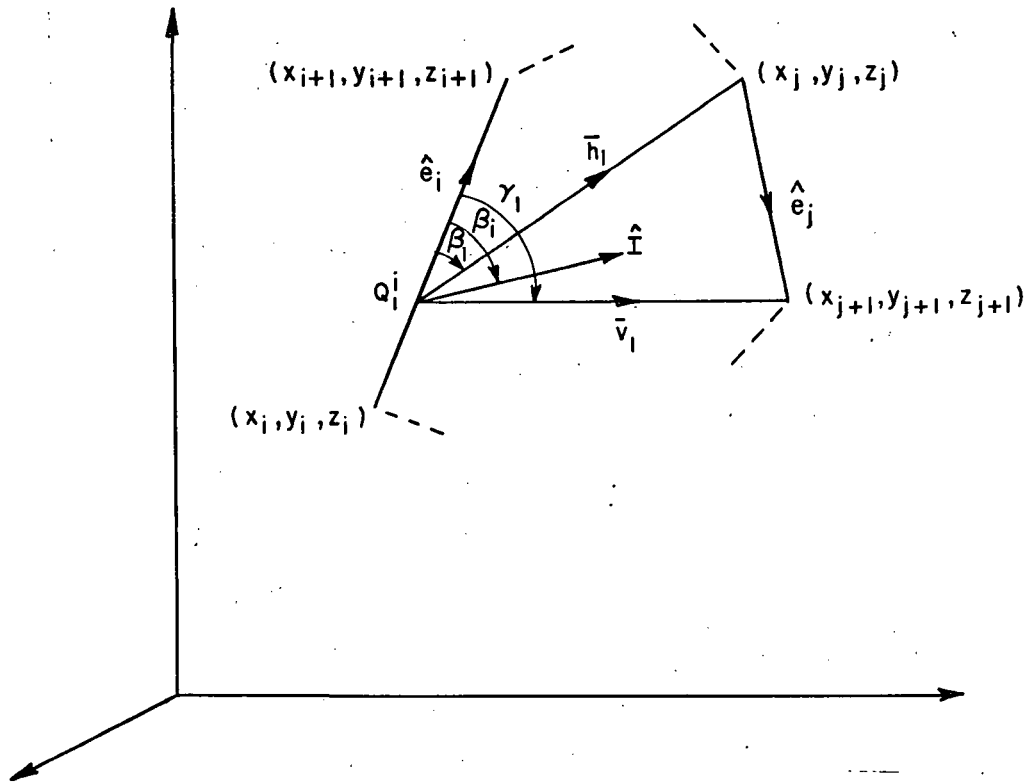
Page #

1 inch

1½ inch

2 inch Chapter Line

1 inch

Figure 220. Parameter definition for the determination of the illuminated region lower bound on edge i and upper bound on edge j.

1 inch

JAB/80

1 inch

1½ inch

<u>Case c:</u>     $\beta_1 < \beta_i < \gamma_1$

Figure 221 defines the geometry parameters where

$$\theta_{j+1} = \cos^{-1} \left[ \hat{e}_j \cdot \hat{v}_1 \right] \qquad , \qquad (142)$$

$$r = \frac{V_1}{\sin \beta_j} \quad \sin \theta_{j+1} \qquad \text{and}$$

$$\bar{r} = r \ \hat{I} \qquad\qquad \text{THESIS / DISSERTATION}$$
Typing Guide Paper

The location of the illuminated region lower bound on edge i is given by $\bar{P}_1^i$ and that of the upper bound on edge j is given by

$$\bar{P}_2^j = \bar{P}_1^i + \bar{r} \qquad\qquad .$$

<u>Case d:</u>     $\beta_i > \gamma_1$

This case is illustrated in Figure 222. We define

$$r = \frac{V_1}{\sin \beta_i} \quad \sin \gamma_1 \qquad \text{and}$$

$$\bar{r} = r \ \hat{I} \qquad\qquad .$$

In this case, the location of the upper bound on edge j is given by

$$\bar{P}_2^j = \bar{C}_{j+1} \qquad \text{1st page Chapter end line} \qquad (143)$$

— — — — — — 1st page Chapter end line

and the lower bound on edge i is modified as

LAST TEXT LINE

Center Guide

1 inch

JAB/80

1 inch

1½ inch

2 inch Chapter line

1 inch
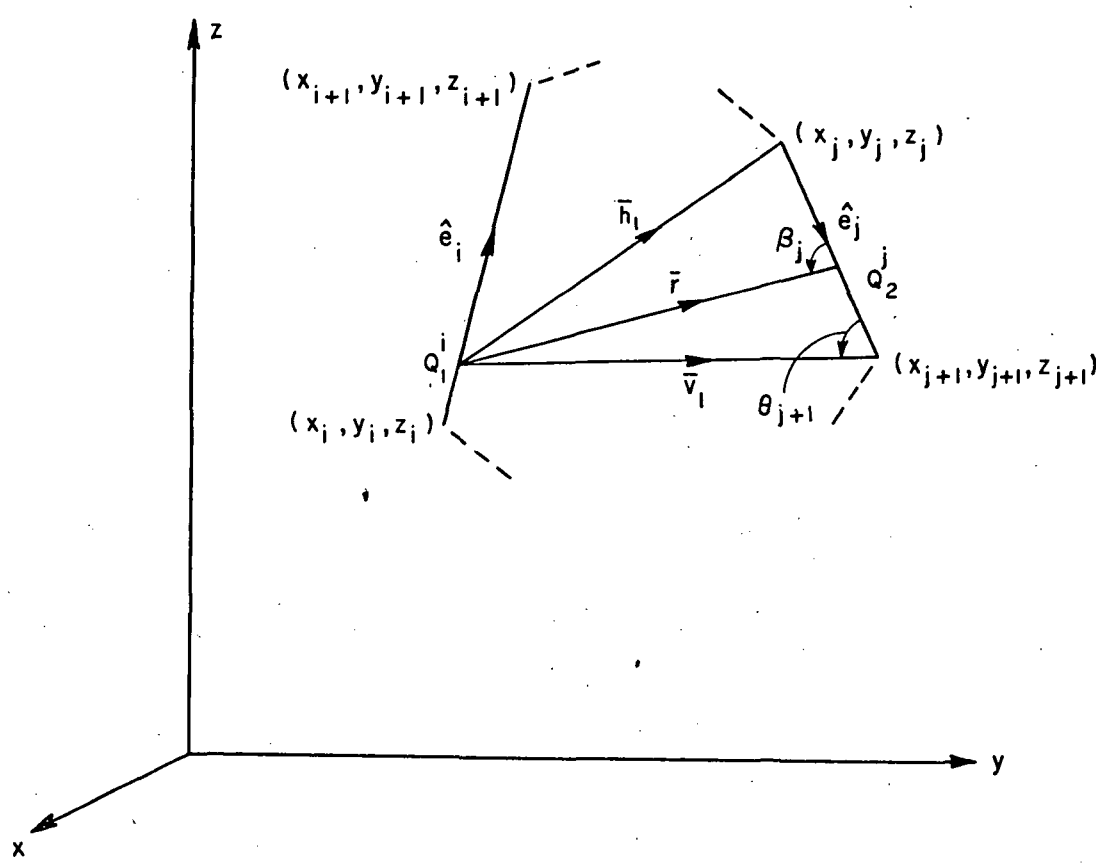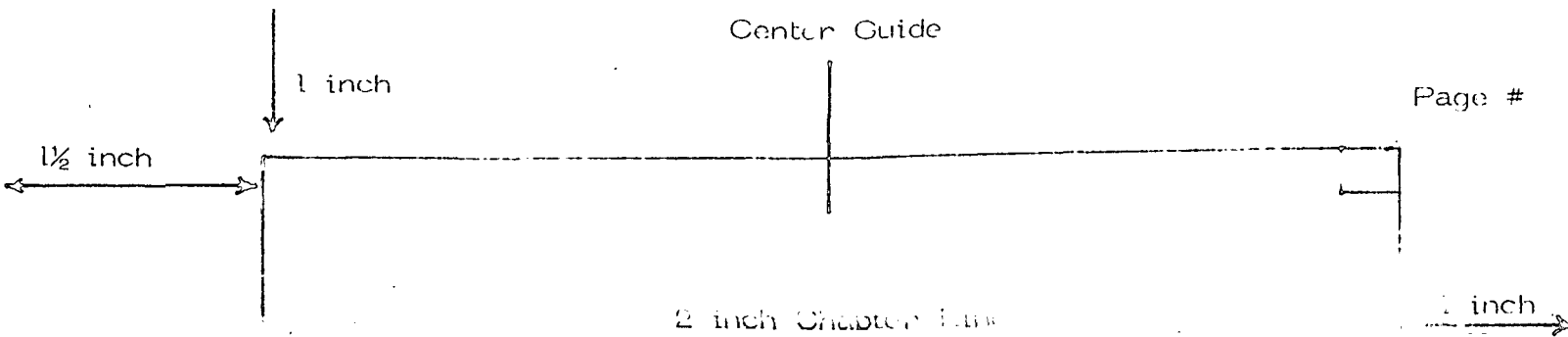


1st page Chapter end line

Figure 221. Determination of illuminated region lower bound on edge i and upper bound on edge j for case c.

1st page Chapter end line

317

JAB/80
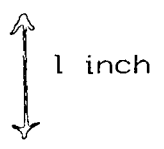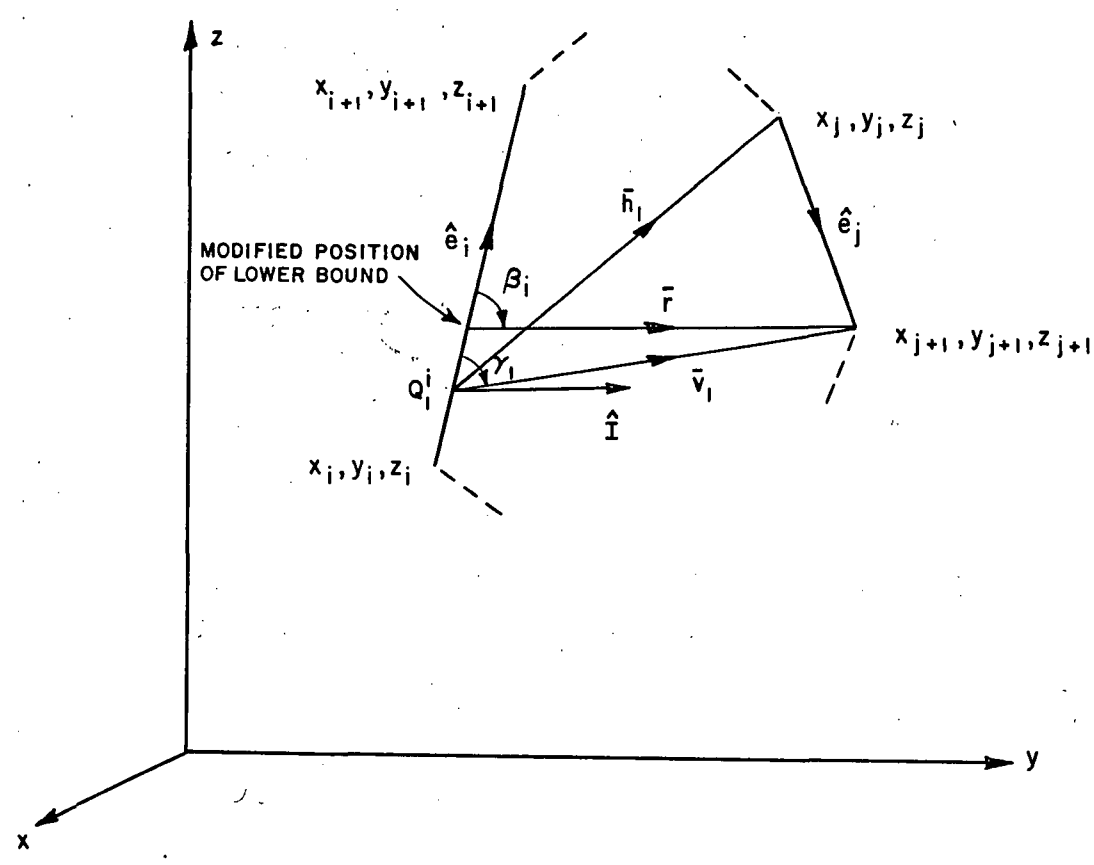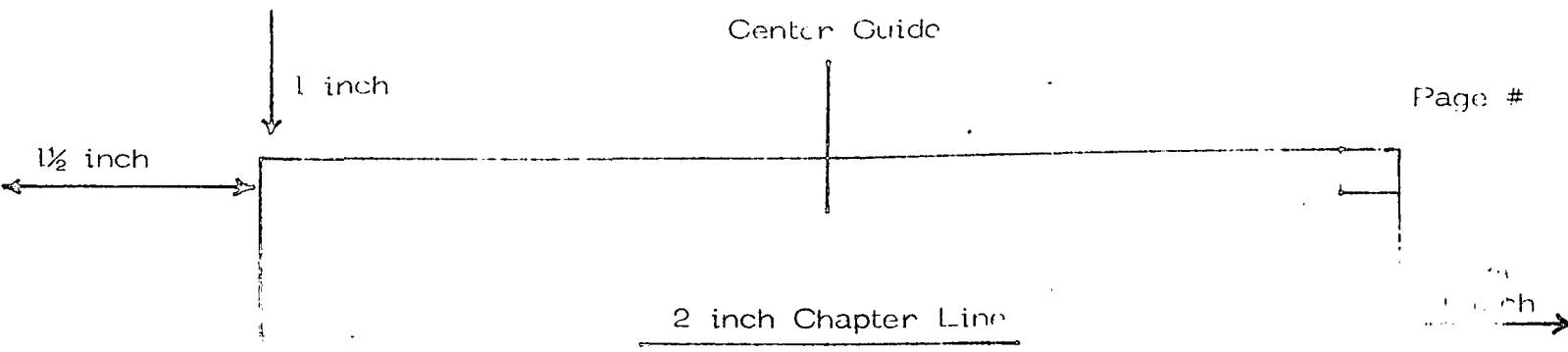
Figure 222. Determination of illuminated region lower bound on edge i and upper bound on edge j for case d.
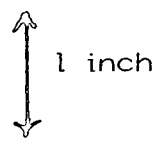
$$\overline{P}_1^i = \overline{P}_2^j - \overline{r}$$

In the special case where $\beta_i = \gamma_1$, the location of the lower bound on edge i is not modified and that of the upper bound on edge j is given by Equation (143).

## B. CASE OF NON-INTERSECTING VECTORS $\overline{h}_1$ AND $\overline{h}_2$

When the vectors $\overline{h}_1$ and $\overline{h}_2$ shown in Figure 216 do not intersect, one has to consider the two special cases shown in Figure 223 where the extension of one edge passes through the physical limits of the other edge defined by its corners.

Consider first the case shown in Figure 223-a and examine Figure 224 where we show the method used to find whether the ray diffracted from edge i illuminates (hits) edge j.  Define

$$\psi = \pi - \beta_i \qquad (144)$$

The ray diffracted from edge i will not illuminate edge j if

$$\pi < \psi < \beta_2$$

where $\beta_i$ and $\beta_2$ are defined in Equations (134, 136).

Based on the value of $\beta_i$ and $\gamma_1$ defined in Equations (134) and (141), one has to consider the following cases:

<u>Case e:</u>   $\beta_i < \gamma_1$

Figure 225 illustrates this case where

1 inch

1½ inch

1 inch

$(x_j, y_j, z_j)$

$\bar{h}_1$

$\hat{e}_j$

$Q_2^i$

$\hat{e}_i$

$\bar{h}_2$

$(x_{j+1}, y_{j+1}, z_{j+1})$

$Q_1^i$

(a)

$(x_j, y_j, z_j)$

$\bar{h}_1$

$Q_2^i$

$\hat{e}_i$

$\hat{e}_j$

$Q_1^i$

$\bar{h}_2$

$(x_{j+1}, y_{j+1}, z_{j+1})$

(b)
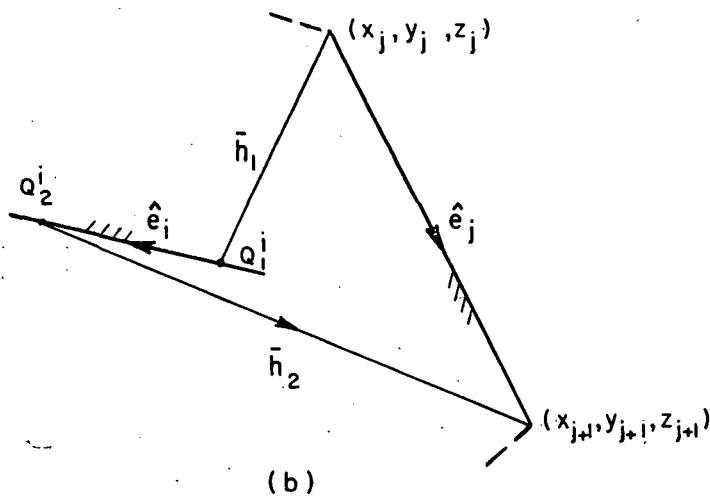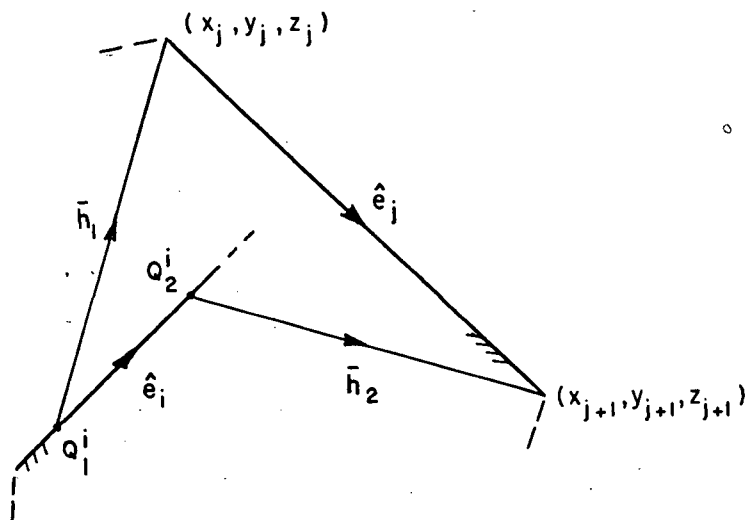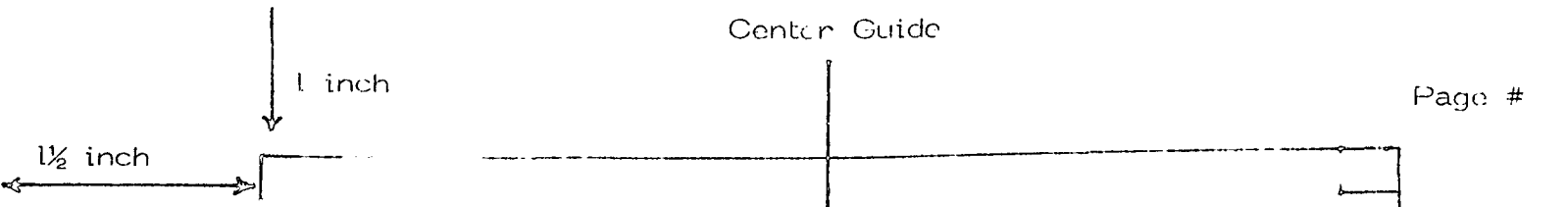
1st page Chapter end line

Figure 223. Cases of non-intersecting vectors $\bar{h}_1$ and $\bar{h}_2$. apter end line

LAST TEXT LINE

320

1 inch

JAB/80

1 inch

1½ inch

1 inch



$(x_j, y_j, z_j)$

$\hat{e}_j$

$(x_{i+1}, y_{i+1}, z_{i+1})$

$\hat{I}$

$Q_2^i$

$\hat{e}_i$

$\psi$

$\beta_2$

$\bar{h}_2$

$(x_i, y_i, z_i)$

$(x_{j+1}, y_{j+1}, z_{j+1})$
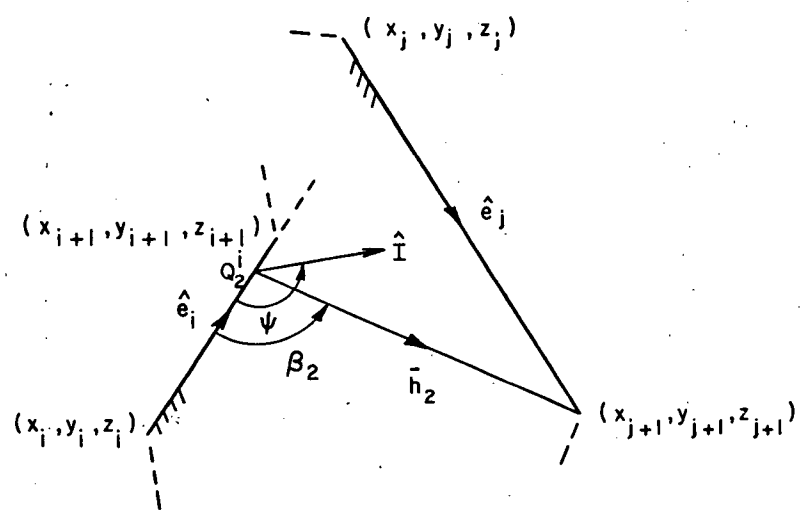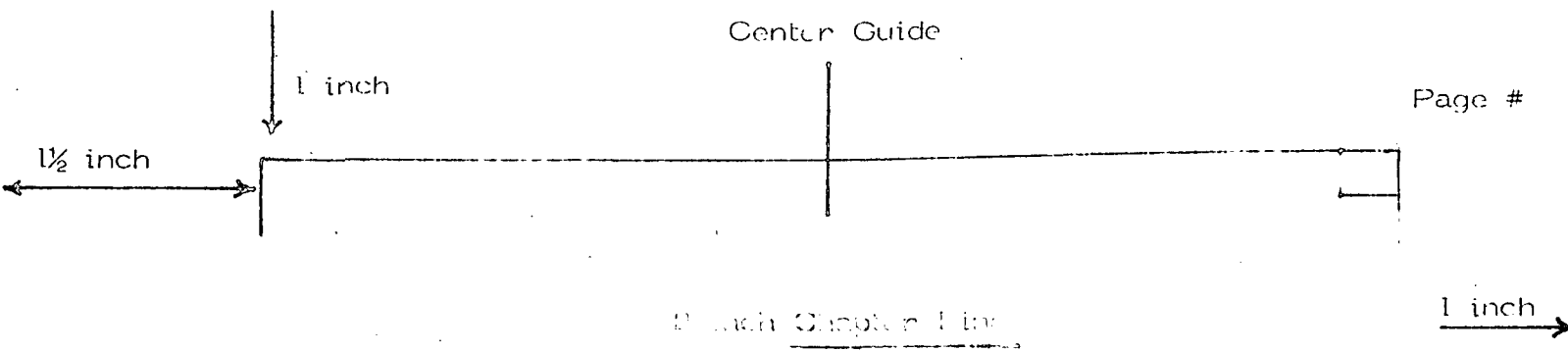
Figure 224. Method used to determine if edge i illuminates edge j when $\bar{h}_1$ does not intersect $\bar{h}_2$.

1st page Chapter end line

LAST TEXT LINE

1 inch

JAB/80
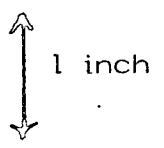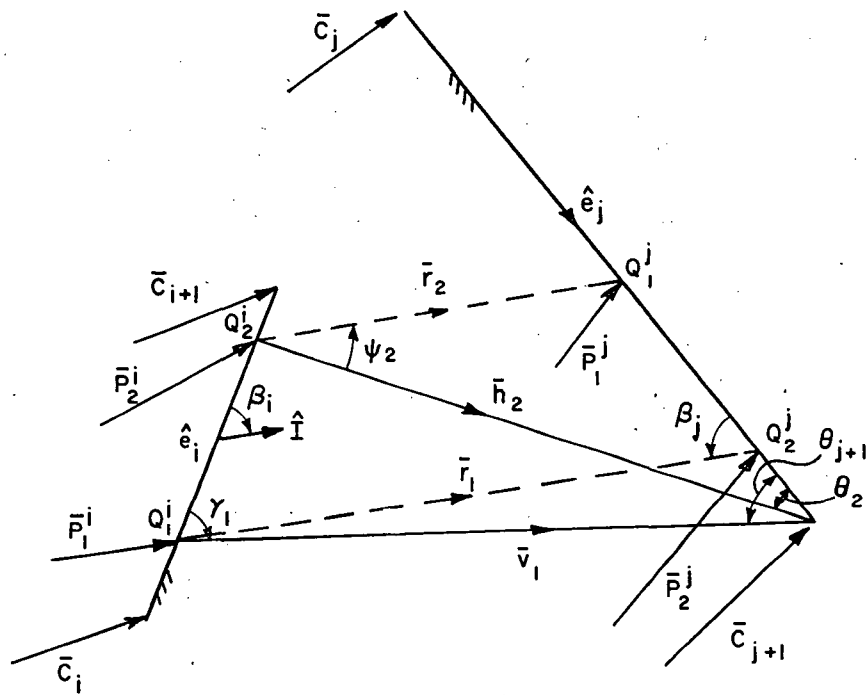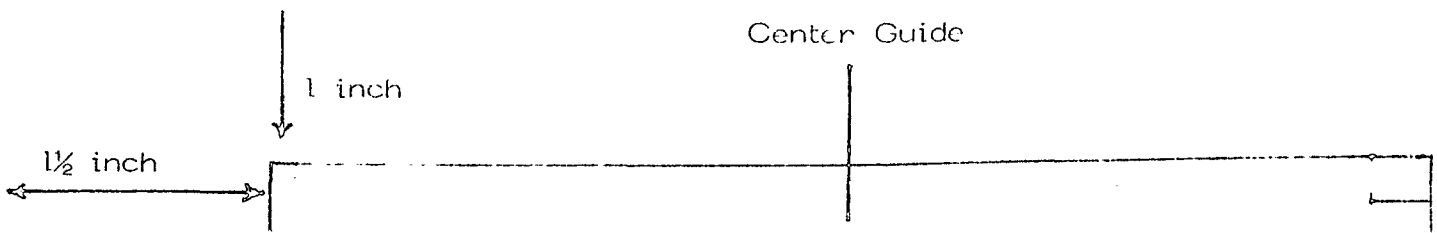
1 inch

1½ inch



Figure 225. Determination of the illuminated region lower and upper bounds on edge j for case e.

1 inch

JAB/80
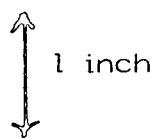
1 inch

1½ inch

$$\psi_2 = \cos^{-1}\left[\hat{I} \cdot \hat{h}_2\right] \quad ,$$

(145)

$$\theta_2 = \beta_j - \psi_2$$

2 inch Chapter Line

$$r_1 = \frac{V_1}{\sin \beta_j} \sin \theta_{j+1} \quad ,$$

$$r_2 = \frac{h_2}{\sin \beta_j} \sin \theta_2 \quad ,$$

THESIS / DISSERTATION
Typing Guide Paper
and

$$\bar{r}_1 = r_1 \, \hat{I}$$

$$\bar{r}_2 = r_2 \, \hat{I} \quad .$$

where $h_2$, $\beta_j$, $V_1$ and $\theta_{j+1}$ are defined in Equations (135), (138), (141), and (142) respectively. The position vectors of the lower and upper bounds of the illuminated region on edge j are given by

$$\bar{P}_1^j = \bar{P}_2^i + \bar{r}_2 \qquad \text{and}$$

(146)

$$\bar{P}_2^j = \bar{P}_1^i + \bar{r}_1 \quad .$$

Case f:    $\beta_i \gtrless \gamma_1$

The geometry associated with this case is shown in Figure 226. The illuminated region lower bound position vector is given by Equation (146) and that for the upper bound is given by

$$\bar{P}_2^j = \bar{C}_{j+1} \quad .$$

1st page Chapter end line

In this case, the location of the lower bound of the illuminated region on edge i has to be modified. We define

1st page Chapter end line

323

1 inch

JAB/80

Center Guide

1 inch

Page #

1½ inch

Branch Chapter line

1 inch



MODIFIED POSITION
OF LOWER BOUND
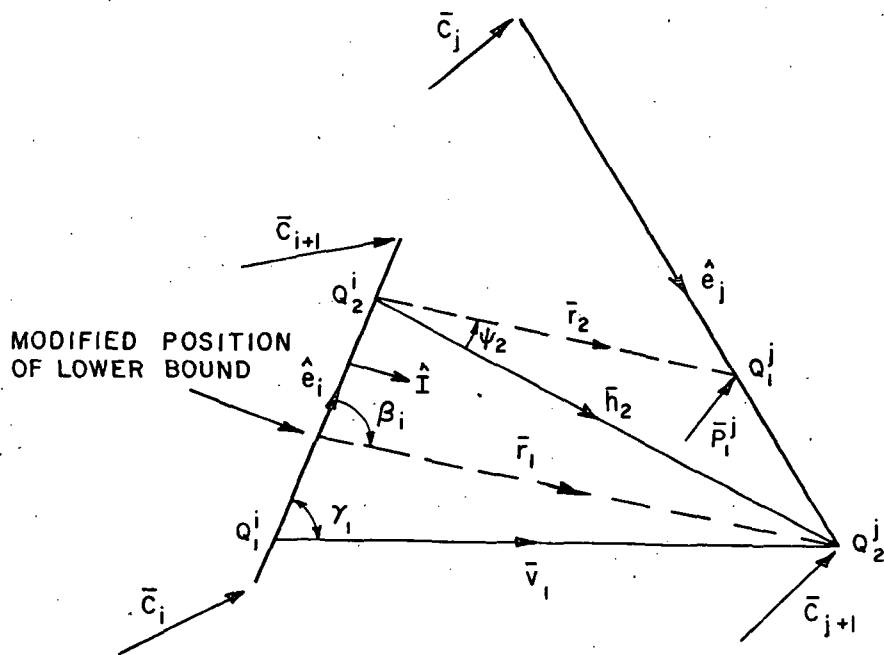
Figure 226. Determination of the illuminated region lower and upper
bounds on edge j for case f.

1st page Chapter end line

1st page Chapter end line

Last text line

324

Bottom Guide

1 inch

1 inch

1½ inch

1 inch

$$r_1 = \frac{V_1}{\sin \beta_i} \sin \gamma_1 \qquad \text{and}$$

2 inch Chapter Line

$$\bar{r}_1 = r_1 \hat{I}$$

Thus,

$$\bar{P}_1^i = \bar{C}_{j+1} - \bar{r}_1$$

Now let us consider the case shown in Figure 223-b. The method used to determine whether the ray diffracted from edge i illuminates edge j, is shown in Figure 227.

THESIS / DISSERTATION
Typing Guide Paper

If

$$\pi < \beta_i < \beta_1$$

then the ray diffracted from edge i <u>will not</u> illuminate edge j. $\beta_i$ and $\beta_1$ are defined in Equations (134) and (136). Depending on the values of $\beta_i$ and $\alpha_1$ defined in Equations (134) and (137), one has to consider the following cases.

<u>Case g</u>:   $\beta_i \lessgtr \alpha_1$

Figure 228 illustrates this case. We define

$$\psi_1 = \cos^{-1} \left[ \hat{I} \cdot \hat{h}_1 \right] \qquad ,$$

$$\theta_1 = \pi - \psi_1 - \beta_j \qquad , \qquad \text{1st page Chapter end line}$$

(147)

$$r_1 = \frac{h_1}{\sin \beta_j} \sin \theta_1 \qquad \text{and}$$

1st page Chapter end line

LAST TEXT LINE

325

1 inch

JAB/80

Center Guide

Page #

1 inch

1½ inch

2 inch Chapter Line

1 inch

$(x_j, y_j, z_j)$

$\beta_i$

$\bar{h}_1$

$(x_{i+1}, y_{i+1}, z_{i+1})$

$\beta_I$

$\hat{e}_i$

$\hat{I}$

$\hat{e}_j$

$Q_1^i$

$(x_i, y_i, z_i)$

$(x_{j+1}, y_{j+1}, z_{j+1})$
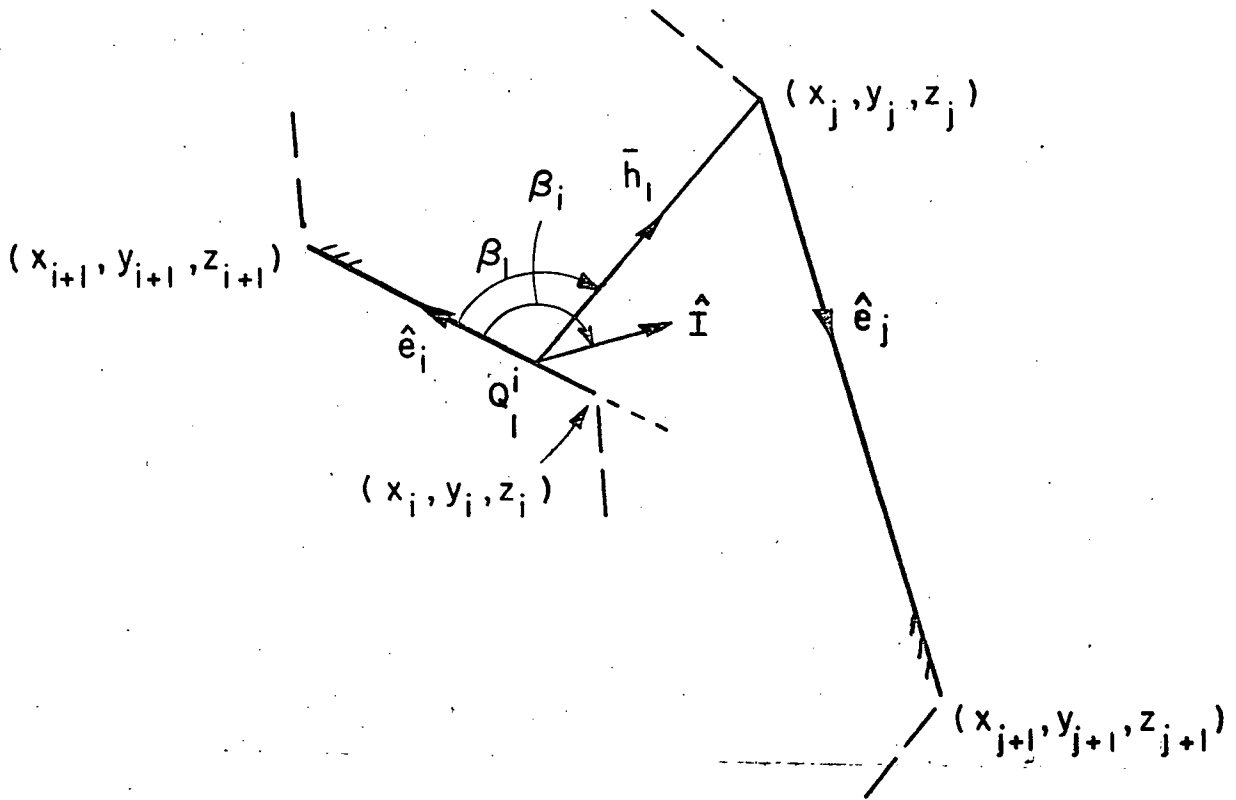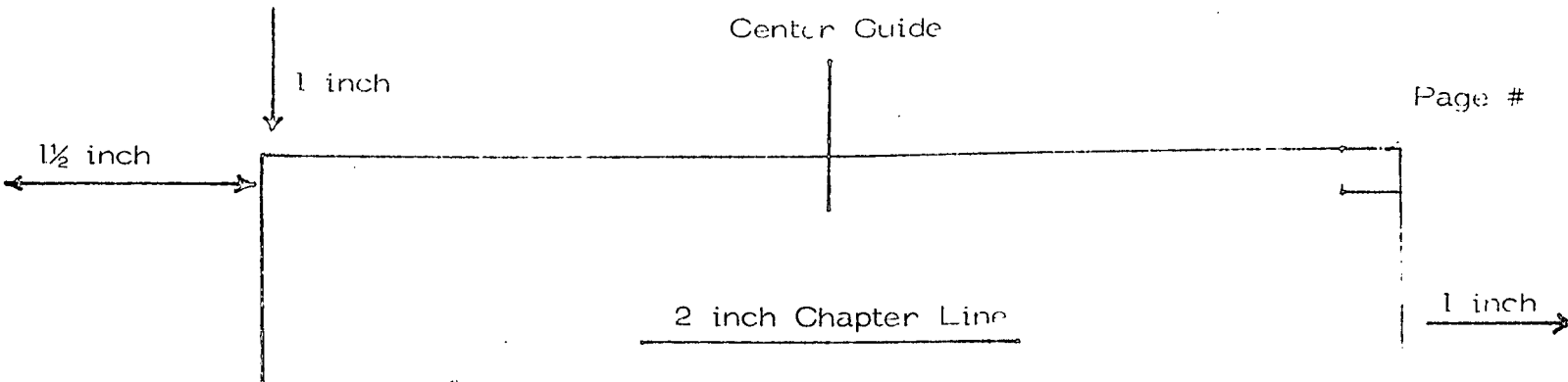
1st page Chapter end line

Figure 227. Method used to determine if edge i illuminates edge j when $\bar{h}_1$ does not intersect $\bar{h}_2$ (case of Figure 203-b).

1 inch

JAB/80

Center Guide

Page #

1 inch

1½ inch

2 inch Chapter Line

1 inch
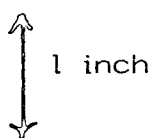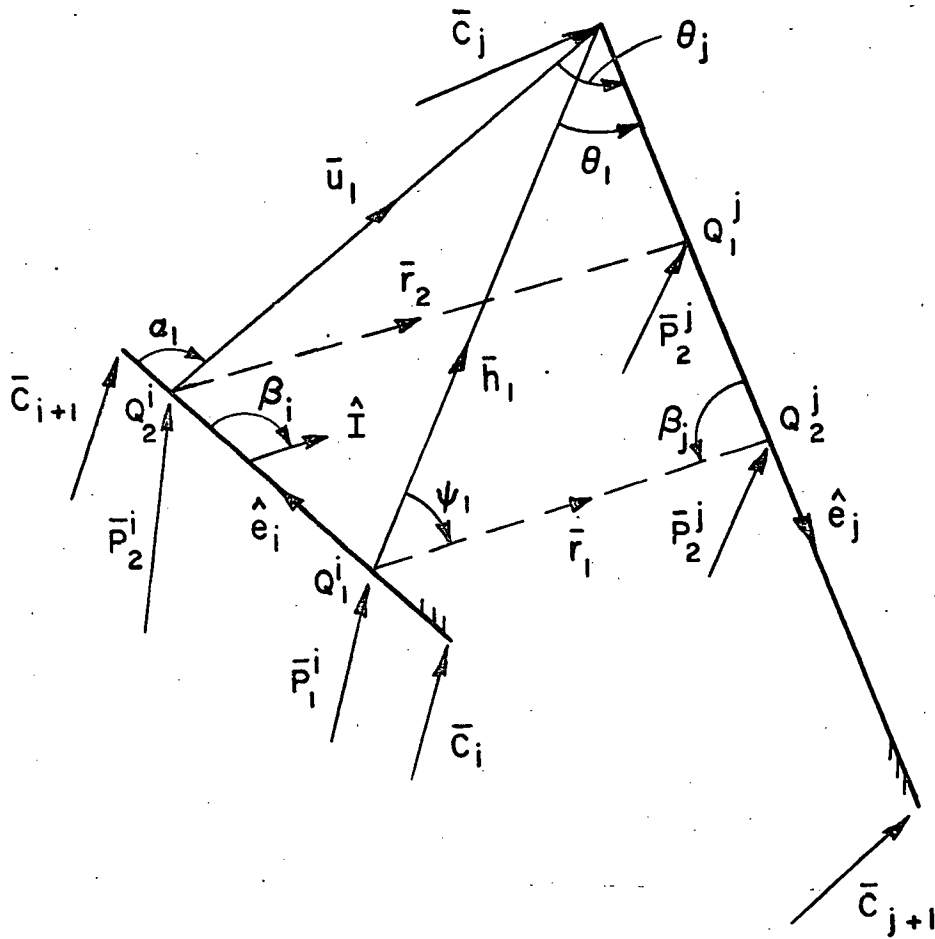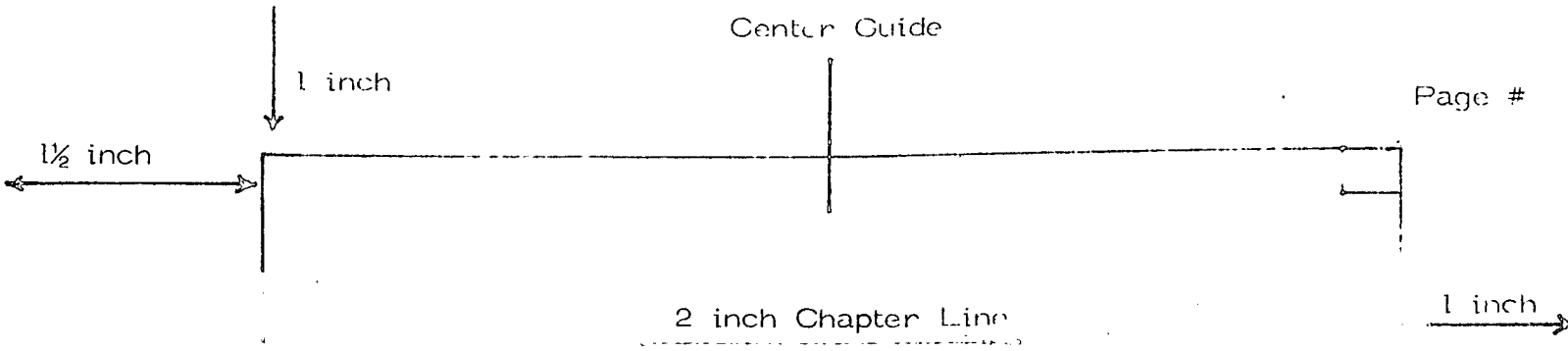
Figure 228. Determination of the illuminated region lower and upper bounds on edge j for case g.

JAB/80

$$r_2 = \frac{U_1}{\sin \beta_j} \sin \theta_j$$

2 inch Chapter Line
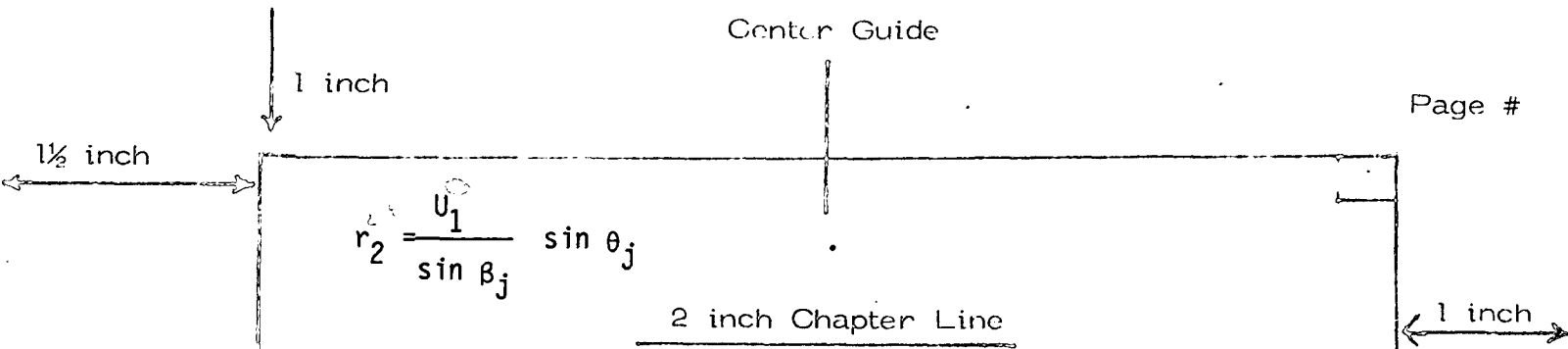
thus

$$\bar{r}_1 = r_1 \hat{I} \qquad \text{and} \qquad \bar{r}_2 = r_2 \hat{I} \, ,$$

where, $h_1$, $U_1$, $\beta_j$ and $\theta_j$ are as defined in Equations (135), (137), and (138) respectively. The position vector of the lower and upper bounds of the illuminated region on edge j are then given by

Typing Guide Paper

$$\bar{P}_1^j = \bar{P}_2^i + \bar{r}_2 \qquad \qquad \text{and}$$

$$\text{(148)}$$

$$\bar{P}_2^j = \bar{P}_1^i + \bar{r}_1$$

<u>Case h:</u>   $\beta_j < \alpha_1$

This case is illustrated in Figure 229 where the upper bound position vector of the illuminated region on edge j is given by Equation (148) and that of the lower bound is given by

$$\bar{P}_1^j = \bar{C}_j$$

For this case the location of the upper bound of the illuminated region on edge i is modified as follows:

$$r_2 = \frac{U_1}{\sin \beta_j} \sin \theta_{j+1} \qquad \text{and}$$

1st page Chapter end line

– – – – – – – – 1st page Chapter end line

$$r_2 = r_2 \hat{I}$$

328

1 inch

1½ inch

1 inch

$\bar{c}_j$　$Q_1^j$

$\bar{u}_1$

$\bar{r}_2$　$\bar{h}_1$

$Q_2^j$

$\theta_{i+1}$

$\beta_i$　$\hat{I}$

$\bar{r}_1$

$\hat{e}_j$

$\bar{c}_{i+1}$　$Q_2^i$

$\hat{e}_i$

$Q_1^i$

$\bar{c}_i$

**MODIFIED POSITION
OF UPPER BOUND**

$\bar{c}_{j+1}$
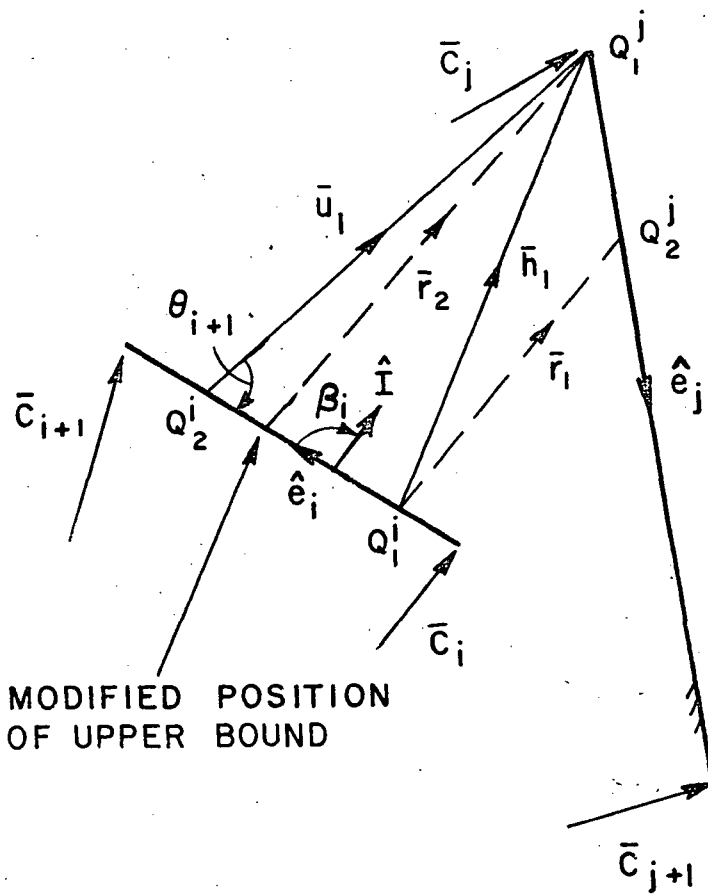
1st page Chapter end line

Figure 229. Determination of the illuminated regions for case c,d line

1 inch

JAB/80

1 inch

1½ inch

1 inch

thus

$$\overline{P}_2^i = \overline{C}_j - \overline{r}_2$$

2 inch Chapter Line

It should be noted that the techniques shown in this Appendix were used to handle the geometry problem associated with the different plates analyzed in our work. However, depending on the plate geometry to be analyzed, one may have to consider other cases associated with the determination of the illuminated region on an edge.

THESIS / DISSERTATION
Typing Guide Paper

1st page Chapter end line

— — — — — — — 1st page Chapter end line

LAST TEXT LINE

330

PAGE GUIDE

1 inch

JAB/80

1½ inch

1 inch

APPENDIX B

## EQUIVALENT CURRENT FORMULATION

From Equations (19) and (20) one has for the Electric and Magnetic Equivalent Currents corresponding to the first order diffraction:

$$I^e_{(1)} = \frac{2j}{Z_0 k} \frac{G^e(n,\phi,\phi')}{\sin^2 \beta_0} E^i_{tan} \tag{149}$$

$$I^m_{(1)} = \frac{2j}{Z_0 k} \frac{G^m(n,\phi,\phi')}{\sin^2 \beta_0} H^i_{tan} \tag{150}$$

where

$$G^{\,e}_{\,m}(n,\phi,\phi') = R(n,\phi-\phi') \mp R(n,\phi+\phi'), \tag{151}$$

$$R(n,\psi) = \frac{1}{n} \sin \frac{\pi}{n} \left( \frac{1}{\cos \frac{\pi}{n} - \cos \frac{\psi}{n}} \right) , \tag{152}$$

$\phi, \phi'$ and $\beta_0$ are defined in Figure 1 and $E^i_{tan}$, $H^i_{tan}$ are the incident field components tangential to the edge. The superscripts on $I^{\,e}_{m\,(1)}$ define type of current, electric or magnetic and the subscripts define the order of diffraction.

The plane wave incident fields are given by

$$\bar{E}^i = (E^i_x \hat{x} + E^i_y \hat{y} + E^i_z \hat{z}) e^{jkg} \tag{153}$$

1 inch

JAB/80
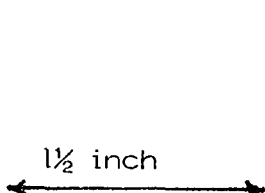
$$\overline{H}^i = (H_x^i \hat{x} + H_y^i \hat{y} + H_z^i \hat{z})\, e^{jkg} \tag{154}$$

where

$$\overline{E}^i \times \overline{H}^i = \frac{\hat{I}}{Z_0} \quad , \text{ and}$$

$\hat{I}$ is the unit vector in direction of propagation, $g = x\,\sin\theta^i\,\cos PH^i + y\,\sin\theta^i\,PH^i + z\,\cos\theta^i$

where

$\theta^i$, $PH^i$ are the $\theta$ and $PH$ angles of incidence defined in the standard spherical coordinate system.

From Equations (153 and 154), one can define

$$E_{tan}^i = \overline{E}^i \cdot \hat{e}_p \tag{155}$$

$$H_{tan}^i = \overline{H}^i \cdot \hat{e}_p \tag{156}$$

where $\hat{e}_p = \overline{x}_p \hat{x} + \overline{y}_p \hat{y} + \overline{z}_p \hat{z}$ is the $p^{th}$ edge unit vector.

The Equivalent Electric Current vector on edge p is then given by

$$\overline{I}_{(1)}^e = \frac{2j}{Z_0 k} \quad \frac{G^e(n,\phi,\phi')}{\sin^2 \beta_0^{(p)}} \quad (\overline{E}^i \cdot \hat{e}_p)\, \hat{e}_p \quad , \tag{157}$$

or

$$\overline{I}_{(1)}^e = (I_x^e\, \hat{x} + I_y^e\, \hat{y} + I_z^e\, \hat{z}) \frac{e^{jkg}}{Z_0} \quad \text{where} \tag{158}$$

$$I_x^e = \frac{2jG^e(n,\phi,\phi')}{k \sin^2\beta_0(p)} \ (E_x\overline{x}_p + E_y\overline{y}_p + E_z\overline{z}_p)\ \overline{x}_p \quad ,$$

2 inch Chapter Line

$$I_y^e = \frac{2jG^e(n,\phi,\phi')}{k \sin^2\beta_0(p)} \ (E_x\overline{x}_p + E_y\overline{y}_p + E_z\overline{z}_p)\ \overline{y}_p \quad , \text{ and}$$

$$I_z^e = \frac{2jG^e(n,\phi,\phi')}{k \sin^2\beta_0(p)} \ (E_x\overline{x}_p + E_y\overline{y}_p + E_z\overline{z}_p)\ \overline{z}_p \quad .$$

Similarly, the Equivalent Magnetic Current is given by

Typing Guide Paper

$$\overline{I}_{(1)}^m = \frac{2j}{Y_0 k}\ \frac{G^m(n,\phi,\phi')}{\sin^2\beta_0(p)}\ (\overline{H}^i \cdot \hat{e}_p)\ \hat{e}_p \quad , \tag{159}$$

or

$$\overline{I}_{(1)}^m = (I_x^m \hat{x} + I_y^m \hat{y} + I_z^m \hat{z})\ e^{jkg} \quad , \text{ where} \tag{160}$$

$$I_x^m = \frac{2jG^m(n,\phi,\phi')}{k \sin^2\beta_0(p)}\ (H_x\overline{x}_p + H_y\overline{y}_p + H_z\overline{z}_p)\ \overline{x}_p \quad ,$$

$$I_y^m = \frac{2jG^m(n,\phi,\phi')}{k \sin^2\beta_0(p)}\ (H_x\overline{x}_p + H_y\overline{y}_p + H_z\overline{z}_p)\ \overline{y}_p \quad , \text{ and}$$

$$I_z^m = \frac{2jG^m(n,\phi,\phi')}{k \sin^2\beta_0(p)}\ (H_x\overline{x}_p + H_y\overline{y}_p + H_z\overline{z}_p)\ \overline{z}_p \quad .$$

where $I_{\binom{x}{y}{z}}^{\binom{e}{m}}$ are the x, y, z rectangular components of the electric

1st page Chapter end line

and magnetic Equivalent currents. — — 1st page Chapter end line

LAST TEXT LINE

333

Ph... LINE

1 inch

JAB/80

1 inch

1½ inch

The θ and PH components of the total scattered field are given by:

$$E^t_{\theta \atop (PH)} \quad E^e_{\theta \atop (PH)} \quad + \quad E^m_{\theta \atop (PH)} \qquad \text{2 inch Chapter Line} \qquad (161)$$

1 inch

where the superscript t indicates total field, e and m indicate fields due to Electric or magnetic equivalent currents.

$$E^t_{\theta} = \frac{jk}{4\pi} \frac{e^{-jkr}}{r} \left\{ (I^m_x \sin PH - I^m_y \cos PH) \right.$$

$$\left. - (I^e_x \cos\theta \cos PH + I^e_y \cos\theta \sin PH - I^e_z \sin\theta) \right\}$$

Typing Guide Paper

$$\int_{\text{edge } p} e^{jk(g+g')} \, d\ell' \qquad (162)$$

$$E^t_{PH} = \frac{jk}{4\pi} \frac{e^{-jkr}}{r} \left\{ (I^m_x \cos\theta \cos PH + I^m_y \cos\theta \sin PH - I^m_z \sin\theta) \right.$$

$$\left. + (I^e_x \sin PH - I^e_y \cos PH) \right\} \int_{\text{edge } p} e^{jk(g+g')} \, d\ell' \qquad (163)$$

where

$$g' = x' \sin\theta \cos PH + y' \sin\theta \sin PH + z' \cos\theta$$

and x', y', z' defines the location of an arbitrary point on edge p.

The integral shown in Equations (162, 163) is given by

1st page Chapter end line

$$\int_{\text{edge } p} e^{jk(g+g')} \, d\ell' = \ell \, \frac{\sin(kA\ell/2)}{(kA\ell/2)} \, e^{jk(B+A\ell/2)} \qquad (164)$$

LAST TEXT LINE

334

PAGE LINE

1 inch

JAB/80

1½ inch

1 inch

where
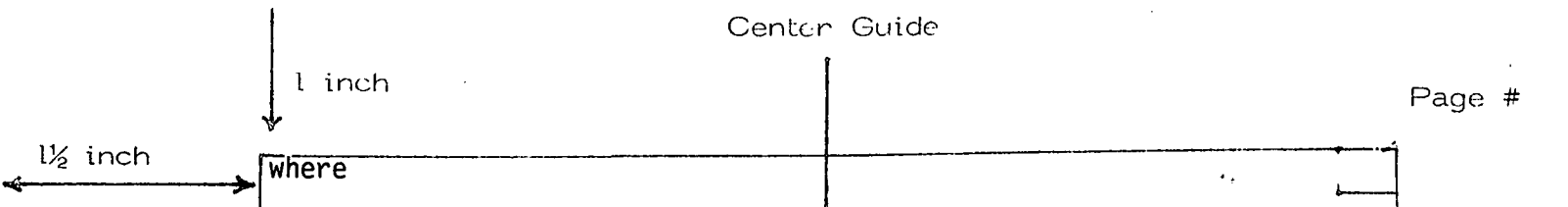
 $\ell$ defines the length of edge p,

3 inch Chapter Line

$$\ell = \sqrt{(x_{p+1} - x_p)^2 + (y_{p+1} - y_p)^2 + (z_{p+1} - z_p)^2} \quad ,$$

$a = \sin\theta \cos PH + \sin\theta^i \cos PH^i,$

$b = \sin\theta \sin PH + \sin\theta^i \sin PH^i,$

$c = \cos\theta + \cos\theta^i,$

$A = a\bar{x}_p + b\bar{y}_p + c\bar{z}_p$   and

$B = ax_p + by_p + cz_p.$

THESIS / DISSERTATION

Note that for backscatter $\theta = \theta^i$ and $PH = PH^i$.

and   $x_p$, $y_p$, $z_p$ are the rectangular components of corner p position vector.

 $\bar{x}_p$, $\bar{y}_p$, $\bar{z}_p$ are the corresponding components of edge p unit vector.

 For the higher order diffraction terms, only Magnetic Equivalent Currents are needed. These currents are derived in a similar way as shown above. Figure 230 illustrates the double diffraction case from edge p to q. The unit vectors $\hat{I}$ and $\hat{d}$ define the incidence and diffraction directions. $Q^{(p)}$ and $Q^{(q)}$ define the diffraction points on edge p and q respectively. $S_1$ is the distance between $Q^{(p)}$ and $Q^{(q)}$.

 The diffracted field from edge p is incident on edge q and is given by

$$\bar{H}^{i(q)}_{\phantom{i}}(Q^{(q)}) = -\frac{1}{2}\beta_0'^{(q)} H^{i(p)}_{\beta_0'^{(p)}}(Q^{(p)}) D_h^{(p)}(S_1, o, \phi'^{(p)}, \beta_0^{(p)})$$
$$\frac{e^{-jkS_1}}{\sqrt{S_1}} \tag{165}$$

1st page Chapter end line
— — — — — — — — 1st page Chapter end line

The Magnetic Equivalent Current due to double diffraction is given by

1 inch

JAB/80
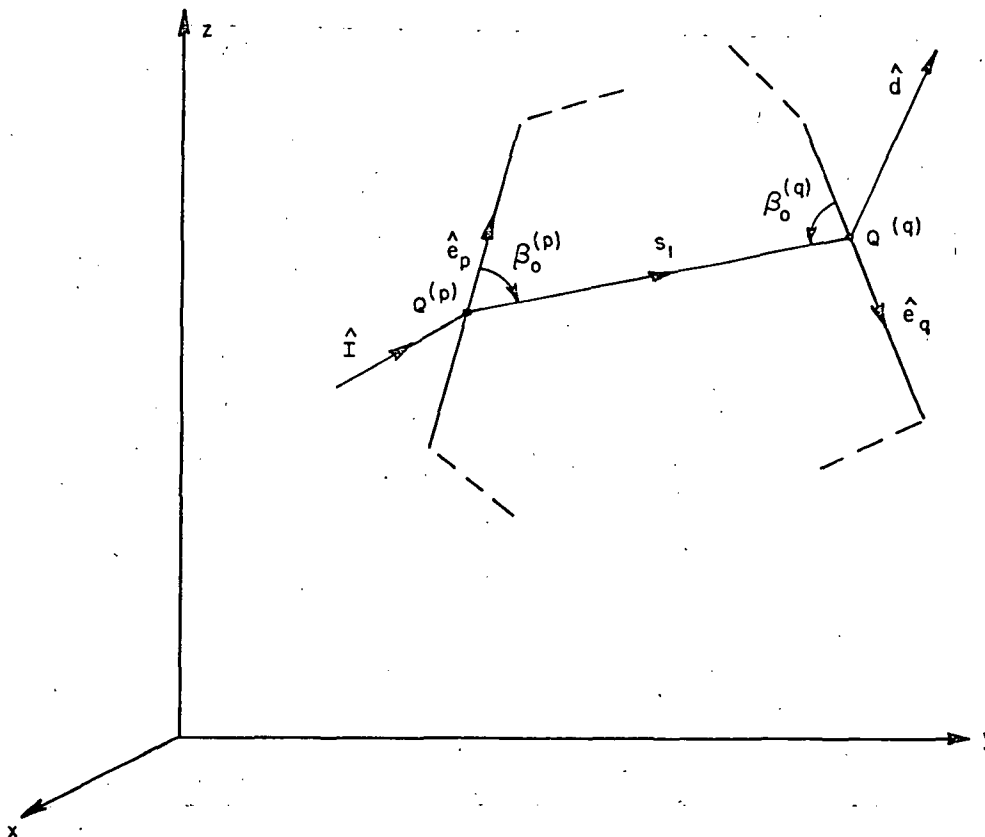
1 inch

1½ inch

2 inch Chapter Line

Figure 230. Parameters definition associated with double edge diffraction
mechanism.

1 inch

JAB/80

$$I^m_{(2)} = \frac{2j}{Y_0 k} \frac{\sqrt{2\pi k}\ e^{j\pi/4}}{\sin \beta^{(q)}_0} D^{(q)}_h (s_1, \phi^{(q)}, o, \beta^{(q)}_0)$$

$$(\overline{H}^{i(q)} (Q^{(q)}) \cdot \hat{e}_q) \tag{166}$$

Substituting Equations (165) into (166), one gets

$$I^m_{(2)} = \frac{-2j}{Y_0 k} \frac{\sqrt{2\pi k}\ e^{j\pi/4}}{\sin \beta^{(q)}_0} \frac{(\overline{H}^{i(p)} (Q^{(p)}) \cdot \hat{e}_p)}{\sin \beta^{(p)}_0}$$

$$D^{(p)}_h (s_1, o, \phi'^{(p)}, \beta^{(p)}_0) \ D^{(q)}_h (s_1, \phi^{(q)}, o, \beta^{(q)}_0) \tag{167}$$

$$\frac{e^{-jks_1}}{\sqrt{s_1}} \quad (\hat{\beta}'^{(q)}_0 \cdot \hat{e}_q)$$

In a similar way to Equation (160), we can write

$$I^m_{(2)} \begin{Bmatrix} x \\ y \\ z \end{Bmatrix} = I^m_{(2)} \begin{Bmatrix} x \\ y \\ z \end{Bmatrix} e^{jkg} \tag{168}$$

Using Equation (167) into Equations (162, 163) with the Electric Equivalent Current set to zero, one can get the required scattered field. Note that the integration in this case must be computed numerically and that the integration is only over the illuminated part of edge q.

The third order diffraction mechanism is shown in Figure 231. The field diffracted from edge q is now the incident field on edge v. Note that as in the strip case, there are 4 rays incident on $Q^{(v)}$ which will contribute to the total diffracted field.

1 inch

1½ inch

2 inch Chapter Line
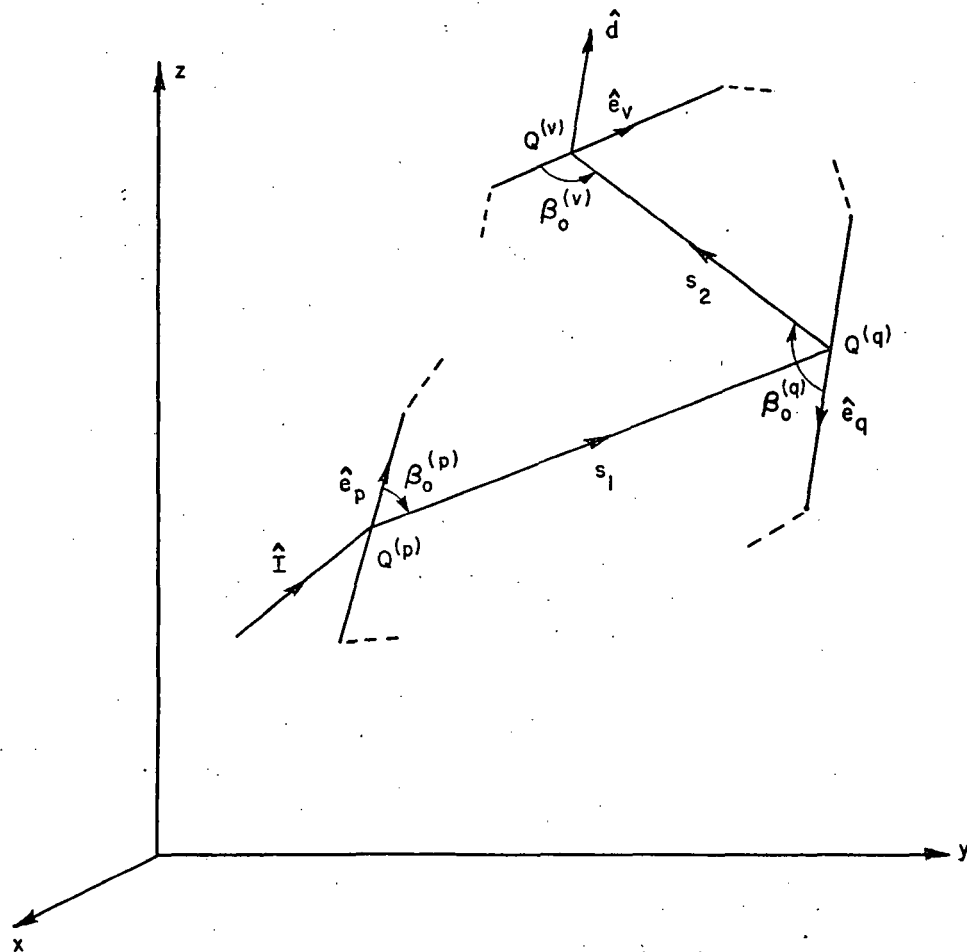
1 inch



Figure 231. Parameter definition associated with triple edge diffraction mechanism. — — — — — — — → 1st page Chapter end line

338

1 inch

JAB/80

The incident field on edge V is

$$\overline{H}^{i(v)}(Q^{(v)}) = -\frac{1}{2}\hat{\beta}_0^{,(v)} \frac{H_{\beta_0^{,}(q)}^{i(q)}(Q^{(q)}) D_h^{i(q)}}{\beta_0^{,}(q)} (L,o,o,\beta_0^{(q)})$$

$$\frac{e^{-jks_2}}{\sqrt{s_2}} \qquad\qquad (169)$$

The $\frac{1}{2}$ factor is introduced because of grazing incidence, and

$$H_{\beta_0^{,}(q)}^{i(q)}(Q^{(q)}) = -\frac{1}{2} \frac{H_{\beta_0^{,}(p)}^{i(p)}(Q^{(p)}) D_h^{(p)}}{Y_0^{i(p)}} (s_1,o,\phi^{,(p)},\beta_0^{(p)})$$

$$\frac{e^{-jks_1}}{\sqrt{s_1}} \qquad\qquad (170)$$

also

$$D_h^{(q)}(L,o,o,\beta_0^{(q)}) = \frac{-e^{-j\pi/4}}{\sqrt{2\pi k}\ \sin\beta_0^{(q)}}$$

Using Equations (169, 170), one can write for the third order Magnetic Equivalent Current

$$I_{(3)}^m = \frac{-2j}{Y_0 k} \frac{(\overline{H}^{i(p)}(Q^{(p)}) \cdot \hat{e}_p)}{\sin\beta_0^{(p)}\ \sin\beta_0^{(q)}\ \sin\beta_0^{(v)}} D_h^{(p)}(s_1,o,\phi^{,(p)},\beta_0^{(p)})$$

$$D_h^{(v)}(s_2,\phi^{(v)},o,\beta_0^{(v)})\ \frac{e^{-jks_1}}{\sqrt{s_1}}\ \frac{e^{-jks_2}}{\sqrt{s_2}}\ (\hat{\beta}_0^{,(v)} \cdot \hat{e}_v) \qquad\qquad (171)$$

or

JAB/80

1 inch

1½ inch

1 inch

$$I^m_{(3)}\left\{\begin{matrix}x\\y\\x\end{matrix}\right\} = I^m_{(3)}\left\{\begin{matrix}x\\y\\z\end{matrix}\right\} e^{-jkg} \qquad (172)$$

2 inch Chapter Line

Using Equation (172) and the radiation integral, one can find the far scattered field due to third order edge diffraction. The integration in this case is also computed numerically and the integration is carried out over the illuminated portion of edge V.

THESIS / DISSERTATION
Typing Guide Paper

1st page Chapter end line
— — — — — — — 1st page Chapter end line

LAST TEXT LINE

340

350 UM

1 inch

JAB/80

1 inch

1½ inch

1 inch
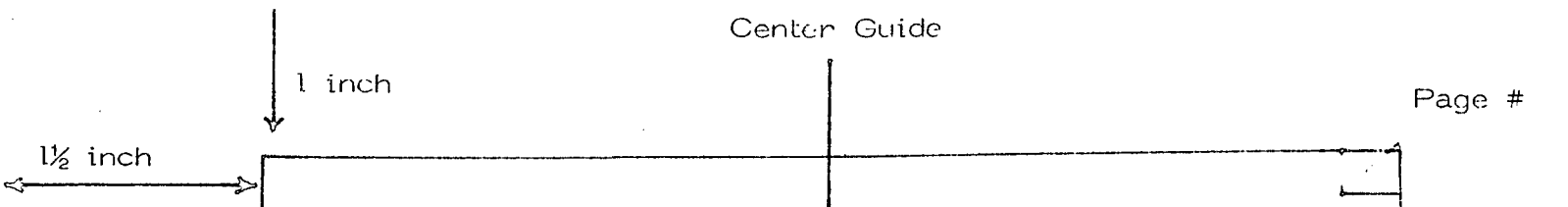
## 2 inch APPENDIX C Line

### EDGE WAVE FORMULATION

Consider Figure 232 which shows a monopole mounted on a perfectly conducting plate.  The field radiated by the monopole is diffracted by corner #2 ($C_2$) along edge #1.  Note that the field on the plate surface is cross-polarized with respect to the diffracted field.  Let us consider just one edge.  Similar results will hold for the other edges.

Typing Guide Paper

**PERFECTLY CONDUCTING PLATE**



**(a) FRONT VIEW**          **(b) SIDE VIEW**
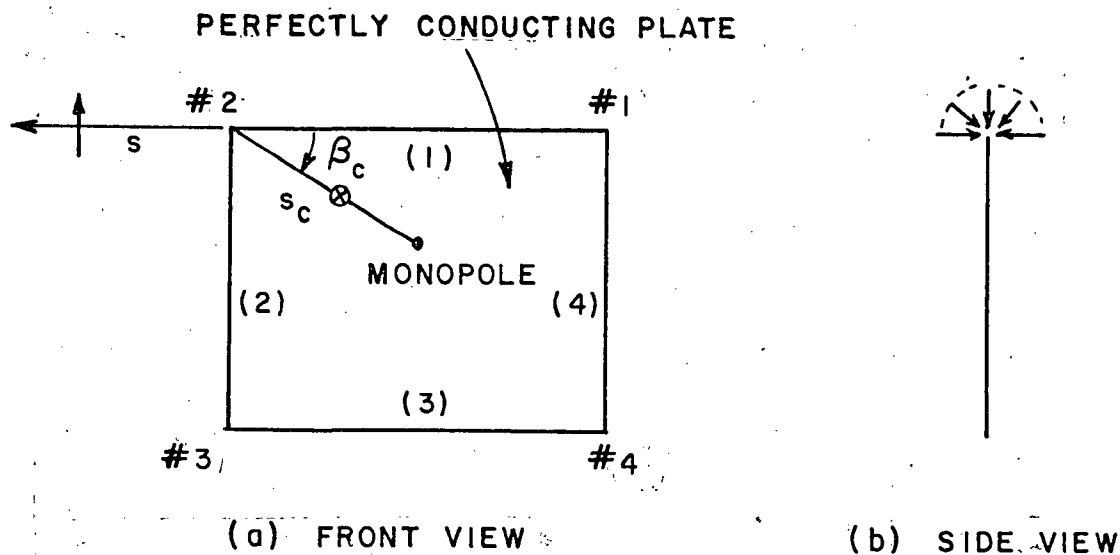
Figure 232.  Edge wave mechanism associated with the radiation problem.

1st page Chapter end line

— — — — — — — 1st page Chapter end line

LAST TEXT LINE

1 inch

JAB/80
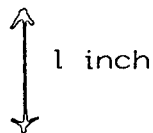
The corner diffracted field is given by

$$
\begin{bmatrix} E_\beta^c \\ E_\phi^c \end{bmatrix} = - \begin{bmatrix} E_\beta^i(Q_c) \; D_s^c(L,L_c,\phi,\phi',\beta_0,\beta_c,\beta_{0_c}) \\ E_\phi^i(Q_c) \; D_h^c(L,L_c,\phi,\phi',\beta_0,\beta_c,\beta_{0_c}) \end{bmatrix}
$$

(173)

$$
\sqrt{\frac{s'}{s''(s'+s'')}} \quad \sqrt{\frac{s(s+s_c)}{s_c}} \quad \frac{e^{-jks}}{s}
$$

where

$$
\begin{Bmatrix} D_s^c \\ D_h^c \end{Bmatrix} = \begin{Bmatrix} C_s(Q_E) \\ C_h(Q_E) \end{Bmatrix} \sqrt{\frac{\sin \beta_c \; \sin \beta_{0_c}}{(\cos \beta_{0_c} - \cos \beta_c)}} \quad F\left[kL_c a(\pi+\beta_{0_c}-\beta_c)\right]
$$

(174)

$$
\sqrt{\frac{8\pi}{k}} \quad \frac{e^{-j\pi/4}}{4\pi}
$$

and

$$
C_{s,h}(Q_E) = \frac{-e^{-j\pi/4}}{2\sqrt{2\pi k}\,\sin \beta_0} \left[ \frac{F\left[kLa(\beta^-)\right]}{\cos \beta^-/2} \middle| F\left\{ \frac{La(\beta^-)/\lambda}{kL_c a(\pi+\beta_{0_c}-\beta_c)} \right\} \middle| \right.
$$

$$
\left. \pm \; \frac{F\left[kLa(\beta^+)\right]}{\cos \beta^+/2} \middle| F\left\{ \frac{La(\beta^+)/\lambda}{kL_c a(\pi+\beta_{0_c}-\beta_c)} \right\} \middle| \right]
$$

(175)

The function $F(x)$ was defined in Equation (26), and $a(\beta) = 2\cos^2(\beta/2)$
where

$$
\beta^\pm = \phi \pm \phi' \quad ,
$$
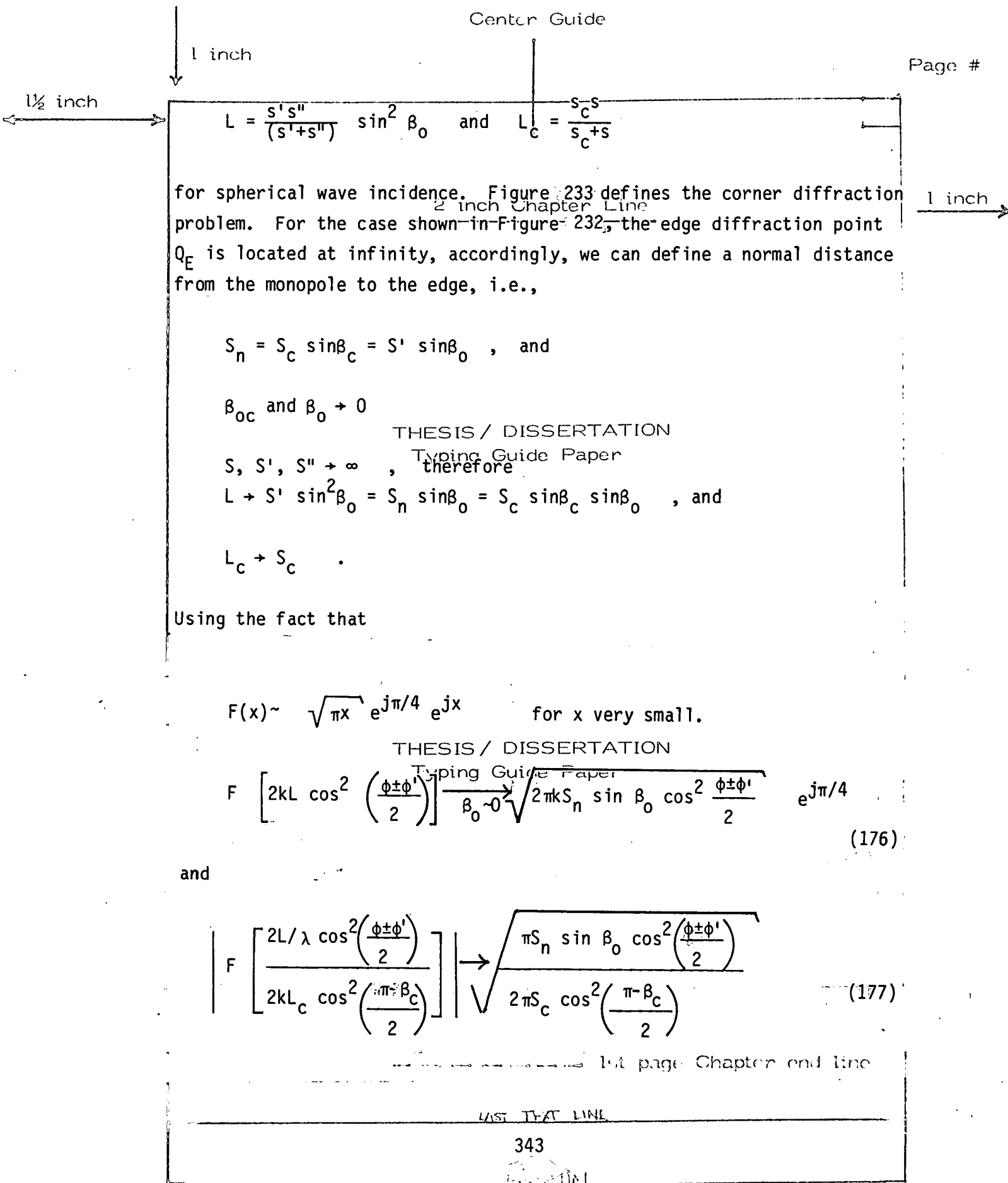
$$L = \frac{s's''}{(s'+s'')} \sin^2 \beta_0 \quad \text{and} \quad L_c = \frac{s_c s}{s_c + s}$$

for spherical wave incidence. Figure 233 defines the corner diffraction problem. For the case shown in Figure 232, the edge diffraction point $Q_E$ is located at infinity, accordingly, we can define a normal distance from the monopole to the edge, i.e.,

$$S_n = S_c \sin\beta_c = S' \sin\beta_0 \quad , \quad \text{and}$$

$$\beta_{oc} \text{ and } \beta_0 \to 0$$

$$S, S', S'' \to \infty \quad , \quad \text{therefore}$$

$$L \to S' \sin^2\beta_0 = S_n \sin\beta_0 = S_c \sin\beta_c \sin\beta_0 \quad , \quad \text{and}$$

$$L_c \to S_c \quad .$$

Using the fact that

$$F(x) \sim \sqrt{\pi x} \, e^{j\pi/4} \, e^{jx} \qquad \text{for x very small.}$$

$$F\left[2kL \cos^2\left(\frac{\phi \pm \phi'}{2}\right)\right] \xrightarrow{\beta_0 \to 0} \sqrt{2\pi k S_n \sin\beta_0 \cos^2\frac{\phi \pm \phi'}{2}} \, e^{j\pi/4} \tag{176}$$

and

$$\left| F\left[\frac{2L/\lambda \cos^2\left(\frac{\phi \pm \phi'}{2}\right)}{2kL_c \cos^2\left(\frac{\pi - \beta_c}{2}\right)}\right] \right| \to \sqrt{\frac{\pi S_n \sin\beta_0 \cos^2\left(\frac{\phi \pm \phi'}{2}\right)}{2\pi S_c \cos^2\left(\frac{\pi - \beta_c}{2}\right)}} \tag{177}$$

343

1 inch

1½ inch

2 inch Chapter Line
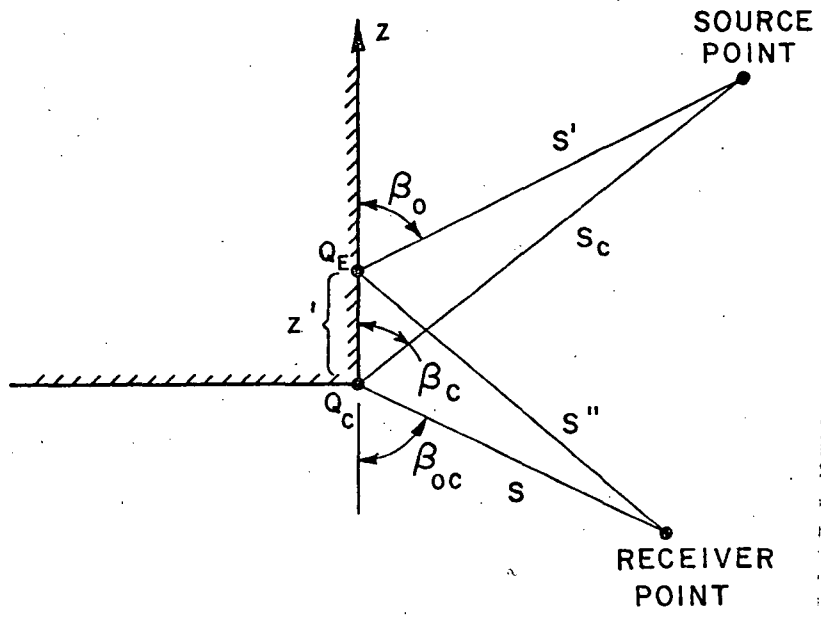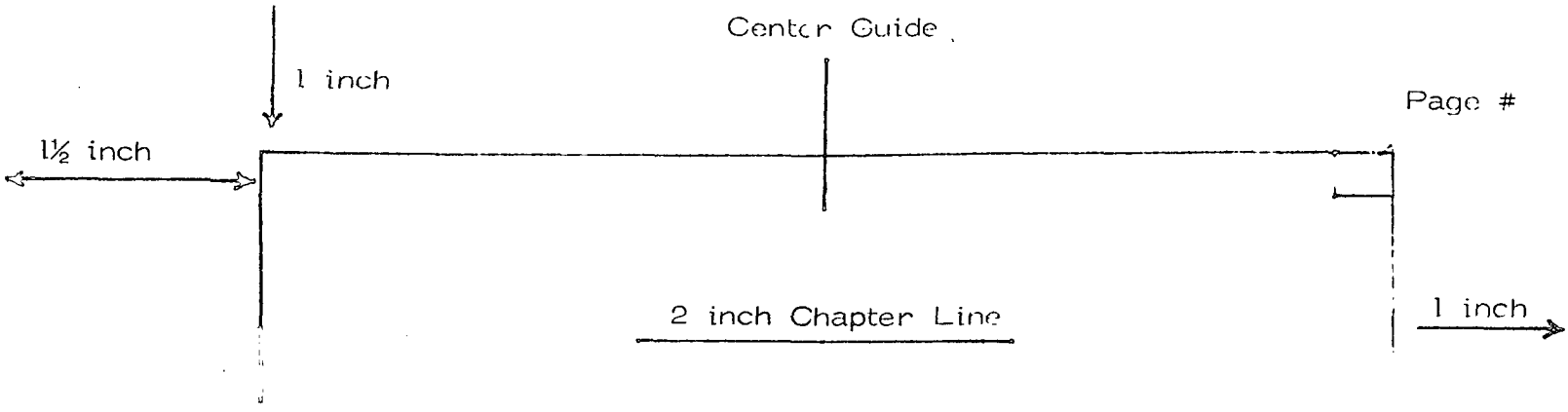
1 inch



Figure 233. Parameter definition associated with the corner
diffraction problem.

1st page Chapter end line

1st page Chapter end line

LAST TEXT LINE

344

1 inch

JAB/80
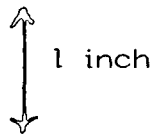
Substituting Equations (176, 177) into Equations (174, 175) one gets

$$C_{s_h} = -\frac{1}{2}\sqrt{\frac{S_n^2}{2S_c \cos^2\left(\frac{\pi-\beta_c}{2}\right)}} \left\{ \cos\frac{\phi-\phi'}{2} \mp \cos\left(\frac{\phi+\phi'}{2}\right) \right\} \tag{178}$$

or

$$C_{s_h} = -\sqrt{\frac{S_n^2}{2S_c \cos^2\left(\frac{\pi-\beta_c}{2}\right)}} \left\{ \begin{array}{ll} \sin\frac{\phi}{2} & \sin\frac{\phi'}{2} \\ \cos\frac{\phi}{2} & \cos\frac{\phi'}{2} \end{array} \right\} \tag{179}$$

THESIS / DISSERTATION

Substituting Equation (174, 179) into (173), and note that

$$\sqrt{\frac{s'}{s''(s'+s'')}} \sqrt{\frac{s(s+s_c)}{s_c}} \rightarrow \sqrt{\frac{s'}{s_c}} \quad , \quad \text{one obtains}$$

$$\left\{ \begin{array}{l} E_{\beta} \\ E_{\phi} \end{array} \right\} = \left\{ \begin{array}{l} E_\beta^i(Q_c) \; D_s^{(ew)}(s_c,\phi,\phi',\beta_c) \\ E_\phi^i(Q_c) \; D_h^{(ew)}(s_c,\phi,\phi',\beta_c) \end{array} \right\} \sqrt{s_c} \; \frac{e^{-jks}}{s} \tag{180}$$

where

$$D_{s_h}^{(ew)}(s_c,\phi,\phi',\beta_c) = \frac{e^{-j\pi/4}}{2\sqrt{\pi k}} \frac{(1+\cos\beta_c)}{\sin\beta_c/2} F\left[2ks_c \sin^2\frac{\beta_c}{2}\right]$$

$$\left\{ \begin{array}{ll} \sin\frac{\phi}{2} & \sin\frac{\phi'}{2} \\ \cos\frac{\phi}{2} & \cos\frac{\phi'}{2} \end{array} \right\} \tag{181}$$

JAB/80

1½ inch

Equation (181) gives the diffraction coefficient associated with the edge wave mechanism.

A similar result could be obtained for the scattering problem shown in Figure 234. The diffracted field is given by:

$$
\begin{Bmatrix} E_\beta \\ E_\phi \end{Bmatrix} = \begin{Bmatrix} E_\beta^i (Q_c) \, D_s^{(ew)} (s, \phi, \phi', \beta_c) \\ E_\phi^i (Q_c) \, D_h^{(ew)} (s, \phi, \phi', \beta_c) \end{Bmatrix} \frac{e^{-jks}}{\sqrt{s}} \qquad (182)
$$

From Equations (180) and (182) and based on previous experience with GTD method, one can write the following for the edge wave field

$$
\begin{Bmatrix} E_\beta \\ E_\phi \end{Bmatrix} = \begin{Bmatrix} E_\beta^i (Q_c) \, D_s^{(ew)} (L, \phi, \phi', \beta_c) \\ E_\phi^i (Q_c) \, D_h^{(ew)} (L, \phi, \phi', \beta_c) \end{Bmatrix} \sqrt{\frac{s_c}{s(s+s_c)}} \, e^{-jks} \qquad (183)
$$

1 (ew)page Chapter end line
1st page Chapter end line

where $L = \dfrac{ss_c}{s+s_c}$

Note that Equation (183) is only used when either the receiver or the transmitter is in the far field region, i.e., either S or $S_c$ is ∞ .

A.  DISCUSSION          2 inch Chapter Line

The Edge wave mechanism is another form of a surface wave.  It is guided by the plate edges and it radiates only at discontinuities such as plate corners.

The Edge wave formulation presented here has some limitations since its derivation is based on the empirically derived corner diffraction coefficient [19].  Such limitations are:

1 inch

JAB/80
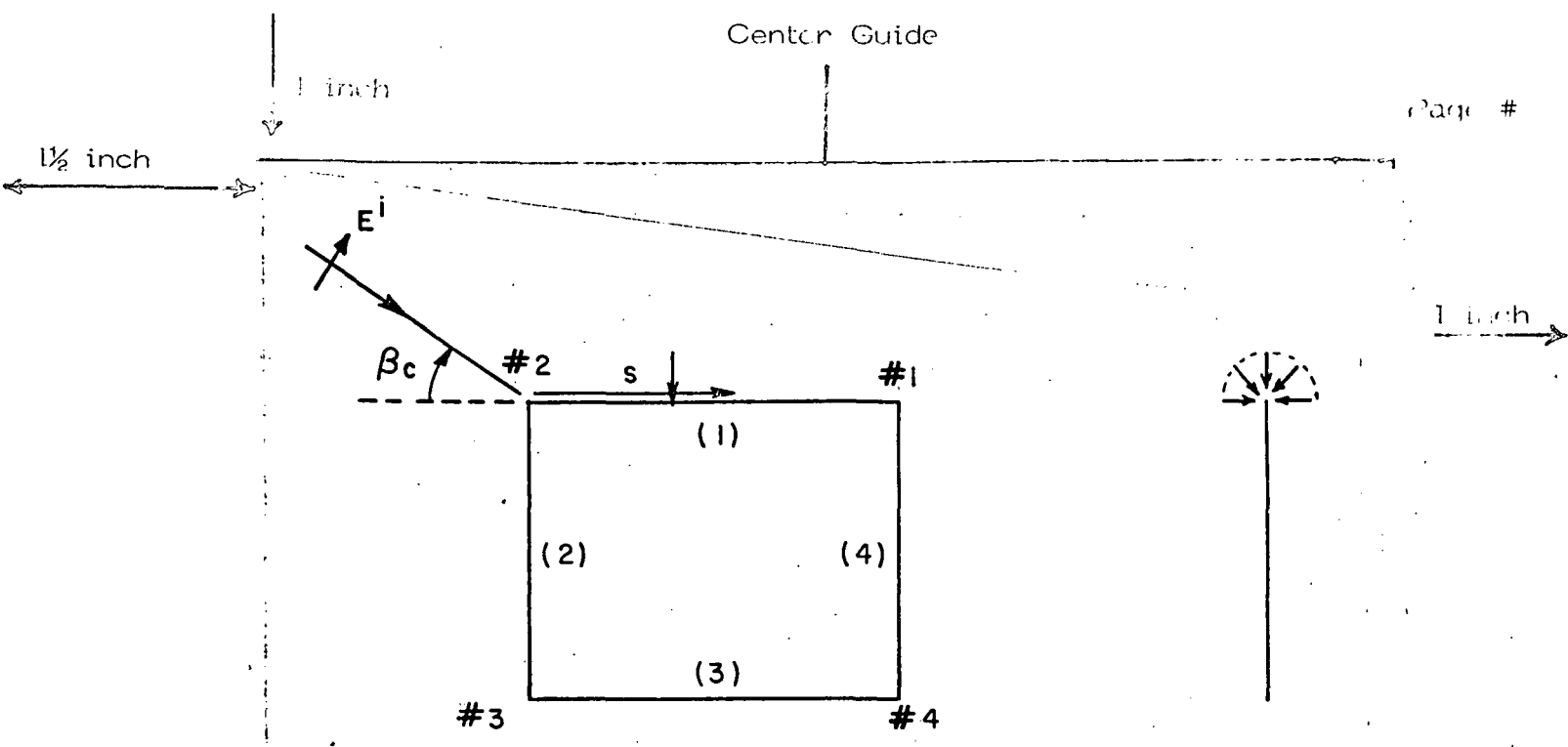
(a) FRONT VIEW                    (b) SIDE VIEW

Figure 234. Edge wave mechanism associated with the scattering
problem.

1. It is only valid for the far field case.

2. If one examines Figure 234 and considers the case shown in
   Figure 235 for the soft boundary condition case, Equation (181)
   will predict zero field for the case in Figure 235 ($\phi=0^o$) and
   a finite value for the case in Figure 234 ($\phi=180^o$). This dis-
   continuity of the field is due to the fact that the Corner dif-
   fraction formulation assumes an infinite half plane exists for
   the case shown in Figure 235 and accordingly a diffracted field
   term associated with the reflected field exists which causes the
   field cancellation to satisfy the boundary condition on the in-
   finite half plane.

1st page Chapter end line

— — — — — — — — 1st page Chapter end line

LAST TEXT LINE

JAB/80

These limitations can be eliminated by properly solving the canon-
ical problem of corner diffraction.

Typing Guide Paper
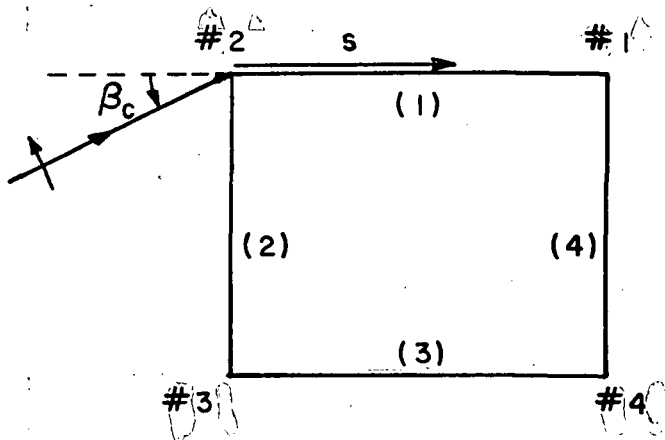
1 inch



Figure 235. Effect of half-plane corner edge wave mechanism.

— — — — — — — 1st page Chapter end line

1st page Chapter end line

— — — — — — — 1st page Chapter end line

LAST TEXT LINE

348

1 inch

JAB/80

## APPENDIX D

SELF-CONSISTENT UTD FORMULATION FOR THE ECHO WIDTH

OF A PERFECTLY CONDUCTING STRIP

The analysis used here is based on the self-consistent (SC) UTD solution. This technique has been pointed out by Rudduck [45]. Wang [46], used this method to compute the scattered fields from infinitely-long perfectly conducting convex cylinders. Yu, et. al., [24], analyzed the scattering from a perfectly conducting strip for the TE case. His solution is based on using the diffraction function $V_B$ obtained by Pauli [47] for a perfectly conducting wedge in the self-consistent formulation, to compute the scattered field due to the multiply diffracted rays between the strip edges.

Here, a self consistent UTD formulation is presented using the Kouyoumjian - Pathak (K-P) form of the diffraction coefficient and the results are compared with the exact Mathieu solution.

The strip geometry is shown in Figure 236, where the incident plane wave field is given by

$$\overline{H}^i = \hat{z} \, e^{jk(x \cos\phi_1^i + y \sin\phi_1^i)} \tag{184}$$

A.   THE SELF-CONSISTENT UTD FORMULATION

For the $TE_z$ case, the total backscattered field consists of singly and multiply diffracted fields between the strip edges. The multiply-diffracted rays are due to those waves traveling, at least once,

1 inch

1½ inch

2 inch Chapter Line

1 inch
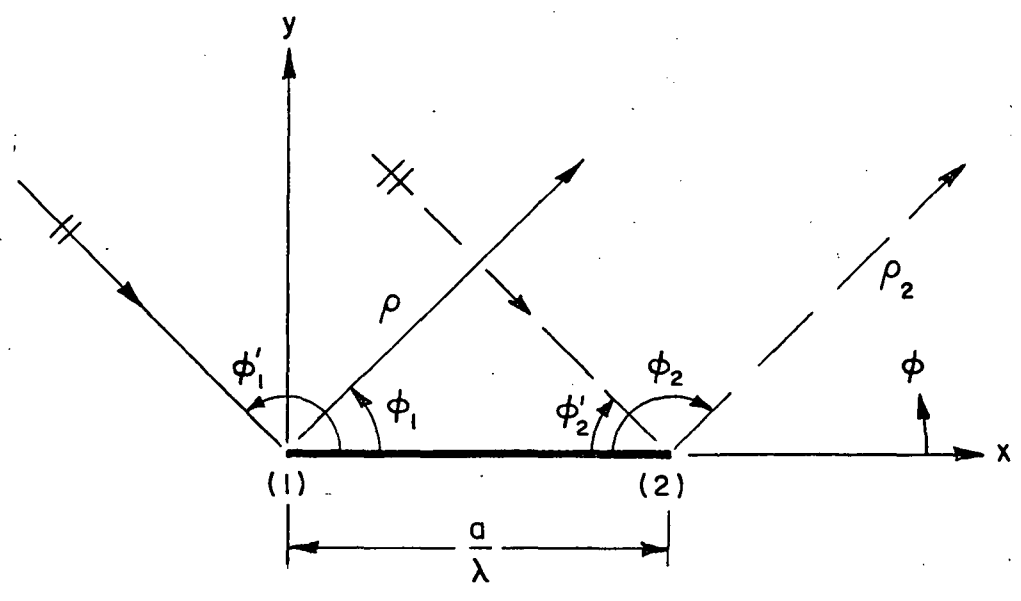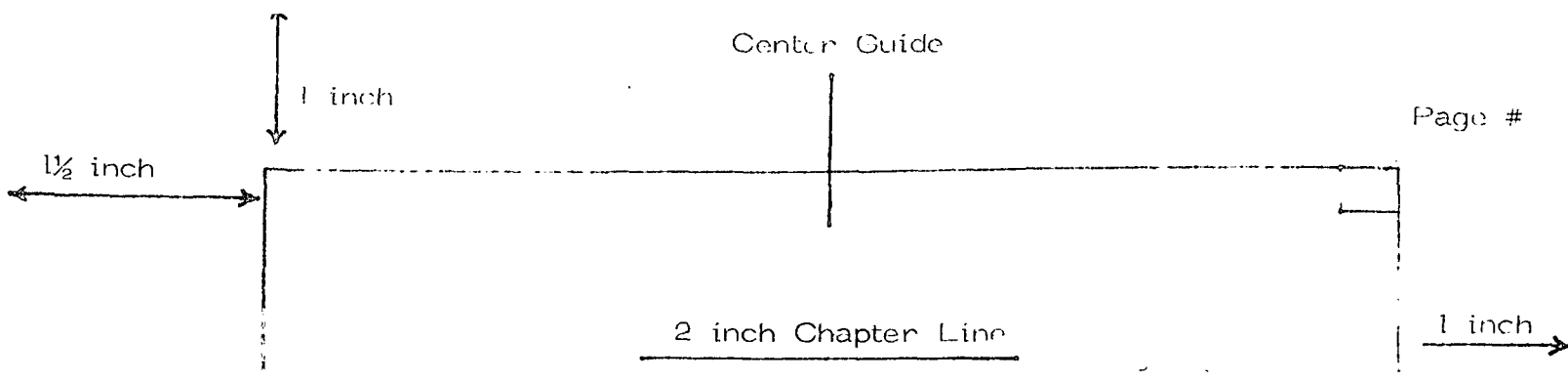


Figure 236. Strip geometry used in self-consistent UTD solution.

1st page Chapter end line

1st page Chapter end line

LAST TEXT LINE

350

1 inch

JAB/80
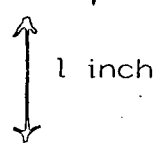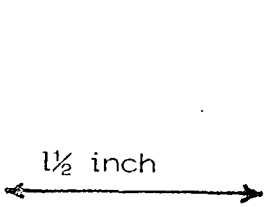
along the surface of the strip. There are infinitely many of these waves on each side of the strip. The self-consistent UTD concept combines all these waves on each face into two surface waves traveling in opposite directions with unknown complex amplitudes as shown in Figure 237.
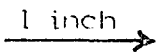
## B.    ANALYSIS

The total backscattered field can be written as

$$H_t = H_t^{sd} + H_t^{md} \tag{185}$$

where the subscript indicates total and the superscripts sd and md indicate single diffraction and multiple diffraction respectively, and

$$H_t^{sd} = H_{(1)}^d + H_{(2)}^d \tag{186}$$
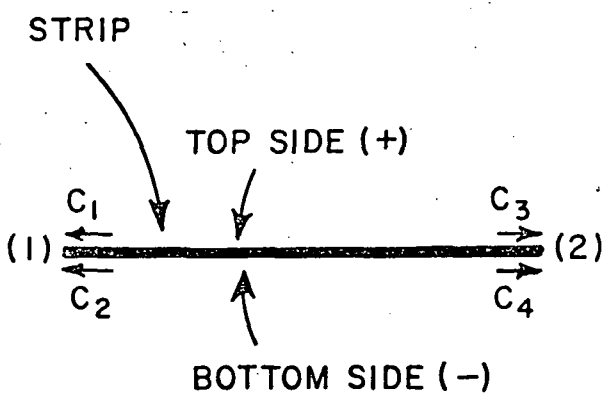


Figure 237.   Self-consistent UTD concept.

351

JAB/80
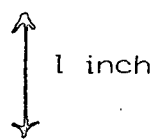
where $H_{(1)}^d$ and $H_{(2)}^d$ are the single diffracted field from edges 1 and 2. They are respectively given by Equations (40) and (41), and

$$H_t^{md} = H_{(1)}^{md} + H_{(2)}^{md} \qquad \text{2 inch Chapter Line} \qquad (187)$$

where $H_{(1)}^{md}$, $H_{(2)}^{md}$ are the total multiply diffracted fields from edges 1 and 2 respectively and are given by

$$H_{(1)}^{md} = \frac{1}{2} \left\{ C_1 D_h (a,\phi_1',o) + C_2 D_h (a,2\pi-\phi_1',o) \right\} \frac{e^{-jk\rho}}{\sqrt{\rho}} \qquad (188)$$

$$H_{(2)}^{md} = \frac{1}{2} \left\{ C_3 D_h (a,\pi-\phi_1',o) + C_4 D_h (a,\pi+\phi_1',o) \right\} \frac{e^{-jk\rho_2}}{\sqrt{\rho_2}} \qquad (189)$$

where $D_h(L,\phi,\phi')$ is given by Equation (46) and the $\frac{1}{2}$ is due to grazing incidence.

From Equation (46), one gets

$$D_h(a,2\pi-\phi_1',o) = -D_h (a,\phi_1',o) \qquad , \qquad \text{and}$$

$$D_h(a,\pi+\phi_1',o) = -D_h (a,\pi-\phi_1',o) .$$

Equations (188), (189) then reduce to

$$H_{(1)}^{md} = \frac{1}{2} (C_1-C_2) D_h (a,\phi_1',o) \frac{e^{-jk\rho}}{\sqrt{\rho}} \qquad (190)$$

$$H_{(2)}^{md} = \frac{1}{2} (C_3-D_4) D_h (a,\pi-\phi_1',o) \frac{e^{-jk\rho_2}}{\sqrt{\rho_2}} \qquad (191)$$

The complex amplitudes $C_1$, $C_2$, $C_3$ and $C_4$ are determined by a self-consistent field procedure. At edge 1, one can write

$$C_1' = H_{12}^{(+)} + \frac{1}{2} \left\{ C_3 D_h(\tfrac{a}{2},o,o) + C_4 D_h(\tfrac{a}{2},2\pi,o) \right\} \frac{e^{-jka}}{\sqrt{a}} \qquad (192)$$

352
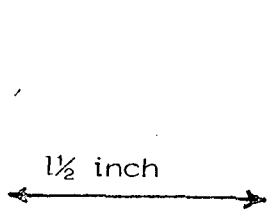
$$C_2 = H_{12}^{(-)} + \frac{1}{2}\left\{C_4 D_h(\tfrac{a}{2},o,o) + C_3 D_h(\tfrac{a}{2},2\pi,o)\right\}\frac{e^{-jka}}{\sqrt{a}} \tag{193}$$

The first term on the R.H.S. of Equations (192) and (193) represents the field at edge 1 due to the ray configuration shown in Figure (238-a and b) respectively, and is given by

$$H_{12}^{(+)} = D_h(a,o,\pi-\phi_1') \, e^{jka\cos\phi_1'} \, \frac{e^{-jka}}{\sqrt{a}} \triangleq A \quad , \tag{194}$$

$$H_{12}^{(-)} = -H_{12}^{(+)} = -A \quad , \tag{195}$$

and the second term on the right of Equations (192) and (193) represents the field at edge 1 due to all edge diffracted rays traveling to the left on the top and bottom side of the strip except those shown in Figure (238 a and b), respectively.

Since $D_h(\tfrac{a}{2},2\pi,o) = -D_h(\tfrac{a}{2},o,o)$ , then

$$C_1 = A + \frac{1}{2}(C_3 - C_4) D_h(\tfrac{a}{2},o,o)\frac{e^{-jka}}{\sqrt{a}} \quad , \text{ and} \tag{195}$$

TOP SIDE

STRIP

(1) —————————— (2)

STRIP

(a)

STRIP

(1) —————————— (2)

BOTTOM SIDE

(b)
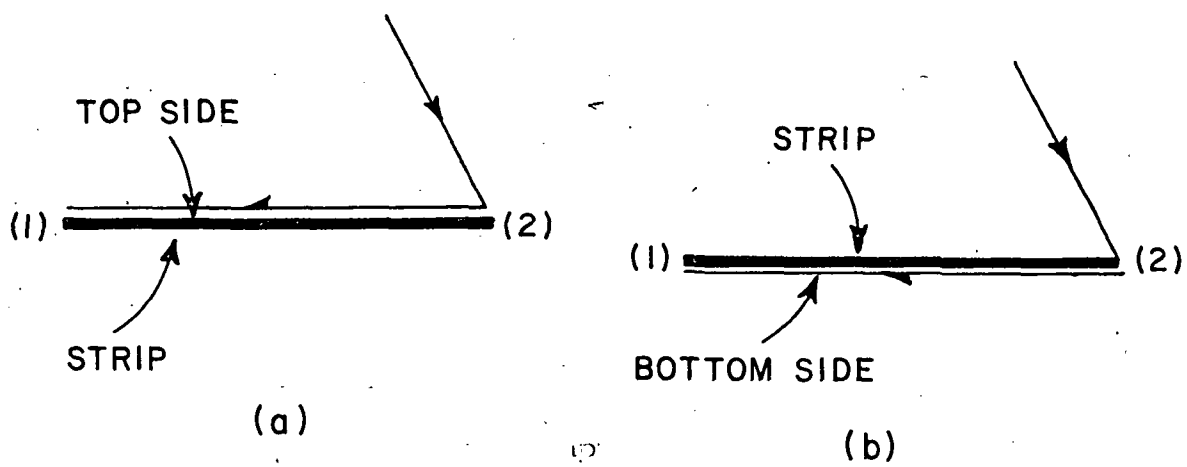
Figure 238.   Ray configuration for self-consistent analysis.
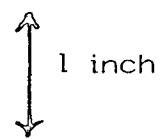
$$C_2 = -A - \frac{1}{2}(C_3 - C_4) \, D_h\left(\frac{a}{2}, o, o\right) \frac{e^{-jka}}{\sqrt{a}} \qquad . \qquad (196)$$

From Equations (195) and (196), one gets

$$C_1 = -C_2 \qquad (197)$$

Similarly, one can prove that

$$C_3 = -C_4 \qquad . \qquad (198)$$

From Equations (197) and (198), one can write

$$C_1 = A + C_3 D_h\left(\frac{a}{2}, o, o\right) \frac{e^{-jka}}{\sqrt{a}} \quad , \text{ and} \qquad (199)$$

$$C_3 = B + C_1 D_h\left(\frac{a}{2}, o, o\right) \frac{e^{-jka}}{\sqrt{a}} \qquad . \qquad (200)$$

or

$$C_1 = A + M\,C_3 \quad , \text{ and} \qquad (201)$$

$$C_3 = B + M\,C_1 \quad . \qquad (202)$$

where $B = D_h(a, o, \phi_1') \dfrac{e^{-jka}}{\sqrt{a}}$ , and

$$M = D_h\left(\frac{a}{2}, o, o\right) \frac{e^{-jka}}{\sqrt{a}} \qquad .$$

Equations (201) and (202) are two simultaneous linear equations from which $C_1$ and $C_3$ can be found. This gives

$$C_1 = \frac{A + MB}{1 - M^2} \quad , \text{ and} \qquad (203)$$

1 inch

1½ inch

$$C_3 = \frac{B + MA}{1 - M^2} \qquad . \tag{204}$$

Substituting Equations (197), (198), into (190) and (191) respectively, one gets

2 inch Chapter Title

1 inch

$$H^{md}_{(1)} = C_1 \, D_h \, (a,\phi_1',0) \, \frac{e^{-jk\rho}}{\sqrt{\rho}} \tag{205}$$

$$H^{md}_{(2)} = C_3 \, D_h \, (a,\pi-\phi_1',0) \, \frac{e^{-jk\rho_2}}{\sqrt{\rho_2}} \tag{206}$$

THESIS / DISSERTATION

First page Chapter Line

The multiply diffracted fields can now be found by substituting Equations (203), (204) into (205) and (206) respectively.

The total backscattered field in the half space $0 \le \phi \le \pi$ can now be found by substituting Equations (186) and (187) into (185). The field in the other half space $\pi \le \phi \le 2\pi$ is the opposite sign of that in the half space $0 \le \phi \le \pi$.

The above analysis is used to compute the E-plane echo width patterns for different strip sizes. The results are compared to the exact solution for the strip in terms of Mathieu functions. The data presented here is normalized to broadside level.

The E-plane echo width pattern for a $3\lambda$ wide strip is shown in Figure 239. The agreement between the SC solution and the exact one is good throughout the pattern. Note that the SC solution gives the same result as that obtained by considering the contribution of single, double and triple edge diffraction mechanisms. This is clearly seen by comparing Figure 19 and 239. The E-plane pattern for a $1.42\lambda$ wide strip is shown in Figure 240. The result is compared with a Reaction method solution obtained by Richmond [48], and the two results agree very well. Figure 241 shows the E-plane pattern results for a $0.25\lambda$

First page Chapter Line

LAST TEXT LINE

PAGE #?? LINE

1 inch

JAB/80
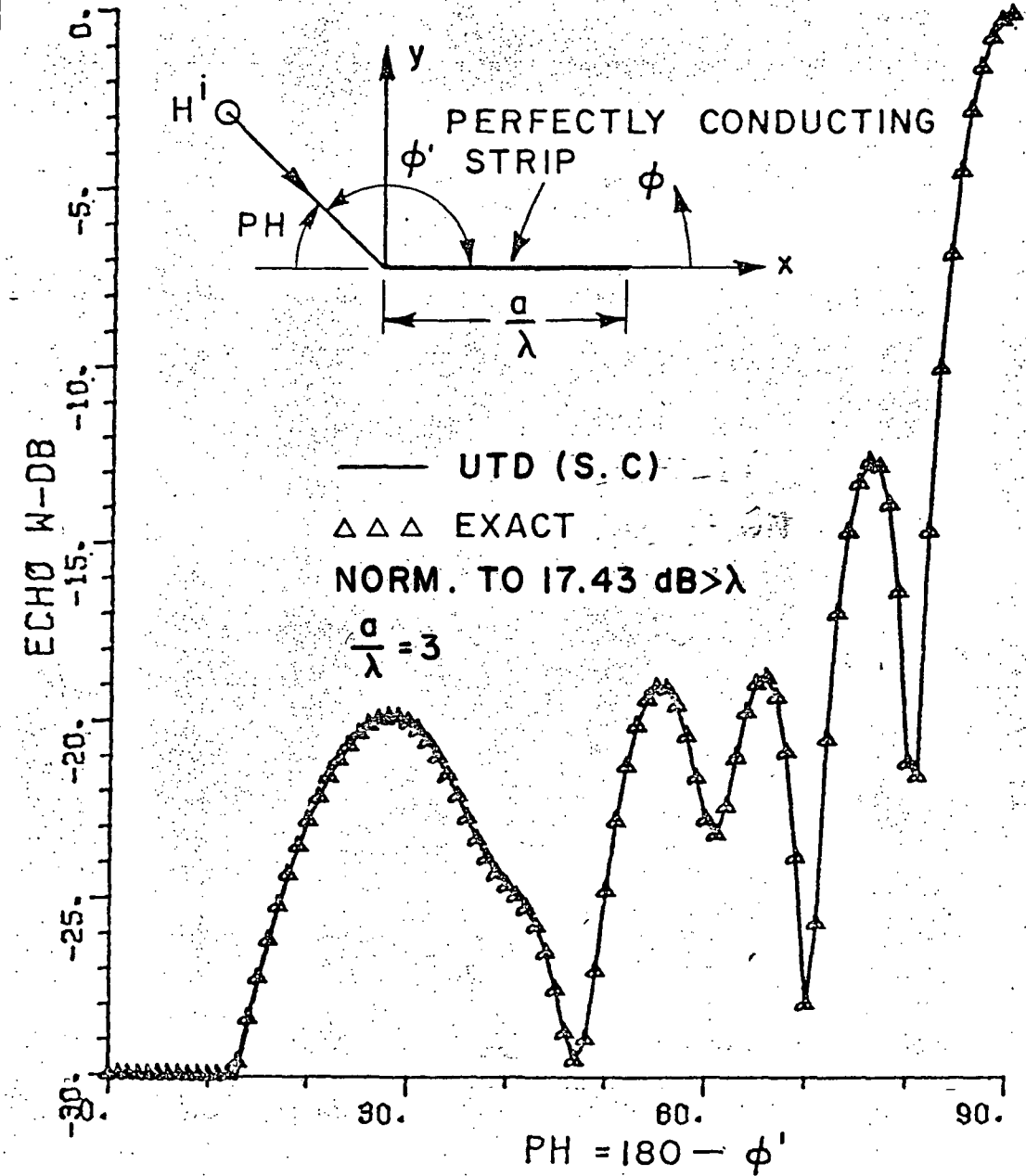
Figure 239. E-plane echo width pattern of 3λ wide strip using the self-consistent UTD concept.

JAB/80

1 inch

1½ inch

1 inch



PERFECTLY CONDUCTING STRIP

—— UTD (S.C.)

×××× REACTION

NORM. TO 11.28 dB>λ

$\dfrac{a}{\lambda} = 1.42$

ECHO W-DB

PH = 180 − φ'
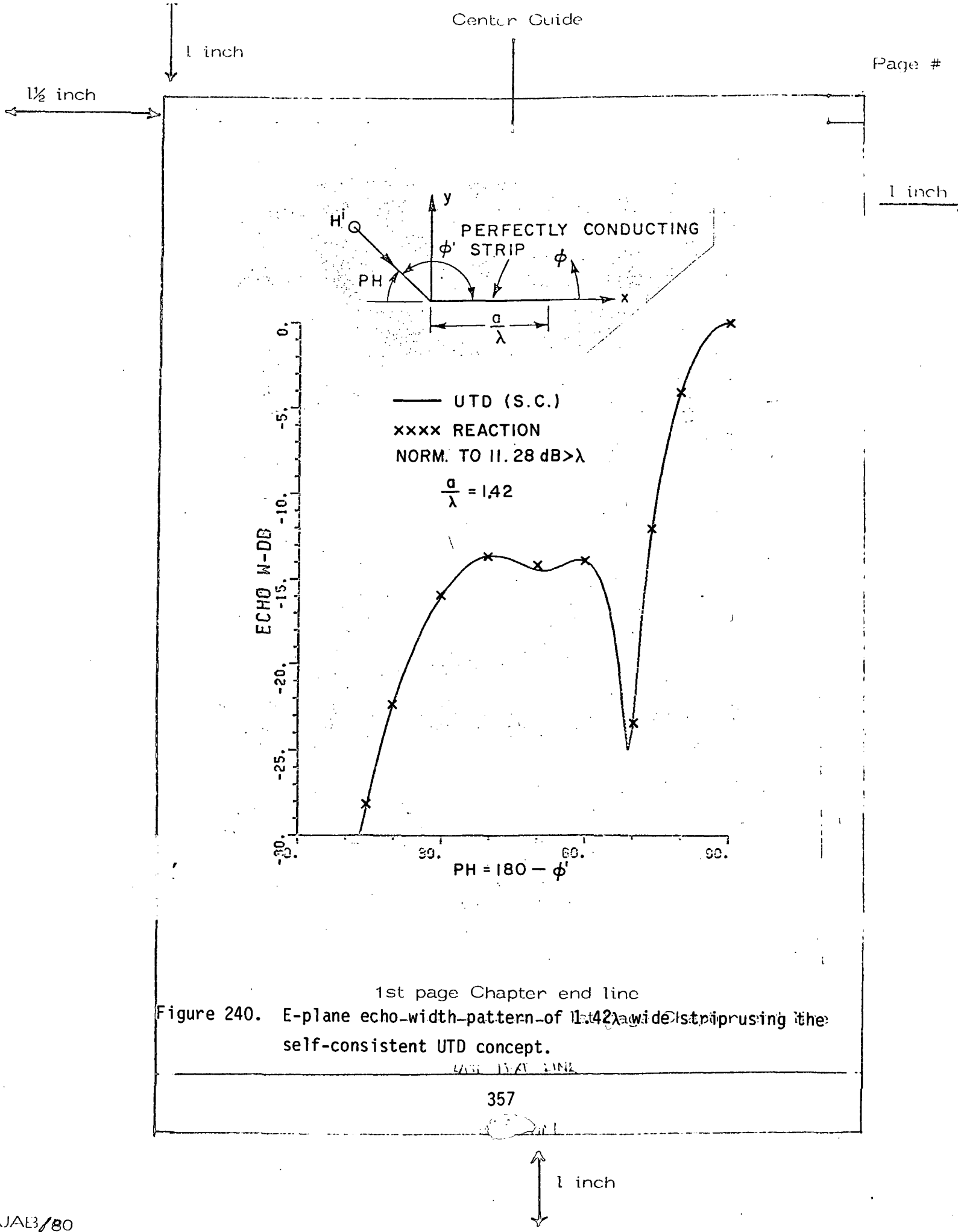
1st page Chapter end line

Figure 240.   E-plane echo-width pattern of 1.42λ wide strip using the self-consistent UTD concept.

1 inch

JAB/80

2 inch Chapter Line
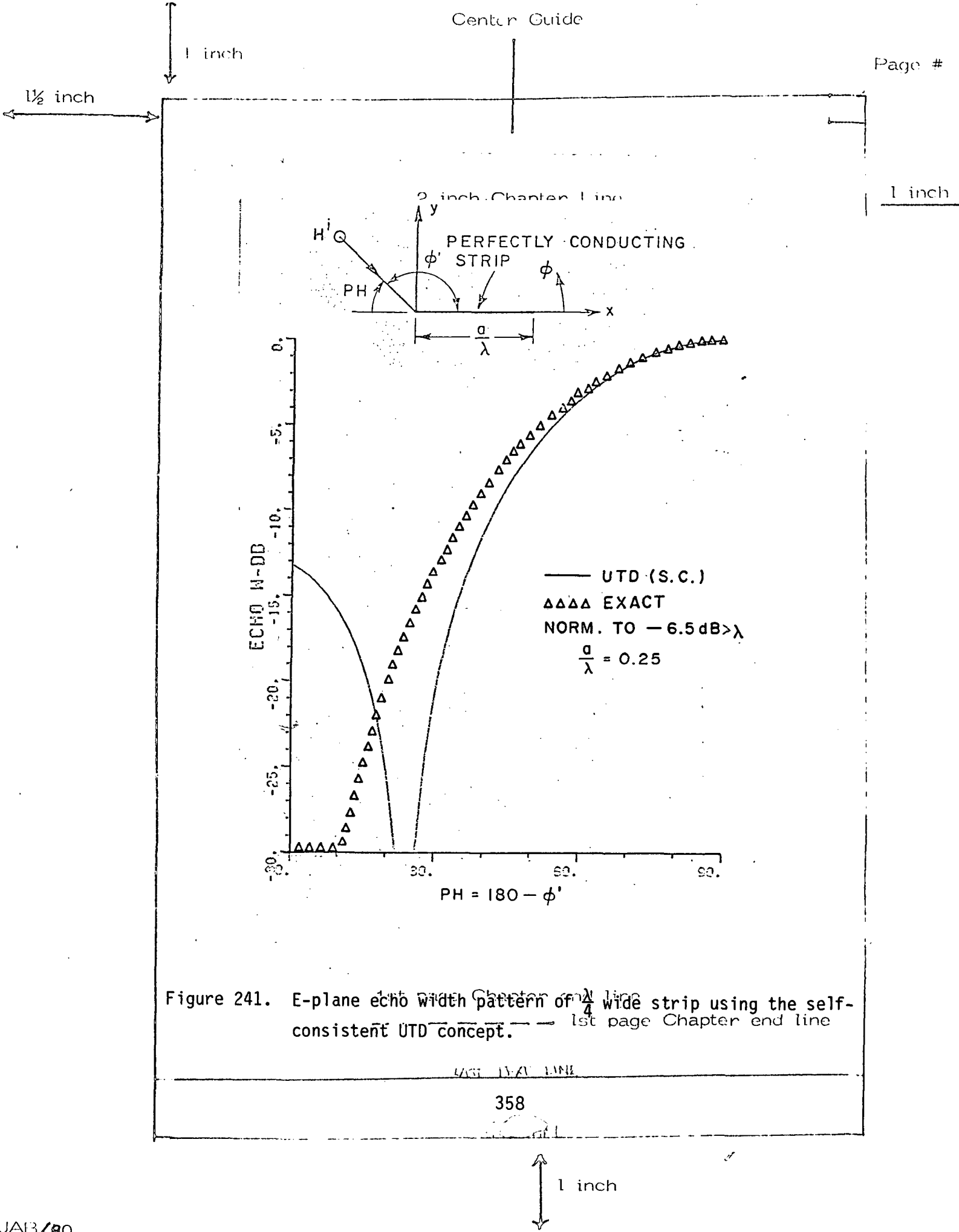


Figure 241. E-plane echo width pattern of $\frac{\lambda}{4}$ wide strip using the self-consistent UTD concept.

1st page Chapter end line

LAST TEXT LINE

1 inch

JAB/80

wide strip. The result deviates appreciably for angles of incidence
less than 40° from edge on. This deviation is caused by the failure
of our model to account for the true nature of the diffracted fields
on the surface of the strip which was assumed to be a homogeneous cyl-
indrical wave. The SC method will give satisfactory results for strip
widths as low as 0.65λ. Figures 242 and 243, show the TE broadside
echo width for different strip widths. The SC results are compared to
the exact and the reaction method solutions [48] and good agreement
is obtained. The TM broadside echo width is shown in Figure 244, where
the SC method result is compared to the exact solution [49]. The ag-
reement between the two results is good.

THESIS/ DISSERTATION
Typing Guide Paper

1st page Chapter end line
— — — — — — — 1st page Chapter end line

LAST TEXT LINE

Center Guide

1 inch

JAB/80
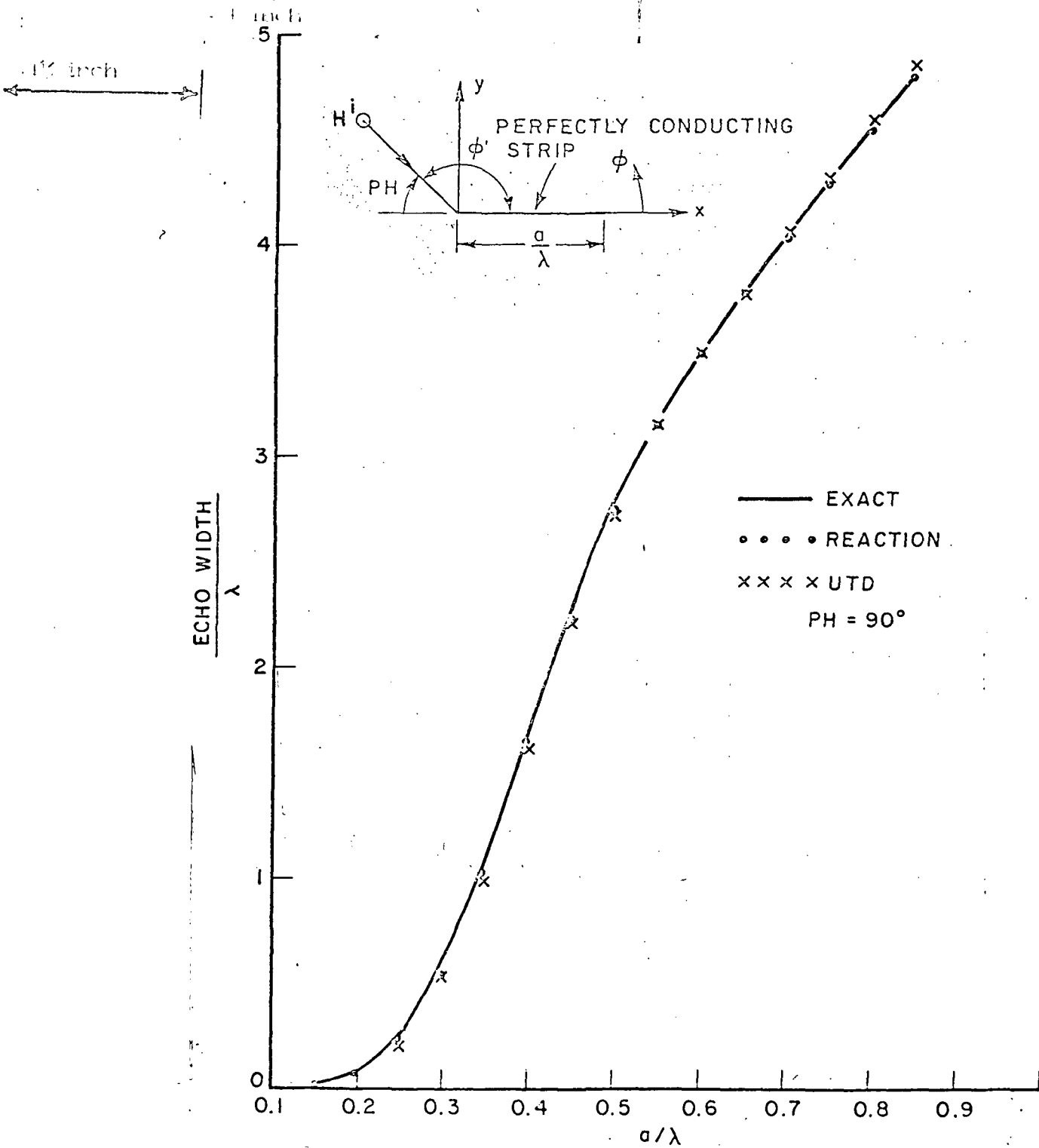
Figure 242. $TE_z$, broadside echo width for a perfectly conducting strip ($\frac{a}{\lambda} = 0.1 - 0.9$).

1½ inch
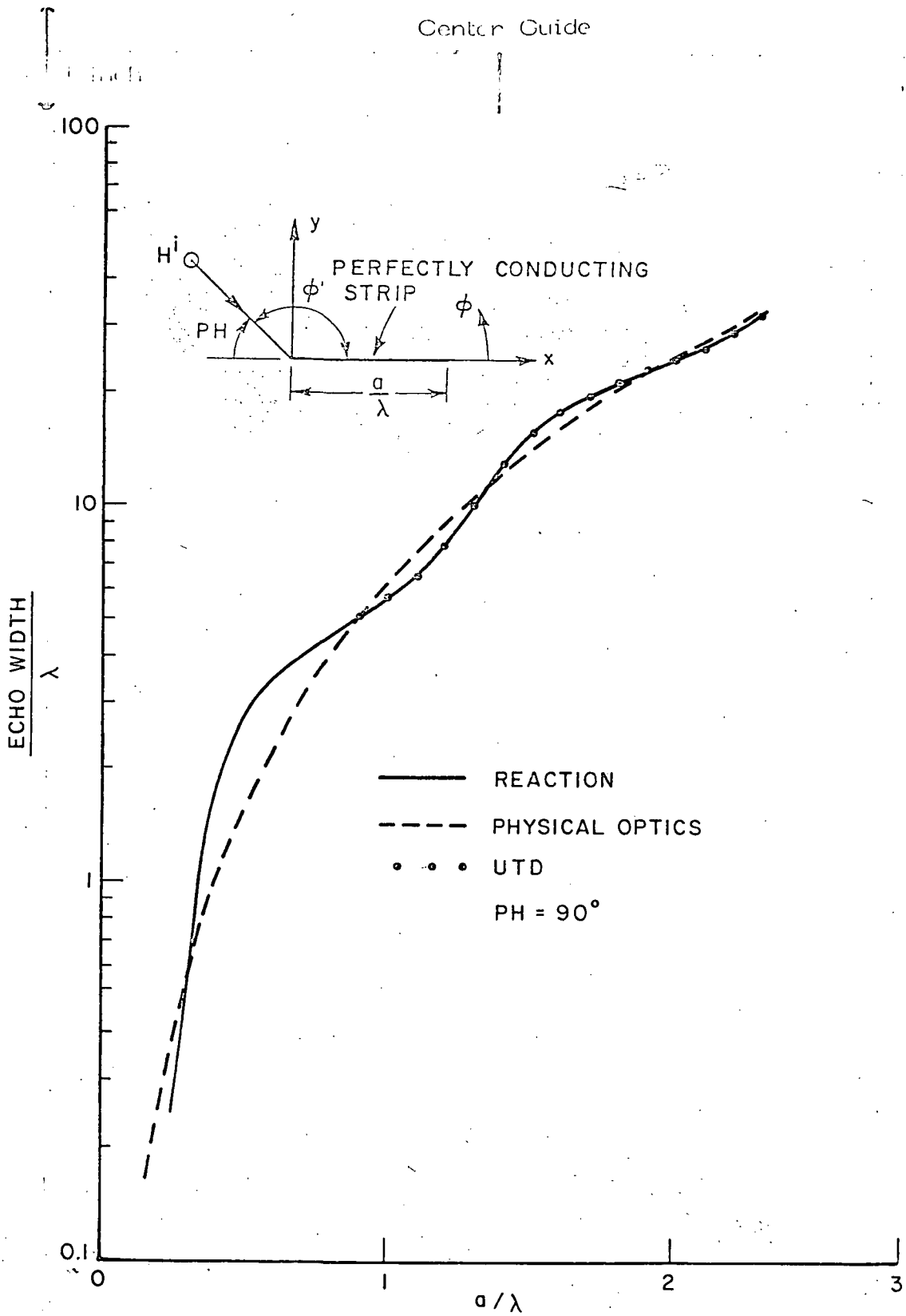
1 inch



Figure 243. TE$_z$, broadside echo width for a perfectly conducting strip ($\frac{a}{\lambda}$ = 1 - 2.3).

JAB/80
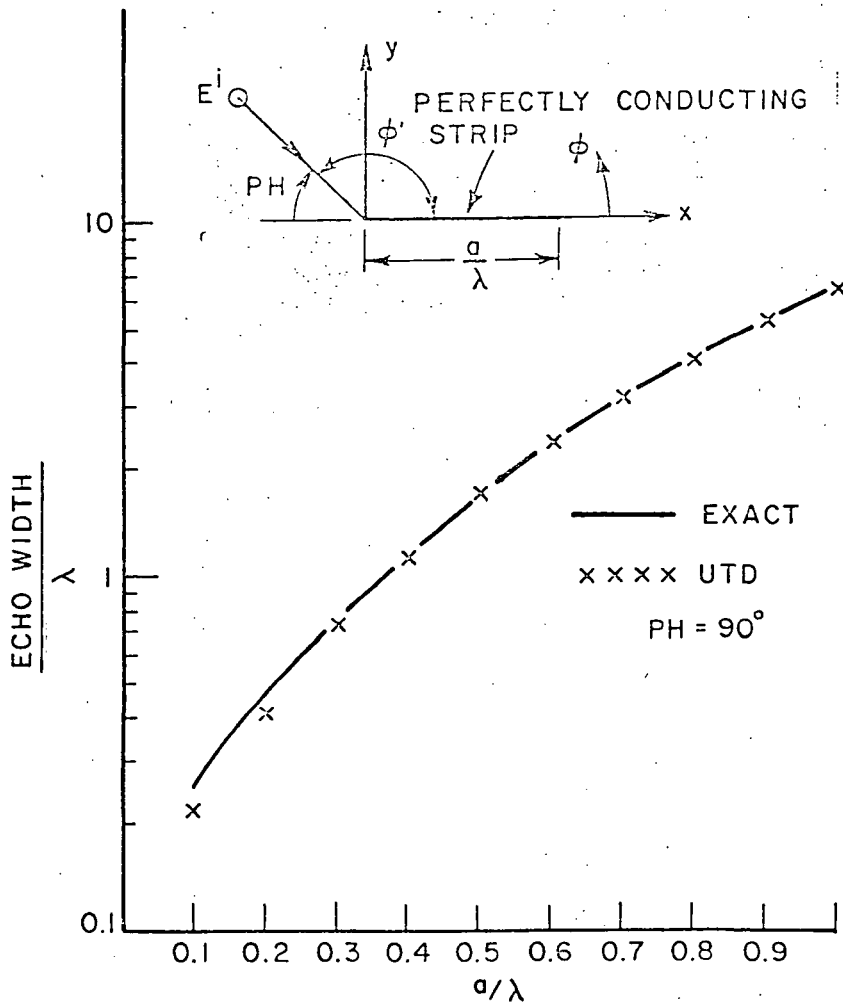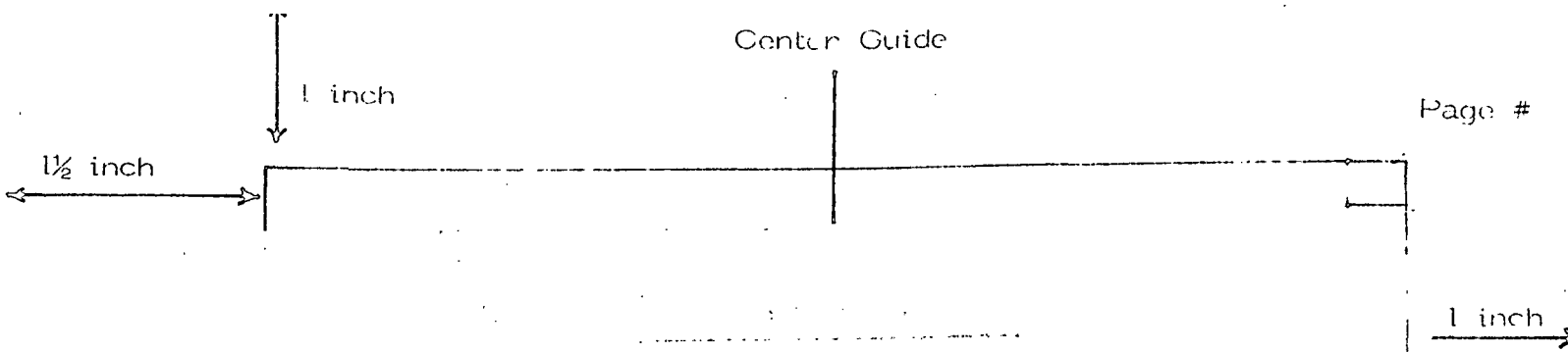
1 inch

Figure 244. TM$_z$ broadside echo width for a perfectly conducting strip ($\frac{a}{\lambda}$ = 0.1 - 1.0).
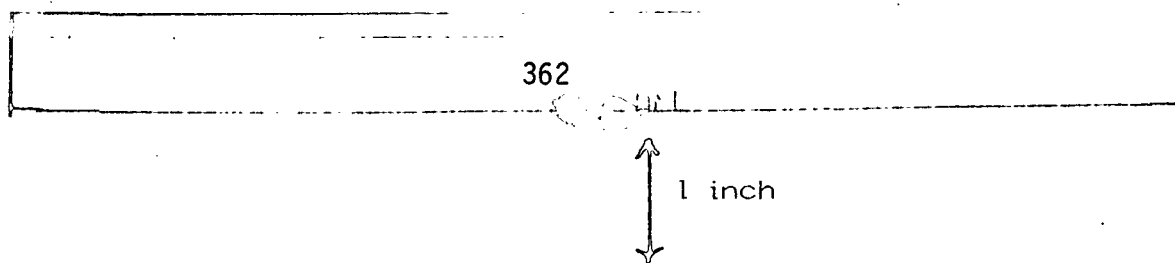
2 inch REFERENCES Line

1. Richmond, J.H., "A Wire-Grid Model for Scattering by Conducting Bodies," IEEE Trans. Antenna and Propagation, Vol. AP-14, pp. 782-786, Nov., 1966.

2. Richmond, J.H., "Computer Analysis of Three-dimensional Wire Antennas," Report 2708-4, 22 December, 1969, The Ohio State University ElectroScience Laboratory, Department of Electrical Engineering; prepared under Contract DAAD-05-69-C-0031 for Ballistic Research Laboratory. Typing Guide Paper

3. Wang, N.N., Richmond, J.H., and Gilreath, M.C., "Sinusoidal Reaction Formulation for Radiation and Scattering from Conducting Surfaces," IEEE Trans. on Antenna and Propagation, Vol. AP-23, No. 3, May 1975, pp. 376-382.

4. Ryan, C.E., Jr., Peters, L., Jr., "Evaluation of Edge Diffracted Fields Including Equivalent Currents for the Caustic Regions," IEEE Trans. on Antenna and Propagation, Vol. AP-17, NO. 3, May 1969.

5. Ryan, C.E., Jr., Rudduck, R.C., "Radiation Patterns of Rectangular Wave Guides," IEEE Trans. Antenna and Propagation, Vol. AP-16, pp. 488-489, July 1968.

6. Mentzer, C.A., "Analysis and Design of High Beam Efficiency Aperture Antennas," Final report 3453-1, April 1974, The Ohio State University ElectroScience Laboratory, Department of Electrical Engineering.

7. Kouyoumjian, R.G., and Pathak, P.H., "A Uniform Geometrical Theory of Diffraction for an Edge of a Perfectly Conducting Surface," Proc. of the IEEE, vol. 62, NO. 11, November, 1974, pp. 1448-1461.

8. Pathak, P.H., and Kouyoumjian, R.G., "The Dyadic Diffraction Coefficient for a Perfectly Conducting Wedge," Scientific Report No. 5, Report 2183-4, 5 June, 1970, The Ohio State University ElectroScience Laboratory, Department of Electrical Engineering, prepared under contract AF19 (628) 5929 for Air Force Cambridge Research Laboratory (AFCRL-69-0546) (AD 707821) Chapter end line

JAB/80

9.  Millar, R.F., "An Approximate Theory of the Diffraction of an Electromagnetic Wave by an Aperture in a Plane Screen," IEE Monograph, No. 152R, October 1955.

10. Millar, R.F., "The Diffraction of an Electromagnetic Wave by a Circular Aperture," IEE Monograph, No. 196R, September 1956.

11. Millar, R.F., "The Diffraction of an Electromagnetic Wave by a Large Aperture," IEE Monograph, No. 213R, December 1956.

12. Ryan, C.E. and Rudduck, R.C., "Radiation Patterns of Rectangular Waveguides," IEEE Trans. Antenna and Propagation, July 1968, p. 488.

13. Ryan, C.E. and Peters, L., Jr., "Evaluation of Edge Diffracted Fields Including Equivalent Currents for the Caustic Regions," IEEE Trans. on Antenna and Propagation, May 1969, pp. 292-299.

14. Ryan, C.E. and Peters, L., Jr., correction to "Evaluation of Edge Diffracted Fields Including Equivalent Currents for the Caustic Region," IEEE Trans. on Antenna and Propagation, March 1970, p. 275.

15. Burnside, W.D. and Peters, L., Jr., "Axial-Radar Cross Section of Finite Cones by the Equivalent Current Concept with Higher Order Diffraction," Radio Science, October 1972, pp. 943-948.

16. Senior, T.B.A. and Uslenghi, P.L.E., "Radiation Patterns of Rectangular Waveguides," IEEE Trans. on Antenna and Propagation, July 1968.

17. Richmond, J.H., personal communication.

18. Knott, E.E. and Senior, T.B.A., "Comparison of Three High Frequency Techniques," Proceeding of IEEE, November 1974, pp. 1468-1474.

19. Burnside, W.D. and Pathak, P.H., "A Corner Diffraction Coefficient," To appear.

20. Keller, J.B., "Diffraction by an Aperture," Journal of Applied Physics, April 1957, Volume 28, No. 4.

21. Ryan, C.E., "Short Course Notes," The Ohio State University, Department of Electrical Engineering, 1969.

22. Burnside, W.D., personal communication.

2 inch Chapter Line

1st page Chapter end line

1 inch

JAB/80

23. Freeland, J., Kouyoumjian, R.G., Pathak, P.H., "A High Frequency Approximation for the Strip Current," Report 2183-5, 23 March, 1970, The Ohio State University, ElectroScience Laboratory, Department of Electrical Engineering; prepared under contract AF19 (628) - 5929 for Air Force Cambridge Research Laboratories.

24. Yu, J.S. and Rudduck, R.C., "On Higher Order Diffraction Concepts Applied to a Conducting Strip," IEEE Trans. on Antenna and Propagation, Vol. AP-15, No. 5.

25. Sommerfield, A., Optics, Academic Press, Inc., New York, (1954), pp. 245-272.

26. Bowman, J.J., Senior, T.B.A., and Uslenghi, P.L.E., "Electromagnetic and Acoustic Scattering by Simple Shapes," Pub. American Elsevier Publishing Company.

27. Harrington, R.F., "Time Harmonic Fields," McGraw Hill Company, pp. 359-360.

28. Ross, R.A., "Radar Cross Section of Rectangular Flat Plates as a Function of Aspect Angle," AP-14, No. 3, May 1966.

29. Yu, J.S., "Radar Cross Section of a Thin Plate Near Grazing Incidence," IEEE Trans. on Antenna and Propagation, September 1970.

30. Ufimtsev, P.I., Secondary Diffraction of Electromagnetic Waves from a Strip," Zh. Tekh. Fiz., Vol. 28, No. 3, pp. 569-582, 1958.

31. Hey, J.S. and Senior, T.B.A., "Electromagnetic Scattering by Thin Conducting Plates at Glancing Incidence," Proc. Phys. Soc., Vol 72, pp. 981-995, December 1958.

32. Knott, E.F., Liepa, V.V. and Senior, T.B.A., "Plates and Edges," IEEE Trans. on Antenna and Propagation, Nov. 1971, pp. 788-789.

33. Newman, E., Personal Communication.

34. Locus, S.S., Heath, H.C., Oshiro, R.K. and Coleman, J.R., "Radar Cross Section Studies," Final Report, Northrup Corporation, April 1974.

35. Chu, T., "Plates Measurements," Ohio State University, ElectroScience Laboratory Measurements Facilities, Department of Electrical Engineering.

36. Meixner, J., Andrejewski, W., Ann. Physic 7, 157 (1950)

37. Flammer, C.J. Appl. Phys., 24, 1224 (1953).

38. Devore, R., Hodge, D.B. and Kouyoumjian, R.G., "Backscattering Cross Sections of Circular Disks for Arbitrary Incidence," J. of Applied Physics, Vol. 42, No. 8, July 1971.

39. Bechtel, M.E., "Application of Geometrical Diffraction Theory to Scattering from Cones and Disks," Proceeding IEEE, August 1965.

40. Ryan, C.E., Jr., and Peters, L., Jr., "A Creeping Wave Analysis of the Edge on Echo Area of Disks, "IEEE Trans. Antennas and Propagation (communication), Vol. AP-16, pp. 274-275, March 1968.

41. Hodge, D.B., "The Calculation of Far Field Scattering by a Circular Metalic Disk," Report 710816-2, The Ohio State University, ElectroScience Laboratory, Department of Electrical Engineering.

42. Chu, T., Personal Communication.

43. Sikta, F.A., Campbell, R.H., Hill, R.A., "Plates Measurements," Ohio State University, ElectroScience Laboratory Measurements Facilities, Department of Electrical Engineering.

44. Peters, L., Jr., "End Fire Echo Area of Long, Thin Bodies," IEEE Trans. on Antenna and Propagation, AP-Vol. 58, pp. 138, 1958.

45. Rudduck, R.C., "Application of Wedge Diffraction and Wave Interaction Methods to Antenna Theory," OSU Short Course Notes for GTD and Numerical Techniques, Vol. 1, Sept. 1975.

46. Wang, N., "Self-Consistent GTD Formulation for Conducting Cylinders with Arbitrary Convex Cross Section", IEEE Trans. on Antenna and Propagation, Vol. AP-24, No. 4, July 1976.

47. Pauli, W., "On Asymptotic Series for Functions in the Theory of Diffraction by Light," Phys. Rev., Vol. 54, pp. 924-931, Dec. 1938.

48. Richmond, J.H., "Computer Analysis and Design of Spacecraft Antennas," Informal Status Report, Project 2902, The Ohio State University ElectroScience Laboratory, 15 March, 1971.

49. Richmond, J.H., "On the Edge Mode in the Theory of TM Scattering by a Strip or Strip Grating," IEEE Trans. on Antenna and Propagation, Vol. AP-28, No. 6, Nov. 1980.

1st page Chapter end line
1st page Chapter end line

LAST TEXT LINE

1 inch

JAB/80